FINAL TECHNICAL REPORT

NASA CONTRACT NSG 5357

INITIAL STUDIES OF MIDDLE AND UPPER TROPOSPHERIC STRATIFORM CLOUDS

COLORADO STATE UNIVERSITY

DEPARTMENT OF ATMOSPHERIC SCIENCE

PRINCIPAL INVESTIGATOR: STEPHEN K. COX

MAY 18, 1982

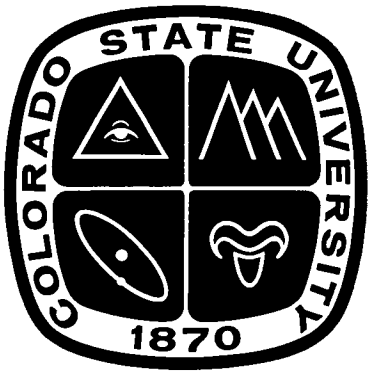

DEPARTMENT OF ATMOSPHERIC SCIENCE
COLORADO STATE UNIVERSITY
FORT COLLINS, COLORADO

TABLE OF CONTENTS

FINAL TECHNICAL REPORT

NASA CONTRACT NSG 5357

INITIAL STUDIES OF MIDDLE AND UPPER TROPOSPHERIC STRATIFORM CLOUDS

SECTION 1.

STATEMENT OF PROJECT OBJECTIVES:

The initial middle and upper tropospheric cloud studies performed under this NASA grant had multiple objectives. These objectives may be summarized as follows: studies of spatial and temporal occurrence of extended middle and upper tropospheric cloud layers; development of a physical-numerical model to simulate the life cycles of middle and upper tropospheric cloud layers; and the design of an observational program to study the physical, radiative and dynamical properties of these cloud layers.

Our initial intent was to study the spatial and temporal extents of middle and upper tropospheric cloud layers using both rawinsonde data and satellite visible and infrared imagery. We successfully completed the rawinsonde summary but found the satellite archives available to be lacking in the time continuity required for such a study. Section 2 reproduces the results of the analysis derived from rawinsonde data.

Much of the resources of this grant have gone into the development of a two dimensional model of the middle and upper tropospheric cloud layer. The two dimensional model is nearly complete and has passed many of the required validation tests. Final validation and utilization of the model is only a few months away. Section 3, a portion of a Ph. D. thesis being prepared by Mr. David Starr, presents a detailed explanation of the model and its development to date.

One of the specific objectives of this grant was the design of an experimental program to complement the climatological and modelling objectives presented in Sections 2 and 3 and referred to above. Section 4 of this final technical report presents the model design for such a program in proposal form. This proposal is being submitted to NASA concurrently with this report with the aim of implementing such a program of observations within the next two years.

Section 5 of this report is a reprint of a paper published in Applied Optics on the variability of the radiative properties of ice clouds across the solar wavelengths. This work was a precurser to the selection of a realistic, simplified solar radiation algorith for the two dimensional physical-numerical model described in Section 3.

Section 6 is composed of a copy of the Ph. D. thesis of Michael Abel. Dr. Able is a member of the Air Weather Service who attended Colorado State University from 1978 - 1980. Dr. Able, under the guidance of the principal investigator, pursued a research topic closely identifiable with the longterm objectives of the middle and upper tropospheric cloud grant. Dr. Able developed an unconventional method of collecting a climatology of the effects of middle and upper tropospheric clouds on the radiative energy budget of the earth. Cloud height and a composite area-radiative property may be inferred from his technique as well. Dr. Able was supported under this grant only to the extent of covering research expenses such as computer time, materials, manuscript preparation and correspondence since his salary was paid by the Air Weather Service.

Appendix 1 of this report lists publications and meeting presentations prepared from material generated by research conducted under NASA grant 5347?

APPENDIX 1 - PAPERS AND MEETING PRESENTATIONS BASED UPON MATERIAL FROM NASA GRANT STUDIES

Cox, S. K., 1979: Initial studies of middle and upper tropospheric stratiform clouds. Six Monthly Interim Report for NASA Grant NSG 5357, 72 pp.

Welch, R. M., S. K. Cox, and W. G. Zdunkowski, 1980: Calculations of the variability of ice cloud radiative properties at selected solar wavelengths. Appl. Opt., 19, 3057-3067.

Starr, D. O'C., and S. K. Cox, 1980: Characteristics of middle and upper tropospheric clouds as deduced from rawinsonde data. Atmospheric Science Paper #327, Colorado State University, Ft. Collins, CO., 71 pp.

Abel, M. D., and S. K. Cox, 1981: A climate index derived from satellite measured spectral infrared radiation. Atmospheric Science Paper #335, Colorado State University, Ft. Collins, CO.

Abel, M. D., and S. K. Cox, 1981: A climate index derived from satellite measured spectral infrared radiation. Submitted for publication to J. Atmos. Sci., (May).

D. SCIENTIFIC MEETINGS - Papers presented after January 1972

*Cox, S. K.: JOC Study Conference on Parameterization of Extended Cloudiness and Radiation for Climate Models. Review of parameterizations of radiation and extended cloudiness. 27 September - 4 October 1978, Oxford, U.K.

Starr, D. O'C., and S. K. Cox: Numerical experiments on the role of radiative processes in the development and maintenance of upper level clouds. Fourth Conference on Atmospheric Radiation of the American Meteorological Society, June 16-18, 1981, Toronto, Ont., Canada.

Abel, M. D., and S. K. Cox: A climate index indicative of cloudiness derived from satellite infrared sounder data. Fourth Conference on Atmospheric Radiation of the American Meteorological Society, June 16-18, 1981, Toronto, Ont., Canada.

CHARACTERISTICS OF MIDDLE AND UPPER TROPOSPHERIC CLOUDS AS DEDUCED FROM RAWINSONDE DATA

By

David O'C. Starr

And

Stephen K. Cox

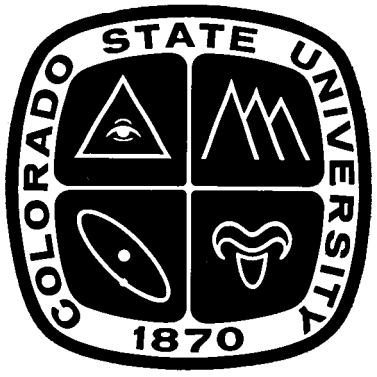

Atmospheric Science
PAPER NO.
327

US ISSN 0067-0340

DEPARTMENT OF ATMOSPHERIC SCIENCE
COLORADO STATE UNIVERSITY
FORT COLLINS, COLORADO

CHARACTERISTICS OF MIDDLE AND UPPER TROPOSPHERIC CLOUDS AS DEDUCED FROM RAWINSONDE DATA

by

David O'C. Starr and Stephen K. Cox

Research supported by
National Aeronautics and Space Administration
Goddard Space Flight Center
under grant NSG 5357

Department of Atmospheric Science
Colorado State University
Fort Collins, Colorado

November, 1980

Atmospheric Science Paper Number 327

ABSTRACT

This study characterizes the static environment of middle and upper tropospheric clouds as deduced from rawinsonde data from 24 locations in the contiguous U.S. for 1977. Computed relative humidity with respect to ice is used to diagnose the presence of cloud layer. The deduced seasonal mean cloud cover estimates based on this technique are shown to be reasonable. Over 3600 cloud cases qualified for the analysis. The cases are stratified by season and pressure thickness, i.e. thick and thin. The dry static stability, vertical wind speed shear and Richardson number are computed for three layers for each case, i.e. the sub-cloud and above cloud layers and an in-cloud layer bounded by the cloud-top level. Mean values for each parameter and, in some instances, the corresponding relative frequency distributions are presented for each stratification and layer. The relative frequency of occurrence of various structures is presented for each stratification, e.g. increasing static stability with height through the three layers.

The observed values of each parameter vary over quite large ranges for each layer. The observed structure of each parameter for the layers of a given case is also quite variable. Structures corresponding to any of a number of different conceptual models, which are reviewed, may be found though some are substantially more common than others. It is of note that moist adiabatic conditions are not commonly observed and that the stratification based on thickness yields substantially different results for each group. Summaries of the results are included in the text.

ACKNOWLEDGMENTS

The authors gratefully acknowledge the support of the computing facility at the National Center for Atmospheric Research, which is sponsored by the National Science Foundation. The primary support for this research was provided by the National Aeronautics and Space Administration under a climate-related grant administered by the Goddard Space Flight Center, under grant NSG 5357.

TABLE OF CONTENTS

1. INTRODUCTION

This study attempts to characterize certain aspects of the environment associated with middle and upper tropospheric stratiform clouds. The results will be utilized in the development of simple realistic models of the thermodynamic energy budgets of these cloud forms in a future study. The models will be used to investigate the role of various physical processes in the formation, maintenance and dissipation of these clouds. The motivation for studying these cloud forms is based on two factors. The first is that these clouds cover very extensive areas of the earth at any given time. Secondly, clouds are the most significant atmospheric constituent affecting the distribution of radiative energy loss or gain in the earth-atmosphere system. In other words, relative changes in cloud cover or cloud optical depth within a typical atmospheric column may lead to larger changes, both in the vertical distribution of net radiative energy gain within that column and in the corresponding surface radiative budget, than do similar relative changes in the concentration of any other constituent, (e.g. Starr, 1976). Middle and upper tropospheric clouds tend to more substantially alter the vertical distribution of net radiative energy gain than low level clouds, (e.g. Starr, 1976). The horizontal and vertical gradients of the net radiation budget comprise the basic forcing function governing the general circulation of the atmosphere.

Much attention has been focused on the simulation of the general circulation and climate modelling in recent years, (e.g. U.S. Committee for the GARP, 1978). A number of general circulation models have been developed by various groups, (see reviews by ISCU, 1974 and Starr and

Cox, 1977). The sensitivity of such models to variations in both the prescription of radiatively active constituents and radiative boundary conditions and in the formulation of the specific radiative scheme is well documented, e.g. Stone and Manabe, 1968; Washington, 1971; Schneider, 1975, Fels and Kaplan, 1975; Schneider et al, 1978. Numerous simple energy balance climate models have also been developed, e.g. Budyko, 1969; Sellers, 1969. The model simulations of mean climate state and its variability are also quite sensitive to the radiative component, e.g. Budyko, 1969; Sellers, 1969; Warren and Schneider, 1979; Coakley, 1979. Based upon the above studies, it is expected that the method of incorporating the effects of middle and upper tropospheric cloud forms into the climate simulations has a significant effect on the results. However, the methods of incorporating the effects of stratiform clouds in these models are generally of a very simple nature. The least complex methods utilize estimates of mean climatological cloudiness and coarse estimates of mean cloud radiative properties to prescribe these factors for the radiative component of the model. The most sophisticated methods utilize the model predicted relative humidity to predict the cloud cover but still employ estimates of mean radiative properties. The method of predicting stratiform cloud cover is generally based on an empirically derived linear relationship between relative humidity and cloud cover. Typically, the relationship used is similar to that reported by Smagorinsky, (1960), which was based on analysis of synoptic data. A requirement for sufficiently large and positive, model predicted, large-scale vertical velocity is also typically used to constrain the diagnosis of cloud cover.

The reason for utilizing such simple methods for the diagnosis of cloud cover and cloud properties in these models is two-fold. First, simplicity is highly desirable in order to minimize the computational requirements for the simulations. This is particularly true for the general circulation models. The limited computational capability available for model simulations dictates the use of parametric diagnosis of stratiform cloudiness, since the horizontal and vertical resolution of the models is limited. Secondly and more importantly, quantitative information on both the actual areal extent and variability of such clouds and their associated radiative properties in the atmosphere is sparse. Possible relationships between these quantities and other observable atmospheric parameters are even less well-known. On a more fundamental level, the basic physics of these clouds is not well understood. Relationships between the role of various physical processes and the physical environment in which they act have not been quantitatively assessed in any universal sense though a few limited case studies have been reported, e.g. Heymsfield, 1977. These issues have been addressed in the report of the JOC AD HOC Working Group on activation of the STRATEX Programme (7 January 1977). The aim of this study is to provide quantitative information which will aid in achieving a better understanding of the atmospheric environment associated with these cloud forms, the role of various physical processes in the life-cycle of these clouds, and their areal extent.

2. DATA ANALYSIS METHODOLOGY

By utilizing synoptic scale rawinsonde data this study investigates the static stability and the vertical wind shear associated with middle and upper tropospheric clouds. In this way the relative applicability of a number of simple conceptual models may be assessed. These conceptual models are summarized below.

2.1 Brief Review of Conceptual Models

The classical view of the environment associated with these cloud forms is depicted in Figure 1. In this view, the clouds are formed in an upgliding air mass above an elevated frontal zone. Vertical motion is positive above the frontal surface and negative below it. Adiabatic cooling due to lifting of the air mass is responsible for the existence of large-scale saturation. The stability of the cloud layer is determined by its pre-condensation stability and the amount of lifting. Sufficient lifting of a layer, which is initially only moderately stable, will produce unstable conditions. Once an unstable layer is produced, the tendency is for this layer to deepen, especially if the lifting persists. Since the vertical motion in the lifted air mass is greatest near the frontal zone, the cloud layer will generally form just above the front. Thus, the cloud layer is bounded below by a very stable layer. If unstable conditions are achieved, then vertical convective circulations may develop as in altocumulus clouds. These circulations are generally presumed to be weak, though Heymsfield (1977) reports that this may not always be the case. Strong vertical shear of the horizontal wind is anticipated across the frontal zone

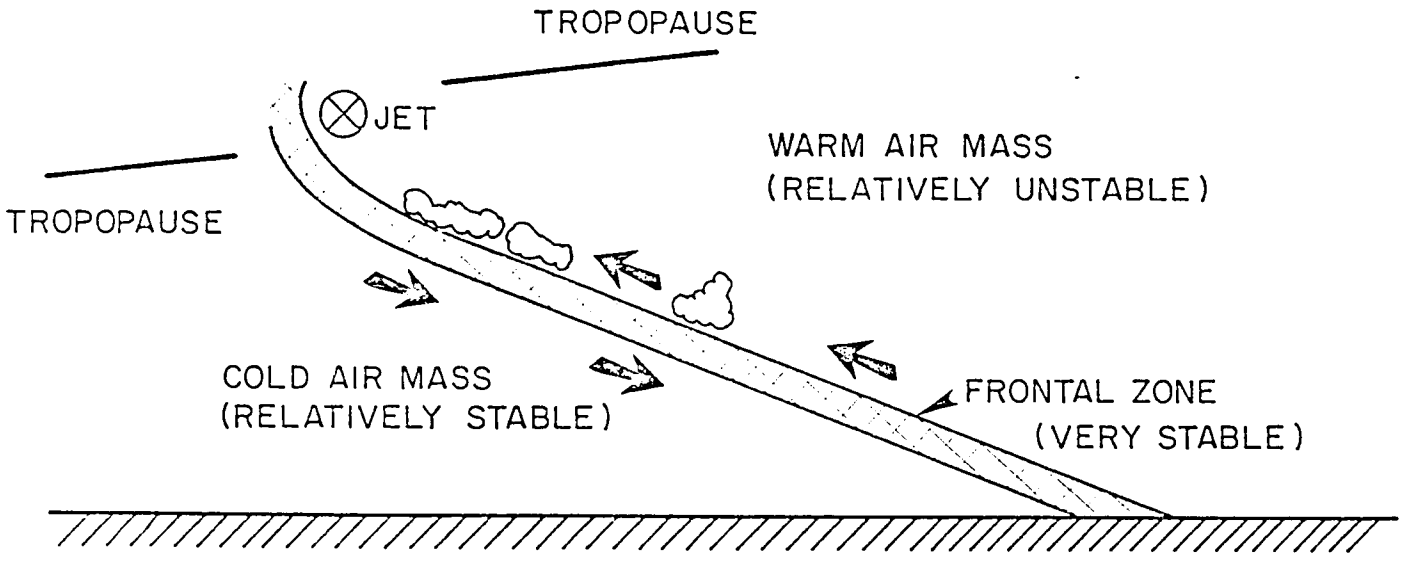

Figure 1. Classical model of the environment associated with middle and upper tropospheric clouds. Arrows indicate air motion relative to the front.

below the cloud layer. This was found in a study by Reuss (1967) of cirrus bands formed along frontal surfaces.

Another viewpoint may be found in the observations reported by Ludlam (1947, 1956), Oddie (1959), Yagi (1969), and Heymsfield (1975a,b). These studies report on the atmospheric environment associated with a few cirrus uncinus cloud cases. A very unstable layer, i.e. an approximately dry adiabatic lapse rate, is associated with the formation of a cloud head. A stable, capping layer, which may correspond to a frontal zone is sometimes observed. However, there is some disagreement about this being a universal feature. Another stable layer bounds the formative region from below, and again, there is disagreement about the stability of this layer. Heymsfield's observations show this layer to be very stable, while Yagi's observations show it to be slightly more stable than the formative zone. Thus, in one instance, the environmental conditions may correspond to the classical view, except possibly for the stable capping layer, while in another the presence of a sub-cloud frontal zone is not indicated. Heymsfield points out that vertical shear of the horizontal wind speed appears to be important in the formation of these clouds, though either positive or negative shear may be present. Heymsfield also notes that the local vertical motion field responsible for the formation of the cloud may be due to wave motion, i.e. gravity waves, originating in the bounding stable layer. If this is correct, then large-scale vertical lifting may not be required for cloud layers to form. There is also some question as to the origin of these structures.

It is also possible that in the later stages of the life-cycle of an elevated frontal zone, when its stability has been diminished by

diffusion and turbulence, that simple mixing across the front of warmer, moist air from above and cooler, not too dry air from below may lead to saturation and condensation. This would be somewhat analogous to the formation of radiation fog. Both vertical shear and stability would tend to be maximized within the cloud layer relative to conditions above or below the cloud. No large-scale lifting would be required.

Persistence of clouds formed by outflow from deep convection may also be responsible for the existence of extensive cloud layers. This may be readily observed in satellite photos. In this instance, large-scale uplift may not be involved in the maintenance of the cloud. There is probably a strong tendency for a stable capping layer since such a feature could play a role in initiating the outflow.

Upper level stratiform clouds are not always directly associated with frontal discontinuities. Orographic cloud forms are a prime example, (e.g. Ludlam, 1956). In this case, the vertical motion field is not due to large-scale uplift but to the flow adjusting to an impedence below. Condensation brought about by adiabatic cooling destabilizes the region about cloud base and stabilizes the region above cloud top, relative to the situation at these levels before lifting. The stability of the internal portions of the cloud layer is a function of the pre-lifted stability and the amount of lifting, i.e. larger amplitude waves produce greater instability. Quite large vertical shears may be associated with the region below the cloud layer as indicated by the presence in many instances, of extreme turbulence and rotor clouds in this region. Another example may be the jet stream cirrus. Although in some instances, these clouds are

undoubtedly associated with the elevated frontal zones coupled with jet streams, Conover (1960) suggests that they may be driven by vertical circulations arising from horizontal vortices due to the jet flow. Though the cloud patterns are observed to closely parallel temperature discontinuities, which are probably associated with old fronts, in some cases they are observed to exist well above these discontinuities. The tropopause may act as a stable capping layer for these clouds. The magnitude of the vertical shear of the horizontal wind should be a minimum near the region of cloud top.

Clouds do form in a lifted air mass well above the frontal zone. This is substantiated not only by Conover's observations, but also by the commonly observed growth of jet contrails into cirrus layers. Thus, lifting may produce saturation well away from the front. Heymsfield (1977) has noted that local upward vertical velocities play a large role in the formation of these clouds. However, since the lifting is weak away from the front, and the jet induced vortical circulations may not always be present, it may be hypothesized that clouds of these types form in layers where the air was initially somewhat unstable so that convective currents might form.

One feature of all the stratiform clouds, which is universal, is that condensation acts to destabilize the region about cloud base and stabilize the region above cloud top.

2.2 The Basic Data Set

For these analyses, rawinsonde data from 24 continental U.S. stations for the year 1977 were used. The stations were chosen so that a roughly uniform geographical distribution over the continental

U.S. between 30°N and 50°N latitude was obtained. These stations are depicted in Figure 2. Only 0000 and 1200 GMT sondes were used. Thus, the total basic data set is comprised of ∿17,500 sondes. The National Center for Atmospheric Research provided the basic rawinsonde data on mass storage for easy access by computer. The data from a particular sonde are comprised of the temperature, relative humidity, geopotential height, wind direction and wind speed at various pressure levels. All standard pressure levels, i.e. 50 mb resolution, and all significant levels are included in the basic rawinsonde data. For this data set, the mean vertical resolution is ∿30 mb for the domain of interest, i.e. surface level up to the 200 mb level.

2.3 Data Processing and Analysis Procedures

For the purposes of these analyses, an atmospheric layer, which is saturated with respect to ice, is taken to be a cloud layer. The justification for this assumption is given in the following section. At that point, the validity of utilizing rawinsonde measured relative humidity for these analyses is also assessed.

The basic data set was divided into seasons. In this study, the summer season corresponds to the months of June, July and August; the fall season corresponds to the months of September, October and November; the winter season corresponds to the months of December, January and February; and the spring season corresponds to the months of March, April and May. All data for each season for all stations were grouped together, i.e. no regional analysis or time of day distinctions were attempted. Regional characteristics of the overall data set will be addressed in a future study already in progress. Each

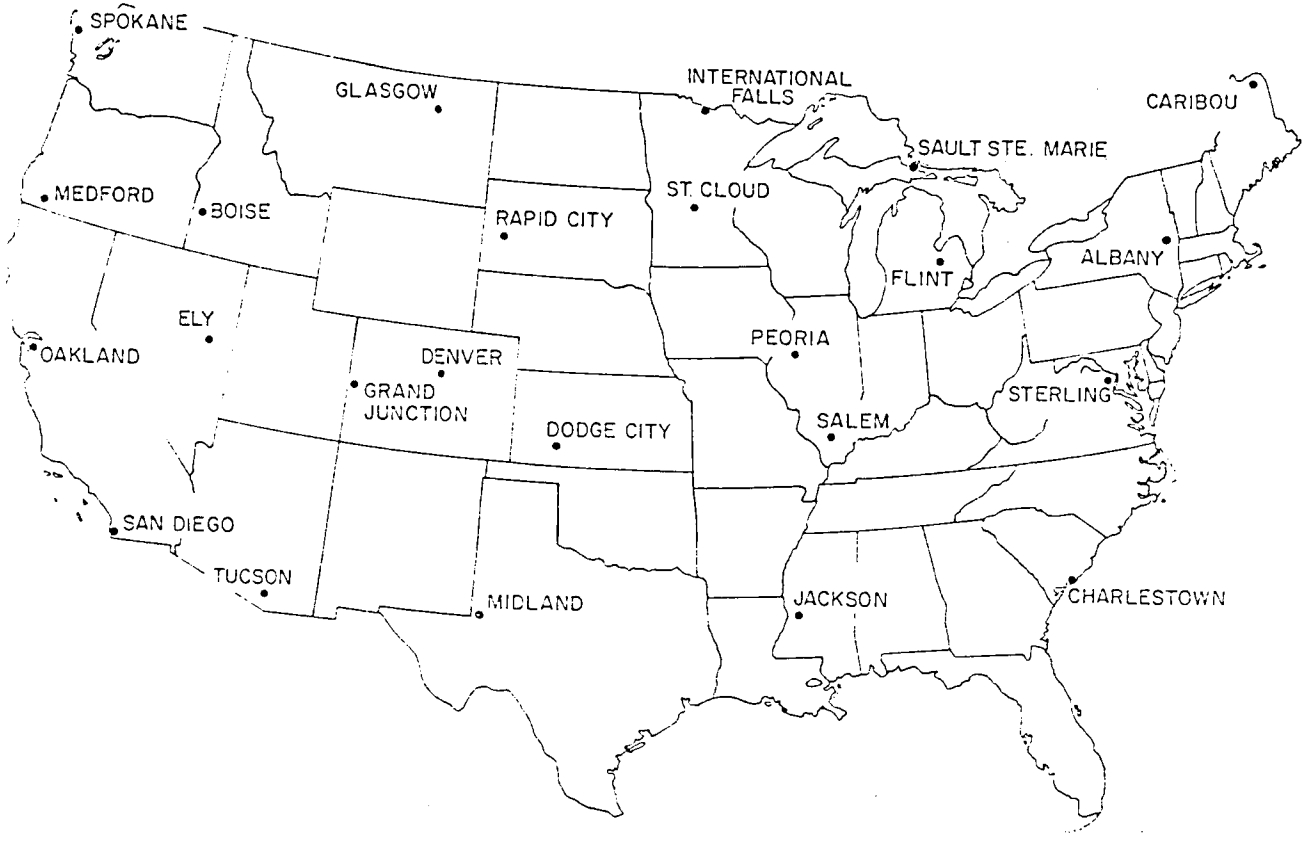

Figure 2. Geographical distribution of National Weather Service rawinsonde stations used for this study.

sonde in a seasonal group was considered to determine if a cloud layer was present.

For these analyses, only data at pressures less than or equal to 500 mb were considered. There is one exception to this, which will be noted later. In addition, only data at pressures less than the lowest pressure having a temperature greater than 0°C were considered. Thus, this study is limited to high level clouds, which are predominantly ice-phase. Relative humidity data at temperatures less than -40°C do not exist in the basic data set. The analysis for a particular sonde was terminated at this level.

List (1966) presents values for the ratio of the saturation water vapor pressure with respect to water to the saturation vapor pressure with respect to ice as a function of temperature, T. These data are a good approximation to the ratio of the relative humidity with respect to ice, RH_i, to the relative humidity with respect to water, RH_w. The data were fit with a second order polynomial. These data and the polynomial fit are presented in Figure 3. At each data level considered, this polynomial was used to compute the relative humidity with respect to ice from the observed temperature and relative humidity. Note that the observed relative humidity is referenced to water and that the data being considered correspond to temperatures between 0°C and -40°C.

For each sonde, all data levels in the pressure and temperature domain noted above, were searched for saturation with respect to ice, i.e. $RH_i \geq 100\%$. Any saturated layer was denoted as a cloud layer. If only one saturated level was found, it was still considered to be a cloud layer. If saturation was found at the lowest data level in the analysis domain, the analysis domain was extended in order to locate

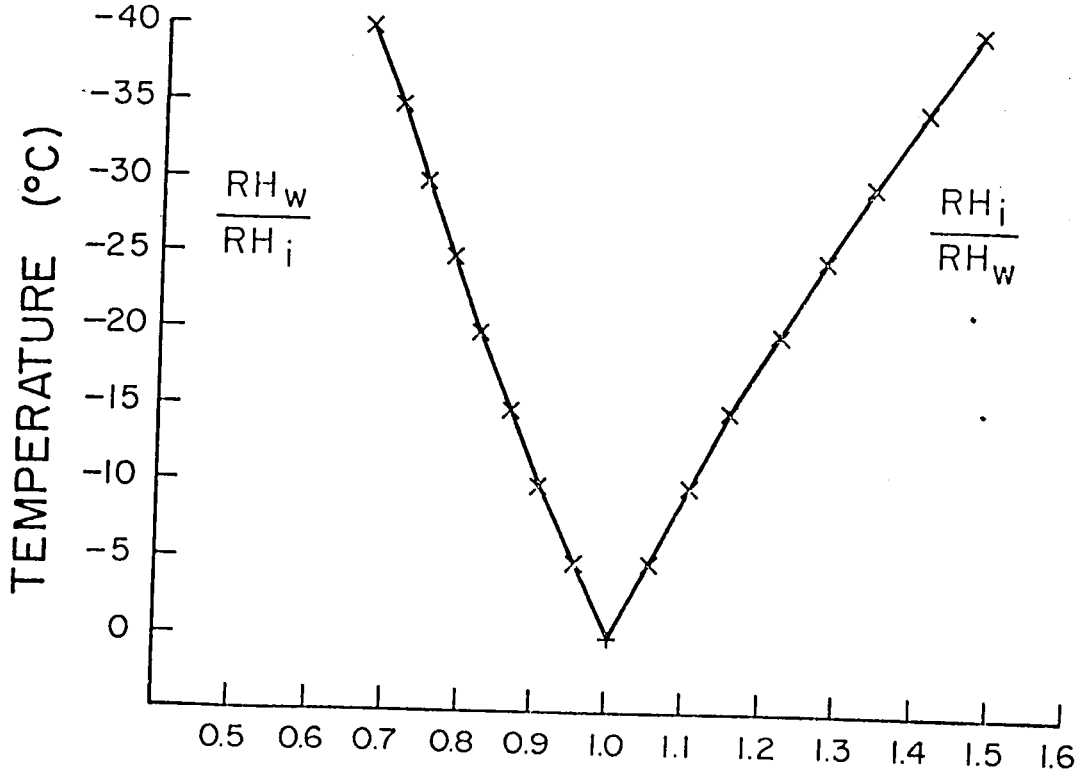

Figure 3. Plotted points represent the ratio of the saturation water vapor pressure with respect to a water surface to the saturation water vapor pressure with respect to an ice surface as a function of temperature (after List, 1966). The plotted curves correspond to the approximation employed in this study for the ratio of relative humidity with respect to ice to relative humidity with respect to water, i.e. RH_i / RH_w, and its inverse.

cloud base, i.e. the lowest saturated level below the 500 mb or 0°C level without any intervening unsaturated levels. If positive temperatures were encountered in the attempt to locate cloud base, then the observed values of RH_w were used to test for saturation, i.e. $RH_w \geq 100\%$ for $T > 0°C$.

When a cloud layer was determined to be present, three layers were defined for these analyses. They are the over-cloud layer, the cloud-top layer and the sub-cloud layer. The over-cloud layer is defined by the uppermost saturated level and the next higher level, which is unsaturated. The cloud-top layer is defined by the uppermost saturated level and the next lower level, which may not be saturated if only one saturated level was encountered. In most cases, at least two adjacent saturated levels were found. Note that the over-cloud layer and the cloud-top layer share a common boundary. The sub-cloud layer is defined by the lowest level at which saturation is found, i.e. no intervening unsaturated levels between this level and the cloud-top level, and the next lower level, which is unsaturated. However, in the case of a cloud layer which is defined by only one saturated level, the sub-cloud layer is defined to be the layer adjacent to and below the cloud-top layer. If any data were missing, i.e. T, RH_w, height, wind direction or wind speed, for the levels needed to define these layers, the case was eliminated from the analyses. For each of these three layers, three quantities were computed, namely: the dry static stability, the vertical shear of the horizontal wind speed and the atmospheric analog of the Richardson number.

Dry static stability, σ, corresponds to the vertical derivative of potential temperature, Θ, i.e.

$$\sigma \equiv \frac{\partial \Theta}{\partial z} \tag{2.1}$$

where z is the height. The potential temperature is given by Poisson's equation:

$$\Theta \equiv T \left(\frac{P}{P_o} \right)^{-\kappa}$$

where P is the pressure, P_o is a constant reference pressure and κ is a constant. Equation (2.1) was evaluated for a given layer as:

$$\sigma = (\Gamma_d - \Gamma) \left(\frac{\overline{P}}{P_o} \right)^{-\kappa} \tag{2.2}$$

where Γ is the temperature lapse rate for the layer, Γ_d is the dry adiabatic lapse rate and $\overline{P}$ is the mean layer pressure. If the upper level of a layer is denoted as the $n^{\underline{th}}$ level and the lower level of a layer is denoted as the $(n-1)^{\underline{th}}$ level, the formulae used to evaluate Eqn. (2.2) are:

$$\Gamma = \frac{(T_{n-1} - T_n)}{z_n - z_{n-1}}$$

and

$$\overline{P} = \frac{(P_n + P_{n-1})}{2.}$$

where

$$\Gamma_d \equiv \frac{g}{C_p} = 9.8 \text{ °K/km},$$

$$P_o \equiv 1000 \text{ mb}$$

and

$$\kappa \equiv \frac{R_g}{C_p} = 0.288$$

where g is the acceleration due to gravity, C_p is the specific heat of dry air at constant pressure and R_g is the real gas constant for dry air. The dry static stability is a measure of the stability of parcels within a layer to small vertical displacements. It quantifies the potential buoyancy force acting on a parcel. A more accurate measure of the stability might be obtained by also considering the vertical derivative of equivalent potential temperature, Θ_e, (e.g. Hess, 1959). However, for the temperature domain of this data set with its correspondingly small values of the saturation vapor pressure, Θ_e very nearly equals Θ. Thus, dry static stability is a good approximation to the stability in this domain.

The vertical shear of the horizontal wind speed, S, for a layer was computed as:

$$S = \frac{| \tilde{v}_n | - | v_{n-1} |}{z_n - z_{n-1}} \qquad (2.3)$$

where $| \tilde{v}_n |$ is the horizontal wind speed at pressure level n. Wind direction has been ignored for the consideration of vertical wind shear in this study. A number of detailed case studies of extensive altostratus and cirrostratus cloud layers by one of the authors led to the conclusion that directional shear is generally small even in

the vicinity of elevated fronts associated with the cloud layers considered. It is for this reason because of a desire for simplicity in the analyses that wind direction is not considered here.

The Richardson number, R, for a layer was computed as:

$$R = \frac{g\,\sigma}{\bar{\Theta}\,S^2} \qquad (2.4)$$

where the mean layer potential temperature is given by:

$$\bar{\Theta} = \frac{(T_n + T_{n-1})}{2.0}\left(\frac{\bar{P}}{P_o}\right)^{-\kappa}.$$

The Richardson number is a non-dimensional number, which corresponds to a ratio of the buoyancy forces to the mechanical forces, i.e. shear stress, acting on a parcel. It is a measure of the production and dissipation of turbulent kinetic energy. Large values of R imply that turbulent kinetic energy is quickly damped, i.e. dissipated, in the mean flow. Small values of R, i.e. $R \lesssim \sim 0.25$, imply that the turbulent kinetic energy imbedded in the mean flow is maintained by the mean flow, i.e. production is greater than or equal to dissipation. Clear air turbulence occurs when a small Richardson number is observed for the mean flow.

We chose to analyze these parameters for a number of reasons. First, they are easy to compute and readily accessible from the basic data set. Second, they enable the identification of typical atmospheric structures, which may be associated with these cloud forms,

e.g. frontal zones, on an automated basis. This eliminates the need to analyze weather maps, which would greatly increase the difficulty and time required to accomplish a survey as extensive as this one. Third, they characterize the static environment associated with these layers. Note that the importance of horizontal advective processes in the life-cycle is currently being evaluated with this data set. Fourth, knowledge of the typical static stability structure associated with cloud forms is very useful in the design of simple thermodynamic budget models of stratified cloud layers, e.g. Schubert (1976) and Albrecht, et al (1979). Also, information on the turbulent kinetic energy budget of a cloud layer is important for design and closure of parametric models of convective energy transports within a layer.

For each layer for each season, frequency distributions were obtained for each parameter. Mean values and standard deviations were also computed. Structure information was compiled based on comparison of the values for each layer of a particular cloud case. Many different stratifications of the cloud case data set were attempted. Most turned out to be not very useful. However, stratifying the data on the basis of thickness of the cloud layer did provide some interesting results. Thin cloud layers were defined to be less than or equal to 50 mb thick, otherwise the cloud case was regarded as a thick cloud layer. The 50 mb thickness criterion was chosen because this is the minimum resolution of the basic data set and because it was felt that it might adequately discriminate between the fair weather thin cirrus and the strongly forced deep clouds associated with cyclones. In this way, it was hoped to distinguish between cases which might best correspond to the classical model and those which might best be described

by other conceptual models. The results of these analyses are presented in Section 3.

2.4 Rawinsonde Observed Relative Humidity and Cloud Cover

In this section, the validity of utilizing relative humidity data from standard rawinsondes for the diagnosis of cloud layers is considered.

Humidity data from standard National Weather Service rawinsondes for ambient temperatures in the range of 0°C to -40°C are commonly regarded as having large inherent errors, especially at the colder temperatures. However, substantial improvements in the basic design of the sonde and the humidity element itself have been made in recent years. Reports by Brousaides (1973) and Brousaides and Morrissey (1974), hereafter referred to as MB, present a synopsis of potential errors in the redesigned sonde. This sonde has been in use since ∿1973 at the National Weather Service launch sites in the U.S. Errors due to solar insolation and thermal lag have been substantially reduced compared to older sondes. However, the remaining errors are still substantial. Brousaides (1973) notes that the reproducibility, i.e. the relative precision, of the humidity sensors is within a range of approximately 6-7% in measured relative humidity. Except in the situation of heavy precipitation, washout was not found to be a severe problem for the new sonde. MB state that errors due to thermal lag are on the order of 6 to 9% in measured relative humidity, while solar insolation induced errors amount to 9 to 14% in the temperature and pressure domain considered in this study. However, for the geographic and height domain of this study and the 0000 and 1200 GMT launch times,

solar insolation problems should be minimal, i.e. only ∿25% of the sondes considered in this study potentially experienced direct solar exposure at some time during their flight at solar elevations corresponding to greater than one hour above the horizon. Even these sondes were typically exposed at relatively small solar elevations. MB note that the rectification of flight data is very difficult due to the variability of the error sources, i.e. solar elevation, cloud conditions, previous thermal and humidity history, etc. This is especially true for standardized data sets, which are used in this study, where the complete minute-by-minute data record is unavailable. Correction of the basic data set employing their formulae was not attempted.

The data were tested for humidity lag. Data and formulae presented in Brousaides (1973) were used to formulate a test criterion of maximum observable response rate. Approximately 5% of the basic data set was tested against this criterion. The sample was random except that humidity was required to increase from the next lower level to the test level. An observed rate of change of humidity equal to or greater than 80% of the maximum observable response rate was found at less than 3% of the levels tested. Thus, in the basic data set, vertical gradients of humidity are rarely large enough to exceed the sensor capability.

Rhea (1978) has found the new sonde to be acceptable for locating cloud layers. Surface observations of cloud layers were compared to relative humidity with respect to ice computed from rawinsonde data for western Colorado. Saturated layers were found to correspond well with observations of cloud layers. Much improvement in this regard was noted, when compared to the last two generations of sondes.

Similar results were found by these authors. A number of case studies of the large-scale energy budgets associated with upper level stratiform cloud layers are in progress by these authors. The purpose of these studies is to try to ascertain the nature of the advective components of the budgets and the corresponding synoptic situation. Surface and satellite observations of cloud layers agreed quite well with deductions based solely on observed relative humidty with respect to ice. Probably the best validation for using post-1973 rawinsonde data to assess the presence of cloud layers may be found by considering the following. The percentage of sondes exhibiting saturation with respect to ice at pressures less than 600 mb and temperatures between 0°C and -40°C for the basic data set are given below for two latitude bands.

	Summer	Fall	Winter	Spring	Annual
30°N - 40°N	26.6 (27.1)	26.3 (32.7)	31.7 (31.4)	30.5 (38.0)	28.8 (32.3)
40°N - 50°N	39.0 (36.1)	36.1 (40.7)	42.4 (39.1)	40.1 (43.4)	36.9 (39.8)

The percentages in parentheses are the mean zonal cloud cover for these latitudes in the northern hemisphere for the middle and upper troposphere, which were derived from data presented in London (1957). London's estimates were based upon surface observations of various cloud forms. The effects of obscuration due to overlap of cloud layers were taken into account in deriving the estimates of cloud cover for the various cloud types presented in London (1957). The percentages given above were computed by summing the given cloud amounts for cirrus, altostratus, nimbostratus and cumulonimbus clouds and then

correcting these sums for overlap. The overlap correction consisted of assuming random distribution of cirrus, altostratus and nimbostratus clouds. Thus, the corrected sums are less than the uncorrected sums.

If saturation with respect to ice determined from rawinsonde data is a good indicator of the presence of a cloud, then for a large data sample, the percentage of sondes exhibiting saturation should correspond to the observed mean middle and upper tropospheric cloud cover. The agreement between seasonal mean zonal cloud cover estimated from surface observations and that based on analysis of rawinsonde data is fairly good. Exact agreement would not be anticipated for a number of reasons. First, this analysis is based on data for the continental U.S. for the year 1977, while London's estimates are based on other years for the entire northern hemisphere in these latitude bands. Thus, year-to-year variability in the cloud cover for the middle and upper troposphere and longitudinal variations in that cloud cover could be sources of disagreement. Also, due to the -40°C limit on the data sample for this analysis, some cirriform clouds cannot possibly be detected. In addition, some of the nimbostratus cloud forms may be too shallow or too warm to be detected by this analysis. This would be particularly true in the warmer seasons. Thus, the seasonal mean zonal cloud cover for the middle and upper troposphere derived from this analysis should be less than that actually observed even if the technique is valid. A compensating effect is that layers, which are saturated with respect to ice, are observed to be cloud free in some cases, e.g. Bigg and Meade (1971), Jayaweera and Ohtake (1972), and Detwiler and Vonnegut (1979). However, this situation occurs relatively infrequently (e.g. Lala, [1969]) reports that only 3% of the

time is this observed at Albany, New York) and normally at temperatures less than -30°C. Since saturation with respect to ice at pressures less than 600 mb and temperatures between 0°C and -40°C was detected in ∿35% of the sondes for Albany in 1977, less than 8% of the saturated layers determined by this analysis are anticipated to be cloud free. It is expected that errors arising from the limited vertical domain of this study are greater than those due to erroneous diagnosis. Therefore, the seasonal mean zonal cloud cover for the middle and upper troposphere derived here is likely to be less than that actually observed even if the technique is valid. It is of note that, except in winter, the estimated cloud cover derived in this study is less than that derived from London (1957) for both latitude bands.

2.5 The Cloud Case Data Set

Before discussing the results of the analyses of cloud characteristics, it is appropriate to consider the cloud case data set. In Table 1, the number of cloud cases, which qualified for these analyses on the basis of the criteria discussed in Section 2.3, are presented for each season for both cloud thickness groups. These are the number of cases for which the analyses of cloud layer characteristics were performed. In the following discussion of results, relative frequency of occurrence always refers to the percentage or fraction of the total number of cases in a particular group, i.e. season and thickness, exhibiting a particular characteristic. Many more thin cloud cases qualified for the analyses than thick cloud cases. This is partly because many of the thick saturated layers, which were found, were

saturated at the -40°C level and, thus, were excluded from the analyses as cloud-top pressure could not be located.

	Summer	Fall	Winter	Spring	Total
Thick Clouds	189	251	246	200	886
Thin Clouds	863	765	524	564	2716
All Clouds	1052	1016	770	764	3602

Table 1. Number of cloud cases included in this study for each season and for each cloud thickness group.

In Figure 4, the relative frequency of occurrence of cloud cases with cloud-top pressure, p_{CT}, within 25 mb of a given pressure level is given for each season for both the thick cloud cases and the thin cloud cases. The corresponding mean cloud-top pressures are also noted. Mean cloud-top pressure is greatest in winter and least in summer. The shapes of the curves are highly influenced by the mean seasonal location of the -40°C isotherm and its variation. The location of the mean seasonal tropopause and its variation also affect the shape of the curves. These two factors cause the observed diminishing relative frequencies above ∿400 mb. Note that the summer and fall curves are similar and that the spring and winter curves are similar for both thick and thin cloud cases. The mean cloud thickness is ∿30 mb for the thin cloud cases and nearly 150 mb for the thick cloud cases. However, only $\sim \frac{1}{3}$ of the thick cloud cases are thicker than 150 mb. Thus, the mean is highly influenced by the very thick cases.

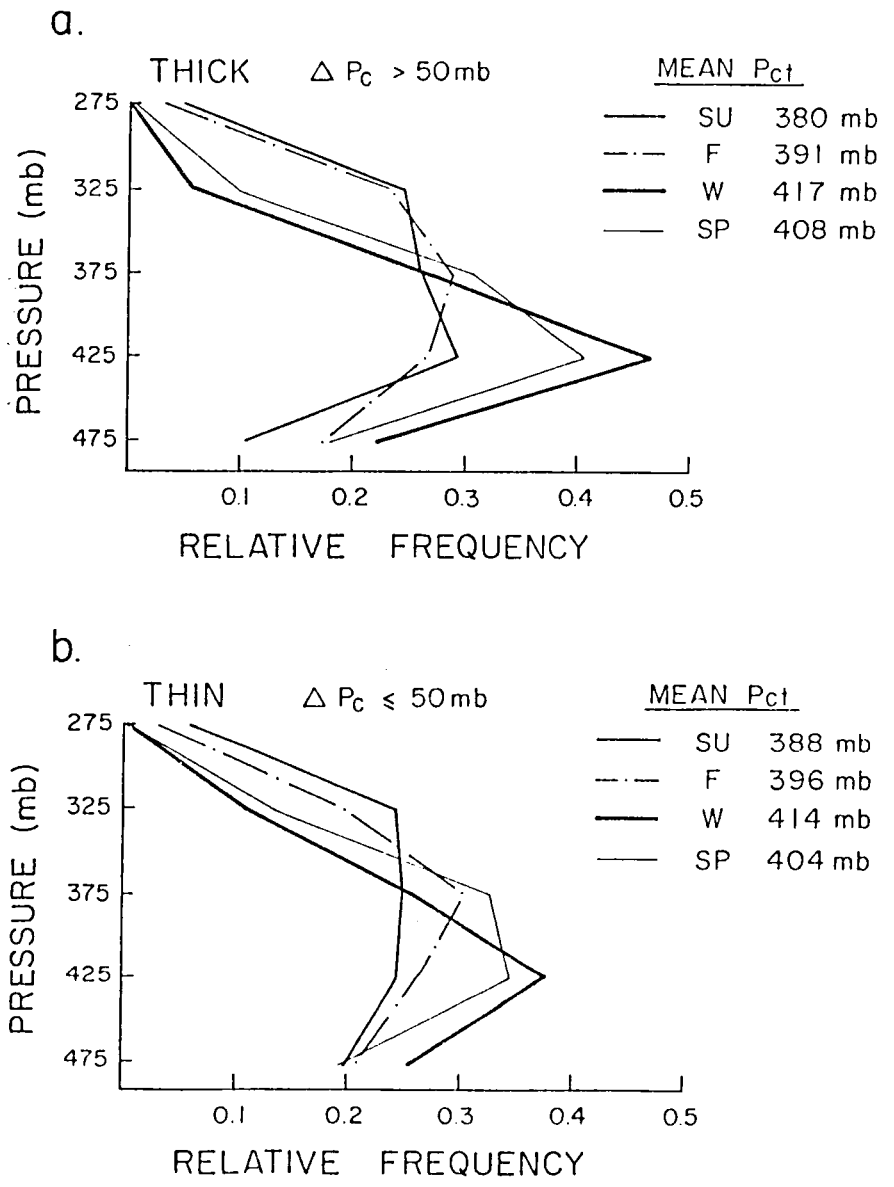

Figure 4. Relative frequency of occurrence for cloud cases with cloud top pressure, p_{CT}, within 25 mb of a given pressure for both (a) thick cloud cases and (b) thin cloud cases for each season. Seasonal mean cloud top pressures are also given.

3. RESULTS

3.1 Stability

3.1.a Mean Stability Structures

The results of the analyses of the dry static stability in the cloud-top layer, σ_T; the over-cloud layer, σ_0; and the sub-cloud layer, σ_S, are presented in this section. The seasonal means for the three layers, i.e. $\overline{\sigma_T}$, $\overline{\sigma_0}$, and $\overline{\sigma_S}$, are given in Figure 5a for the thick cloud cases and in Figure 5b for the thin cloud cases. The seasonal means for the 350 mb to 450 mb layer, $\overline{\sigma_4}$, and for the 650 mb to 750 mb layer, $\overline{\sigma_7}$, computed from all sondes are included in each figure for comparison.

Comparing the $\overline{\sigma_4}$ and $\overline{\sigma_7}$ curves, dry static stability is seen to decrease with increasing height in all seasons. The seasonal range of $\overline{\sigma_4}$ is only 0.36°K/km with relative maxima, i.e. more stable, occurring in summer and winter. The winter maximum may be partly due to the inclusion of some cases, where the tropopause is within the 350 mb to 450 mb layer. This may occur when a deep, cold trough is located over a station at launch time and would lead to a more stable value of $\overline{\sigma_4}$. The seasonal range of $\overline{\sigma_7}$ is nearly 1.5°K/km. Thus, the middle troposphere undergoes a much larger seasonal variation of mean dry static stability, when compared to the upper troposphere. The winter season is the most stable and the summer season is the most unstable at the 700 mb level. In terms of $\overline{\sigma_7}$, spring resembles summer and fall is intermediate between winter and summer. The seasonal behavior of $\overline{\sigma_7}$ may be partly attributed to the increased frequency and strength of elevated fronts occurring the the 650 mb to 750 mb layer during the cold seasons. Stabilization of the lower troposphere due to infrared

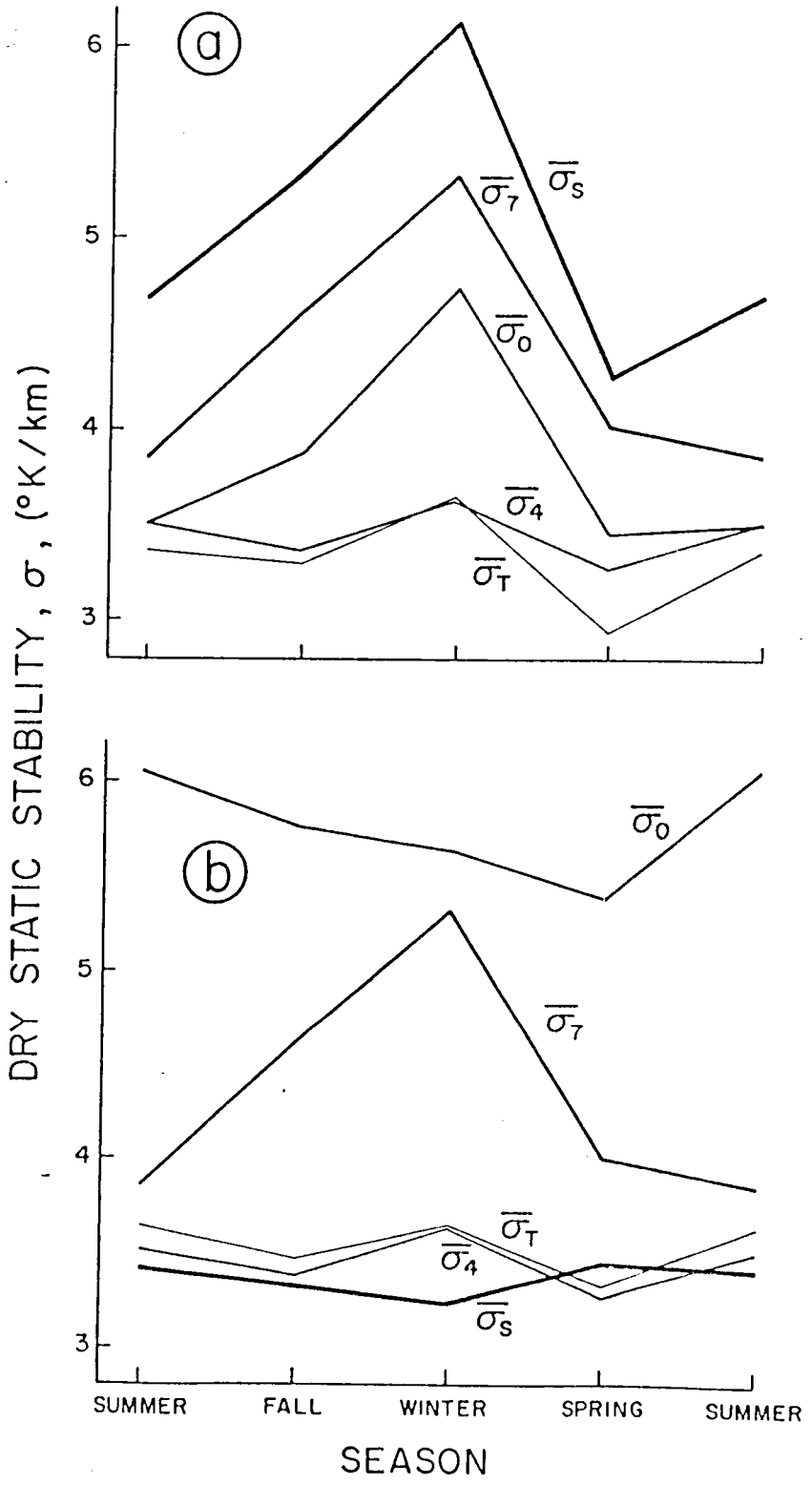

Figure 5. Seasonal mean dry static stability for the cloud-top layer, $\overline{\sigma}_T$; the over-cloud layer, $\overline{\sigma}_0$; and the sub-cloud layer, $\overline{\sigma}_S$, for (a) thick cloud cases and (b) thin cloud cases. Mean seasonal dry static stability at 400 mb, $\overline{\sigma}_4$, and at 700 mb, $\overline{\sigma}_7$, are included for comparison. See text for further explanation.

radiative processes acting at night may also play a role in raising $\overline{\sigma_7}$ in the winter, especially at the high elevation stations. Also, enhanced convective mixing in summer may play a role in lowering $\overline{\sigma_7}$ in that season. If only sondes exhibiting saturation with respect to ice at a level above the 500 mb level are used to compute $\overline{\sigma_4}$ and $\overline{\sigma_7}$, the curves are altered somewhat. In this case, $\overline{\sigma_7}$ is decreased by less than 0.1°K/km in each season, when compared to the plotted values. The values of $\overline{\sigma_4}$ are increased by approximately 0.1°K/km in winter and spring and by 0.3 and 0.2°K/km in summer and fall, respectively. Thus, the mean difference in dry static stability between the upper and lower troposphere is less for cloud case sondes, when compared to all sondes. In summer, this difference is negligible for the cloud case sondes.

The observed values of $\overline{\sigma_4}$ and $\overline{\sigma_7}$ may be used to compute the seasonal mean rate of change of dry static stability with respect to pressure, i.e. $(\overline{\sigma_7} - \overline{\sigma_4})$ / 300 mb. If this linear rate of change is assumed to be valid for the pressure domain considered here, the seasonal mean dry static stability at any pressure level in this domain may be computed as a linear function of that pressure. In order to compare the observed values of $\overline{\sigma_T}$, $\overline{\sigma_0}$ and $\overline{\sigma_S}$ to mean atmospheric conditions, "expected" mean values of $\overline{\sigma_T}$, $\overline{\sigma_0}$ and $\overline{\sigma_S}$ were computed from the observed respective mean mid-layer pressures by the above method. The assumption of linear decrease of σ with pressure should not have much effect on the computations of the "expected" mean values, since, except for the sub-cloud layer for the thick cloud cases, the mid-layer pressures occur predominantly in the 350 mb to 450 mb layer (see

Fig. 4). Thus, the expected mean values are based on small adjustments to the value of $\overline{\sigma_4}$.

Considering $\overline{\sigma_T}$, $\overline{\sigma_0}$ and $\overline{\sigma_S}$ for the thick cloud cases, the cloud-top layer is the most unstable layer and the sub-cloud layer is the most stable layer of the three in the mean for each season. The mean cloud-top layer is less stable than expected from mean conditions. The difference is nearly 0.5°K/km in spring, ∿0.2°K/km in winter, and ∿0.1 °K/km in the other seasons. If the virtual dry static stability, i.e. using the moist adiabatic lapse rate instead of the dry adiabatic lapse rate in Eq. 2.2, is computed, the mean cloud-top layer is an additional ∿0.5°K/km more unstable than mean conditions. Therefore, it is primarily the moisture content of the mean cloud-top layer that distinguishes it from mean conditions in terms of stability to small vertical displacements.

The mean over-cloud layer for the thick cloud cases is more stable than expected from mean conditions by 0.1, 0.6, 1.1 and 0.2°K/km in summer, fall, winter and spring, respectively. The seasonal range of $\overline{\sigma_0}$ is greater than that of $\overline{\sigma_T}$ by a factor of ∿3.5, which is surprising in that the mean difference between the mid-layer pressures is only ∿30 mb. The difference between $\overline{\sigma_0}$ and $\overline{\sigma_T}$ is 0.1, 0.6, 1.1 and 0.5°K/km in summer, fall, winter and spring, respectively. Thus, particularly in winter, the mean thick cloud layer is capped by a layer which is more stable than the cloud-top layer, even if differences in water vapor content are ignored.

The mean sub-cloud layer is the most stable layer and also exhibits the largest seasonal range in dry static stability of the three layers, which might have been anticipated from mean conditions, i.e.

$\overline{\sigma_7}$. However, the observed values of $\overline{\sigma_S}$ are greater than the values expected from mean conditions by approximately 1.1, 1.5, 1.8 and 0.7 °K/km in summer, fall, winter and spring, respectively. These values suggest the presence of an elevated front in the sub-cloud layer. This may be seen by considering that in winter the value of $\overline{\sigma_S}$ corresponds to a temperature lapse rate of only 4.7°K/km, which is absolutely stable even under saturated conditions at this pressure, i.e. ∿550 mb.

Considering $\overline{\sigma_T}$, $\overline{\sigma_0}$ and $\overline{\sigma_S}$ for the thin cloud cases, the over-cloud layer is observed to be the most stable of the three in the mean for each season, while the sub-cloud layer is the least stable except in spring. The observed values of $\overline{\sigma_T}$ are greater than those expected from mean conditions by ∿0.1°K/km in summer and fall, nearly equal in spring, and are less by ∿0.2°K/km in winter. Thus, unlike the thick cloud cases, the mean cloud-top layer for the thin cloud cases tends to be slightly more stable than mean conditions. The seasonal range in $\overline{\sigma_T}$ for the thin cloud cases is less than half that for the thick cloud cases, though the patterns are similar. The mean cloud-top layers for the thick and thin cloud cases are not that different in terms of dry static stability and in both cases it is primarily the water vapor content of the layers that distinguishes them from mean conditions.

The mean over-cloud layer for the thin cloud cases is more stable than expected from mean conditions by 2.6, 2.5, 2.0 and 2.2°K/km in summer, fall, winter and spring, respectively. These values suggest the presence of an elevated front above the thin cloud layer. In some cases, this stable layer is likely to correspond to the tropopause. The value of $\overline{\sigma_0}$ in summer corresponds to a temperature lapse rate of

only ∿5.4°K/km, which is a very stable layer at this pressure level, (∿370 mb). The seasonal range of $\overline{\sigma_0}$ is much smaller for the thin cloud cases, when compared to the thick cloud cases, and the seasonal patterns are dissimilar, except that each exhibits a spring minimum. In each season, the mean over-cloud layer is much more stable for the thin cloud cases compared to the thick cloud cases even though the stability of the respective mean cloud-top layers is not too different.

Mean conditions suggest that for the thin cloud cases, $\overline{\sigma_S}$ should be greater than $\overline{\sigma_T}$, however, this is not observed. The values of $\overline{\sigma_S}$ are less than those expected from mean conditions by ∿0.1°K/km in spring and summer and ∿0.2°K/km in the other seasons. The stability of the mean sub-cloud layer is not too different from that of the mean cloud-top layer for the thin cloud cases. There is no indication of an elevated frontal zone in the mean sub-cloud layer for the thin cloud cases as there was for the thick cloud cases.

3.1.b. Relative Frequency of Various Stability Structures

Thus far, the mean stratification in terms of dry static stability in the vicinity of both thick and thin cloud layers have been quantified for each season. Differences in the mean dry static stability between the thin and thick cloud cases have been noted. However, the correspondence of the mean structures to the actual observed case by case structure must be established before any quantitative model of the typical stratification can be put forth, i.e. is the mean structure representative of the typical structure or is it the result of averaging multiple and different typical structures? In Table 2, the observed relative frequency of occurrence of various stratifications in

(a)

Thick Cloud Cases

	Su	F	W	Sp	Average
σ_0 and $\sigma_S \geq \sigma_T$	27	34	34	27	30
$\sigma_S < \sigma_T \leq \sigma_0$	11	11	12	12	11
$\sigma_S \geq \sigma_T > \sigma_0$	35	35	34	34	35
σ_0 and $\sigma_S < \sigma_T$	27	20	20	28	24
$\sigma_0 \geq \sigma_T$	38	45	46	39	42
$\sigma_S \geq \sigma_T$	62	69	68	61	65

(b)

Thin Cloud Cases

	Su	F	W	Sp	Average
σ_0 and $\sigma_S \geq \sigma_T$	43	40	38	41	41
$\sigma_S < \sigma_T \leq \sigma_0$	21	17	21	17	19
$\sigma_S \geq \sigma_T > \sigma_0$	14	16	17	17	16
σ_0 and $\sigma_S < \sigma_T$	22	27	24	25	24
$\sigma_0 \geq \sigma_T$	64	57	59	58	60
$\sigma_S \geq \sigma_T$	57	56	55	58	57

Table 2. Relative frequency of occurrence in percent of various stratifications of dry static stability among the over-cloud layer, σ_0; the cloud-top layer, σ_T; and the sub-cloud layer, σ_S, for each season and the "average" season for (a) thick cloud cases and for (b) thin cloud cases.

terms of dry static stability among the cloud-top, over-cloud and sub-cloud layers are presented for both cloud thickness groupings for each season. In the top data row, the relative frequency of cases in a group exhibiting a minimum in dry static stability in the cloud-top layer relative to the other two layers is given. The second and third data rows correspond to increasing and decreasing stability with height through the three layers, respectively. The fourth row corresponds to maximum stability in the cloud-top layer relative to the other two layers. In the last two rows, the relative frequency of cases where the over-cloud layer is more stable than the cloud-top layer and where the sub-cloud layer is more stable than the cloud-top layer are presented for each group. Simple inspection of the entries reveals that based upon this analysis any possible stratification may be observed for any given group. However, some stratifications are substantially more common than others.

3.1.b.i. Thick Cloud Cases

For the thick cloud cases, the most likely stratification is that with decreasing stability with height through the three layers. The relative frequency of occurrence of this structure is nearly constant with respect to season. This is also true of the structure with increasing stability with height, which is the least likely. Minimum stability in the cloud-top layer tends to be the second most likely structure, and is most common in fall and winter. Maximum stability in the cloud-top layer has the opposite seasonal variation. In spring and summer, these two stratifications are nearly equally likely to occur. In order to properly interpret each structure physically, the

corresponding values of $\overline{\sigma_0}$, $\overline{\sigma_T}$ and $\overline{\sigma_S}$ must be considered together with the relative frequency of occurrence of the two layer stratifications shown in the last two data rows in Table 2.

In an average season, the value of σ_0 is greater than σ_T in only 42% of the thick cloud cases, however, $\overline{\sigma_0}$ minus $\overline{\sigma_T}$ is positive and equal to $\sim$0.6°K/km. This implies that, for cases where $\sigma_0 > \sigma_T$, the difference $(\overline{\sigma_0} - \overline{\sigma_T})$ is larger than the difference $(\overline{\sigma_T} - \overline{\sigma_0})$, for cases where $\sigma_T > \sigma_0$. The situation of a small decrease in dry static stability from the cloud-top layer to the over-cloud layer strongly suggests that both layers are located in the same air mass. This applies to cases when the observed structures are those with either maximum stability in the cloud-top layer or decreasing stability with height through the three layers. If an expected decrease is computed for these cases, which is based upon an assumption that mean conditions are representative of those in a uniform air mass, then an estimate of a typical value of $(\sigma_0 - \sigma_T)$ may be made for the cases when $\sigma_0 > \sigma_T$. This value is $\sim$1.4°K/km. Thus, in the thick cloud cases where $\sigma_0 > \sigma_T$, the over-cloud layer tends to be stable and caps the cloud layer. This relatively stable layer may possibly be interpreted as an elevated frontal zone, since the stability of a frontal zone at this level is not nearly as great as at lower levels due to the cumulative effect of diffusion over its lifetime. However, other interpretations are possible and are considered below.

In an average season, the value of σ_S is greater than σ_T in 65% of the thick cloud cases and $\overline{\sigma_S} - \overline{\sigma_T}$ equals $\sim$1.75°K/km, which is substantial. The implication is that for cases where $\sigma_T > \sigma_S$, the difference $(\overline{\sigma_T} - \overline{\sigma_S})$ is relatively small and that for cases where $\sigma_S > \sigma_T$,

the difference $(\overline{\sigma_S} - \overline{\sigma_T})$ is large. In the manner used above, $(\overline{\sigma_S} - \overline{\sigma_T})$ is estimated to be $\sim$2.4°K/km, for cases where $\sigma_S > \sigma_T$. Thus, the structure with decreasing stability with height through the three layers corresponds very well to the classical notion of a very stable layer or front below the cloud layer and where the cloud-top layer and over-cloud layer exist in the same lifted air mass. This is observed to be the most likely structure for the thick cloud cases. The interpretation of the structure with minimum stability in the cloud-top layer is similar to the classical notion, except for the relatively stable capping layer.

In addition to the interpretation that the stable over-cloud layer is another frontal zone, which might exist in the case of thick clouds to be west of the center of a mature or occluded cyclone, a second interpretation is that the enhanced stability of this layer is due to both strong infrared radiative cooling and evaporative cooling in the region of cloud-top, which are greatest near the lower boundary of the over-cloud layer and, thus, tend to stabilize the over-cloud layer. Nighttime cases would show these effects more than daytime cases due to the compensating effect of solar absorption.

Observations reported by Griffith et al, 1979, of the radiative characteristics of tropical cirrus clouds lead to the conclusion that the lapse rate of a 25 mb thick over-cloud layer, as defined here, may be potentially stabilized at a rate of up to $\sim$20°K/km/day due to infrared radiative processes. These results correspond to the case of a high, very cold cloud (i.e. $\sim$ -50°C), which is essentially a black body with respect to infrared radiation and represents the situation of maximum radiative effect. The potential stabilization of the over-

cloud layer due to evaporative processes may be evaluated by noting that typical ice water contents may range from 0.001 to 0.3 g/m^3 and typical mean vertical velocities in the cloud layer may range from 1 to 100 cm/s (from Griffith et al, 1979, and Heymsfield, 1977). If the cloud-top level is assumed to remain constant and the ice crystals are assumed to be transported upward at the observed vertical velocity and are sublimated at cloud-top, the lapse rate of the over-cloud layer may be potentially stabilized at a rate of from $\sim$0.005 to $\sim$150 °K/km/day. A vertical velocity of 2 cm/s and an ice water content of 0.1 g/m^3 result in a lapse rate stabilization rate of $\sim$10°K/km/day in the over-cloud layer due to evaporative cooling.

Subsidence and its associated adiabatic warming may also lead to increased stability in a layer. However, in the case of a relatively stable layer directly above a relatively unstable layer, a very strong or enduring subsidence field would be required in the upper layer to explain the observed magnitude of the stability differences if both layers are initially assumed to be similar. For example, a vertical velocity of $\sim$ -2 cm/s results in the lapse rate being stabilized at a rate of $\sim$0.3 °K/km/day at these levels. Large vertical gradients of both the vertical motion field and the divergence would also be required near the interface between the two layers for the observed structure to evolve by this mechanism. Such gradients may exist across elevated fronts but the vertical circulations required are opposite to those corresponding to the classical model. Compensating subsidence in the region of strong convection may affect the stability structure of middle and upper tropospheric outflow layers. However, the required vertical gradients in the circulation are not likely to be due to the

convection but rather due to some pre-existing structure. Thus, radiative and evaporative effects may readily account for the observed stability of the over-cloud layer, while adiabatic effects due to vertical motion are much less likely to be the source of the observed structure.

The structure with increasing stability with height does not correspond to the classical structure. However, if the location of cloud-top pressure is slightly in error in these cases, i.e. above the actual cloud-top level, then the stability of the cloud-top layer is overestimated since the over-cloud layer tends to be much more stable. Since, where $\sigma_T > \sigma_S$, the difference in stability between the cloud-top layer and the sub-cloud layer tends to be relatively small, it may be hypothesized that they are in the same air mass and that the sign of the difference, which is inconsistent with this hypothesis, arises from slight errors in the location of the cloud-top level. In any event, these cases do not appear to be forced by frontal lifting from directly below the cloud layer.

The above arguments, also, lead to the conclusion that, in the case of the structure with maximum stability in the cloud-top layer, the differences in dry static stability between the three layers tend to be relatively small. Thus, the presence of a very stable layer is not indicated for any of the layers. The observations of maximum stability in the cloud-top layer may be due to the effects of infrared radiation or evaporation near cloud-top coupled with a slight mislocation of the cloud-top level. In this instance, maximum stability occurs just above cloud-top. It should be noted, that the interpretations, which rely on assumed errors in the location of cloud-top, lead to the conclusion that $\overline{\sigma_T}$ has been overestimated.

Combining all the results from the analysis of the stratification about thick clouds, the following conclusions may be put forth:

1. In 65% of the cases, the mean sub-cloud layer is estimated to be ∿2°K/km more stable than mean conditions. This strongly suggests the presence of a frontal zone corresponding to the classical model.
2. In nearly half of the cases with the stable sub-cloud layer, the mean over-cloud layer is also relatively stable, i.e. estimated to be ∿1.3°K/km more stable than mean conditions.
3. In ∿35% of the cases, which do not show the stable sub-cloud layer, ∿ $\frac{1}{3}$ do exhibit the stable capping layer, while the rest show a weak tendency for maximum stability in the vicinity of cloud-top.
4. The stability of the mean cloud-top layer has probably been slightly overestimated due to the mislocation of the cloud-top level in some cases. However, even if $\overline{\sigma_T}$ is adjusted to compensate for this effect, the corresponding temperature lapse rate is still 1 to 2°K/km less than the moist adiabatic lapse rate. It is primarily the moisture content of this layer, which distinguishes it from mean atmospheric conditions.

These conclusions were based on an average season. They are most valid in winter, where the magnitude of the differences are larger than for the average season.

3.1.b.ii. Thin Cloud Cases

For the thin cloud cases, the structure with minimum stability in the cloud-top layer is the most likely stratification in each season. However, maximum stability in this layer is the next most commonly observed structure. Increasing stability with height through the three layers is slightly more common than decreasing stability with height. The observed relative frequency of occurrence for each structure for the thin cloud cases exhibits a seasonal range of ∿5%. No obvious pattern is evident in this seasonal variation. The observed relative frequency of occurrence for the different stratifications indicates substantial differences between the thick and thin cloud cases.

In an average season, the value of σ_0 is greater than σ_T in ∿60% of the thin cloud cases and the difference $\overline{\sigma_0} - \overline{\sigma_T}$ is ∿2.2°K/km. This difference is very large considering the proximity of these two layers and the above percentage. If for the cases where $\sigma_0 < \sigma_T$, the over-cloud layer and the cloud-top layer are assumed to exist in the same air mass and an expected value of $(\overline{\sigma_T} - \overline{\sigma_0})$ is computed based on mean conditions, then an estimate can be made for $(\overline{\sigma_0} - \overline{\sigma_T})$ for the cases when $\sigma_T < \sigma_0$. This estimate is that $(\overline{\sigma_0} - \overline{\sigma_T})$ equals ∿3.7°K/km. This indicates a very stable capping layer for the cases when $\sigma_0 > \sigma_T$. This conclusion relies on the above estimate only in degree and not in substance. The stability of the over-cloud layer when $\sigma_0 > \sigma_T$, is much greater for the thin cloud cases when compared to the corresponding thick cloud cases. Whereas the interpretation that these cases represent cloud layers capped by a frontal zone is somewhat open to question, as noted previously for the thick cloud cases; it is much more plausible here, given the estimated magnitude of $\overline{\sigma_0}$ for the thin cloud cases. The estimated value of $\overline{\sigma_0} \simeq 7$°K/km for the thin cloud

cases where $\sigma_0 > \sigma_T$, corresponds to a temperature lapse rate of only ∿4.5°K/km. Radiative and evaporative processes may be responsible for the evolution of this structure.

In an average season, the value of σ_S is greater than σ_T in 57% of the cases. The difference $\overline{\sigma_T} - \overline{\sigma_S}$ is relatively small and equal to ∿0.2°K/km. This difference is expected to be ∿ -0.1°K/km if both layers exist in the same air mass. If this is correct for the thin cloud cases, where $\sigma_T < \sigma_S$; then for the cases where $\sigma_S < \sigma_T$, the difference may be estimated to be ∿0.6°K/km. This implies that, for the structures exhibiting either maximum stability in the cloud-top layer or increasing stability with height, the cloud-top layer is somewhat more stable than the sub-cloud layer but not so stable as to suggest a frontal zone.

In light of the above arguments, the observed stratifications for the thin cloud cases may be interpreted in an average sense for a mean season. The structure with decreasing stability with height through the three layers appears to be associated with the situation of all three layers existing in the same air mass. There is no indication of a frontal zone in the sub-cloud layer for this structure as there is for the thick cloud cases. Also, where this structure was the most frequently observed stratification for the thick cloud cases, it is the least frequently observed for the thin cloud cases. The stratification where minimum stability is observed in the cloud-top layer of thin clouds corresponds to the situation where the cloud layer and sub-cloud layer are located in the same air mass. A very stable layer is observed in the over-cloud layer and no indication of a frontal zone is found for the sub-cloud layer. The structure with increasing

stability with height, also, shows the very stable over-cloud layer and no sub-cloud front. The enhanced stability of the cloud-top layer, i.e. 0.6°K/km greater than σ_S is most likely due to small errors in the location of the cloud-top level. This interpretation seems reasonable given the very stable nature of the over-cloud layer. This interpretation leads to the conclusion that $\overline{\sigma_T}$ has been overestimated. For the structure with maximum stability in the cloud-top layer, the cloud-top layer and over-cloud layer appear to be located in the same air mass due to the small decrease with height of dry static stability for the layers. However, the stability of the cloud-top layer is not sufficiently great to warrant an interpretation based on the presence of a frontal zone. It is possible that errors in the location of the cloud-top level together with radiative and evaporative effects lead to the observed maximum. In any event, this stratification is very similar to the decreasing stability with height structure except for the weak maximum, i.e. none of the three layers exhibit sufficient stability for a frontal zone.

Combining the above results, the conclusions from the analysis of the stratification about thin cloud layers may be summarized as:

1. In ∿60% of the cases, a very stable mean over-cloud layer exists, whose stability strongly suggests the presence of a front, i.e. $\sigma_0 \sim 7$°K/km.
2. In the other 40% of the cases, the presence of a frontal zone or a very stable layer is not indicated for any of the three mean layers. However, in 60% of these cases there is an indication of enhanced stability in the vicinity of mean cloud-top level.

3. It is likely that, when maximum stability is observed to increase with height through the three layers, the location of cloud-top is slightly in error. If this is true, then $\overline{\sigma_T}$ has been overestimated. If the magnitude of this error is estimated from mean conditions, then a corrected value of $\overline{\sigma_T}$ may be computed, which is slightly less than $\overline{\sigma_S}$.

The above inferences for the thin cloud cases are nearly equally valid for any season. The conclusions for both the thin and thick cloud cases are based upon observed means and the relative frequency of occurrence of various structures. It must be emphasized that they only apply to the average case exhibiting such a structure.

3.1.c. Relative Frequency Distributions of Stability

As was stated previously, any possible stability stratification may be observed for these three layers for a cloud case. In fact, the observed stability values range over a wide domain. Conditions ranging from super-adiabatic to strong inversions are observed in each of the three layers in each season. Errors in the location of cloud-top pressure have been assumed to account for some of the observations of stable cloud-top layers. At this point, it is appropriate to examine the observed distribution of dry static stability for each layer.

In Figure 6, the observed relative frequency of occurrence is given for various stability classes. In each panel, the distributions are given for each season for one of the three layers for a particular cloud thickness group. Each class represents a 1°K/km range of observed dry static stability, except for class 1. Cases included in class 1 correspond to observations of super adiabatic or dry adiabatic

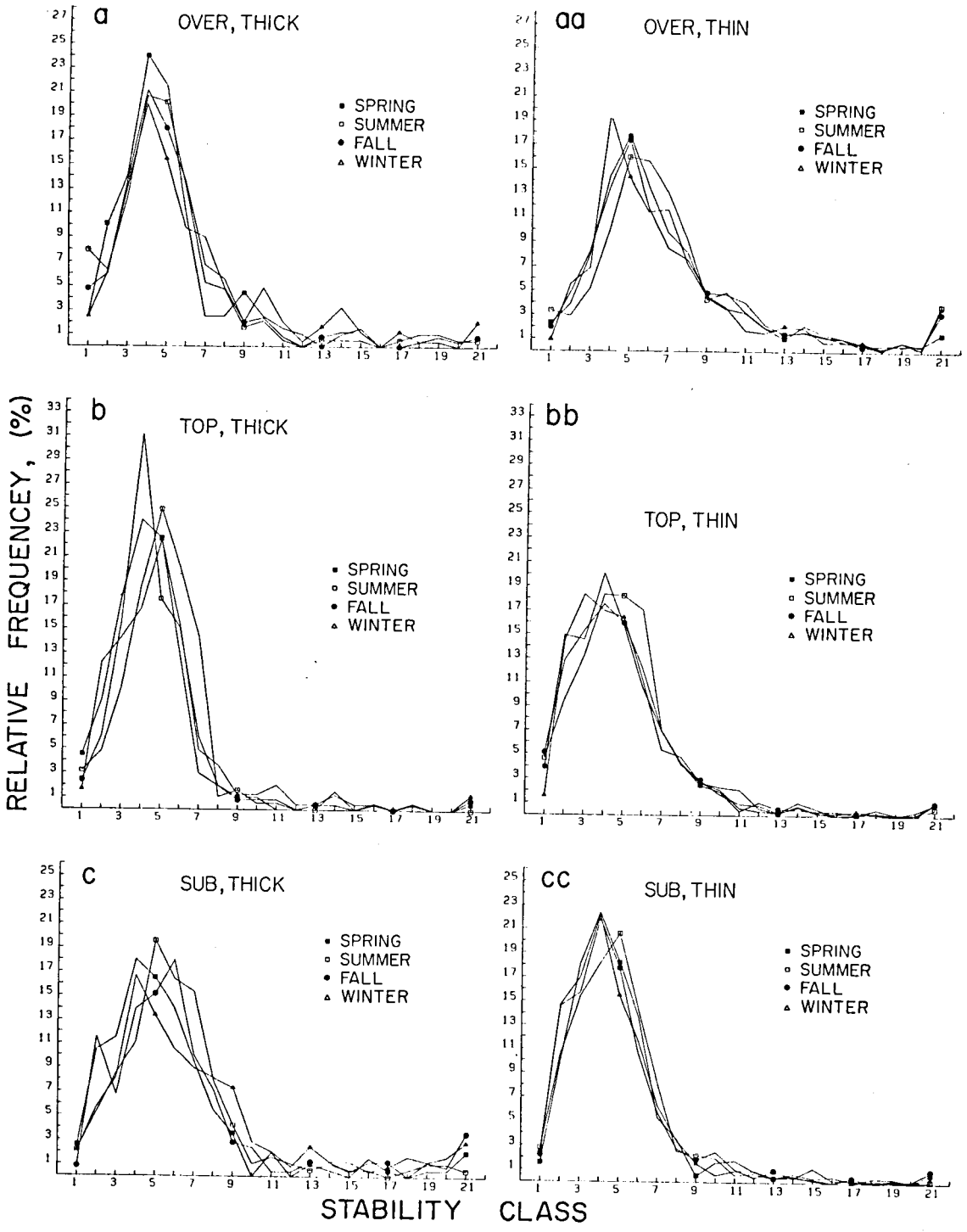

Figure 6. Relative frequency of occurrence of various stability classes for each season for the thick cloud cases for each layer, (i.e. (a) over-cloud layer, (b) cloud-top layer, (c) sub-cloud layer) and, similarly, for the thin cloud cases (i.e. (aa), (bb) and (cc), respectively). See text for definition of stability classes and further explanation.

conditions, i.e. $\sigma \lesssim 0°K/km$. Class number 2 includes observations where $0°K/km < \sigma \lesssim 1°K/km$. Similarly, class N includes cases where $(N-2)°K/km < \sigma \lesssim (N-1)°K/km$. Note that class 2 represents cases, where conditions are approximately moist adiabatic for the pressure and temperature domain of these cloud cases. Some of the cases included in class 3 may also correspond to moist adiabatic conditions. In general for this domain, class 14 corresponds to near isothermal conditions in a layer, though some cases in classes 13 and 15 may also show this due to their respective pressure levels. Classes 16 through 21 correspond to cases exhibiting an inversion in the layer with the strength of the observed inversion increasing with class number, e.g. class 21 includes cases where temperature typically increases at a rate of greater than $\sim 5°K/km$ from the base to the top of the layer. In order to facilitate the consideration of these data, the corresponding cumulative frequency distributions are given in Figures 7 and 8 for the thick cloud cases and for the thin cloud cases, respectively. The relative frequencies are accumulated progressively from class 1 through class 21, e.g. the cumulative frequency plotted for class 3 corresponds to the sum of the relative frequencies of classes 1, 2 and 3. In each panel, the observed distributions for each of the layers are given for a particular season and cloud thickness group.

In general, the relative frequency distributions are broader for the thin cloud cases in the over-cloud layer and the cloud-top layer, when compared to the thick cloud cases. The opposite is true of the sub-cloud layer. Narrow distributions correspond to uniform conditions observed on a case by case basis. In winter, the distributions tend to be broader than in other seasons. There is also a tendency for a seasonal shift in the distributions, i.e. the summer peak is generally to

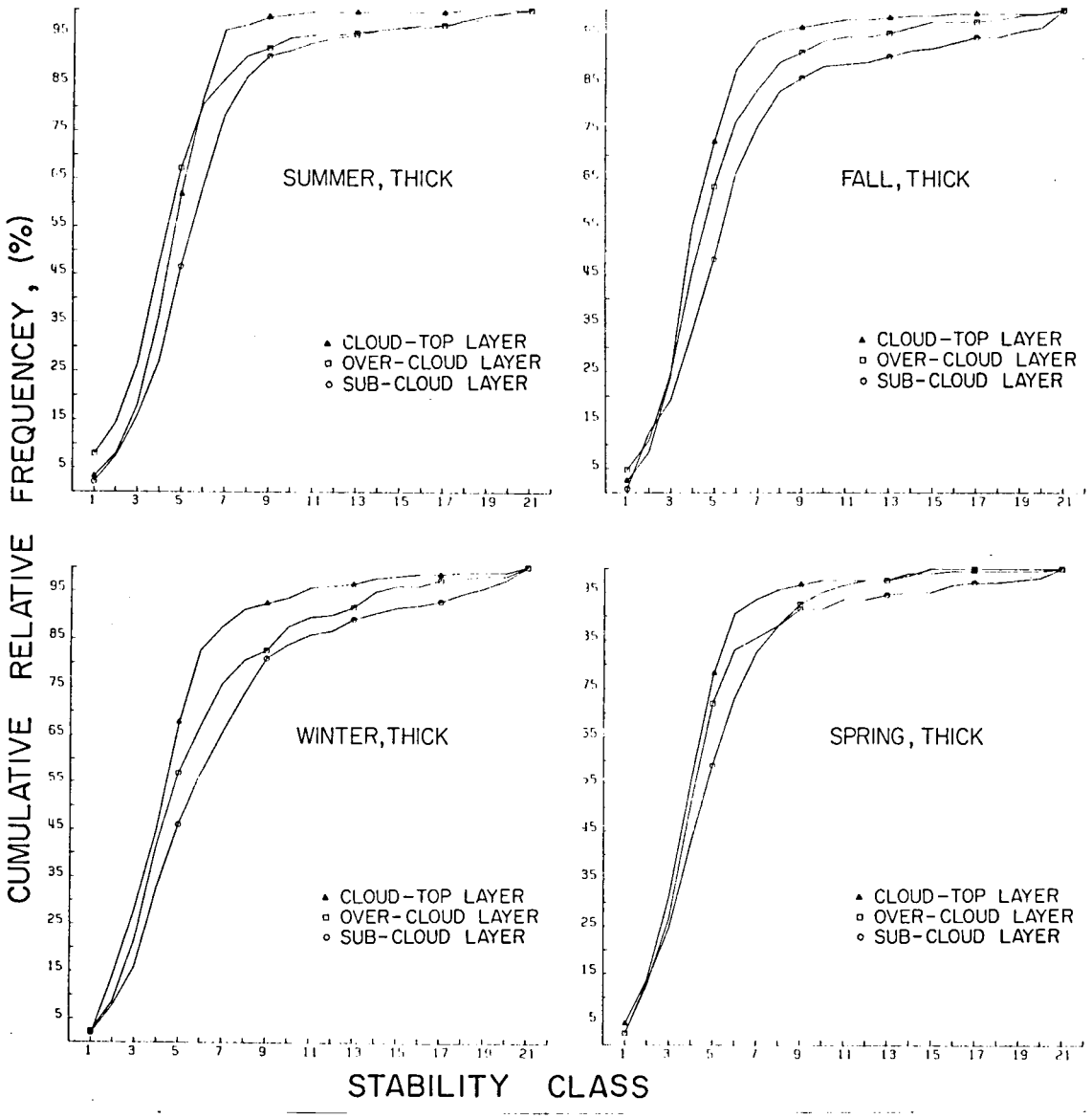

Figure 7. Cumulative relative frequency distributions of stability class for the thick cloud cases for each of the over-cloud, cloud-top and sub-cloud layers. See text for further explanation.

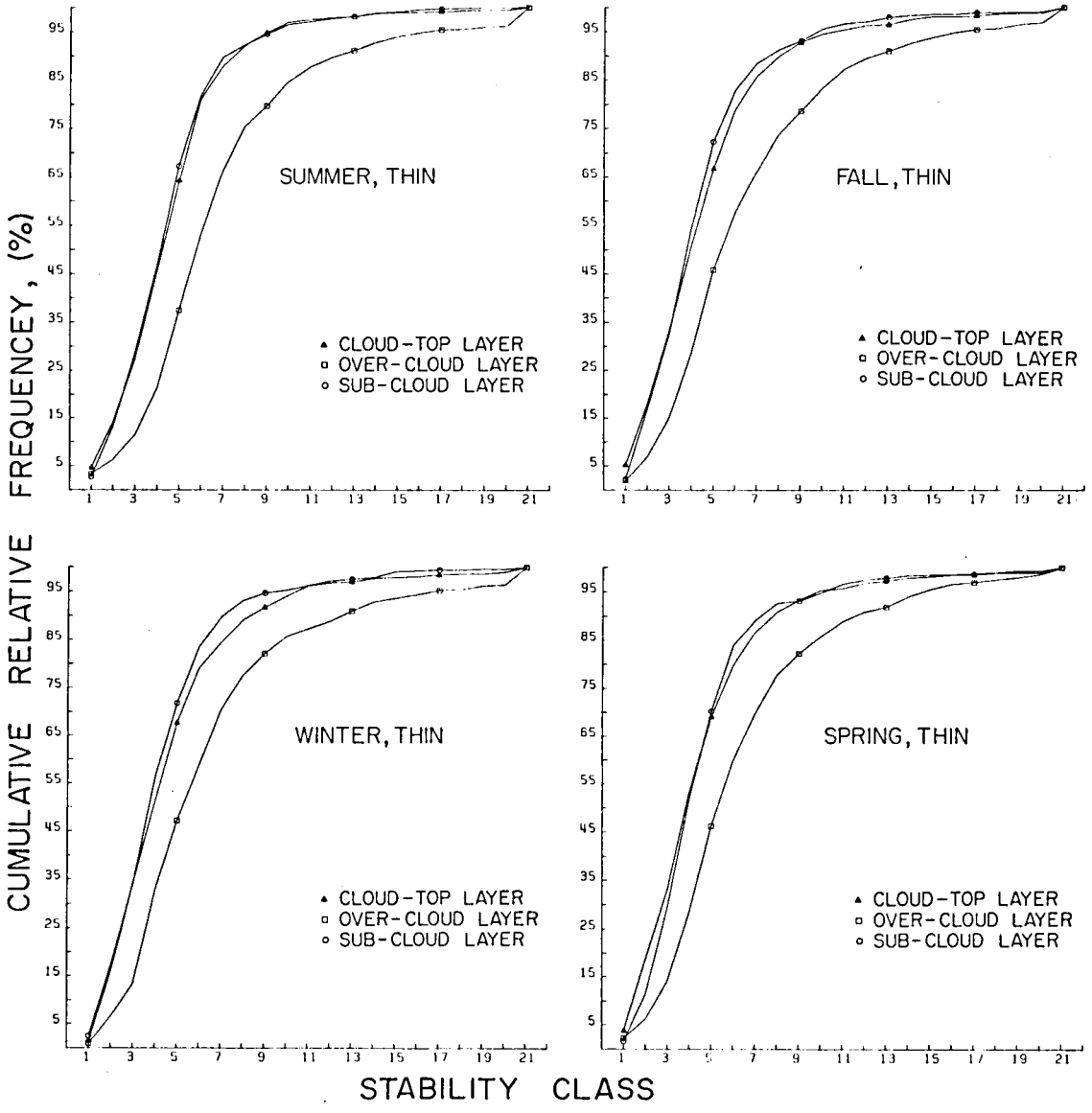

Figure 8. Same as for Figure 7, except for thin cloud cases.

the right and the winter peak tends to be to the left of the peaks for spring and fall. It should also be noted that the over-cloud layer distributions show a relatively large frequency of very stable conditions, especially for the thin cloud cases. The sub-cloud layer distributions for the thick cloud cases, also, exhibit a relatively large frequency of very stable conditions.

The median values of σ_0, σ_T and σ_S (i.e. cumulative frequency = 50%, see Figs. 7 and 8) exhibit the same relative pattern as the mean values depicted in Figure 5, except for thick cloud cases in summer. However, the differences between the median values of σ_0, σ_T and σ_S for a given season are smaller than noted for the means. Thus, the relative frequency of very stable conditions for the various layers has a substantial influence on the computed means. The median values of σ_T and σ_S for the thin cloud cases are within 1 to 2°K/km of the stability associated with moist adiabatic conditions, while the median values of σ_0 are an additional 1.5°K/km more stable. For the thick cloud cases, the median values of σ_T and σ_0 are within 1 to 2°K/km of moist adiabatic conditions, while the median value of σ_S is an additional 1°K/km more stable. Note that dry adiabatic or super adiabatic conditions tend to be most common in the over-cloud layer for the thick cloud cases and in the cloud-top layer for the thin cloud cases, when compared to the other layers.

For the thin cloud cases, the cumulative relative frequency distributions for the sub-cloud layer and the cloud-top layer are very similar. There is a slight tendency for the cloud-top layer to exhibit more extreme values, when compared to the sub-cloud layer. Fewer than 5% of the observations of σ_T or σ_S indicate isothermal or inversion

conditions. The distributions for σ_0 are substantially different. Approximately 10% of the observations of σ_0 correspond to isothermal or inversion conditions. Moderately stable to very stable conditions dominate the σ_0 distributions. The σ_0 distributions for the thin cloud cases are the most stable of all the layers for either thickness group.

Noting the distributions for the thick cloud cases, in no season do two layers exhibit the degree of similarity seen between the cloud-top and sub-cloud layers for the thin cloud cases. Also, no two layers are as different as the over-cloud and cloud-top layers for the thin cloud cases. The seasonal variation in the distributions is greater than for the thin cloud cases. In summer, the over-cloud layer and the sub-cloud layer exhibit very stable conditions in nearly the same percentage of cases, while in the other seasons the sub-cloud layer is approximately twice as likely to show this. As in the thin cloud distributions, the cloud-top layer exhibits very stable conditions, i.e. isothermal, less than $\sim$5% of the time.

3.2 Vertical Wind Shear

The results of the analyses of the vertical shear of the horizontal wind speed in the cloud-top layer, S_T; the over-cloud layer, S_0; and the sub-cloud layer, S_S, are presented in this section. Recall that the wind direction is ignored in these analyses.

Considering the sign of the shear, it is apparent that negative shear occurs relatively infrequently in these layers. For the thin cloud cases in a given season, the relative frequency of occurrence of negative shear is nearly the same for each layer. Seasonal variation is also negligible, except for the summer season, where

approximately 20% of the cases exhibit negative shear in a given layer compared to 15 to 16% in the other seasons. The thick cloud cases have both a more pronounced seasonal variation and more significant differences between the layers in a given season, than the thin cloud cases. For the thick cloud cases, S_T; S_0 and S_S are negative in 11, 11 and 14% of the winter cases; in 13, 15 and 18% of the fall cases; in 17, 19 and 26% of the spring cases; and in 17, 24 and 29% of the summer cases, respectively. Thus, as in the thin cloud cases, negative shear occurs most frequently in the summer for each layer. Negative shear is least likely in winter and the cloud-top layer is the layer least likely to exhibit negative shear in each season for the thick cloud cases. However, the difference between this layer and the over-cloud layer is relatively small except in summer. Differences between the cloud-top layer and the sub-cloud layer are larger and are most pronounced in spring and summer. Thus, for a given cloud thickness group in a given season, the relative frequency of negative shear does not vary substantially among layers in close proximity, i.e. all three layers of the thin cloud cases or the upper two layers for the thick cloud cases.

In terms of the relative frequency of occurrence of negative shear in the three layers for the thick cloud cases, spring is more similar to summer than to fall and fall is more similar to winter than to spring. The seasonal variation for the thick cloud cases may be at least partly explained by noting that the thick cloud is likely to occur in a region of strong or deep vertical lifting in the middle and upper levels, i.e. in association with either an elevated warm front or to a lesser degree an elevated cold front of a cyclone. This is

particularly true in the cold seasons. This region is located near the fastest upper level flow associated with the cyclone, i.e. the jet stream core, whose strength is coupled to the cyclone intensity. The intensification of the flow, particularly at high levels, over the region of strong uplift makes positive shear more likely in layers below the jet stream level and above the front. Thus, the seasonal cycle in cyclone intensity and the associated upper level flow may produce the observed seasonal variation in the relative frequency of negative shear for thick cloud layers. Since the thin cloud is likely to occur in a region of weak vertical lifting, seasonal changes in cyclone intensity are more likely to affect the areal extent than the shear environment of the thin clouds. This is because even though a more intense cyclone has a stronger jet core and a larger area of faster flow, the region of strong uplift is larger and, thus, the weak uplift region is located farther away from the jet core compared to the less intense cyclone case.

Another factor, which might influence the seasonal cycle, is the role of vertical transport of water by deep convection in the formation of some of these clouds. Deep convection is most common in summer and spring, less common in fall and rare in winter for this domain. Thus, the seasonal cycle of deep convection resembles the seasonal variation in the relative frequency of negative shear for the thick cloud cases. Deep convection tends to occur in close proximity to a cold front at the surface and the associated upper level jet stream, particularly in spring. This region is generally upstream from the jet maximum and is not in an area of strong middle or upper level large-scale lifting. Horizontal propagation of the convection away

from the surface front or horizontal transport of water after injection into the middle and upper levels may cause the outflow cloud layer to exist away from under the jet core. Thus, if deep convection is important in the formation of some of these thick cloud cases, then these cases may exist in a substantially different environment in terms of large-scale vertical motion and the strength of the upper level flow compared to cases associated with elevated fronts, which are typical of the winter season.

There are eight possible configurations for the sign of the shear in the three layers of a given cloud case. In Table 3, the observed relative frequency of occurrence for each of these configurations is given for each season for the thick cloud cases, (a), and for the thin cloud cases, (b). The predominance of positive shear may be further emphasized by noting that positive shear of the horizontal wind speed is observed in two or more of the three layers in 84% to 94% of the thick cloud cases and in 86% to 92% of the thin cloud cases depending on the season. Positive shear in all three layers is the most common configuration in every season for either cloud thickness group. Nearly one-half to greater than two-thirds of the cases exhibit this structure in a given season for either group. The next most likely configurations are those involving negative shear in only one of the layers. For the thin cloud cases, none of these three structures is significantly more likely than any other, except in summer. In fact, the spring, winter and fall seasons show almost no seasonal variability in the relative frequency of any given configuration. This lack of seasonal variability in the occurrence of the different configurations corresponds exactly to the result noted above, from the analysis of

(a)

Thick Cloud Cases

S_0,	S_T,	S_S	Su	F	W	Sp	Average	Range
+	+	+	47	63	70	51	58	23
+	+	-	19	14	11	16	15	7
-	+	+	9	7	6	12	9	6
-	+	-	8	2	1	4	4	7
+	-	+	9	6	7	8	7	3
+	-	-	1	2	1	5	2	4
-	-	+	6	5	3	4	4	3
-	-	-	1	1	1	0	1	1

(b)

Thin Cloud Cases

			Su	F	W	Sp	Average	Range
+	+	+	56	65	65	66	63	9
+	+	-	13	9	9	7	10	5
-	+	+	10	10	8	10	10	2
-	+	-	2	1	2	1	2	1
+	-	+	7	8	7	8	7	1
+	-	-	5	3	4	2	3	3
-	-	+	5	3	4	4	4	2
-	-	-	2	1	1	2	1	1

Table 3. Relative frequency of occurrence in percent of cases having various configurations for the sign of the vertical shear of the horizontal wind speed in the over-cloud, cloud-top and sub-cloud layers, i.e. sign of S_0, S_T and S_S, respectively, for each season (a) for thick cloud cases and (b) for thin cloud cases. Values for the average season and the seasonal range are also given for each configuration.

the sign of the shear in each layer independently. In summer, the configuration with negative shear in only the sub-cloud layer is somewhat more likely than in other seasons and the configurations with negative shear in at least two layers tend to be slightly more common. The relative frequency of occurrence for the other two structures with positive shear in only two of the layers does not change significantly even in summer, i.e. only the structure with all positive shear is less likely in summer.

For the thick cloud cases, the seasonal range of relative frequency for each configuration is larger than for the thin cloud cases. In general, the spring/fall season values are most similar to the summer/winter values. These results are the same as those derived from the analysis of each layer independently. Other than the seasonal variation, the primary difference between the thick and thin cloud cases is that the structure with negative shear in only the sub-cloud layer is substantially more likely for the thick cloud cases in all seasons. Considering the average of the seasonal values, the increased frequency of this structure is almost equal to the decreased frequency of the structure with all positive shear compared to the thin cloud cases. This is not true on a season by season basis, where the relative frequency of occurrence for the other structures with at least one positive shear layer and negative shear in the sub-cloud layer are also somewhat different, when comparing the thin and thick cloud cases.

For the analysis of the magnitude of the vertical shear of the horizontal wind speed in each of the three layers, cases exhibiting positive shear and cases exhibiting negative shear in the layer of

interest are considered independently. The following discussion is limited to seasonal means. As in the case of the dry static stability, the means encompass quite a wide range of observed values. The standard deviations for the various means typically range from nearly equal to the mean to approximately twice the mean value. In Table 4, the average shear in each layer for each season is given for cases with positive shear in the layer, $\overline{S_+}$, and for cases with negative shear in the layer, $\overline{S_-}$, for the thick cloud cases (a) and for the thin cloud cases (b). The values of $\overline{S_+}$ and $\overline{S_-}$ may be combined with the corresponding observed relative frequency of occurrence given above to obtain either $\overline{S}$ or $\overline{|S|}$, i.e. the seasonal mean shear or the seasonal mean magnitude of the shear, respectively.

Considering $\overline{S_+}$, both the thick cloud and thin cloud cases show a maximum in winter, a minimum in summer, and spring values larger than fall values for each layer. The seasonal pattern for $\overline{S_-}$ is somewhat more confused. Due to the small relative frequency of negative shear, the pattern for $\overline{|S|}$ resembles that for $\overline{S_+}$ very closely. The seasonal range of $\overline{S_-}$ is generally less than one-half that of $\overline{S_+}$ for each layer for either thickness group. Thus, the seasonal cycle in cyclone intensity and speed of the upper level flow affects the positive shear cases much more than the negative shear cases. As in the case of the sign of the shear, the thick cloud cases have a substantially greater seasonal range in both $\overline{S_+}$ and $\overline{S_-}$ for a given layer, when compared to the thin cloud cases. This supports the earlier conclusion based on the analysis of the sign of the shear, that the thin cloud cases are not as sensitive as the thick cloud cases to the seasonal cycle in cyclone intensity. In general, $\overline{S_+}$ is greater and $|\overline{S_-}|$ is less for the

(a)

Thick Cloud Cases

	Su	F	W	Sp
O	4.0	4.9	6.5	6.1
	-4.5	-4.9	-5.5	-4.6
T	3.3	4.8	6.5	5.5
	-3.8	-4.5	-5.4	-4.6
S	4.1	5.1	6.8	5.5
	-5.7	-5.0	-5.5	-4.4

(b)

Thin Cloud Cases

	Su	F	W	Sp
O	4.1	4.7	6.0	4.9
	-5.3	-5.4	-4.9	-5.2
T	3.8	4.6	5.4	5.2
	-5.0	-5.4	-5.9	-5.9
S	3.4	4.7	5.4	5.1
	-5.3	-5.4	-5.4	-4.7

Table 4. Mean vertical shear of the horizontal wind speed in m/s/km for each season (a) for thick cloud cases and (b) for thin cloud cases for the over-cloud, cloud-top, and sub-cloud layers, i.e. O, T and S, respectively. The positive entries are the means for cases with positive shear in that layer, i.e. $\overline{S_+}$, and the negative entries are the means for cases with negative shear in that layer, i.e. $\overline{S_-}$.

thick cloud cases, when compared to the thin cloud cases for a given season and layer. For the thin cloud cases, $|\overline{S_-}| > \overline{S_+}$ in most instances, while except in summer, $\overline{S_+} > |\overline{S_-}|$ for the thick cloud cases. Thus, in the mean for a season, when negative shear occurs in one of the layers of a thin cloud, the magnitude of the shear tends to be greater than when positive shear occurs in that layer. This is a surprising result.

For the thick cloud cases, the minimum values of $\overline{S_+}$, $|\overline{S_-}|$, and $\overline{|S|}$ occur in the cloud-top layer for each season except in spring, where the minimum values of $|\overline{S_-}|$ and $\overline{|S|}$ occur in the sub-cloud layer. The maximum values occur in the sub-cloud layer in each season except spring, where the maximum values of $|\overline{S_-}|$ and $\overline{|S|}$ occur in the cloud-top layer. For the thin cloud cases, the maximum values of $\overline{S_+}$ and $\overline{|S|}$ occur in the over-cloud layer in each season except spring, where the maximum values occur in the cloud-top layer. The maximum value of $|\overline{S_-}|$ occurs in the cloud-top layer in each season except summer, where it occurs in the sub-cloud layer. The pattern for minimum values of $\overline{S_+}$, $|\overline{S_-}|$ or $\overline{|S|}$ is confused. Except in winter, the difference between the maximum and minimum values of either $\overline{S_+}$, $|\overline{S_-}|$ or $\overline{|S|}$ observed for the three layers in a season is larger for the thick cloud cases than for the thin cloud cases. Thus, more variability between the layers is observed for the thick cloud cases than for the thin cloud cases, except in winter.

On a case-by-case basis, four possible structures for the magnitude of the shear may occur. These are: maximum $|S|$ in the cloud-top layer, decreasing $|S|$ with height through the three layers, increasing $|S|$ with height, and minimum $|S|$ in the cloud-top layer. In Table 5,

(a)

Thick Cloud Cases

	Su	F	W	Sp	Average	Range
$\|S_T\| \gtrsim \|S_0\|$ and $\|S_S\|$	32	33	31	28	31	5
$\|S_S\| > \|S_T\| \gtrsim \|S_0\|$	18	22	20	22	20	4
$\|S_0\| > \|S_T\| \gtrsim \|S_S\|$	16	19	23	17	19	7
$\|S_T\| < \|S_0\|$ and $\|S_S\|$	34	26	26	33	30	8

(b)

Thin Cloud Cases

	Su	F	W	Sp	Average	Range
$\|S_T\| \gtrsim \|S_0\|$ and $\|S_S\|$	34	34	33	37	34	4
$\|S_S\| > \|S_T\| > \|S_0\|$	20	22	21	22	21	2
$\|S_0\| > \|S_T\| \gtrsim \|S_S\|$	20	20	21	22	21	2
$\|S_T\| < \|S_0\|$ and $\|S_S\|$	26	24	25	19	24	7

Table 5. Relative frequency of occurrence in percent of cases having various relative configurations of the magnitude of the vertical shear of the horizontal wind speed in the over-cloud, cloud-top and sub-cloud layers, i.e. $|S_0|$, $|S_T|$ and $|S_S|$, respectively, for each season. Values for the average season and the seasonal range are also given for each configuration.

the observed relative frequency of occurrence of each of these structures for each season for both the thick cloud cases (a) and the thin cloud cases (b) is given.

The seasonal variability of the relative frequency of occurrence of each structure is larger for the thick cloud cases than for the thin cloud cases. The two most commonly observed structures for the thick cloud cases in each season are those with either maximum or minimum shear magnitude in the cloud-top layer. On an annual basis, they are ∿50% more likely than the other two structures. In spring, the structure with maximum |S| in the cloud-top layer is somewhat less likely than in the other seasons. The structure with minimum shear in the cloud-top layer is substantially less likely in fall and winter when compared to spring and summer, where it is the most commonly observed structure. This structure corresponds to the mean structure for each season, noted above, which was derived from the analysis of each layer independently. Thus, in fall and winter, the most likely structure does not correspond to the observed mean structure. If the cases of increasing or decreasing |S| with height can be assumed to cancel in the computation of the mean structure, this implies that if a typical case with minimum |S| in the cloud-top layer is compared to a typical case with a maximum |S| in the cloud-top layer, the minimum would be more pronounced than the maximum.

For the thin cloud cases, the structure with maximum |S| in the cloud-top layer is the most likely structure in each season. The observed relative frequency of occurrence for each structure is nearly constant with respect to season except in spring where the structure with minimum |S| in the cloud-top layer is less likely and the

structure with maximum |S| in the cloud-top layer is more likely than in the other seasons. This is opposite to what is observed in the thick cloud cases. Except in spring, the most likely structure for the thin cloud cases does not correspond to the mean structure for a season, given in Table 4b.

3.3 Richardson Number

The results of the analyses of the Richardson number in the over-cloud, cloud-top, and sub-cloud layers, i.e. R_0, R_T and R_S, respectively, are discussed in this section. Richardson numbers for the 350 mb to 450 mb layer, R_4, and the 650 mb to 750 mb layer, R_7, are also considered.

Seasonal mean Richardson number for a layer is not a very useful quantity. This is primarily due to the inverse-square dependence of R on the vertical wind shear, S. For cases where S is small, R is very large and greatly affects the means and corresponding standard deviations. For these analyses, if S = 0 or if $R \geq 60$, then R is arbitrarily set equal to 60. For all the layers considered, both the seasonal mean Richardson numbers and the corresponding standard deviations are largest in summer and smallest in winter. The fall and spring values are generally close to the winter values, i.e. always closer to winter than to summer. For the thick cloud cases, the values of $\overline{R_0}$, $\overline{R_T}$ and $\overline{R_S}$ each range from $\sim$12 to $\sim$18 with corresponding standard deviations of from $\sim$19 to $\sim$31. For the thin cloud cases, the value of $\overline{R_0}$ ranges from $\sim$14 to $\sim$19 with standard deviations of from $\sim$18 to $\sim$24, respectively. The values of $\overline{R_T}$ and $\overline{R_S}$ each range from $\sim$13 to $\sim$16 with standard deviations from $\sim$18 to $\sim$22, respectively. The values of

$\overline{R_4}$ and $\overline{R_7}$, each range from ∿14 to ∿16. The analysis of Richardson number over thick layers, such as for R_4 and R_7, is not very interesting. Less than 1% of all sondes have either R_4 or R_7 values within a factor of two of the turbulence threshold, i.e. $R \lesssim 0.5$. This result is unchanged if only cloud case sondes are used. The percentage of all sondes exhibiting values of R_7 or R_4 less than or equal to 4.0 ranges from ∿10% to ∿30% for R_4 and from ∿15% to ∿20% for R_7 with the minimum values occurring in summer and the maximum values occurring in winter. These values are increased by a couple of percentage points, if only cloud case sondes are used.

For the following discussion, no distinction is made between thick and thin cloud cases. Differences between these groups are considered later. In Figure 9, the relative frequency of occurrence of cloud cases with Richardson number less than or equal to a given value in each of the over-cloud, cloud-top, and sub-cloud layers is given for both the summer and winter seasons. Similar plots for fall and spring lie between the corresponding winter and summer curves and are generally closer to the winter curve. In summer, a higher percentage of the cloud cases have values of R_0, R_T and R_S less than or equal to 0.25, when compared to the winter season. However, the winter cases show a larger relative frequency of R_0, R_T and R_S less than or equal to 4.0, i.e. relatively small Richardson number, when compared to the summer season. In all seasons, the relative frequency of cases with Richardson number less than some given value is greatest for the cloud-top layer and smallest for the over-cloud layer. This does not hold for the smallest Richardson numbers, as in winter, the sub-cloud layer most frequently exhibits values less than ∿0.2 and in summer, the

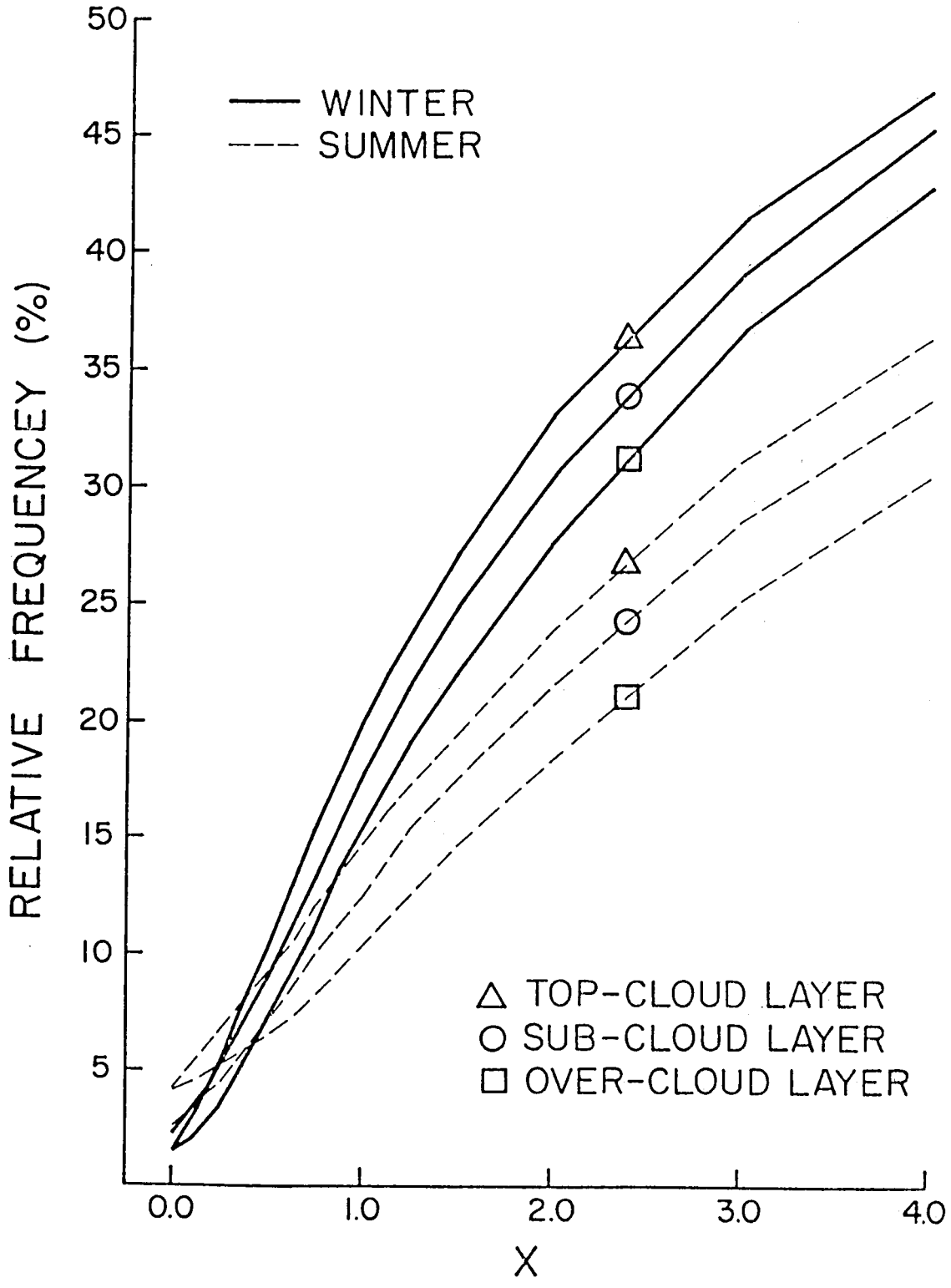

Figure 9. Relative frequency of occurrence of cloud cases having Richardson number less than or equal to X for each of the over-cloud, cloud-top and sub-cloud layers in winter and in summer.

sub-cloud layer least frequently exhibits values less than ∿0.4. The cloud-top layer possesses the maximum Richardson number of the three layers in nearly 40% of the cases in an average season. However, in nearly 35% of the cases, minimum Richardson number is observed in this layer.

The data shown in Figure 9 and the preceeding discussion are most applicable to the thin cloud cases due to the dominance of these cases in the total cloud case sample. For the thick cloud cases, the smallest values of Richardson number tend to be less common for the sub-cloud and cloud-top layers and more likely for the over-cloud layer, when compared to the thin cloud cases. The differences in relative frequency amount to less than 3% between the two groups at Richardson numbers less than 0.5 in each season. Considering cases exhibiting Richardson numbers less than or equal to 4.0, the same pattern is found though the differences between the thin and thick cloud cases for a given layer are larger, i.e. ∿12% maximum difference.

A Richardson number of ∿0.25 or less for the mean flow is required for turbulence and turbulent transports to be maintained by the mean flow. Since only a small percentage of these cases exhibit such small Richardson numbers, it is concluded that, in general, these clouds are not formed as a result of widespread turbulence generated by the mean flow. The Richardson number quantifies the relative importance of buoyancy forces and mechanical forces, i.e. shear, in the production of turbulent kinetic energy and, thus, also the turbulent energy transports. Considering the cloud-top layer, in only 20% of the winter cases and in only 15% of the summer cases, is the mechanical production greater than or equal to the buoyancy production. Thus, in

general, buoyancy forces are the more dominant factor influencing the production of turbulent kinetic energy and the associated convective energy transports for middle and upper tropospheric stratiform clouds. Therefore, it is primarily thermal perturbations and not wind speed perturbations that are responsible for vertical eddy circulations within these clouds.

These analyses seem to be sensitive to the vertical resolution of the data set. This may be seen by comparing the relative frequency of the very small values of Richardson number, i.e. $\lesssim 0.25$, for the cloud-top layer to that of the 350 mb to 450 mb layer for cloud case sondes. The difference in relative frequency is more than an order of mangitude. The mean cloud-top layer is $\sim \frac{1}{3}$ the pressure thickness of the 350 mb to 450 mb layer. It is possible that with better vertical resolution, the smallest values of Richardson number may occur more frequently. However, since all significant levels are included in the rawinsonde data set, we suggest that this problem in minor.

Recall that slight errors in the location of cloud-top pressure were hypothesized based on the analysis of dry static stability, i.e. Section 3.1. If this is true, then the effect on the frequency distribution of Richardson numbers is to reduce the relative frequency of small values for the over-cloud layer and increase the relative frequency of small values for the cloud-top layer. It is unlikely that these adjustments would substantially alter the above conclusions.

4. SUMMARY AND CONCLUSIONS

This study characterizes the static environment of middle and upper tropospheric stratiform clouds as deduced from rawinsonde data from 24 continental U.S. stations between 30°N and 50°N latitude for the year 1977. The analyses are limited to pressures less than 500 mb and temperatures between 0°C and -40°C. Thus, primarily ice-phase cloud forms are considered. Computed relative humidity with respect to ice is used to diagnose the presence of a cloud layer. Good agreement is found between climatological estimates of seasonal mean middle and upper tropospheric cloud cover deduced from surface observations and estimates based on this technique.

Thin cloud layers and thick cloud layers are treated independently. A saturated layer which is less than or equal to 50 mb thick is designated as a thin cloud case. Otherwise, the saturated layer is defined as a thick cloud case. The analyses are performed on a seasonal basis. No regional distinctions are attempted.

Three layers are defined for the analysis of a cloud case. These are the uppermost saturated layer, the next higher layer and the layer below the lowest saturated layer, i.e. the cloud-top layer, the over-cloud layer and the sub-cloud layer, respectively. Cloud cases with missing data at any of the levels defining these layers are eliminated from the analyses. Over 3600 cloud cases qualified for the analysis. For each of the layers, the dry static stability, the vertical shear of the horizontal wind speed and the atmospheric analog of the Richardson number are computed. Seasonal means for each of these quantities for both cloud thickness groups are presented. The

corresponding relative frequency distributions are also presented for some of these quantities. In addition, various structures for each parameter are defined in terms of the relative values of the parameter in each of the three layers, e.g. increasing stability with height through the three layers. The relative frequency of occurrence of these structures is presented for each season and thickness group.

A number of different conceptual models of the stability stratification and shear structure associated with these cloud forms are briefly reviewed. This study attempts to establish (in a quantitative way) the applicability of each of these models for the domain of this analysis.

On a case by case basis, the observed values of the dry static stability, the vertical shear of the horizontal wind speed and the Richardson number may vary over quite large ranges for each layer for either cloud thickness group. The observed stability stratification and vertical wind shear structure about cloud layers is found to be quite variable. Cloud cases exhibiting structures corresponding to each of the different conceptual models may be found in all seasons for both cloud thickness groups. Some structures are found to be substantially more common than others. Some of the observed variability may possibly be explained as arising from errors in locating the actual cloud-top level. These errors may arise due to the differing response rates of the humidity and temperature sensors, (i.e. hysterisis of the humidity sensor may lead to an indication of continuing saturation for a small distance after the sonde has exited the cloud layer). However, the corresponding indicated temperatures and, thus, stability

pertain to the over-cloud layer as the response of the temperature sensor is much faster, especially for these temperatures and pressures.

The major conclusions resulting from these analyses are presented below.

1. In all aspects, the thick cloud cases exhibit larger seasonal variability, than the thin cloud cases. Since cyclone intensity and the associated upper level flow undergo substantial seasonal cycles, it is concluded that the environment of thick middle and upper level cloud forms is much more strongly tied to cyclone intensity than that associated with thin cloud forms.
2. Buoyancy forces are the primary factor influencing the generation of turbulent kinetic energy, and, hence are the primary forces maintaining the vertical transports in middle and upper tropospheric clouds. In only 15-20% of the cloud cases is the mechanical generation, i.e. shear production, of turbulent kinetic energy of equal or greater magnitude. Only rarely is production greater than dissipation of turbulent kinetic energy in the mean flow. Thus, the turbulent energy transports associated with these cloud forms do not result from turbulence maintained by the mean flow.
3. Thick Cloud Layers
   a. The classical model of the cloud layer existing just above an elevated frontal zone is appropriate

for a majority of the thick cloud cases. However, a substantial portion of the cases do not exhibit the very stable sub-cloud layer associated with a front. This may be partly due to problems in locating cloud base or to the actual extension of the cloud layer below the front due to precipitation processes occurring in its mature stage.

b. A majority of the cases, also, exhibit a relatively stable layer in the vicinity of cloud-top. It is not clear whether this feature may be typically explained as a frontal zone or simply due to radiative and evaporative processes occurring in this region.

c. Well mixed conditions are not commonly observed in any of the three layers, i.e. $< \sim 15\%$ of the cases for either of the layers exhibit a moist adiabatic lapse rate. However, lapse rates within 1°K/km to 2°K/km of moist adiabatic are typically observed in the cloud-top layer.

d. The vertical shear of the horizontal wind speed is most commonly a maximum in either the sub-cloud layer or the cloud-top layer. This supports the conclusion that a frontal zone is typically associated with the sub-cloud layer and that a stable capping layer exists in many cases. The structure with maximum vertical shear of the horizontal wind speed occurring in the sub-cloud layer is the mean structure observed.

4. Thin Cloud Layers

a) The typical structure observed for the thin cloud cases does not correspond to the classical model. In fact, the sub-cloud frontal zone is not commonly observed.

b) The over-cloud layer is very stable in a majority of the cases. The observed stability strongly suggests the presence of a frontal zone. However, the potential effects of radiative and evaporative processes could possibly account for this structure. A majority of the cases, which do not exhibit the very stable over-cloud layer, do show a tendency for a weak stability maximum in the vicinity of cloud-top.

c) The cloud-top layer and the sub-cloud layer are found to be very similar in most regards. Approximately 25% of the cases exhibit lapse rates corresponding to near moist adiabatic conditions in these two layers, i.e. the layers are well mixed. Typically, the observed stability of these two layers corresponds to lapse rates within 1°K/km to 2°K/km of the moist adiabatic lapse rate.

d) In the mean, vertical wind shear is a maximum in the over-cloud layer though maximum or minimum shears are most commonly observed in the cloud-top layer. A surprising result is that the magnitude of the shear is observed to be larger when negative shear

is observed, than when positive shear is observed for each of the layers for the thin cloud cases. We do not have an explanation of this occurrence. The thick cloud cases show the opposite tendency.

References

Albrecht, B. A., A. K. Betts, W. H. Schubert and S. K. Cox, 1979: A model of the thermodynamic structure of the trade-wind boundary layer: Part I. Theoretical formulation and sensitivity tests. J. Atmos. Sci., 36, 73-89.

Bigg, E. K., and R. T. Meade, 1971: Clear air seeding in the presence of ice supersaturation. Proc. Int. Conf. Wea. Mod. (Canberra, Australia), 141-142.

Brousaides, F. J., 1973: An assessment of the carbon humidity element in radiosonde systems. Air Force Cambridge Research Laboratories, Instrumentation Papers, No. 197 AFCRL-TR-73-0423, 46 pp.

_____, and F. J. Morrissey, 1974: Residual temperature-induced humidity errors in the National Weather Service radiosonde, Final Report. Air Force Cambridge Research Laboratories, Instrumentation Papers, No. 215, AFCRL-TR-74-0111, 40 pp.

Budyko, M. I., 1969: The effects of solar radiation variations on the climate of the earth. Tellus, 21, 611-619.

Coakley, J. A., Jr., 1979: A study of climate sensitivity using a simple energy balance model. J. Atmos. Sci., 35, 260-269.

Conover, J., 1960: Cirrus patterns and related air motions near the jet stream as derived by photography. J. Meteor., 17, 532-546.

Detwiler, A., and B. Vonnegut, 1979: Clear-air seeding. Extended Abstracts 7th Conf. on Inadvertent and Planned Wea. Mod., (Banff, Canada), 15-17.

Fels, S. B., and L. D. Kaplan, 1975: A test of the role of longwave radiative transfer in a general circulation model. J. Atmos. Sci., 32, 779-789.

Griffith, K. T., S. K. Cox and R. G. Knollenberg, 1979: Infrared radiative properties of tropical cirrus clouds inferred from aircraft measurements. Submitted for publication to the J. Atmos. Sci.

Hess, S. L., 1959: Introduction to Theoretical Meteorology. Chapter 7. Holt, Rinehart and Winston, New York. 362 pp.

Heymsfield, A. J., 1975a: Cirrus uncinus generating cells and the evolution of cirriform clouds. Part I. Aircraft measurements of the growth of the ice-phase. J. Atmos. Sci., 32, 799-808.

_____, 1975b: Cirrus uncinus generating cells and the evolution of cirriform clouds. Part II. Structure and circulations of the cirrus uncinus generating head. J. Atmos. Sci., 32, 809-819.

Heymsfield, A. J., 1977: Precipitation development in stratiform ice clouds: A microphysical and dynamical study. J. Atmos. Sci., 34, 367-381.

International Council of Scientific Unions, 1974: Modelling for the First GARP Global Experiment. GARP Publications Series No. 14, World Meteorological Organization, 261 pp.

Jayaweera, K.O.L.F., and T. Ohtake, 1972: Artificial cloud formation in the atmosphere. Science, 178, 504-505.

Lala, G. G., 1969: Structure and modification of clouds and fogs. Ed. by B. Vonnegut, D. C. Blanchard, R. A. Cudney. Research Foundation of State University of N.Y., Albany, 84-100.

List, R. J., 1966: Smithsonian Meteorological Tables. Page 370, Smithsonian Institution, Washington, D. C., 527 pp.

London, J., 1957: A study of the atmospheric heat balance. Final Report, Contract No. AF19(122)-165, Department of Meteorology and Oceanography, New York University, July, 99 pp.

Ludlam, F. H., 1947: The forms of ice clouds. Quart. J. Roy. Met. Soc., 74, 39-56.

_____, 1952: Orographic cirrus clouds. Quart. J. Roy. Met. Soc., 78, 554-562.

_____, 1956: The forms of ice clouds, II. Quart. J. Roy. Met. Soc., 82, 257-265.

Oddie, B.C.V., 1959: Some cirrus cloud observations made by the Westminster Shiant Isles Expedition, 1958. Weather, 4, 204-208.

Reuss, J. H., 1967: Wolken-Steromessbildreichen, II, Grossraunige cirrus bandes als merhale von Luftmassengrenzen der hohes troposphare and ihrer Eigenshaften. Beitr. Phys. Atmos., 36, 7-15.

Rhea, J. O., 1978: Orographic precipitation model for hydrometeorological use. Colorado State University, Atmos. Sci. Paper No. 287, 221 pp.

Schneider, S. H., 1975: On the carbon-dioxide-climate confusion. J. Atmos. Sci., 32, 2060-2066.

_____, W. M. Washington and R. M. Chervin, 1978: Cloudiness as a climate feedback mechanism: Effects on cloud amounts of prescribed global and regional surface temperature changes in the NCAR GCM. J. Atmos. Sci., 35, 2207-2221.

Schubert, W. H., 1976: Experiments with Lilly's cloud-topped mixed layer model. J. Atmos. Sci., 33, 436-446.

Sellers, W. D., 1969: A global climate model based on the energy balance of the earth-atmosphere system. J. Appl. Meteor., 8, 392-400.

Smagorinsky, J., 1960: On the dynamical prediction of large-scale condensation by numerical methods. Geophys. Mono. No. 5, Amer. Geophys. Union, Washington, D. C., 71-78.

Starr, D. O'C., 1976: The sensitivity of tropical radiative budgets to cloud distribution and the radiative properties of clouds. Colorado State University Atmos. Sci. Paper No. 254, NTIS No. PB-263-227, 117 pp.

_____, and S. K. Cox, 1977: Review of the radiation computations in large scale atmospheric models. Unpublished report available from authors, 26 pp.

Stone, H. M., and S. Manabe, 1968: Comparison among various numerical models designed for computing infrared cooling. Mon. Wea. Rev., 96, 735-741.

U. S. Committee for the Global Atmospheric Research Program, 1978: Elements of the research strategy for the United States Climate Program. National Academy of Sciences, Washington, D. C. 46 pp.

Warren, S. G., and S. H. Schneider, 1979: Seasonal simulation as a test for uncertainties in the parameterizations of a Budyko-Sellers zonal climate model. J. Atmos. Sci., 36, 1377-1391.

Washington, W. M., 1971: On the role of radiation in dynamical climate simulation and numerical weather prediction. Proc. of Miami Workshop on Remote Sensing, 29 - 31 March, Miami, Florida, NOAA, 39-67.

Yagi, T., 1969: On the relation between the shape of cirrus clouds and the static stability of the cloud level. Studies of cirrus clouds: Part IV. J. Meteor. Soc. of Japan, 47, 59-64.

BIBLIOGRAPHIC DATA SHEET	1. Report No. CSU-ATS-327	2.	3. Recipient's Accession No.
4. Title and Subtitle CHARACTERISTICS OF MIDDLE AND UPPER TROPOSPHERIC CLOUDS AS DEDUCED FROM RAWINSONDE DATA			5. Report Date November, 1980 6.
7. Author(s) David O'C. Starr and Stephen K. Cox			8. Performing Organization Rept. No. CSU-ATS-327
9. Performing Organization Name and Address Department of Atmospheric Science Colorado State University Fort Collins, Colorado 80523			10. Project/Task/Work Unit No. 11. Contract/Grant No. NSG 5357
12. Sponsoring Organization Name and Address National Aeronautics and Space Administration Goddard Space Flight Center Washington, D. C. 20546			13. Type of Report & Period Covered 14.

15. Supplementary Notes:

16. Abstracts This study characterizes the static environment of middle and upper tropospheric clouds as deduced from rawinsonde data from 24 locations in the contiguous U.S. for 1977. Computed relative humidity with respect to ice is used to diagnose the presence of cloud layer. The deduced seasonal mean cloud cover estimates based on this technique are shown to be reasonable. Over 3600 cloud cases qualified for the analysis. The cases are stratified by season and pressure thickness, i.e. thick and thin. The dry static stability, vertical wind speed shear and Richardson number are computed for three layers for each case, i.e. the sub-cloud and above cloud layers and an in-cloud layer bounded by the cloud-top level. Mean values for each parameter and, in some instances, the corresponding relative frequency distributions are presented for each stratification and layer. The relative frequency of occurrence of various structures is presented for each stratification, e.g. increasing static stability with height through the three layers.

The observed values of each parameter vary over quite large ranges for each layer. The observed structure of each parameter for the layers of a given case is also quite variable. Structures corresponding to any of a number of different conceptual models, which are reviewed, may be found though some are substantially more common than others. It is of note that moist adiabatic conditions are not commonly observed and that the stratification based on thickness yields substantially different results for each group. Summaries of the results are included in the text.

17. Key Words and Document Analysis 17a. Descriptors

Clouds Ice Clouds Tropospheric cloud characteristics

17b. Identifiers/Open-Ended Terms

17c. COSATI Field/Group

18. Availability Statement	19. Security Class (This Report) UNCLASSIFIED	21. No. of Pages 71
	20. Security Class (This Page) UNCLASSIFIED	22. Price

5 (Rev. 3-72)

A MIDDLE AND UPPER TROPOSPHERIC CLOUD MODEL. Final Technical Report.

NASA CR-168,971
Section 3

SECTION 3

I. INTRODUCTION

In recent years, middle and upper tropospheric stratiform clouds have been increasingly recognized as an important factor in modulating climate (Schneider et al., 1978). This is particularly true of cirrus clouds (Cox, 1971). The reason for this importance is twofold. First, middle and upper tropospheric stratiform clouds cover extensive areas of the earth. Based on surface observations, London (1957) estimated the seasonal mean zonal cloud cover at these levels to range from $\sim$ 20% to $\sim$ 40% depending on the season and latitude zone. Starr and Cox (1980) gave similar results based upon their analysis of rawinsonde data. Second, clouds are very radiatively active. Particularly for cirrus clouds, the radiative effects are further enhanced due to their vertical location relative to the vertical radiative structure of the clear atmosphere. This effect has been previously noted by Starr (1976), Cox (1971) and Manabe and Strickler (1964) among others. The potential magnitude of the radiative effects of clouds may be seen in Figure 1. The data points correspond to computed broadband infrared heating rates for the entire atmospheric column in a maritime tropical atmosphere for various specified cloud top pressures and cloud infrared radiative properties. Note that ε^* may be interpreted as the product of the area cloud cover and the broadband infrared cloud emittance. The effect of cloud location and, thus, cloud temperature is clearly seen in the increasing sensitivity of the total atmospheric cooling to the specification of cloud cover and cloud emittance as cloud top pressure and, thus, temperature decrease. It is of note that radiatively black high level cirrus clouds can halve the total column cooling. It

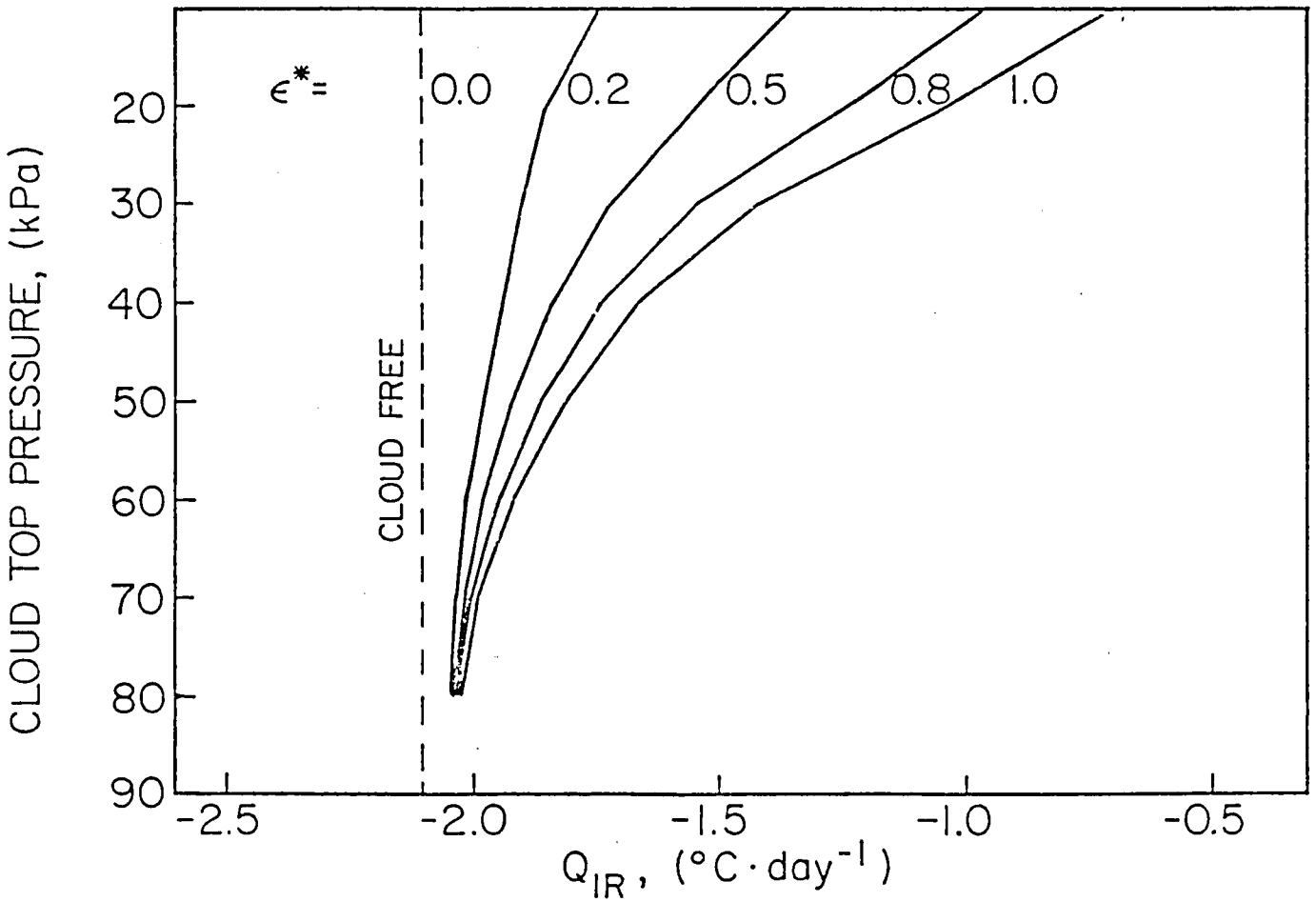

Figure 1. Broadband infrared heating rates, Q_{IR}, for the total atmospheric column as a function of cloud top pressure in a maritime tropical atmosphere (after Starr, 1976). Cloud layers are assumed to be 10 kPa thick and are also assumed to behave as grey bodies in the infrared spectral region with a broadband emittance ϵ^* specified as noted.

is precisely the latitudinal gradient of radiative heating which drives the general circulation and, thus, is a primary factor in determining global climate (Lorentz, 1967).

As noted by Starr (1976), the radiative effects of upper level clouds on the static stability structure of the atmosphere are potentially even more significant, i.e. changes in the vertical structure of radiative heating. It follows that upper level clouds may have a significant effect on the way that the atmosphere responds to the radiative forcing. This may be seen in the results of Yanai et al. (1976), where the response of cumulus convection to the large-scale radiative environment is very sensitive to the vertical radiative structure. At the least, clouds and particularly high level clouds are potentially the single most important atmospheric parameter modulating the local radiative budget of the atmosphere.

However, the interaction and relative importance of the various physical processes involved in the formation, maintenance and dissipation of upper level cloud layers are not well understood. In addition, quantitative information as to the physical properties of these cloud types has been lacking. The reasons for this lack of basic knowledge are primarily twofold. The impact on man of upper level cloudiness has been widely believed to be minimal. These clouds are not a direct source of economic or life damaging severe weather nor are they directly responsible for precipitation which may harm or benefit man.

Besides their potential importance on climatic time scales, it has, also, been suggested that cirriform clouds may play a significant role in enhancing the precipitation efficiency of mid-latitude cyclone systems by acting as a natural cloud seeding agent (Braham and

Spyers-Duran, 1967, Douglas et al., 1957 and Marshall et al., 1952) and, also, in modulating the intensity of tropical weather systems by means of their radiative effects (McBride and Gray, 1980 and Foltz and Gray, 1979). Cox (1969) has shown that the radiative effects of cirrus clouds may enhance both the growth and decay stages of mid-latitude cyclones. It is also obvious that the presence of upper level clouds may affect the subsequent initiation and intensity of mesoscale convection by modulating the incipient environment through their radiative influence on surface and atmospheric temperatures. For similar reasons, upper level cloudiness may significantly impact agricultural production particularly for crops which are crucially sensitive to surface temperature, e.g. corn. Relatively small changes in agricultural production, including the forecasting thereof, are becoming increasingly important to society as a whole due to the pressures of growing population and the subsequent economic ramifications. For these reasons, inadvertent weather modification due to cirrus cloud formation in the wake of jet aircraft has received increased attention of late (e.g. Machta and Carpenter, 1971). Thus, it is now apparent that upper level cloudiness may have a substantial impact on man and, thus, is a worthy topic for research.

The second reason that cirriform clouds are not well understood resides in one simple fact. They are located high in the atmosphere. Until the advent of jet aircraft, in situ observations were very difficult to make and, thus, very sparse (Heymsfield, 1975a). Even with high altitude research aircraft, sampling problems are substantial, primarily due to the required aircraft speed at such altitudes. Only recently, with the introduction of optical particle sampling devices

with very fast sampling rates (Knollenberg, 1970), have substantial quantities of microphysical observations been made, e.g. Griffith et al. (1980), Varley (1978), Heymsfield (1975a, 1977), and Hobbs et al. (1975). It should also be noted that until the mid 1970's, even rawinsonde humidity data at middle and upper tropospheric levels were inaccurate and highly unreliable especially during daylight hours (Starr and Cox, 1980, Rhea, 1978 and Betts, 1973a). In addition, observations of the radiative properties of cirrus clouds are now becoming more plentiful, e.g. Paltridge and Platt (1980), Griffith et al. (1980), Cox (1976) and Allen (1971). Thus, the information available has now increased to the point where a detailed consideration of the physical processes involved in the life cycle of upper level cloud layers is now feasible and warranted.

To date, studies in this area have been of limited scope and very qualitative, e.g. Yagi (1969), Matvejev (1965), Conover (1960), Oddie (1959) and Ludlam (1947, 1956). Exceptions to this are the excellent studies of Heymsfield (1975c, 1977), where dynamical and microphysical aspects were considered in some detail. The study presented here may be regarded as a theoretical extension of these preliminary studies.

The deficiencies in our understanding of cirrus clouds are probably best exemplified by noting the very simplistic treatment of these cloud types in general circulation models (i.e. GCMs). When cloudiness is carried as an interactive model component, (which is not the case in many simulations reported in the literature where climatology is specified), the diagnosis of upper level cloud amounts is based on a formulation given by Smagorinsky (1960) or something very similar where the large-scale relative humidity is the determining factor. A large-scale

vertical velocity criterion is also used in many instances. The widespread use of this specific formulation (Starr and Cox, 1977) is more a consequence of its availability than any assurance as to its actual appropriateness. Though it may fortuitously have some statistical significance (Sommeria and Deardorff, 1977), it was originally derived from upper air relative humidity data which were nortoriously inaccurate at that time, as noted previously. In addition, it implicitly relies on the appropriateness of what may be called the "classical model" for slope convection. In this model, which is depicted in Figure 2, upper level cloud layers result from the lifting and subsequent adiabatic cooling to saturation of air masses in association with frontal motions. Conover (1960) points out that this does not seem to be the case with jet stream cirrus layers. Starr and Cox (1980) reported that based on an extensive climatological study of the static stability and wind shear structures associated with upper level clouds, that the classical model was inappropriate in a large portion of the total cases. This was particularly evident with thin fair weather cloud forms. The observational studies of fair weather cirrus, alluded to earlier generally support this conclusion. As pointed out by Roach and Bader (1977), once formed, ice phase clouds are observed to persist for significant time periods in seemingly unfavorable environments, where the classical model would fail to diagnose their presence.

Furthermore, cirrus cloud layers are generally assumed to be half black in the infrared. As pointed out by Allen (1971), this choice seems to be more a result of knowing that the emittance had to be less than one but greater than zero than any real theoretical or observationally based criteria.

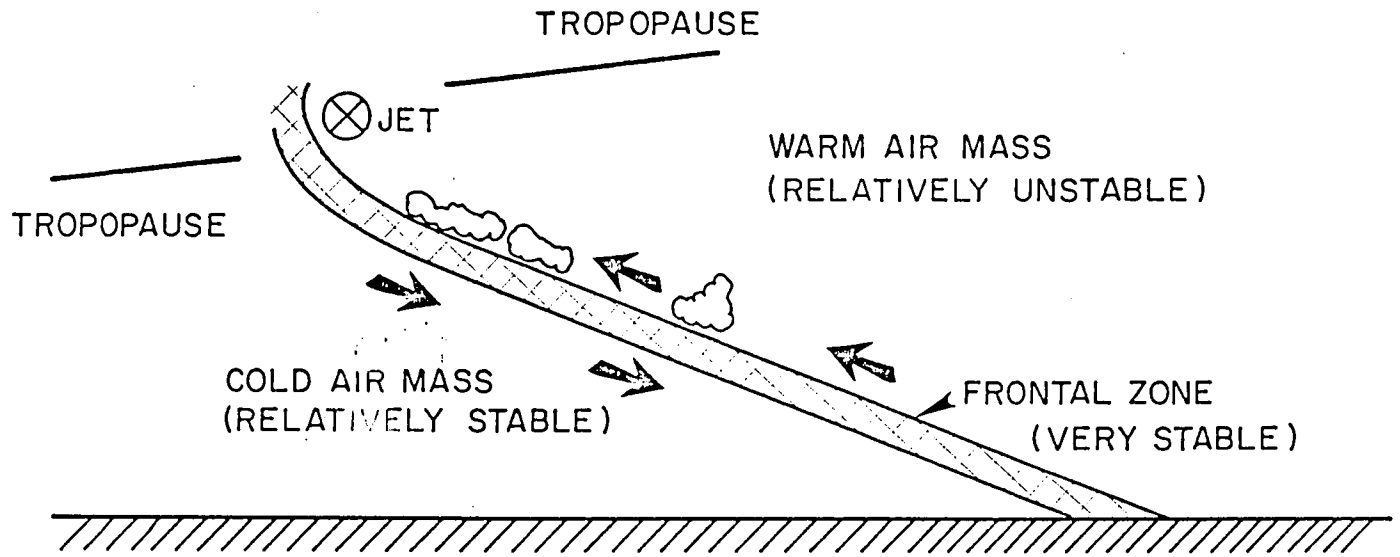

Figure 2. Classical model of the environment associated with slope convection. Note that strong vertical shear of the horizontal wind direction exists across the frontal zone.

Thus, the parameterizations of cirrus clouds generally employed in GCM's are seen to have only a weak physical basis. It is the aim of this study to begin to form a comprehensive physical basis upon which future improvements in this area may be made. It should be noted that recently, more realistic treatments of middle level stratiform cloudiness have been reported (Sundquist, 1978, 1980) where cloud water is actually carried in the model. However, this parameterization is more appropriate to liquid phase clouds. As will be shown later, the differences between liquid and ice phase stratiform clouds are substantial.

The objective of this study is to gain a basic understanding of the interplay of the various physical processes involved in the formation, maintenance and decay of middle and upper tropospheric stratiform clouds. The focus of the study is limited primarily to ice phase, fair weather cloud forms. Thus, mixed phase clouds are not considered. In addition, deep cloud layers associated with regions of strong lifting in cyclones are not directly addressed. A modelling approach is adopted, where simulations of cirriform clouds, which attempt to incorporate the important physical processes in an interactive manner, are performed.

The choice of a specific modelling approach is highly influenced by the fact that the interrelationship between a number of presumably important physical parameters are unknown or, at the least, highly speculative at this time. For example, the bulk radiative properties of a cloud such as its infrared emittance and solar absorptance must be related through the microphysical properties of the cloud. Only recently have theoretical studies of ice clouds, which address this issue, been reported, (e.g. Stephens, 1980 and Liou, 1972). However,

such theoretical relationships rely critically on the assumed crystal habit and size spectrum and also possibly on the assumed crystal orientations. How these properties depend on the dynamic, thermodynamic and radiative environment of the cloud is uncertain. Empirical studies, e.g. Paltridge and Platt (1980) and Griffith et al. (1980), also suffer from uncertainty due to the scatter of the observations. Because of these uncertainties, the modelling philosophy adopted here is to choose an approach which is the most simple method capable of yielding realistic simulations. In this way, the sensitivity of simulations to the choice of various parameters may be economically established in a realistic manner.

A two-dimensional, time-dependent, Eulerian numerical model, which incorporates all of the important physical processes in a simplified way is employed to investigate the role of these processes in the evolution of a cloud in an isolated atmospheric layer. A time-dependent approach was adopted so that the changing roles of various processes at different stages of the cloud life cycle might be investigated. A Eulerian model is employed due to the abundance of knowledge available as to the mechanics of this type of model. By two-dimensional, denoted 2-D, we mean that solutions are obtained for dependent model variables in two space dimensions, e.g. (x, z, t).

A full 3-D modelling approach, e.g. Sommeria (1976), Cotton and Tripoli (1978), was rejected primarily because of the substantial increases in computing requirements and complexity. While a 3-D model has the advantages of being capable of simulating the effects of spacial variability of the large-scale environment and full three-dimensional turbulent transport processes, the focus of this study is

on local scale control, i.e. cloud forms, which are not dominated by large-scale processes. The neglect of turbulent transports in a third space dimension is not felt to be too severe of a drawback to the 2-D approach especially considering the present state of knowledge.

A 1-D modelling approach was rejected primarily because of uncertainty as to the appropriateness of the required closure assumption and the desire to capture more detail in the simulations as an aid in gaining understanding. The primary advantages of a 1-D modelling approach are the overall simplicity of the model and the resulting computational economy. In the case of entrainment type models, e.g. Lilly (1968), Schubert, et al. (1979), and Randall (1980), these advantages are at least partially offset by their limited applicability. The assumed thermodynamic and dynamic structure of the environment, which is necessary and crucial to the entrainment closure assumption, may not be nearly as applicable to the problem here as to the stratocumulus problem which they considered. This conclusion is supported by the work of Starr and Cox (1980). A more global 1-D approach as been employed by Oliver, et al. (1978). They employ a second order turbulence closure, where the required correlation coefficients for turbulence parameters are diagnosed from the structure of the basic state based on empirical relationships derived primarily from observations in the atmospheric boundary layer. These relationships are believed to be more general but may not be universal.

An obvious important advantage of a 2-D or 3-D modelling approach, when compared to the 1-D approach, is that horizontal structure is explicitly resolved on the grid scale. This may be a substantial aid in clarifying the interpretation of results, particularly if the

evolution of such structure is important in the understanding of the cloud life cycle process as noted by Ludlam (1947) and Heymsfield (1975b). Furthermore, if a reasonably small grid interval is used, much of the turbulent transports are explicitly resolved. In this case, the choice of a particular turbulence closure scheme for the model, which accounts for processes acting at a scale less than the grid interval, may not be as crucial to the results. In this sense, the universality of the closure need not be as rigorously established as in the case of a 1-D model where essentially all turbulent transport processes are parametrically represented. Asai and Nakamura (1978), Arnason et al., (1968) and Lilly (1962) among others have successfully applied the 2-D approach in studies of convection in the atmospheric boundary layer and lower troposphere.

II. THEORY

The theoretical framework, which forms the basis for the numerical model, is developed in this chapter. Before presenting the governing equations, some general interpretive considerations must be made. Time dependent solutions to the governing equations are obtained on a rectangular, two-dimensional, vertical plane of constant elevation. Locations within this plane are specified in terms of a horizontal coordinate, x, and a vertical coordinate, z. No particular geographic significance in terms of orientation should be ascribed to the direction of the x-axis.

Consistent with the use of a two-dimensional approach as developed here, solutions may be interpreted for the full three space dimensional case as corresponding to a slice perpendicular to some mean horizontal wind component as depicted in Figure 3. In this sense, the solution domain may be viewed as being advected along the direction of this mean wind component. Thus, the model is not formally applicable to the situation where vertical or horizontal shears of the mean current are present within the plane of interest. A second interpretation, which might be invoked, is that the solution domain is fixed relative to the earth. In this case, the plane must again be oriented perpendicular to the mean horizontal current where no wind shears are permitted in this current. However, it is explicitly assumed in this instance that the slice under consideration is exactly the same as any other similar-oriented slice. Thus, the solutions might best be interpreted as corresponding to the case of structures which appear in three dimensions as longitudinal rolls relative to a basic current. The best

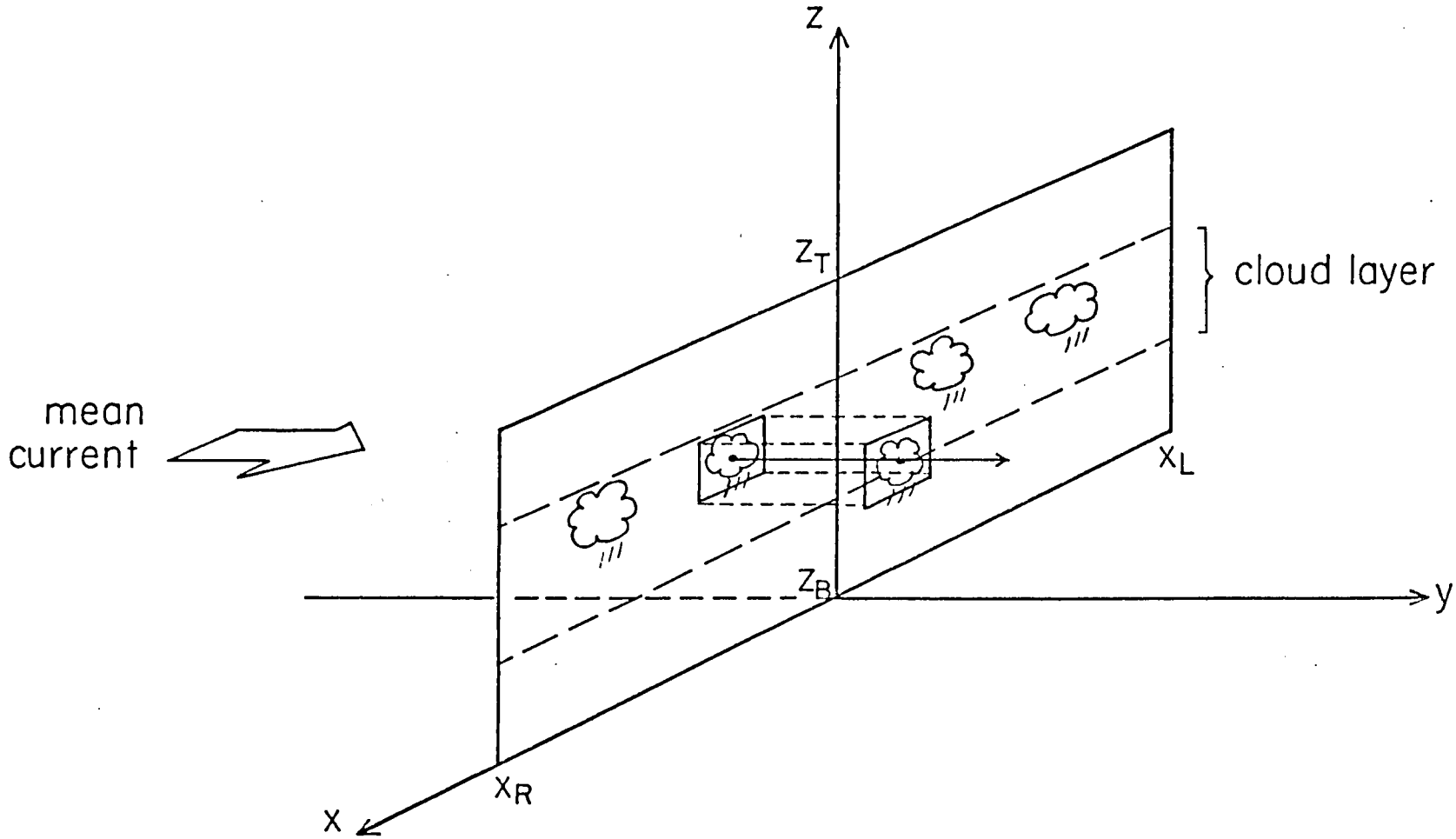

Figure 3. Schematic representation of the spacial domain adopted for this study.

atmospheric analogy would be the jet stream cirrus cloud streaks described by Conover (1960), which are typically oriented parallel to the jet axis. Hopefully, extensions of these model results may be made to the full three dimensional case. Note that the two-dimensional modelling approach can be adapted for a mean current in the plane of interest as in Lipps (1971). However, this is generally not convenient for the purposes here, although some attempt to investigate the role of vertical shear of a lateral wind component on cirrus cloud formation is made.

In this model, the plane of interest is generally specified as $\sim$ 3 km in depth. The horizontal dimension is generally specified as either $\sim$ 6 km or $\sim$ 12 km though periodic lateral boundary conditions are imposed, as will be seen in the following. In this sense, the horizontal domain may be viewed as infinite subject to the constraints imposed by the lateral boundary condition.

The dynamics of two-dimensional fluids are governed by the principle of conservation of momentum i.e. Newton's Laws, which may be expressed by a reduced form of the Navier-Stokes equations as:

$$\frac{d(\rho u)}{dt} = -\frac{\partial p}{\partial x} + \frac{\partial \sigma_x}{\partial x} + \frac{\partial \tau_{xz}}{\partial z}$$

and (2.1)

$$\frac{d(\rho w)}{dt} = -\rho g - \frac{\partial p}{\partial z} + \frac{\partial \sigma_z}{\partial z} + \frac{\partial \tau_{zx}}{\partial z}$$

where u and w are the velocity components in the x and z directions, respectively; ρ is the density; p is the static pressure; and g is the acceleration due to gravity. The viscous stress components for a

Newtonian fluid are represented by the last two terms in each equation where:

$$\sigma_x \equiv \mu \left[2 \frac{\partial u}{\partial x} - \frac{2}{3} \left(\frac{\partial u}{\partial x} + \frac{\partial w}{\partial z}\right)\right] ,$$

$$\sigma_z \equiv \mu \left[2 \frac{\partial w}{\partial z} - \frac{2}{3} \left(\frac{\partial u}{\partial x} \quad \frac{\partial w}{\partial z}\right)\right] ,$$

$$\tau_{xz} = \tau_{zx} \equiv \mu \left[\frac{\partial u}{\partial z} + \frac{\partial w}{\partial x}\right] \qquad (2.2)$$

and μ is the dynamic viscosity of air. Note that

$$\frac{d}{dt} \equiv \frac{\partial}{\partial t} + u \frac{\partial}{\partial x} + w \frac{\partial}{\partial z} .$$

In addition to the usual assumptions, which are appropriate for tropospheric air, where the net electrical, magnetic, etc. forces are neglected, the following assumptions have been made. The flow is limited to two dimensions where either the velocity component into the plane of interest is regarded as zero or the gradients in that direction of all quantities are similarly regarded as zero. Furthermore, Stokes' hypothesis has been employed for the stress terms along the direction of interest, i.e. σ_x and σ_z, as in Schlichting (1968). In addition, terms due to the curvature and rotation of the earth have been neglected except of course in the usual definition of g where effects due to gravitational forces and apparent centrifugal forces are included. This is consistent with the application here, where these equations are to be applied to a domain which has a relatively small horizontal dimension (Holton, 1972). It is, also, consistent with the

interpretations, noted previously, where the geographic orientation of the plane of interest is determined by its orientation to some basic current. Thus, Coriolis effects may be regarded as operating on the basic current, though this is not explicitly considered here.

A second governing principle is the conservation of mass, which may be expressed for a two-dimensional fluid by the continuity equation in the form:

$$\frac{\partial \rho}{\partial t} + \frac{\partial}{\partial x}(\rho u) + \frac{\partial}{\partial z}(\rho w) = 0. \qquad (2.3)$$

Following from Kraus (1972), for atmospheric motions where the vertical displacements are small compared to the atmospheric scale height ($\sim$ 8 km for the troposphere), the continuity equation is well approximated as:

$$\frac{\partial u}{\partial x} + \frac{\partial w}{\partial z} = 0 . \qquad (2.4)$$

Thus, the atmosphere is regarded as locally incompressible or anelastic and the wind fields are consequently non-divergent.

In a consistent manner, if compressibility effects are neglected in the viscous stress terms, Equations (2.3) and (2.4) allow Equation (2.1) to be expressed as:

$$\rho \frac{du}{dt} = -\frac{\partial p}{\partial x} + \frac{\partial \sigma_x}{\partial x} + \frac{\partial \tau_{xz}}{\partial z}$$

and (2.5)

$$\rho \frac{dw}{dt} = -\rho g - \frac{\partial p}{\partial z} + \frac{\partial \sigma_z}{\partial z} + \frac{\partial \tau_{zx}}{\partial x}$$

5

where:

$$\sigma_x = 2\mu \frac{\partial u}{\partial x} \quad \text{and} \quad \sigma_z = 2\mu \frac{\partial w}{\partial z} \quad .$$

Again following from Kraus (1972), for relatively shallow atmospheric disturbances, the perturbations of density from the mean value of the layer under consideration may be neglected except when coupled with the gravity term in the momentum equations. This is consistent with the previous assumption leading to Equation (2.4) and represents the familiar Bousinesque approximation, which has been discussed in great detail by Ogura and Phillips (1962). This approximation has been widely used in studies of atmospheric convection. Its validity rests on the relative shallowness of the disturbance and the implicit assumption that wave motion with time scales less than N^{-1} are unimportant in the solution where N is the well known Brunt-Väisälä frequency. Thus, waves moving faster than gravity waves, e.g. sound waves, will not be present in the solution. This approximation is valid in the problem here, though probably not as valid as in studies of the atmospheric boundary layer where it is normally applied. This approximation allows the governing momentum equations to be further simplified to:

$$\frac{du}{dt} = -\frac{1}{\rho_{oo}} \frac{\partial p}{\partial x} + \frac{\partial \sigma_x}{\partial x} + \frac{\partial \tau_{xz}}{\partial z}$$

and (2.6)

$$\frac{dw}{dt} = -\frac{\rho'}{\rho_{oo}} g - \frac{1}{\rho_{oo}} \frac{\partial p}{\partial z} + \frac{\partial \sigma_z}{\partial z} + \frac{\partial \tau_{zx}}{\partial x}$$

where ρ_{oo} is the mean density in the layer of interest and ρ' is the local deviation of density from the mean value at any level. This definition of ρ' involves a slight approximation, which is generally very valid for atmospheric layers (Kraus, 1972). Note that the stress components have been redefined in Equation (2.6) where:

$$\sigma_x = 2\nu \frac{\partial u}{\partial x}, \quad \sigma_z = 2\nu \frac{\partial w}{\partial z},$$
$$\tau_{xz} = \tau_{zx} = \nu \left(\frac{\partial u}{\partial z} + \frac{\partial w}{\partial x}\right), \tag{2.7}$$

and ν is the kinematic viscosity of air, consistently defined as:

$$\nu \equiv \frac{\mu}{\rho_{oo}}. \tag{2.8}$$

Thus, the spacial derivatives of $1/\rho$ have been neglected in formulating these terms. Hereafter, ν is regarded as a constant. Though ν has temperature and pressure dependencies (Schlichting, 1968), these assumptions are consistent with the previous approximations. Also, when applied in discrete space, the meaning of this term is substantially altered as will be seen later.

The approximate momentum equations may now be combined to yield:

$$\frac{d\zeta}{dt} = -g \frac{\partial}{\partial x}\left(\frac{\rho'}{\rho_{oo}}\right) + \nu \nabla^2 \zeta \tag{2.9}$$

where ζ is the component of vorticity into the plane of interest defined as:

$$\zeta = \frac{\partial w}{\partial x} - \frac{\partial u}{\partial z} \tag{2.10}$$

and ∇^2 is the two-dimensional Laplacian operator defined as:

$$\nabla \equiv \frac{\partial^2}{\partial x^2} + \frac{\partial^2}{\partial z^2} \quad . \tag{2.11}$$

Note that the sign of ζ as defined here is opposite to that conventionally used, i.e.

$$\zeta \equiv -\hat{j} \circ \mathbb{\nabla} \times \mathbb{V}$$

where $\hat{j}$ is a unit vector into the plane of interest and $\mathbb{\nabla}$ and $\mathbb{V}$ are the three dimensional divergence operator and wind velocity vectors, respectively. This is done purely for convenience and has no effect on the dynamics.

Given the developments to this point, it is now appropriate to introduce the streamfunction ψ, where:

$$u \equiv -\frac{\partial \psi}{\partial z} \quad \text{and} \quad w \equiv \frac{\partial \psi}{\partial x} \tag{2.12}$$

and, thus,

$$\zeta = \nabla^2 \psi \quad . \tag{2.13}$$

This allows the Equation (2.9) to be rewritten as:

$$\frac{\partial \zeta}{\partial t} = J(\zeta, \psi) - g \frac{\partial}{\partial x} \left(\frac{\rho'}{\rho_{oo}}\right) + \nu \nabla^2 \zeta \tag{2.14}$$

where the Jacobian operator is defined as:

$$\mathcal{J}(A,\psi) \equiv \frac{\partial A}{\partial x}\frac{\partial \psi}{\partial z} - \frac{\partial A}{\partial z}\frac{\partial \psi}{\partial x} \tag{2.15}$$

for any quantity A. The utility of employing ψ resides in the fact that given the integration in time of the prognostic Equation (2.14), the new wind fields may be readily diagnosed by inverting the diagnostic Equation (2.13) for ψ and employing Equation (2.12). Solutions of Equation (2.13), which is of the form of a Poisson's equation, are available.

Now, following from Ball (1956) and consistent with the approximations employed here for a shallow layer, local pressure perturbations from the horizontal mean pressure may be ignored in the equation of state. The equation of state for moist tropospheric air is well approximated as:

$$p = \rho R_g \left(\frac{1 + q/\varepsilon}{1 + q}\right) T \tag{2.16}$$

where R_g is the real gas constant for dry tropospheric air, T is the temperature, q is the specific humidity of water vapor and ε is the ratio of the molecular weight of water to that of dry air. Note that, except for the water content, the composition of tropospheric air is assumed to be constant and van der Waal's effects have been neglected. Thus,

$$\frac{\rho'}{\rho_o} \simeq -\frac{T_v'}{T_{v_o}} \tag{2.17}$$

where the subscript 0 denotes a horizontally averaged quantity and

$$T_v \equiv T\left(\frac{1 + q/\varepsilon}{1 + q}\right) . \tag{2.18}$$

Noting that $q << 1$, binomial expansion of Equation (2.18) yields a highly accurate approximation for T_v as:

$$T_v \cong T + T\left(\frac{1-\varepsilon}{\varepsilon}\right) q .$$

Neglecting the mean level cross correlation $(q'T')_o$ compared to $q_o T_o$ allows:

$$T_{v_o} \cong T_o + T_o\left(\frac{1-\varepsilon}{\varepsilon}\right) q_o$$

which may be further approximated as:

$$T_{v_o} \simeq T_o \tag{2.19}$$

since

$$\left(\frac{1-\varepsilon}{\varepsilon}\right) q_o << 1 .$$

Thus, with some manipulation,

$$\frac{T_v'}{T_{v_o}} \simeq \frac{T'}{T_o}\left\{1 + \left(\frac{1-\varepsilon}{\varepsilon}\right)\left(q_o + q' + \frac{(q'T')_o}{T'}\right)\right\} + \left(\frac{1-\varepsilon}{\varepsilon}\right) q'$$

which may be further reduced as:

$$\frac{T_v'}{T_{v_o}} \simeq \frac{T'}{T_o} + \left(\frac{1-\varepsilon}{\varepsilon}\right) q' \tag{2.20}$$

since

$$\left(\frac{1-\varepsilon}{\varepsilon}\right)\left(q_o + q' + \frac{(q'T')_o}{T'}\right) \ll 1 .$$

In a consistent manner,

$$\frac{T'}{T_o} \cong \frac{\Theta'}{\Theta_o} \tag{2.21}$$

where

$$\Theta \equiv \frac{T}{\pi_o} , \tag{2.22}$$

$$\pi_o \equiv \left(\frac{p_o}{p_{ref}}\right)^{R_g/c_p} \tag{2.23}$$

and p_{ref} is some reference pressure. Effects due to the presence of water vapor have been ignored in the definition of potential temperature Θ, i.e. c_p and R_g are the specific heat and real gas constant for dry air, respectively. Pressure perturbations have been neglected in the definition of Θ (i.e. $\pi \cong \pi_o$), which is consistent with the above as in Ball (1956). Thus, Equations (2.17), (2.20) and (2.21) may be combined to yield:

$$-\frac{\rho'}{\rho_{oo}} \equiv B \cong \frac{\Theta'}{\Theta_{oo}} + \left(\frac{1-\varepsilon}{\varepsilon}\right) q' - \ell \tag{2.24}$$

where consistent with the Bousinesque approximation, Θ_{oo} has replaced Θ_o. Note that the contribution of non-vapor phase water to the buoyancy parameter B has been incorporated by the additional term ℓ which is the specific humidity of non-vapor phase water, i.e. ice water.

Subsititution of Equation (2.24) into Equation (2.14) allows:

$$\frac{\partial \zeta}{\partial t} = J(\zeta,\psi) + g\frac{\partial B}{\partial x} + \nu \nabla^2 \zeta . \tag{2.25}$$

Integration of this equation in time is an initial value problem, where boundary conditions for the various terms must be specified. For this study, the layer of interest is regarded as at rest with respect to some predefined basic state. In this sense, ζ and ψ are, therefore, regarded as purely perturbation quantities and are initially everywhere zero within the domain. Disturbances within the layer are regarded as isolated from the environment external to the layer. Thus, the appropriate boundary conditions at the top (T) and base (B) of the layer are that:

$$\zeta_T = \zeta_B = 0 \tag{2.26}$$

$$\psi_T = \psi_B = 0 \tag{2.27}$$

and

$$\left.\frac{\partial \zeta}{\partial z}\right|_{z = z_T \text{ or } z_B} = 0 \, . \tag{2.28}$$

The first two conditions confine any disturbance which evolves to remain entirely within the region of interest. The last condition states that there is no stress at the boundaries. In addition,

$$\theta'_T = \theta'_B = 0$$

$$q'_T = q'_B = 0$$

and

$$\ell_T = \ell_B = 0 \tag{2.29}$$

will, also, be imposed.

Noting the desired interpretations as stated in the beginning of this chapter, periodic boundary conditions are imposed in the lateral direction, i.e.

$$S(x_L, z) \equiv S(x_R, z) \tag{2.30}$$

where S is any quantity and x_L and x_R denote the left and right boundaries of the domain, respectively. Consequently, no net horizontal pressure forces, including the horizontal stress forces, are allowed at any level at any time. Thus, except for the initial conditions on Θ_{oo}, Θ', q' and ℓ, all the initial conditions and boundary conditions necessary for the solution of Equation (2.25) have been specified.

One additional feature is incorporated into the model. A basic state vertical motion is allowed. As a consequence of the previous developments, the basic state vertical velocity, w_o, is constrained to be everywhere a constant. Furthermore, w_o must remain constant in time and must, therefore, be regarded as an initial condition. Equation (2.25) is appropriately modified as:

$$\frac{\partial \zeta}{\partial t} = J(\zeta,\psi) - w_o \frac{\partial \zeta}{\partial z} + g \frac{\partial B}{\partial x} + \nu \nabla^2 \zeta \ . \tag{2.31}$$

Equation (2.31) is the governing dynamic equation adopted for this study. The terms on the right-hand side describe the contributions to the tendency of ζ due to advection by the perturbation wind field, advection by the basic state wind field, generation and destruction of ζ by buoyancy forces and viscous dissipation of perturbation kinetic energy via diffusion processes.

The governing thermodynamic principle is conservation of total energy, i.e. the first law of thermodynamics. An approximate statement of this principle is:

$$c_V \frac{dT}{dt} + p \frac{d\alpha}{dt} = \Phi + Q_R + Q_c + \kappa_T \nabla^2 T \qquad (2.32)$$

where α is the specific volume and c_V is the specific heat of air at constant volume. The first term on the left-hand side represents changes in internal energy, i.e. the energy associated with purely random molecular and intra molecular motions. The second term represents the work done in expansion and compression. In addition to the usual assumptions, which are generally valid for tropospheric air where net changes in electrical, magnetic, etc. energies are neglected, it has also been assumed that net work done by bulk pressure gradient forces including dynamic pressure forces and the force of gravity are exactly balanced by the corresponding changes in kinetic energy, i.e. the energy associated with the net non-random motions of large groups of molecules. Thus, these terms do not appear in Equation (2.32). The first term on the right-hand side of Equation (2.32) represents the frictional heat source due to the viscous dissipation of kinetic energy, i.e. the energy transformation associated with the degradation of non-random to random molecular motions. This term will be neglected, hereafter, because for tropospheric air, it is typically very much smaller than the remaining terms. The next two terms represent the heat sources due to radiative processes and phase changes of water. The last term accounts for heat conduction. This term is generally neglected in atmospheric studies. It is retained here only because when the governing equation is applied in discrete space a term of similar form but very different meaning occurs.

If tropospheric air is assumed to behave as an ideal gas and, thus, obey the kinetic theory of gases, noting Equations (2.22), (2.23)

and (2.16) with q assumed equal to zero, Equation (2.32) may be rewritten as:

$$\frac{d\theta}{dt} = \frac{1}{c_p \pi_o} \left\{ g \frac{\partial F_R}{\partial p_o} + L C \right\} + \kappa_\theta \nabla^2 \theta \qquad (2.33)$$

where F_R is the net upward radiative flux, C is the net rate of phase change of water and L is the appropriate specific latent heat of water phase change, e.g. L is the specific heat of condensation when C is the condensation rate. Consistent with the previous developments, c_p is assumed equal to the specific heat of dry air at constant pressure and the horizontally averaged values of p_o and π_o have been employed. Similarly, the spacial gradients of π have been neglected in formulating the conduction term.

In addition to the neglect of the water vapor contribution to both c_p and the gas constant when deriving Equation (2.33), the source terms on the right-hand side are presumed to input energy to only the gaseous components of the system. As pointed out by Betts (1973b), Equation (2.33) describes pseudo moist adiabatic processes in the presence of the noted diabatic energy sources, where it is explicitly assumed that changes in the mass per unit volume of the gases considered due to phase changes of water are negligible and that no energy changes other than that directly realizable via the phase change processes may occur due to advection of non-vapor phase water into or out of a given volume of air.

Noting the derivation of the governing dynamic equation, Equation (2.33) may be written in a similar form as:

$$\frac{\partial \Theta}{\partial t} = \mathcal{J}(\Theta,\psi) - w_o \frac{\partial \Theta}{\partial z} + \frac{1}{c_p \pi_o} \left\{ g \frac{\partial F_R}{\partial p_o} + LC \right\} + \kappa_\theta \nabla^2 \Theta \, . \qquad (2.34)$$

This equation may be further modified as:

$$\frac{\partial \theta}{\partial t} = \mathcal{J}(\Theta_o + \theta, \psi) - w_o \frac{\partial(\theta_o + \theta)}{\partial z} + \kappa_\theta \nabla^2 \theta$$

$$+ \frac{1}{c_p \pi_o} \left\{ g \frac{\partial F_R}{\partial p} + LC \right\} \qquad (3.35)$$

where Θ_o represents the horizontally averaged initial potential temperature at a level and θ represents the local perturbations from this basic state value, i.e. previously denoted Θ'. This is the governing thermodynamic equation adopted for this model. Note that thermal conduction (diffusion) is presumed to act only on the perturbation quantity θ.

In addition to the previously imposed lateral boundary condition and the boundary conditions on θ at the top and base of the layer, the additional condition that:

$$\frac{\partial \theta}{\partial z}\Big|_{z=z_T \text{ or } z_B} = \qquad (2.36)$$

is imposed. Thus, no conduction (diffusion) is allowed across either boundary. Thus, disturbances are totally confined within the layer of interest. The manner of specifying the terms F_R and LC are deferred to Sections (3.11) and (3.9), respectively. Thus, it remains only to specify the initial conditions for Θ_o and θ in order that Equation (2.35) may be integrated in time. Generally, the perturbation

potential temperature field is employed to initiate a disturbance as developed in Section (3.12).

Conservation of total water is invoked as a fourth governing principle. For this model, the total water budget equation is partitioned into two equations as:

$$\frac{\partial q}{\partial t} = J(q + q_o, \psi) - w_o \frac{\partial (q + q_o)}{\partial z} - C + \kappa_q \nabla^2 q \qquad (2.37)$$

and

$$\frac{\partial \ell}{\partial t} = J(\ell, \psi) - w_o \frac{\partial \ell}{\partial z} - \frac{\partial}{\partial z} v^* \ell + C + \kappa_\ell \nabla^2 \ell \qquad (2.38)$$

which describe the budgets of water vapor and non-vapor phase water (generally ice water), respectively. These budgets are expressed in terms of the respective specific humidities. In a manner similar to that employed in the governing thermodynamic equation, q_o represents the initial horizontally averaged water vapor specific humidity and q represents the local perturbations from this value at a level. Note that C is now specifically defined as the condensation or vapor to ice sublimation rate. Furthermore, the initial condition for non-vapor phase water is that none exists within the domain such that no basic state exists for ℓ, i.e. $\ell_o = 0$. Therefore, all non-vapor phase water which might occur is regarded as a perturbation of the initial basic state.

Noting the desired application to discrete space, diffusion terms have been included in each of the governing water budget equations where the diffusion processes have been presumed to act only on the

perturbation quantities q and ℓ. The coefficients κ_q and κ_ℓ are the respective diffusion coefficients. These terms will be considered in more detail later.

In addition to the lateral boundary conditions and the vertical boundary conditions and q and ℓ noted previously, the further conditions that:

$$\left.\frac{\partial q}{\partial z}\right|_{z=z_T \text{ or } z_B} = 0$$

and

$$\left.\frac{\partial \ell}{\partial z}\right|_{z=z_T \text{ or } z_B} = 0 \qquad (2.39)$$

are imposed. Thus, no diffusion is permitted across the horizontal boundaries of the domain.

The term $v^* \ell$ in Equation (2.38) represents the flux of ℓ due to the effects of the gravity induced relative fall velocity of the particles comprising ℓ. The parameter v^* is the effective relative fall velocity. The manner of specifying this term is considered in Section (3.10). It should be noted that the boundary condition on ℓ at the base of the layer of interest is relaxed when considering this term as developed in Section (3.3). Thus, precipitation will be allowed to exit the domain at the lower boundary by virtue of its relative fall velocity.

Thus, four prognostic equations, (i.e. (2.31), (2.35), (2.37) and (2.38)) have been derived, which govern moist convection in a relatively shallow atmospheric layer. Integration in time of these coupled equations requires the additional diagnostic relationship given by

Equation (2.13). Diagnostic relationships to specify F_R, C and v^* are also required. These terms are specified in a parametric fashion as described in the next chapter. Note that microphysical growth equations are not explicitly incorporated into the model as prognostic governing equations. The required boundary conditions for the integration of the set of governing prognostic equations over a finite domain are given by Equations (2.26), (2.27), (2.28), (2.29), (2.30), (2.36) and (2.39). In addition, initial conditions, where θ_o, θ_{oo}, q_o, p_o, π_o and w_o must be specified, are required. The required initial conditions for perturbation quantities are specified as:

$$q = 0 \qquad \psi = 0$$

$$\ell = 0 \text{ and } \zeta = 0 \tag{2.40}$$

everywhere within the domain. Thus, disturbances are initiated via the initial prescription of θ where the mean value of θ at any level is required to be zero.

It should be noted that the basic state quantities have only a vertical dependence, except of course θ_{oo} and w_o which are constants. All quantities may be reinitialized at any point during an integration of the model. This would require the adjustment of the values of θ, q and ℓ to reflect changes in the basic state pressure field and the new horizontal mean basic state values in order that the relevant conservation principles are obeyed. In the case where substantial trends in the horizontal means of θ and q occur during a

simulation, such a reinitialization procedure would yield more accurate solutions given the approximations made in this chapter. However, this is generally not done. The reason for this approach is that the resulting increases in complexity and computational requirements outweigh the gain in accuracy, which would generally be small in the simulations reported here, especially given the level of approximation already involved in the governing equations.

Before proceeding to the specific design of the numerical model, a general consideration of the application of the continuous governing equations to a discrete grid point space must be made. When applied to a specific grid point which represents a corresponding grid area, all basic state and perturbation quantities in the governing equations formally represent the mean value of that quantity in that grid area. However, perturbations about the grid area mean value of any quantity may exist in that grid area. Mean cross correlations between any pair of quantities within a grid area are, therefore, not formally taken into account in the governing equations. Net transports, which may result from these mean cross-correlations are not resolved and are normally referred to as turbulent processes. For example, if $\overline{\theta}$ is the mean value of perturbation potential temperature on the boundary between two vertically adjoining grid areas and $\overline{w}$ is the corresponding mean vertical velocity, the net flux of perturbation potential temperature across the boundary is given by:

$$\overline{w\theta} = \overline{w}\,\overline{\theta} + \overline{w'\theta'}$$

where the primed quantities represent the local deviation from the mean

value on the boundary. As given, the model accounts for only the $\overline{w}\,\overline{\theta}$ term.

The manner of specifying the turbulent transport terms is normally referred to as the turbulence closure assumption. A non-trivial closure assumption is generally required when considering a grid resolution such as will be employed here. Lilly (1962) gives a good discussion of first order turbulence closure assumptions. The simplest non-trivial closure assumption is called k-theory, where the terms:

$$\left(\overline{u' \frac{\partial \zeta'}{\partial x}}\right), \left(\overline{w' \frac{\partial \zeta'}{\partial z}}\right) \quad \text{in Equation (2.31),}$$

$$\left(\overline{u' \frac{\partial \theta'}{\partial x}}\right), \left(\overline{w' \frac{\partial \theta'}{\partial z}}\right) \quad \text{in Equation (2.35),}$$

$$\left(\overline{u' \frac{\partial q'}{\partial x}}\right), \left(\overline{w' \frac{\partial q'}{\partial z}}\right) \quad \text{in Equation (2.37)}$$

and

$$\left(\overline{u' \frac{\partial \ell'}{\partial x}}\right), \left(\overline{w' \frac{\partial \ell'}{\partial z}}\right), \frac{\partial(\overline{v^{*\prime} \ell'})}{\partial z} \quad \text{in Equation (2.38)}$$

which result from an expansion of the respective equations, as above, are parametrically represented by the diffusion terms $\nu \nabla^2 \zeta$, $\kappa_\theta \nabla^2 \theta$, $\kappa_q \nabla^2 q$ and $\kappa_\ell \nabla^2 \ell$, respectively. Note that contributions due to density perturbations, which result in additional two-parameter and three parameter mean cross-correlation terms are neglected in a manner consistent with the previous approximations. In k-theory, the eddy diffusion coefficients ν, κ_θ, κ_q and κ_ℓ are specified constants. This is the approach adopted here. The reasons for this approach have already been alluded to in the introduction.

Lilly (1962) describes a more complicated first order closure scheme where the diffusion coefficients are not constant in space and time. Thus, they appear inside the spacial derivative operators similar to μ in Equation (2.1). His scheme has some physical basis but relies on the rather arbitrary choice of some numerical constants in the determination of the local eddy diffusion coefficients. Though such a scheme may be more realistic than the rather simple assumption employed here, it is unclear whether the improvement is significant. This is particularly true when considering that in a numerical grid point model, the eddy diffusion terms have the additional role of suppressing numerical noise and the occurrence of non-physical solutions and are therefore not as physically significant. Given the uncertainty as to the proper choice of coefficients in either scheme, especially when considering an application to middle or upper tropospheric conditions where observational support for such a choice is very limited, the simpler scheme was chosen. This scheme reduces the computational complexity and cost of the model. Furthermore, it straightforwardly obeys the relevant conservation principles. Though it is possible to derive conservative diffusion schemes for more complicated first order turbulence closure assumptions, this is generally not done due to the added complexity.

For similar reasons, second order turbulence closure assumptions (e.g. Oliver et al., 1978) are also rejected. For this study, the eddy diffusion coefficients are regarded as "tuneable" model constants. The role of these terms and the sensitivity of simulations to the choice of specific numerical values is established in Chapter 4. Comparisons

are made with other schemes. It should be noted that Asai and Nakamura (1978) have taken an approach similar to that adopted here for their study of convection in the atmospheric boundary layer. Their simulations exhibited a high degree of realism. Thus, it is hoped that the first order turbulence closure assumption invoked here will not adversely impact the realism of the simulations to a significant degree.

In Chapter 3, the numerical design of the model is presented. For the reader, who is not concerned with the specific details of the numerical techniques, a number of sections may be omitted. Sections (3.9), (3.10) and (3.11) describe the theoretical and observational basis for the diagnosis of the quantities v^*, C and F_R, respectively. The other sections are largely concerned with specific finite differencing schemes and may be conveniently omitted, if desired.

III. DESIGN OF THE NUMERICAL MODEL

In this chapter, the numerical model is described in detail. The spacial grid and the corresponding notation conventions are given in the first section. In addition, the general spacially discrete form of the governing equations and the manner of imposing the periodic lateral boundary conditions in discrete space are presented there. The vertical boundary conditions are considered in the following sections as appropriate. In Sections (3.2), (3.3) and (3.4), the specific finite difference formulations of the terms accounting for advective processes, which are resolved by the grid, are presented. The terms accounting for unresolved advective processes, i.e. eddy diffusion processes, are formulated in Section (3.5). In the next section, the finite difference form of the energy conversion term, i.e. generation/destruction of vorticity by buoyancy forces, is given. The time integration schemes, which are employed in the model, are detailed in Section (3.7). The method of solving Poisson's equation for the diagnosis of streamfunction from the predicted vorticity field on a discrete grid is described in Section (3.8). In the succeeding sections, the parameterizations for the diagnosis of phase changes of water, effective ice water terminal velocity and radiative heating rates are developed. The initialization procedure is given in Section 3.12. The overall computational procedure is also presented there in schematic form.

3.1 General Considerations

In this section, the spacial grid along with the corresponding notation conventions are presented. Also, the general form of the

governing equations and the periodic boundary conditions in the lateral direction are presented in a spacially discrete form.

The spacial grid, which is adopted for the model, is the "staggered" grid. This grid is staggered in that it is actually a superposition of two sub-grids which are offset. This is illustrated in Figure 4. The streamfunction and vorticity are defined at the grid points labeled x, hereafter referred to as dynamic grid points. The potential temperature, water vapor specific humidity and ice water specific humidity are defined at the grid points labeled 0, hereafter referred to as thermodynamic grid points. The spacial separation between dynamic grid points (or thermodynamic grid points), which are adjacent in either the x or z directions, is a constant, i.e. d. The thermodynamic grid points are offset by a distance d/2 in both the x and z directions when compared to the dynamic grid points.

The "staggered" grid has been commonly used in studies of atmospheric convection, e.g. Lilly (1965), Lipps (1971), and Asai and Nakamura (1978). A primary advantage in using the "staggered" grid, when compared to a grid where all of the prognostic variables are defined at the same locations, is that the winds are well defined when computing the advection of θ, q or ℓ. This may be seen by comparing the advective schemes for ζ given in Section 3.2 and θ or q given in Section 3.3. Another significant advantage is that the vertical boundary conditions on θ, q and ℓ are well defined. This is more evident when the specific advective schemes are presented. Note that the boundaries are defined to coincide with dynamic grid points. Thus, each thermodynamic grid point represents a corresponding grid area d^2 as does each interior dynamic grid point. The bounding dynamic grid

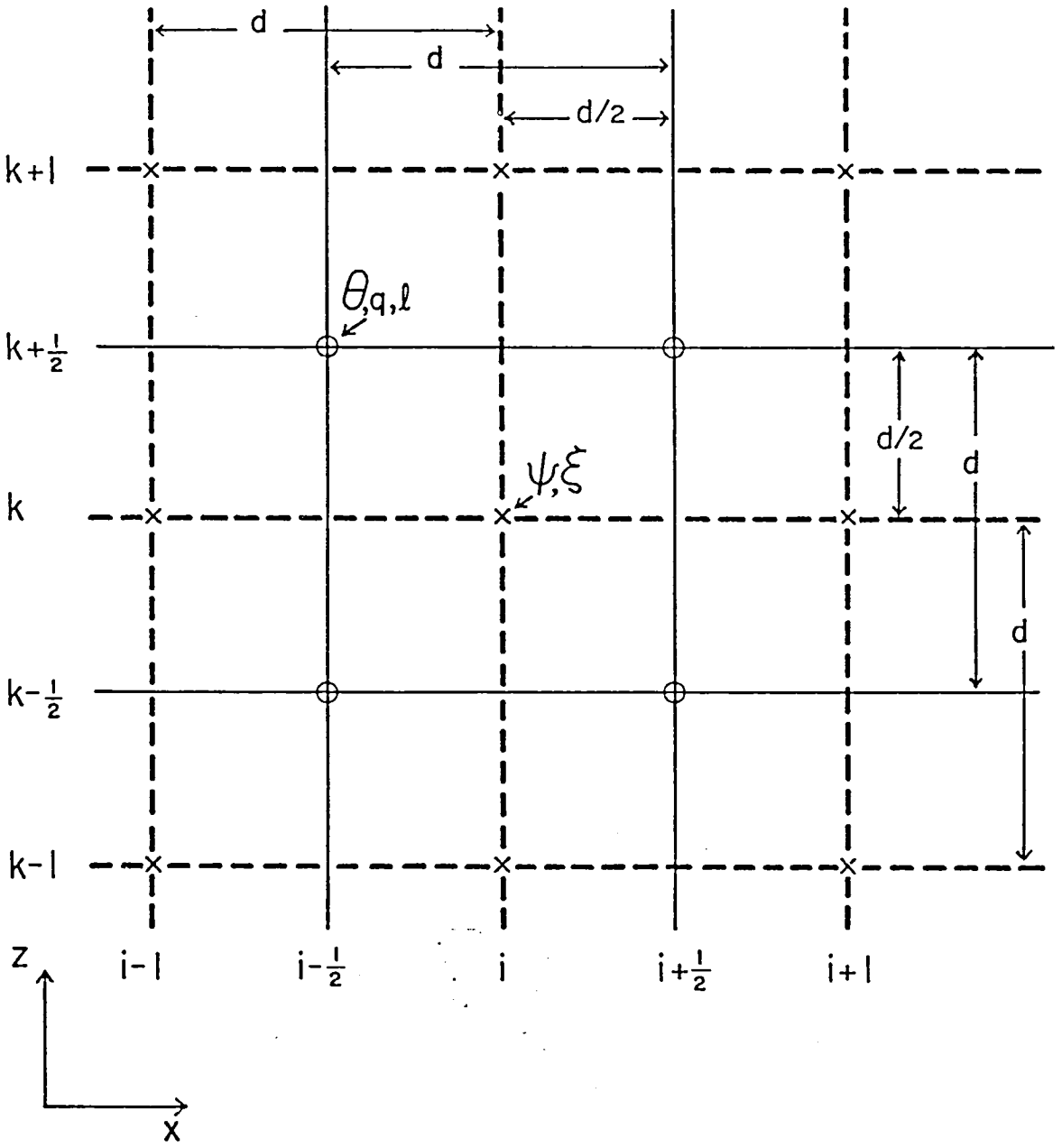

Figure 4. The grid configuration adopted for this study. The quantities ψ and ζ are defined at the points labeled x and the quantities θ, q and ℓ are defined at the points labeled 0. The grid interval is d and the coordinate orientation and grid point indexing are as indicated.

points each represent a corresponding grid area $d^2/2$ (see Figure 5b), except at the corners where the grid area is $d^2/4$.

In this paper, the notation convention is to use whole integers to index the column and level of dynamic grid points, i.e. i and k, respectively; as depicted in Figure 4. Furthermore,

$$x_{i=1} \equiv 0$$

and (3.1.1)

$$z_{k=1} \equiv h_B$$

where h_B is the height of the lower boundary. Thus, the (x,z) coordinates of a dynamic grid point (i,k) are given by:

$$x_i = (i-1)\, d \qquad \text{for } i = 1, 2, \ldots, I-1, I$$

and

$$z_k = h_B + (k-1)\, d \quad \text{for } k = 1, 2, \ldots, K-1, K \qquad (3.1.2)$$

where I and K are defined as the total number of dynamic grid points in the x and z directions, respectively.

The thermodynamic grid points are indexed as whole integers plus ½. Thus,

$$x_{i+\frac{1}{2}} = (i - \tfrac{1}{2})\, d \qquad \text{for } i = 1, 2, \ldots, I-2, I-1$$

and

$$z_{k+\frac{1}{2}} = h_B + (k - \tfrac{1}{2})\, d \quad \text{for } k = 1, 2, \ldots, K-2, K-1 \qquad (3.1.3)$$

are the (x,z) coordinates of a thermodynamic grid point ($i+\frac{1}{2}$, $k+\frac{1}{2}$). Note that there is one less thermodynamic grid level and grid column when compared to the dynamic grid. The specification of d, h_B, I and K totally determines the location of all grid points and the extent of the domain.

Observations indicate that major convective cells in cirriform clouds are organized on a horizontal space scale of $\sim$ 1 km, e.g. Heymsfield (1975b) and Plank, et al. (1955), among others. Approximately 6 to 8 grid points are required to adequately resolve a wave (Phillips, 1956). Thus, for the simulations reported here, the grid interval is usually specified as d = 100 m, which should be adequate. For a model, which is similar to that reported here, Asai and Nakamura (1978) found that d = 100 m adequately resolved convection in the atmospheric boundary layer. Recall that the importance of the sub-grid scale transports represented by the eddy diffusion terms in the governing equations decreases as the grid interval is decreased and the turbulent fields are better resolved. Thus, the impact of the rather simple first order turbulence closure scheme invoked here may be reduced by decreasing d. Tests, where d = 50 m, are reported here. The domain is generally specified as K = 64 and I = 128, i.e. $(z_K - z_1)$ = 3.1 km and $(x_I - x_1)$ = 12.7 km for d = 100 m. This should allow the convective cells to choose their own scale (Asai and Nakamura, 1978). However, for the preliminary test phase of the model development, I = 64 is specified in many cases for primarily economic reasons.

It is convenient to discuss the periodic lateral boundary conditions at this point. They will not be explicitly considered in any of the succeeding sections. The lateral boundaries correspond to the

dynamic grid points (1,k) and (I,k) for k = 1, 2, ..., K-1, K. As noted above, these grid points represent grid areas $d^2/2$. However, the periodic boundary conditions require:

$$S_{1,k} \equiv S_{I,k} \tag{3.1.4}$$

for S = ψ or ζ and k = 1, 2, ..., K-1, K. Thus, the two bounding grid points at a given level are effectively the same point and represent the combined corresponding grid area d^2 (except, of course, at the upper and lower boundaries where the combined grid area is $d^2/2$).

Computationally, when a parameter $S_{i+j,k}$ or $S_{i-j,k}$ occurs in a specific formulation and

if i+j > I, then:

$$i + j \equiv i - (I-1) + j$$

or if i-j < 1, then:

$$i - j \equiv i + (I-1) - j \tag{3.1.5}$$

for j = 1, 2, ... in the case of S = ψ or ζ for j = $\frac{1}{2}$, $\frac{3}{2}$, ... in the case of S = θ, q or ℓ. Thus, $\theta_{\frac{3}{2},k}$ and $\theta_{I-\frac{1}{2},k}$ represent the perturbation potential temperature of two horizontally adjacent thermodynamic grid areas.

The spacially discrete form of the governing equations may be written in flux form using Equation (2.4) as:

$$\frac{\partial \zeta_{i,k}}{\partial t} = D\, J_{i,k}(\zeta, \psi) - \left.\frac{\partial (w_o \zeta)}{\partial z}\right|_{i,k} + g \left.\frac{\partial B}{\partial x}\right|_{i,k} + \nu \nabla^2_{i,k} \zeta \,. \tag{3.1.6}$$

$$\frac{\partial \theta_{i+\frac{1}{2},k+\frac{1}{2}}}{\partial t} = T\, J_{i+\frac{1}{2},k+\frac{1}{2}}(\theta + \theta_o, \psi) - \left.\frac{\partial [w_o(\theta + \theta_o)]}{\partial z}\right|_{i+\frac{1}{2},k+\frac{1}{2}}$$

$$+ \kappa_\theta \nabla^2_{i+\frac{1}{2},k+\frac{1}{2}} \theta + \frac{1}{C_p \pi_{o_{k+\frac{1}{2}}}} \left\{ (LC)_{i+\frac{1}{2},k+\frac{1}{2}} + QR_{i+\frac{1}{2},k+\frac{1}{2}} \right\} \tag{3.1.7}$$

$$\frac{\partial q_{i+\frac{1}{2},k+\frac{1}{2}}}{\partial t} = T\, J_{i+\frac{1}{2},k+\frac{1}{2}}(q + q_o, \psi) - \left.\frac{\partial [w_o(q + q_o)]}{\partial z}\right|_{i+\frac{1}{2},k+\frac{1}{2}}$$

$$+ \kappa_q \nabla^2_{i+\frac{1}{2},k+\frac{1}{2}} q - C_{i+\frac{1}{2},k+\frac{1}{2}} \tag{3.1.8}$$

$$\frac{\partial \ell_{i+\frac{1}{2},k+\frac{1}{2}}}{\partial t} = -\frac{\partial}{\partial x}\left\{\left(-\frac{\partial \psi}{\partial z}\right)\ell\right\}_{i+\frac{1}{2},k+\frac{1}{2}} - \frac{\partial}{\partial z}\left\{\left(\frac{\partial \psi}{\partial x} + w_o + v^*\right)\ell\right\}_{i+\frac{1}{2},k+\frac{1}{2}}$$

$$+ \kappa_\ell \nabla^2_{i+\frac{1}{2},k+\frac{1}{2}} \ell + C_{i+\frac{1}{2},k+\frac{1}{2}} \tag{3.1.9}$$

and

$$\zeta_{i,k} = \nabla^2_{i,k} \psi \,. \tag{3.1.10}$$

The index subscripts indicate operators in discrete space as described in the succeeding sections. Note that the discrete form of the

Jacobian operator for evaluation at dynamic grid points is different than that for thermodynamic grid points. The prognostic equations must be integrated in time as described in Section 3.7. For this integration, the right hand side of Equation (3.1.6) must be evaluated for $i = 1, 2, \ldots, I-1, I$ and $k = 1, 2, \ldots, K-1, K$. Note that the computations at $i = 1$ and $i = I$ are redundant. The diagnostic equation, i.e. Equation (3.1.10) must be solved at these same grid points. For the integration of the remaining prognostic equations, the right hand sides of Equations (3.1.7), (3.1.8) and (3.1.9) must be evaluated for $i = 1, 2, \ldots, I-2, I-1$ and $k = 1, 2, \ldots, K-2, K-1$.

3.2 Vorticity Advection

The advection of vorticity by the perturbation component of the velocity field is evaluated at the dynamic grid points by means of the flux form of the nine-point finite difference approximation reported by Arakawa (1966). This formulation is a linear combination of three basic second order schemes and, thus, has second order accuracy. Furthermore, it has the desirable properties of conservation of vorticity, squared vorticity and kinetic energy, which is not true of the more basic schemes from which it was derived (Arakawa, 1966). Thus, this approximation is computationally stable in these regards.

Recall that in this model, advection of vorticity by the mean flow component of the velocity field is limited to advection by a basic state vertical velocity, i.e. w_o, which is everywhere an externally specified constant. This term is evaluated in a manner which maintains the desirable properties of the advective scheme noted above.

The advection of vorticity at a dynamic grid point (i,k) by the total velocity field is computed as:

$$ {}^{D}J_{i,k}(\zeta,\psi) - \left.\frac{\partial(w_o\zeta)}{\partial z}\right|_{i,k} = $$

$$ \frac{-1}{12d^2}\Big\{ {}^{D}F_1(i,k) - {}^{D}F_2(i,k) + {}^{D}F_3(i,k) - {}^{D}F_4(i,k) $$

$$ + {}^{D}F_5(i,k) - {}^{D}F_6(i,k) + {}^{D}F_7(i,k) - {}^{D}F_8(i,k)\Big\} \quad (3.2.1) $$

where

$$ {}^{D}F_1(i,k) \equiv (\psi_{i,k-1} + \psi_{i+1,k-1} - \psi_{i,k+1} - \psi_{i+1,k+1}) $$

$$ (\zeta_{i+1,k} + \zeta_{i,k}), \quad (3.2.2) $$

$$ {}^{D}F_2(i,k) \equiv (\psi_{i-1,k-1} + \psi_{i,k-1} - \psi_{i-1,k+1} - \psi_{i,k+1}) $$

$$ (\zeta_{i,k} + \zeta_{i-1,k}), \quad (3.2.3) $$

$$ {}^{D}F_3(i,k) \equiv (4\Psi_o + \psi_{i+1,k} + \psi_{i+1,k+1} - \psi_{i-1,k} - \psi_{i-1,k+1}) $$

$$ (\zeta_{i,k+1} + \zeta_{i,k}), \quad (3.2.4) $$

$$ {}^{D}F_4(i,k) \equiv (4\Psi_o + \psi_{i+1,k-1} - \psi_{i+1,k} - \psi_{i-1,k-1} - \psi_{i-1,k}) $$

$$ (\zeta_{i,k} + \zeta_{i,k-1}), \quad (3.2.5) $$

$$ {}^{D}F_5(i,k) \equiv (\Psi_o + \psi_{i+1,k} - \psi_{i,k+1})(\zeta_{i+1,k+1} + \zeta_{i,k}), \quad (3.2.6) $$

$$ {}_{D}F_{6}(i,k) \equiv (\Psi_{o} + \psi_{i,k-1} - \psi_{i-1,k})(\zeta_{i,k} + \zeta_{i-1,k-1}), \qquad (3.2.7) $$

$$ {}_{D}F_{7}(i,k) \equiv (\Psi_{o} + \psi_{i,k+1} - \psi_{i-1,k})(\zeta_{i-1,k+1} + \zeta_{i,k}), \qquad (3.2.8) $$

$$ {}_{D}F_{8}(i,k) \equiv (\Psi_{o} + \psi_{i+1,k} - \psi_{i,k-1})(\zeta_{i,k} + \zeta_{i+1,k-1}) \qquad (3.2.9) $$

and

$$ \Psi_{o} \equiv w_{o}d . \qquad (3.2.10) $$

Note that if $\Psi_{o} = 0$, then Equation (3.2.1) reduces exactly to that given by Arakawa (1966).

Each ${}_{D}F_{j}(i,k)$ essentially represents the flux of vorticity between the grid point (i,k) and one of the surrounding eight grid points, directed as in Figure 5a. In this sense, Equation (3.2.1) represents a weighted average of flux convergences computed at various orientations. The basic state component is a weighted mean of the vertical flux convergence at the grid point (i,k) and the two horizontally adjacent grid points (i+1,k) and (i-1,k). The vorticity exchanges between points are mutually conservative, i.e.

$$ {}_{D}F_{1}(i,k) = {}_{D}F_{2}(i+1,k) $$

$$ {}_{D}F_{2}(i,k) = {}_{D}F_{1}(i-1,k) $$

$$ {}_{D}F_{3}(i,k) = {}_{D}F_{4}(i,k+1) $$

$$ {}_{D}F_{4}(i,k) = {}_{D}F_{3}(i,k-1) $$

$$ {}_{D}F_{5}(i,k) = {}_{D}F_{6}(i+1,k+1) $$

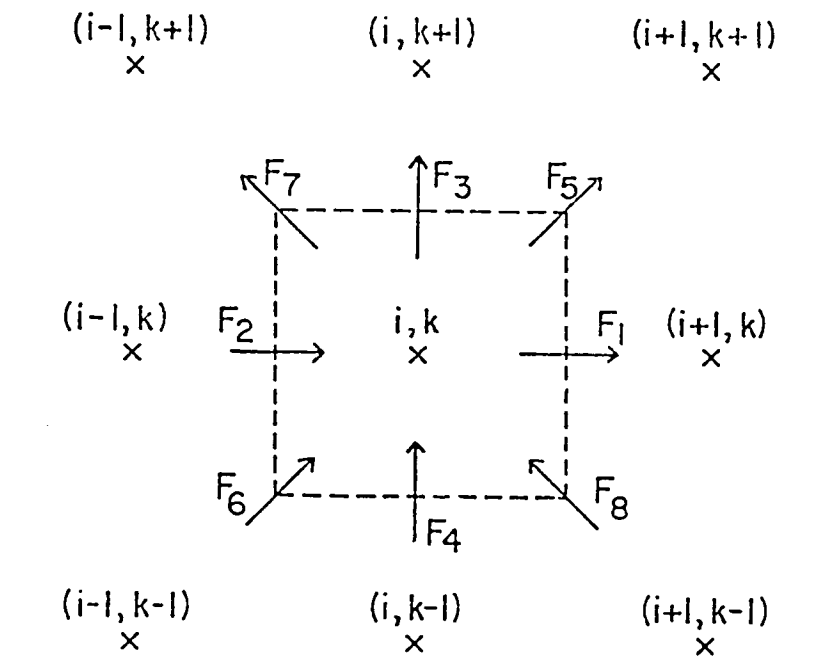

(a)

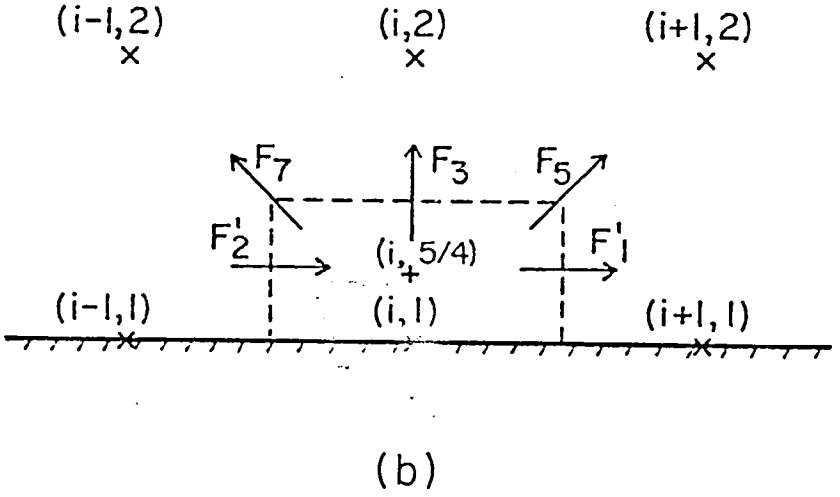

(b)

Figure 5. Orientation of the flux components accounting for the mutual interactions between grid points when evaluating the advective term in the governing dynamic equation (a) at a general interior dynamic grid point (i,k), (b) at a bounding dynamic grid point (i,1). See text for definitions and discussion.

$$_{D}F_{6}(i,k) = {}_{D}F_{5}(i-1,k-1)$$

$$_{D}F_{7}(i,k) = {}_{D}F_{8}(i-1,k+1)$$

$$_{D}F_{8}(i,k) = {}_{D}F_{7}(i+1,k-1). \qquad (3.2.11)$$

This leads to the computational advantage of employing the flux form in that only four of the flux terms need be evaluated at each grid point, e.g. $_{D}F_{1}(i,k)$, $_{D}F_{3}(i,k)$, $_{D}F_{5}(i,k)$, $_{D}F_{7}(i,k)$.

The grid points on the horizontal boundaries, i.e. (i,1) and (i,K), represent rectangular grid areas of vertical depth d/2 as in Figure 5b for the grid point (i,1). Following from Arakawa (1966), the above scheme is modified when evaluated at the bounding grid points as:

$$_{D}J_{i,1}(\zeta,\psi) - \left.\frac{\partial(w_{o}\cdot)}{\partial z}\right|_{i,1} =$$

$$\frac{-2}{12d^{2}}\left\{{}_{D}F_{1}(i)_{1} - {}_{D}F_{2}(i)_{1} + {}_{D}F_{3}(i,1) + {}_{D}F_{5}(i,1) + {}_{D}F_{7}(i,1)\right\} \qquad (3.2.12)$$

and

$$_{D}J_{i,K}(\zeta,\psi) - \left.\frac{\partial(w_{o}\zeta)}{\partial z}\right|_{i,K} =$$

$$\frac{-2}{12d^{2}}\left\{{}_{D}F_{1}(i)_{K} - {}_{D}F_{2}(i)_{K} - {}_{D}F_{4}(i,K) - {}_{D}F_{6}(i,K) - {}_{D}F_{8}(i,K)\right\} \qquad (3.2.13)$$

where

$$_{D}F_{1}(i)_{1} \equiv (\psi_{i,1} + \psi_{i+1,1} - \psi_{i,2} - \psi_{i+1,2})(\zeta_{i+1,1} + \zeta_{i,1}), \qquad (3.2.14)$$

$$_{D}F_{2}(i)_{1} \equiv (\psi_{i-1,1} + \psi_{i,1} - \psi_{i-1,2} - \psi_{i,2})(\zeta_{i,1} + \zeta_{i-1,1}), \qquad (3.2.15)$$

$$ {}_{D}F_{1}(i)_{K} \equiv (\psi_{i,K-1} + \psi_{i+1,K-1} - \psi_{i,K} - \psi_{i+1,K})(\zeta_{i+1,K} + \zeta_{i,K}) \tag{3.2.16} $$

and

$$ {}_{D}F_{2}(i)_{K} \equiv (\psi_{i-1,K-1} + \psi_{i,K-1} - \psi_{i-1,K} - \psi_{i,K})(\zeta_{i,K} + \zeta_{i-1,K}) \cdot \tag{3.2.17} $$

Note that:

$$ {}_{D}F_{1}(i)_{k} = {}_{D}F_{2}(i+1)_{k} $$

and

$$ {}_{D}F_{2}(i)_{k} = {}_{D}F_{1}(i-1)_{k} \tag{3.2.18} $$

for k = 1 or K.

These expressions account for the altered area and geometry of the boundary grid areas and preserve the desirable conservation properties noted previously. Note that the purely horizontal flux terms have been modified, i.e. compare Equations (3.2.2) and (3.2.3) to Equations (3.2.14)-(3.2.17). Otherwise the flux terms accounting for exchanges with interior points remain the same and the terms representing interactions with points outside the domain have been omitted in Equations (3.2.12) and (3.2.13) when compared to Equation (3.2.1). In effect, the vertical boundary conditions on ζ are already incorporated into Equations (3.2.12) and (3.2.13). The following interpretation of the above formulations clarifies this point.

Due to the nature of the grid employed here and the desire for a conservative advective scheme, the values of $\zeta_{i,1}$ and $\zeta_{i,K}$ must be regarded as representing the mean vorticity of the corresponding half-grid

areas and not ζ_B or ζ_T, respectively. Thus, $\zeta_{i,1}$ and $\zeta_{i,K}$ may be viewed as corresponding to the grid points $(i,\frac{5}{4})$ and $(i,K-\frac{1}{4})$, as shown in Figure 5b. Arakawa (1966) gives a modified version of his scheme which accounts for variable grid geometry at interior points. Direct application of this scheme to the geometry of the bounding grid areas and comparison to Equations (3.2.12) and (3.2.13) yields the following conclusions. The geometric difference between $(i,1)$ and $(i,\frac{5}{4})$ and (i,K) and $(i,K-\frac{1}{4})$ have been ignored in computing the mutual interaction of boundary layer grid points and internal grid points in order that the conservation principles are maintained. The purely horizontal advection terms are approximate but consistent with the desired conservation properties and the above approximation (Arakawa, 1966). Noting that interpolations are unnecessary for determining ζ on the boundaries, the terms omitted may be effectively viewed as corresponding to the imposition of the boundary conditions, $\zeta_B \equiv \zeta_T \equiv 0$. This interpretation also holds for the components due to the basic state vertical velocity. Thus, no additional modification of the above formulations is required in order that the vertical boundary conditions on perturbation vorticity be obeyed.

The perturbation streamfunction may be regarded as representative at discrete points and not necessarily representative of the mean value of the corresponding grid areas. In this sense, the vertical boundary conditions on ψ may be applied straightforwardly as:

$$\begin{aligned} \psi_{i,1} &\equiv 0 \\ \psi_{i,K} &\equiv 0 \end{aligned} \qquad (3.2.19)$$

for i = 1, 2, ..., I-1, I.

Thus, these terms may be eliminated from Equations (3.2.12) and (3.2.13) though it is only computationally convenient to do so for the ${}_{D}F_{1}(i)_{1}$, ${}_{D}F_{2}(i)_{1}$, ${}_{D}F_{1}(i)_{K}$ and ${}_{D}F_{2}(i)_{K}$ terms, e.g.

$$ {}_{D}F_{1}(i)_{1} = (-\psi_{i,2} - \psi_{i+1,2})(\zeta_{i+1,1} + \zeta_{i,1}) \qquad (3.2.20) $$

and

$$ {}_{D}F_{1}(i)_{K} = (\psi_{i,K-1} + \psi_{i+1,K-1})(\zeta_{i+1,K} + \zeta_{i,K}) . \qquad (3.2.21) $$

The computational procedure is given by the following steps:

a) Compute ${}_{D}F_{1}(i)_{1}$ and ${}_{D}F_{1}(i)_{K}$ for i = 1, 2, ..., I-1, I as given by Equations (3.2.20) and (3.2.21) respectively.

b) Compute ${}_{D}F_{1}(i,k)$ for i = 1, 2, ..., I-1, I and k = 2, 3, ..., K-2, K-1 as given by Equation (3.2.2).

c) Compute ${}_{D}F_{3}(i,k)$, ${}_{D}F_{5}(i,k)$, ${}_{D}F_{7}(i,k)$ for i = 1, 2, ..., I-1, I and k = 1, 2, ..., K-2, K-1 as given by Equations (3.2.4), (3.2.6) and (3.2.8), respectively.

d) Utilizing the identities given in Equations (3.2.11) and (3.2.18), compute ${}_{D}J_{i,k}(\zeta,\psi) - \left.\frac{\partial(w_o\zeta)}{\partial z}\right|_{i,k}$ for i = 1, 2, ..., I-1, I and k = 1; k = 2, 3, ..., K-2, K-1; and k = K from Equations (3.2.12), (3.2.1) and (3.2.13), respectively.

3.3 Advection of Potential Temperature and Water Vapor

For the purposes here, let the dummy variable S represent either the potential temperature or water vapor specific humidity such that S denotes either θ or q and $S + S_o$ denotes either $\theta + \theta_o$ or $q + q_o$.

The advection of $S + S_o$ by the perturbation component of the velocity field is evaluated at thermodynamic grid points by means of

the flux form of the finite difference approximation reported by Lilly (1965). This scheme is of second order accuracy and was designed for application to a staggered grid as here. It incorporates values at five thermodynamic grid points and at four dynamic grid points. This formulation conserves $(S + S_o)$ and $(S + S_o)^2$ and, thus, is computationally stable in these regards. As in the previous section, the advection of $(S + S_o)$ by the basic state vertical velocity may be evaluated in a manner consistent with the above scheme. The desirable conservation properties of the scheme are maintained in the modified formulation.

The advection of $(S + S_o)$ by the total velocity field is computed at a thermodynamic grid point $(i+\frac{1}{2},k+\frac{1}{2})$ as:

$$ {}_T J_{i+\frac{1}{2},k+\frac{1}{2}}(S + S_o, \psi) - \left.\frac{\partial [w_o (S + S_o)]}{\partial z}\right|_{i+\frac{1}{2},k+\frac{1}{2}} = $$

$$ \frac{-1}{d^2}\left\{ {}_T F_1(i+\tfrac{1}{2},k+\tfrac{1}{2}) - {}_T F_2(i+\tfrac{1}{2},k+\tfrac{1}{2}) \right. $$

$$ \left. + {}_T F_3(i+\tfrac{1}{2},k+\tfrac{1}{2}) - {}_T F_4(i+\tfrac{1}{2},k+\tfrac{1}{2}) \right\} \qquad (3.3.1) $$

where

$$ {}_T F_1(i+\tfrac{1}{2},k+\tfrac{1}{2}) \equiv $$

$$ (\psi_{i+1,k} - \psi_{i+1,k+1}) \left[\frac{(S_{i+\frac{1}{2},k+\frac{1}{2}} + S_{i+\frac{3}{2},k+\frac{1}{2}})}{2} + S_{o_{k+\frac{1}{2}}} \right] \qquad (3.3.2) $$

$$ {}_{T}F_{2}(i+\tfrac{1}{2},k+\tfrac{1}{2}) \equiv $$

$$ (\psi_{i,k} - \psi_{i,k+1}) \left[\frac{(S_{i-\frac{1}{2},k+\frac{1}{2}} + S_{i+\frac{1}{2},k+\frac{1}{2}})}{2} + S_{o_{k+\frac{1}{2}}} \right], \qquad (3.3.3) $$

$$ {}_{T}F_{3}(i+\tfrac{1}{2},k+\tfrac{1}{2}) \equiv $$

$$ (\Psi_{o} + \psi_{i+1,k+1} - \psi_{i,k+1}) \left[\frac{(S_{i+\frac{1}{2},k+\frac{3}{2}} + S_{i+\frac{1}{2},k+\frac{1}{2}})}{2} + \frac{(S_{o_{k+\frac{1}{2}}} + S_{o_{k+\frac{3}{2}}})}{2} \right] \qquad (3.3.4) $$

and

$$ {}_{T}F_{4}(i+\tfrac{1}{2},k+\tfrac{1}{2}) \equiv $$

$$ (\Psi_{o} + \psi_{i+1,k} - \psi_{i,k}) \left[\frac{(S_{i+\frac{1}{2},k+\frac{1}{2}} + S_{i+\frac{1}{2},k-\frac{1}{2}})}{2} + \frac{(S_{o_{k+\frac{1}{2}}} + S_{o_{k-\frac{1}{2}}})}{2} \right]. \qquad (3.3.5) $$

Each ${}_{T}F_{j}(i+\tfrac{1}{2},k+\tfrac{1}{2})$ essentially represents the flux of $(S + S_{o})$ between the thermodynamic grid point $(i+\tfrac{1}{2},k+\tfrac{1}{2})$ and one of the surrounding four thermodynamic grid points directed as in Figure 6. The computational advantage of the flux form of the advective scheme may be seen in that only two fluxes, e.g. ${}_{T}F_{1}(i+\tfrac{1}{2},k+\tfrac{1}{2})$ and ${}_{T}F_{3}(i+\tfrac{1}{2},K+\tfrac{1}{2})$, need be computed at each thermodynamic grid point since:

$$ \begin{aligned} {}_{T}F_{1}(i+\tfrac{1}{2},k+\tfrac{1}{2}) &= {}_{T}F_{2}(i+\tfrac{3}{2},k+\tfrac{1}{2}) \\ {}_{T}F_{2}(i+\tfrac{1}{2},k+\tfrac{1}{2}) &= {}_{T}F_{1}(i-\tfrac{1}{2},k+\tfrac{1}{2}) \\ {}_{T}F_{3}(i+\tfrac{1}{2},k+\tfrac{1}{2}) &= {}_{T}F_{4}(i+\tfrac{1}{2},k+\tfrac{3}{2}) \\ {}_{T}F_{4}(i+\tfrac{1}{2},k+\tfrac{1}{2}) &= {}_{T}F_{3}(i+\tfrac{1}{2},k-\tfrac{1}{2}) \, . \end{aligned} \qquad (3.3.6) $$

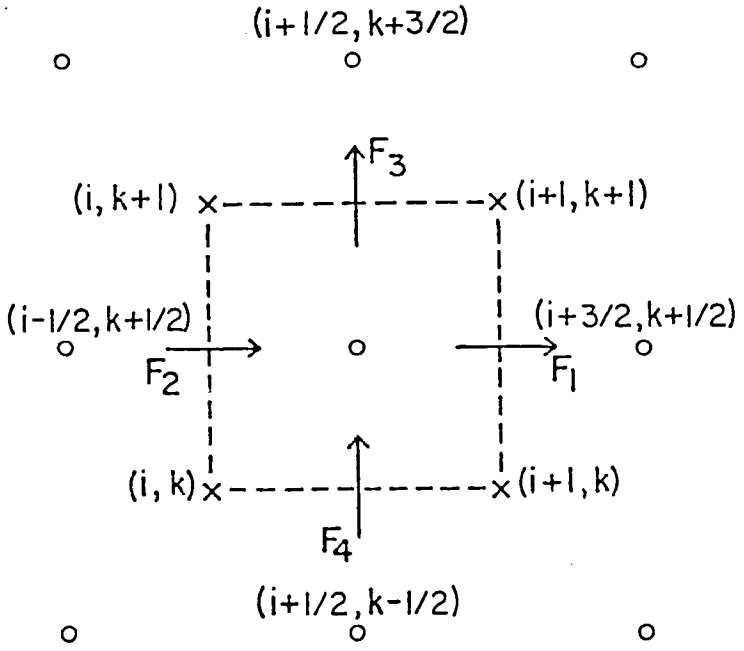

Figure 6. Orientation of the flux components accounting for the mutual interactions between grid points when evaluating the advective term in the governing equations for θ, q and ℓ at a general thermodynamic grid point $(i+\frac{1}{2}, k+\frac{1}{2})$. See text for definitions and discussion.

Due to the geometry of the grid (see Figure 4), the vertical boundary conditions on S and S_o may be applied directly at discrete points along the dynamic grid levels k = 1 and k = K. These points do not correspond to any thermodynamic grid areas and, thus, $S_{i+\frac{1}{2},k}$ and S_{o_k} for k = 1 or K represent discrete point values and not area means. Thus, the boundary conditions on S correspond to:

$$S_{i+\frac{1}{2},k} = 0 \qquad (3.3.7)$$

for k = 1 or K.

The formulas for the vertical flux components employ a linear interpolation between vertically adjacent thermodynamic grid points to determine midpoint values. Since S and S_o are specified on the boundaries, the interpolation for S and S_o at these levels is unnecessary. Thus, the cross boundary fluxes are determined as:

$$T^{F_4}(i+\tfrac{1}{2},\tfrac{3}{2}) = (\Psi_o + \psi_{i+1,1} - \psi_{i,1})(S_{i+\frac{1}{2},1} + S_{o_1}) \qquad (3.3.8)$$

and

$$T^{F_3}(i+\tfrac{1}{2},K-\tfrac{1}{2}) = (\Psi_o + \psi_{i+1,K} - \psi_{i,K})(S_{i+\frac{1}{2},K} + S_{o_K}) . \qquad (3.3.9)$$

Together with Equation (3.3.7), the vertical boundary condition on ψ, i.e. Equation (3.2.19), allows:

$$T^{F_4}(i+\tfrac{1}{2},\tfrac{3}{2}) = \Psi_o S_{o_1} \qquad (3.3.10)$$

and

$$T^{F_3}(i+\tfrac{1}{2},K-\tfrac{1}{2}) = \Psi_o S_{o_K} . \qquad (3.3.11)$$

Recall that Ψ_o is an externally specified parameter. Similarly, S_{o_1} and S_{o_K} are externally specified parameters. Thus, the cross-boundary fluxes may be regarded as adjustable model constants and do not depend on processes acting within the layer.

Note that the formulations for the horizontal flux terms in the bounding layers might be simplified to reflect the boundary conditions on ψ. Computationally, this is not convenient.

The computational procedure is given by the following steps.

a) Compute ${}_TF_1(i+\frac{1}{2},k+\frac{1}{2})$ for i = 1, 2, ..., I-2, I-1 and k = 1, 2, ..., K-2, K-1 from Equation (3.3.2).

b) Compute ${}_TF_4(i+\frac{1}{2},\frac{3}{2})$ and ${}_TF_3(i+\frac{1}{2},K-\frac{1}{2})$ for i = 1, 2, ..., I-2, I-1 from Equations (3.3.10) and (3.3.11), respectively. (Note that this step is performed only once at the initial time step.)

c) Compute ${}_TF_3(i+\frac{1}{2},k+\frac{1}{2})$ for i = 1, 2, ..., I-2, I-1 and k = 2, 3, ..., K-3, K-2 from Equation (3.3.4).

d) Utilizing the identities given in Equation (3.3.6), compute ${}_T\mathcal{J}_{i+\frac{1}{2},k+\frac{1}{2}}(S + S_o, \psi) - \frac{\partial[w_o(S + S_o)]}{\partial z}\Big|_{i+\frac{1}{2},k+\frac{1}{2}}$ from Equation (3.3.1) for i = 1, 2, ..., I-2, I-1 and k = 1, 2, ..., K-2, K-1.

3.4 Ice Water Advection

The advection of ice water specific humidity is evaluated at thermodynamic grid points by means of an "upstream" flux form finite difference approximation, which is appropriate to a staggered grid. This scheme is similar to that described in the last section for θ and q, except that the value of ℓ specified on the grid area boundary

between two adjacent thermodynamic grid points is not interpolated from the values of ℓ at those grid points. Instead, the midpoint value of ℓ is directly specified as equal to the value of ℓ at the upstream grid point. The direction of the appropriate component of the total wind at the midpoint between the two grid points determines which is the upstream grid point, i.e. the wind is directed from the upstream grid point to the downstream grid point. Effectively, ice water has been assumed to be uniformly distributed within each thermodynamic grid area.

As before, the contributions due to both the perturbation velocity field and the basic state vertical velocity are incorporated into the scheme. In addition, the relative, vertical fall velocity of ice water particles is taken into account. The upstream advective scheme is conservative with respect to ℓ and ℓ^2 and is computationally stable in these regards. Subject to the appropriateness of the aforementioned assumption, this formulation also has second order accuracy.

The primary advantage in using the upstream scheme for computing the advection of ℓ, when compared to the scheme described for θ or q, is that it eliminates the occurrence of the $\ell < 0$ computation mode in the solution. This mode arises in the previous scheme due to truncation errors. These truncation errors may be viewed as a result of the incompatibility of using interpolation and requiring that the grid point value of ℓ is representative of the mean value of the corresponding grid area. For example, in the case of water vapor specific humidity, the effect of truncation errors on q will be relatively small compared to $q + q_o$, since in general, $q_o >> q$. Thus, the non-physical mode $(q + q_o) < 0$ is unlikely to occur. Diffusive damping may be applied to q to effectively suppress what may be viewed as numerical

noise generated by truncation errors (Chapter 4). However, since $\ell_o \equiv 0$, the occurrence of $\ell < 0$ due to truncation error corresponds to a non-physical mode in the solution in that negative ice water does not exist. In the presence of the diabatic processes, the initial amplitude of the $\ell < 0$ computational mode may be relatively large. Reasonable diffusive damping can reduce the amplitude but will not eliminate this mode from the domain. The occurrence of the $\ell < 0$ mode presents a substantial problem in that if total water is to be conserved, these values may not be simply ignored. However, such values would have a substantial adverse impact on the evaluation of the buoyant generation of vorticity. The use of the "upstream" formulation eliminates these problems and this advantage is felt to far outweigh the disadvantages noted below.

The primary disadvantage of using the upstream flux scheme, when compared to the previous scheme, is that it is more complex and substantially less efficient computationally. Furthermore, the assumed spacial distribution of ℓ is likely to be a much poorer representation of the continuous case when compared to the linear variation over distances of $O(d)$ assumed for the previous scheme. It is for this last reason, that the upstream flux scheme is not used for θ or q, since it would not be any more inefficient computationally than the previous scheme once the wind directions are determined.

The advection of ℓ by the total velocity field, where the relative vertical velocity of suspended ice water particles is taken into account, is evaluated at a thermodynamic grid point $(i+\frac{1}{2},k+\frac{1}{2})$ as:

$$\left[- \frac{\partial}{\partial x} \left\{ \ell \left(\frac{-\partial \psi}{\partial z} \right) \right\} - \frac{\partial}{\partial z} \left\{ \ell \left(\frac{\partial \psi}{\partial x} + w_o + v^* \right) \right\} \right]_{i+\frac{1}{2}, k+\frac{1}{2}} =$$

$$\frac{-1}{d^2} \left\{ {}_L F_1(i+\tfrac{1}{2}, k+\tfrac{1}{2}) - {}_L F_2(i+\tfrac{1}{2}, k+\tfrac{1}{2}) \right.$$

$$\left. + {}_L F_3(i+\tfrac{1}{2}, k+\tfrac{1}{2}) - {}_L F_4(i+\tfrac{1}{2}, k+\tfrac{1}{2}) \right\} \qquad (3.4.1)$$

where the horizontal flux terms are determined as follows:

If $(\psi_{i+1,k} - \psi_{i+1,k+1}) \geq 0$, then:

$${}_L F_1(i+\tfrac{1}{2}, k+\tfrac{1}{2}) = (\psi_{i+1,k} - \psi_{i+1,k+1}) \, \ell_{i+\frac{1}{2}, k+\frac{1}{2}} ,$$

otherwise:

$${}_L F_1(i+\tfrac{1}{2}, k+\tfrac{1}{2}) = (\psi_{i+1,k} - \psi_{i+1,k+1}) \, \ell_{i+\frac{3}{2}, k+\frac{1}{2}} . \qquad (3.4.2)$$

If $(\psi_{i,k} - \psi_{i,k+1}) \geq 0$, then:

$${}_L F_2(i+\tfrac{1}{2}, k+\tfrac{1}{2}) = (\psi_{i,k} - \psi_{i,k+1}) \, \ell_{i-\frac{1}{2}, k+\frac{1}{2}} ,$$

otherwise:

$${}_L F_2(i+\tfrac{1}{2}, k+\tfrac{1}{2}) = (\psi_{i,k} - \psi_{i,k+1}) \, \ell_{i+\frac{1}{2}, k+\frac{1}{2}} . \qquad (3.4.3)$$

The evaluation of the vertical flux components is further complicated by the presence of the effective relative fall velocity term v^*. It is convenient to let:

$$ {}_{L}F_{3}(i+\tfrac{1}{2},k+\tfrac{1}{2}) \equiv {}_{L}F_{3+}(i+\tfrac{1}{2},k+\tfrac{1}{2}) + {}_{L}F_{3-}(i+\tfrac{1}{2},k+\tfrac{1}{2}) $$

and

$$ {}_{L}F_{4}(i+\tfrac{1}{2},k+\tfrac{1}{2}) \equiv {}_{L}F_{4+}(i+\tfrac{1}{2},k+\tfrac{1}{2}) + {}_{L}F_{4-}(i+\tfrac{1}{2},k+\tfrac{1}{2}) \qquad (3.4.4) $$

where the plus and minus subscripts denote the potential components of the flux across a grid area boundary due to the interaction of the perturbation and basic state vertical velocities with the relative fall velocity of suspended particles in the region just above (+) and just below (-) the boundary. Thus, it is possible for two vertically adjacent grid areas to actually exchange some ice water, i.e. some falls from the upper to the lower grid area and some is advected from the lower to the upper grid area. These components are determined as follows:

If $(\Psi_o + \psi_{i+1,k+1} - \psi_{i,k+1} + \Psi^*_{i+\frac{1}{2},k+\frac{3}{2}}) < 0$, then:

$$ {}_{L}F_{3+}(i+\tfrac{1}{2},k+\tfrac{1}{2}) = (\Psi_o + \psi_{i+1,k+1} - \psi_{i,k+1} + \Psi^*_{i+\frac{1}{2},k+\frac{3}{2}})\, \ell_{i+\frac{1}{2},k+\frac{3}{2}}, $$

otherwise:

$$ {}_{L}F_{3+}(i+\tfrac{1}{2},k+\tfrac{1}{2}) \equiv 0. \qquad (3.4.5) $$

If $(\Psi_o + \psi_{i+1,k+1} - \psi_{i,k+1} + \Psi^*_{i+\frac{1}{2},k+\frac{1}{2}}) > 0$, then:

$$ {}_{L}F_{3-}(i+\tfrac{1}{2},k+\tfrac{1}{2}) = (\Psi_o + \psi_{i+1,k+1} - \psi_{i,k+1} + \Psi^*_{i+\frac{1}{2},k+\frac{1}{2}})\, \ell_{i+\frac{1}{2},k+\frac{1}{2}}, $$

otherwise:

$$ {}_{L}F_{3-}(i+\tfrac{1}{2},k+\tfrac{1}{2}) \equiv 0. \qquad (3.4.6) $$

If $(\Psi_o + \psi_{i+k,k} - \psi_{i,k} + \Psi^*_{i+\frac{1}{2},k+\frac{1}{2}}) < 0$, then:

$$L^F_{4+}(i+\tfrac{1}{2},k+\tfrac{1}{2}) = (\Psi_o + \psi_{i+1,k} - \psi_{i,k} + \Psi^*_{i+\frac{1}{2},k+\frac{1}{2}})\, \ell_{i+\frac{1}{2},k+\frac{1}{2}},$$

otherwise:

$$L^F_{4+}(i+\tfrac{1}{2},k+\tfrac{1}{2}) \equiv 0. \qquad (3.4.7)$$

If $(\Psi_o + \psi_{i+1,k} - \psi_{i,k} + \Psi^*_{i+\frac{1}{2},k-\frac{1}{2}}) > 0$, then:

$$L^F_{4-}(i+\tfrac{1}{2},k+\tfrac{1}{2}) = (\Psi_o + \psi_{i+1,k} - \psi_{i,k} + \Psi^*_{i+\frac{1}{2},k-\frac{1}{2}})\, \ell_{i+\frac{1}{2},k-\frac{1}{2}},$$

otherwise:

$$L^F_{4-}(i+\tfrac{1}{2},k+\tfrac{1}{2}) \equiv 0. \qquad (3.4.8)$$

Now,

$$\Psi^*_{j,m} \equiv v^*_{j,m}\, d \qquad (3.4.9)$$

where j and m are dummy thermodynamic grid indices in the x and z directions, respectively and $v^*_{j,m}$ is the effective relative fall velocity of the suspended ice water particles in a thermodynamic grid area (j,m) and is determined parametrically as developed in Section 3.10. Note that $\Psi^*_{j,m}$ is always less than or equal to zero.

Due to the presence of conditional terms, the evaluation of the advection of ℓ is not efficient computationally. However, this is mitigated somewhat by the identities:

$$
\begin{aligned}
{}_{L}F_{1}(i+\tfrac{1}{2},k+\tfrac{1}{2}) &= {}_{L}F_{2}(i+\tfrac{3}{2},k+\tfrac{1}{2}) \\
{}_{L}F_{2}(i+\tfrac{1}{2},k+\tfrac{1}{2}) &= {}_{L}F_{1}(i-\tfrac{1}{2},k+\tfrac{1}{2}) \\
{}_{L}F_{3}(i+\tfrac{1}{2},k+\tfrac{1}{2}) &= {}_{L}F_{4}(i+\tfrac{1}{2},k+\tfrac{3}{2}) \\
{}_{L}F_{4}(i+\tfrac{1}{2},k+\tfrac{1}{2}) &= {}_{L}F_{4}(i+\tfrac{1}{2},k-\tfrac{1}{2}) \qquad (3.4.10)
\end{aligned}
$$

and

$$
\begin{aligned}
{}_{L}F_{3+}(i+\tfrac{1}{2},k+\tfrac{1}{2}) &= {}_{L}F_{4+}(i+\tfrac{1}{2},k+\tfrac{3}{2}) \\
{}_{L}F_{3-}(i+\tfrac{1}{2},k+\tfrac{1}{2}) &= {}_{L}F_{4-}(i+\tfrac{1}{2},k+\tfrac{3}{2}) \\
{}_{L}F_{4+}(i+\tfrac{1}{2},k+\tfrac{1}{2}) &= {}_{L}F_{3+}(i+\tfrac{1}{2},k-\tfrac{1}{2}) \\
{}_{L}F_{4-}(i+\tfrac{1}{2},k+\tfrac{1}{2}) &= {}_{L}F_{3-}(i+\tfrac{1}{2},k-\tfrac{1}{2}) \; . \qquad (3.4.11)
\end{aligned}
$$

Thus, only two fluxes need be computed at each grid point, e.g. ${}_{L}F_{1}(i+\tfrac{1}{2},k+\tfrac{1}{2})$ and ${}_{L}F_{3}(i+\tfrac{1}{2},k+\tfrac{1}{2})$.

The boundary conditions on ℓ are imposed in discrete space in roughly the same manner as described for θ and q in the last section. Strict enforcement of the boundary conditions require:

$$
\begin{aligned}
\ell_{i+\frac{1}{2},1} &= 0 \\
\ell_{i+\frac{1}{2},K} &= 0 \; . \qquad (3.4.12)
\end{aligned}
$$

In this sense, the assumption of uniform distribution of ℓ within grid areas has been relaxed in the neighborhood of the upper and lower boundaries. Consequently, the upstream approach is not employed for

computing the vertical fluxes at the k = 1 or k = K levels. Rather, the cross boundary fluxes may be directly specified as:

$$ {}_{L}F_{4}(i+\tfrac{1}{2},\tfrac{3}{2}) \equiv 0 \qquad (3.4.13a) $$

and

$$ {}_{L}F_{3}(i+\tfrac{1}{2},K-\tfrac{1}{2}) \equiv 0 \quad . \qquad (3.4.13b) $$

However, the above conditions may lead to a build up of ℓ in the lower bounding layer. It is physically realistic to allow precipitation to exit the domain at the lower boundary by virtue of its relative fall velocity. This may be accomplished by effectively relaxing the lower boundary condition on ℓ. In the interests of clarity, let:

$$ {}_{L}F_{4}(i+\tfrac{1}{2},\tfrac{3}{2}) \equiv P(i+\tfrac{1}{2}) = {}_{L}F_{4^{+}}(i+\tfrac{1}{2},\tfrac{3}{2}) \qquad (3.4.14) $$

where $P(i+\frac{1}{2})$ is the precipitation rate at $(i+\frac{1}{2},1)$. In this sense, an additional term has been added to the governing equation for the lowest bounding layer, which accounts for precipitation falling out of that layer. Note that the total water may not be conserved within the domain by virtue of this term.

Recalling Equation (3.2.19), the cross boundary flux at the lower boundary is determined as follows.

$$ \left.\begin{aligned} &\text{If} \quad (\Psi_o + \Psi^*_{i+\frac{1}{2},\frac{3}{2}}) < 0, \text{ then} \\ &\qquad P(i+\tfrac{1}{2}) = (\Psi_o + \Psi^*_{i+\frac{1}{2},\frac{3}{2}})\, \ell_{i+\frac{1}{2},\frac{3}{2}} \quad , \\ &\text{otherwise} \\ &\qquad P(i+\tfrac{1}{2}) = 0 \quad . \end{aligned}\right\} \qquad (3.4.15) $$

No advection of ice water into the domain is allowed at either boundary and no advection of ice water out of the domain is allowed at the upper boundary.

The computational procedure is given by the following steps.

a) Diagnose $\Psi^{*}_{i+\frac{1}{2},k+\frac{1}{2}}$ for i = 1, 2, ..., I-2, I-1 and k = 1, 2, ..., K-2, K-1 as in Section 3.10.

b) Compute $P(i+\frac{1}{2})$ for i = 1, 2, ..., I-2, I-1 from Equation (3.4.15).

c) Compute ${}_{L}F_{3+}(i+\frac{1}{2},k+\frac{1}{2})$ and ${}_{L}F_{3-}(i+\frac{1}{2},k+\frac{1}{2})$ from Equations (3.4.5) and (3.4.6), respectively, for i = 1, 2, ..., I-2, I-1 and k = 1, 2, ..., K-3, K-2.

d) Compute ${}_{L}F_{1}(i+\frac{1}{2},k+\frac{1}{2})$ from Equation (3.4.2) for i = 1, 2, ..., I-2, I-1 and k = 1, 2, ..., K-2, K-1.

3) Noting Equation (3.4.13b) and utilizing the identities given in Equations (3.4.14), (3.4.4), (3.4.10) and (3.4.11), compute the net advective convergence of ℓ at the grid point $(i+\frac{1}{2},k+\frac{1}{2})$ by means of Equation (3.4.1) for i = 1, 2, ..., I-2, I-1 and k = 1, 2, ..., K-2, K-1.

3.5 Sub-grid Scale Diffusion

In each of the discrete, prognostic, governing equations a diffusion term appears in the form of a constant times the Laplacian operator applied to the relevant field. These diffusion terms serve two purposes. They account for the physical effects of turbulent transport processes occurring at space scales not resolved by the grid. They, also, serve a purely computational role in suppressing numerical noise and unwanted non-physical computational modes in the solution. In this

sense, the model constants ν, κ_θ, κ_q and κ_ℓ are "tuneable". The manner of choosing the appropriate values for these eddy diffusion coefficients will be considered in Chapter 4. . The formulation of the discrete form of the Laplacian operator, i.e. ∇^2, is considered here.

The finite difference approximation to the Laplacian operator, which is used in this model, is:

$$\nabla^2_{j,m} S = \frac{1}{d^2} \left\{ S_{j+1,m} + S_{j-1,m} + S_{j,m+1} + S_{j,m-1} - 4\, S_{j,m} \right\} \qquad (3.5.1)$$

where S is any one of the prognostic variables, (i.e. ζ, θ, q, or ℓ) and j and m are dummy grid indices in the x and z directions, respectively. Thus, if $S = \zeta$; $j \equiv i$ and $m \equiv k$ and Equation (3.5.1) is applicable for $i = 1, 2, \ldots, I-1, I$ and $k = 3, 4, \ldots, K-3, K-2$. If $S = \theta$, q or ℓ; $j \equiv i+\frac{1}{2}$ and $m \equiv k+\frac{1}{2}$ and Equation (3.5.1) is applicable for $i = 1, 2, \ldots, I-2, I-1$ and $k = 2, 3, \ldots, K-3, K-2$. This formulation is fairly standard.

The boundary conditions are enforced numerically by simply allowing no exchange of S between interior grid points and the boundaries, i.e. for the first row of interior grid points:

$$\nabla^2_{j,m} S = \frac{1}{d^2} \left\{ S_{j+1,m} + S_{j-1,m} + \delta_{M_T,m+1} + \delta_{M_B,m-1} - 3\, S_{j,m} \right\} \qquad (3.5.2)$$

where

$$\delta_{M',m'} \equiv \begin{cases} 0, & M' = m' \\ S_{j,m'}, & M' \neq m' , \end{cases}$$

$$M_T = K \quad \text{and} \quad M_B = 1 \quad \text{for } S = \zeta,$$

and $$M_T = K-\tfrac{1}{2} \quad \text{and} \quad M_B = \tfrac{3}{2} \quad \text{for } S = \theta,\ q \text{ or } \ell.$$

Thus, Equation (3.5.2) is applied at the k = 2 and k = K-1 levels for S = ζ and i = 1, 2, ..., I-1, I and at the k = 1 and k = K-1 levels for S = θ, q or ℓ and i = 1, 2, ..., I-2, I-1 where i and k are related to j and m as noted above.

Effectively, Equation (3.5.2) incorporates the fact that the vertical derivative of S is known on the boundary and, thus, no finite difference computation of $\partial S/\partial z$ is necessary at those points. It should be noted that when applied to ζ, Equation (3.5.2) explicitly assumes no stress at the interface of a bounding half layer and the adjacent interior layer. This was found to be computationally convenient. Since the diffusion terms have the additional role of suppressing numerical noise in the model, a horizontal diffusion term was added for the bounding layers as:

$$\nabla^2_{i,k}\zeta = \frac{1}{d^2}\left(\zeta_{i+1,k} + \zeta_{i-1,k} - 2\,\zeta_{i,k}\right) \qquad (3.5.3)$$

for k = 1 or K. Equations (3.5.1), (3.5.2) and (3.5.3) are conservative in S.

3.6 Vorticity Generation/Destruction by Buoyancy Forces

The buoyancy parameter B may be evaluated at a thermodynamic grid point as:

$$B_{j,m} = \frac{\theta_{j,m}}{\theta_{oo}} + \frac{(1-\varepsilon)}{\varepsilon}\, q_{j,m} - \ell_{j,m}, \qquad (3.6.1)$$

where j and m are dummy grid indices in the x and z directions, respectively. The finite difference approximation to the buoyant generation of vorticity term evaluated at the dynamic grid point (i,k) is given by:

$$g \frac{\partial B}{\partial x}\Big|_{i,k} = \frac{g}{d} [ff^n (B_{i+\frac{1}{2},k+\frac{1}{2}} - B_{i-\frac{1}{2},k+\frac{1}{2}}) + (1 - ff^n) (B_{i+\frac{1}{2},k-\frac{1}{2}} - B_{i-\frac{1}{2},k-\frac{1}{2}})] \quad (3.6.2)$$

where ff^n is a time dependent weighting factor, n indicates the time step, and

$$ff^n \equiv 1 - ff^{n-1} . \quad (3.6.3)$$

The initial value of the "flip-flop" weighting factor, i.e. ff^0, is an externally specified model constant. A value of $ff^0 = \frac{1}{2}$ gives the generation of vorticity at the k level as the linear average of the generation at the $k+\frac{1}{2}$ and $k-\frac{1}{2}$ levels and is the most physically realistic value. However, this may lead to the indefinite maintenance of "checkerboard" noise patterns in B, which may occur, Schubert (1980, personal communication). For the simulations reported here, $ff^0 = \frac{1}{3}$ is specified and, thus, $ff^n = \frac{2}{3}$ at all odd time steps and $ff^n = \frac{1}{3}$ at all even time steps. In this way, "checkerboard" noise patterns are inhibited from perpetrating themselves. The effects of choosing a specific value of ff^0 are considered in Section 4.1.

Recalling the discrete form of the boundary conditions for θ, q and ℓ as developed in the last two sections, strict enforcement of the boundary conditions requires that:

$$B_{i+\frac{1}{2},1} = 0$$

and

$$B_{i+\frac{1}{2},K} = 0 . \qquad (3.6.4)$$

Noting the interpretation of $\zeta_{i,1}$ and $\zeta_{i,k}$ is given in Section (3.2), the proper formulation of the generation term for the bounding layers is:

$$g \frac{\partial B}{\partial x}\Big|_{i,1} = \frac{g}{d} \left\{ ff^n (B_{i+\frac{1}{2},\frac{3}{2}} - B_{i-\frac{1}{2},\frac{3}{2}}) \right\} \qquad (3.6.5)$$

and

$$g \frac{\partial B}{\partial x}\Big|_{i,K} = \frac{g}{d} \left\{ (1 - ff^n) (B_{i+\frac{1}{2},K-\frac{1}{2}} - B_{i-\frac{1}{2},K-\frac{1}{2}}) \right\} . \qquad (3.6.6)$$

The computational procedure is given by the following steps.

a) Compute $B_{i+\frac{1}{2},k+\frac{1}{2}}$ for i = 1, 2, ..., I-2, I-1 and k = 1, 2, ..., K-2, K-1 from Equation (3.6.1).

b) Evaluate $g \frac{\partial B}{\partial x}\Big|_{i,k}$ for i = 1, 2, ..., I-1, I and k = 1; k = 2, 3, ..., K-2, K-1; and k = K from Equations (3.6.5), (3.6.2) and (3.6.6), respectively.

3.7 Time Integration

Two distinct time integration schemes are utilized in this model. Following the general description of both schemes, the specific time integration procedure, which is employed, is presented. The rationale for this procedure is also addressed.

The governing prognostic equations are each of the form of a first order differential equation in time, i.e.

$$\frac{\partial S}{\partial t} = f^*(S, r_1, r_2, \ldots, r_m) \qquad (3.7.1)$$

where S is the dependent variable and f^* is a known function of S and m independent variables $r_1, r_2, \ldots, r_m$. A method of numerically integrating equations of this form in discrete time is desired. Let:

$$t^{n+1} = \Delta t + t^n = n\,\Delta t + t^o \qquad (3.7.2)$$

for n = 1, 2, 3, ...

where n is the time step index and Δt is the integration time step interval and is an externally specified model constant. The problem is an initial value problem in that a prediction of S at some discrete time t^{n+1} is desired where S, $r_1, r_2, \ldots, r_m$ and, thus, f^* are known at the previous time t^n.

If S^{n-1} is also regarded as known, a convenient finite difference approximation to Equation (3.7.1) is:

$$\left.\frac{\partial S}{\partial t}\right|_n \doteq \frac{S^{n+1} - S^{n-1}}{2\,\Delta t} = f^{*n}$$

which may be manipulated to:

$$S^{n+1} = 2\,\Delta t\, f^{*n} + S^{n-1} \quad . \tag{3.7.3}$$

This is the "leap frog" scheme, which is commonly used in meteorological and hydrodynamic models. Note that the time derivative has been approximated in a centered fashion over two time steps. This scheme allows the prediction of S^{n+1} from the known values of S^{n-1} and f^{*n}, i.e. S^n, r_1^n, r_2^n, ..., r_m^n. The leap frog scheme is of better than first order accuracy.

A second time integration scheme results from the finite difference approximation:

$$\left.\frac{\partial S}{\partial t}\right|_n \doteq \frac{S^{n+1} - S^n}{\Delta t} = f^{*n}$$

which may be manipulated to:

$$S^{n+1} = \Delta t\, f^{*n} + S^n \quad . \tag{3.7.4}$$

This is the Euler forward scheme where the time derivative is approximated over one time step interval. Essentially, the tendency at time step n is used to extrapolate from time step n to time step n+1. It allows the prediction of S^{n+1} from the known values of S^n and f^{*n}, i.e. S^n, r_1^n, r_2^n, ..., r_m^n. This scheme is of first order accuracy.

Centered time differencing schemes, such as the leap frog scheme, may show time splitting in the solution. This arises due to the

presence of terms within f^*, which may be highly non-linear in time, e.g. advection terms. Lilly (1965) notes that this may lead to a weak numerical instability where the solution at odd time steps and the solution at even time steps may vary smoothly when viewed separately but may diverge from each other. This oscillation of the solution at high frequency, i.e. $\sim 2\,\Delta t$, corresponds to a non-physical computational mode. It is desirable to damp this mode.

A number of methods have been developed to eliminate the time splitting computational mode in the leap frog scheme. Here, a time filter is employed at all steps as in Asselin (1972). Computationally, this routine is fast though it does increase the storage requirements for time dependent variables. Asselin (1972) found this filter to be an excellent damper for the computational time splitting mode arising in the leap frog time integration scheme. The time filter is applied as:

$$\bar{S}^{n-1} = S^{n-1} + \frac{\eta}{2}(\bar{S}^{n-2} - 2\,S^{n-1} + S^{n}) \qquad (3.7.5)$$

where the over bar denotes a filtered quantity and η is an externally specified filter parameter limited to positive values less than 1. The leap frog scheme is correspondingly modified as:

$$S^{n+1} = 2(\Delta t)\, f^{*n} + \bar{S}^{n-1} \qquad (3.7.6)$$

where the value of S^n employed in evaluating f^{*n} is not filtered in time except that it is based on an integration from a previously

filtered value, i.e. $\bar{S}^{n-2}$. For this study, $\eta = 0.25$ is specified, see (Section 4.1). This value adequately damps the computational mode in test simulations and minimizes phase errors due to the filter (Asselin, 1972).

Another modification which must be made in order to insure computational stability, is to evaluate the diffusion term in f^* at the "lag" time step, (Phillips, 1956). Let:

$$f^n \equiv f^{*n} - \kappa_S \nabla^2 S^n. \qquad (3.7.7)$$

where κ_S is the appropriate eddy diffusion (viscosity) coefficient and f^n corresponds to the appropriate advective and diabatic (buoyant generation) terms evaluated at t^n. The lag step procedure is incorporated into the filtered leap frog (Equation 3.7.6) and Euler forward (Equation 3.7.4) schemes as:

$$S^{n+1} = 2\Delta t \, (f^n + \kappa_S \nabla^2 \bar{S}^{n-1}) + \bar{S}^{n-1} \qquad (3.7.8)$$

and

$$S^{n+1} = \Delta t \, (f^n + \kappa_S \nabla^2 S^{n-1}) + S^n , \qquad (3.7.9)$$

respectively.

In general, the filtered leap frog time integration scheme (Equation 3.7.8) is utilized in this model. Its computational stability and accuracy are superior to the Euler forward scheme as formulated here. However, in certain instances the leap frog scheme will yield unrealistic results. In these cases, the Euler forward scheme is used. These cases will be detailed later in this section.

The time step interval Δt must satisfy the Courant-Friedricks-Lewy condition for computational stability of a two dimensional flow, i.e.

$$\frac{1}{\sqrt{2}} \geq \begin{cases} V_{max} \frac{\Delta t}{d} \\ \\ C_{max} \frac{\Delta t}{d} \end{cases} \qquad (3.7.10)$$

whichever is greater, where V_{max} is the maximum wind speed and C_{max} is the maximum wave speed within the domain, e.g. Phillips, (1956) and Haltiner (1971).

For cirriform clouds, observations indicate that $v_{max} \lesssim 0.8$ m s^{-1} even in highly unstable convective conditions (Heymsfield, 1975b). However, the contribution of the relative terminal velocity of ice particles to an effective velocity must also be considered. In Section (3.10), the parameterization of the effective relative terminal velocity of ice water v^* is presented. The maximum value of v^* is the relevant parameter for the consideration here and is $\sim$ 1.6 m s^{-1}. Thus, Δt = 30s will satisfy the above computational stability requirement in the case of d = 100 m for the most extreme conditions anticipated, i.e. a maximum relative effective terminal velocity superimposed on a maximum expected downdraft air velocity. Note that when d = 50 m, Δt = 15s would be required.

Recall that sound waves have been filtered from the governing equations. Thus, the wave speed requirement is here limited to internal gravity waves, which may occur in stable environments. Following from Haltiner (1971), the phase speed of a horizontally propagating internal gravity wave in the basic state environment is:

$$C \doteq \frac{L_x L_z^2}{2\pi(L_x^2 + L_z^2)} \left(\frac{g}{\theta_o} \frac{\partial \theta_o}{\partial z} \right)^{\frac{1}{2}}$$

where L_x and L_z are the horizontal and vertical wavelengths of the disturbance and the last term is the environmental Brunt-Vaisalla frequency N. Based on the observational study of Starr and Cox (1980), layers more stable than $(\partial\theta/\partial z) \cong 15°K\ km^{-1}$ are extremely rarely observed in the middle to upper troposphere. The corresponding lapse rate is $\sim -10°K\ km^{-1}$, i.e. a very strong temperature inversion. Such very stable layers in the middle to upper troposphere would be of limited vertical extent, i.e. < 1 km (Starr and Cox, 1980). Choosing a typical value of $\Theta_o = 310°K$ leads to $N = 0.02\ s^{-1}$, in the case of $(\partial\theta_o/\partial z) \sim 15°K\ km^{-1}$. Noting that C increases as the scale of a disturbance in such a stable layer increases, an extreme case would be $L_x = L_z = 1$ km. (Note that symmetric disturbances tend to have the fastest wave speeds.) Thus, in a very extreme case, $C_{max} \sim 1.7\ m\ s^{-1}$. This value is less than the value of v_{max} estimated above. Thus, the above values of Δt should insure computational stability even in a very extreme case and are, therefore, adopted for this study.

In practice, it is highly economical to avoid evaluating the diabatic terms in f at every time step due to their complexity as seen in Sections (3.9) and (3.11). However, the number of time steps between times at which the radiative (QR) and water phase change C terms are diagnosed should not be so large that excess numerical noise is generated or that the physics of a simulation become unrealistic. Let N_R and N_C be the number of time steps between evaluations of QR and C, respectively. It is reasonable to require $N_R \leq N_C$, since the distribution of ℓ is the primary modulator of QR (Section 3.11). In this study, $N_R = N_C$ is employed. The proper choice of N_C is deferred until Sections 3.9 and 4.5. A somewhat different approach is adopted for the QR and C terms.

The diagnosed radiative heating rate at the $n = jN_R$ time step, where $j = 1, 2, \ldots,$ is applied at all intervening time steps until the next diagnosis at $n = (j+1)N_R$, i.e.

$$QR^n \doteq QR^{jN_R} \tag{3.7.11}$$

for $n = jN_R, jN_R + 1, \ldots, jN_R + (N_R - 1)$ is assumed. This reduces the shock to the system compared to the method of incorporating the water phase change term described below. The filtered leap frog scheme is an effective filter of high frequency numerical noise which may occur due to the highly non-linear step function nature of QR^n.

Phase changes of water are diagnosed by an adjustment process, i.e. Section (3.9). As such, the term computed is $N_C(\Delta t)\,\tilde{C}^{jN_C}$, where $\tilde{C}^{jN_C}$ is the mean water phase change rate over the time period $n = (j-1)N_C$ to $n = jN_C$. Thus, formally this term is not included in the time integration schemes developed above but is rather an adjustment of the θ, q and ℓ fields at $n = jN_C$ accounting for water phase changes over the previous N_C time steps. The adjustment is made subsequent to the prediction of θ, q and ℓ at the $n = jN_C$ time step.

The use of an adjustment procedure for the diagnosis of the phase change terms leads to problems when evaluating the diffusion terms at the lag step for the prediction of the fields at the $jN_C + 1$ time step. This may be seen in that errors due to not diagnosing C at every time step have been allowed to build up from $n = (j-1)N_C + 1$ to $n = jN_C - 1$. The change in the perturbation fields of θ, q and ℓ may be significant from $n = jN_C - 1$ to $n = jN_C$ once the phase change adjustment has been

made. In this sense, the lag step diffusion terms evaluated at $n = jN_C - 1$ for the prediction to the $n = jN_C + 1$ time step may be very unrealistic when considering the actual current distribution of the perturbation fields. For example, the diffusion processes may attempt to reduce the amplitude of a peak perturbation value when in actuality this peak value has already been largely eliminated in the adjustment process.

A very similar problem arises if the leap frog scheme is used to predict the $jN_C + 1$ time step, since the S^{jN_C-1} values are employed. For these reasons, the diffusion terms are not evaluated and the Euler forward scheme, rather than the filtered leap frog scheme, is utilized to predict the $n = jN_C + 1$ fields of θ, q and ℓ. For θ and q, the filtered leap frog scheme is then restarted to predict the values at $n = jN_C + 2$. The filter is reinitialized as:

$$\bar{S}^{jN_C} \equiv S^{jN_C}. \qquad (3.7.12)$$

For the initial time step from the prescribed fields at n = 0 to n = 1, the centered time integration scheme is inappropriate. Thus, the Euler forward scheme with no diffusion is utilized for this step. Note that the time filter is initialized as in Equation (3.7.12) with j = 0 before the filtered leap frog scheme is applied to predict the fields at n = 2.

One additional consideration must be made. In this model, the Euler forward time integration scheme is always employed for the prediction of ℓ. This is done for primarily two reasons. The first is

that it effectively suppresses the $\ell < 0$ computational mode. As noted in Section 3.4, the occurrence of this non-physical computational mode is particularly troublesome. It arises in the leap frog scheme because the effective wind field for the advection of ℓ may be very divergent due to the presence of the effective relative terminal velocity term for ice water. In this sense, particularly when $\ell^{n-1} < \ell^{n}$, the advective term evaluated at n may remove more ice water than is available at n-1. This does not occur with the Euler forward scheme. The second reason is that when used with an upstream (uncentered) space differencing, the Euler forward scheme is very stable (Haltiner, 1971). This is not true when used with centered space differencing schemes, as for ζ, θ and q, where the Euler forward scheme may lead to computational instability if used repetitively. In fact, the solution is slightly damped when using the Euler forward time integration scheme with upstream space differencing. This damping, though not desirable in and of itself, is far more desirable than permitting the $\ell < 0$ computational mode.

In summary, the computational procedure is as follows:

1. Predict fields at n = 1

   Euler forward scheme with $\kappa_S = 0$ for S = ζ, θ, q and ℓ, (Equation 3.7.9).

2. Initialize time filter $\bar{S}^0$ for S = ζ, θ and q (Equation 3.7.12 with j = 0).

3. Successively predict fields at n = $jN_C + 2$ to n = $(j+1)N_C$.

   a) Filtered leap frog scheme with lag step diffusion for S = ζ, θ and q (Equation 3.7.8) where $\bar{S}^{n-1}$ is evaluated after each step (Equation 3.7.5).

b) Euler forward scheme with lag step diffusion for S = ℓ (Equation 3.7.9).

4. Adjust θ, q and ℓ fields for diagnosed phase changes of water (Section 3.9).

5. Predict fields at $n = jN_C + 1$

   a) Filtered leap frog scheme with lag step diffusion for $S = \zeta$ (Equation 3.7.8).

   b) Euler forward scheme with $\kappa_S = 0$ for S = θ, q, ℓ (Equation 3.7.9).

6. Reinitialize time filter $\bar{S}^{n-1}$ for S = θ and q (Equation 3.7.12).

7. Let j = j + 1 and proceed to step 3.

3.8 Solution of Poisson's Equation

Direct numerical time integration of the governing prognostic equations requires that the perturbation streamfunction field be specified in order that the integration may proceed over the next time step. Thus, diagnostic Equation (3.1.10) must be solved at each dynamic grid point after each time step. Note that $\zeta_{i,k}$ is known and $\psi_{i,k}$ is the unknown at each grid point once the integration step has been performed. Thus, a solution of I x K coupled equations of the form:

$$\zeta_{i,k} = \nabla^2_{i,k}\,\psi = \frac{1}{d^2}\left(\psi_{i+1,k} + \psi_{i-1,k} + \psi_{i,k+1} + \psi_{i,k-1} - 4\,\psi_{i,k}\right) \tag{3.8.1}$$

for i = 1, 2, ..., I-1, I and k = 1, 2, ..., K-1, K is desired. The solutions must obey the boundary conditions given by Equations (3.1.4) and (3.2.19).

Efficient and highly accurate numerical methods exist to solve this type of system, e.g. Lorentz (1976) and Sweet (1977). A fortran program of the cyclic reduction algorithm of Sweet (1977) was obtained from the National Center for Atmospheric Research Software Library (named FISHPAK) and is a revised version of the program described by Swarztrauber and Sweet (1975). They state that the use of this program entails a loss of no more than 3 significant digits for I and K as large as 64. It should be noted that in addition to Equations (3.1.4) and (3.2.9) the program enforces the condition:

$$\zeta_{i,1} = \zeta_{i,K} = 0 ,$$

which may be viewed as consistent with the continuous form boundary conditions on ζ (Equation 2.26) but not with the interpretation here (Section 3.2). This does not appear to cause a substantial problem. Tests of the program by this author verified the stated accuracy.

3.9 Phase Changes of Water

Recall that the model is limited to a consideration of only one non-vapor phase of water. In general, only the ice phase is treated. However, for comparison, liquid/vapor phase simulations are also performed. This section describes the manner of diagnosing the phase changes of water and is specifically directed to the vapor to ice ($v \rightarrow i$) and ice to vapor ($i \rightarrow v$) sublimation processes. Comments on

differences with condensation/evaporation processes are made where appropriate.

The phase changes of water are evaluated in a diagnostic manner. Thus, rather than directly evaluating the sublimation rate by means of some consideration of the microphysical growth equation, the sublimation rate is evaluated indirectly through an adjustment of the local thermodynamic ($T + T_o$) and water ($q + q_o$ and ℓ) values to some assumed equilibrium state. The adjustment at a discrete time t^{jN_C} reflects the phase changes required over the previous time period $\Delta t^* = N_C \Delta t$ such that any non-equilibrium state which has evolved in that time is eliminated (Section 3.7). It is implicitly assumed that the adjustment time scale Δt^* is sufficiently larger than the corresponding true microphysical time scales such that the assumed equilibrium may be realistically achieved. The validity of this assumption as well as the specification of the assumed equilibrium state are considered later in this section. These are essentially the parametric components of the diagnostic routine described here.

The mechanics of the adjustment process are fairly straightforward and are discussed presently. For the moment, the equilibrium assumptions are that no supersaturations with respect to ice may occur and that no subsaturations with respect to ice may occur in the presence of ice water.

When the phase change diagnosis is made (i.e. $n = jN_C$ for $j = 1, 2, \ldots$), the adjustment process is initiated at a thermodynamic grid point $(i+\frac{1}{2}, k+\frac{1}{2})$ only if:

$$(q + q_o) > q^*(T + T_o, p_o) \qquad (3.9.1)$$

or if:

$$(q + q_o) < q^*(T + T_o, p_o) \text{ and } \ell > 0 \qquad (3.9.2)$$

where q^* is the saturation water vapor mixing ratio with respect to ice and is a function of the temperature $(T + T_o)$ and pressure. Note that $q + q_o$ is assumed equal to the total water vapor mixing ratio for the phase change diagnosis. The grid location indices have been neglected for convenience. Note that effects due to pressure perturbations have been neglected. Errors due to this approximation are exceedingly small ($<< 0.1\%$) for the simulations reported here. Statements (3.9.1) and (3.9.2) explicitly assume uniform distributions of $(T + T_o)$, $(q + q_o)$ and ℓ in any thermodynamic grid area. Thus, the effects of sub-grid scale variability (e.g. Sommeria and Deardorff, 1977) have been neglected.

The temperature and saturation water vapor specific humidity may be approximated as:

$$T + T_o \doteq (\theta + \Theta_o)\,\pi_o \qquad (3.9.3)$$

and

$$q^*(T + T_o, p_o) \doteq \frac{\varepsilon\, e_s(T + T_o)}{(p_o - e_s(T + T_o))}, \qquad (3.9.4)$$

respectively, where e_s is the saturation vapor pressure of water with respect to a plane pure ice surface and is a function of temperature alone. The manner of computing $e_s(T + T_o)$ is described in Appendix A and is accurate to within $\pm$ 0.1% over the range of temperatures considered here. A similar representation of the saturation vapor pressure of water with respect to a plane surface of pure liquid water is also given in Appendix A. The error in the above approximations for

e_s and, thus, q^* are due primarily to errors in the diagnosis of $T + T_o$ by means of Equation (3.9.3). In the case where the entire layer is cooled by 5°C, the effect of using π_o rather than π, to compute $T + T_o$ would lead to an error of $\sim$ 5% in e_s and q^* at the top of the domain. Much better accuracy is generally expected as this is a worst case. This problem may be further minimized by periodically updating the values of p_o and π_o.

The values of $(T + T_o)$, $(q + q_o)$ and ℓ are adjusted according to:

$$(T + T_o)' = (T + T_o) + \frac{L}{c_p}(C\,\Delta t^*) \qquad (3.9.5)$$

$$(q + q_o)' = (q + q_o) - (\tilde{C}\,\Delta t^*) \qquad (3.9.6)$$

and

$$\ell' = \ell + (\tilde{C}\,\Delta t^*) \qquad (3.9.7)$$

where the primed quantities denote the new diagnosed values, once the equilibrium adjustment has been made. Note that $\tilde{C}$ is the sublimation rate averaged over the time interval $N_c\,\Delta t$. For sublimation processes, the coefficient of latent heat L is very nearly a constant at tropospheric temperatures. The value employed here as well as the manner of computing the temperature dependent value of L for condensation/evaporation processes is given in Appendix B. Note that subsequent to the adjustment process, the new equilibrium perturbation potential temperature is computed by inverting Equation (3.9.3) as:

$$\theta' = \frac{(T + T_o)'}{\pi_o} - \theta_o \,. \qquad (3.9.8)$$

One additional relationship is needed to close the system of Equations (3.9.5), (3.9.6) and (3.9.7). The first equilibrium assumption leads to:

$$(q + q_o)' = q^*((T + T_o)', p_o) . \qquad (3.9.9)$$

This is, also, a valid representation of the second equilibrium assumption except when Equation (3.9.2) is true and

$$(q + q_o + \ell) \leq q^* \left\{ (T + T_o) + \frac{L\,\ell}{c_p} , p_o \right\} \qquad (3.9.10)$$

in which case:

$$(\tilde{C}\,\Delta t^*) = \ell \qquad (3.9.11)$$

is appropriate. In this instance, Equation (3.9.11) allows the adjustment to proceed directly from Equations (3.9.5), (3.9.6) and (3.9.7).

When Equations (3.9.1) or (3.9.2) are true and Equation (3.9.10) is not true, Equations (3.9.5), (3.9.6) and (3.9.9) may be combined as in Hack and Schubert (1976) to yield:

$$(q + q_o) - q^*((T + T_o)', p_o) - \frac{c_p}{L}\left\{(T + T_o) - (T + T_o)'\right\} = 0 \qquad (3.9.12)$$

where $(q + q_o)'$ and $(\tilde{C}\,\Delta t^*)$ have been eliminated. This is a closed equation for $(T + T_o)'$. Due to the complicated nature of the function q^*, an analytic solution for $(T + T_o)'$ is not readily available. However, an iterative solution is easily obtained by applying Newton's method (Carnahan, et al, 1969) as follows:

i. Make an initial guess of $(T + T_o)'$ and set the iteration index $\nu = 1$. Note that if Equation (3.9.1) is true, then

$$(T + T_o)^{-(\nu=1)} > (T + T_o)$$

or if Equation (3.9.2) is true, then

$$(T + T_o)^{-(\nu=1)} < (T + T_o) .$$

ii. Compute a new estimate $(T + T_o)^{-(\nu+1)}$ from:

$$(T + T_o)^{-(\nu+1)} = (T + T_o)^{-(\nu)} + \left[\frac{L}{c_p} \left\{ (q + q_o) - q^*((T + T_o)^{-(\nu)}, p_o) \right\} \right.$$

$$\left. - \left\{ (T + T_o)^{-(\nu)} - (T + T_o) \right\} \right] * \left[1 + \frac{L \varepsilon \Lambda^{(\nu)}}{c_p (p_o - e_s(T + T_o))} \right]^{-1} \quad (3.9.13)$$

where

$$\Lambda^{(\nu)} \equiv \left. \frac{\partial e_s(y)}{\partial y} \right|_{y=(T + T_o)^{-(\nu)}} . \quad (3.9.14)$$

The manner of computing Λ is described in Appendix A for both sublimation and evaporation/condensation processes. Note that the saturation vapor pressure term in the denominator of Equation (3.9.4) has been regarded as a constant when determining Λ.

iii. Compute the new estimates of $(\tilde{\tilde{C}} \Delta t^*)^{(\nu+1)}$, $(q + q_o)^{-(\nu+1)}$ and $\ell^{-(\nu+1)}$ from Equations (3.9.5), (3.9.6) and (3.9.7), respectively, where $(T + T_o)^{-(\nu+1)}$ is substituted for $(T + T_o)^{-}$ in Equation (3.9.5).

iv. Test convergence of iteration. If:

$$\left| \left\{ q^*((T + T_o)^{-(\nu+1)}, p_o) - (q + q_o)^{-(\nu+1)} \right\} \right.$$

$$\left. \left\{ q^*((T + T_o)^{(\nu+1)}, p_o) \right\}^{-1} \right| < err \qquad (3.9.15)$$

then consider the estimates correct. If Equation (3.9.15) is not true, then let $\nu = \nu+1$ and repeat the procedure from step ii.

The convergence parameter is usually specified as $err = 10^{-4}$, which corresponds to an error of 0.01% in the relative humidity compared to the equilibrium assumption. Convergence is usually achieved in less than four iterations.

Once convergence is achieved the adjusted values of θ, q and ℓ are specified at the thermodynamic grid point $(i+\frac{1}{2},k+\frac{1}{2})$ at time step $n = jN_C$ as:

$$\theta = \frac{(T + T_o)^{-(\nu+1)}}{\pi_o} - \theta_o$$

$$q = (q + q_o)^{(\nu+1)} - q_o \qquad (3.9.16)$$

and $$\ell = \ell^{-(\nu+1)},$$

respectively.

The equilibrium assumptions actually employed in the model are now considered. The above adjustment procedure is correspondingly modified only in the definition of some terms. The approach adopted here is highly empirical though guided by some theoretical considerations. Three distinct phase change processes are considered. These are the vapor to ice sublimation processes in clear air ($v \rightarrow i$), the vapor to

ice sublimation process in the presence of ice particles ($v \rightarrow i+i$) and the ice to vapor sublimation process ($i \rightarrow v$).

For the ($v \rightarrow i$) process, theoretical computations reported by Heymsfield (1975c) indicate that supersaturations with respect to ice on the order of 50% may be required to initiate homogeneous nucleation at temperatures typical of cirriform cloud levels. However, for d = 100 m, the results of Sommeria and Deardorff (1977) indicate that supersaturations of this order may be expected locally within a grid area when the mean grid area supersaturation is on the order of 20-30%. Heymsfields computations show that ice crystals may grow to lengths of $\sim$ 300 μm within $\sim$ 10 minutes where the water vapor supply is depleted to near saturation in this time. These results are consistent with the results of Jayaweera (1971). Recall that ideally, $N_C \Delta t \gtrsim \tau_{v \rightarrow i}$ is required, where $\tau_{v \rightarrow i}$ is the time scale corresponding to the ($v \rightarrow i$) process. The microphysical response times in the presence of ice crystals are much faster (Heymsfield, 1975c or Jayaweera, 1971). Substantial further modification of the particle size spectrum may occur within time intervals less than 5 minutes, i.e. $\tau_{v \rightarrow i+i} \lesssim 5$ minutes. Thus, if $N_C \Delta t \sim 10$ minutes, the physics may be very substantially in error at the time steps between phase change diagnoses. Economic considerations as well as the above suggest $N_C \Delta t = 5$ minutes (i.e. $N_C = 10$ for Δt = 30s) may be adequate for the purposes here. The sensitivity of simulations to the choice of N_C will be established in Section 4.5. With this choice and noting the results above, a reasonable modification of the adjustment process is to substitute $1.2\ q^*$ for q^* in Equation (3.9.1). Noting that $\tau_{v \rightarrow i} > \tau_{v \rightarrow i+i}$, it is assumed rather

arbitrarily that the existing supersaturation is only half depleted in 5 minutes. This is consistent with the results of Heymsfield (1975c). This may be incorporated into the adjustment procedure by substituting 1.12 q^* for q^* in Equations (3.9.9), (3.9.12), (3.9.13) and (3.9.15). In addition, the same factor must be applied to $\Lambda^{(v)}$ in Equation (3.9.13). The use of 1.12 is clarified below.

For the ($v \rightarrow i+1$) process, Heymsfield's computations indicate that no modifications are required. However, in an unpublished companion study to Starr and Cox (1980), they found that supersaturations with respect to ice up to 15% are very common in cirriform cloud layers. They observed a mean value of $\sim$ 8% and a median value of $\sim$ 5%. This result may be readily incorporated into the model by substituting 1.05 q^* for q^* in Equations (3.9.1), (3.9.9), (3.9.12), (3.9.13) and (3.9.15) and, also, multiplying 1.05 times the factor $\Lambda^{(v)}$ in Equation (3.9.13).

A modification of this parameterization at cloud top level may also be appropriate. Roach and Bader (1977) have noted that based on microphysical computations where radiative effects were taken into account, that the infrared radiative budget of an ice crystal near cloud top is such that the larger crystals may continue to grow in significantly subsaturated conditions. Thus, particularly at night, the original equilibrium assumption is probably more valid near cloud top. In the daytime, absorption of solar radiation may largely negate this effect. Thus, at night, the factor 1.0 is applied as above and in the daytime the factor 1.02 is applied for the cloud top layer.

When considering the ($i \rightarrow v$) sublimation process, one factor which must be considered is the hardiness of ice crystals. Observations (e.g. Braham and Spyers-Duran (1967), Berson (1967)) and theoretical

computations (e.g. Roach and Bader (1977) and Hall and Pruppacher, 1976)) indicate that $\tau_{i \to v} >> \tau_{v \to i+i}$. For example, Roach and Bader show that large ice crystals with length dimensions greater than $\sim$ 200 μm may fall more than 1 km in still clear air where the environmental relative humidity with respect to ice is 80%. However, the incorporation of such Lagrangian information into a Eulerian model, such as here, is not straightforward. The effective relative terminal velocity of ice water ranges from $\sim$ 0.6 m s^{-1} to $\sim$ 1.6 m s^{-1} in magnitude when significant numbers of large ice crystals are present as developed in Section (3.10). The exact magnitude depends on the ice water content, $\rho_o \ell$. Thus, in a Lagrangian sense, a precipitation stream may propagate downward 1 km in $\sim$ 10 to $\sim$ 30 minutes in this Eulerian model given a sufficiently large $\rho_o \ell$ at all times. Noting that the falling ice water is subject to the $(i \to v)$ phase change, a mean fall speed of $\sim$ 1 m s^{-1} might be associated with the entire lifetime of the precipitation stream. In this case, all ice water present in an environment with a relative humidity with respect to ice of 80% should be converted to the vapor phase within $\sim$ 15 to $\sim$ 20 minutes. This time scale is less in the case of a more moist environment (Roach and Bader, 1977).

A simple parameterization is to allow only a fraction f_ℓ of the ice water present to undergo the $(i \to v)$ sublimation process at a given time. The amount $f_\ell \ell$ is of course a maximum value, since in order to be consistent with the previous developments, the $(v \to i+i)$ equilibrium assumption must also be maintained. This may be seen in that if Equation (3.9.10) is modified as above for the $(v \to i+i)$ process and $f_\ell \ell$ is substituted for ℓ, and the statement is not true, then the in-cloud equilibrium assumption would be violated if Equation (3.9.11), with

f_{ℓ} ℓ substituted for ℓ, is used for the direct diagnosis of the phase change (i.e. the maximum case). In this instance, Equation (3.9.9), modified as above for the ($v \rightarrow i+i$) process, is invoked and diagnosis of the phase change proceeds iteratively from the correspondingly modified form of Equation (3.9.12). If the modified form of Equation (3.9.10) is true, the phase change adjustment proceeds directly from Equation (3.9.11) with f_{ℓ} ℓ substituted for ℓ.

Since as developed in Section (3.10), $\rho_o \ell = 10^{-4} g\ m^{-3}$ corresponds roughly to the threshold for the diagnosis of significant numbers of large ice crystals, potentially all the ice water present may undergo the ($i \rightarrow v$) process for ice water contents less than this amount, i.e. if $\rho_o \ell \lesssim 10^{-4} g\ m^{-3}$, then

$$f_{\ell} = 1.0 \quad . \tag{3.9.17}$$

Given this condition and noting the proposed value of $N_C \Delta t = 5$ minutes, the function f_{ℓ} should allow $\rho_o \ell$ to be reduced to less than $10^{-4}\ g\ m^{-3}$ within ~ 3 phase change diagnoses (i.e. ~ 15 minutes) at a relative humidity of 80%. The following scheme is proposed in the case where $N_C \Delta t = 5$ minutes:

if $RH_I \gtrsim 0.8$, then:

$$f_{\ell 5} = \max \begin{cases} 0 \\ 4.5\ (1 - RH_I)\ , \end{cases} \tag{3.9.18}$$

otherwise,

$$f_{\ell 5} = \min \begin{cases} 1.0 \\ (6.2 - RH_I)\ /\ 6 \end{cases} \tag{3.9.19}$$

where

$$RH_I \equiv \left[\frac{q + q_o}{q^*(T + T_o, p_o)}\right] \qquad (3.9.20)$$

and the subscript 5 on f_ℓ denotes the corresponding value of $N_C \Delta t$.

This parametric function $f_{\ell 5}$ as defined by Equations (3.9.18) - (3.9.20) is admittedly rather crude. However, in the case where the environmental relative humidity with respect to ice is maintained at 80%, i.e. $RH_I = 0.8$, all ice water is converted to vapor in 20, 15, 10 and 5 minutes beginning with a diagnosis at $\rho_o \ell = 1.0$, 0.1, 0.01 and 0.001 g m^{-3}, respectively. Based on the observation of ice water contents in cirriform clouds (see Section 3.10), 15 minutes or less will generally be required. This agrees with the previously noted studies of ice crystal survival times. Note that for $RH_I = 1.0$, 0.9, 0.8, 0.6, 0.4 and $\lesssim 0.2$, $f_{\ell 5} = 0.00$, 0.45, 0.90, 0.93, 0.97 and 1.0. A value of $RH_I = 0.26$ effectively halves the response time to 10 and 5 minutes in the case where an initial diagnosis is made for $\rho_o \ell = 1.0$ and 0.01 g m^{-1}, respectively.

The function $f_{\ell 5}$ has been tuned to both the specified value of $N_C \Delta t$ and the observations. Thus, any modification of $N_C \Delta t$ requires an adjustment of the function f_ℓ. This may be readily accomplished by noting that:

$$f_\ell = (1 - f_{\ell 5})^{(N_C \Delta t / 5 \text{ min})} \qquad (3.9.21)$$

is required to achieve the same time scales for any specified $N_C \Delta t$ where $f_{\ell 5}$ is determined from Equations (3.9.18) - (3.9.20).

The computational procedure followed for the parametric water phase change diagnosis in the model is summarized by the following steps.

1. If $n = j\,\Delta t^*$, where n is the time step index, $\Delta t^* \equiv N_C\,\Delta t$, Δt is the time step interval and $j = 1, 2, 3, \ldots$; then proceed to step 2. If $n \neq j\,\Delta t^*$, then no diagnosis is performed at this time step.

2. At each thermodynamic grid point $(i+\frac{1}{2}, k+\frac{1}{2})$, compute $T + T_o$ and $q^*(T + T_o, p_o)$ from Equation (3.9.3) and (3.9.4), respectively, test for the assumed equilibrium between the phases of water as in steps (2a-d). (Note that the grid indices are omitted here).

   a) If $\ell = 0$ and $(q + q_o) \geq 1.2\, q^*(T + T_o, p_o)$, then let $\Gamma \equiv 1.2$[1] and proceed to step 4.

   b) If $\ell > 0$ and $(q + q_o) \geq \Gamma\, q^*(T + T_o, p_o)$, where $\Gamma \equiv 1.05$ if $k < KT - 1$, $\Gamma \equiv 1.00$ if $k = KT - 1$ and $\vartheta^n < 90°$, and $\Gamma \equiv 1.02$ if $k = KT - 1$ and $\vartheta^n \geq 90°$ then proceed to step 4. Note that $KT - \frac{1}{2}$ is the cloud top grid area and ϑ^n is the solar zenith angle as defined in Section 3.11.

   c) If $\rho_o\,\ell < 10^{-4}$ g m^{-3} and $(q + q_o) < \Gamma\, q^*(T + T_o, p_o)$, where Γ is defined as in step 2b, then let $f_\ell = 1.0$ and proceed to step 3.

   d) If $\rho_o\,\ell \geq 10^{-4}$ g m^{-3} and $(q + q_o) < \Gamma\, q^*(T + T_o, p_o)$, where Γ is defined as in step 2b, then compute f_ℓ as in Equation (3.9.18) - (3.9.21) and proceed to step 3.

---

[1] Consistently $\Gamma = 1.05$ or 1.16 in the case of $N_C\,\Delta t = 10$ or 2.5 minutes, respectively.

3. Substitute $f_\ell \ell$ for ℓ and Γq^* for q^* in Equation (3.9.10) and test to see if the statement is true. If true, substitute $f_\ell \ell$ for ℓ in Equation (3.9.11) and proceed directly with the adjustment from Equations (3.9.5), (3.9.6), (3.9.7) and (3.9.16).

4. Substitute Γq^* for q^* and $\Gamma\Lambda$ for Λ in Equations (3.9.13) and (3.9.15) and proceed with iteration as described previously, i.e. steps (i) to (iv), until convergence is achieved. Complete the adjustment as in Equation (3.9.16).

When a liquid/vapor water phase simulation is performed, the adjustment proceeds under the original equilibrium assumptions, i.e. $\Gamma \equiv 1.0$ and $f_\ell \equiv 1.0$ in all cases. This is consistent with microphysical observations of liquid phase middle tropospheric stratiform clouds as summarized by Mason (1971).

Recall that effects due to sub-grid scale variability of T, q and ℓ have been neglected in this development. A desire for simplicity and a basic lack of knowledge have dictated this approach. This may be seen in that the schemes proposed by Manton and Cotton (1977) and Sommeria and Deardorff (1977) were designed primarily for models of cumulus convection and boundary layer processes in the lower atmosphere. Furthermore, the validity of the assumptions, which form the basis of those parametric schemes, has not been rigorously established by observations. The neglect of sub-grid scale variability for water phase change processes is somewhat consistent with the rather simple treatment of sub-grid scale processes employed elsewhere in this model, i.e. eddy diffusion processes. It is hoped that the use of d = 100 m will

minimize the impact of these assumptions. However, Sommeria and Deardorff (1977) state that use of this assumption leads to somewhat less extensive and intense convection in a simulation compared to the case where their parameterization is employed.

3.10 Effective Relative Fall Velocity

In the governing equation for the ice phase water budget, the quantity $v^* \ell$ appears, which accounts for the vertical flux of ℓ due to the gravity induced vertical fall velocity of the ice particles comprising ℓ relative to a coordinate system moving at the vertical air velocity $(w + w_o)$. The manner of specifying v^*, which is the effective relative fall velocity of the ice phase water, is developed in this section.

A parametric approach is adopted. The resulting parameterization is most valid for ice phase stratiform clouds at temperatures less than $\sim -20°C$. This is consistent with the limitations of the model, where only one non-vapor phase of water, which is generally specified as the ice phase, may be taken into account. The parameterization is computationally efficient and, hopefully, yields a realistic diagnosis of v^* as a function of ice water content, $\rho \ell$. A liquid phase parameterization is, also, given.

Since the full microphysical growth equations are not incorporated into the model for the reasons stated previously, it is virtually impossible to account for all the variations in v^* which may occur in natural clouds. In particular, the effects of particle size sorting by virtue of the interaction of the dynamics and microphysics are not

taken into account. This may not be too severe of a problem for the cloud layer itself but may limit the validity of the parameterization for precipitation trails emanating from the cloud layer.

Let r be some characteristic length of a given water particle of type j, where $v_j(r)$ and $m_j(r)$ are the corresponding relative vertical fall speed and mass of that particle. The type of particle refers to the particle habit, e.g. liquid water drop, a columnar ice crystal, a plate form ice crystal, etc. It is assumed that the relative vertical fall velocity of a particle equals its terminal velocity in still air. Let $n_j(r')$ be the number density of particles of type j and characteristic length r in the size interval,

$$(r' - \frac{\Delta}{2}) < r \leq (r + \frac{\Delta}{2})$$

where Δ is some small length interval. For the computations reported here, $\Delta \equiv 10^{-6}$ m. Now,

$$\ell = \frac{1}{\rho} \sum_{i=1}^{I'} \sum_{j=1}^{J} n_j(r_i)\, m_j(r_i),$$

$$-v^*\ell = \frac{1}{\rho} \sum_{i=1}^{I'} \sum_{j=1}^{J} n_j(r_i)\, m_j(r_i)\, v_j(r_i)$$

and, thus,

$$-v^* = \frac{\sum_{i=1}^{I'} \sum_{j=1}^{J} n_j(r_i)\, m_j(r_i)\, v_j(r_i)}{\sum_{i=1}^{I'} \sum_{j=1}^{J} n_j(r_i)\, m_j(r_i)} \qquad (3.10.1)$$

where

$$r_i = (i - \tfrac{1}{2})\,\Delta ,$$

ρ is the air density and $r_{I'}$ is the characteristic length of the largest particle present. For the computations reported here, $I' = 5 \times 10^3$ corresponding to $r_{I'} \doteq 5 \times 10^{-3}$ m, unless a point of insignificance is reached first, i.e. numerical underflow. The number density size distribution may be represented as:

$$n_j(r_i) = N_j\, n_j^*(r_i)$$

where N_j is the number density of all particles of habit j and $n_j^*(r_i)$ is a dimensionless normalized size distribution function.

Many ice crystal habits may be found in stratiform ice clouds. Weickmann (1947) reported that at temperatures less than -25°C, hexagonal prisms are the most common crystal forms. He found the bullet rosette to be the primary crystal habit in convectively active cirrus clouds, while in less convectively active cirrostratus clouds eroded single bullets, columns and plates were predominant. Based upon laboratory experiment, aufm Kampe et al. (1951) found that irregular aggregates of plates and columns, bullet rosettes and single columns should be the most common crystal habits at temperatures between -20°C and -40°C. Based on his own extensive observations and those of other workers, Ono (1970) reported that, at temperatures less than -22°C, single columns, bullets and thick plates, bullet rosettes and irregular

aggregates of plates and columns are the predominant crystal habits. Heymsfield and Knollenberg (1972) found that, in convectively active cirrus generating cells, the crystal forms were about 75% bullets, columns and bullet rosettes and about 25% plates. They also noted that the observed plate form ice crystals invariably corresponded to the smallest particle sizes observed ($r < 10^{-4}$ m). Similar results were reported by Heymsfield (1974) for sub-tropopause thin cirrus. Heymsfield (1975a) found that, in convectively active cirrus uncinus clouds, the predominant ice crystal types were bullet rosettes, single bullets, banded columns and plates in that order. Hobbs, et al. (1975) reported that, in numerous samples of cirrostratus clouds, irregular aggregates of columns and plates and single columnar forms were the most commonly observed ice crystal habits. Based on observations in numerous cirriform clouds at temperatures less than -22°C, Heymsfield (1977) found that columns and thick plates were predominant with weak convective activity, while in convectively active layers, bullet rosettes and hollow columns were the most common crystal habits. Varley (1978) and Varley and Brooks (1978) found that in cirrostratus clouds, the larger particles were most commonly irregular aggregates and bullet rosettes, while plate form crystals were predominant for the smallest particle sizes.

The observations of Hobbs, et al. (1975) and Heymsfield (1977) indicate, that for temperatures less than $\sim$ -20°C, the contribution of liquid phase water to the total non-vapor phase water content is insignificant. This is consistent with the conclusions of Schaefer (1951), where the initiation of ice crystals in cirrus clouds is attributed primarily to spontaneous nucleation.

Ono (1970) and Heymsfield (1977) note that at warmer temperatures planar crystal forms, e.g. dendrites, and high aspect ratio columnar forms, e.g. needles, may be predominant. Locatelli and Hobbs (1974) found that riming may also be an important factor in modifying the ice crystal types at warmer temperatures. In addition, as temperature increases toward 0°C, the liquid phase particle habit becomes increasingly more significant until at $T \gtrsim -5°C$, it may be predominant. However, over the range of temperatures where the ice phase and liquid phase of water may coexist in significant quantities, i.e. $T \cong 15$ C°to 0°C, the liquid phase particles are predominantly very small, (Heymsfield, 1977).

For the parameterization developed here, only two water particle habits are considered. These are the column and the bullet rosette aggregate ice crystal types. Thus, the parameterization is most applicable for temperatures less than $\sim -20°C$. Since both the mass and terminal velocity of ice particles are monotonically increasing functions of r, both the total ice water content, $\rho \ell$, and the effective terminal velocity corresponding to a given particle size distribution are dominated by the contributions due to the largest particles present in significant abundance. Based upon this fact and the fact that the mass-length relations and terminal velocities of the smallest particles present are not too different for the different ice crystal habits in an absolute sense, the plate form ice crystal habit is neglected in this development. Errors in the computed v^* due to this assumption are minimal. A similar justification for neglecting the liquid phase water particle habit may also be invoked.

In Table 1, mass-length relations for various ice crystal types, which are based upon numerous observations and empirically derived by

the authors noted, are presented. The characteristic length of r of an ice crystal is defined here as the maximum length dimension of that crystal. These relationships are plotted in Figure 7. Note that single columns are more massive than bullet rosettes for $r \leq 5 \times 10^{-4}$ m and that the curve for plates lies between these curves for the smaller particle sizes. Except for very large particles, irregular aggregates are the most massive particles at any given characteristic length.

Particle habit	$m(g) = A\, r^{B}$ (10^{-6} m) A	B	Source
Columns (j=1)	1.35×10^{-10}	1.7	Heymsfield (1972)
Bullet rosettes (j=2)	4.4×10^{-14}	3.0	"
Plates	8.22×10^{-13}	2.5	"
Unrimed aggregates of plates, bullets and columns	7.36×10^{-11}	1.9	Locatelli and Hobbs (1974)

Table 1. Mass-length relationships.

Heymsfield (1972) states that the standard error of these formulas is on the order of $\pm$ 20% for individual ice crystals. However, much better accuracy may be expected when considering large populations of ice crystals as here.

Based on the exacting computations of Heymsfield (1972), the magnitude of the terminal velocities of single column, bullet and plate -type ice crystals in still air as a function of characteristic length may be represented by the relations presented in Table 2. These relationships are plotted in Figure 8. These data correspond to an ambient

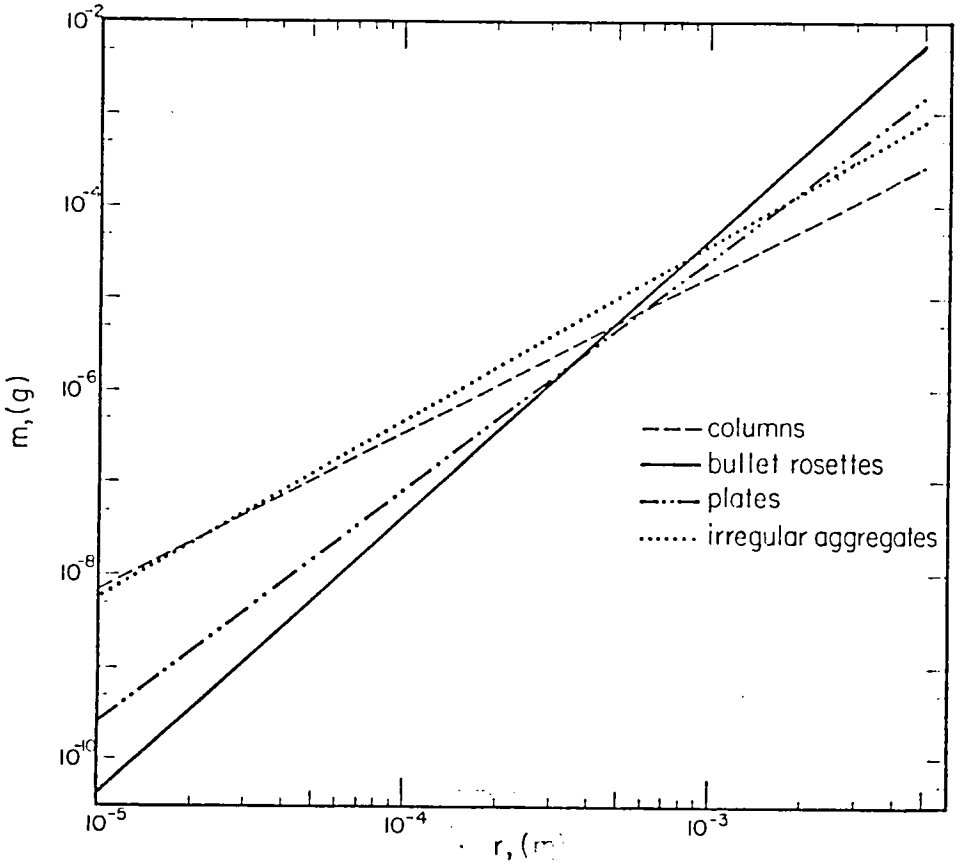

Figure 7. Empirical relationships between particle characteristic length, r, and the corresponding particle mass, m, for various ice particle habits. See text for source and discussion.

pressure of 40 kPa (400 mb) and an ambient air temperature of -20°C. These relations were fit to his results over the range 10^{-4} to 10^{-3} m. For $r < 10^{-4}$ m and $r > 10^{-3}$ m, simple extrapolation from the nearest size interval was employed.

$v(\text{m s}^{-1}) = A\, r^{B}\ (10^{-6}\ \text{m})$

$r\ (10^{-6}\text{m})$	Columns (j=1) A	Columns (j=1) B	Bullets (j=2) A	Bullets (j=2) B	Plates A	Plates B
0-200	8.114×10^{-5}	1.585	5.666×10^{-5}	1.663		
200-400	4.995×10^{-3}	0.807	3.197×10^{-3}	0.902	1.480×10^{-3}	0.926
400-600	2.223×10^{-2}	0.558	2.977×10^{-2}	0.529	[illegible]	000
600-800	4.352×10^{-2}	0.453	2.144×10^{-2}	0.581	[illegible]	[illegible]
800-5000	3.833×10^{-2}	0.472	3.948×10^{-2}	0.489	[illegible]	[illegible]

Table 2. Terminal fall speed-length relationships [illegible].

In a relative sense, plate form ice crystals fall [illegible] rapidly than single column or bullet ice crystals at small particle sizes. However, in an absolute sense, the differences amount to no more than 2×10^{-2} m s^{-1} for $r < 10^{-2}$ m. Comparing columns and bullets at any given characteristic length, the more massive particle tends to fall faster but there is a superimposed aerodynamic effect. Heymsfield (1975c) states that the relationship for bullet rosettes corresponds closely to that for single bullets (at least to within the [illegible] of the computations). This is also assumed here. Heymsfield [illegible] states that the standard error of his computations for individual crystals is on the order of ± 20% and is due primarily to the [illegible]

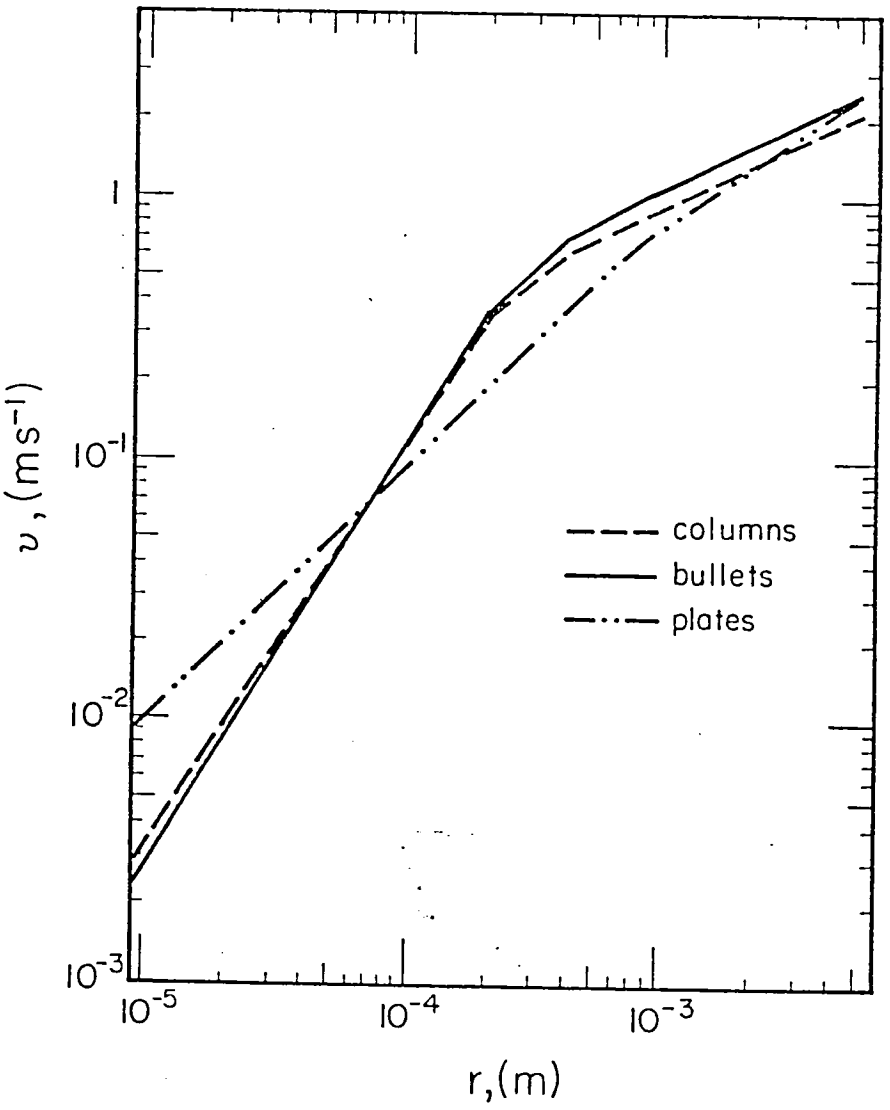

Figure 8. Empirical relationships between particle characteristic length, r, and the corresponding particle terminal fall speed, v, for various ice particle habits. See text for source and discussion.

noted uncertainty in the empirical mass-length relationships, which were employed. However, as before, much better accuracy may be anticipated when considering large populations of crystals as here.

Presumably, the irregular aggregate type particle would have a larger terminal velocity than the bullet rosette for a given characteristic length by virtue of its larger mass for most values of r. However, an opposing effect is that due to its less aerodynamic shape, the irregular aggregate crystal would experience more drag and, thus, fall slower than a bullet rosette at a given value of r. Because of the lack of an appropriate empirical terminal velocity-length relationship for the irregular particles, all aggregate particles have been assumed to be bullet rosettes. It is hoped that the compensating effects noted above will mitigate the effect of neglecting the irregularly shaped aggregate ice particle habit.

Thus, $j = 2$ is assumed in Equation (3.10.1), where $j = 1$ and $j = 2$ correspond to the single column and bullet rosette ice crystal habits, respectively. The appropriate relations from Tables 1 and 2 are employed for $m_j(r_i)$ and $v_j(r_i)$, respectively. Since it is unclear from the previously discussed observations exactly what relation might be invoked concerning the relative abundance of these two crystal habits, it is arbitrarily assumed that:

$$\frac{N_1}{N} = \frac{n_1(r_i)}{n(r_i)} \equiv WW$$

where

$$N \equiv N_1 + N_2$$

and

$$n(r_i) \equiv n_1(r_i) + n_2(r_i)$$

are the total number density and number density size distribution function for all ice particles present, respectively, and WW is some constant, positive fraction. Thus,

$$n_1(r_i) = (WW)\, n(r_i)$$

and

$$n_2(r_i) = (1\text{-}WW)\, n(r_i) \qquad (3.10.2)$$

where

$$n(r_i) = N\, n^*(r_i),$$

are assumed. Formally, the relative abundance of the two ice crystal habits has been assumed to be independent of particle size. However, due to the dominant influence of the largest particles present in significant quantities on the computed v^*, the choice of WW may be interpreted as effectively specifying the relative abundances of these largest particles.

The computations reported here are performed for specified values of WW = 0, 0.5 and 1.0 corresponding to an assumption that all particles are bullet rosettes, that there is an equipartitioning between single columns and bullet rosettes and that all particles are single columns, respectively.

The form of the particle size distribution functions associated with stratiform ice phase clouds is not well-known. Heymsfield (1975a), Varley (1978), and Varley and Brooks (1978) all indicate that in all cases the smallest particles dominate the total number density with a peak in the number density distribution at a characteristic length less

than $\sim 10^{-5}$ m. Hobbs et al. (1975) present data which implies that a large particle mode with a modal length on the order of 5×10^{-4} m or greater tends to be found with ice water contents greater than ~ 0.1 g m^{-3}. At smaller values of ice water content, a peak in the particle size distribution tends to occur at a characteristic length of 10^{-4} m to 3×10^{-4} m. Heymsfield (1975a) observed a distinct peak in the particle size distribution at $r \sim 5 \times 10^{-4}$ m in cirrus uncinus clouds with an ice water content of $\sim .25$ g m^{-3}. He, also, shows what may be interpreted as a weak modal peak at $r \sim 10^{-4}$ m for cirrostratus clouds with an ice water content of ~ 0.02 g m^{-3}. These observations agree reasonably well with those of Varley (1978) and Varley and Brooks (1978), who found a fairly strong tendency for peaks in the number density distribution at a characterstic length of 10^{-4} m to 3×10^{-4} m for ice water contents ranging from 10^{-4} to 10^{-2} g m^{-3}. The modal length of the large particle mode tended to increase with increasing ice water content. Their data tend to support the observations of Hobbs et al. (1975) for the larger ice water contents, i.e. $\rho \ell > 10^{-2}$ g m^{-3}. Griffith et al. (1980) observed a modal length of $\sim 2 \times 10^{-4}$ m corresponding to ice water contents in the range of 0.05 to 0.15 g m^{-3} in cirrus anvil clouds.

Heymsfield (1975a) notes that the ice water content and total ice crystal number density tend to increase with increasing convective activity. Furthermore, particle sizes and concentrations were found to be a function of temperature with sizes decreasing and concentration increasing with decreasing temperature. To some degree, this may be the result of size sorting by virtue of the interaction of the dynamics and particle terminal velocities with the cloud.

In summary, the observations indicate a predominant bimodal structure in the particle size distribution function where the characteristic modal length of the large particle mode tends to increase with increasing ice water content. Though there is evidence in the observations for additional size modes, only bimodal distributions are considered here. This greatly simplifies the following developments. It is assumed that the normalized particle size distribution function for all ice crystals may be partitioned as:

$$n^*(r_i) = W\, n_S^*(r_i) + (1-W)\, n_L^*(r_i) \qquad (3.10.3)$$

where W is a positive fraction and $n_S^*(r_i)$ and $n_L^*(r_i)$ are the normalized particle size distribution functions corresponding to a small and large particle size mode, respectively.

It is convenient to define:

$$\ell_k^* \equiv \sum_{i=1}^{I'} \left\{ n_k^*(r_i) \left[(WW)\, m_1(r_i) + (1 - WW)\, m_2(r_i) \right] \right\} \qquad (3.10.4)$$

and

$$v_k^* \equiv \frac{1}{\ell_k^*} \sum_{i=1}^{I'} \left\{ n_k^*(r_i) \left[(WW)\, m_1(r_i)\, v_1(r_i) + (1 - WW)\, m_2(r_i)\, v_2(r_i) \right] \right\} \qquad (3.10.5)$$

for k = S or L. These quantities correspond to a normalized ice water specific humidity and a normalized effective ice water fall speed, respectively, for both the small (k=S) and large (k=L) modal normalized particle size distributions for the assumed partition of particle habit.

Equations (3.10.1)-(3.10.5) may now be combined to yield:

$$-v^* = \frac{W\, v_S^*\, \ell_S^* + (1-W)\, v_L^*\, \ell_L^*}{W\, \ell_S^* + (1-W)\, \ell_L^*} . \qquad (3.10.6)$$

Thus, it remains only to specify W in order that the magnitude of v^* may be determined for any assumed forms of $n_S^*(r_i)$ and $n_L^*(r_i)$ given WW.

Heymsfield (1977) gives the following relationship between the mean characteristic length of ice crystals longer than 10^{-4} m and the corresponding observed total ice water content, which was deduced from observations in numerous types of stratiform ice clouds:

$$\bar{r} = 698 + 366\ \mathrm{Log}(\rho\ell) + 122\ \mathrm{Log}^2(\rho\ell) + 13.6\ \mathrm{Log}^3(\rho\ell) \qquad (3.10.7)$$

where $\rho\ell$ has dimensions g m^{-3} and $\bar{r}$ has dimensions 10^{-6} m. This relationship is plotted in Figure 9. Note that this empirical relation was derived from observations where $\rho\ell$ was not less than 10^{-4} g m^{-3} However, the behavior of the empirical fit at smaller values of $\rho\ell$ is not unreasonable and is adopted here.

This same parameter may be computed for any assumed particle size distribution. Let:

$$N_k^* \equiv \sum_{i=100}^{I'} n_k^*(r_i) \qquad (3.10.8)$$

and

$$\bar{r}_k \equiv \frac{1}{N_k^*} \sum_{i=100}^{I'} n_k^*(r_i)\, r_i \qquad (3.10.9)$$

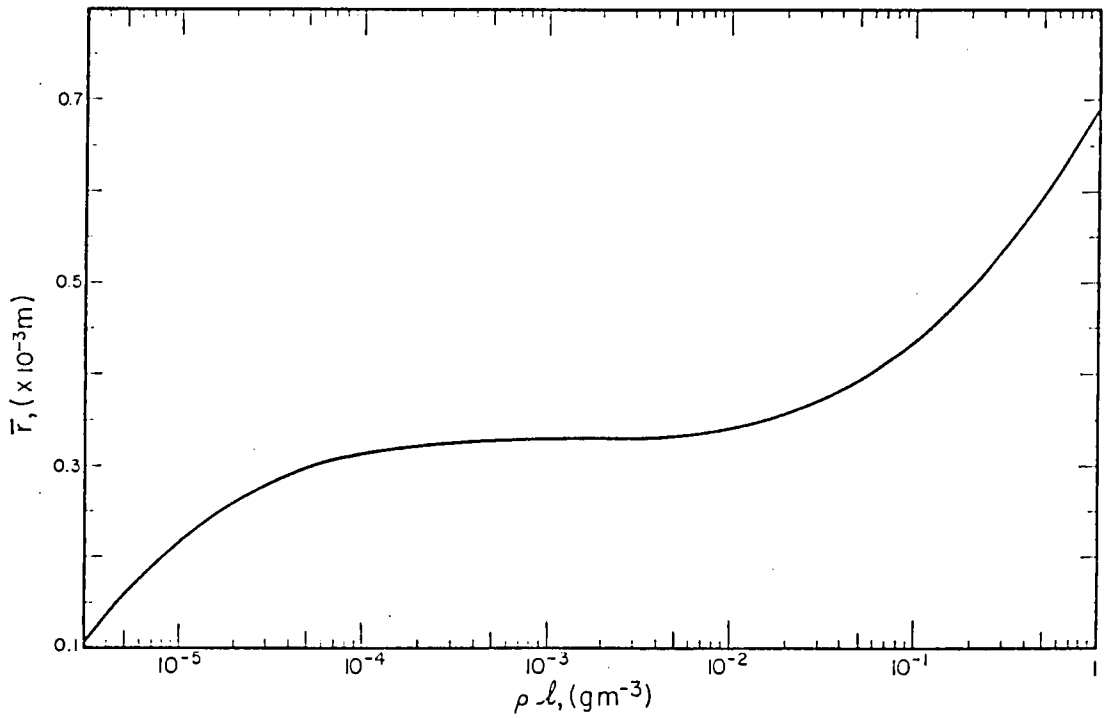

Figure 9. Empirical relationship between the observed ice water content, $\rho\ell$, and the mean characteristic length of ice crystals whose characteristic length is greater than 10^{-4} m (after Heymsfield, 1977).

for k = S or L. Thus, N_k^* and $\bar{r}_k$ are the fraction of the total number of particles in the small or large particle size distribution with a length greater than 10^{-4} m and the mean length of those particles, respectively. In a manner similar to the derivation of Eq. (3.10.6),

$$\bar{r} = \frac{W\, N_S^*\, \bar{r}_S + (1-W)\, N_L^*\, r_L^*}{W\, N_S^* + (1-W)\, N_L^*}$$

which may be rearranged to yield:

$$W = \frac{N_L^* (\bar{r}_L - \bar{r})}{N_S^* (\bar{r} - \bar{r}_S) + N_L (\bar{r}_L - \bar{r})} \quad . \qquad (3.10.10)$$

Thus, given the previous assumptions and empirical relations, v^* may be computed as a function of ice water content for any assumed functional forms of $n_S^*(r_i)$ and $n_L^*(r_i)$. Note that solutions for $v^*(\rho\ell)$ may only be obtained when:

$$\bar{r}_S \lesssim \bar{r} \lesssim \bar{r}_L \, . \qquad (3.10.11)$$

Following from Deirmendjian (1969) and Mason (1971), a normalized monomodal particle size distribution function may be represented by a modified gamma function distribution. Welch et al. (1980) note that a normalized bi-modal size distribution function may be represented by a superposition of two modified gamma function distributions corresponding to a large particle mode and a small particle mode. This approach is adopted here. Thus,

$$n_k^*(r_i) = \frac{r_i^{\alpha_k} \exp(- b_k r_i^{\gamma_k})}{C_k}$$

where

$$b_k \equiv \left(\frac{\alpha_k}{\gamma_k}\right) r_k^{-\gamma_k}$$

and

$$C_k \equiv \gamma_k^{-1} b_k^{-(\alpha_k+1)/\gamma_k} \Gamma\left(\frac{\alpha_k+1}{\gamma_k}\right) \qquad (3.10.12)$$

for k = S or L. Note that r_i and r_k have dimensions of 10^{-6} m when evaluating $n_k^*(r_i)$, which has dimensions $(10^{-6}$ m interval$)^{-1}$. The specified modal characteristic crystal length is r_k and α_k and γ_k are tuneable shape parameters for a distribution. For convenience,

$$\frac{(\alpha_k + 1)}{\gamma_k} = m ,$$

where m is a positive integer, is required such that:

$$\Gamma \frac{(\alpha_k + 1)}{\gamma_k} = (m-1)! \quad .$$

A single small particle mode normalized particle size distribution function was assumed for all the computations reported here. The modal length was specified as 10^{-5} m. The assumed distribution parameters and the resulting computed parameters are given in Table 3. This function, $n_S^*(r_i)$, is plotted in Figure 10. Note that the computations were made for $\Delta = 10^{-6}$ m and then summed to the $(1.5 \times 10^{-5}$ m interval$)^{-1}$ shown. The shape of this distribution function agrees reasonably with

k		S										0
r_k (μm)		10		200			300			500		9
α_k		2		2			2			2		5
γ_k		0.5	1.5	1.0	0.75	1.5	1.0	0.75	1.5	1.0	0.75	1.0
$\bar{r}_k$ (m)		0.126	0.264	0.319	0.386	0.381	0.462	0.558	0.625	0.755	0.911	—
	WW 1	0.130	0.672	0.852	1.049	0.869	1.066	1.292	1.143	1.380	1.644	
v_k^* (m s^{-1})	WW 5	0.069	0.586	0.749	0.937	0.785	0.972	1.196	1.068	1.303	1.571	0.009
	WW 0	0.065	0.529	0.645	0.764	0.692	0.812	0.944	0.906	1.047	1.205	

Table 3. Shape parameters (α_k and γ_k), mean large particle characteristic length ($\bar{r}_k$) and effective relative fall speed (v_k^*) for various monomodal particle size distributions with modal characteristic length $\bar{r}_k$ for ice crystals (k = S or L) and liquid water drops (k = 0). See text for definitions and discussion.

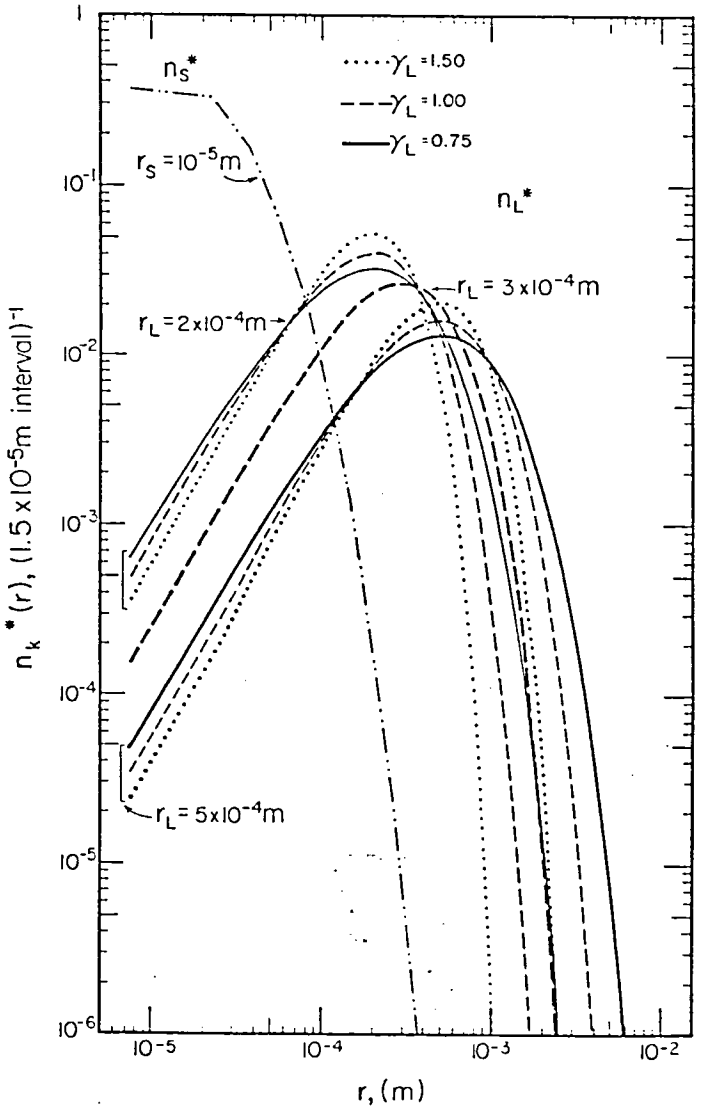

Figure 10. Normalized ice particle number density functions. See text for definition and discussion.

those observed by Heymsfield (1975a), Varley (1978) and Varley and Brooks (1978) for the smallest particle sizes.

A number of distributions were tried for the large particle mode. Modal lengths of 2×10^{-4} m, 3×10^{-4} m and 5×10^{-4} m were used. The assumed shape parameters and the resulting computed parameters $\bar{r}_k$ and v_k^*, defined previously, are given in Table 3. The corresponding normalized particle size distribution functions are plotted in Figure 10. Note that for a given r_L and α_L, the effect of decreasing γ_L is to broaden the distribution which increases the magnitude of the computed values of $\bar{r}_L$ and v_L^*. Also, all things being equal, the more the particle habit is dominated by bullet rosettes, the larger the computed v_L^*. The exceptions to this are for the small particle distribution and the narrowest distribution for $r_L = 2 \times 10^{-4}$ m. The shape of these large particle distributions span the range of observations discussed previously. For example, the shape of the 5×10^{-4} m large particle mode observed by Heymsfield (1975a) in a cirrus uncinus cloud lies between the $\gamma_L = 1.0$ and $\gamma_L = 1.5$ curves for $r_L = 5 \times 10^{-4}$ m and $r \gtrsim 6 \times 10^{-4}$ m. His distribution is somewhat more peaked right at $r = 5 \times 10^{-4}$ m but the disagreement is comparable to the uncertainty of the observations themselves.

Computations of $v^*(\rho\ell)$ by means of Equations (3.10.6) and (3.10.10) were performed for each of the assumed $n_L^*(r_i)$ functions utilizing the assumed $n_s^*(r_i)$ function and the given empirical relations for $m_j(r_i)$, $v_j(r_i)$ and $\bar{r}(\rho\ell)$ for WW = 0, 0.5 and 1.0. The results are graphically displayed in Figures 11, 12 and 13, respectively. In addition to the constraint given by Eq. (3.10.11), the computations were terminated if $W < 0.80$ was encountered. This condition was imposed

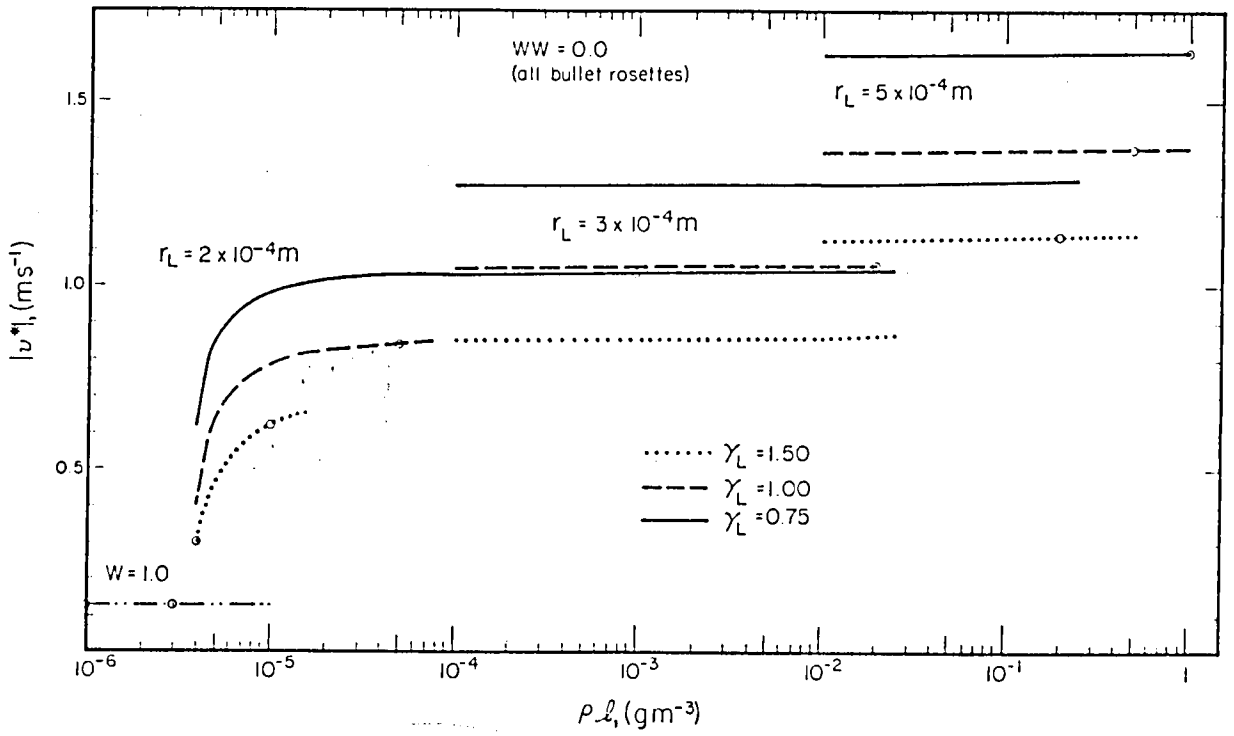

Figure 11. Magnitude of the effective ice water terminal velocity $|v^*|$ versus ice water content, $\rho\ell$, for various particle size distribution functions assuming all particles are bullet rosettes. See text for definitions and discussion.

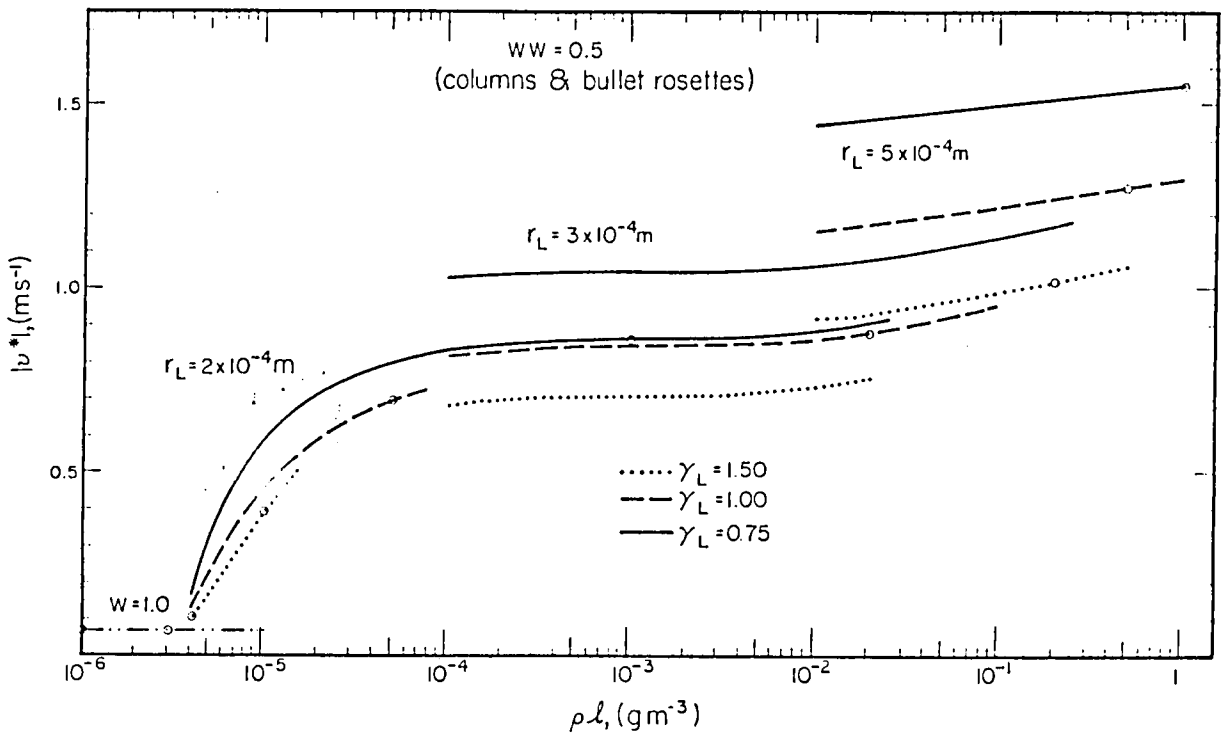

Figure 12. Same as Figure 11, except assuming an equipartition between columns and bullet rosettes for the ice particle habit.

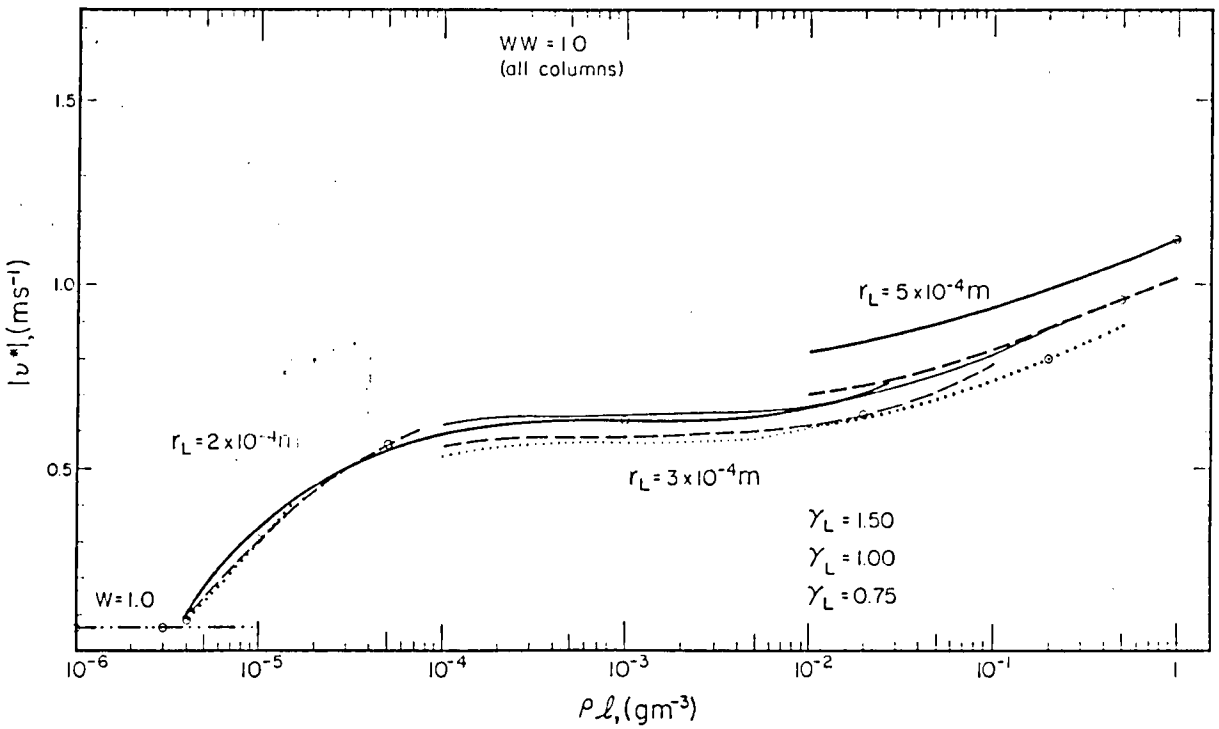

Figure 13. Same as Figure 11, except assuming all particles are single columns.

based on analysis of the previously noted observations of $n(r)$ and determines the maximum value of $\rho\ell$ for which a solution may be obtained for any assumed $n_L^*(r_i)$. Note that solutions when $r_L = 3 \times 10^{-4}$ m and 5×10^{-4} m for $\rho\ell < 10^{-4}$ and 10^{-2} g m^{-3}, respectively, have not been displayed since the observations indicate that these modes are unlikely at these values of $\rho\ell$.

For each assumed large particle distribution, the contribution of the large particles dominates v^* once $\rho\ell$ exceeds 10^{-5} to 10^{-4} g m^{-3}. Thus, the magnitude of v^* increases rapidly at small values of $\rho\ell$ and becomes nearly constant for moderate to large values. This is most evident for the case where all particles are assumed to be bullet rosettes (WW = 0.0). It is of note that the assumed form of $n_k^*(r_i)$ becomes much more critical when the particle habit is predominatly bullet rosettes as compared to columns.

Based on the limited observations available, it seems reasonable to increase the large particle modal characteristic length and to broaden the large particle mode size distribution function as $\rho\ell$ increases. Somewhat arbitrarily, the circled points in Figures 11, 12 and 13 are assumed to be representative. The assumed distribution functions at these values of $\rho\ell$ do roughly correspond to the previously noted observations. They are then connected as in Figure 14 to yield three basic parameterizations, i.e. WW0, WW5 and WW1 corresponding to WW = 0, 0.5 and 1.0, respectively. Effectively, r_L and γ are allowed to increase in a somewhat continuous fashion between the circled points, where specific solutions are assumed. The scenario assumed here may be summarized as:

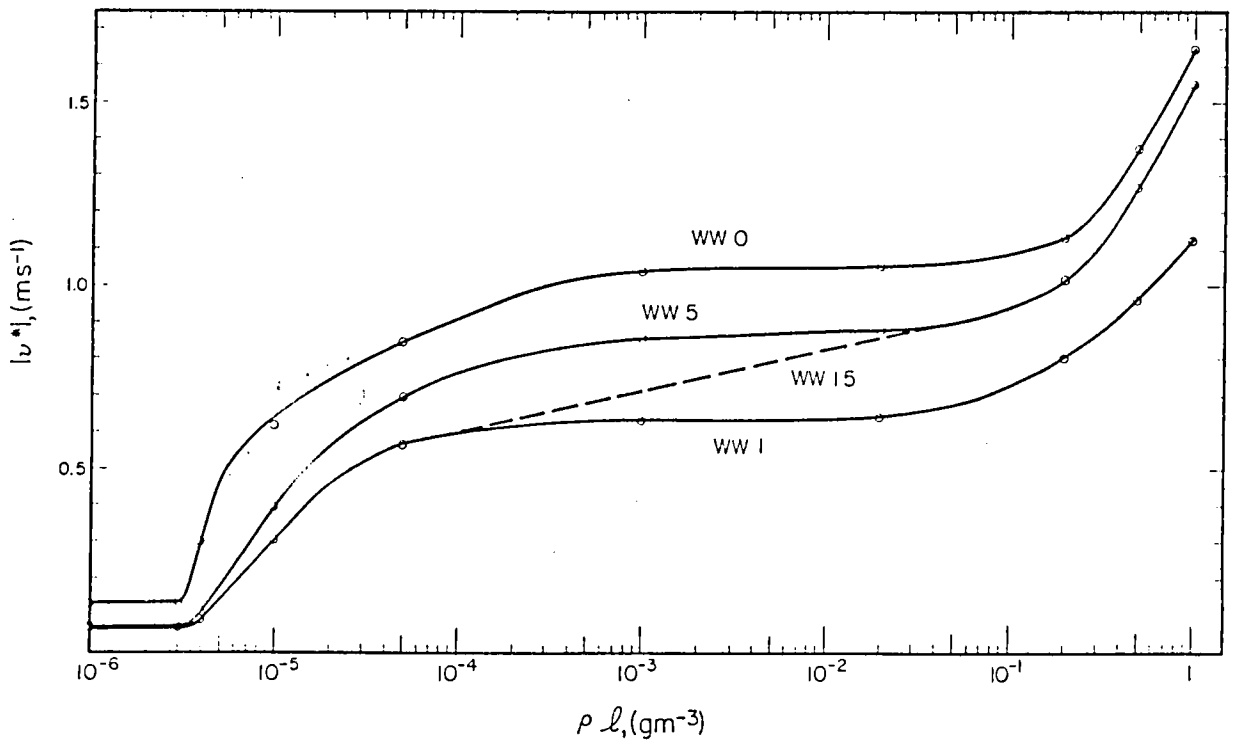

Figure 14. Magnitude of the effective ice water terminal velocity v^*_ℓ versus ice water content, $\rho\ell$, for realistic scenarios describing the evolution of number density size distribution function. The curves correspond to a particle habit assumption of all bullet rosettes (WW0), equipartition of bullet rosettes and columns (WW5), all single columns (WW1) and a realistic evolution of the all columns assumption to the equipartition assumption (WW15). See text for definition and discussion.

(1) For $\rho\ell < 3 \times 10^{-6}$ g m^{-3}, only the small particle size mode exists.

(2) For 3×10^{-6} g $m^{-3} < \rho\ell < 10^{-3}$ g m^{-3}, a large particle size mode with a modal length of 2×10^{-4} m is also present. This mode broadens with increasing $\rho\ell$ to where at $\rho\ell = 4 \times 10^{-6}$ g m^{-3} to 10^{-5} g m^{-3}, 5×10^{-5} g m^{-3} and 10^{-3} g m^{-3} the normalized particle size distribution function for the large particle mode is given by $\gamma_L = 1.5$, 1.0 and 0.75, respectively.

(3) At larger values of $\rho\ell$, the large particle modal characteristic length increases to where at $\rho\ell = 2 \times 10^{-2}$ g m^{-3}, $r_L = 3 \times 10^{-4}$ m and $\gamma_L = 1.0$. This is a relatively broad size distribution. By the time $\rho\ell = 0.2$, the modal characteristic length is 5×10^{-4} m and $\gamma_L = 1.5$.

(4) At even larger values of $\rho\ell$, the large particle size mode broadens to where at $\rho\ell = 0.5$ g m^{-3} and 1.0 g m^{-3}, $\gamma_L = 1.0$ and 0.75, respectively, for the large particle mode at $r_L = 5 \times 10^{-4}$ m.

This scenario agrees reasonably with the observations noted previously. However, recalling the observations of Heymsfield (1977) as regards the intensity of convective activity and the observed magnitude of $\rho\ell$ and the numerous observations of the relationship between the intensity of convective activity and the predominance of particular particle habits, it seems likely that the WW1 parameterization is most applicable at relatively small values of $\rho\ell$ and that the WW5 or WW0 parameterizations are more appropriate at larger values of $\rho\ell$. Thus, a fourth parameterization, i.e. WW15, is proposed, where for $\rho\ell < 5 \times 10^{-5}$ g m^{-3}, the WW1 scheme is employed and for $\rho\ell \geq 5 \times 10^{-2}$ g m^{-3}, the WW5 scheme is used. Intermediate between these values of $\rho\ell$, the

bullet rosette crystal habit beomes increasingly more common as $\rho\ell$ increases. The assumed dependence of $v^*(\rho\ell)$ in this region is given by the dashed curve in Figure 14. The WW15 parameterization seems to be the most reasonable based on the observations.

It should be noted that the assumed total ice crystal number density $N(\rho\ell)$ corresponding to the above parameterizations is realistic. Comparison with the limited observations available yields disagreements on the order of one order of magnitude in total particle number within a cubic meter in most cases. This is comparable to the uncertainty in the observations themselves.

For model simulations, it is most efficient computationally to evaluate $v^*(\rho\ell)$ by means of look-up tables. The advantage of this method over a more direct technique where v^* is evaluated by means of some functional fit may be seen in that in all cases v^* is at least cubic in $\text{Log}(\rho\ell)$. Evaluation of logrithms is very inefficient computationally. The tabular representation of $\left|v^*(\rho\ell)\right|$ for the WW15 parameterization is given in Appendix C. Note that only one significant digit of $\rho\ell$ is resolved and v^* is specified as the value corresponding to the center of the $\rho\ell$ interval. Given the uncertainties and approximations involved in developing the parameterization, this resolution is deemed adequate.

Based on analyses of the results of Heymsfield's (1972) computations of the terminal velocity of ice crystals and the measurements of Beard and Pruppacher (1969) for the terminal velocity of liquid water drops in various ambient environments, a correction for variations in the ambient pressure and temperature which yields good agreement with their results for typical atmospheric conditions is given by:

$$v_j(r_i)\Big|_p = \left(\frac{p_{ref}}{p}\right)^{\frac{1}{3}} v_j(r_i)\Big|_{p_{ref}} \qquad (3.10.13)$$

where p is the ambient pressure and p_{ref} is the ambient pressure to which their observations or computations pertain. This correction yields better agreement than the $(p_{ref}/p)^{\frac{1}{2}}$ correction factor they propose. Noting Equations (3.10.5) and (3.10.6), this correction may be applied directly to v^*. For the parameterizations developed here, p_{ref} = 40 kPa. The ambient pressure and density are approximated as the basic state values. Thus,

$$v^*_{i+\frac{1}{2},k+\frac{1}{2}} = -\left(\frac{40\ \text{kPa}}{p_{o_{k+\frac{1}{2}}}}\right)^{\frac{1}{3}} \left| v^*(\rho_{o_{k+\frac{1}{2}}} \ell_{i+\frac{1}{2},k+\frac{1}{2}}) \right| \qquad (3.10.14)$$

for i = 1, 2, ..., I-2, I-1 and k = 1, 2, ..., k-2, k-1, which denote the grid location, where $\left|v^*(\rho_{o_{k+\frac{1}{2}}} \ell_{i+\frac{1}{2},k+\frac{1}{2}})\right|$ is determined from the table given in Appendix C. Note that since the basic state pressure is employed for the pressure correction, the correction factor need only be computed once for each grid level. Note that the downward direction of v^* is accounted for by the minus sign in Equation (3.10.14).

Mason (1971) provides a summary of observations by various authors of the microphysical properties of liquid phase stratiform clouds at mid-tropospheric levels. The observations indicate that these cloud forms have predominantly monomodal drop size distributions and are composed almost exclusively of relatively small drops. The observed distributions are well reproduced by the shape parameters given in Table 3, i.e. k = 0. Beard and Pruppacher (1969) give mass and terminal velocity relationships for water drops as a function of

characteristic drop diameter for an ambient air pressure of 50 kPa and a temperature of -8°C. These allow the computation of the v_o^* corresponding to normalized drop size distribution function defined by the shape parameters given in Table 3. The resulting v_o^* is given in Table 3. This value, corrected for ambient pressure as for the WW15 ice phase parameterization and multiplied by minus one, is employed for liquid phase simulations.

3.11 Determination of Radiative Heating Rates

This section describes the manner of specifying the radiative heating rates, QR, at all thermodynamic grid points at a given time step n. These heating rates are incorporated in the model as described in Section (3.7).

The radiative heating rates are partitioned into two components. These are the infrared component, QIR, and the shortwave or solar, QSW, component, which pertain to radiative processes acting in the spectral intervals of 3.0 μm to 50 μm and 0.3 μm to 3.0 μm, respectively. Two radiative transfer models are utilized for some of the computations. These are, hereafter referred to as IRADIR and IRADSW and pertain to the infrared and shortwave spectral regions, respectively. These models are briefly described below.

IRADIR is a broadband, infrared, flux emittance radiative transfer model and closely corresponds to that reported by Cox (1973). The radiative transfer equation is solved in finite difference form at the vertical resolution of the input data assuming a horizontally homogeneous atmosphere and isotropic diffuse fluxes. Isothermal conditions are assumed for each atmospheric layer resolved by the input data at

the linearly interpolated mid-point temperature. Perfect Plankian emission from the earth's surface is, also, assumed. The model accounts for the contributions due to gaseous absorption by the 6.3 μm, continuum and rotational water vapor absorption bands; the carbon dioxide absorption bands (including primarily the 14.7 μm band); and the 9.6 μm ozone absorption band. A correction for the overlap of the rotational water vapor band and the carbon dioxide bands is applied. The effect of pressure and temperature broadening of an absorption band is taken into account in parametric fashion. The parametric formulation as well as the sources of the gaseous emittance data for each band considered are given in Cox, et al. (1976).

The input data for IRADIR are the atmospheric vertical profiles of pressure, temperature, water vapor specific humidity, carbon dioxide mixing ratio and ozone concentration. These profiles must include both the regions above and below the vertical domain of interest here (including surface values). Within the domain of interest, the input data are specified at all dynamic grid levels such that the computed flux convergence profiles are well defined for the thermodynamic grid levels. In addition, a cloud layer may be defined. For the IRADIR model, clouds are assumed to act as grey body absorbers/emitters, i.e. no spectral dependence. Both an upward $\varepsilon^*(\uparrow)$ and a downward $\varepsilon^*(\downarrow)$ bulk effective broadband infrared cloud emittance are specified as input data, in addition, to the cloud top and base levels. A correction for the overlap of the gaseous absorption bands and cloud absorption for the cloud layer is applied as in Griffith, et al. (1980). Note that for the computations performed here with the IRADIR model, the in-cloud flux profiles are computed as in Griffith, et al. (1980) such that the

effective radiating level is not the cloud boundary level. This is not particularly significant in terms of the heating rates actually employed in the model.

The IRADSW model is a simplified, broadband shortwave, flux transmittance radiative transfer model and closely corresponds to that reported by Manabe and Strickler (1964) and Manabe and Wetherald (1967). The model assumes a horizontally homogeneous atmosphere and considers the contributions due to gaseous absorption by water vapor, carbon dioxide and ozone. The absorptance data are taken from Manabe and Strickler (1964) and include a pressure broadening correction. Overlap of the absorbing bands is ignored. A conservative Rayleigh scattering parameterization is included. The solar constant is specified as 1372 $W\ m^{-2}$ and is corrected for sun-earth geometry. Atmospheric vertical profiles of temperature, etc. must be specified as for the IRADIR model. In addition, the date and solar zenith angle, ϑ, must, also, be specified as input data. The surface shortwave albedo is specified as zero since at typical cirriform cloud levels the absorption of solar radiation reflected from the earth's surface is negligible. A cloud layer may, also, be defined where IRADSW is applied to compute the upward flux profiles above cloud top due to reflection of downward shortwave radiation by the cloud layer. In addition to the cloud top level, the bulk, broadband cloud shortwave reflectance must be specified. For the IRADSW model, clouds are assumed to act as "grey" body reflectors, where the reflected shortwave fluxes are assumed diffuse and isotropic. For the computation of the gaseous optical paths, the cloud top level is regarded as a mirrored surface.

In the parameterization developed here, the effects due to the perturbations of temperature, pressure and water vapor mixing ratio from their basic state values are ignored. Errors due to this assumption for typical perturbations simulated here are relatively small, (Starr, 1976). In addition, the determination of the QSW profile for any grid column is assumed independent of the determination in the adjacent columns. This is done since the azimuthal orientation of the grid plane relative to the sun's position is unknown. In effect, a grid column is assumed representative of conditions along the solar azimuth. Furthermore, effects due to the finite geometry of cloud elements (e.g. Welch et al. 1980 and Davis, et al. 1978) are ignored for both the infrared and shortwave schemes.

The output of the IRADIR and IRADSW models are the upward and downward irradiance profiles at the vertical resolution of the input data. The corresponding atmospheric radiative heating rates for a layer may be determined as:

$$QR \equiv QIR + QSW \tag{3.11.1}$$

where

$$QIR = \frac{g}{c_p} \frac{\left\{(H_T(\downarrow) + H_B(\uparrow)) - (H_B(\downarrow) + H_T(\uparrow))\right\}}{(p_B - p_T)} , \tag{3.11.2}$$

H is the infrared flux in the upward ($\uparrow$) or downward ($\downarrow$) directions at the top T or base B of the layer,

$$QSW \equiv QSW^{(\downarrow)} + QSW^{(\uparrow)} , \tag{3.11.3}$$

$$QSW^{(\downarrow)} = \frac{g}{c_p} \frac{\left\{I_T^{(\downarrow)} - I_B^{(\downarrow)}\right\}}{(p_B - p_T)} \quad , \qquad (3.11.4)$$

$$QSW^{(\uparrow)} = \frac{g}{c_p} \frac{\left\{I_B^{(\uparrow)} - I_T^{(\uparrow)}\right\}}{(p_B - p_T)} \quad , \qquad (3.11.5)$$

I is the shortwave flux in the direction and at the level indicated, and p is the pressure at the top or base of the layer. The pressure values are always specified as the basic state values. Note that the heating due to absorption of solar energy is partitioned into that resulting from absorption of downward and upward propagating fluxes. $QSW^{(\uparrow)}$ is neglected except for the layers above cloud top, when a cloud is diagnosed in a particular grid column.

The parametric scheme described in the next sub-sections allows the determination of QIR, $QSW^{(\downarrow)}$ and $QSW^{(\uparrow)}$ at every thermodynamic grid point (i.e. $(i+\frac{1}{2},k+\frac{1}{2})$ for i = 1, 2, ..., I-2, I-1 and k = 1, 2, ..., K-2, K-1) and a given time step n.

A cloud is diagnosed in the $i+\frac{1}{2}$ thermodynamic grid column if:

$$\ell_{i+\frac{1}{2},k+\frac{1}{2}} \neq 0$$

for k = 1, 2, ..., K-2, or K-1. The grid level corresponding to cloud top level is diagnosed as:

$$KT_{i+\frac{1}{2}} = k' \qquad (3.11.6)$$

where

$$\ell_{i+\frac{1}{2},k-\frac{1}{2}} \neq 0$$

and

$$\ell_{i+\frac{1}{2},k+\frac{1}{2}} = 0$$

for k = k', k'+1, ..., K-2, K-1. Similarly, the cloud base grid level is diagnosed as:

$$KB_{i+\frac{1}{2}} = k' \qquad (3.11.7)$$

where

$$\ell_{i+\frac{1}{2},k+\frac{1}{2}} \neq 0$$

and

$$\ell_{i+\frac{1}{2},k+\frac{1}{2}} = 0$$

for k = 1, 2, ..., k'-2, k'-1.

The solar zenith angle ϑ^n and the local sun time t^n_{SOL} must also be determined at time step n. The local sun time is specified as:

$$t^n_{SOL} = t^o_{SOL} + n\,\Delta t \qquad (3.11.8)$$

where t^o_{SOL} is the externally specified solar time corresponding to the initiation of a simulation and Δt is the time step increment. The hour angle of the sun may be computed as:

$$h^n = 2\pi \left| 0.5 - t^n_{SOL} \right| \qquad (3.11.9)$$

where t_{SOL}^{n} is expressed as the fraction of a day past local midnight. No distinction between morning and afternoon is necessary for the purposes here. The specification of the simulation latitude, ϕ, allows the computation of the solar zenith angle at time step n as:

$$\vartheta^{n} = \cos^{-1}\left\{\sin\phi \sin\delta + \cos\phi \cos\delta \cos h^{n}\right\} \qquad (3.11.10)$$

where the solar declination, δ, is approximated as:

$$\delta \doteq -0.1306\,\pi \cos\left(\frac{2\pi}{365}(JD + 9)\right) \qquad (3.11.11)$$

for a given Julian day number (day of year), JD. The sunrise time of a simulation for a given Julian day and latitude is given by:

$$SR = 0.5 - \left(\frac{1}{\pi}\right) \cos^{-1}\left\{\frac{-\sin\phi \sin\delta}{\cos\phi \cos\delta}\right\} \qquad (3.11.12)$$

where SR is expressed as the fraction of one day past local midnight. Now, if:

$$t_{SOL}^{n} \leq SR$$

or

$$t_{SOL}^{n} \geq 1 - SR$$

then:

$$\vartheta^{n} \equiv 90°$$

and

$$QSW \equiv 0 . \qquad (3.11.13)$$

The next sub-section describes the manner of diagnosing the bulk radiative properties of a cloud layer which is diagnosed in a given grid column at time step n. The parameterization is highly empirical. The infrared radiative properties are $\varepsilon^*(\uparrow)$ and $\varepsilon^*(\downarrow)$, which will be defined in the following sub-section. The bulk shortwave properties are the broadband shortwave reflectance, transmittance and absorptance defined as:

$$\rho_{s_{i+\frac{1}{2}}} = \frac{I^{(\uparrow)}_{KT_{i+\frac{1}{2}}}}{I^{(\downarrow)}_{KT_{i+\frac{1}{2}}}}, \qquad t_{s_{i+\frac{1}{2}}} = \frac{I^{(\downarrow)}_{KB_{i+\frac{1}{2}}}}{I^{(\downarrow)}_{KT_{i+\frac{1}{2}}}} \qquad (3.11.14)$$

and $$a_{s_{i+\frac{1}{2}}} = 1 - \rho_{s_{i+\frac{1}{2}}} - t_{s_{i+\frac{1}{2}}},$$

respectively. The succeeding two sub-sections describe the scheme to determine QIR and QSW, respectively. It is of note that the radiative heating rates in the model domain are modulated primarily by the diagnosis of cloud and its corresponding radiative properties. These determinations are made for every grid column. A diurnal cycle is taken into account and, thus, is a secondary modulator of the diagnosed radiative heating rates. The determinations of the radiative heating rates in cloudy columns are not only sensitive to the diagnosis of the bulk cloud radiative properties and the diurnal cycle but also to the vertical distribution of ice water in that column.

3.11.a. Parameterization of the Bulk Radiative Properties of Cloud Layers

A general relationship between the vertically integrated ice water content ($\widetilde{IWP}$) of a cloud layer and the corresponding broadband infrared emittance (ε) and reflectance (ρ_{IR}) of that cloud layer is desired. That such a relationship exists for natural cirriform clouds is uncertain. Most theoretical work in this area has concentrated on deducing the functional relationship between cloud optical depth and the corresponding ε and ρ_{IR} for various model clouds. The optical depth of a cloud layer is related to the $\widetilde{IWP}$ through the extinction coefficient which in turn is determined by the microphysical characteristics of the cloud. It is fundamentally the relationship between ice water content and the corresponding microphysical characteristics of natural cirriform clouds which is unknown. However, as discussed in Section (3.10), observations indicate that some general relationship between the ice water content and the corresponding microphysical characteristics does exist for natural cirriform clouds. Thus, it is likely that some general relationship between ε and ρ_{IR} and the $\widetilde{IWP}$ may exist. The approach adopted here is to develop such a relationship, which is based on direct observations.

Following from Cox (1976), Stephens (1980) and others, the bulk infrared radiative properties of a cloud layer may be described by two effective broadband infrared emittances, $\varepsilon^*(\uparrow)$ and $\varepsilon^*(\downarrow)$, which pertain to the upward and downward propagating fluxes, respectively. These parameters account for effects due to both the broadband infrared emittance and reflectance of the cloud. The utility of this approach is that these parameters may be readily deduced from observations of

the infrared fluxes, without distinguishing between the transmitted/emitted and reflected components. They are defined as:

$$\varepsilon^*(\uparrow) = \frac{H_{KB}(\uparrow) - H_{KT}(\uparrow)}{H_{KB}(\uparrow) - \sigma T_{KT}^4}$$

and (3.11.15)

$$\varepsilon^*(\downarrow) = \frac{H_{KB}(\downarrow) - H_{KT}(\downarrow)}{\sigma T_{KB}^4 - H_{KT}(\downarrow)}$$

where σ is the Stephan-Boltzmann constant; H is the broadband infrared flux propagating in the upward ($\uparrow$) or downward ($\downarrow$) direction at cloud top (KT) or cloud base (KB) and T is the temperature of the level indicated.

Assuming uniform microphysical conditions in the cloud layer, the effective emittances are related to the emittance as:

$$\varepsilon^*(\uparrow) \doteq \varepsilon + \rho_{IR} \frac{(H_{KT}(\downarrow) - H_{KB}(\uparrow))}{(\sigma T_{KT}^4 - H_{KB}(\uparrow))}$$

and

$$\varepsilon^*(\downarrow) \doteq \varepsilon - \rho_{IR} \frac{(H_{KB}(\uparrow) - H_{KT}(\downarrow))}{(\sigma T_{KB}^4 - H_{KT}(\downarrow))}$$

where cloud top and cloud base temperature are assumed representative of the true effective radiative temperature of the emergent emitted fluxes at the respective cloud boundaries.

Yamamoto, et al. (1970) and Stephens (1980) have shown that ρ_{IR} is a relatively small quantity, i.e. $\sim$ 0.03 to 0.06 for cirriform clouds. However, the resultant effect on the infrared radiative divergence of a cloud layer may be substantial due to the magnitude (compared to σT^4 (cloud)) and spectral composition of the incident fluxes which may alter both ρ_{IR} and ε^* when considering fluxes propagating in a given direction. Thus, the differences between $\varepsilon^*(\uparrow)$ and $\varepsilon^*(\downarrow)$ and ε are significant in terms of the radiative heating rate, which is the primary concern here.

Following from Paltridge (1974), Griffith, et al. (1980) and others, infrared radiative flux profiles in cirriform cloud layers may be represented by the corresponding effective emittance profiles for the upward or downward ($\uparrow$ or $\downarrow$) propagating fluxes as:

$$\varepsilon^*(z)\,(\uparrow,\downarrow) = 1 - \exp\left(-\beta(\uparrow,\downarrow)\,\overline{IWP(z)}\,(\uparrow,\downarrow)\right)$$

where

$$\overline{IWP(z)}\,(\uparrow,\downarrow) \equiv \int_{(z,z_{KB})}^{(z_{KT},z)} \rho(z')\,\ell(z')\,dz'$$

and $\beta(\uparrow)$ and $\beta(\downarrow)$ are effective mass absorption coefficients for the upward and downward propagating infrared fluxes. Thus, the bulk cloud layer effective emittances are:

$$\varepsilon^*(\uparrow) = 1 - \exp\left(-\beta(\uparrow)\,\widetilde{IWP}\right)$$

and

$$\varepsilon^*(\downarrow) = 1 - \exp\left(-\beta(\downarrow)\,\widetilde{IWP}\right) \qquad (3.11.16)$$

where

$$\overline{IWP} \equiv \int_{z_{KB}}^{z_{KT}} \rho(z')\, \ell(z')\, dz'.$$

Theoretically, a mass absorption coefficient can be expressed as the ratio of the absorption cross section to the ice water content of the corresponding particle size distribution (Paltridge, 1974). Thus, $\beta(\uparrow)$ and $\beta(\downarrow)$ may be expected to have a vertical dependence based on the vertical structure of ice water content and particle size distributions. However, Griffith, et al. (1980) and Paltridge and Platt (1980) have shown that observations of infrared radiative flux profiles in cirrus cloud layers may be accurately reproduced by a proper choice of effective mass absorption coefficients, which are independent of height. The simplicity of this approach and its apparent representativeness of conditions in natural cirriform clouds are ideal for development of a parametric scheme. Thus, it is assumed here that $\beta(\uparrow)$ and $\beta(\downarrow)$ are independent of location within a cloud.

Paltridge and Platt (1980) reported that a value of $\beta \cong 0.056$ $m^2\ g^{-1}$ reproduces their observations of infrared radiative flux profiles in cirrostratus cloud layers. No distinction between $\beta(\uparrow)$ and $\beta(\downarrow)$ was attempted. The observations were made at 35°N latitude in March and included microphysical parameters as well as the radiative fluxes. The scatter of the data is significant. An envelope of $\beta \cong$ 0.03 to 0.07 $m^2 g^{-1}$ encompasses the observations. Part of this scatter may be attributed to sampling problems associated with horizontal inhomogeneities in the cloud layers. It is of note that the deduced values of β are highly sensitive to the reduction of the microphysical

data. There are a number of uncertainties in the interpretation of the data for the particle size ranges sampled and more significantly in the manner of estimating, by means of extrapolation, the contribution of larger ice particles to the total ice water content (Griffith, et al. 1980). Using very similar instrumentation and data reduction procedures, Griffith, et al. (1980) found that a mean value of $\beta(\downarrow) \cong 0.06$ $m^{-2}g^{-1}$ accurately reproduced their observed downward infrared radiative flux profiles in tropical cirriform clouds. Note that a correction for gaseous absorption was applied to the data and, thus, the bulk value of $\beta(\downarrow)$, as in Paltridge and Platt (1980), should be slightly larger than this value. Again, significant scatter of the data was observed. They note that this estimate of $\beta(\downarrow)$ may be as much as 40% too small depending on the manner of estimating the corresponding ice water content. However, based on the observations of large particle size distributions discussed in Section 3.10, the method employed by Paltridge and Platt (1980) and Griffith, et al. (1980) to deduce the above values is very reasonable.

Griffith, et al. (1980) note that the relative vertical distribution of radiative heating, is less sensitive to the choice of $\beta(\uparrow)$ and $\beta(\downarrow)$ than the flux profiles themselves. However, the net infrared radiative heating of the cloud layer is sensitive to the difference $\beta(\uparrow) - \beta(\downarrow)$. Stephens (1980) notes that the difference $(\varepsilon^{*}(\uparrow) - \varepsilon)$ and, thus, $\beta(\uparrow)$ is relatively insensitive to reasonable seasonal and geographic variations in the radiative environment of high level clouds. Given these facts and the relatively good agreement of the observations, a value of $\beta(\uparrow) = 0.050$ $m^{2}g^{-1}$ is assumed here. The rationale for choosing a seemingly small value of $\beta(\uparrow)$ will become more clear in

the following. The value of $\beta(\downarrow)$ is determined from:

$$\beta(\downarrow) = R_\beta \, \beta(\uparrow) \qquad (3.11.17)$$

where the manner of specifying R_β is considered below.

Cox (1976) gives observed mean values of $\varepsilon^*(\downarrow)$ and $\varepsilon^*(\uparrow)$ as functions of cloud pressure for mid-latitude and tropical regions, which were deduced from numerous nighttime radiometersonde flights in all seasons. Assuming that some mean non-vapor phase water path may be associated with the pair $\varepsilon^*(\downarrow)$ and $\varepsilon^*(\uparrow)$ observed in the mean for clouds at a particular pressure level, these data allow the computation of the mean ratio

$$R_\beta \equiv \beta(\downarrow) \, / \, \beta(\uparrow)$$

by means of Equation (3.11.16) as a function of pressure for each region. In Table 4, Cox's reported mean values of $\varepsilon^*(\downarrow)$ and $\varepsilon^*(\uparrow)$ and the deduced values of R_β are given as functions of cloud pressure.

The magnitude of the ratio R_β is indicative of the relative importance of the reflection of incident infrared radiation at cloud top and at cloud base in determining the difference between $\varepsilon^*(\downarrow)$ and $\varepsilon^*(\uparrow)$. Ignoring differences in the spectral distribution of radiant energy between the incident fluxes at cloud top and cloud base and assuming that the cloud microphysical properties are vertically homogeneous, values of R_β greater than unity may be loosely interpreted as corresponding to the situation where the incident upward flux at cloud base is larger in magnitude than the incident downward flux at cloud top.

Pressure (kPa)	Mid-latitude $\varepsilon^*(\downarrow)$	Mid-latitude $\varepsilon^*(\uparrow)$	Mid-latitude R_β	Tropical $\varepsilon^*(\downarrow)$	Tropical $\varepsilon^*(\uparrow)$	Tropical R_β
15				0.27	0.17	1.69
25				0.47	0.35	1.47
35	0.45	0.41	1.13	0.84	0.61	1.95
45	0.64	0.55	1.28	0.68	0.54	1.47
55	0.64	0.53	1.35	0.81	0.59	1.86
65	0.57	0.50	1.22	0.69	0.61	1.24
75	0.48	0.43	1.16	0.63	0.60	1.09
85	0.54	0.54	1.00	0.69	0.69	1.00
95	0.48	0.56	0.80	0.62	0.67	0.87

Table 4. Observed mean upward and downward broadband infrared effective emittances for clouds occurring in the 10 kPa thick layer centered on the indicated pressure level (after Cox, 1976) and the corresponding ratio of the mass absorption coefficients (see text for definitions and discussion).

Thus, the observed mean values of R_β for clouds in the middle and upper troposphere simply verify that the incident upward flux, which is dominated by the contribution from the relatively warm underlying surface, is larger than the incident downward flux, which has originated in the relatively cold atmosphere above. Similarly, since the observed mean values of R_β are larger at nearly every level for the tropics when compared to the mid-latitudes, it may be concluded that the differences are due more to differences in the mean annual nighttime surface temperature of these regions than to any differences in the temperature of the overlying atmosphere. The observed mean values of R_β in the lower troposphere, which are less than unity, may be due to a number of factors. The effective radiating temperature of the overlying atmosphere is much greater for low level clouds when compared to high level clouds. Also, low level clouds may tend to be associated with cooler surface temperatures, i.e. cold air masses, when compared to upper level clouds. This is probably most true for the mean annual mid-latitude case. It is, also, possible that low level clouds frequently exist under relatively warm middle level clouds. Stephens (1978) computed a theoretical value of R_β of ~ 1.22 corresponding to the case of a low level cloud existing in the U.S. Standard Atmosphere. This supports the latter two explanations of the observed smallness of R_β in the mean for low level clouds in the mid-latitude region.

Since the theory (Stephens, 1980) and the observations indicate that R_β is very dependent on surface temperature, both annual and diurnal cycles of R_β may be required. However, since both the annual and diurnal cycles of surface temperature are relatively small in amplitude for tropical regions, R_β would not significantly vary either

seasonally or diurnally in these regions. Thus, the observed mean annual nighttime values deduced from the data of Cox (1976) are probably very representative of all seasons and times of day. The substantial vertical variation of observed mean values of R_β for middle and high level clouds in tropical regions may be mostly due to biases in the data set toward situations where relatively cold (compared to the surface) underlying cloud layers tended to be present when upper level clouds were sampled at some levels, i.e. the levels where R_β is observed to be small. Thus, $R_\beta \simeq 2$ is likely to be representative of high level clouds in tropical regions when no underlying clouds are present. For mean cloud conditions, a value of $R_\beta \simeq 1.6$ is appropriate for cloud layers above 50 kPa.

For cloud layers at pressures less than 50 kPa, a vertically averaged value of $R_\beta = 1.2$ is very representative of mean nighttime conditions at any of these levels in the mid-latitudes. This value is most representative of spring/fall conditions. Rather arbitrarily, a value of 1.4 and 1.0 are assumed to be representative of summer and winter nighttime conditions, respectively. These choices seem reasonable for mean seasonal conditions given the comparison to the tropical case. During the daytime, R_β would increase to some maximum afternoon value due to the diurnal cycle of surface temperature. It is assumed that the cycle may be described by a cosine response where the peak value of R_β occurs at 1400 hr local solar time. The proposed maximum daytime values are 1.2, 1.4 and 1.8 for the winter, spring/fall and summer seasons, respectively, in the mid-latitudes.

In summary, based on the limited climatological data available and noting that the model here does not carry surface temperature as a

prognostic or diagnostic variable, a reasonable parameterization of R_β, which should correspond fairly well to the mean radiative environment of upper level clouds is assumed. Thus,

$$R_\beta(t_{SOL}) = \begin{cases} R_\beta(\min) \quad , & SR \gtrsim t^n_{SOL} \gtrsim SS \\ R_\beta(\max)\cos(SA) \ , & SS > t^n_{SOL} > SR \end{cases} \qquad (3.11.18)$$

where

$$SA \equiv \frac{\pi}{2}\left[1 - \left\{\frac{t^n_{SOL} - SR}{t_\beta - SR}\right\}\right]$$

for $SR \lesssim t^n_{SOL} \lesssim t_\beta$;

and

$$SA \equiv \frac{\pi}{2}\left\{\frac{SS - t^n_{SOL}}{SS - t_\beta}\right\}$$

for $t_\beta < t^n_{SOL} \lesssim SS$,

where

$$SS \equiv 1 - SR,$$

$$t_\beta \equiv 0.583 \ ,$$

t^n_{SOL} is the local solar time, and $R_\beta(\min)$ and $R_\beta(\max)$ are specified as in Table 5. Note that SR, SS, t_β and t^n_{SOL} are all expressed as the fraction of a day past midnight local time. It should be noted that the mid-latitude scheme is most representative of continental conditions and the tropical scheme is more representative of oceanic conditions.

A general relationship between the bulk broadband shortwave reflectance (ρ_S), absorptance (a_S) and transmittance (t_S) and the $\overline{IWP}$ of a cloud layer is desired. For the same reasons as discussed above,

Mid-latitude	R_β (min)	$\beta(\downarrow)$	R_β (max)	$\beta(\downarrow)$
winter	1.0	0.05	1.2	0.06
spring/fall	1.2	0.06	1.4	0.07
summer	1.4	0.07	1.8	0.09
tropical	1.6	0.08	—	—

Table 5. Specified values of the R_β parameter and the corresponding downward mass absorption coefficients $\beta(\downarrow)$ in $m^2\ g^{-1}$ for $\beta(\uparrow) = 0.05$ $m^2\ g^{-1}$.

such a relationship may exist. The approach adopted here is to propose such a relationship based on theory and observations. It is highly empirical.

Reynolds and Vonder Haar (1977) have deduced an empirical relation between the visible albedo (ρ_v) and the effective upward infrared emittance in the atmospheric window spectral region ($\varepsilon_w^*(\uparrow)$) for cirriform clouds based on analysis of satellite data and other observational and theoretical studies (e.g. Shenk and Curran (1973), Hunt (1973), and Liou (1973, 1974). Note that anisotropic effects were taken into account in their study. Their results are shown in Figure 15a. This relation is well represented by:

$$\rho_v(\vartheta = 60°) = 0.505\ \varepsilon_w^*(\uparrow) + 0.095\ \varepsilon_w^*(\uparrow)^2 .$$

Now, $\varepsilon_w^*(\uparrow)$ is generally about 6% smaller than $\varepsilon^*(\uparrow)$ due to the spectral distribution of the emitted infrared fluxes at typical tropospheric temperatures (Stephens, 1980). However, the $\varepsilon_w^*(\uparrow)$ deduced by Reynolds and Vonder Haar is likely to be $\sim$ 6% larger than the actual vertical $\varepsilon_w^*(\uparrow)$ due to the satellite viewing angles employed. Thus, it is assumed here that $\varepsilon^*(\uparrow)$ may be substituted for $\varepsilon_w^*(\uparrow)$ in the above expression. Welch et al. (1980) present data on the spectral distribution of reflected shortwave radiant energy for various model cirriform clouds based on detailed Mie calculations and Monte Carlo simulations. For their most realistic model clouds (i.e. C.5 bullets and C.5 columns)

$$\rho_s / \rho_v \equiv 0.91$$

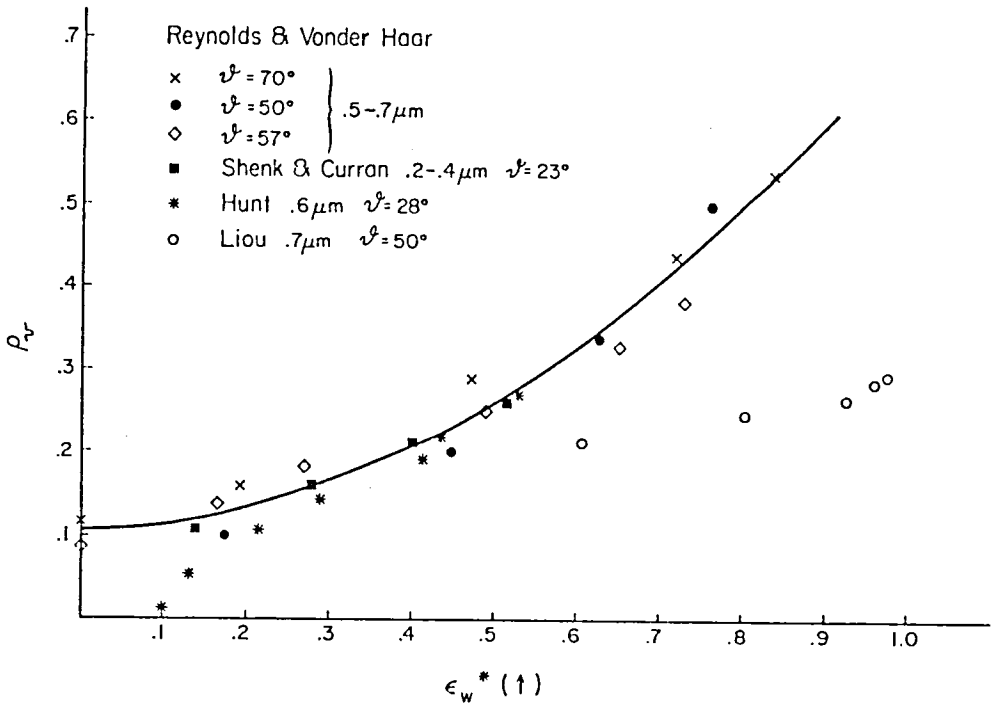

Figure 15a. Relationship between visible cirrus cloud reflectance, ρ_v, and effective upward infrared window emittance $\varepsilon_w^*(\uparrow)$ reported by Reynolds and Vonder Haar (1977) based on observations and theory.

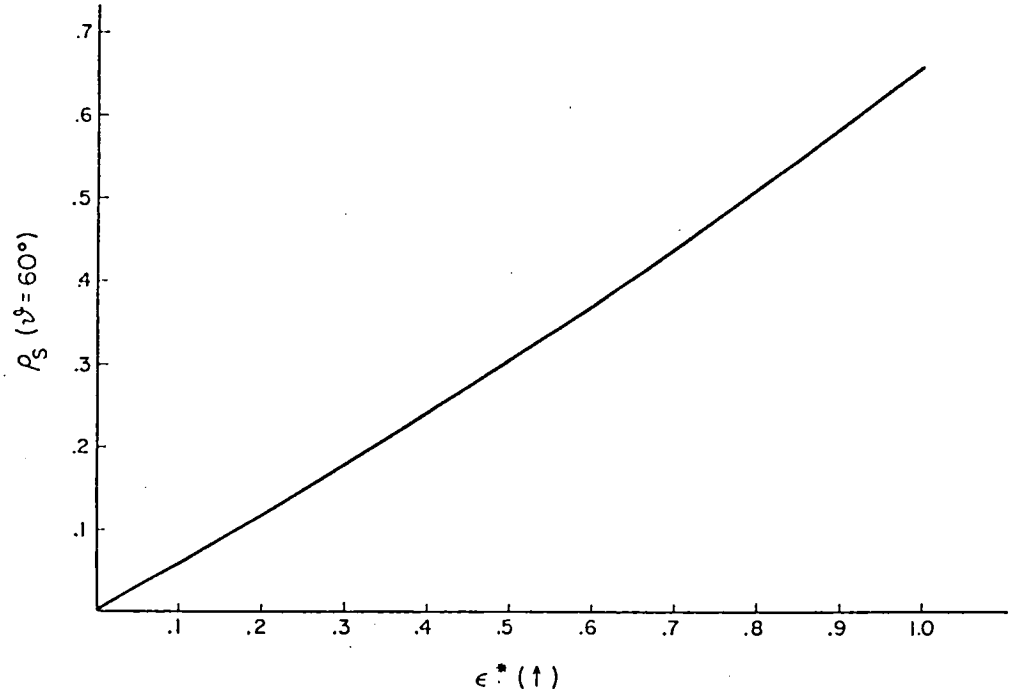

Figure 15b. Empirical relationship between the effective upward broadband infrared cloud emittance $\varepsilon^*(\uparrow)$ and the broadband shortwave reflectance ρ_s at a solar zenith angle of 60° adopted for this study. See text for definition and discussion.

where $\rho_S \cong 0.61$ and $a_S = 0.14$ for $\vartheta = 0°$. Since the reflection of visible radiation and the absorption and reflection of near infrared shortwave radiation are both determined to a large extent by the number of in-cloud scatters, which occur in the respective spectral regions, it is assumed that this ratio is representative for all ρ_S and ϑ. Thus,

$$\rho_S\,(\vartheta = 60°) = 0.557\,\varepsilon^*(\uparrow) + 0.105\,\varepsilon^*(\uparrow)^2 \qquad (3.11.19)$$

is employed here. This relation is plotted in Figure 15b.

The broadband bulk shortwave reflectance of a given cloud is a function of solar zenith angle. Following from Stephens (1978), this functional dependence of ρ_S on ϑ varies slightly depending on the magnitude of $\rho_S(\vartheta)$ as a function of cloud optical depth for low level liquid water clouds, (Figure 16a). For a given $\rho_S(\vartheta = 60°)$ determined as above for a cirriform cloud, the zenith angle dependence of ρ_S is assumed to be the same as in Stephens (1978) for a liquid water cloud of the same $\rho_S(\vartheta = 60°)$. The following formula reproduces his results quite well for most values of $\rho_S(\vartheta = 60°)$ and ϑ:

$$\begin{aligned}\rho_S(\vartheta) &= (0.161 + 0.117 \times 10^{-1}\,\vartheta \qquad (3.11.20)\\ &+ 0.386 \times 10^{-4}\,\vartheta^2)\,\rho_S(\vartheta = 60°)\\ &+ (0.914 - 0.152 \times 10^{-1}\,\vartheta)\,\rho_S(\vartheta = 60°)^2\end{aligned}$$

where ϑ is in degrees. This fit underestimates his values of $\rho_S(\vartheta)$ by about 0.05 to 0.10 at $\vartheta = 80°$ given $\rho_S(\vartheta = 0°)$. In support of the

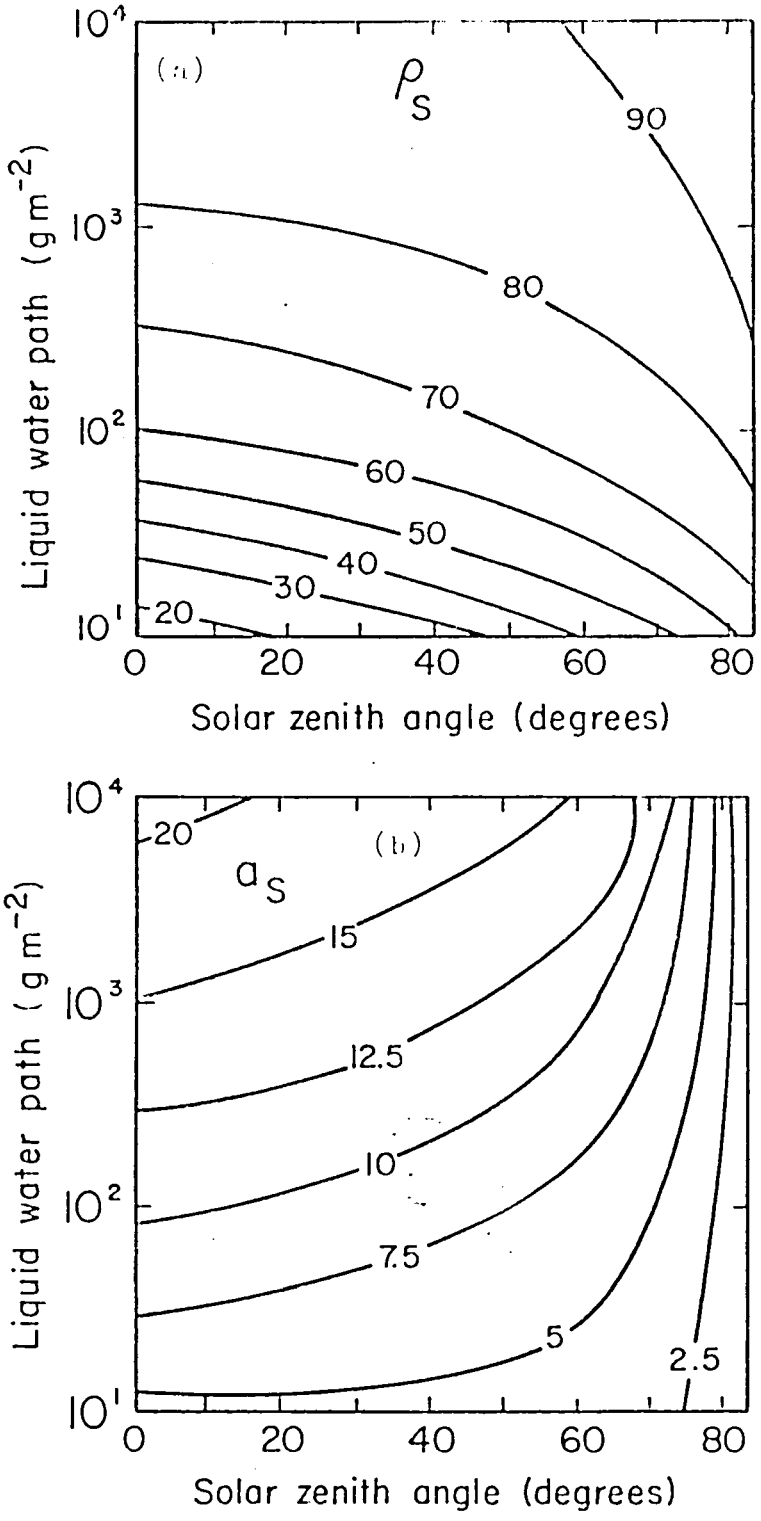

Figure 16. Broadband cloud shortwave reflectance ρ_S (a) and absorptance a_S (b) as a function of liquid water path and solar zenith angle for a liquid phase model cloud determined theoretically by Stephens (1978). For the purposes here, the water path units on the ordinate may be regarded as arbitrary.

assumption of the representativeness of this scheme for ice clouds, the scheme was applied to the results of Platt et al. (19[illegible] simultaneous observations of $\varepsilon_w^*(\uparrow)$ and $\rho_v(\vartheta \simeq 35°)$ deduced from satellite data were reported for cirriform clouds. Equation (3.11.19) was applied to their observed values of $\varepsilon_w^*(\uparrow)$ to compute $\rho_v(\vartheta = 60°)$ and Equation (3.11.20) was then used to compute $\rho_v(\vartheta = 35°)$. The agreement was nearly perfect.

Observations of a_s are most difficult and, thus, have not been widely reported in the literature. The primary problem with such observations is that the finite character of natural [illegible] significant quantities of shortwave energy escaping out the sides of a cloud (Davis et al. 1978). This leads to problems in interpreting direct observations and may be largely responsible for some of the rather large values of a_s which have been reported (e.g. Herman et al. 1975). Twoomey (1976) notes that the absorption of shortwave solar energy in a cloud has a theoretical limit of ~ 20% given the spectral distribution of the incident flux.

Paltridge and Platt (1980) have reported concurrent measurements of ρ_s and a_s for cirrostratus clouds. Much care was taken to sample very horizontally uniform clouds. The measurements were made at a solar zenith angle of 35°. They, also, measured ε^*. Assuming $\varepsilon^* = \varepsilon^*(\uparrow)$ and transforming the observed $\rho_s(\vartheta = 35°)$ to $\rho_s(\vartheta = 60°)$ by Equation (3.11.20), yielded very good agreement with the proposed relationship between $\varepsilon^*(\uparrow)$ and $\rho_s(\vartheta = 60°)$. The disagreements were of the same order as the scatter of the data originally reported by Reynolds and Vonder Haar (1977). In Figure 17, the concurrently measured values of a_s and $\rho_s(\vartheta = 35°)$ are depicted along with error bars representing an

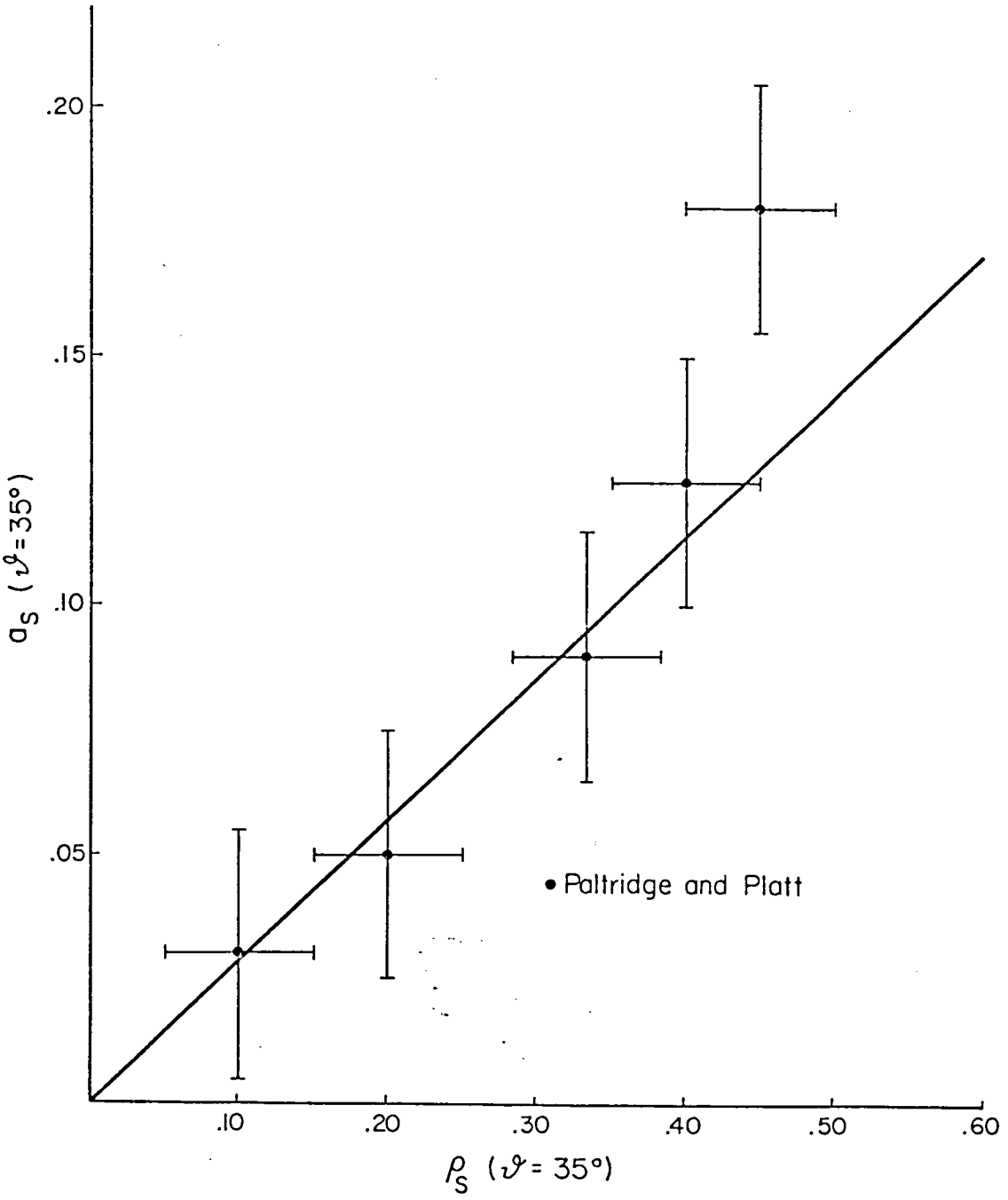

Figure 17. Empirical relationship between broadband shortwave cloud reflectance ρ_S and absorptance a_S at a solar zenith angle of 35° adopted for this study. Data points are from Paltridge and Platt (1980), where the estimated uncertainty of these observations is indicated. See text for definition and discussion.

estimate of the uncertainty. A simple linear fit reproduces their observations quite well and is given by:

$$a_S(\vartheta=35°) = 0.283\ \rho_S(\vartheta=35°)\ . \qquad (3.11.21)$$

Noting that Equations (3.11.19) and (3.11.20) lead to a maximum value of $\rho_S(\vartheta=35°) \cong 0.66$ in the case of $\varepsilon^*(\uparrow) = 1.0$, a corresponding maximum value of $a_S(\vartheta=35°) \cong 0.19$ results. This is a reasonable value. The author notes that this relationship (i.e. Equation 3.11.21) is probably the most tenuous and least well documented of all the empirical relationships invoked in this section. However, is is employed in lieu of better information.

In a manner similar to that employed to deduce $\rho_S(\vartheta)$ given $\rho_S(\vartheta=60°)$, the results of Stephens (1978) (see Figure 14b) are utilized to deduce $a_S(\vartheta)$ given $a_S(\vartheta=35°)$. It is of note that the results of Stephens (1978) agree quite well with the results of Davis et al. (1978) in terms of the ϑ dependence of a_S for a similar situation. The resulting fit is given by:

$$\begin{aligned} a_S(\vartheta) \cong\ & (1.01\ a_S(\vartheta=35°) + 0.716\ a_S(\vartheta=35°)^2) \qquad (3.11.22) \\ & + (-0.246 \times 10^{-2}\ a_S(\vartheta=35°) + 0.765 \times 10^{-2}\ a_S(\vartheta=35°)^2)\vartheta \\ & - 0.493 \times 10^{-3}\ a_S(\vartheta=35°)^2\ \vartheta^2\ . \end{aligned}$$

This formulation produces slightly higher values of $a_S(\vartheta)$ compared to the results of Stephens (1978) for $\vartheta > 80°$ given $a_S(\vartheta=0°)$. Also, the values of $a_S(\vartheta)$ are slightly low ($\sim 5\%$) for small values of $a_S(\vartheta=35°)$.

Given the uncertainties already present, this formulation should be sufficient for the purposes here.

The value of the bulk broadband shortwave transmittance of the cloud layer may then be specified as:

$$t_S(\underline{\vartheta}) = 1 - \rho_S(\underline{\vartheta}) - a_S(\underline{\vartheta}) \; . \qquad (3.11.23)$$

To review the parameterization scheme developed here to deduce the bulk radiative properties of cirriform cloud layers, the logical sequence of determinations is depicted in the flow diagram given in Figure 18. The relevant equations are noted where appropriate. This scheme allows the determination of $\varepsilon^*(\uparrow)_{i+\frac{1}{2}}$, $\varepsilon^*(\downarrow)_{i+\frac{1}{2}}$, $\rho_S(\vartheta^n)_{i+\frac{1}{2}}$, $a_S(\vartheta^n)_{i+\frac{1}{2}}$ and $t_S(\vartheta^n)_{i+\frac{1}{2}}$ given ϑ^n and $\widetilde{IWP}_{i+\frac{1}{2}}$ computed as:

$$\widetilde{IWP}_{i+\frac{1}{2}} = \sum_{k=1}^{K-1} \rho_{o_{k+\frac{1}{2}}} \ell_{i+\frac{1}{2},k+\frac{1}{2}} \; d \qquad (3.11.24)$$

for i = 1, 2, ..., I-2, I-1 at time step n.

3.11.b. Determination of Infrared Radiative Heating Rates

Prior to the initiation of a simulation, the IRADIR model is applied to the basic state vertical profiles of pressure, temperature, water vapor, carbon dioxide and ozone, as noted previously. This allows the specification of $QIR_{o_{k+\frac{1}{2}}}$ for k = 1, 2, ..., K-2, K-1; which is the basic state clear sky vertical infrared radiative heating rate profile. This heating rate profile is applied in every clear column

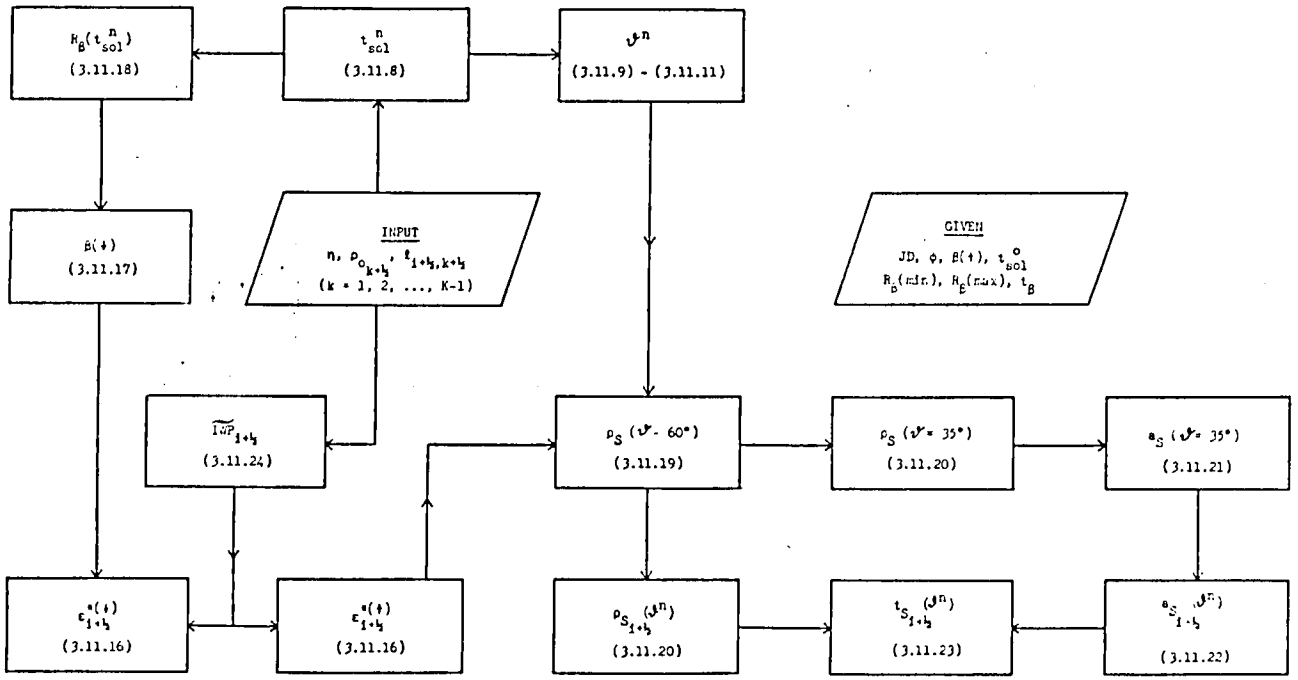

Figure 18. Flow diagram depicting the logical sequence of determinations for computing the bulk radiative properties of a cloud layer in a given grid column $i+\frac{1}{2}$. The relevant equations are as noted. See text for discussion.

which is diagnosed at a given time, i.e.

$$QIR_{i+\frac{1}{2},k+\frac{1}{2}} = QIR_{o_{i+\frac{1}{2}}} \qquad (3.11.25)$$

for k = 1, 2, ..., K-2, K-1 when $\ell_{i+\frac{1}{2},k+\frac{1}{2}} = 0$ for k = 1, 2, ... K-2, K-1.

Cox (1981, personal communication) and this author (Starr, 1976) have observed that the infrared radiative heating rates computed by IRADIR for atmospheric layers above cloud top and below cloud base are very nearly linear functions of the specified [illegible] cloud emittances in the upward and downward directions, respectively, for a given basic state. This suggests a very convenient method of specifying the heating rates in these layers, when a cloud is present in a column.

At the same time as the computation of the QIR_o profile, the IRADIR model is applied to the basic state profiles with a radiatively black (i.e. $\varepsilon^*(\uparrow) = \varepsilon^*(\downarrow) \equiv 1.0$) cloud specified with cloud top at $z_{KT'}$ and cloud base at $z_{KB'}$. The KT' and KB' grid levels are preselected to correspond to the expected location of cloud top and cloud base. The resulting infrared heating rate profiles are denoted as $(QIR)_{cloud}$ for k = 1, 2, ..., KB' - 2, KB' - 1 and k = KT', KT' + 1, ..., K-2, K-1. Employing the fact that the heating rates in these layers may be accurately approximated as linear functions of the corresponding $\varepsilon^*(\downarrow)$ and $\varepsilon^*(\uparrow)$, respectively, allows the specification of the infrared radiative heating rates in the clear portion of cloudy columns as:

$$QIR_{i+\frac{1}{2},k+\frac{1}{2}} = QIR_{o_{k+\frac{1}{2}}} + \varepsilon^{*}(\downarrow)_{i+\frac{1}{2}} \left\{ QIR_{c_{k'+\frac{1}{2}}} - QIR_{o_{k+\frac{1}{2}}} \right\}$$

for $k = 1, 2, \ldots, KB_{i+\frac{1}{2}}-2, KB_{i+\frac{1}{2}}-1$ (3.11.26a)

and

$$QIR_{i+\frac{1}{2},k+\frac{1}{2}} = QIR_{o_{k+\frac{1}{2}}} + \varepsilon^{*}(\uparrow)_{i+\frac{1}{2}} \left\{ QIR_{c_{k'+\frac{1}{2}}} - QIR_{o_{k+\frac{1}{2}}} \right\}$$

(3.11.26b)

for $k = KT_{i+\frac{1}{2}}, KT_{i+\frac{1}{2}}+1, \ldots, K-2, K-1$

where $\ell_{i+\frac{1}{2},k+\frac{1}{2}} \neq 0$ for some k and where $KB_{i+\frac{1}{2}}$ and $KT_{i+\frac{1}{2}}$ are the corresponding diagnosed cloud base and cloud top grid levels, respectively; and $\varepsilon^{*}(\downarrow)_{i+\frac{1}{2}}$ and $\varepsilon^{*}(\uparrow)_{i+\frac{1}{2}}$ are the diagnosed bulk effective downward and upward infrared emittances of the cloud layer in that column, respectively. Note that:

$$k' \equiv \begin{cases} 1 \\ k - (KB_{i+\frac{1}{2}} - KB') \end{cases}, \text{ whichever is greater}$$

in Equation (3.11.26a) and

$$k' \equiv \begin{cases} K \\ k - (KT_{i+\frac{1}{2}} - KT') \end{cases}, \text{ whichever is less}$$

in Equation (3.11.26b).

Thus, the heating rates above and below the cloud boundaries are adjusted assuming that the response to the presence of a locally defined cloud layer relative to its boundaries is the same as relative to the boundaries of the pre-defined expected cloud layer. This is a very good assumption.

For the cloud filled portion of a diagnosed cloudy column (i.e. $K_{B_{i+\frac{1}{2}}} \leq k < KT_{i+\frac{1}{2}}$), an explicit, though crude, radiative transfer computation is made. When the IRADIR model is used to compute the QIR_o profile, corresponding vertical profiles of effective gaseous infrared emittances are also computed as:

$$\varepsilon_g^*(\uparrow)_{k+\frac{1}{2}} \equiv \frac{H_o(\uparrow)_k - H_o(\uparrow)_{k+1}}{H_o(\uparrow)_k - \sigma\, T_o{}^4{}_{k+\frac{1}{2}}}$$

and (3.11.27)

$$\varepsilon_g^*(\downarrow)_{k+\frac{1}{2}} \equiv \frac{H_o(\downarrow)_k - H_o(\downarrow)_{k+1}}{\sigma\, T_o{}^4{}_{k+\frac{1}{2}} - H_o(\downarrow)_{k+1}}$$

where H_o is the upward ($\uparrow$) or downward ($\downarrow$) infrared flux at the indicated level computed by model IRADIR for the clear sky basic state profiles and T_o is the basic state temperature at the subscripted level.

Recalling that the bulk infrared effective emittances of the cloud may be consistently partitioned such that the corresponding in-cloud vertical flux profiles may be generated (Griffith et al., 1980), both upward and downward effective vertical cloud emittance profiles are computed as:

$$\varepsilon_c^*(\uparrow)_{i+\frac{1}{2},k+\frac{1}{2}} = 1 - \exp(-\beta(\uparrow)\, IWP_{i+\frac{1}{2},k+\frac{1}{2}})$$

and (3.11.28)

$$\varepsilon_c^*(\downarrow)_{i+\frac{1}{2},k+\frac{1}{2}} = 1 - \exp(-\beta(\downarrow)\, IWP_{i+\frac{1}{2},k+\frac{1}{2}})$$

for $k = KB_{i+\frac{1}{2}}, KB_{i+\frac{1}{2}}+1, \ldots, KT_{i+\frac{1}{2}}-2, KT_{i+\frac{1}{2}}-1$;

when $\ell_{i+\frac{1}{2},k+\frac{1}{2}} \neq 0$ for some k, where

$$IWP_{i+\frac{1}{2},k+\frac{1}{2}} \equiv \rho_{o_{k+\frac{1}{2}}} \ell_{i+\frac{1}{2},k+\frac{1}{2}} \, d \, . \qquad (3.11.29)$$

A simple correction for the overlap of the gaseous and cloud contribution to the total effective emittance profiles is applied following Griffith et al., (1980) as:

$$\varepsilon^*_T(\uparrow)_{i+\frac{1}{2},k+\frac{1}{2}} = 1 - (1 - \varepsilon^*_c(\uparrow)_{i+\frac{1}{2},k+\frac{1}{2}}) \, (1 - \varepsilon^*_g(\uparrow)_{k+\frac{1}{2}})$$

and (3.11.30)

$$\varepsilon^*_T(\downarrow)_{i+\frac{1}{2},k+\frac{1}{2}} = 1 - (1 - \varepsilon^*_c(\downarrow)_{i+\frac{1}{2},k+\frac{1}{2}}) \, (1 - \varepsilon^*_g(\downarrow)_{k+\frac{1}{2}})$$

for $k = KB_{i+\frac{1}{2}}, KB_{i+\frac{1}{2}}+1, \ldots, KT_{i+\frac{1}{2}}-2, KT_{i+\frac{1}{2}}-1$.

The in-cloud vertical flux profiles are then computed as:

$$H(\uparrow)_{i+\frac{1}{2},k+1} = (1 - \varepsilon^*_T(\uparrow)_{i+\frac{1}{2},k+\frac{1}{2}}) \, H(\uparrow)_{i+\frac{1}{2},k} + \varepsilon^*_T(\uparrow)_{i+\frac{1}{2},k+\frac{1}{2}} \, \sigma \, T_{o_{k+\frac{1}{2}}}^4$$

for $k = KB_{i+\frac{1}{2}}, KB_{i+\frac{1}{2}}+1, \ldots, KT_{i+\frac{1}{2}}-2, KT_{i+\frac{1}{2}}-1$

and (3.11.31)

$$H(\downarrow)_{i+\frac{1}{2},k} = (1 - \varepsilon^*_T(\downarrow)_{i+\frac{1}{2},k+\frac{1}{2}}) \, H(\downarrow)_{i+\frac{1}{2},k+1} + \varepsilon^*_T(\downarrow)_{i+\frac{1}{2},k+\frac{1}{2}} \, \sigma \, T_{o_{k+\frac{1}{2}}}^4$$

for $k = KT_{i+\frac{1}{2}}-1, KT_{i+\frac{1}{2}}-2, \ldots, KB_{i+\frac{1}{2}}+1, KB_{i+\frac{1}{2}}$

where $H(\downarrow)_{i+\frac{1}{2},KT} \equiv H_o(\downarrow)_{KT}$,

and $H(\uparrow)_{i+\frac{1}{2},KB} \equiv H_o(\uparrow)_{KB}$.

Thus, the basic state clear sky fluxes for the expected cloud top and base levels must also be stored in addition to the clear and cloudy sky basic state heating rate profiles and the clear sky basic state gaseous effective emittance profiles. The in-cloud infrared heating rate profile may now be computed for a cloudy column $i+\frac{1}{2}$ as:

$$QIR_{i+\frac{1}{2},k+\frac{1}{2}} = \frac{g}{c_p} \left\{ H(\uparrow)_{i+\frac{1}{2},k} + H(\downarrow)_{i+\frac{1}{2},k+1} - H(\uparrow)_{i+\frac{1}{2},k+1} - H(\downarrow)_{i+\frac{1}{2},k} \right\} \Big/ \left\{ P_{o_k} - P_{o_{k+1}} \right\} \qquad (3.11.)$$

for $k = KB_{i+\frac{1}{2}}, KB_{i+\frac{1}{2}}+1, \ldots, KT_{i+\frac{1}{2}}-2, KT_{i+\frac{1}{2}}-1$.

This completes the determination of the infrared radiative heating rates. In summary, prior to a simulation, basic state vertical profiles of pressure, temperature, water vapor specific humidity, carbon dioxide mixing ratio and ozone concentration, both internal and external to the model domain, are input to the IRADIR broadband infrared radiative transfer model to generate the clear sky basic state infared fluxes $H_o(\uparrow)_{KB'}$ and $H_o(\downarrow)_{KT'}$, clear sky and cloudy sky basic state infrared radiative heating rate profiles QIR_o and QIR_c, and clear sky profiles of effective infrared gaseous emittance $\varepsilon_g^*(\uparrow)$ and $\varepsilon_g^*(\downarrow)$, which are all stored in the model for the model vertical domain. The effective cloud mass absorption coefficient $\beta(\uparrow)$ is prespecified along with the conditions to determine the parameters $R_\beta(\min)$ and $R_\beta(\max)$. The model diagnosed solar time t_{SOL}^n then allows the computation of $\beta(\downarrow)$. With all these quantities and the prespecified basic state profiles of pressure, temperature and density and a few physical constants, the appropriate infrared radiative heating rate profile may be computed for

each column in the domain depending on whether a cloud is present in the column or not and depending on the vertical profile of ice water specific humidity in the column if it is cloudy. The determination is parametric primarily in the specification of the empirical constants $\beta(\uparrow)$, $R_\beta(\min)$, $R_\beta(\max)$ and t_β. Effects due to the diurnal variation of surface and atmospheric temperatures external to the model domain are taken into account in two ways. The parametric quantity $R_\beta(t^n_{SOL})$ yields a climatological response for the cloud layer and some limited response in the sub-cloud layer. In addition, the prespecified basic state fluxes, heating rate profiles and gaseous emittance profiles may be reinitialized at any time during a simulation by simply redefining the basic state profile of temperature, water vapor, etc. outside (below) the model domain and reapplying the IRADIR model as noted above. In this way, the radiative effects of diurnal variations of surface temperature and lower atmospheric thermodynamic structure may be incorporated in a simulation.

3.11.c. Determination of Shortwave Radiative Heating Rates

Prior to the initiation of a simulation, the IRADSW model is applied to the basic state vertical profiles of pressure, temperature, water vapor specific humidity, carbon dioxide mixing ratio and ozone concentration, as noted previously, for six prespecified solar zenith angles, ϑ_m. These solar zenith angles are specified as:

$$80^\circ \equiv \vartheta_1 > \vartheta_2 > \ldots > \vartheta_6$$

where the range is determined such that ϑ_6 is the minimum solar zenith

angle, which will be encountered during the simulation. Thus, six profiles of clear sky basic state shortwave radiative heating rates are generated, i.e. $QSW^{(\downarrow)}_{o_{k+\frac{1}{2}}}(\vartheta_m)$ for k = 1, 2, ..., K-2, K-1 and m = 1, 2, ..., 6. By simple linear interpolation, the clear sky basic state shortwave radiative heating rate profile at solar zenith angle ϑ^n is specified as:

$$QSW^{(\downarrow)}_{o_{k+\frac{1}{2}}}(\vartheta^n) = \alpha^n \, QSW^{(\downarrow)}_{o_{k+\frac{1}{2}}}(\vartheta_{m'+1}) + (1-\alpha^n) \, QSW^{(\downarrow)}_{o_{k+\frac{1}{2}}}(\vartheta_{m'}) \qquad (3.11.33)$$

where

$$\alpha^n \equiv \frac{(\vartheta_{m'} - \vartheta^n)}{(\vartheta_{m'} - \vartheta_{m'+1})}$$

and ϑ^n is the solar zenith angle diagnosed at time step n. Note that:

$$QSW^{(\downarrow)}_{o_{k+\frac{1}{2}}}(\vartheta_{m=0} = 90°) \equiv 0. \qquad (3.11.34)$$

In addition, the downward shortwave irradiance at the prespecified expected cloud top level $I^{(\downarrow)}_{o_{KT'}}(\vartheta_m)$ and the total flux convergence in the total atmospheric column above this level $\Delta I^{(\downarrow)}_{o_{KT'}}(\vartheta_m)$ computed by IRADSW and corresponding to each of the six basic state clear sky shortwave heating rate profiles are, also, stored in the model. This allows the determination of $I^{(\downarrow)}_{o_{KT'}}(\vartheta^n)$ and $\Delta I^{(\downarrow)}_{o_{KT'}}(\vartheta^n)$ in the same way as noted above for $QSW^{(\downarrow)}_{o_{k+\frac{1}{2}}}(\vartheta^n)$. All these basic state shortwave radiative parameters are based on a consideration of only the downward direct solar irradiances in clear sky conditions.

Similarly, six profiles of $QSW^{(\uparrow)}_{o_{k+\frac{1}{2}}}(\vartheta m)$ for k = KT', KT'+1, ..., K-2, K-1 and six values of $\Delta I^{(\uparrow)}_{KT'}(\vartheta m)$ are determined from application of the IRADSW model to the basic state profiles. These quantities are the shortwave radiative heating rate profiles and total flux convergences in the atmospheric column above KT' due to only reflected shortwave radiation from a reference cloud layer, respectively. The reference cloud top level is KT' and the broadband shortwave reflectance of the cloud is specified as $\rho_S = 0.61$. In the same manner as above, this allows the determination of $QSW^{(\uparrow)}_{o_{k+\frac{1}{2}}}(\vartheta^n)$ and $\Delta I^{(\uparrow)}_{KT'}(\vartheta^n)$ and $\Delta I^{(\uparrow)}_{KT'}(\vartheta^n)$.

For clear columns, the shortwave radiative heating rates are specified as the basic state downward profiles, i.e.

$$QSW_{i+\frac{1}{2},k+\frac{1}{2}} = QSW^{(\downarrow)}_{o_{k+\frac{1}{2}}}(\vartheta^n) \qquad (3.11.35)$$

where $\ell_{i+\frac{1}{2},k+\frac{1}{2}} = 0$

for k = 1, 2, ..., K-2, K-1.

The determination of the shortwave radiative heating rate profiles in columns where a cloud is diagnosed must now be considered.

For the layers above cloud top, the absorption of the downward direct solar radiation is specified as the value in the clear sky case. However, the absorption of shortwave radiant energy reflected from cloud top may be significant and must be considered.

The spectral distribution of shortwave radiant energy in the upward reflected flux emergent from cloud top may be substantially different when compared to the incident direct solar beam due to interactions within the cloud layer, (Welch et al., 1980). At any

wave length ν, the ratio of the short-wave energy absorbed from the reflected component to that absorbed from the downward beam in the total atmospheric column above cloud top is given by:

$$R_{\nu p} = R_{\nu_{2\ell}} \rho_{\nu}$$

where

$$R_{\nu_{2\ell}} \equiv \frac{a_{\nu}(u^{*})(1 - a_{\nu}(u_{2\ell}))}{a_{\nu}(u_{2\ell})} ,$$

ρ_{ν} is the spectral reflectance of the cloud layer and a_{ν} is the spectral gaseous absorptance of the atmospheric column above cloud top, and is a function of the appropriate optical path of the absorbing gas. Note that the parameter $I_{o_{\nu}}$, the incident spectral solar irradiance at the top of the atmosphere, has been eliminated from the numerator and denominator. The optical path parameters are computed as:

$$u_{2\ell} = u \sec(2\ell)$$

and $$u^{*} = 1.66\ u$$

where

$$u \equiv \int_{o}^{P_{KT}} q(p') \frac{dp'}{g}$$

is the vertical optical path and q is the mixing ratio of the absorbing gas. For the moment, water vapor is considered to be the only gaseous absorber since it is the primary gaseous atmospheric absorber,

(Yamamoto, 1962). Note that $u_{\mathscr{l}}$ corresponds to the vertical optical path corrected for the path traversed by the direct solar beam at some solar zenith angle $\mathscr{l}$. The reflected radiation stream is assumed to be isotropic and diffuse for the computation u^*, (Goody, 1964).

For convenience, the 0.94 μm 1.10 μm, 1.38 μm and 1.87 μm absorbing bands of water vapor are considered as one band, i.e. $\nu = 1$. Similarly, the 2.7 μm, 3.3 μm and 6.3 μm absorbing bands are collectively denoted as $\nu = 2$. The absorptance functions a_1 and a_2 are taken from Yamamoto (1962) and properly normalized to I_{o_1} and I_{o_2} as in Welch et al. (1976) for $\mathscr{l} = 0°$. Welch et al. (1980) give spectral reflectances for each of the sub-bands at $\mathscr{l} = 0°$ for a number of optically thick model clouds based on detailed Mie calculations and Monte Carlo simulations, (their Table 4.8). Their C.5 (bullets) and C.5 (columns) model clouds yield the most realistic bulk short-wave radiative cloud properties (i.e. $\rho_S \simeq 0.61$ and $a_S \simeq 0.14$). These values roughly agree with the empirical relation for ρ_S versus a_S proposed earlier. In addition, the microphysical properties of their model clouds correspond well to the small particle size mode employed elsewhere in this study. They state that the presence of a large particle size mode does not substantially alter their results. Thus, the average properties of these two model clouds are adopted as a reference case in this study. The mean values of ρ_ν are normalized to I_{o_ν} and combined to yield $\rho_1 = 0.574$ and $\rho_2 = 0.009$. Thus, in the near infrared spectral region, the spectral reflectance decreases dramatically as wave length increases. It is assumed that for $\rho_S = 0.61$, ρ_1 and ρ_2 are independent of $\mathscr{l}$.

For cirrus clouds (i.e. $p_{KT} \sim 40$ kPa), a reasonable range of expected values of u is $\sim$ 0.01 cm to 0.2 cm precipitable water corresponding to very dry and very moist conditions above cloud top. For this range of u values, $R_{1\mathcal{l}}$ and $R_{2\mathcal{l}}$ were found to be nearly independent of u, though there was a distinct dependence on $\mathcal{l}$ through $u_{\mathcal{l}}$.

The ratio of the solar energy absorbed from the reflected component to that absorbed from the direct component summed over the $\nu = 1$ and $\nu = 2$ bands is given by:

$$R_\rho = \frac{R_{1\rho}\, a_1(u_{\mathcal{l}})\, I_{o_1}(\mathcal{l}) + R_{2\rho}\, a_2(u_{\mathcal{l}})\, I_{o_2}(\mathcal{l})}{a_1(u_{\mathcal{l}})\, I_{o_1}(\mathcal{l}) + a_2(u_{\mathcal{l}})\, I_{o_2}(\mathcal{l})} .$$

Recall that $I_{o_\nu}(\mathcal{l}) = \cos(\mathcal{l})\, I_{o_\nu}(\mathcal{l}=0°)$, where $I_{o_\nu}(\mathcal{l}=0°)$ is specified as in Welch et al. (1976). For the reference model cloud considered here, $R_\rho \doteq 0.45$, 0.44, 0.33 and 0.23 for $\mathcal{l}=0°$, 30°, 60° and 80°. The absorption of reflected energy in the $\nu = 2$ band is negligible and results in $R_\rho \simeq (2/3)\, R_{1\rho}$ at any $\mathcal{l}$. The $\mathcal{l}$ dependence of R_ρ for the reference case may be empirically represented as:

$$R_{\mathcal{l}} = 0.44 - 0.287 \times 10^{-2}\,(\mathcal{l}-30°) - 0.267 \times 10^{-4}\,(\mathcal{l}-30)^2$$

for $30° \leq \mathcal{l} < 90°$ (3.11.36)

and $R_{\mathcal{l}} = 0.45$ for $\mathcal{l} < 30°$

which is valid over the range of u considered here. This function is plotted in Figure 19.

For lack of better information, it is assumed that the relative spectral distribution of reflected solar radiation is independent of ρ_S and $\mathcal{l}$. This is equivalent to assuming that the cumulative effect on the emergent reflected radiation component of both scattering and

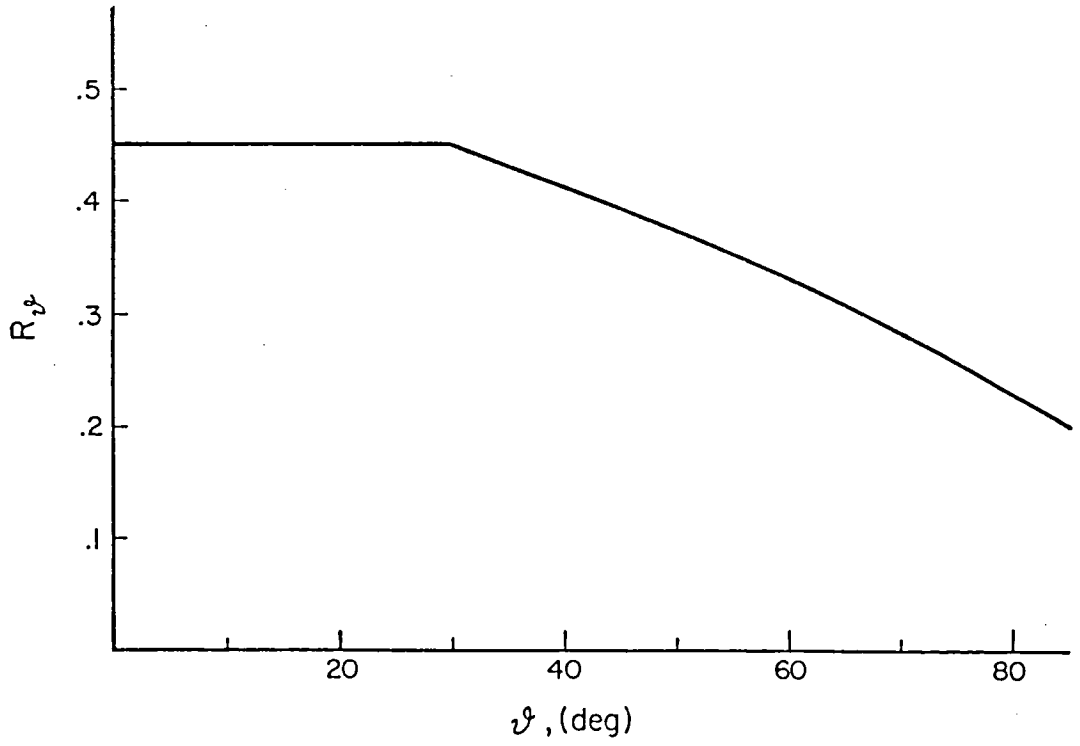

Figure 19. Empirical solar zenith angle dependence function R_ϑ. See text for definition and discussion.

absorption processes acting within the cloud layer are linearly related for the absorbing and nonabsorbing bands. Hopefully, this assumption is not too bad. Consequently, for a given $\nu\ell$, R_ρ is a linear function of ρ_S and equals zero at $\rho_S = 0$. Thus, employing the results from the reference case, this assumption yields:

$$R_\rho = \frac{\rho_S}{0.61} R_{\nu\ell}$$

where $R_{\nu\ell}$ is determined from Equation (3.11.36). Note that the fractional increase in total solar energy absorbed due to water vapor absorption of the short-wave radiant energy reflected from cloud top is maximized for small zenith angles and large broadband cloud short-wave reflectances.

Absorption of solar radiation by ozone and carbon dioxide are substantially smaller, that due to water vapor and behave analogously to the $\nu = 1$ and $\nu = 2$ bands considered here, respectively. Thus, R_ρ is assumed representative for all gaseous absorption of the reflected short-wave component.

The validity of the above expression, when applied to the case of cirrus clouds, is most crutially dependent on the representativeness of the results taken from Welch et al. (1980) and the assumption that ρ_ν/ρ_S = constant at a given ν.

The total resultant increase in short-wave radiative heating must now be partitioned in the model layers above cloud top. The reference basic state heating rate profile, $QSW^{(\uparrow)}_{o_{k+\frac{1}{2}}}(\nu\ell^n)$, due to gaseous absorption of reflected radiation for k = KT´, KT´+1, ..., K-2, K-1 is utilized. Note that IRADSW assumes $\rho_\nu = \rho_S$. However, for any ρ_S,

the relative vertical distribution of solar heating is representative due to the similarity in shape of the various absorptance functions with respect to u (Yamamoto, 1962). Let:

$$R_\rho^* \equiv R_\rho \frac{\Delta I^{(\downarrow)}_{o_{KT'}}(\tilde{\nu}\ell^n)}{\Delta I^{(\uparrow)}_{o_{KT'}}(\tilde{\nu}\ell^n)} \quad .$$

Thus, $R_\rho^* \Delta I^{(\uparrow)}_{KT'}(\tilde{\nu}\ell^n)$ is the total convergence due to absorption of reflected radiation corresponding to ρ_S, where both the spectral changes and angular redistribution of the radiation stream emergent from cloud top have been taken into account. R_ρ^* is, therefore, a normalizing factor and may be applied directly to the reference case heating rate profile $QSW^{(\uparrow)}_{o_{k+\frac{1}{2}}}(\tilde{\nu}\ell^n)$ to yield both the proper magnitude and distribution of heating. Thus, if a cloud is diagnosed in column $i+\frac{1}{2}$, then:

$$QSW_{i+\frac{1}{2},k+\frac{1}{2}} = QSW^{(\downarrow)}_{o_{k+\frac{1}{2}}}(\tilde{\nu}\ell^n) + R_\rho^* \, QSW^{(\uparrow)}_{o_{k+\frac{1}{2}}}(\tilde{\nu}\ell^n) \qquad (3.11.37)$$

for $k = KT_{i+\frac{1}{2}}, KT_{i+\frac{1}{2}}+1, \ldots, K-2, K-1$

where $k' \equiv k - (KT_{i+\frac{1}{2}} - KT')$,

$$R_\rho^* = \frac{\rho_{S_{i+\frac{1}{2}}}}{0.61} R_{\tilde{\nu}\ell}(\tilde{\nu}\ell^n) \frac{\Delta I^{(\downarrow)}_{o_{KT'}}(\tilde{\nu}\ell^n)}{\Delta I^{(\uparrow)}_{o_{KT'}}(\tilde{\nu}\ell^n)} \quad .$$

and $R_{\tilde{\nu}\ell}(\tilde{\nu}\ell^n)$ is given by Equation (3.11.36). Note that as in the case of the infrared heating rate determinations, the response of the heating rates above a locally defined cloud top relative to cloud top level has been assumed to be distributed as relative to the cloud top level of the reference case.

Data on the vertical distribution of solar heating within cirrus cloud layers are virtually nonexistent. Welch et al. (1976), Davis et al. (1978) and Welch et al. (1980) present data on the vertical distribution of in-cloud absorption for a few liquid phase model clouds. In each study, the cloud microphysical properties were assumed spacially homogeneous. They show that the short-wave radiative heating is concentrated in the upper portion of the cloud layer. Welch et al. (1976) show that the shape of the in-cloud heating rate profile depends to some degree on the assumed microphysics. A dependence on $\mathscr{l}$ is also evident (Davis et al., 1978).

It seems reasonable to assume that the vertical profile of short-wave heating rates is functionally related to the vertical profile of ice water content vertically integrated from cloud top level. Accordingly, the solar heating of a layer within a cloud diagnosed in grid column $i+\frac{1}{2}$ may be expressed as:

$$QSW_{i+\frac{1}{2},k+\frac{1}{2}} = \frac{g\, a_{S_{i+\frac{1}{2}}}\, I^{(\downarrow)}_{o_{KT'}}(\mathscr{l}^n)}{c_p\,(p_{o_k} - p_{o_{k+1}})} \left\{ \frac{\bar{\bar{\bar{IWP}}}^{\alpha_S}_{i+\frac{1}{2},k} - \bar{\bar{\bar{IWP}}}^{\alpha_S}_{i+\frac{1}{2},k+1}}{IWP^{\alpha_S}_{i+\frac{1}{2}}} \right. \qquad (3.11.38)$$

for $k = KT_{i+\frac{1}{2}}-1,\ KT_{i+\frac{1}{2}}-2,\ \ldots,\ KB_{i+\frac{1}{2}}+1,\ KB_{i+\frac{1}{2}}$

where

$$\bar{\bar{\bar{IWP}}}_{i+\frac{1}{2},k'} \equiv \sum_{j=k'}^{KT_{i+\frac{1}{2}}-1} \rho_{o_{j+\frac{1}{2}}}\, \mathscr{l}_{i+\frac{1}{2},j+\frac{1}{2}}\, d \qquad (3.11.39)$$

and α_S is some distribution shape parameter. Note that the solar energy absorbed between the $KB_{i+\frac{1}{2}}$ and $KT_{i+\frac{1}{2}}$ levels is a $a_{S_{i+\frac{1}{2}}} I^{(\downarrow)}_{o_{KT'}}(\mathscr{l}^n)$. The last term simply partitions this energy into the various in-cloud layers.

The profiles of in-cloud solar absorption given by Welch et al. (1976) and Davis et al. (1978) may be accurately produced by a function as above. The required values of α_S range from ~ 1/3 to ~ 3/4 with the largest values associated with small solar zenith angles and small values of a_S. Note that as α_S increases, the heating is more uniformly distributed in the vertical, i.e. not as concentrated in the upper portion of the cloud. Since it is uncertain exactly how appropriate their results are for cirrus cloud layers and since not enough data exist to reliably establish the dependence of α_S on $z\ell$ of a_S; a_S = 0.5 is assumed for this study. This seems reasonable for the relatively thin ice clouds considered here.

An approach similar to that employed earlier for the reflected short-wave component may be adopted for the transmitted short-wave radiation in the subcloud region. Let $R_{\nu t}$ be the ratio of the transmitted solar radiation absorbed in a layer extending down from cloud base to level k to that absorbed in clear sky conditions in the same layer at wave length ν, i.e.

$$R_{\nu t} = R_{\nu z\ell} t_\nu$$

where

$$R'_{\nu z\ell} = \frac{a_\nu(u^*(KB \rightarrow k))(1 - a_\nu(u_{z\ell}(0 \rightarrow KT)))}{a_\nu(u_{z\ell}(0 \rightarrow k)) - a_\nu(u_{z\ell}(0 \rightarrow KB))},$$

t_ν is the spectral transmittance of the cloud layer and the arguments of u^* and $u_{z\ell}$ refer to the vertical domain over which the corresponding u is evaluated (0 incidates the top of the atmosphere). Note that I_{o_ν} has been eliminated from this expression as before. The expression for $R'_{\nu z\ell}$ is very similar to the previous expression for $R_{\nu z\ell}$. Since $R_{\nu z\ell}$ was nearly independent of u over an appropriate range of u

and since the vertical optical paths within the domain are likely to be of the same order (i.e. $\lesssim$ 0.2 cm), $R'_{\nu,\mathcal{l}}$ should also be relatively independent of the vertical optical paths. Therefore, it is assumed that:

$$R'_{\nu,\mathcal{l}} \doteq R_{\nu,\mathcal{l}}.$$

Thus, $R_{\nu t}$ is assumed to have the same dependence on $\mathcal{l}$ as $R_{\nu\rho}$. This simplifies matters as unlike the case of the reflected solar component, multiple vertical structures of u must be considered rather than simply a reasonable range of single layer values.

From Welch et al. (1980), employing the same model cloud results and procedures as before, $t_1 \cong 0.09$ and $t_2 \cong 2 \times 10^{-5}$ for $t_S \cong 0.25$, $\rho_S \cong 0.61$ and $a_S \cong 0.14$. By analogy to the reflected case where $(\rho_1/\rho_S) >> (\rho_2/\rho_S)$ allows $R_\rho \sim (2/3)\, R_{1\rho}$, let $R_t \sim (2/3)\, R_{1t}$. Combining this result with the previous results and approximations allows:

$$R_t = (t_1/\rho_1)\, R_\rho = 0.159\, R_{\mathcal{l}}$$

for their model cloud.

Assuming that the relative spectral distribution of short-wave radiant energy transmitted through the cloud layer is independent of $\mathcal{l}$ and t_S and noting that $R_t = 1.0$ for $t_S = 1.0$ is required, the above result for $t_S = 0.25$ leads to:

$$R_t = \left\{ \begin{array}{l} 1.0 - \left\{\dfrac{1 - t_S}{1 - 0.25}\right\} \left\{1 - 0.159\, R_{\mathcal{l}}\right\} \\ 0 \end{array} \right\} \qquad (3.11.41)$$

whichever is greater. Note that $R_t = 0$ for $t_S \lesssim 0.10$, 0.14 and 0.18 when $\mathcal{l} = 30°$, 60° and 80°, respectively. Thus, for very optically thick cloud layers, essentially all of the transmitted solar radiation

is at visible wave lengths and not subject to gaseous absorption in the subcloud region.

The short-wave radiative heating rates resulting from the absorption of transmitted solar radiation in the subcloud layers are, therefore, determined in cloudy column $i+\frac{1}{2}$ as:

$$QSW_{i+\frac{1}{2},k+\frac{1}{2}} = R_t \; QSW^{(\downarrow)}_{o_{k+\frac{1}{2}}}(\mathscr{l}^n) \tag{3.11.42}$$

for k = 1, 2, ..., $KB_{i+\frac{1}{2}}-2$, $KB_{i+\frac{1}{2}}-1$

where R_t is determined from Equations (3.11.41) and (3.11.36) as a function of $t_{S_{i+\frac{1}{2}}}$ and $\mathscr{l}^n$.

In summary, prior to the initiation of a simulation six basic state profiles of $QSW^{(\downarrow)}_o$ and $QSW^{(\uparrow)}_o$ and the corresponding values of $I^{(\downarrow)}_{o_{KT'}}$, $\Delta I^{(\downarrow)}_{o_{KT'}}$ and $\Delta I^{(\uparrow)}_{o_{KT'}}$ are computed by means of the IRADSW model for the basic state profile of pressure, temperature, etc. for six prespecified solar zenith angles. The diurnal cycle of these quantities is approximated by a linear interpolation in terms of zenith angle. In the presence of a cloud layer, the appropriate basic state radiative heating rate profiles in the subcloud and above cloud regions are adjusted based on the diagnosed bulk short-wave radiative properties of the cloud, where the angular and spectral distribution of the radiation emergent from the cloud layer is parametrically taken into account. The in-cloud short-wave radiative heating rate profiles are computed based upon the appropriate incident basic state flux and the diagnosed broadband absorptance where the distribution is determined parametrically based on the vertical distribution of ice water.

3.12. Initialization and Procedural Summary

In this section, the overall computational procedure employed in the model is briefly summarized in schematic form. A logical listing of all model parameters is, also, presented. Definitions and details not found in this section may be found in the appropriate section of this chapter. The required model input parameters and the manner of initializing the model for a simulation are described here in detail.

The following is a list of all model parameters, where these parameters have been classified according to their computational utilization. These parameters have all been defined in the previous sections. Parameters employed strictly for analysis of model output have not been included. The temporal and spacial dependencies of the model parameters are noted in a shorthand fashion. The dependencies are given within the brackets and refer to all quantities on that line. The absence of a bracketed quantity denotes constants. The notation is such that the presence of n, N_R or N_c denotes the time steps at which the parameters are evaluated, i.e. every time step, only every N_R time steps or only every N_c time steps, respectively. The presence of i or $i+\frac{1}{2}$ denotes a parameter nominally evaluated at every dynamic or thermodynamic grid level, respectively. The absence of a reference to any dependency indicates no dependency.

Physical Constants and Functions:

R_g, c_p, g, ε, σ, L, e_S, Λ, solar constant

Geometric Constants:

d, h_B, I, K

Computational Constants:

Δt, η, ff^{o}, N_c, N_R, err

Parametric Constants:

ν, κ_θ, κ_q, κ_ℓ $\beta^{(\uparrow)}$, t_β, $R_\beta(\min)$, $R_\beta(\max)$, α_S

Initialization Parameters:

JD, ϕ, t^{o}_{SOL}, KT´, KB´, $\mathscr{l}_m$, (δ, SR)

Primary Basic State Quantities:

Θ_{oo}, w_o, Θ_o, q_o, p_o, π_o, T_o, $_o$[@ k+½ and k = 1,K]

Secondary Basic State Parameters:

QIR_o, QIR_c, $\varepsilon_g^{*(\uparrow)}$, $\varepsilon_g^{*(\downarrow)}$ $QSW_o^{(\downarrow)}$ ($\mathscr{l}_m$) [@ k+½]

$QSW_o^{(\uparrow)}$ ($\mathscr{l}_m$) [@ k+½ > KT´]

$H^{(\downarrow)}_{o_{KT´}}$, $H^{(\uparrow)}_{o_{KB´}}$, $I^{(\downarrow)}_{o_{KT´}}$ ($\mathscr{l}_m$), $\Delta\, I^{(\downarrow)}_{o_{KT´}}$ ($\mathscr{l}_m$), $\Delta\, I^{(\uparrow)}_{o_{KT´}}$ ($\mathscr{l}_m$)

Prognostic (Perturbation) Fields:

ζ [@ i, k, n]

θ, q, ℓ [@ i+½, k+½, n]

Primary Diagnostic Quantities (Nonparametric):

ψ [@ i, k, n]

t [@ n]

Primary Diagnostic Quantities (Parametric):

ν^{*} [@ i+½, k+½, n]

Secondary Diagnostic Quantities (Nonparametric):

T, q^{*} [@ i+½, k+½, N_c]

IWP [@ i+½, k+½, N_R]

$\bar{\bar{I}}\bar{\bar{W}}\bar{\bar{P}}$ [@ $i+\frac{1}{2}$, k, N_R]

IWP, KT, KB [@ $i+\frac{1}{2}$, N_R]

$QSW_o^{(\downarrow)}$ ($\mathcal{L}$) [@ $k+\frac{1}{2}$, N_R]

$QSW_o^{(\uparrow)}$ ($\mathcal{L}$) [@ $k+\frac{1}{2} > KT'$, N_R]

t_{SOL}, $\mathcal{L}$, $I_{o_{KT'}}^{(\downarrow)}$ ($\mathcal{L}$), $\Delta I_{o_{KT'}}^{(\downarrow)}$ ($\mathcal{L}$), $\Delta I_{o_{KT'}}^{(\uparrow)}$ ($\mathcal{L}$) [@ N_R]

Secondary Diagnostic Quantities (Parametric):

QIR, QSW, $QSW^{(\downarrow)}$, $\varepsilon_T^{*(\uparrow)}$, $\varepsilon_T^{*(\downarrow)}$ [@ $i+\frac{1}{2}$, $k+\frac{1}{2}$, N_R]

C, f_ℓ, Γ [@ $i+\frac{1}{2}$, $k+\frac{1}{2}$, N_c]

$QSW^{(\uparrow)}$ [@ $i+\frac{1}{2}$, $k+\frac{1}{2} > KT$, N_R]

$H^{(\uparrow)}$ [@ $i+\frac{1}{2}$, $KT > k+\frac{1}{2} > KB$, N_R]

$H^{(\downarrow)}$ [@ $i+\frac{1}{2}$, $KT > k+\frac{1}{2} > KB$, N_R]

$\varepsilon_c^{*(\uparrow)}$, $\varepsilon_c^{*(\downarrow)}$ [@ $i+\frac{1}{2}$, $KB < k+\frac{1}{2} < KT$, N_R]

$\varepsilon^{*(\uparrow)}$, $\varepsilon^{*(\downarrow)}$, ρ_S, a_S, t_S, R_ρ^*, R_t [@ $i+\frac{1}{2}$, N_R]

R_β, $\beta^{(\downarrow)}$, $R_{\mathcal{L}}$ [@ N_R]

The overall computational procedure is schematically outlined in Figure 20. This flow diagram may be logically partitioned into two phases, which are the preliminary phase and the simulation phase. The preliminary phase is broken down into three general areas, i.e. model setup, input and initialization. The model setup requires that the physical constants and functions, the geometric constants, the computational constants and the parametric constants be specified. In addition, all the functional relationships to determine the parametric quantities must be specified. The sensitivity of simulations to the specific choice of the parametric constants and these functional relationships is established in Chapters 4 and 5.

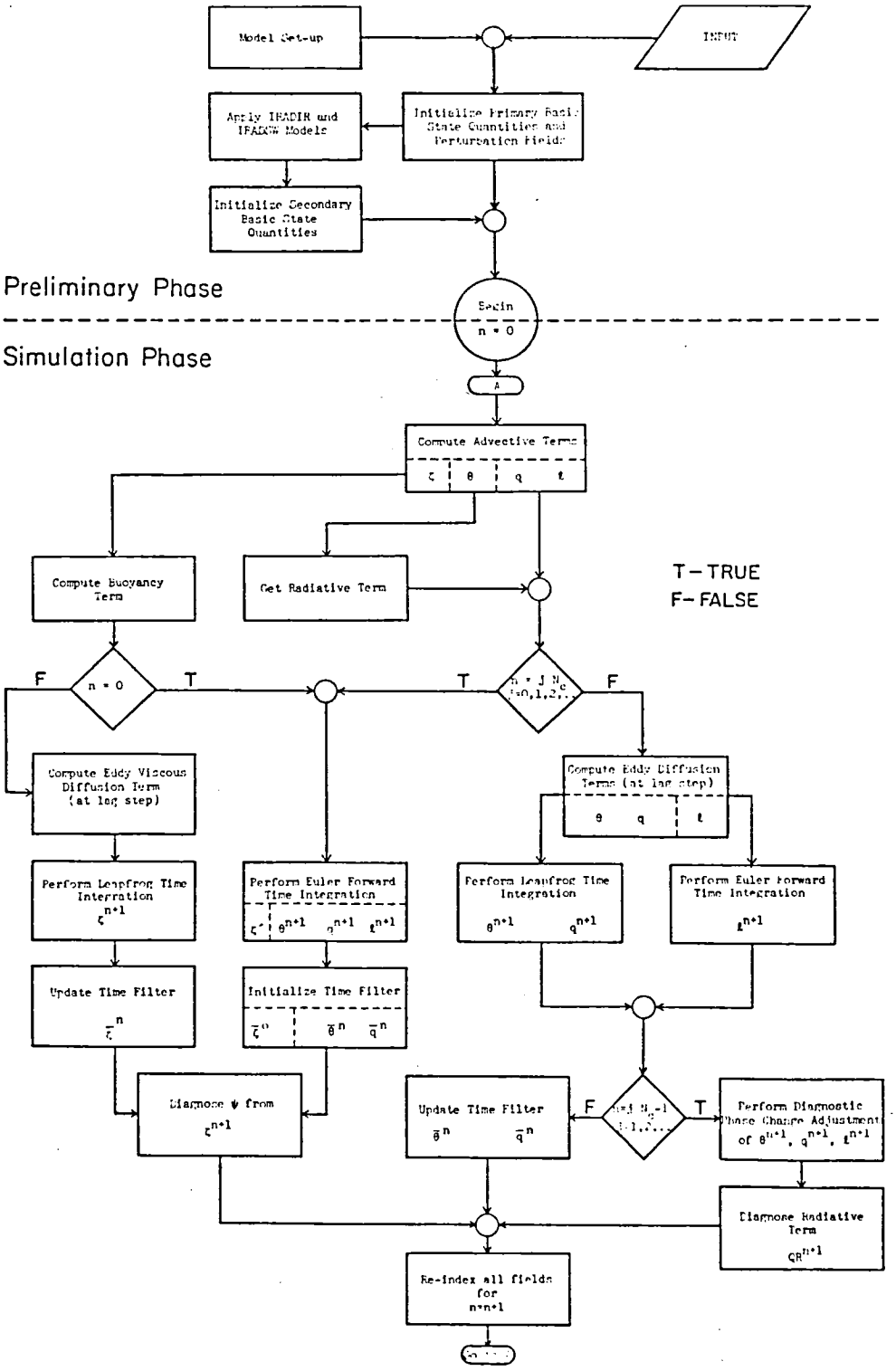

Figure 20. Flow diagram depicting the overall computational procedure employed in the model. See text for discussion.

The initialization portion of the preliminary phase determines the primary and secondary basic state parameters and initializes the perturbation fields and primary diagnostic quantities as well as the radiative term QR. This initialization proceeds from the model setup and the input parameters. The input parameters are: T_{o_1}, p_{o_1}, RH_{o_k}, Γ_{o_k} or Γ_{T_k} and w_o, which are the basic state temperature and pressure at the lower boundary, the relative humidity (with respect to ice) at all dynamic and thermodynamic levels, a basic state temperature lapse rate parameter for each sublayer resolved by the dynamic and thermodynamic grid levels and the basic state vertical velocity. Two options may be employed for the initialization of the primary basic state quantities. These are the direct method (input Γ_{o_k}) and the indirect method (input Γ_{T_k}). The indirect method is discussed presently. The direct method is a simplification of the indirect method. Note that both methods may be employed for a given simulation, i.e. some sublayers initialized from the direct method and some by the indirect method. In each method, the initialization proceeds from the lowest sublayer, i.e. between the k = 1 and k = 3/2 levels, to the highest sublayer. An iterative solution for the primary basic state parameters at the upper boundary of each successive sublayer is employed.

For the indirect method, the temperature lapse rate of a layer is initialized as the saturated pseudo-moist adiabatic lapse rate, Γ_m, minus some offset, Γ_T, which is an input parameter. Following from Hess (1959), the saturated pseudo-moist adiabatic lapse rate is well approximated as:

$$\Gamma_m(p, T) = \frac{g}{c_p} \left[\frac{1 + \frac{L}{R_g} \frac{\varepsilon\, e_S(T)}{(p - e_S(T))\, T}}{1 + \frac{L^2\, \varepsilon^2}{c_p\, R_g} \frac{e_S(T)}{(p - e_S(T))\, T^2}} \right] \tag{3.12.1}$$

at a pressure, p, and temperature, T; where $e_S(T)$ and L are determined as in Appendices A and B, respectively. The pressure at the upper boundary, p_T, of a layer, where the pressure at the lower boundary, p_B, as well as the temperature, T, and water vapor specific humidity, q, at both boundaries are known, is well approximated as:

$$p_T(p_B, T_T, T_B, q_T, q_B) = p_B \exp \left\{ \frac{-g}{R_g} \frac{d}{2} \left[\frac{T_T + T_B}{2} \right]^{-1} \left[1 + \frac{(1-\varepsilon)}{\varepsilon} \frac{q_T + q_B}{2} \right]^{-1} \right\} \tag{3.12.2}$$

where d/2 is the vertical thickness of the layer. The water vapor specific humidity is given by

$$q_T(p, T, RH) = RH \frac{e_S(T)}{(p - e_S(T))} \tag{3.12.3}$$

where RH is the specified relative humidity (with respect to ice).

Since,

$$T_T = T_B - \left(\frac{d}{2}\right) \left\{ \Gamma_m \left(\frac{p_T + p_B}{2}, \frac{T_T + T_B}{2} \right) - \Gamma_T \right\} \tag{3.12.4}$$

and iterative solution for the indirect method is readily available. Let ν be the iteration index. As a first approximation,

$$\Gamma^1_{m_k} \doteq \Gamma_m \left(p_{o_{k-\frac{1}{2}}}, T_{o_{k-\frac{1}{2}}} \right)$$

$$T^1_{o_k} = T_{o_{k-\frac{1}{2}}} - \frac{d}{2} \left(\Gamma'_{m_k} - \Gamma_{T_k} \right)$$

$$p^1_{o_k} = p_T(p_{o_{k-\frac{1}{2}}}, T^1_{o_k}, T_{o_{k-\frac{1}{2}}}, 0, q_{o_{k-\frac{1}{2}}})$$

and $$q^1_{o_k} = q_T(p^1_{o_k}, T^1_{o_k}, RH_{o_k}) \qquad (3.12.5)$$

where the functions Γ_m, p_T and q_T are given by Equations (3.12.1), (3.12.2) and (3.12.3), respectively, and the values of $P_{o_{k-\frac{1}{2}}}$, $T_{o_{k-\frac{1}{2}}}$, $q_{o_{k-\frac{1}{2}}}$, Γ_{T_k} and RH_{o_k} are known. The iteration proceeds as:

$$\Gamma^{\nu}_{m_k} \doteq \Gamma_m \left(\frac{p_{o_{k-\frac{1}{2}}} + p^{\nu-1}_{o_k}}{2}, \frac{T_{o_{k-\frac{1}{2}}} + T^{\nu-1}_{o_k}}{2} \right)$$

$$T^{\nu}_{o_k} = T_{o_{k-\frac{1}{2}}} - \frac{d}{2}(\Gamma^{\nu}_{m_k} - \Gamma_{T_k})$$

$$p^{\nu}_{o_k} = p_T(p_{o_{k-\frac{1}{2}}}, T^{\nu}_{o_k}, T_{o_{k-\frac{1}{2}}}, q^{\nu-1}_{o_k}, q_{o_{k-\frac{1}{2}}})$$

and $$q^{\nu}_{o_k} = q_T(p^{\nu}_{o_k}, T^{\nu}_{o_k}, RH_{o_k}). \qquad (3.12.6)$$

The solution is regarded as correct, when:

$$\frac{\Gamma^{\nu}_{m_k} - \Gamma^{\nu-1}_{m_k}}{\Gamma^{\nu}_{m_k}} < err \qquad (3.12.7)$$

and

$$\frac{q^{\nu}_{o_k} - q^{\nu-1}_{o_k}}{q^{\nu-1}_{o_k}} < err \qquad (3.12.8)$$

where err is some convergence criterion and is usually specified as 0.0001. Convergence is rapid and is usually achieved in one or two iterations.

For the direct method, the temperature lapse rate is directly specified as Γ_o. Thus,

$$T_{o_k} = T_{o_{k-\frac{1}{2}}} - \left(\frac{d}{2}\right) \Gamma_{o_k} \quad . \tag{3.12.9}$$

Thus, as a first approximation,

$$p^1_{o_k} = p_T \left(p_{o_{k-\frac{1}{2}}}, T_{o_k}, T_{o_{k-\frac{1}{2}}}, 0, q_{o_{k-\frac{1}{2}}}\right)$$

and

$$q^1_{o_k} = q_T \left(p^1_{o_k}, T_{o_k}, RH_{o_k}\right) \quad . \tag{3.12.10}$$

The iteration proceeds as:

$$p^{\nu}_{o_k} = p_T \left(p_{o_{k-\frac{1}{2}}}, T_{o_k}, T_{o_{k-\frac{1}{2}}}, q^{\nu-1}_{o_k}, q_{o_{k-\frac{1}{2}}}\right)$$

and

$$q^{\nu}_{o_k} = q_T \left(p^{\nu}_{o_k}, T_{o_k}, RH_{o_k}\right) \tag{3.12.11}$$

where Equation (3.12.7) is utilized to test for convergence.

By employing the appropriate method for each successive level (i.e. $k = \frac{1}{2}, 2, \frac{1}{2}, \ldots, K=\frac{1}{2}, K$), the primary basic state parameters T_o, p_o and q_o are determined at all levels. This allows the specification of the other primary basic state parameters as:

$$\pi_{o_k} = \left(\frac{p_{o_k}}{p_{ref}}\right)^{R_g/c_p} \tag{3.12.12}$$

and

$$\theta_{o_k} = \frac{T_{o_k}}{\pi_{o_k}} \tag{3.12.13}$$

$$\rho_{o_k} = \frac{p_{o_k}}{R_g T_{o_k}} \left[(1+q_{o_k}/\varepsilon)/(1 + q_{o_k})\right] \tag{3.12.14}$$

and

$$\theta_{oo} = \frac{1}{K} \sum_{k=1}^{K} \theta_{o_k} \quad . \tag{3.12.15}$$

Recall that for the simulation phase, T_o, p_o, q_o, π_o, θ_o and ρ_o are required at only the k = 1; k = $\frac{3}{2}$, $\frac{5}{2}$, ..., K-$\frac{1}{2}$; and k = K grid levels. Though the basic state parameters might be retained for dynamic grid levels for the computation of the vertical advection terms (rather than employing interpolation), this is inconsistent with the desired conservation properties when utilizing the staggered grid. For the same reason, the input values of Γ_o of Γ_T as well as the initialization method are required to be the same for the two sublayers adjoining any dynamic grid level.

Once the primary basic state parameters are deduced, the secondary basic state parameters may be determined from the IRADIR and IRADSW models as described in Section 3.11. Note that this requires the additional input of vertical profiles of atmospheric pressure, temperature and water vapor specific humidity for the regions external to the model domain, i.e. from the surface to the lower boundary and from the upper boundary to the top of the atmosphere. Similarly, vertical profiles of carbon dioxide mixing ratio and ozone concentration are required for the regions both internal and external to the model domain. In addition, the initialization parameters must be input.

The radiative term, i.e. QR and its component parts, is specified as the appropriate clear sky basic state value at all thermodynamic grid points for the initiation of a simulation. The perturbation fields of water vapor specific humidity and ice water specific humidity are initialized as:

$$q_{i+\frac{1}{2},\ k+\frac{1}{2}} = 0 \qquad (3.12.16)$$

and $$\ell_{i+\frac{1}{2},\ k+\frac{1}{2}} = 0$$

for i = 1, 2, ..., I-2, I-1 and k = 1, 2, ..., K-2, K-1.

In general, the dynamic perturbation fields are initialized as:

$$\zeta_{i,k} = 0$$

and $$\psi_{i,k} = 0 \qquad (3.12.17)$$

for i = 1, 2, ..., I-1, I and k = 1, 2, ..., K-1, K. An alternative dynamic initialization, which is employed is:

$$\psi_{i,k} = \psi_{o_k}$$

and $$\zeta_{i,k} = \frac{1}{d^2} (\psi_{o_{k+1}} + \psi_{o_{k-1}} - 2\ \psi_{o_k})$$

for k = 2, 3, ..., K-2, K-1; and

$$\psi_{i,k} = 0$$

$$\zeta_{i,k} = 0 \qquad (3.12.18)$$

for k = 1 and k = K and i = 1, 2, ..., I-1, I where the vertical profile ψ_{o_k} is a model input parameter. Note that this formulation is consistent with the developments in Sections 3.5 and 3.8. This alternative initialization allows the specification of a mean lateral wind component, u_{o_k}, which has a vertical shear structure. Note that there is no mean layer horizontal wind, i.e.

$$\sum_{k=1}^{K} \psi_{o_k} = 0 \ . \qquad (3.12.19)$$

The ramifications of this initialization procedure for a simulation are discussed in the succeeding chapters where it is employed.

The thermal perturbation field is employed to initiate a disturbance. In general, a uniform random number generator (RNDM (SEED)) is used where SEED is the seed number for RNDM. Each call to RNDM (SEED) yields a fraction RN, where:

$$-1 \leq RN \leq 1.$$

The call is made M = (K-1) (I-1) times yielding a series of uniformly distributed random numbers RN'_m where m = 1, 2, ..., M. These are normalized as:

$$RN_m = RN'_m - \sum_{m'=1}^{M} RN'_{m'} . \tag{3.12.20}$$

The thermal perturbation field is then initialized as:

$$\theta_{i+\frac{1}{2},k+\frac{1}{2}} = \Theta_{max}\, RN_m \tag{3.12.21}$$

where m = i + (k-1)(I-1) for i = 1, 2, ..., I-2, I-1 and k = 1, 2, ..., K=2, K-1. Now, θ_{max} is the maximum magnitude of thermal perturbation which may occur at the initial time and is a model input parameter. Note that:

$$\sum_{i=1}^{I-1} \sum_{k=1}^{K-1} \theta_{i+\frac{1}{2},k+\frac{1}{2}} = 0. \tag{3.12.22}$$

The initial disturbance is sometimes confined within a limited vertical region of the model domain, i.e. $\theta_{i+\frac{1}{2},k+\frac{1}{2}} \equiv 0$ outside the initial disturbed region and inside, $\theta_{i+\frac{1}{2},k+\frac{1}{2}}$ is initialized as above. Note that an appropriate value of M is chosen and Equation (3.12.21) is modified in a consistent manner such that Equation (3.12.22) is true. For the preliminary model testing (i.e. Chapter 4), alternative

thermal perturbation initializations were tried, e.g. a warm bubble. These are described where appropriate.

In summary, the input parameters for a simulation (other than for the model setup) are: T_{o_1}, p_{o_1}, RH_{o_k}, Γ_{o_k} or Γ_{T_k}, w_o, θ_{max} or some alternate thermal pattern, ψ_{o_k} if desired, the initialization parameters and the atmospheric environment external to the model domain.

Once the initialization phase is complete, the simulation proceeds as in Figure 20. Within each rectangle, the computational procedure given in the appropriate preceeding sections is followed. Thus, the enclosed operation is performed at all the relevant grid points before proceeding to the next operation. The rationale for the overall computational procedure adopted during a simulation is also discussed in Section 3.7.

IV. VALIDATION OF THE NUMERICAL MODEL

The purpose of this chapter is to present some of the general model characteristics. In this sense, the model performance is baselined. The series of experiments, which are described, provide a rational basis upon which the choices of specific numerical values for certain model constants are made. The sensitivity of simulations to these specific choices are interrelated to varying degrees. Limited versions of the model are used for many of the simulations reported here, e.g. a dry version. The sensitivity of the specific parametric representation of the ν^*, C and Q_R terms is deferred until the next chapter, i.e. until the elementary model is validated. Some comparisons to other works are made as appropriate.

The model constants, which are considered here, are:

ff^o : the initial buoyancy flip-flop weighting factor;

η : the filter factor for the filtered leap frog time integration scheme;

ν : the eddy viscosity;

κ_0 : the thermal eddy diffusivity;

κ_q : the water vapor eddy diffusivity;

κ_ℓ : the ice water eddy diffusivity;

$N_C \Delta t$: the phase change adjustment time scale;

d : the spacial grid interval;

and $(I-1)d$: the horizontal grid domain.

Except for the diffusivity coefficients, these parameters are purely computational in nature. As will be seen, the choices of specific numerical values for the eddy diffusivity coefficients are also partially based on computational consideration.

In the course of performing these experiments, the stated conservation properties of the finite difference formulations of the advective terms, as developed in Sections (3.2)-(3.4), were verified. Conservation of the relevant quantities was found to ten significant digits. When the advective schemes are coupled with the time integration scheme, the same accuracy is found for the primary quantities, e.g. $\bar{\zeta}$, $\bar{\theta}$ or $\bar{\ell}$. However, trends may be present in squared quantities, i.e. ζ^2 or $(\theta + \theta_o)^2$. This is due to the phase shifting properties of the filtered leap frog scheme. These trends may be suppressed by the proper choice of η.

4.1 Time Filter and Buoyancy Weighting Factors

The use of the flip-flop weighting scheme for the evaluation of the buoyancy vorticity generation term stimulates the time-splitting computational mode in the leap frog time integration scheme. In this sense, the choice of ff^o and η are coupled to some degree. Though there are other sources which may stimulate the time-splitting mode in the full model, it is instructive to consider just these two parameters. The model used for these tests has been stripped of the phase change, radiative, diffusive and basic state vertical velocity components. Thus, the model incorporates only the perturbation advective terms in the governing prognostic equations for ζ, θ and q in addition to the vorticity generation/destruction term. The ice water equation is not evaluated.

The model is initialized with a basic state, denoted BASIC 1 as depicted in Figure 21. The stability structure is similar to that commonly observed in conjunction with middle and upper tropospheric cloud layers in the midlatitudes (e.g. Heymsfield, 1975a; Yagi, 1969

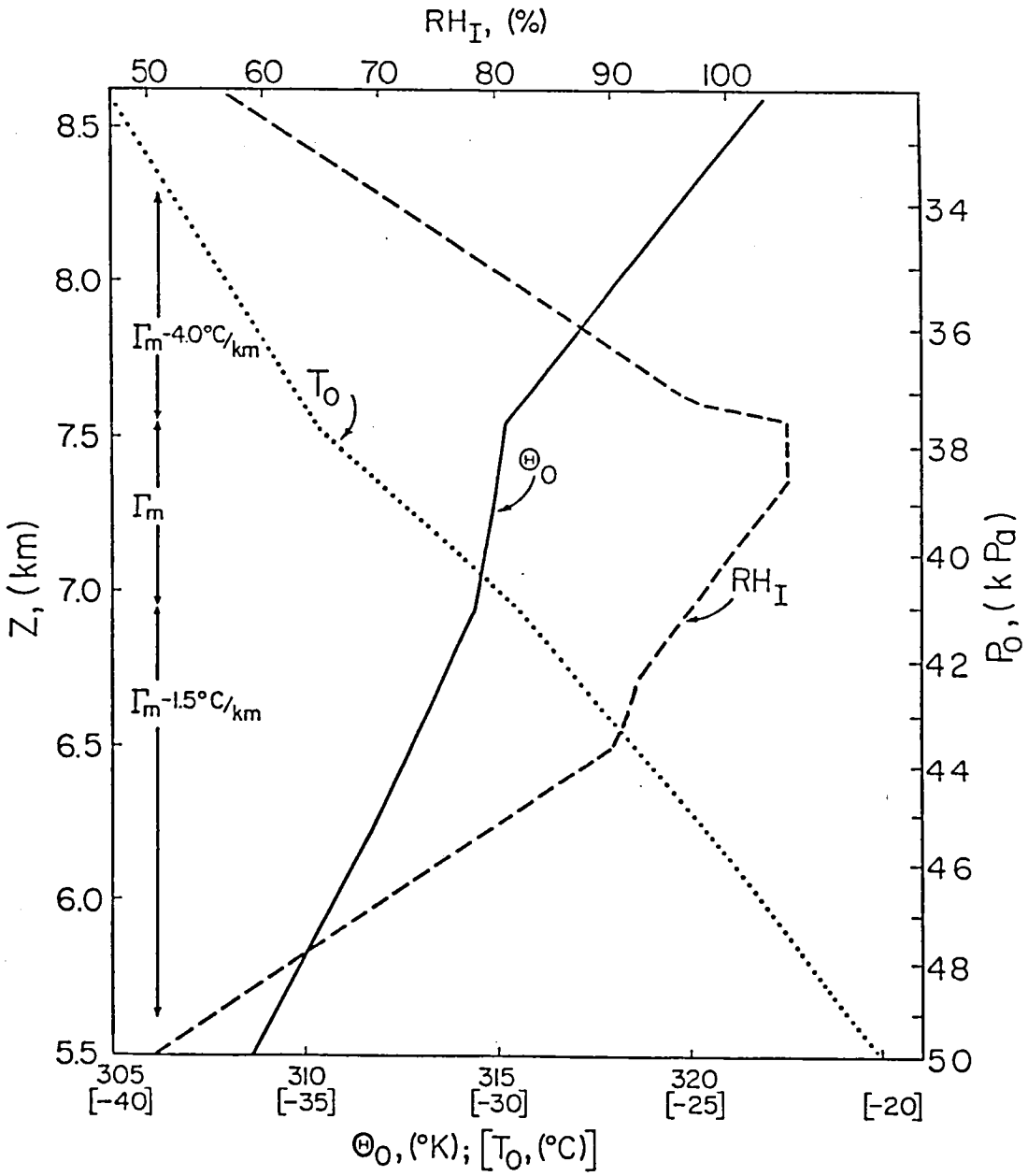

Figure 21. BASIC 1 initial state for potential temperature Θ_0; temperature, T_0; and relative humidity with respect to ice, RH_I. The corresponding basic state static stability structure is noted on the left where Γ_m denotes a pseudo moist adiabatic stratification.

and Starr and Cox, 1980). In the upper portion of the layer, the basic state stratification is 4°K/km more stable than neutral, i.e. psuedo-moist adiabatic. In the central region, the basic state is neutrally stratified and in the lower portion it is 1.5°K/km more stable than neutral. The assumed moisture structure is plotted in terms of the relative humidity with respect to ice, RH_I. The neutral layer is 0.6 km thick. The domain is specified as K = 32 and I = 64, i.e. 6.3 km in the horizontal. All perturbation fields are initialized to zero except for θ, which is randomly perturbed in the region from 6.5 km to 7.6 km elevation. The maximum perturbation magnitude is $\sim$ 0.1°K corresponding to that observed by Heymsfield (1975b) in a cirrus uncinus cloud. This value is appropriate for the case here where d = 100 m. The mean perturbation magnitude is $\sim$ 0.05°K over the perturbed region.

The previously stated choice of $ff^o = \frac{1}{3}$ (section 3.7) is somewhat arbitrary. This value is sufficiently less than $\frac{1}{2}$ such that "checkerboard" noise patterns do not persist. In Figure 22, the layer mean kinetic energy, $\bar{\bar{TKE}}$, is plotted as a function of time for three simulations employed different value of η for $ff^o = \frac{1}{3}$. Kinetic energy is defined in the usual way as:

$$TKE_{i+\frac{1}{2},k+\frac{1}{2}} = \frac{u^2_{i+\frac{1}{2},k+\frac{1}{2}}}{2} + \frac{w^2_{i+\frac{1}{2},k+\frac{1}{2}}}{2} \qquad (4.1)$$

at thermodynamic grid point $(i+\frac{1}{2},k+\frac{1}{2})$, where for analysis purposes:

$$u_{i+\frac{1}{2},k+\frac{1}{2}} = \frac{1}{d}\left\{\frac{(\psi_{i,k} + \psi_{i+1,k})}{2} - \frac{(\psi_{i,k+1} + \psi_{i+1,k})}{2}\right\}$$

and

$$w_{i+\frac{1}{2},k+\frac{1}{2}} = \frac{1}{d}\left\{\frac{(\psi_{i+1,k} + \psi_{i+1,k+1})}{2} - \frac{(\psi_{i,k} + \psi_{i,k+1})}{2}\right\}. \qquad (4.2)$$

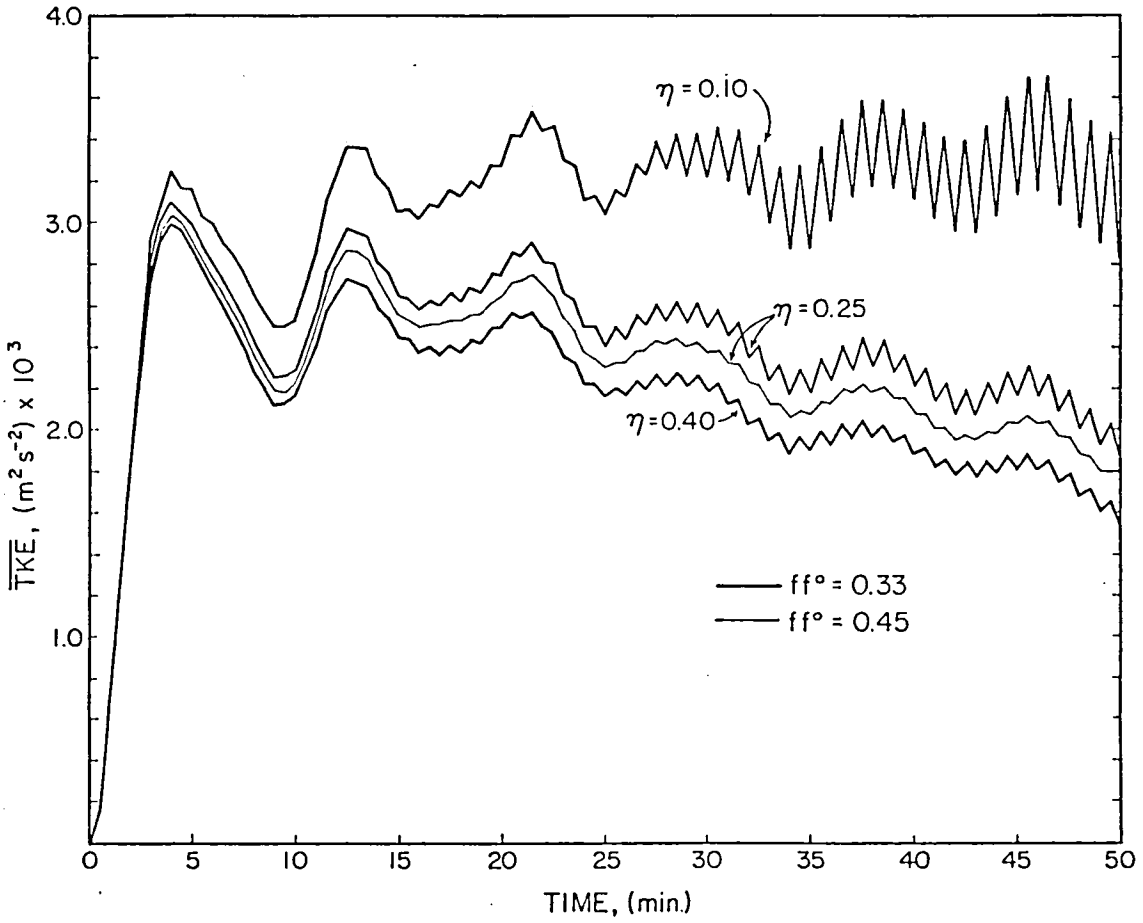

Figure 22. Mean layer perturbation kinetic energy, $\overline{TKE}$, versus time for simulations from an identical initial state (i.e. BASIC 1 and random perturbations of θ) using a model version which is identical in each case except for the specification of the time filter factor, η, and the buoyancy weighting factor, ff°. (No phase change, radiation, or eddy diffusion processes included).

Now,

$$S \equiv \frac{1}{I'K'} \sum_{i=1}^{I'} \sum_{k=1}^{K'} S_{i',\,k'} \tag{4.3}$$

for any quantity S where $I' = I$, $K' = K$, $i' = i$ and $k' = k$ when S is defined at dynamic grid points and $I' = I=1$, $K' = K-1$, $i' = i+\frac{1}{2}$ and $k' = k+\frac{1}{2}$ when S is defined at thermodynamic grid points as with TKE.

As defined by Equation (4.1), the kinetic energy excludes contribution due to the basic state vertical velocity and is therefore denoted TKE, i.e. turbulent or perturbation kinetic energy. Recall that in these simulations $\nu = \kappa_\theta = \kappa_q \equiv 0$.

What is of interest here are the short period oscillations in the solution, i.e. $\sim 2\Delta t = 60s$. These show the time-splitting nature of the leap frog scheme. Note that the Euler forward scheme is never employed once the simulation is initiated. With this initialization, the simulation should proceed as an adjustment process where potential energy available via the horizontal gradients of perturbation potential temperature is converted to kinetic energy. The generated kinetic energy may be destroyed by buoyancy forces as is the case of a positively buoyant bubble penetrating the relatively stable layer in the upper portion of the domain. In this sense, the kinetic energy is converted back to potential energy and the net effect has been simply a redistribution of potential temperature. This end state should be stably or neutrally stratified every where and horizontally uniform. Oscillations about this end state are anticipated and physical since internal gravity waves are produced when a buoyant plane penetrates a relatively stable layer. Furthermore, since the initial perturbations

are randomly distributed and of varying amplitudes, one may expect local disturbances to evolve on varying space scales with different propagation speeds. Thus, even in the continuous case, monotonically smooth behavior of $\bar{\bar{\bar{TKE}}}$ is not expected. Therefore, the long period ($\sim$ 8 min) oscillation of the solution is not cause for concern.

What is seen in these simulations is that after $\sim$ 13 minutes some time-splitting is evident in each case. The amplitude of the time-splitting oscillation diminishes as η is increased. In the case of $\eta = 0.10$, the oscillation is becoming unstable as time progresses. However, computational instability due to the time-splitting mode as in Lilly (1965) was not encountered after one hour of simulated time. This may be more a fortuitous result of damping due to the structure of the prescribed basic state than due to the time filter. In either of the other cases, though time-splitting is evident, no unstable growth of the $2\Delta t$ oscillation occurs.

For $\eta < 0.25$, the mean thermal perturbation amplitude (i.e. $\bar{\bar{\bar{\theta}}}$, which is analogous to $(\theta + \Theta_o)^2$) amplified with time, while for $\eta > 0.25$ it decayed. This is consistent with the results of Asselin (1972), where a choice of $\eta = 0.25$ yielded essentially no phase error in the filtered leap frog time integration scheme. Note that these trends were computed by a two time step running mean though this was unnecessary in the case of $\eta \geq 0.25$ where the $2\Delta t$ oscillations were not found in $(\theta + \Theta_o)^2$ to ten significant digits. The same relative trends were found for ζ^2 and $\bar{\bar{\bar{TKE}}}$ in the $2\Delta t$ averages, i.e. compared to $\eta = 0.25$. It is concluded that for $\eta > 0.25$, the solution is computationally damped, while for $\eta < 0.25$ it exhibits some computational

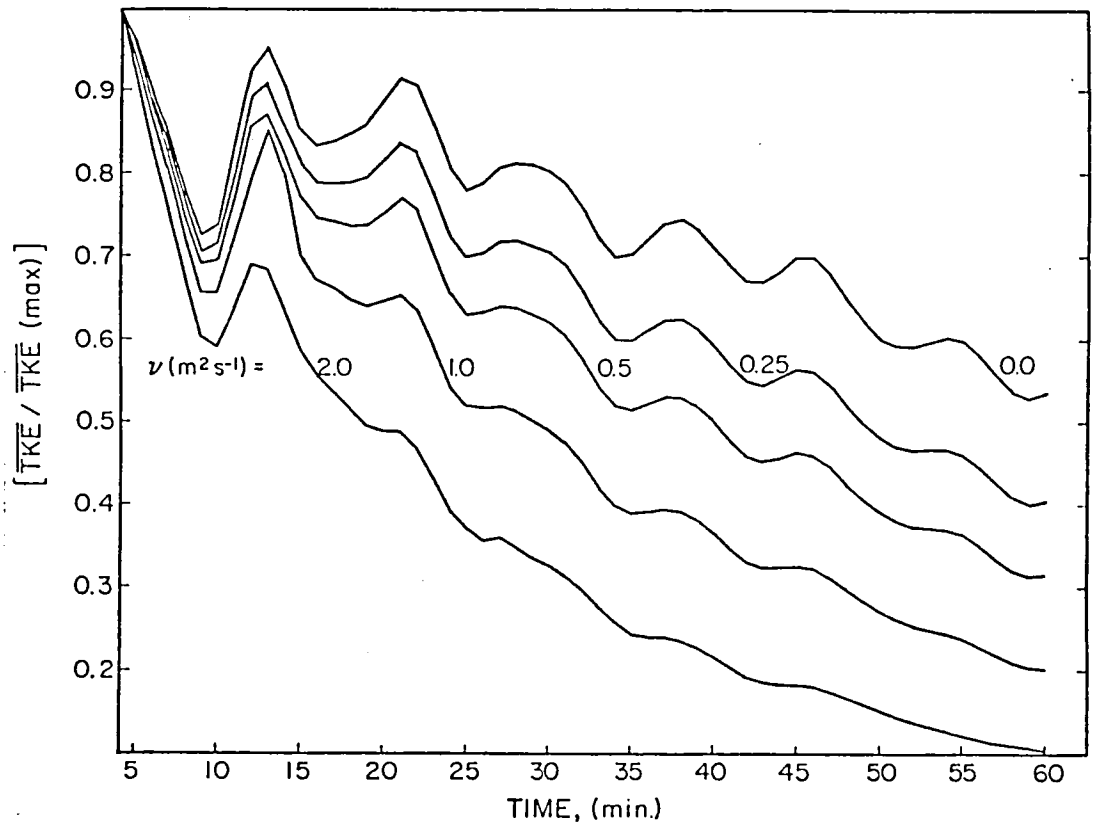

Figure 23. Mean layer perturbation kinetic energy, $\overline{TKE}$, versus time for simulations from an identical initial state (i.e. BASIC 1 and random perturbations of θ) using a model version which is identical in each case except for the specification of the eddy viscosity, ν. (No phase change, radiation or eddy thermal or water vapor diffusion processes included.)

instability. The choice of $\eta = 0.25$ yields the desired behavior of the advective schemes (Arakawa, 1966).

A different value of ff^o was tried, i.e. $ff^o = 0.45$. As seen in Figure 22, in the case of $\eta = 0.25$, the time-splitting mode is smaller in amplitude than in the case of $\eta = 0.25$ and $ff^o = \frac{1}{3}$. In all respects, the solution was damped in the case of $ff^o = 0.45$ compared to the case of $ff^o = \frac{1}{3}$ when $\eta = 0.25$, e.g. $\bar{\bar{\theta}}^{-}$ decreased with time. This may be attributed to some locking in of "checkerboard" patterns in θ which prevent the proper generation of TKE. Hereafter $\eta = 0.25$ and $ff^o = \frac{1}{3}$ are prescribed in all experiments unless noted otherwise.

4.2 Eddy Viscosity

The coefficient of eddy viscosity is now considered. Two series of experiments were performed. In the first, the same basic state and perturbation initialization, as described in Section 4.1, was employed. The same model version was used except that the eddy viscosity term was turned on. In Figure 23, the time dependent behavior of the ratio $[\bar{\bar{TKE}}/\bar{\bar{TKE}}\ (\max)]$ is shown for various specified values of ν. The maximum value of $\bar{\bar{TKE}}$ occurred at $t = 4$ min in each experiment. Only the one-minute values are plotted. Thus, the time-splitting mode does not show up in these plots. The $\bar{\bar{TKE}}$ reaches smaller maximum values and decays more rapidly as ν is increased. The ratios of $[\bar{\bar{TKE}}\ (\max)_{\nu} / \bar{\bar{TKE}}\ (\max)_{\nu=0}]$ were 0.984, 0.968, 0.938, 0.880 in the case of $\nu = 0.25$, 0.50, 1.0 and 2.0 $m^2\ s^{-1}$, respectively. It is seen that the larger values of ν also increase the damping of the longer period oscillations in the solution. Increasing the prescribed value of the eddy viscosity coefficient causes a larger proportion of the $\bar{\bar{TKE}}$ to be

found at longer wave lengths as it effectively damps the smallest waves as time progresses. It also damps the propagation speed of any thermals which are present and reduces the amplitude of any internal gravity waves which evolve. In addition, the amplitude of the time-splitting oscillation in the solution is reduced.

In prescribing the value of ν, one is essentially setting a decay time scale for motions at various scales. In this sense, the rate at which a given disturbance runs down via viscous diffusion is a function of the wave-length dependent kinetic energy power spectrum, i.e. a disturbance with most of its energy at the shorter wave length will decay faster than one which is organized at larger scales for a given value of ν. Given the initialization employed here, most of the energy is initially concentrated at the shorter wave lengths.

If a disturbance decay time scale τ is defined as the time it takes a disturbance to decay to 1/e of its maximum intensity where the intensity is evaluated in terms of $\bar{\bar{TKE}}$, $\tau \simeq 50$, 36 and 22 minutes for the simulations with $\nu = 0.5$, 1.0 and 2.0, respectively. An alternate definition of τ where ζ^2 is used to evaluate the intensity yields essentially the same results. However, τ is not an eddy viscous relaxation time scale since it includes the effects of buoyancy processes. A second set of experiments was performed in an attempt to establish an eddy viscous decay time scale τ_ν for various values of ν. The value of τ_ν is evaluated similarly to τ.

These simulations are based on a model version where the thermodynamic and water equations are eliminated. Thus, only the perturbation advection term and the eddy viscous term are retained in the remaining prognostic equation for ζ. The domain geometry is identical

to that noted previously. The initialization procedure involves specifying only a perturbation vorticity value at all dynamic grid points. This was done in a fashion similar to that noted in Section (3.12) for θ. A different seed number was employed to generate two initial fields. These fields were substantially different in their respective random organization of TKE at various scales. In Figure 24, the temporal decay from their initial values of both $\bar{\bar{T}}\bar{\bar{K}}\bar{\bar{E}}$ and ζ^2 is shown for various specified values of ν for each initial state. The slight damping of the solutions in the cases where $\nu = 0$ is due to the time filter ($\eta = 0.2$).

The differences in the rates at which $\bar{\bar{T}}\bar{\bar{K}}\bar{\bar{E}}$ decays between simulations from each prescribed initial state for a given value of ν reflect the differences in scale organization in the respective initial disturbances. The value of τ_ν based on $\bar{\bar{T}}\bar{\bar{K}}\bar{\bar{E}}$ is $\sim$ 2 hr and $\sim$ 4 hr for $\nu = 1.0\ m^2\ s^{-1}$ and $\sim$ 19 min and 67 min for $\nu = 5.0\ m^2\ s^{-1}$ for the two respective initial states. The magnitude of τ_ν in these cases is indicative of the fact that the initial $\bar{\bar{T}}\bar{\bar{K}}\bar{\bar{E}}$ may be dominated by larger scale motions by virtue of Equations (2.12), (2.13) and (4.1) even though the initial wave-length power spectrum of ζ^2 is dominated by the shorter wave lengths. Based on ζ^2, $\tau_\nu \sim$ 24 minutes in both of these cases where $\nu = 1.0\ m^2\ s^{-1}$. The value of τ_ν based on ζ^2 is a better measure of the eddy viscous decay time scale for the smallest scale resolved motions in these cases.

Observations indicate that for environments, which are similar to BASIC 1, small scale convective updrafts in cirriform clouds have lifetimes of order $\sim$ 15 - 20 minutes (Heymsfield, 1975 b, c; Ludlam,

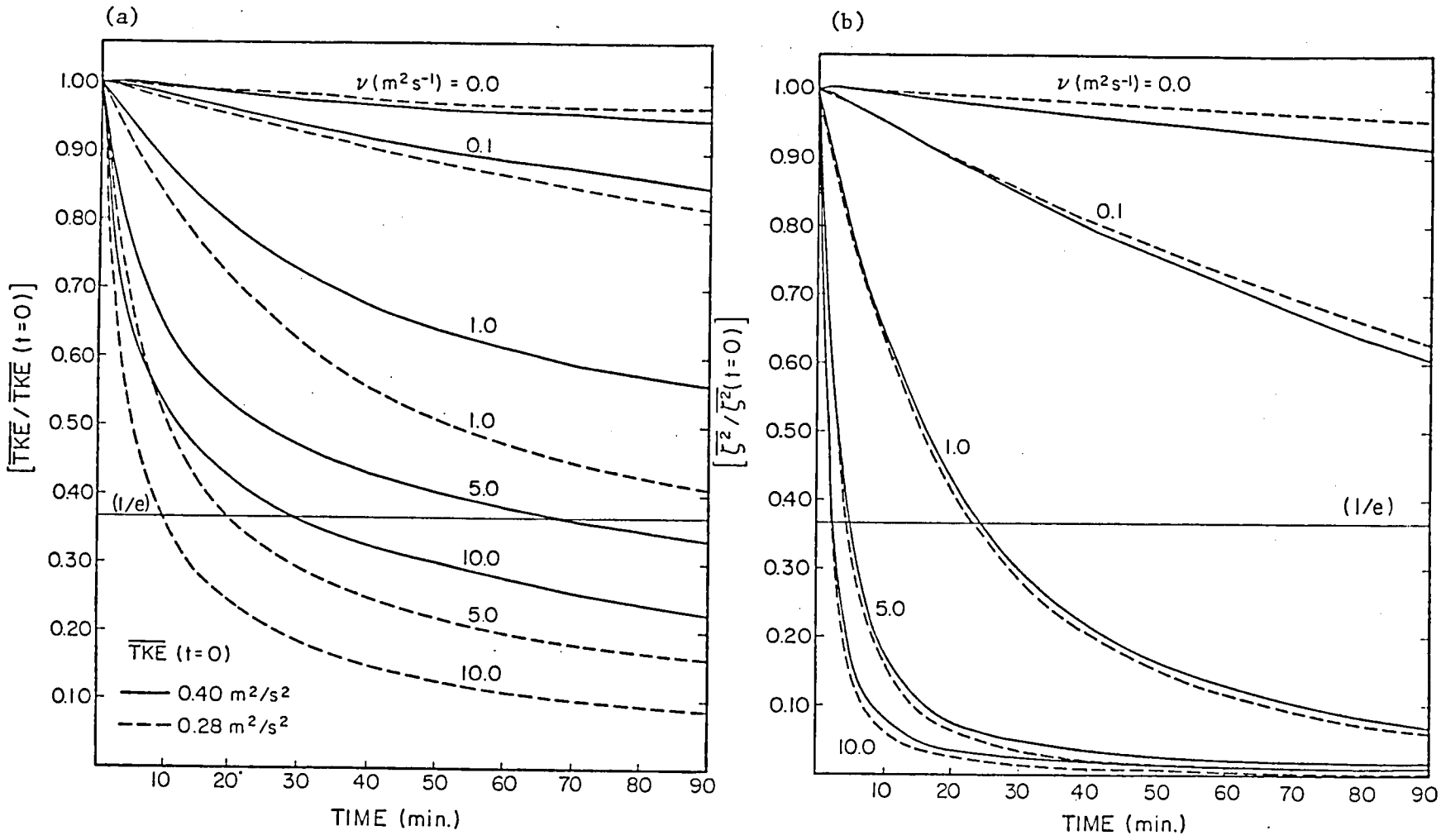

Figure 24. (a) Mean layer perturbation kinetic energy, $\overline{TKE}$, and (b) mean layer perturbation enstrophy, $\overline{\zeta^2}$, versus time for simulations from two different initial states (dashed and solid, respectively) for various specified eddy viscosity coefficients, ν, using a model version where only the advective and eddy viscosity terms are evaluated in the governing dynamic equation. The initial states are each based on random perturbations of the perturbation vorticity, ζ.

1947). A specification of $\tau_\nu \cong 24$ minutes, i.e. $\nu = 1.0\ m^2\ s^{-1}$, seems reasonable since when the thermal and water vapor eddy diffusivity terms are engaged, the value of $\tau = 36$ minutes, noted previously for $\nu = 1.0\ m^2\ s^{-1}$, where buoyancy processes are acting, will be reduced. This is shown in the next section. Hereafter, except where noted, $\nu = 1.0\ m^2\ s^{-1}$ is specified for all simulations. It must be recognized that although the corresponding eddy viscous relaxation time scale seems reasonable, this is a somewhat arbitrary choice. Asai and Nakamura (1978) have used the same value in a similar model (d = 100 m) which successfully simulated atmospheric convection in the atmospheric boundary layer. Only analyses of observation data on turbulent quantities at space scales less than 100 m would allow the most appropriate value of ν to be established. Such data do not presently exist for cirriform cloud layers.

4.3 Thermal and Water Vapor Eddy Diffusivities

The choice of specific numerical values for K_θ and K_q is influenced by both computational and physical considerations. Recall that the eddy diffusivity terms represent the physical process of subgrid scale unresolved transports as described in Chapter 2 and, also, act to eliminate unwanted computational modes due to truncation errors resulting from the finite difference approximations to the continuous form of the advective terms as noted in Section 3.4. Since physically both the thermal and water vapor diffusion are highly related to the unresolved turbulent velocity fields and both are properties of the gas, it seems reasonable to impose the condition that:

$$K \equiv K_q = K_\theta \ . \tag{4.4}$$

Hereafter, this assumption is always made though not always explicitly mentioned. The validity of this assumption is further supported by the computational consideration that the same advective schemes are employed for θ and q. The choice of κ_{ℓ} is deferred since ℓ is not a gas property and the corresponding subgrid scale turbulent wind field must reflect the particle nature of the components of ℓ (e.g. drag forces). The advective scheme also differs from that employed for θ or q.

Two series of experiments were performed. The first is similar to those described in the preceeding sections. The second set of experiments is an attempt to generate results, which are directly comparable to the classic experiments of Arnason et al. (1968) on buoyant convection. The latter experiments are focussed on establishing the computational requirements on κ_{θ}.

The model employed for the first set of experiments incorporates all terms in the governing equations except the phase change, radiative and large scale vertical velocity terms. Thus, the ice water equation is not evaluated. The initial state is BASIC 1 and the perturbation fields are initialized as noted previously, i.e. random perturbations on θ only. In Figure 25, the time dependent behavior of $[\bar{\bar{T}}\bar{\bar{K}}\bar{\bar{E}}/\bar{\bar{T}}\bar{\bar{K}}\bar{\bar{E}}\ (\max)]$ is depicted in the case where κ is specified as equal to 0.0, 1.0, 2.0 and 4.0 $m^2\ s^{-1}$, respectively. In each case, ν = 1.0 $m^2\ s^{-1}$ is specified. Again, only the one-minute values are plotted. As the value of κ_{θ} is increased, the maximum value of $\bar{\bar{T}}\bar{\bar{K}}\bar{\bar{E}}$ achieved during a simulation is decreased. The ratio $[\bar{\bar{T}}\bar{\bar{K}}\bar{\bar{E}}(\max)_{\kappa}/\bar{\bar{T}}\bar{\bar{K}}\bar{\bar{E}}(\max)_{\kappa=0}]$ is 0.928, 0.862, 0.756 in the case of κ = 1.0, 2.0 and 4.0 $m^2\ s^{-1}$, respectively. It should, also, be noted that for κ = 4.0 $m^2\ s^{-1}$, $\bar{\bar{T}}\bar{\bar{K}}\bar{\bar{E}}$

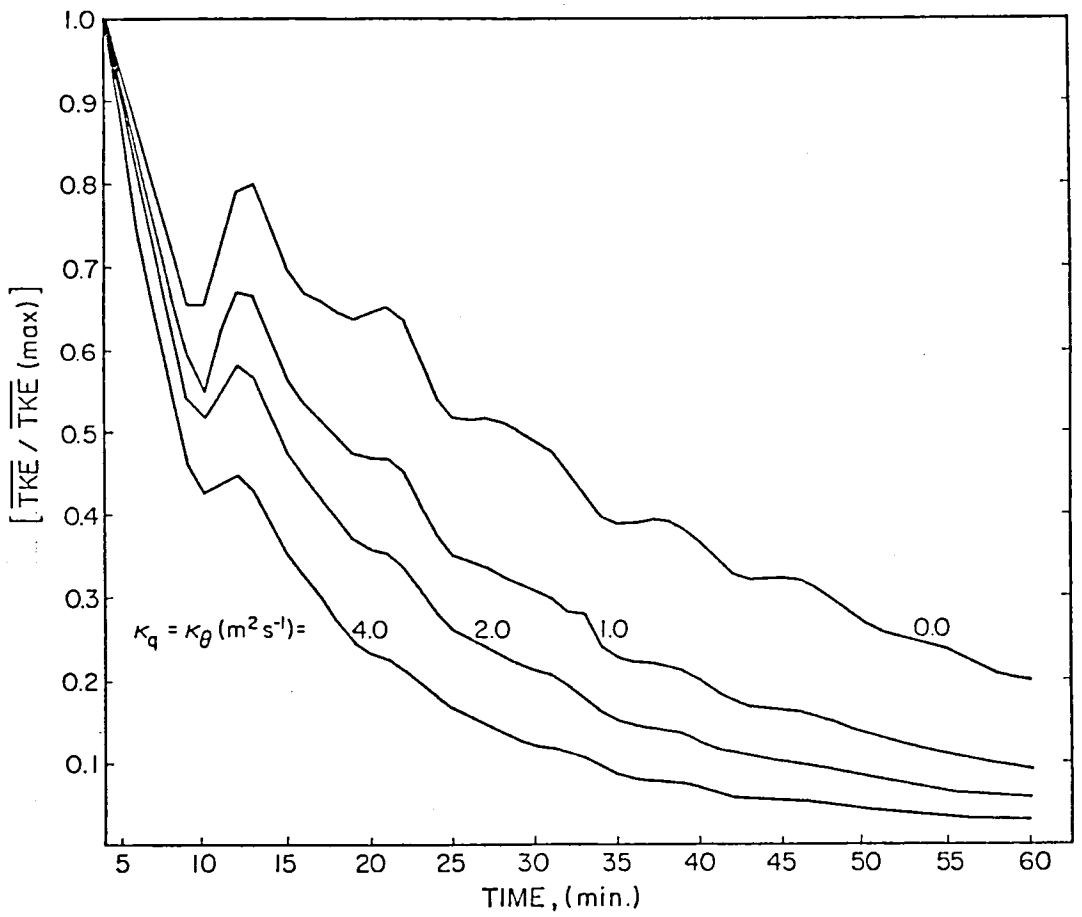

Figure 25. Mean layer perturbation kinetic energy, $\overline{TKE}$, versus time for simulations from an identical initial state (i.e. BASIC 1 and random perturbations of θ) using a model version which is identical in each case except for the specification of the thermal and water vapor eddy diffusivities, K_θ and K_q, respectively. (No phase change or radiative processes included).

(max) occurs at 3.5 minutes instead of 4 minutes as in the other simulations.

The effect of the diffusion terms for θ and q is to smooth the respective gradients of these quantities in space. The smoothing is primarily active on 2d scale waves though as time progresses it affects all scales of the disturbance. Thus, as κ is increased, the horizontal gradients responsible for the buoyant generation of TKE are reduced. Therefore, not only does $\overline{\overline{TKE}}$ (max) decrease as κ is increased, but the decay rate from maximum disturbance intensity is increased. For these simulations, $\tau \cong 36$, 20, 15 and 10 minutes for κ = 0.0, 1.0, 2.0 and 4.0 $m^2\ s^{-1}$. Based on the observations discussed previously, a value of κ = 1.0 - 2.0 $m^2\ s^{-1}$ yields reasonable decay time scales for a disturbance such as simulated here.

An assumption generally employed in first order turbulence closure schemes is that $\nu = \kappa_\theta = \kappa_q$. Asai and Nakamura (1978) make this assumption for a simple first order scheme as here. A comparable assumption is commonly made in more complicated first order schemes (Lilly, 1962). The physical basis for such an assumption is rather tenuous. Fundamentally, the observational information necessary to justify such an assumption is almost totally lacking in the case of middle and upper tropospheric cloud layers.

Before choosing κ_θ, some computational considerations must be made. Such considerations are particularly appropriate for κ_θ, where nonphysical modes in the solution may be readily identified, e.g. the occurrence of negative values of θ in the case of dry convection in a neutral environment. This type of nonphysical mode results from truncation errors due to the finite difference approximation of the

advective term, i.e. linear interpolation for midpoint values between grid points may be inadequate to resolve the true continuous behavior on this space scale. The diffusion term acts to smooth the field on this scale such that the interpolation assumption is more valid and the nonphysical modes are correspondingly suppressed.

The model employed for the following simulations is a dry version. Only the governing dynamic and thermodynamic equations are evaluated. The water terms in the governing dynamic equation, i.e. in B, are eliminated as are the phase change and radiative terms in the thermodynamic equation. Also deleted are the eddy viscous diffusion term (i.e. $\nu = 0$) and the basic state vertical velocity term. The eddy thermal diffusion term is retained. This version of the model is very similar to a dry model reported by Arnason et al. (1968), hereafter denoted A. Their numerical techniques are substantially different than those employed here. The major difference is in the time integration scheme employed for the thermodynamic equation. They use the Lax-Wendroff two-step scheme described by Richtmyer (1962). Effectively, this scheme simulates an eddy diffusion term where the local thermal eddy diffusivity is diagnosed from the specified values of d, Δt and the local wind component. In this sense, their model incorporates a variable κ_θ. As will be seen later, the advective scheme, when coupled with the time integration scheme, is consequently nonconservative in θ. The thermal eddy diffusion term is formally retained in the model here though it does not formally appear in their governing equations.

The same spacial domain and grid geometry, noted previously, are employed. These are identical in the case of d and nearly identical

in the case of I and K to those employed by A. The potential temperature basic state is initialized to 294°K everywhere, i.e. neutral, and the disturbance is initialized via perturbation potential temperature to a warm bubble as shown in Figure 26. Again this is nearly identical to that employed by A. Note that the fields are symmetric about x = 3.15 km. Also, $z = h_B \equiv 0$. The maximum value of θ is 0.38°K. Recall that this value is much larger than anticipated in the case of cirriform cloud layers. A time step of Δt = 15 seconds is prescribed due to the anticipated wind speeds.

Simulations from this initial state were carried out for four specified values of κ_θ, i.e. κ_θ = 0.0, 2.5, 5.0 and 7.5 $m^2\ s^{-1}$. The simulations were terminated after 20 minutes as the boundary conditions begin to influence the disturbance in an unrealistic manner at this point. In Figures 27, 28 and 29, the fields of perturbation potential temperature are shown after 5, 10 and 20 minutes of simulated time, respectively, for each κ_θ experiment. The corresponding fields of ψ are shown in Figures 30, 31 and 32. They are negatively symmetric about x = 3.15 km. For comparison, the fields of θ and ψ after 5 and 10 minutes of simulated time, which were given by A, are reproduced in Figure 33. Note that the units employed here for ψ are different by a factor of 10^2 from those employed by A.

As seen in Figure 27, the effect of increasing the specified value of κ_θ is to decrease the maximum thermal perturbation, which is very noticeable even after 5 minutes for the values employed here. Similarly, the growth in the intensity of the circulation is comparably reduced (Figure 30). These effects persist in time as seen in the remaining figures. It is of note that the thermal pattern evolves

t = 0 minutes

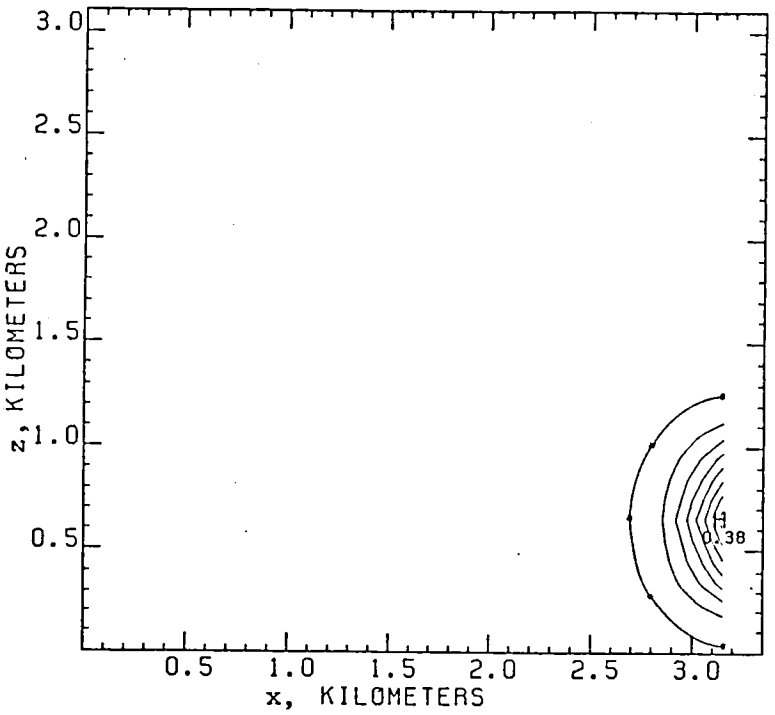

Figure 26. Initial perturbation potential temperature, θ, in °C as in Arnason et al. (1968). Note that the field is symmetric about x = 3.15 km. The contour interval is 0.05°C and the * line indicates the θ = 0°C contour (in this case, θ = 0°C everywhere outside this contour).

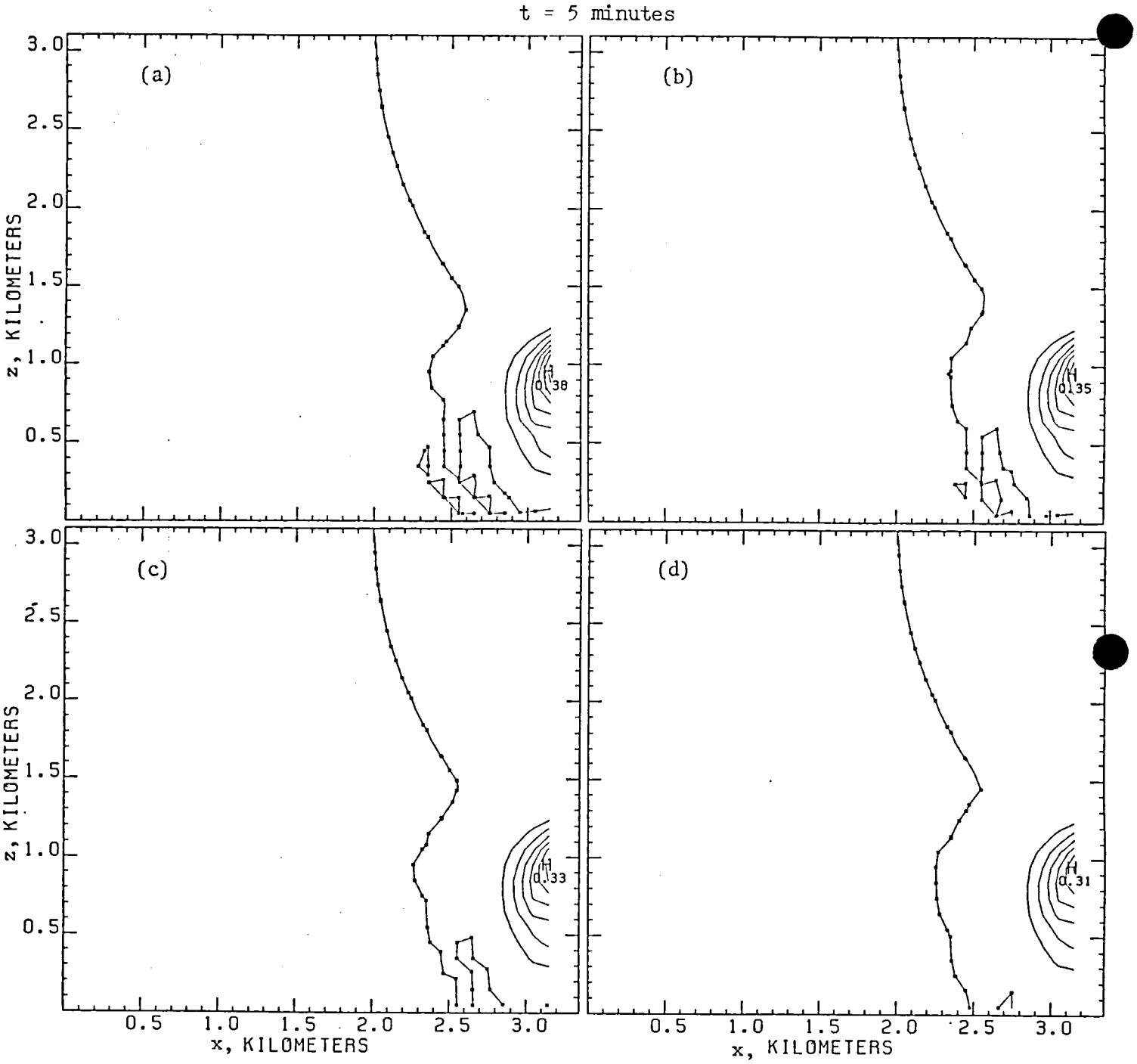

Figure 27. Perturbation potential temperature, θ, in °C after 5 minutes of simulated time for simulations from an identical initial state (i.e. statically neutral basic state and initial thermal perturbation field as depicted in Figure 26) using a dry model version identical in each case except for the specification of the thermal eddy diffusivity, κ_θ = 0.0 (a), 2.5 (b), 5.0 (c), 7.5 (d) $m^2\ s^{-1}$. Note that the simulations are symmetric about x = 3.15 km. The contour interval is 0.05°C and the * line indicates the θ = 0°C contour.

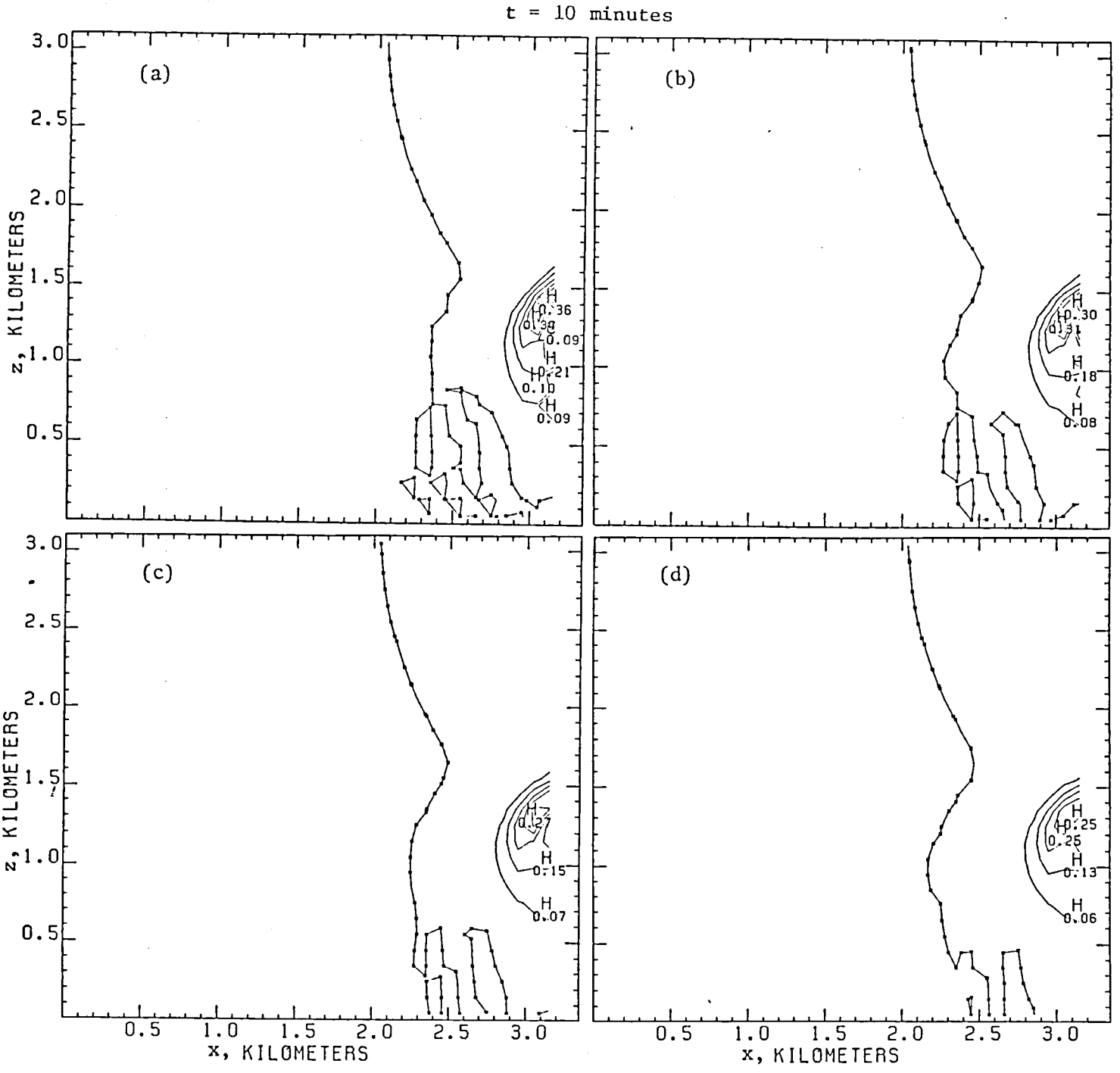

Figure 28. Same as Figure 27, except at t = 10 minutes simulated time.

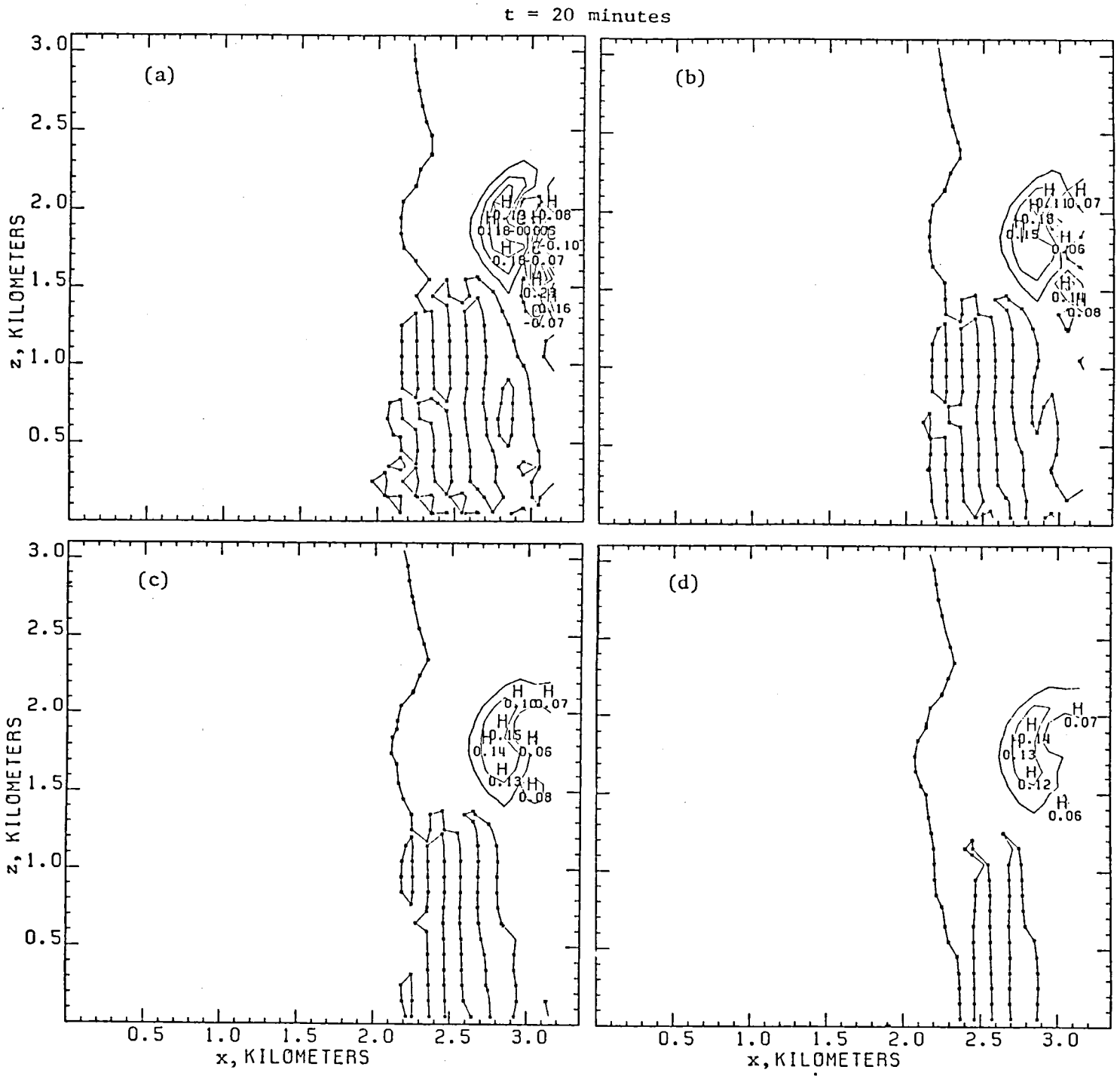

Figure 29. Same as Figure 27, except at t = 20 minutes simulated time.

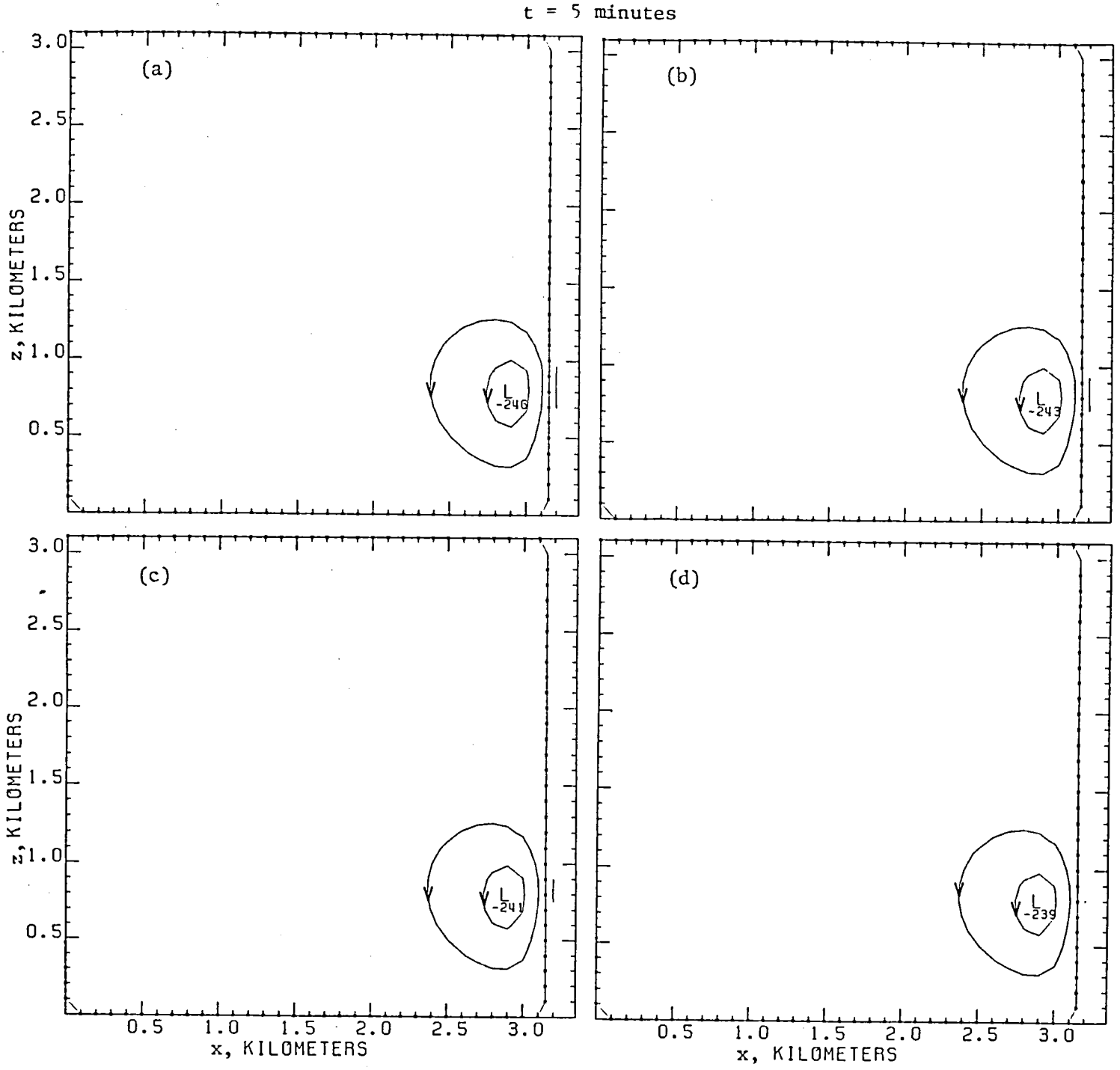

Figure 30. Perturbation stream function, ψ, in $m^2 \cdot s^{-1}$ after 5 minutes simulated time for simulations from an identical initial state (i.e. statically neutral basic state and initial thermal perturbation field as depicted in Figure 26) using a dry model version identical in each case except for the specification of the thermal eddy diffusivity, K_θ = 0.0 (a), 2.5 (b), 5.0 (c) and 7.5 (d) $m^2\ s^{-1}$. Note that the simulations are symmetric about x = 3.15 km. The contour inverval is 100 $m^2\ s^{-1}$ and the arrows indicate the direction of the flow.

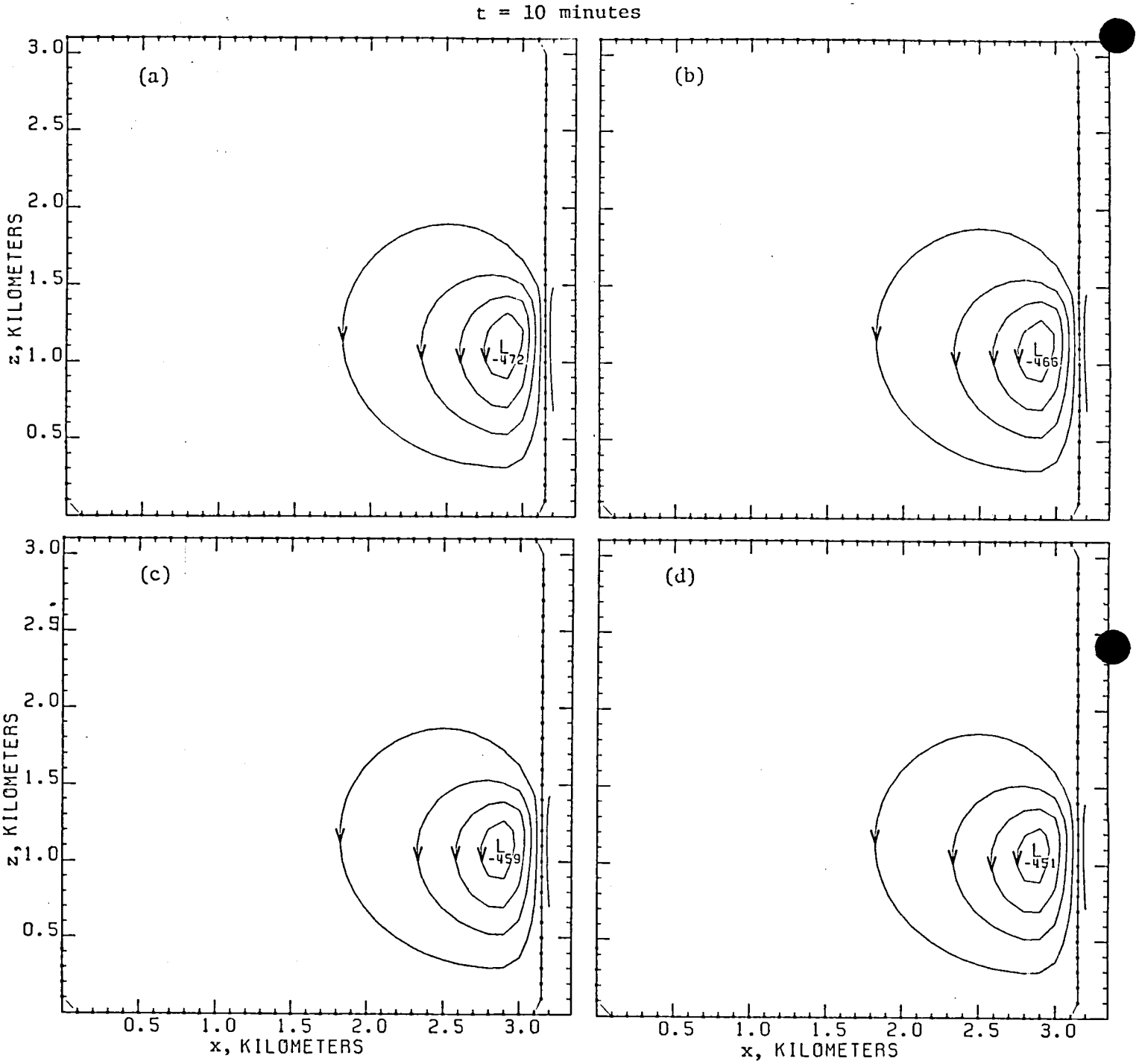

Figure 31. Same as Figure 30, except at t = 10 minutes simulated time.

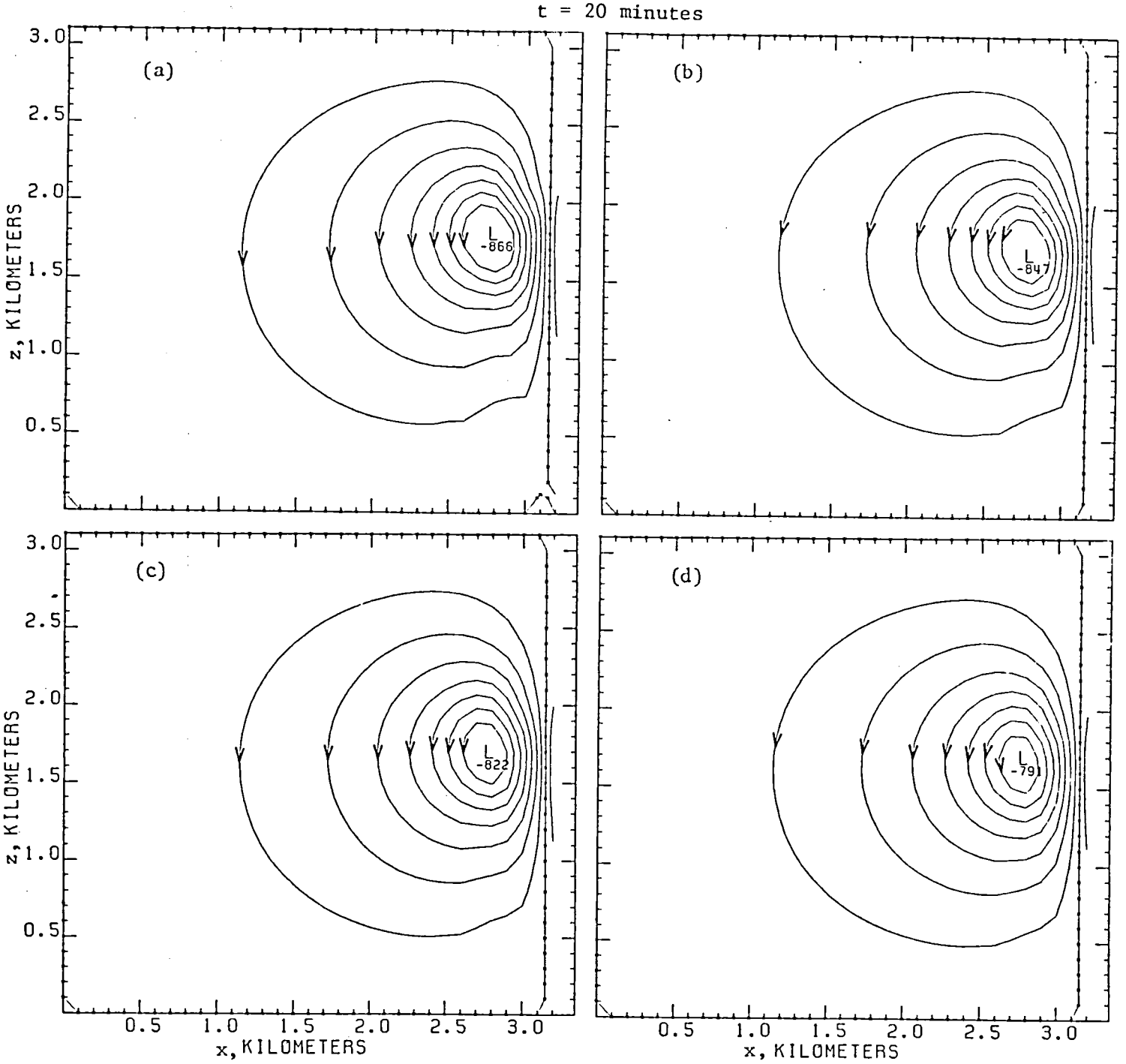

Figure 32. Same as Figure 30, except at t = 20 minutes simulated time.

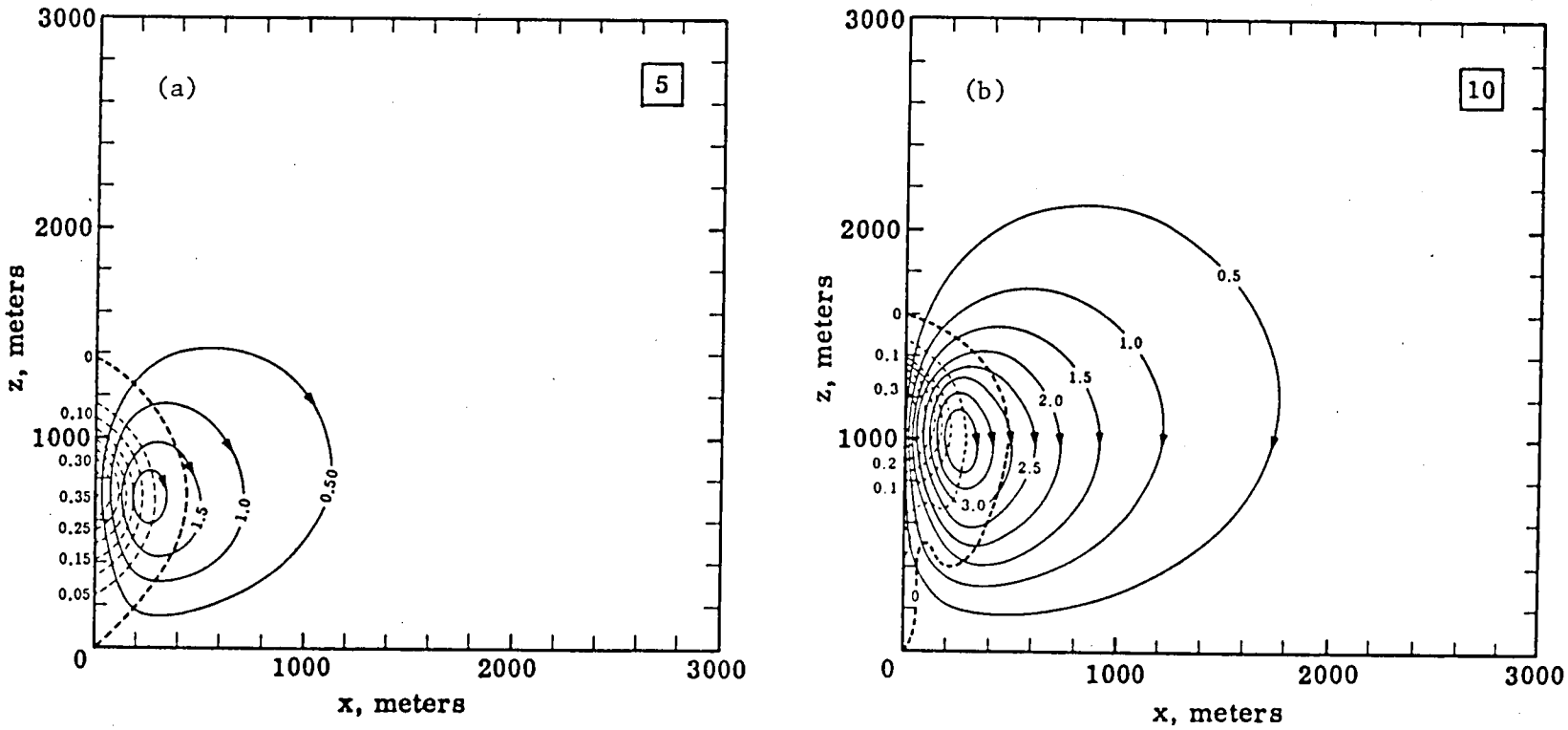

Figure 33. Perturbation potential temperature, θ, in °C (dashed lines) and perturbation streamfunction, ψ, in $m^2\ s^{-1}$ times 10^{-2} (solid lines) after (a) 5 minutes and (b) 10 minutes simulated time for simulations of dry convection in a statically neutral environment initialized approximately as in Figure 26. (From Arnason et al., 1968).

to a mushroom-shaped bubble by 10 minutes (Figure 28). This is very similar to the results of A (Figure 33). At this time, the first significant indication of a nonphysical mode, i.e. $\theta < 0$, occurs in the center of the disturbance in the case of $\kappa_\theta = 0$. After 20 minutes, the thermal perturbation pattern has become even more deformed in all cases (Figure 29). In three dimensions, the pattern may be interpreted as a ring in the horizontal much like a smoke ring. In the case of $\kappa_\theta = 0$, the nonphysical mode predominates in the central core of the bubble. The amplitude of this mode is substantial. This region corresponds to the region of highest wind velocity as may be deduced from Figure 32.

The $\theta < 0$ mode occurs in each simulation though its magnitude is suppressed as κ_θ is increased. This may be seen in Figure 34, where the minimum value of θ occurring within the domain is plotted as a function of time at one-minute intervals for each simulation. Prior to t = 8 minutes, the $\theta < 0$ mode is relatively insignificant in all cases. In the case of $\kappa_\theta = 7.5\ m^2\ s^{-1}$, the $\theta < 0$ mode is almost totally suppressed at all times. The maximum amplitude of the $\theta < 0$ mode may be tolerable in the case of $\kappa_\theta = 5\ m^2\ s^{-1}$ while for $\kappa_\theta = 2.5\ m^2\ s^{-1}$, it is too large to ignore.

The time dependent behavior of the maximum thermal perturbation is shown in Figure 35 for each simulation. Only the one-minute values are plotted as the 15-second values are somewhat more noisy. The data points corresponding to the simulation reported by A are included for comparison. Physically, each curve should be monotonically decreasing with time as it is impossible to mix two parcels of air and achieve a higher potential temperature than either had initially. Again, the

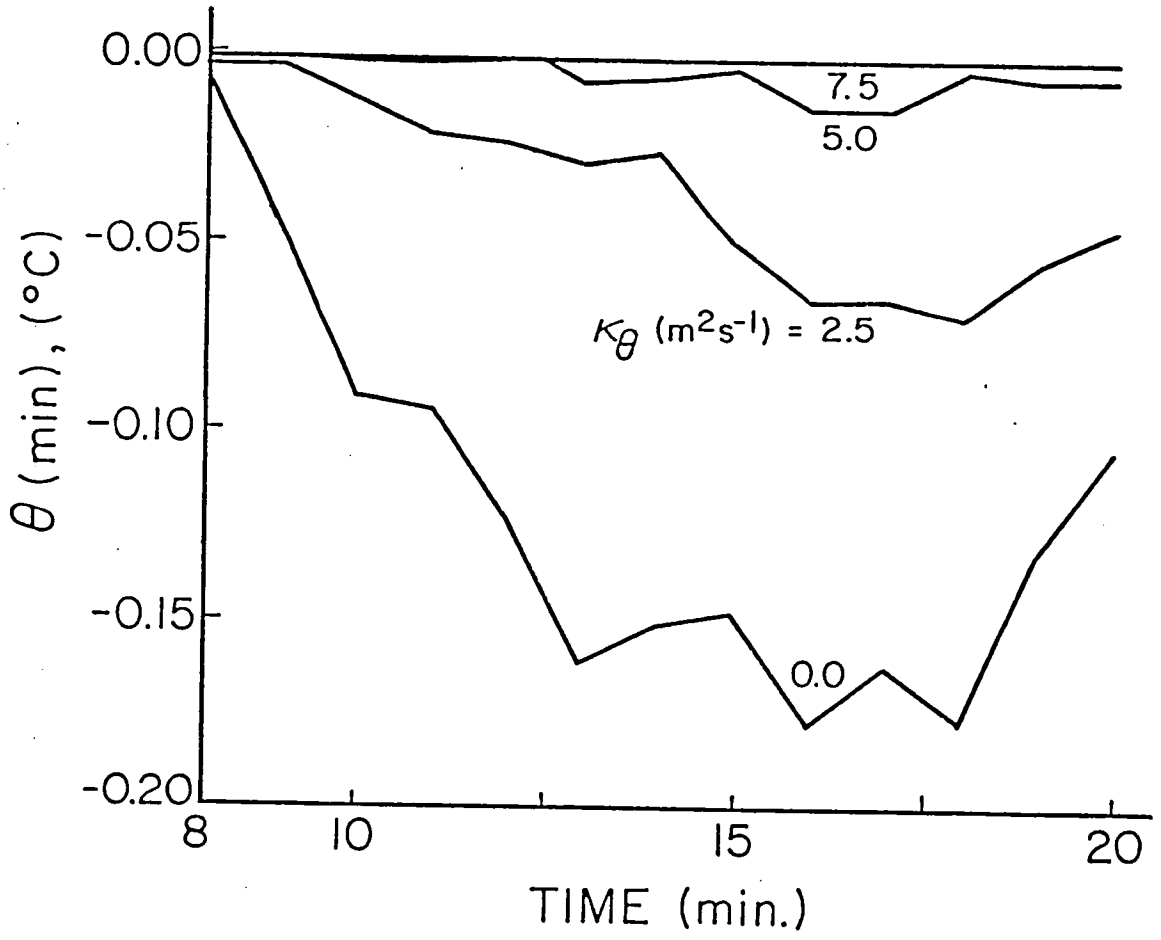

Figure 34. Minimum value of perturbation potential temperature, θ, occurring within the domain as a function of time for simulations from the same initial state (neutral basic state and initial thermal perturbation fields depicted in Figure 26) using a dry model version identical in each case except for the specification of the thermal eddy diffusivity, κ_θ.

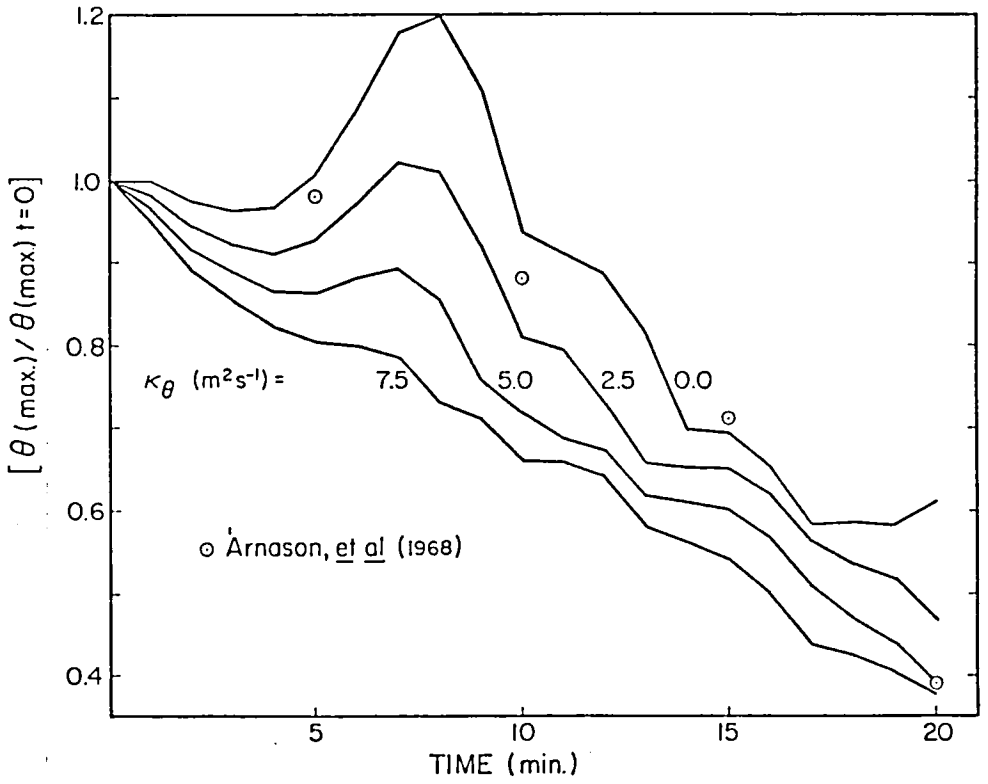

Figure 35. Same as Figure 34, except for maximum value of perturbation potential temperature.

κ_θ = 7.5 m^2 s^{-1} simulation almost totally suppressed this computational mode while the results for κ_θ = 5.0 m^2 s^{-1} exhibit a tolerable error. The diffusive effect of the resolved wind field may be quantified by the decay of $\theta_{max}(t)$ from its maximum value in the case of κ_θ = 0. The additional diffusive effect of the unresolved turbulent wind field, i.e. thermal eddy diffusion, is seen to be of secondary importance in modulating θ_{max} in all cases for the values of κ_θ invoked here.

It is of note that vertical wind speeds in excess of 2.5 m s^{-1} occur after $\sim$ 10 minutes simulated time in all cases. This together with the fact that the initial thermal perturbation is over twice the magnitude that is anticipated in the model application here, i.e. cirriform cloud layers, leads to the conclusion that truncation errors and the resulting nonphysical modes will be much less of a problem than in these example cases. For the cirriform cloud application, where the vertical wind speeds are likely to be less than 0.8 m^2 s^{-1}, $\kappa_\theta \simeq$ 1.0 m^2 s^{-1} yields relative errors comparable to the κ_θ = 5.0 m^2 s^{-1} case here.

For completeness, the energetics of these simulations are considered. Following from A, the potential energy is defined here as:

$$PE = - (\theta/\theta_o)\ g\ z \qquad (4.4)$$

and, thus, is a perturbation potential energy and is always negative. In Table 6, the simulation here with κ_θ = 5 m^2 s^{-1} is compared to that of A. It may be immediately concluded that the model of A is not conservative in potential temperature, i.e. $\bar{\theta}$. As noted previously, this is a consequence of their formulation of the Lax-Wendroff scheme where

Time (min)	$[\bar{\theta}/\bar{\theta}(t=0)]$		$\bar{T}\bar{K}\bar{E}$ $(m^2\ s^{-2}) \times 10^2$		$[(\bar{P}\bar{E}(t=0) - \bar{P}\bar{E})/\bar{T}\bar{K}\bar{E}]$	
0	1.00	1.00	0.0	0.0	-	-
5	1.00	1.00	1.3	1.5	1.00	1.01
10	0.99	1.00	5.2	5.1	0.94	1.01
15	0.93	1.00	10.0	9.1	0.88	1.01
20	0.86	1.00	13.8	12.5	0.81	1.01

Table 6. Comparison between the present experiment with $\kappa_\theta = 5\ m^2\ s^{-1}$ (right-hand columns) and that of Arnason *et al.* (1968) (left-hand columns). See text for definition and discussion.

the point-point exchanges are not mutually conservative. The model here is much superior in this regard. The buoyant generation of $\bar{\bar{T}}\bar{\bar{K}}\bar{\bar{E}}$ is very comparable in the two simulations. The model of A exhibits a somewhat more intense circulation through the latter stages of the simulations. As a consequence of the nonconservation of θ, the energy transformation PE → TKE shows a loss in total energy as time progresses in the experiment of A, i.e. PE is being lost without being transformed to TKE. Given this, it is somewhat surprising that their values of $\bar{\bar{T}}\bar{\bar{K}}\bar{\bar{E}}$ are larger than the values here at most times. However, this may be explained by noting that their effective thermal diffusivity may be less than 5 m^2 s^{-1} when averaged over the disturbed region though it is locally much larger in the core. For example, the κ_θ = 2.5 m^2 s^{-1} simulation yielded larger values of $\bar{\bar{T}}\bar{\bar{K}}\bar{\bar{E}}$ by about 4% at all times when compared to the κ_θ = 5.0 simulation. The seeming gain in total energy for the present experiment is not actually a gain. The filtered leap frog scheme employed here leads to a slight damping (η = 0.3) in the $\bar{\bar{T}}\bar{\bar{K}}\bar{\bar{E}}$. Thus, a small amount of $\bar{\bar{T}}\bar{\bar{K}}\bar{\bar{E}}$ is being continuously lost after the PE → TKE conversion. This effect is comparable to a slight eddy viscous damping of the system.

In conclusion, the model performance is very satisfactory to this point. The simulations show a high degree of realism when considering the evolution of the shape of a warm bubble in a neutral environment. In some aspects, namely the numerical techniques and the enforcement of physical conservation laws, the model may be regarded as superior to some previously reported models of an essentially similar nature. For the application envisioned here, a choice of $\kappa_\theta = \kappa_q$ = 1.0 m^2 s^{-1} should adequately suppress nonphysical computational modes arising

from truncation errors. Given the previous choice of $\nu = 1.0\ m^2\ s^{-1}$ this value gives a reasonable decay time ($\tau \simeq 20$ min) for disturbances typical of cirrus cloud layers where only buoyancy forces and eddy processes are acting (i.e. viscous, thermal and water vapor diffusion) in the absence of any internal energy sources or external forcing. Taken together, these choices for ν, κ_θ and κ_q are consistent with those made by other workers, e.g. Asia and Nakamura (1978) and Lilly (1965). These values are used in all succeeding simulations unless noted otherwise.

REFERENCES

Allen, J. R., 1971: Measurement of cloud emissivity in the 8-13 μ waveband. J. Appl. Meteor., 10, 260-265.

Arakawa, A., 1966: Computational design for long-term numerical integration of the equations of fluid motion: two-dimensional incompressible flow. Part I. J. Comp. Phys., 1, 119-143.

Arnason, G., R. S. Greenfield and E. A. Newburg, 1968: A numerical experiment in dry and moist convection including the rain stage. J. Atmos. Sci., 25, 404-415.

Asai, T., and K. Nakamura, 1978: A numerical experiment of airmass transformation over warmer sea. Part I: Development of a convectively mixed layer. J. Meteor. Soc. Japan, 56, 424-434.

Asselin, R., 1972: Frequency filter for time integrations. Mon. Wea. Rev., 100, 487-490.

aufm Kampe, H. J., H. K. Weickmann and J. J. Kelly, 1951: The influence of temperature on the shape of ice crystals growing at water saturation. J. Meteor., 8, 168-174.

Ball, F. K., 1956: Energy changes involved in disturbing a dry atmosphere. Quart. J. Roy. Meteor. Soc., 82, 15-29.

Beard, K. V., and H. R. Pruppacher, 1969: A determination of the terminal velocity and drag of small water drops by means of a wind tunnel. J. Atmos. Sci., 26, 1066-1072.

Berson, F., 1967: Layer echoes from under a canopy of high cloud. Aust. Meteor. Mag., 15, 205-224.

Betts, A. K., 1973a: A composite mesoscale cumulonimbus budget. J. Appl. Meteor., 30, 597-610.

_____, 1973b: Non-precipitating cumulus convection and its parameterization. Quart. J. Roy. Meteor. Soc., 99, 178-196.

Braham, R. R., Jr., and P. Spyers-Duran, 1967: Survival of cirrus crystals in clean air. J. Appl. Meteor., 6, 1053-1061.

Carnahan, B., H. A. Luther and J. O. Wilkes, 1969: Applied Numerical Methods. John Wiley and Sons, New York, 604 pp.

Conover, J., 1960: Cirrus patterns and related air motions near the jet stream as derived by photography. J. Meteor., 17, 532-546.

Cotton, W. R., and G. J. Tripoli, 1978: Cumulus convection in shear flow, three dimensional numerical experiments. J. Atmos. Sci., 35, 1503-1521.

Cox, S. K., 1969: Radiation models of midlatitude synoptic features. Mon. Wea. Rev., 97, 637-651.

_____, 1971: Cirrus clouds and the climate. J. Atmos. Sci., 28, 1513-1515.

_____, 1973: Infrared heating calculations with a water vapor pressure broadened continuum. Quart. J. Roy. Meteor. Soc., 99, 669-679.

_____, 1976: Observations of cloud infrared effective emissivity. J. Atmos. Sci., 33, 287-289.

_____, M. C. Polifka, K. Griffith, A. Rockwood and D. Starr, 1976: Radiative transfer computational routines for atmospheric science applications. Colorado State University Atmospheric Science Report, Ft. Collins, CO., 75 pp.

Davis, J. M., S. K. Cox and T. B. McKee, 1978: Solar absorption in clouds of finite horizontal extent. Atmos. Sci. Paper 282, Colo. State Univ., Ft. Collins, CO., 92 pp. (NTIS PB 286 834)

Deirmendjian, D., 1969: Electromagnetic Scattering on Spherical Polydispersions. Elsevier, New York, 290 pp.

Douglas, R. H., K. L. X. Gunn and J. S. Marshall, 1957: Pattern in the vertical of snow generation. J. Meteor., 14, 95-108.

Foltz, G. S., and W. M. Gray, 1979: Diurnal variation in the troposphere's energy balance. J. Atmos. Sci., 36, 1450-1466.

Goody, R. M., 1964: Atmospheric Radiation: Theoretical Basis. Clarendon Press, Oxford, 436 pp.

Griffith, K. T., S. K. Cox and R. C. Knollenberg, 1980: Infrared radiative properties of tropical cirrus clouds inferred from aircraft measurements. J. Atmos. Sci., 37, 1073-1083.

Hack, J. J., and W. H. Schubert, 1976: Design of an axisymmetric primitive equation tropical cyclone model. Atmos. Sci. Paper 263, Colo. State Univ., Ft. Collins, CO., 70 pp. (NTIS PB 268 813)

Hall, W. D., and H. R. Pruppacher, 1976: The survival of ice particles falling from cirrus clouds in subsaturated air. J. Atmos. Sci., 33, 1995-2006.

Haltiner, G. J., 1971: Numerical Weather Prediction. John Wiley and Sons, New York, 317 pp.

Hess, S. L., 1959: Introduction to Theoretical Meteorology. Holt, Rinehart and Winston, New York, 362 pp.

Heymsfield, A. J., 1972: Ice crystal terminal velocities. J. Atmos. Sci., 29, 1348-1356.

_____, and R. G. Knollenberg, 1972: Properties of cirrus generating cells. J. Atmos. Sci., 29, 1358-1366.

_____, 1974: Ice crystal growth in deep cirrus systems. Preprints Vol., Conf. on Cloud Physics, A.M.S., Tucson, 311-316.

_____, 1975a: Cirrus uncinus generating cells and the evolution of cirriform clouds. Part I: The structure and circulations of the cirrus uncinus generating head. J. Atmos. Sci., 32, 799-808.

_____, 1975b: Cirrus uncinus generating cells and the evolution of cirriform clouds. Part II: The structure and circulations of the cirrus uncinus generating head. J. Atmos. Sci., 32, 809-819.

_____, 1975c: Cirrus uncinus generating cells and the evolution of cirriform clouds. Part III: Numerical computations of the growth of the ice phase. J. Atmos. Sci., 32, 820-830.

_____, 1977: Precipitation development in stratiform ice clouds: A microphysical and dynamical study. J. Atmos. Sci., 34, 367-381.

Hobbs, P. V., L. F. Radke and D. G. Atkinson, 1975: Airborne measurements and observations in cirrus clouds. AFCRL-TR-75-0249, 117 pp.

Holton, J. R., 1972: An Introduction to Dynamic Meteorology. Academic Press, New York, 319 pp.

Hunt, G. E., 1973: Radiative properties of terrestrial clouds at visible and infrared thermal window wavelengths. Quart. J. Roy. Meteor. Soc., 99, 346-369.

Jayaweera, K. O. L. F., 1971: Calculations of ice crystal growth. J. Atmos. Sci., 28, 728-736.

Knollenberg, R. G., 1970: The optical array: An alternative to scattering or extinction for airborne particle size determinations. J. Appl. Meteor., 9, 86-103.

Kraus, E. B., 1972: Atmosphere-Ocean Interaction. Clarendon Press, Oxford, 275 pp.

Lilly, D. K., 1962: On the numerical simulation to buoyant convection. Tellus, 14, 148-172.

_____, 1965: On the computational stability of numerical solutions of time-dependent non-linear geophysical fluid dynamics problems. Mon. Wea. Rev., 93, 11-26.

Lilly, D. K., 1968: Models of cloud-topped mixed layers under a strong inversion. Quart. J. Roy. Meteor. Soc., 105, 303-306.

Liou, K. N., 1972: Light scattering by ice clouds in the visible and infrared: A theoretical study. J. Atmos. Sci., 30, 524-536.

_____, 1973: Transfer of solar irradiance through cirrus cloud layers. J. Geophys. Res., 78, 1409-1418.

_____, 1974: On the radiative properties of cirrus in the window region and their influence on remote sensing of the atmosphere. J. Atmos. Sci., 31, 522-532.

Lipps, F. B., 1971: Two-dimensional numerical experiments in thermal convection with vertical shear. J. Atmos. Sci., 28, 3-19.

List, R. J., 1966: Smithsonian Meteorological Tables. Smithsonian Institution, Washington, D.C., 527 pp.

Locatelli, J. P., and P. V. Hobbs, 1974: Fall speeds and masses of solid precipitation particles. J. Geophys. Res., 79, 2185-2197.

London, J., 1957: A study of the atmospheric heat balance. Final Report, Contract No. AF19(122)-165, Department of Meteorlogy and Oceanography, New York University, July, 99 pp.

Lorentz, E. N., 1967: The nature and theory of the general circulation of the atmosphere. World Meteorological Organization, No. 218, TP 115, 161 pp.

_____, 1976: A rapid procedure for inverting Del-Square with certain computers. Mon. Wea. Rev., 104, 961-966.

Lowe, P. R., 1977: An approximating polynomial for the computation of saturation vapor pressure. J. Appl. Meteor., 16, 100-103.

Ludlam, F. H., 1947: The forms of ice clouds. Quart. J. Roy. Meteor. Soc., 74, 39-56.

_____, 1956: The forms of ice clouds, II. Quart. J. Roy. Meteor. Soc., 82, 257-265.

Machta, L., and T. Carpenter, 1971: Trends in high cloudiness at Denver and Salt Lake City. STUDY of Man's Impact on Climate, MIT Press, Cambridge, 410-415.

Manabe, S., and R. F. Strickler, 1964: Thermal equilibrium of the atmosphere with a convective adjustment. J. Atmos. Sci., 21, 361-385.

_____, and R. T. Wetherald, 1967: Thermal equilibrium of the atmosphere with a given distribution of relative humidity. J. Atmos. Sci., 21, 241-259.

Manton, J. J., and W. R. Cotton, 1977: Formulation of approximate equations for modelling moist deep convection on the mesoscale. Atmos. Sci. Paper 266, Colo. State Univ., Ft. Collins, CO., 62 pp. (NTIS PB 267 592)

Marshall, J. S., M. P. Langleben and E. C. Rigby, 1952: Precipitation trajectories and patterns. McGill University Stormy Weather Group Scientific Report MW-8, 23 pp.

Mason, B. J., 1971: The Physics of Clouds. Clarendon Press, Oxford, 671 pp.

Matvejev, L. T., 1965: The dynamics of formation and the forecast of stratiform cloud systems. International Symposium of Dynamics of Large-Scale Processes in the Atmosphere, Academy of Sciences of the U.S.S.R., Moscow, 36 pp.

McBride, J. L., and W. M. Gray, 1980: Mass divergence in tropical weather systems. Paper I: Diurnal variations. Quart. J. Roy. Meteor. Soc., 106, 501-516.

Oddie, B. C. V., 1959: Some cirrus cloud observations made by the Westminster Shiant Isles Expedition, 1958. Weather, 4, 204-208.

Ogura, Y., and N. A. Phillips, 1962: Scale analysis of deep and shallow convection in the atmosphere. J. Atmos. Sci., 19, 173-179.

Oliver, D. A., W. S. Lewellen and G. G. Williamson, 1978: The interaction between turbulent and radiative transport in the development of fog and low-level stratus. J. Atmos. Sci., 35, 301-316.

Ono, A., 1970: Growth made of ice crystals in natural clouds. J. Atmos. Sci., 27, 649-658.

Paltridge, G. W., 1974: Infrared emissivity, shortwave albedo, and the microphysics of stratiform water clouds. J. Geophys. Res., 79, 4053-4058.

_____, and C. M. R. Platt, 1980: Aircraft measurements of solar and infrared radiation and the microphysics of cirrus clouds. Vol. of Extended Abstracts, International Radiation Symposium, Ft. Collins, CO., Aug. 11-16, 419-421.

Phillips, N. A., 1956: The general circulation of the atmosphere: A numerical experiment. Quart. J. Roy. Meteor. Soc., 82, 123-164.

Plank, V. G., D. Atlas and W. H. Paulsen, 1955: The nature and detectability of clouds and precipitation as determined by 1.25 centimeter radar. J. Meteor., 12, 358-378.

Platt, C. M. R., D. W. Reynolds and N. C. Abshire, 1980: Satellite and lidar observations of the albedo, emittance and optical depth of cirrus compared to model calculations. Mon. Wea. Rev., 108, 195-204.

Randall, D. A., 1980: Entrainment into a stratocumulus layer with disturbed radiative cooling. J. Atmos. Sci., 37, 148-159.

Reynolds, D. W., T. H. Vonder Haar and S. K. Cox, 1975: The effect of solar radiation in the tropical troposphere. J. Appl. Meteor., 14, 433-444.

_____, and T. H. Vonder Haar, 1977: A bispectral method for cloud parameter determination. Mon. Wea. Rev., 105, 446-457.

Rhea, J. O., 1978: Orographic precipitation model for hydrometeorological use. Atmos. Sci. Paper 287, Colo. State Univ., Ft. Collins, CO., 221 pp. (NTIS PB 296 514)

Richtmyer, R. D., 1962: A survey of different methods for non-steady fluid dynamics. NCAR Tech. Notes, 63-2, 1-25.

Roach, W. T., and M. J. Bader, 1977: On the effects of radiative transfer on the growth of droplets and ice crystals in layer clouds. Proc. Sym. on Radiation in the Atmos., Garmisch-Partenkirchen, FRG., Aug., Scientific Press, Princeton, 239-241.

Schaefer, V. J., 1951: Snow and it's relationship to experimental meteorology. Comp. of Meteor., AMS, 221-234.

Schlichting, H., 1968: Boundary Layer Theory. 6th Edition, Mc-Graw-Hill, New York, 748 pp.

Schneider, S. H., W. M. Washington and R. M. Chervin, 1978: Cloudiness as a climate feedback mechanism: Effects on cloud amounts of prescribed global and regional surface temperature changes in the NCAR GCM. J. Atmos. Sci., 35, 2207-2221.

Schubert, W. H., J. S. Wakefield, E. J. Steiner and S. K. Cox, 1979: Marine stratocumulus convection, Part I: Governing equations and horizontally homogeneous solutions. J. Atmos. Sci., 36, 1286-1307.

Shenk, W. E., and R. J. Curran, 1973: A multispectral method for estimating cirrus cloud top heights. J. Appl. Meteor., 12, 1213-1216.

Smagorinsky, J., 1960: On the dynamical prediction of large-scale condensation by numerical methods. Geophys. Mono., No. 5, Amer. Geophys. Union, Washington, D.C., 71-78.

Sommeria, G., 1976: Three dimensional simulation of turbulent processes in the undisturbed trade wind boundary layer. J. Atmos. Sci., 33, 216-241.

_____, and J. W. Deardorff, 1977: Sub-grid scale condensation in models of nonprecipitating clouds. J. Atmos. Sci., 34, 344-355.

Starr, D. O'C., 1976: The sensitivity of tropical radiative budgets to cloud distribution and the radiative properties of clouds. Atmos. Sci. Paper 254, Colo. State Univ., Ft. Collins, CO., 117 pp. (NTIS PB 263 227)

_____, and S. K. Cox, 1977: Review of the radiation computations in large scale atmospheric models. Unpublished report available from authors, 26 pp.

_____, and S. K. Cox, 1980: Characteristics of middle and upper tropospheric clouds as deduced from rawinsonde data. Atmos. Sci. Paper 327, Colo. State Univ., Ft. Collins, CO., 72 pp.

Stephens, G. L., 1978: Radiation profiles in extended water clouds. Part II: Parameterization schemes. J. Atmos. Sci., 35, 2123-2132.

_____, 1980: Radiative transfer on a linear lattice: Applications to anisotropic ice crystal clouds. J. Atmos. Sci., 39, 2095-2104.

Sundquist, H., 1978: A parameterization scheme for non-convective condensation including prediction of cloud water content. Quart. J. Roy. Meteor. Soc., 104, 677-690.

_____, 1980: Stratiform clouds as a prognostic variable in a global prediction model: Results from a five day forecast. Report DM-31, Dept. of Meteorology, Univ. of Stockholm, 38 pp.

Swarztrauber, P., and R. Sweet, 1975: Efficient Fortran subprograms for the solution of elliptic equations. NCAR TN/IA-109, July, 138 pp.

Sweet, R. A., 1977: A cyclic reduction algorithm for solving black tridiagonal systems of arbitrary dimension. SIAM J. Numer. Anal., 14, 706-720.

Twomey, S., 1976: Computations of the absorption of solar radiation by clouds. J. Atmos. Sci., 33, 1087-1091.

Varley, D. J., 1978: Cirrus particle distribution study, Part I. AFGL-TR-78-0192, 71 pp.

_____, and D. M. Brooks, 1978: Cirrus particle distribution study, Part II. AFGL-TR-78-0248, 108 pp.

Weickmann, H. K., 1947: Die eisphase in der atmosphere. Library Trans. 273, Royal Aircraft Establishment, Farnborough, 96 pp.

Welch, R. M., J. G. Geleyn, W. G. Zdunkowski and G. Korb, 1976: Radiative transfer of solar radiation in model clouds. Beitr. Phys. Atmos., 49, 128-146.

Welch, R. M., S. K. Cox and J. E. Davis, 1980: Solar Radiation and Clouds. Meteorological Monographs, Vol. 17, No. 39, American Meteorological Society, 93 pp.

Yagi, T., 1969: On the relation between the shape of cirrus clouds and the static stability of the cloud level. Studies of cirrus clouds: Part IV. J. Meteor. Soc. Japan, 47, 59-64.

Yamamoto, G., 1962: Direct absorption of solar radiation by atmospheric water vapor, carbon dioxide and molecular oxygen. J. Atmos. Sci., 19, 182-188.

_____, G. M. Tanaka and A. Asano, 1970: Radiative transfer in water clouds in the infrared region. J. Atmos. Sci., 27, 282-292.

Yanai, M., J. H. Chu, T. E. Stark and T. Nitta, 1976: Response of deep and shallow tropical maritime cumuli to large-scale processes. J. Atmos. Sci., 33, 976-991.

APPENDIX A: COMPUTATION OF SATURATION VAPOR PRESSURE

The evaluation of saturation water vapor pressure, e_s, is based on saturation with respect to a plane surface of liquid or ice water depending on which non-vapor phase is being considered. Effects due to the shape of the particles or the presence of contaminating substances are ignored. A sixth order polynomial representation of $e_s(T)$ is used. The polynomial was obtained by fitting the Goff-Gratch formulation, which is taken as the standard (List, 1966). The computational economy of this approach has been well documented (Lowe, 1977).

The fitting procedure is similar to that employed by Lowe (1977). The procedure is to pose the problem as a minimization problem where the coefficients of Chebyshev polynomials are the unknowns. Numerical techniques are available to solve this problem and are generally available on most computers. The use of Chebyshev polynomials allows a good fit over a substantially larger temperature range than is possible with a more basic polynomial representation. The best fit Chebyshev polynomial is then converted into the form:

$$e_s(T) = a_0 + a_1 (T + a_2 (T + a_3 (T + a_4 (T + a_5 (T + a_6))))) \quad (A1)$$

($10^2 P_a$)

where $e_s(T)$ is in mb and T is in °K. A good fit over the entire range of realistic tropospheric temperatures was not possible due to the exponential behavior of $e_s(T)$. Thus, a number of polynomials were derived, which are each applicable to a specific range of temperatures. The derived polynomial coefficients applicable to specific temperature ranges when considering ice or liquid water phases are given in Tables

A1 and A2, respectively. The accuracy of these polynomials when compared to the Goff-Gratch formulation is better than ± 0.1% over the noted temperature range.

A similar approach was adopted to represent the derivative of e_s with respect to temperature, i.e.

$$\frac{\partial e_s(T)}{\partial T} = b_0 + b_1(T + b_2 (T + b_3 (T + b_4 (T + b_5 (T + b_6))))) . \quad (A2)$$

The derived polynomial coefficients applicable for various temperature ranges when considering ice or liquid water phases are given in Tables A3 and A4, respectively. The accuracy of these fits when compared to the formulas given by List (1966) are better than ± 0.05% over the noted temperature range.

TABLE A1: Polynomial coefficients for computation of e_s (ice)

Temp. Range =	- 75°C to - 40°C	- 59°C to - 20°C	- 40°C to 0°C
a_0 =	.2063861920E+04	.9965965426E+04	.3693113251E+05
a_1 =	-.6072373651E+02	-.2713843220E+03	-.9336988892E+03
a_2 =	.7454997900E+00	.3085305704E+01	.9863423592E+01
a_3 =	-.4889078071E-02	-.1874848114E-01	-.5574396896E-01
a_4 =	.1806747948E-04	.6424209891E-04	.1778237564E-03
a_5 =	-.3567969433E-07	-.1177213769E-06	-.3037007404E-06
a_6 =	.2942273428E-10	.9015651780E-10	.2170412857E-09

TABLE A2: Polynomial coefficients for computation of e_s (liquid water)

Temp. Range =	- 50°C to - 10°C	- 25°C to + 25°C	- 10°C to + 50°C
a_0 =	.6165189065E+04	.7676749690E+04	-.6831653575E+04
a_1 =	-.1667439376E+03	-.2056793389E+03	.1012101269E+03
a_2 =	.1886839551E+01	.2301179803E+01	-.4024185804E+00
a_3 =	-.1143897897E-01	-.1377392223E-01	-.1076593467E-02
a_4 =	.3920338183E-04	.4656025967E-04	.1303140958E-04
a_5 =	-.7204942038E-07	-.8434798769E-07	-.3714823651E-07
a_6 =	.5550437565E-10	.6403236206E-10	.3635860564E-10

TABLE A3: Polynomial coefficients for computations of d e_s (ice) / d T

Temp. Range	=	- 75°C to - 40°C	- 59°C to - 20°C	- 40°C to 0°C
b_0	=	.1331727716E+03	.4335100895E+03	.1125524155E+04
b_1	=	-.3947443692E+01	-.1200964475E+02	-.2916288078E+02
b_2	=	.4885191077E-01	.1390118584E+00	.3161616127E+00
b_3	=	-.3231598594E-03	-.8608106940E-03	-.1836491646E-02
b_4	=	.1205461023E-05	.3008638463E-05	.6031171831E-05
b_5	=	-.2404821784E-08	-.5629640721E-08	-.1062315136E-07
b_6	=	.2005062406E-11	.4407720998E-11	.7844897550E-11

TABLE A4: Polynomial coefficients for computation of d e_s (liquid water / d T.

Temp. Range	=	- 50°C to - 10°C	- 25°C to + 25°C	- 10°C to + 50°C
b_0	=	.5112232690E+02	-.4564371585E+03	-.1028975624E+04
b_1	=	-.1639223720E+01	.1013305498E+02	.2240655345E+02
b_2	=	.2168286602E-01	-.9211352474E-01	-.2016900254E+00
b_3	=	-.1519800912E-03	.4348429226E-03	.9563519268E-03
b_4	=	.5969451501E-06	-.1105709261E-05	-.2501195356E-05
b_5	=	-.1248422426E-08	.1387113002E-08	.3377718061E-08
b_6	=	.1087992994E-11	-.6123247164E-12	-.1794906427E-11

APPENDIX B:

The value of the latent heat, $L_{j,m}$, is specified according to whether the ice phase or the liquid phase is being considered. For ice phase simulations,

$$L_{j,m} \equiv 2.836 \times 10^6 \text{ j / kg}^{-1} \qquad \text{(B1)}$$

for $193.16\ ^\circ\text{K} \leq T \leq 273.16\ ^\circ\text{K}$.

For liquid phase simulations, the temperature dependence of the latent heat is retained for the initiation of the adjustment process but is ignored during the adjustment process, i.e.

$$L_{j,m} \equiv (3.156 \times 10^6 - 2.4 \times 10^3\ T_{j,m})\ \text{j / kg}^{-1}$$

for

$$273.16\ ^\circ\text{K} \leq T_{j,m} \leq 313.16\ ^\circ\text{K} \qquad \text{(B2)}$$

or

$$L_{j,m} \equiv (3.183 \times 10^6 - 2.501 \times 10^3\ T_{j,m})\ \text{j / kg}$$

for

$$224.16\ ^\circ\text{K} \leq T_{j,m} < 273.16 \qquad \text{(B3)}$$

where $T_{j,m}$ is in °K. The values of $L_{j,m}$ specified, as above, are accurate to within ± 0.1%, when compared to the values given by List (1966) based on the Goff-Gratch standard formulations.

APPENDIX C

EFFECTIVE RELATIVE FALL SPEED OF ICE WATER

The tabular representation of the WW15 parameterization for v^*, which was derived in Section 3.10 and depicted in Figure 12, is given below.

B \ A	1	2	3	4	5	6	7	8	9
6	0.065	0.065	0.065	0.088	0.135	0.177	0.214	0.248	0.279
5	0.307	0.438	0.501	0.540	0.566	0.575	0.583	0.590	0.596
4	0.602	0.637	0.658	0.673	0.684	0.694	0.701	0.708	0.714
3	0.720	0.755	0.776	0.791	0.802	0.812	0.820	0.826	0.832
2	0.838	0.857	0.894	0.909	0.925	0.937	0.948	0.958	0.966
1	0.973	1.022	1.134	1.213	1.274	1.347	1.409	1.463	1.510
0	1.552	1.559	1.559	1.559	1.559	1.559	1.559	1.559	1.559

Table C1. Effective relative gravity induced fall speed, $|\vec{v}^*|$, in m s^{-1} as a function of $\rho\ell$ in gm^{-3}, where $|v^*|(A,B)$ corresponds to $(A - 0.5)\ 10^{-B} \leq \rho\ell < (A + 0.5)\ 10^{-B}$.

SECTION 4

A PROPOSAL SUBMITTED TO NASA HEADQUARTERS

by

Department of Atmospheric Science
Colorado State University

TITLE: OBSERVATIONS OF UPPER AND MIDDLE TROPOSPHERIC CLOUDS

PRINCIPAL INVESTIGATOR: Stephen K. Cox
Professor
Department of Atmospheric Science
Colorado State University
Fort Collins, CO 80523
(303) 491-8594

PROPOSED STARTING DATE: October 1, 1982

PROPOSED ENDING DATE: September 30, 1986

TABLE OF CONTENTS

PREFACING REMARKS

This proposal has been prepared in a rather unconventional but, in the author's opinion, effective way. The bulk of the proposal (Sections 1 - 4) outlines an extensive investigation of "Radiation and Extended Middle and Upper Tropospheric Cloudiness." The complete investigation has the national and international relevance to dictate that it be carried out, however the scope of the investigation exceeds the ability and resources of any one institution or agency to successfully carry out.

The specific research components which I (the principal investigator) propose to carry out are listed in Section 5. These are only a modest fraction of the total effort required to do the complete experiment. From several quotes in the proposal it is obvious that this problem has the scientific support essential to carry it to a successful conclusion. The remaining question is -- Are the agencies which are capable of supporting such an effort with their facilities and resources willing to make the appropriate commitment?

1.0 RATIONALE

Recent recommendations from the JOC and WMO and ICSU stress the need for increasing our knowledge of the radiative characteristics and the temporal and spatial regimes of extended cloud fields. (Report of the JOC AD HOC Working Group on Extended Cloudiness and the Radiation Budget.) In the JOC document two observational programs have been proposed. They are STRATEX I dealing with boundary layer stratus cloud systems and STRATEX II dealing with extended cirrostratus cloud systems. A number of efforts have already been mounted or proposed for STRATEX I [i.e. Paltridge (1974), Wakefield and Schubert (1976), Schmetz and Raschke, (1980) and Fouquart, et al. (1980)]. In addition, several missions of the U.S.S.R. IL-18M during GATE explored the radiative characteristics of the stratocumulus boundary layer regime. The STRATEX II regime has not received the same amount of observational attention to date, largely due to the requirement for high performance aircraft to reach the cirrus layers. Notable exceptions to this are the CV-990 and Sabreliner flights made during GATE for the express purpose of measuring cirrus cloud radiation characteristics. In addition, Kuhn (1963) and Cox (1971, 1976) have reported results of observations of infrared radiative characteristics of cirrus clouds derived from radiometersonde observations. The following three paragraphs are quoted directly from the report of the JOC AD HOC Working Group on activation of the STRATEX Programme (7 January 1977).

STRATEX II

> A number of fundamental gaps exist in our understanding of the growth and maintenance of high level extended clouds. The questions that still need to be answered involve such things as the relative importance of mean vertical motion and of turbulence induced by the radiation field around the cloud itself; and such things as whether there are important distinguishing characteristics between "frontal type" cirrus and the cirrus blown from the tops of cumulo-nimbus.
>
> In view of the lack of knowledge of the processes and character of upper level clouds, the ad-hoc group agreed that proposals

directed to any (and preferably as many as possible) of the following areas should be encouraged:

1. Simple mapping of variability (of the cloud and its radiative characteristics) in terms of the meteorological environment of the cloud.

2. Representative case studies involving observations of the cloud microphysics and radiation characteristics.

3. Programmes to investigate the processes responsible for the generation, maintenance and dissipation of the cloud system.

Some of the proposed programmes listed under STRATEX I above contained aspects that could involve the primary goals of STRATEX II. However, none of these programmes, at least in their preliminary phase, has been specifically directed towards those goals.

Again, it is recommended that future programmes be designed to have central objectives tuned to the STRATEX II requirements.

This proposal deals with STRATEX II objectives. As was pointed out in the JOC document noted above, the specific radiative and cloud microphysical characteristics of cirroform clouds should be determined from aircraft observations conducted at different geographical locations for limited periods of time.

1.1 Purpose

The principal needs of climate studies relating to middle and upper tropospheric clouds may be placed into two categories: modeling and monitoring (M & M). Inherent in each of these applications is the belief that these clouds are important to both the stability and to the magnitude of potential change in the earth's climate. It should be noted that many of the modeling applications apply to GCM's and NWP as well as climate models. While it is convenient to divide the needs into the M & M categories we shall see that the information required to satisfy one area of investigation is highly complementary to the other.

The climate modeling requirements for middle and upper tropospheric clouds may be loosely stated as specifying the temporal and spatial (3D) distributions of these clouds and their radiative properties. Two philosophically different ways of achieving this goal are immediately apparent. A deterministic approach would seek to understand the basis for the formation, maintenance and dissipation of middle and upper tropospheric cloud fields and incorporate these mechanisms or a parameterized version of them into a climate model. Similarly the radiative properties of these model clouds would be related in a physically meaningful way to the microphysical variables within the model. On the other hand, a probabilistic approach might be adopted to meet these same needs. In this approach data describing the average values and variability of the temporal and spatial distributions and the radiative properties of middle and upper tropospheric clouds would be collected, analyzed and expressed as empirical representations of extended cloudiness.

Of course the deterministic approach is the more attractive one, if it proves feasible. It alone, being based upon fundamentals of physics, might allow middle and upper tropospheric cloud regimes much different from our present day climate to evolve in models. On the other hand, the details and complexities of such an approach may extend well beyond our GCM, NWP and climate modeling capabilities. A probabilistic approach would necessarily restrict us to the middle and upper tropospheric cloud regimes of our present climate. While this might be useful in investigating some contemporary climate problems it will restrict the universality of any model which uses it. Interestingly though, the statistical relationships developed in a probabilistic analysis will also serve as a check, guide and/or constraint on a deterministic parameterizaiton incorporated in a model.

The deterministic approach will serve as a guide in the investigation outlined below. It's obvious advantages as well as it's intellectually

satisfying appeal dictate this decision. However, since the probabilistic approach represents a reasonable fallback position should the deterministic tactic fail, and since it represents a check on any deterministic parameterization scheme, we shall also strive to meet the data requirements for a statistical analysis of these cloud properties.

This proposal may be divided into two components which are closely related. First there is the continued development and utilization of a 2D, time-dependent, physical-numerical model of upper and middle tropospheric clouds. In addition to investigating sensitivity of cloud formation, maintenance and dissipation to various physical components, the model results will be used to refine the design of a middle and upper tropospheric cloud observation program - the second component of this proposal.

Middle and upper tropospheric cloud monitoring requires essentially the same data forms as the modeling applications mentioned above; the primary difference is in the expanded time and space scales required for the monitoring application.

The primary goals of an upper and middle tropospheric cloud experiment are listed below:

1) Observe the magnitudes of the dynamic, thermodynamic and moisture (includes liquid and ice phase) variables in the presence of upper and middle tropospheric clouds in order to verify cloud model calculations.

2) Observe the properties of the large scale flow coincident with the observations in goal number one to serve as an initial condition data base for the study of relationships between large scale variables and extended cloudiness effects.

3) Observe simultaneously spectral and broadband radiative properties and cloud microphysical structure. Microphysical structure includes phase, crystal habit and orientation as well as vertical and horizontal structure of these variables; these observations will allow verification, modification and simplification of radiative transfer

techniques in order to make them more compatible with model constraints.

4) Observe cloud regions from satellite coincident with observations noted in goal number 3 in order to establish the potential to infer cloud radiative and microphysical properties from satellite measurements (cloud truth). This is an essential step to effective utilization of any satellite-deduced cloud climatology.

5) Observe, principally from satellite, life cycles of upper and middle tropospheric cloud systems both regionally and globally. These data will allow generation of statistical summaries of the areal, temporal and cloud height characteristics of these systems.

There are numerous specific experimental goals which fit into one or more of the general goals listed above. I shall not attempt to enumerate these at this point. The purpose of listing the primary goals above is so that they may be related to the resources required to carry them out.

2.0 BACKGROUND

The most definitive modeling work to date on stratoform clouds has concentrated upon low-level stratocumulus clouds. Lilly (1968) and more recently Schubert (1976) reported physical-numerical models capable of describing the basic dynamic, thermodynamic and water budget requirements of stratocumulus clouds.

Much less is known concerning the mass, moisture and energy budgets associated with upper tropospheric clouds.

2.1 Prior modeling and thermodynamic budget studies

A number of interesting, qualitative observations of cirrus uncinus clouds have been reported by Ludlam (1948), Oddie (1958) and Yagi (1969). In addition, Ludlam (1956) and Conover (1960) give fascinating descriptions of other upper tropospheric clouds. However, there is a dramatic void of quantitative information relating to the life cycle of a middle or upper tropospheric layer cloud. While pieces of this puzzle may be found in the literature, the relationships and dependencies of the layer cloud to large and small scale motions and to radiation have been largely ignored. While one may find these components treated separately, they have not been considered simultaneously for the cloud layer as a whole [c.f. Schubert (1976) and Lilly (1968)].

Very little research has been reported on total energy and mass budgets of upper tropospheric clouds, however, components of these energy and mass budgets have been explored independently by a number of authors.

The most common approach has been to examine the formation, growth and decay of cloud droplets or crystals. These studies include papers by Jiusto (1971), Jayawerra (1971), Braham and Spyers-Duran (1967), Heymsfield (1975a,b), Hall and Pruppacher (1976) and Heymsfield (1977). These studies concentrate on the microphysical aspects and energy and water mass budgets in order to explain the presence and lifetime of individual droplets or crystals. In general, the investigator's attention was focused on the crystal itself in a lagrangian sense and constraints

offered by the energy and mass budgets of the layer of the atmosphere was ignored.

Studies by Heymsfield (1975c) did attempt to quantitatively incorporate layer air motion in making numerical computations of crystal growth of cirrus uncinus clouds. However, even this study focused on a single, local comma-like circulation required to form and/or sustain the visually observable cirrus uncinus element. In a very recent paper, Heymsfield (1977) discusses precipitation development in stratiform ice clouds. As in previous papers, the emphasis of this paper is on microphysical processes and crystal interaction with the vertical velocity field while largely ignoring the total mass-energy budget of the layer.

2.2 Prior studies of radiative characteristics of upper tropospheric clouds

Previous studies may be grouped into two categories: theoretical and observational. The theoretical work may be further subdivided into spherical particles and ice crystals. The observational studies may be conveniently classified by platform. Studies conducted from surface, aircraft, balloon and satellite data are referenced.

2.2.1 Theoretical studies

Pioneering theoretical work on the subject of radiative characteristics of water clouds with spherical droplets has been reported by Deirmendjian (1960, 1962, 1967); Korb and Moller (1962), Feigel'son (1973), Yamamoto et al. (1971, 1975), Hansen (1969), Herman (1962) and Zdunkowski et al. (1965, 1969, 1971, 1974). Welch et al. (1976) have added wavelengths beyond 2.8 μm and shown that significant solar in-cloud heating is to be expected from these longer wavelengths.

Plass (1968) reported computations made using a Monte Carlo technique. Jacobositz (1970) and Coleman and Liou (1980) studied the equivalent sphere radius of a composite of hexagonal crystals while Liou (1975 a,b,c) and Hunt (1973) report computations of cirroform cloud radiation characteristics.

Fleming and Cox (1974) reported the energy budget ramifications of a series of possible configurations of radiative characteristics of cirrus clouds. Recently Liou and Wittman (1979) reported parameterized equations for the radiative properties of cirrus clouds as a function of cloud ice content while Liou et al. (1980) studied radiative equilibrium temperatures in a cirrus cloudy atmosphere. Welch, Cox and ZdunKowski (1980) examined the variability of cirrus radiative properties with different crystal shape configurations. Stephens (1980) has shown that ice crystal orientation may be a significant factor in determining the radiative properties of cirrus clouds.

In summary, the modeling of radiative characteristics of clouds with spherical droplets is reasonably well advanced with a number of significant published contributions. The case for ice crystal clouds is not as well documented and relatively few theoretical contributions may be found.

2.2.2. Observational studies

Surface data in the 8 to 13 μm range were used by Allen (1971) to infer effective infrared emissivity values of cirrus clouds. Platt (1973, 1975) and Platt and Gambling (1971) used simultaneous surface laser, radiometer and satellite radiance data to infer cirrus characteristics.

Kuhn and Weickmann (1969) and Kuhn (1970) reported aircraft observations of cirrus infrared extinction for cases of natural cirrus and jet aircraft contrails. Davis (1971) reported on cirrus extinction characteristics inferred from airborne ruby laser data and simultaneous radiometric observations. Griffith and Cox (1977) reported tropical cirrus characteristics deduced from GATE aircraft data. Murcray, et al. (1974) reported spectral emission observations from cirrus clouds in the 10 to 12 μm region. These observations were conducted from a balloon platform.

Radiometersonde observations served as the source of data on radiative characteristics of upper tropospheric clouds in the studies reported by Kuhn (1963a), Kuhn and Suomi (1965) and Cox (1969, 1971, 1976).

Fritz and Rao (1967) and Platt (1975) utilized satellite radiance data

for inferring the radiative characteristics of cirrus clouds.

Recent studies by Griffith and Cox (1977) and Griffith, Cox and Knollenberg (1980) and Paltridge and Platt (1980) show cirroform cloud characteristics which are different from those predicted from theory and also significantly different from many other observations. Figure 1 illustrates these differences from theory and Figure 2 shows the agreement among observations. The differences are so dramatic that they readily show the need for more observational corroboration as well as theoretical explanation. These differences are much larger than observational errors could introduce, and, therefore, must be real. One should note that the data used by Griffith and Cox (1977) were collected during GATE primarily in the anvil-outflow area of mesoscale cumulonimbi cloud systems.

In summary, relatively few observations studies of the radiative characteristics of upper tropospheric cloudiness have been reported. Most of the studies referred to above, investigated only the radiative characteristics of the cloud layer for a relatively narrow spectral interval and/or for a narrow angle increment. Only the studies by Kuhn (1963b), Kuhn and Suomi (1965), Cox (1969, 1971, 1976) and Griffith and Cox (1977) have studied the broadband irradiance characteristics. While these few studies range from case studies to composite summaries, there has been no methodically-designed observational study of the radiative characteristics of upper tropospheric clouds as called for in STRATEX II documentation supplied by the GARP Climate Dynamics Working Group.

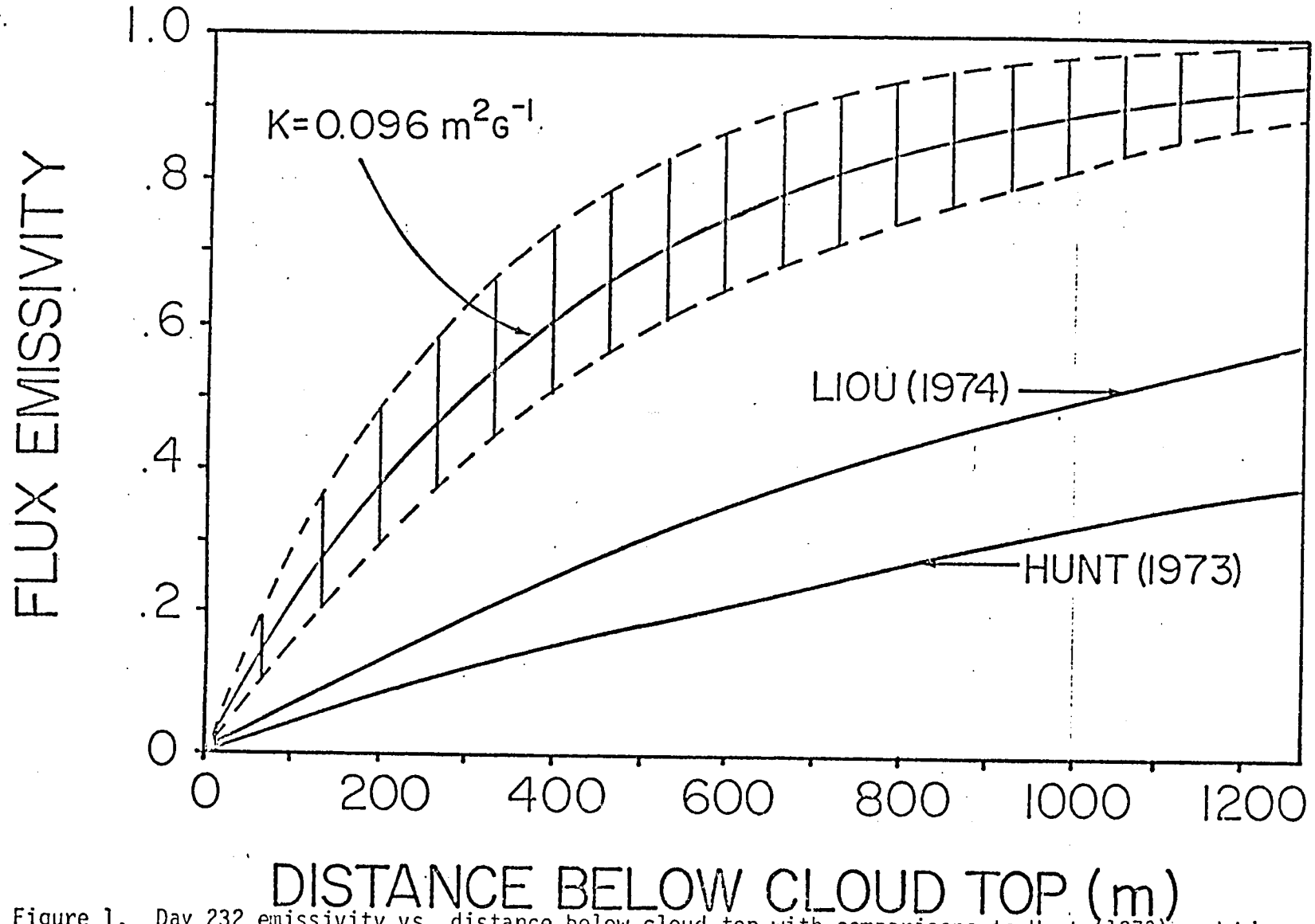

Figure 1. Day 232 emissivity vs. distance below cloud top with comparisons to Hunt (1973) and Liou (1974). (Dashed line envelope indicates uncertainty).

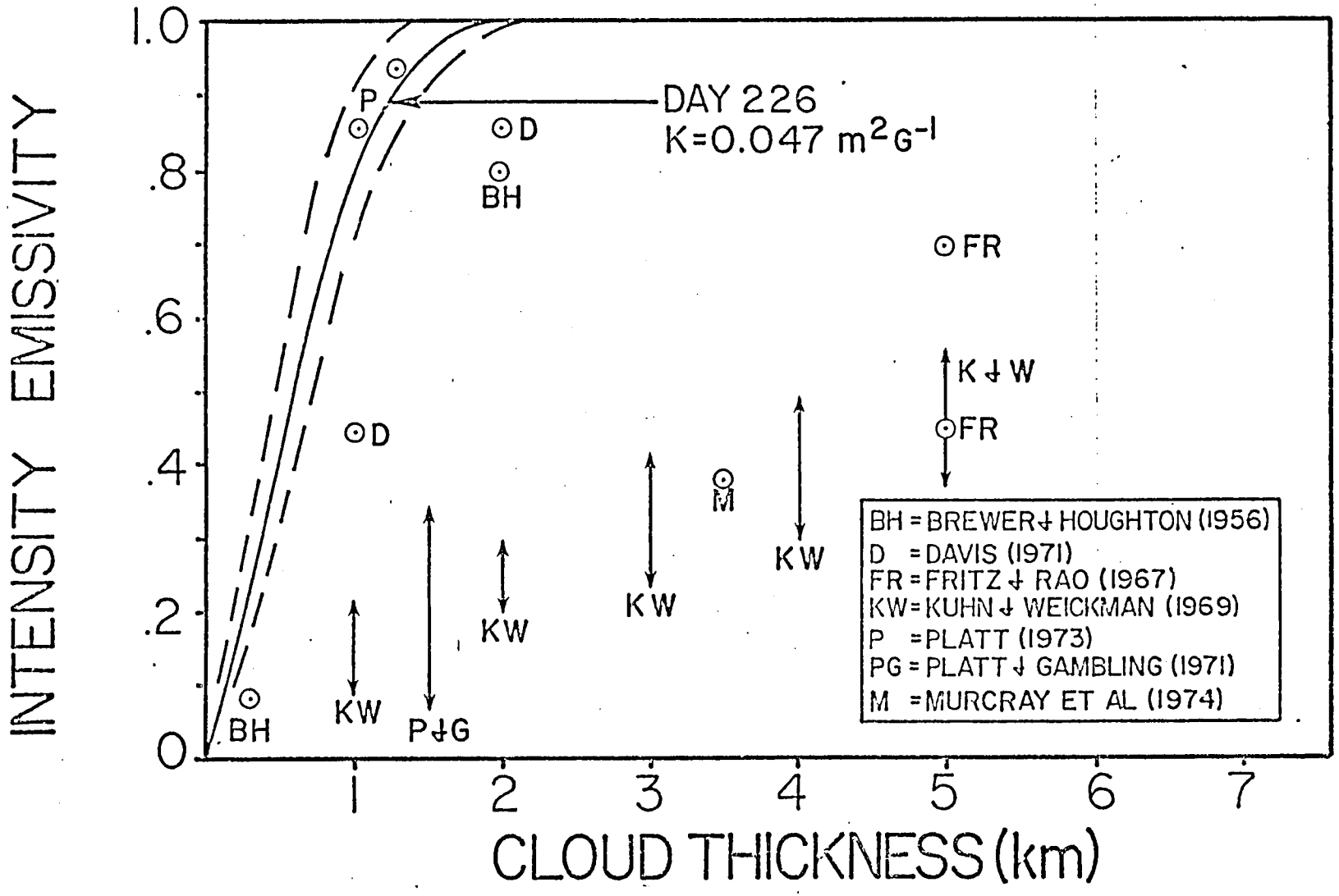

Figure 2. Comparison Between Present Study and Previous Observations of Intensity Emissivity vs. Cloud Thickness. (Dashed line envelope indicates uncertainty).

3.0 THE MODELING COMPONENT

3.1 Modeling Approach

(Note - A modeling effort of this type, outlined below, has been proposed to the National Science Foundation.) The modeling objective of this research effort is to gain a basic understanding of the interplay of the various physical processes involved in the formation, maintenance and decay of middle and upper tropospheric stratiform clouds. Furthermore, the initial focus of this study is limited to cloud forms, in which large scale dynamical forcing is not likely to be the dominant physical factor, i.e. deep, precipitating cloud forms associated with regions of strong lifting in a cyclone and not considered. The choice of a modeling approach is highly influenced by the fact that the interrelationships between a number of presumably important physical parameters are unknown or at the least highly speculative at this time.

For example, the bulk radiative properties of a cloud such as its effective infrared emissivity and effective solar absorptivity must be related through the optical depth of the cloud. Only recently have theoretical studies of ice clouds, which address this issue, been reported, e.g. Stephens (1980). However, such theoretical relationships rely critically on the assumed crystal habit and size spectrum and also possibly on the assumed crystal orientations. How these properties depend on the dynamic, thermodynamic and radiative environment of the cloud is uncertain. Empirical studies, e.g. Paltridge and Platt (1980), also suffer from uncertainty due to the scatter of the observations. Because of these uncertainties, the modeling philosophy adopted here is to choose an approach which is the most simple method capable of yielding realistic simulations. In this way, the sensitivity of simulations to the choice of various parameters may be economically established in a realistic manner.

The modeling approach adopted for this study is to employ a two-dimensional, time-dependent, Eulerian numerical model, which incorporates all of the important physical processes in a simplified way,

to investigate the role of these processes in the evolution of a cloud form in an isolated atmospheric layer, e.g. Asai and Nakamura (1978), Lipps (1971). Other modeling approaches were considered. Only time-dependent approaches were examined so that the changing roles of various processes at different stages of the cloud life cycle might be investigated. Only Eulerian models were considered due to the abundance of knowledge available as to the mechanics of these models. By two-dimensional, denoted 2-D, we mean that solutions are obtained for dependent model variables in two space dimensions, e.g. (x, z, t). Similarly, a model, which simulates dependencies in only one or in three space dimensions, i.e. (z,t) or (x, y, z, t), respectively, is denoted as a 1-D or 3-D model, respectively.

A full 3-D modeling approach, e.g. Sommeria (1976), Cotton and Tripoli (1978), was rejected primarily because of the substantial increases in computing requirements and complexity. While a 3-D model has the advantages of being capable of simulating the effects of spatial variability of the large-scale environment and full three-dimensional turbulent transport processes, the initial focus of this study is on local scale control, i.e. cloud forms, which are not dominated by large-scale processes. The neglect of turbulent transports in a third space dimension is not felt to be too severe of a drawback to the 2-D approach especially considering the present state of knowledge.

A 1-D modeling approach was rejected primarily because of uncertainty as to the appropriateness of the required closure assumption and the desire to capture more detail in the simulations as an aid in gaining understanding. The primary advantages of a 1-D modeling approach are the overall simplicity of the model and the resulting computational economy. In the case of entrainment type models, e.g. Lilly (1968), Schubert, et al. (1979), and Randall (1980), these advantages are at least partially offset by their limited applicability. The assumed thermodynamic and dynamic structure of the basic state, which is necessary and crucial to

the entrainment closure assumption, may not be nearly as applicable to the problem here as to the stratocumulus problem which they considered. This conclusion is supported by previous work, i.e. Starr and Cox (1979). A more global 1-D approach has been employed by Oliver, et al. (1978). They employ a second order turbulence closure, where the required correlation coefficients for turbulence parameters are diagnosed from the structure of the basic state based on empirical relationships derived primarily from observations in the atmospheric boundary layer. These relationships are believed to be more general but may not be universal.

An obvious important advantage of a 2-D or 3-D modeling approach, when compared to the 1-D approach, is that horizontal structure is explicitly resolved on the grid scale. This may be a substantial aid in clarifying the interpretation of results, particularly if the evolution of such structure is important in the understanding of the cloud life cycle process. Furthermore, if a reasonably small grid interval is used, much of the turbulent transports are explicitly resolved. In this case, the choice of a particular turbulence closure scheme for the model, which accounts for processes acting at a scale less than the grid interval, may not be as crucial to the results. In this sense, the universality of the closure need not be as rigorously established as in the case of a 1-D model where essentially all turbulent transport processes are parametrically represented.

3.2 Description of the Model

The governing system of equations for the model is composed of four prognostic equations and three primary diagnostic equations together with a number of secondary diagnostic relationships. The system is anelastic and employs the Bousinesque approximation appropriate for shallow convection. Thus, the hydrodynamics are non-divergent. Consistent with the two-dimensional approach and the local scale focus of this study, the basic state or large-scale environment is assumed horizontally uniform and Coriolis effects are neglected. Table 1 identifies the model variables and

LIST OF MODEL VARIABLES AND NOTATION

u, w: the horizontal and vertical components of the two-dimensional velocity vector, $\mathbb{V}$.

ψ: the stream function or velocity potential field, where

$$u \equiv -\frac{\partial \psi}{\partial z} \qquad \text{and} \qquad w \equiv \frac{\partial \psi}{\partial x} .$$

ζ: the component or vorticity normal to the (x,z) - plane, where

$$\zeta \equiv \nabla^2 \psi = \frac{\partial w}{\partial x} - \frac{\partial u}{\partial z} . \tag{5}$$

Θ: the layer mean basic state potential temperature.

$\theta_o(z)$, $q_o(z)$: the basic state potential temperature and water vapor specific humidity.

θ, q, ℓ: the perturbation potential temperature, water vapor specific humidity, and liquid/ice phase water specific humidity.

$\pi_o(z)$: a representation of the hydrostatic basic state pressure, $P_o(z)$, where

$$\pi_o \equiv \left(\frac{P_o}{P_{REF}}\right)^{R/c_p}$$

ν, k_θ, k_q, k_ℓ: the viscosity, thermal diffusivity, water vapor diffusivity and liquid/ice phase water diffusivity, respectively.

C: the condensation/sublimation rate per unit mass for water.

F_R: the net radiative flux per unit area defined as positive when the net flux is directed upward.

L: the specific latent heat of condensation/sublimation for water.

R: the real gas constant for dry air.

c_p: the specific heat capacity of dry air at constant pressure.

g: the acceleration due to gravity.

TABLE 1

e: the ratio of the molecular weight of water to the molecular weight of dry air, i.e.

$$e \equiv \frac{M_{H_2O}}{M_a} .$$

P_{REF}: a constant reference pressure.

∇^2: the two-dimensional Laplacian operator, where

$$\nabla^2 \equiv \frac{\partial^2}{\partial x^2} + \frac{\partial^2}{\partial z^2} .$$

J: the Jacobian operator, where

$$J(A, \psi) \equiv \frac{\partial A}{\partial x}\frac{\partial \psi}{\partial z} - \frac{\partial A}{\partial z}\frac{\partial \psi}{\partial x} .$$

TABLE 1

notation used below. The prognostic equations are:

$$\frac{\partial \zeta}{\partial t} = J(\zeta, \psi) + g \frac{\partial}{\partial x}\left\{\frac{\theta}{\bar{\theta}} + \frac{(1 - e)}{e} q - \ell\right\} + \nu \nabla^2 \zeta \qquad (1)$$

$$\frac{\partial \theta}{\partial t} = J(\theta + \theta_o, \psi) + \frac{1}{c_p \pi_o}\left\{L C + g \frac{\partial F_R}{\partial P_o}\right\} + k_\theta \nabla^2 \theta \qquad (2)$$

$$\frac{\partial q}{\partial t} = J(q + q_o, \psi) - C + k_q \nabla^2 q \qquad (3)$$

$$\frac{\partial \ell}{\partial t} = J^*(\ell, \psi) + C + k_\ell \nabla^2 \ell \qquad (4)$$

where the notation is as given below.

Equation (1) is the vorticity equation, which is the governing dynamic equation, appropriate to this model. The individual terms on the right-hand side account for the advection of vorticity, the generation of vorticity by buoyancy forces, and the diffusion of vorticity, which leads to the viscous dissipation of kinetic energy. Equation (2) is the governing thermodynamic equation. The first term accounts for the advection of potential heat while the last term accounts for thermal diffusion. Note that thermal diffusion is assumed not to act on the basic state and recall that for a Bousinesque system the perturbation potential temperature may be regarded as a constant times the temperature deviation from the basic state temperature distribution e.g. Ogura and Phillips (1962). In addition, the contributions due to diabatic (source/sink) processes, i.e. radiation and water substance phase changes, are taken into account. Equations (3) and (4) are budget equations for water vapor and non-vapor water substance, respectively. Advection and diffusion effects and phase change source/sinks are included. The advective term in Eq. (4) may be modified in order to account for the fall velocities of water drops/ice crystals, i.e. J^*.

A basic state vertical velocity, w_o, may be readily incorporated into this model. In this case, the following terms would be required on the right-hand sides of equations (1)-(4), respectively,

$$- w_o \frac{\partial \zeta}{\partial z} \qquad (1.1)$$

$$- w_o \frac{\partial(\theta + \theta_o)}{\partial z} \qquad (2.1)$$

$$- w_o \frac{\partial(q + q_o)}{\partial z} \qquad (3.1)$$

$$- w_o^* \frac{\partial \ell}{\partial z} \, . \qquad (4.1)$$

Also, equations describing the resulting temporal dependence of the thermodynamic structure of the basic state would be required.

The primary diagnostic equations are Equation (5) which diagnoses the stream function field from the predicted vorticity field, and diagnostic equations to determine $F_R(x,z)$ and $C(x,z)$. In this regard, secondary diagnostic relations are required to determine the pertinent local radiative characteristics and microphysical characteristics including the modification of $J(l,\Psi)$ to $J^*(l,\Psi)$ and the diagnosis of saturation water vapor pressure. The methods employed for the diagnosis of F_R and C are now being developed and will be parametric to some degree.

The lateral boundary condition employed is that the solution is periodic in the horizontal direction. The, $w_o(t)$ must be everywhere a constant. The dynamic boundary condition evoked at the upper and lower boundaries is that the perturbation velocity is zero at these levels, i.e. $\Psi(x,z_{TOP}) = \Psi(x,z_{BOTTOM}) = \text{constant}$.
Note that the basic state is regarded as at rest, except when w_o +

0. This is not too limiting as the plane of interest may be regarded as perpendicular to a mean flow and advected with the mean flow. Furthermore, a no stress condition is imposed at the upper and lower boundaries. Similarly, no thermal, water vapor or non-vapor phase water substance diffusion is permitted across the upper and lower boundaries. These boundaries are also required to maintain thermodynamic properties determined entirely from the basic state, i.e.

$$\theta = q = l = 0 \text{ at } z = z_{TOP}, z_{BOTTOM}.$$

It may be necessary to relax this requirement for l at some later time, when the model may be modified in order to account for precipitation processes. The spacial grid employed is a staggered grid as in Asai and Nakamura (1978). For this grid, dynamic quantities, i.e. Ψ and ζ, are defined on all boundaries and at regularly spaced grid points in the interior. The thermodynamic quantities, i.e. θ, q, and l, are defined at points equally spaced between the nearest four dynamic grid points, i.e. at half levels in both x and z. This system has substantial computational advantages, i.e. Lilly (1965). The grid interval is currently specified as 100 m and the domain is 3.1 km in the vertical and 6.3 km in the horizontal. A larger horizontal domain may be used for the actual simulations. The resulting time step required for computational stability is on the order of 30 seconds. A finer grid will be tested.

The essential numerical techniques employed follow from Arakawa (1966) for the advective term in the dynamic equation, Lilly (1965) for the advective term in Eqs. (2) and (3), and Swarztrauber and Sweet (1975) for the solution of Eq. (5). The advective term in Eq. (4) is evaluated by a modified version of Lilly's method. The Laplacian operator is evaluated in its standard finite difference form. The time integration scheme is a filtered leapfrog method following from Asselin (1972). The preliminary diagnostic solution for C utilizes Newton's method, e.g. Hack and Schubert (1976). The evaluation of the vorticity generation term is

standard except that a vertical flip-flop weighting scheme is employed to prevent locking in of a checkerboard noise pattern.

The viscous and diffusion terms account for the effects of subgrid scale turbulent mixing processes, which are not resolved by the model. As such, these terms are parametric in nature. They also serve the purpose of minimizing computational errors, e.g. truncation errors, which may result in the generation of non-physical modes in the solution. At present, the eddy viscosity and diffusion coefficients are specified constants. A true first order closure for the turbulent transports, e.g. Lilly (1962) may be tried, where these constants are locally diagnosed from the velocity deformation field and a few specified constants. However, it is unclear if any advantages from such a method outweigh the added computational requirements.

The performance of the numerical schemes is currently being tested. Preliminary results based on a dry version of the model, i.e., prognostic Equations (1-3), indicate a very satisfactory performance. The physical conservation principles, i.e. conservation of total energy, are well obeyed. The advective terms are conservative to better than 10 decimal places and no instabilities have been encountered, e.g. growth of

$$(\theta + \theta_0)^2 \text{ or } \xi^2$$

and mean layer kinetic energy in the absence of buoyancy generation or diffusion from an initial noisy pattern of ξ. In order to baseline the dry model, the numerical experiments of Arnason, et al. (1968) on dry convection in a neutral environment have been reproduced. Their numerical techniques are substantially different than those used here. In most regards, the performance of our model was much superior to theirs in terms of the above concepts. However, an explicit thermal diffusion scheme was required in our model in order to suppress nonphysical computational modes. They use an advective scheme, which effectively adjusts the diffusion coefficient to the value required locally to suppress truncation errors. However, their scheme is apparently non-conservative, which is a

serious drawback. Also, based on an analysis of their results compared to experiments performed with our model, they may substantially overestimate the required local smoothing necessary for reasonable suppression of computational modes due to truncation error. In summary, the numerical techniques incorporated into the model have yielded very good results to date and warrant further development along these lines.

4.0 THE OBSERVATIONAL COMPONENT

4.1 Types of Phenomenon to be Observed

Following the directives of the JOC, WMO document quoted previously we specifically target four types of middle and upper tropospheric cloudiness. These cloud types meet the following specifications: They are of sufficiently large time and space scales to allow collection of an adequate data set; they occur sufficiently frequently and are of sufficient areal extent to significantly impact the earth's radiation budget; and they are types of cloudiness for which no adequate parameterizations exist in GCM's.

The specific cloud types are listed below:

1) pre warm frontal CiSt

2) subtropical CiSt, not associated directly with active convection

3) extended Acu associated with overrunning of Gulf moisture in central midwestern U.S.

4) Cb anvil cirrus at various distances from source region.

In addition, the above cloud types have the following common characteristics. These cloud types may be found relatively isolated from other cloud features which complicate observations and interpretations and are observed to cover very large areas which emphasizes their importance to the planetary radiation budget. Category 4 was selected for observation so that mid-latitude radiative characteristics of Cb anvils could be compared with the results reported by Griffith and Cox (1977) and in view of their potential importance in tropical rainfall generation (Webster and Stephens, 1980).

4.2 Experiment Setting

In an attempt to logically select a geographical location and time period which would optimize chances for observing the phenomenon of interest, we have examined five years of continental U. S. radiosonde data. Although a number of variables were analyzed the most useful variables were middle and upper tropospheric relative humidities with respect to both liquid water and ice.

4.2.1 Location

An examination of both mean values and variability of these climatological relative humidities clearly indicates the preferred location and timing. Figures 3-7 for the spring season (MAM) suggest an experiment location bounded by 82°W and 95°W longitude and 43°N and 31°N latitude. This region shows, during the spring season, a tendency for high relative humidities with low variability.

4.2.2. Timing

The timing of the experiment phase requires at least one additional piece of information. Although the mean relative humidities are slightly higher in late spring, their variability also increases as does the frequency of occurrence of convection. Since we are not concerned with strong convective-dynamic systems in this study, and convection is likely to produce strong local anomalies in the middle and upper tropospheric moisture and cloud fields, it would be preferred to hold the experiment in the early part of the spring season. A tentative start date for the experiment would be late February with completion targeted by 15 April.

Because of the complexities in making upper tropospheric observations of most variables and the lack of a priori observations it will be highly

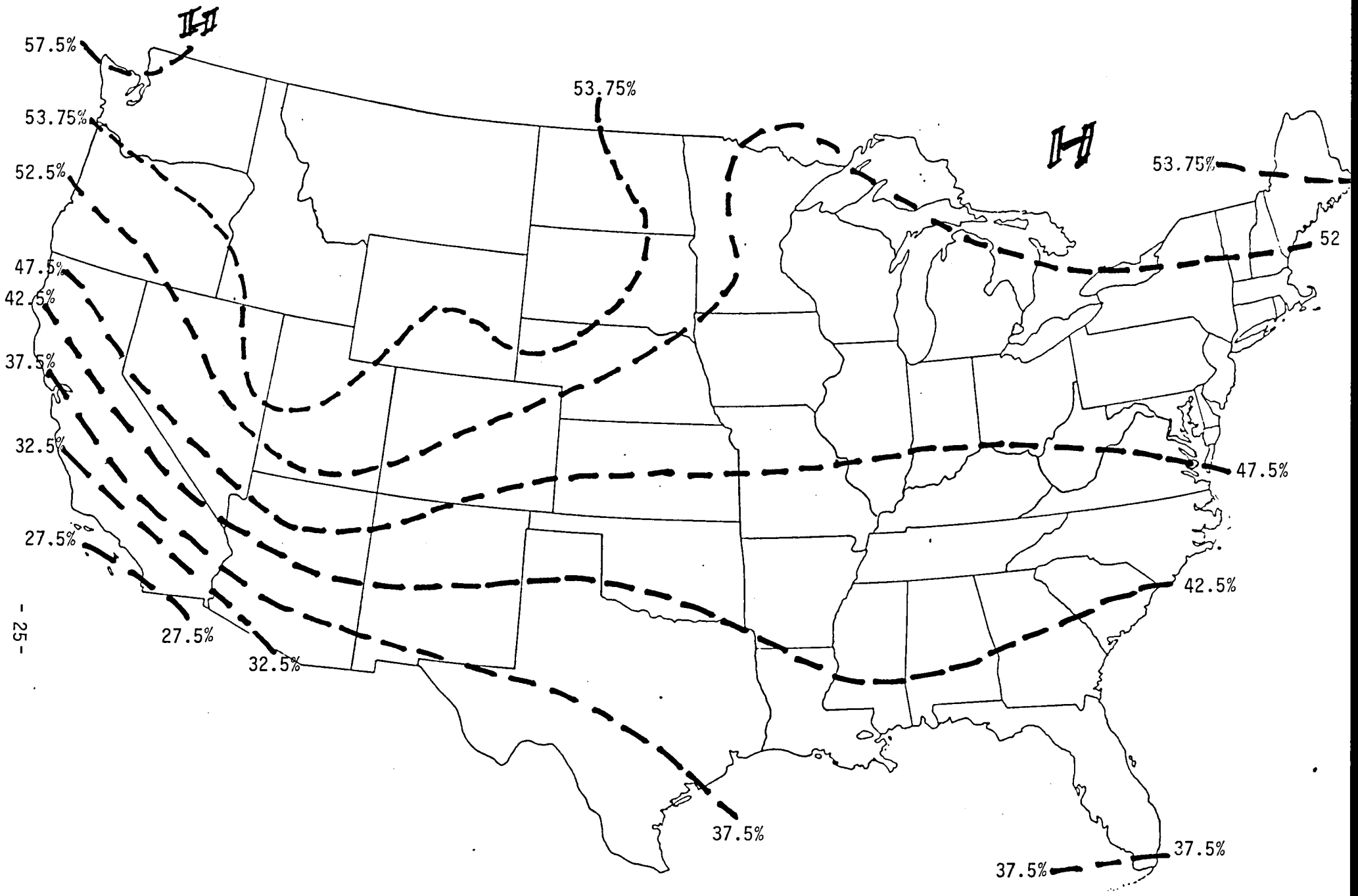

Figure 3. Mean relative humidity of the 700-500 mb layer for the spring season.

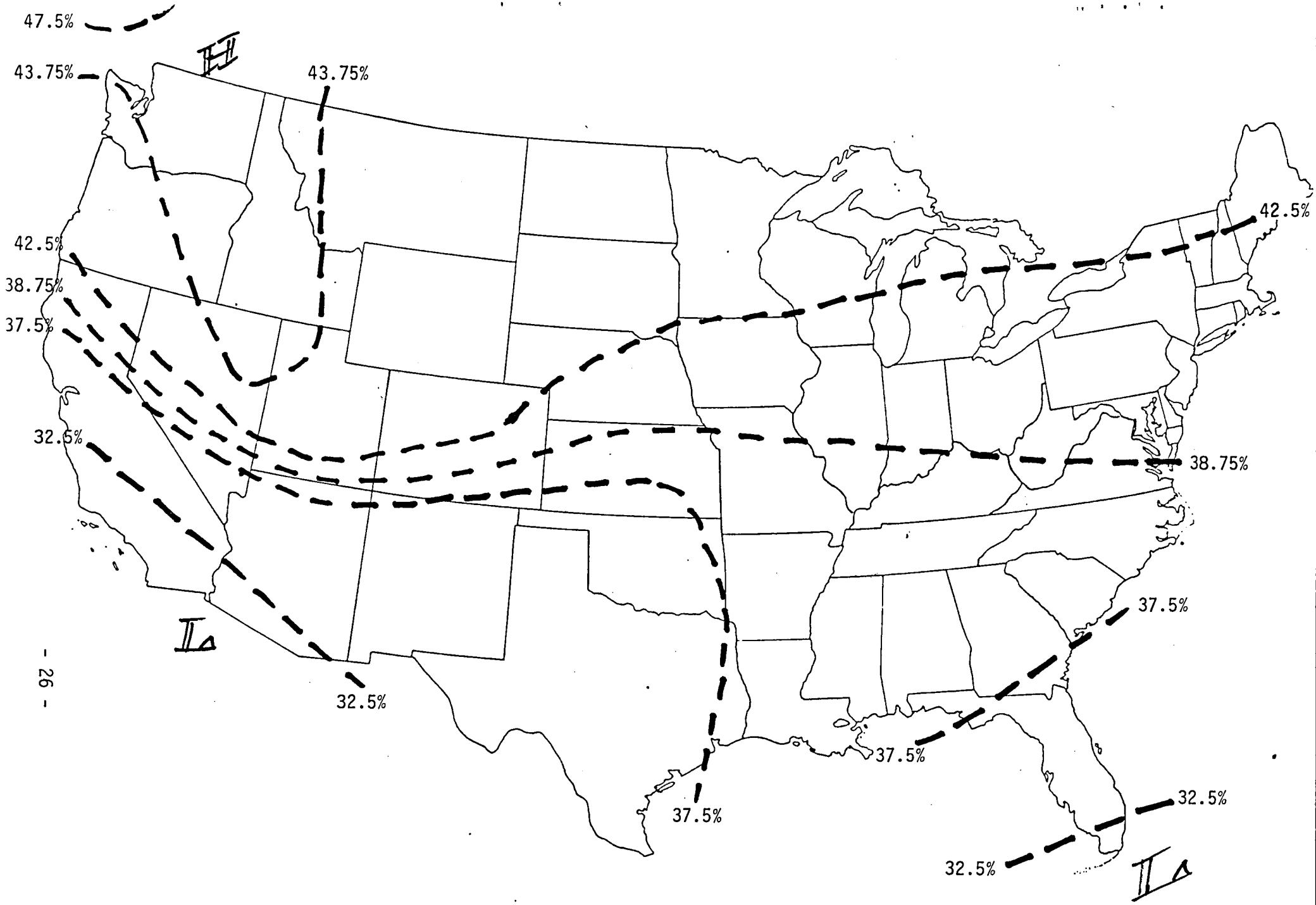

Figure 4. Mean relative humidity for the 500-200 mb layer for the spring season.

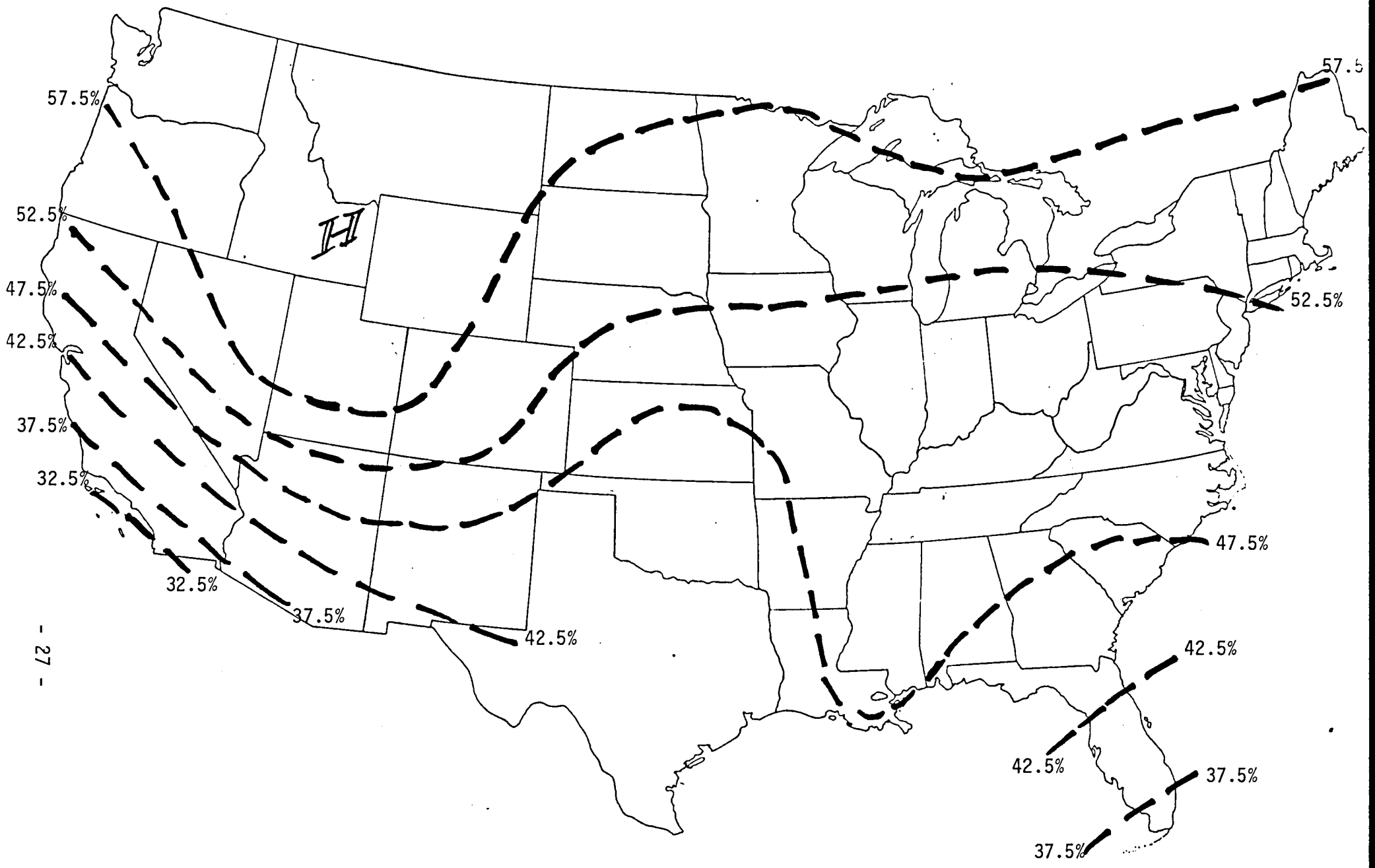

Figure 5. Mean relative humidity with respect to ice for the 500-200 mb layer for the spring season.

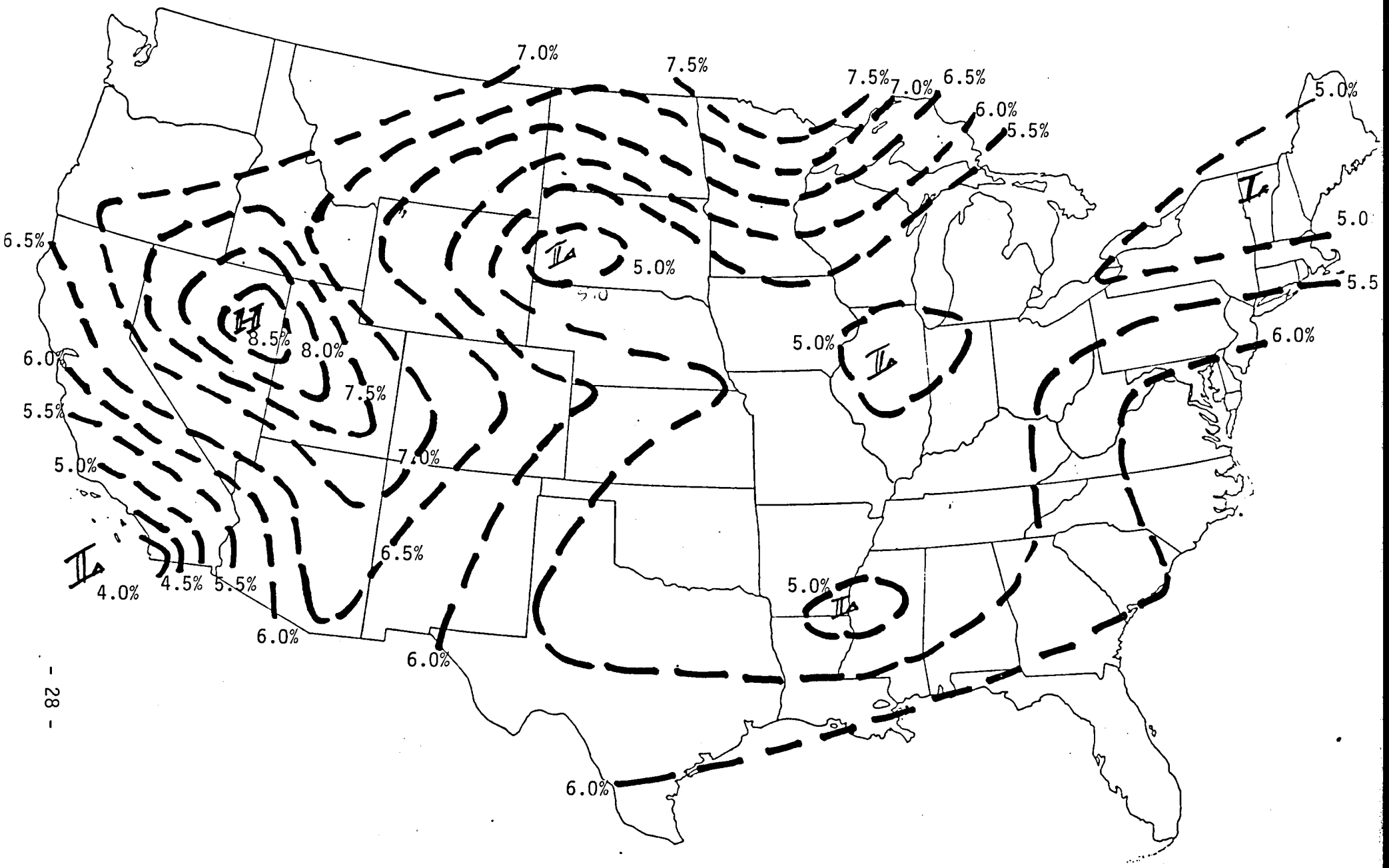

Figure 6. Standard deviation of the relative humidity of the 700-500 mb layer for the spring season.

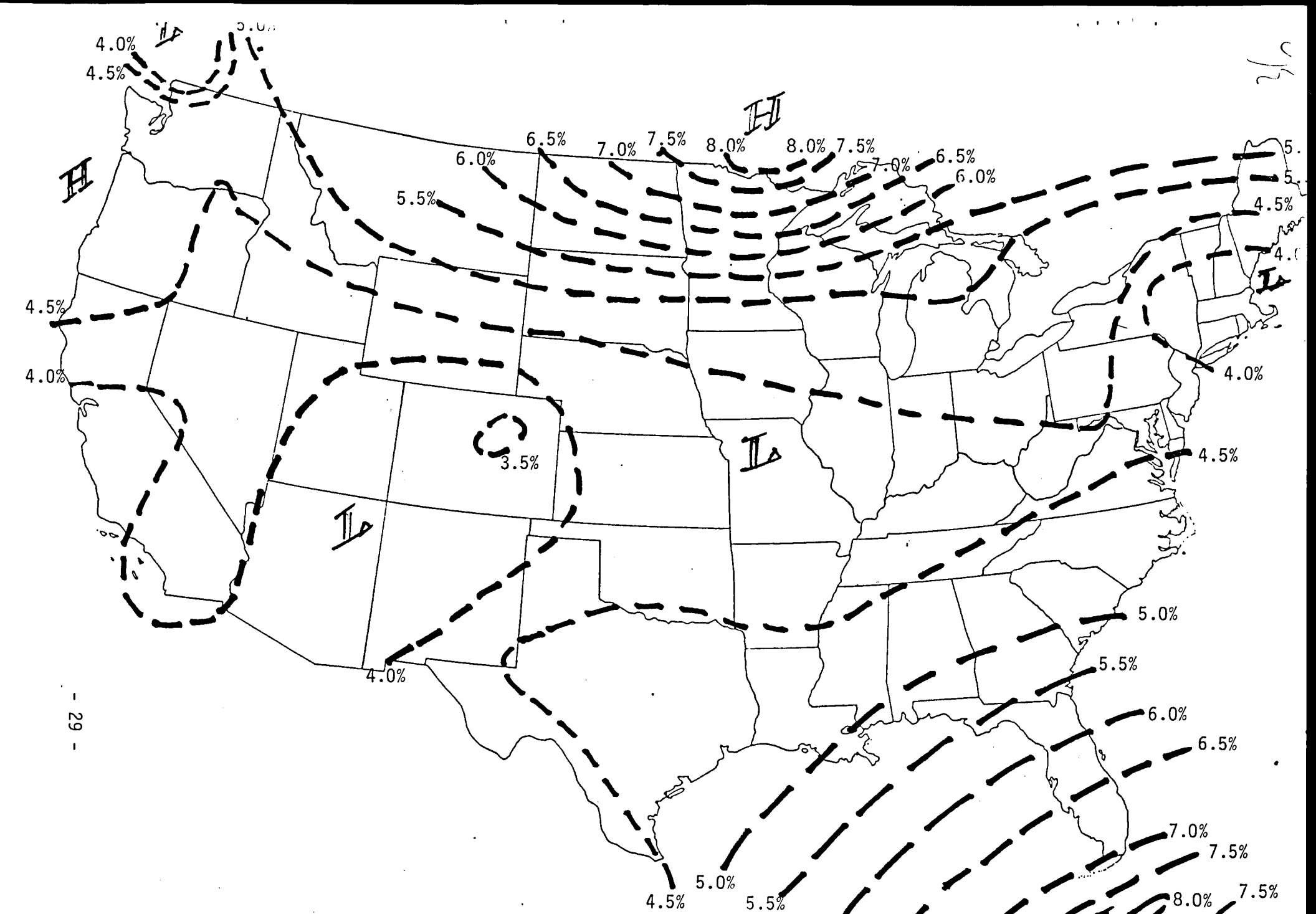

Figure 7. Standard deviation of the relative humidity of the 500-200 mb layer for the spring season.

desirable to conduct the observation phase in two stages, one year apart. This will allow observation strategy and hardware innovation to develop as we gain more knowledge from the earlier set of observations. This logical, stepwise progression of the experiment is crucial to assuring the success of these efforts. The first year program would be conducted during a four week period and the second year during a six week period.

4.3 Required observations and platforms

Table 2 outlines the required observations for the middle and upper tropospheric cloud experiment. These observations are broken into two space scales, cloud scale and meso-synoptic scale. It is essential to observe both scales since one expects significant sensitivity of the cloud formation and maintenance to both scales of motion.

Table 3 presents two lists of required platform resources for this experiment, the first list is for the minimum platform resources required to meet most experiment objectives. We estimate that 60% of the objectives could be met with these resources. The second list contains the optimum platform configuration; with these resources available virtually all experimental objectives could be addressed.

TABLE 2

REQUIRED OBSERVATIONS

STATE PARAMETERS	CLOUD SCALE PLATFORM	MESO-SYNOPTIC SCALE PLATFORM
Temperature (x,y,z)	A/C	Rawinsonde-satellite
Water vapor (x,y,z)	A/C	" "
Surface Temperature	A/C	Satellite
DYNAMIC PARAMETERS		
Wind Components		
u (x,y,z)	A/C	Rawinsonde
v (x,y,z)	A/C	"
w (x,y,z)	Sfc. Doppler Lidar	"
MICROPHYSICAL PARAMETERS		
Liquid water content, l		
l (x,y,z)	A/C	-
Ice water content	A/C	-
Crystal habit		
Crystal orientation	A/C	-
Freezing nuclei		
Type		
Concentration	A/C	-
Size Distributions (ice & liquid)		
BULK CLOUD FEATURES		
Height	A/C	Satellite
Translation	Sfc. Lidar	Satellite
Areal extent	A/C Photo.	Surface, Satellite
3-D neph	A/C Photo.	Surface, Satellite
Cloud topography uniformity	A/C Lidar & Surface Lidar	Satellite
RADIATION		
K↑↓ TOT, VIS, NIR (x,y,z) $\Delta\lambda$ [C,S]	A/C	Surface-Satellite
L↑↓ TOT, 10μm (x,y,z) $\Delta\lambda$ [C,S]	A/C	Surface-Satellite

$I_\lambda(\xi)$	A/C	Surface-Satellite
10 μm, vis, 1.6 μm....[C,S]		

$K_{\downarrow\lambda}$ = spectral shortwave irradiance
$L_{\downarrow\lambda}$ = spectral long wave irradiance
$I_\lambda(\xi)$ = spectral radiance at selected wavelengths, λ, and angles ξ

TABLE 2

TABLE 3

MINIMUM REQUIRED PLATFORM RESOURCES

-- AIRCRAFT (2)

1 microphysical + radiation + state + dynamical

1 radiation + microphysical + state + dynamical

-- SATELLITE

1 GEO SAT with IR + VIS imagery

-- SURFACE

NWS 00 and 12 Z rawinsonde

NWS 3 hour surface data

1 Surface Lidar

OPTIMUM PLATFORM RESOURCES

-- AIRCRAFT (3)

1 microphysical + state + dynamical + radiation

1 radiation + microphysical + state + dynamical

1 dynamical + state + microphysical + radiation

-- SATELLITE

2 GEO SAT with VAS

2 Low orbit with sounder and imaging

-- SURFACE

2 Surface Doppler Lidar

1 Surface Lidar

NWS on six hour rawinsonde schedule during study periods

Hourly surface data including all-sky continuous photography

4.3.1 Types of Aircraft Required

In the optimum configuration three aircraft are required. Ideally all three would be capable of operating between altitudes of 12,000 feet to 50,000 feet at airspeeds less than 100 mps. This is, of course unrealistic. Considering the type and availability of instrumentation, compromises on both airspeed and altitude ceiling are probably necessary. We state following minimum criteria:

1. One aircraft with operating capability to at least 41,000 feet, and airspeed less than 150 mps.

2. Two aircraft capable of operating to 35,000 feet with airspeeds less than 150 mps.

Table 4 lists the specific observations required for the three aircraft in the optimum platform configuration referred to in Table 3. The common measurements column insures the redundancy of a basic complement of measurements. The advantages of this configuration are discussed in the following section.

4.3.2 Modes of Platform Utilization

The mode of operation of the various observational systems will vary from system to system. For the purposes of this proposal we shall outline the normal operations mode for the major measurement systems referred to in Table 2. Under each observing system a semi-quantitative attempt is made to assess the impact this requirement will have on the corresponding facility or the estimated cost of the service.

TABLE 4.

REQUIRED AIRCRAFT OBSERVATIONS

	Common measurements for all A/C	Specific additional measurements for A/C	
Housekeeping	Time Heading Position Pitch Roll Ground Speed/Airspeed Radar Altitude	1, 2 and 3 (refer to Aircraft specialization) 1. radiation 2. cloud physics 3. dynamic	
State parameters	Static pressure Air temperature Front/Dew point temperature T_{cld} (side looking radiometer) T_{sfc} (downward looking radiometer)		
Dynamic parameters	Wind speed/Direction (u, v)	u, u′ v, v′ w, w′	3
Radiation parameters	$K\uparrow\downarrow_{TOT,VIS,NIR}$ $I_{\Delta\lambda}(\theta)$=10μm 5μm 1.6μm $L\uparrow\downarrow_{TOT}$ Satellite ground truth radiometers N↑ 10μm (T_{sfc}) Lidar (downward looking)		
Microphysical parameters	LWC IWC n(r) or n(Δx, Δy	Ice crystal Habit Orientation	1 & 2
Other	Photography Down looking Side looking	Nuclei Freezing Giant Aitken Composition	

NWS Rawinsonde and Surface Observations

During a six week experiment period the NWS support activities (surface + rawinsonde) would be their normal SOP. During this same six week period we would anticipate eight 48 hour periods with rawinsondes released at three hour intervals. During the same intensive periods surface observations would be collected hourly.

IMPACT: 96 additional rawinsonde releases + personnel/station

Aircraft

During the six week experiment period each aircraft would be based within or close to the experiment region. Based upon prediction of the desired phenomenon and real time satellite and aircraft data, the aircraft would be deployed to the specific experiment target. We would anticipate 20 four hour sorties per plane during the six week experiment. There would be more sorties than NWS intensive periods since most systems will require more than one sorti and some targets (i.e. Cb anvil cirrus) will not require intensive NWS support.

IMPACT: 80 aircraft flight hours/AC.

In addition to the platform requirements and committments outlined above, considerable resource committments must be made for aircraft radiation, microphysical, state and dynamics hardware, archive and data reduction.

In the optimum 3 aircraft configuration we envision three highly similar instrumentation configurations for radiation, microphysics, state and dynamic measurements. As such, the aircraft could be deployed serially to observe evolution of middle and upper tropospheric cloud

fields or at the same time to reveal a more nearly simultaneous 3D structure of the radiation, microphysics, state and dynamic variables. The similarity of capability also protects the experiment from inevitable aircraft and/or instrumentation malfunctions at critical times.

IMPACT: Experiments/hardware support for each aircraft 200 K

(for three aircraft total 500 K)

Lidar

Ranging - continuous (5 sec.) profiling for at least the six week experiment period. This may be relaxed during periods when middle and upper tropospheric clouds are obviously absent.

Doppler - continuous operations during aircraft operations periods and during portions of NWS intensive operations.

IMPACT: Ranging - approximately 720 operating hours

Doppler - approximately 150 operating hours

Satellite

During the entire six week experiment period all satellite imagery and radiometric data collected from geostationary and low orbiting meteorological satellites over the experiment area will be archived. In addition, real-time infrared and visible imagery from the appropriate sector of a geostationary image must be available to experiment planners throughout the experiment.

IMPACT: A) Continuous operation of ground receiving station for archival and mission planning, execution. Impact 6 weeks @ $37,500

B) Satellite data archive requirements not yet ascertained, but significant.

4.4 Options for the Observational Program

Faced with current realities of restricted resources available for pursuing worthwhile scientific goals, we will now consider several different options for the observational program. The most attractive option, number 1, which could meet nearly all the scientific objectives outlined in section 1.1 requires the resources listed in Table 4. This is in essence the full complement of platforms discussed in section 4.3.

OPTION 1

--Augmented National Weather Service rawinsonde releases
--Dopler Lidar (NOAA, ERL)
--Real time GOES support
--Satellite data archive
--Three research aircraft
    a. Radiation specialization
    b. Microphysical specialization
    c. Dynamics specialization

OPTION 2:

--Same as option 1 above except only two aircraft
--Two research aircraft
    a. Radiation specialization
    b. Microphysical specialization

OPTION 3:

--Conventional NWS rawinsonde operations (00 and 12 Z)
--Real time GOES support
--Satellite data archive
--Two research aircraft
    a. Radiation specialization
    b. Microphysical specialization

OPTION 4:

--Conventional NWS rawinsonde observations (00 and 12 Z)
--Satellite data archive
--One researach aircraft - radiation specialization

TABLE 4.4.1.

ALTERNATIVE EXPERIMENTAL PROGRAM LEVELS OF EFFORT

Option 2 would be similar to option 1 with the exception of one fewer aircraft. Relying on two instead of three aircraft would affect the experiment in two ways. Aircraft data could not be collected in as near a simultaneous time frame as with three aircraft; and the experiment would become more vulnerable to aircraft and instrumentation failures. These latter problems could largely be compensated for by increasing the length of the experiment.

Option 3, outlined in Table 4 significantly decreases the resources required, but at the same time, limits the ability of the experiment to meet the full complement of scientific goals. Option 3 would rely on only the 00 and 12 Z soundings available from the NWS rawinsonde network. This would severely limit our ability to define the synoptic scale conditions and only the most static cases could be considered for model verification studies. In addition by not utilizing the doppler lidar, we give up an opportunity to define the smaller scales of vertical motion in these cloud systems.

In summary, with option 3 a substantial reduction of resources required has been made at the expense of developing a complete physical representation of synoptic and micro scale motions.

Option 4 puts this experiment back at a single institution level. In addition to the compromises noted above, option 4 in essence relies upon only one aircraft and other conventional data. While such a limited investigation would yield some new information on the radiative and microphysical properties of upper tropospheric clouds, the complete set of objectives outlined in section 1.1 could not be met.

Probably the best compromise available from the above options would be to adopt option 4 for the first year observation program as a forerunner to implementing option 1 or 2 in the following year. In this way, a rather modest investment could satisfy the needs outlined in the last paragraph of Section 4.2.2: the development of strategy and hardware innovation for the most complex component of the experiment, the aircraft.

Then, the second year would see the implementation of a full scale observational program aimed at the broader set of scientific goals.

5.0 SPECIFIC COLORADO STATE UNIVERSITY OBJECTIVES, GOALS AND RESPONSIBILITIES

As mentioned in the opening remarks and is obvious from the text, the scope of the Extended Cloud and Radiation Program is beyond that of one group or agency. Therefore, besides participation in the planning and overall execution of the experimental program, we propose to take responsibility for the following specific activities.

1. Continue development and utilization of time dependent physical-numerical model to study the relative importance of physical processes in the formation, maintenance and dissipation of middle and upper tropospheric clouds. (Proposal pending with the National Science Foundation.)

2. Apply the aforementioned model results to further specifically define time and space scales, critical parameters and accuracy requirements of observational program.

3. Take lead responsibility in aircraft radiometer development and deployment for measurements of $K\uparrow\downarrow_{TOT,VIS,NIR}$; $LW\uparrow\downarrow_{TOT}$; $I(\theta)$ .5 - .7 μm; T_{cld}; T_{sfc}

4. Analyze observational data in a manner enabling comparison with upper tropospheric cloud model results.

5. Utilize verified model to investigate cloud property sensitivity to various processes and conditions.

Our CSU research group has been working for the past two years on essential precedent problems to the successful design and execution of a meaningful upper and middle tropospheric cloud experiment. These activities have focused upon a study of the environmental characteristics surrounding extensive areas of upper and middle tropospheric clouds, development of a physical-numerical model to simulate the roles of the various physical processes acting upon the upper and middle tropospheric cloud layer and gathering statistical information on the duration and geographic origin of these systems. A report containing the results of

the investigation into the attendant environmental structures is given in Appendix I. Section 3.0 described the physical-numerical model currently under development and expected to be operational in mid 1982. The third effort is currently under way.

In addition to these three efforts designed principally to investigate all physical processes interacting in upper and middle tropospheric clouds, we have performed numerous studies to examine specifically the radiative properties of these clouds. The most recent examples of these efforts are Griffith, Cox and Knollenberg, (1980), Welch, Cox, and Davis (1980) Welch, Cox and Zdunkowski (1980) and Paltridge et al. (1981).

The Principal Investigator has enjoyed a productive involvement in many previous airborne radiation measurement programs, the most recent of which have been GATE (1974) and MONEX (1979).

6.0 ADMINISTRATIVE ORGANIZATION OF THIS RESEARCH

It is obvious from the scope of the middle and upper tropospheric cloud research program that its execution transcends any one institution. The involvement of several government agencies and universities is essential to the successful completion of this work. The participation may be conveniently divided into two categories: operations and facility support and research support.

The platform resources required clearly dictate the participation of some specific agencies. In addition it will be highly desirable to have research personnel from these same agencies participate in the experiment and subsequent data reduction and analysis. The biggest contribution of the university community will be in conducting specific experiments with specific hardware and in the analysis of much of the data.

The obvious operations and facility support required and associated agencies are listed in Table 5.

TABLE 5

Ranging Lidar	Universities
Doppler Lidar	NOAA (ERL, SELS)
Aircraft	NASA, NOAA, NSF (NCAR)
Aircraft Operations	FAA
Satellite	NASA, NOAA
Rawinsonde	NOAA, (NWS)

From the list compiled in Table 2 and the breadth of scientific talent required to accomplish this experiment, it is obvious that some centralized focal point for coordination and resource deployment must be established. The bureaucratic term for this is a lead agency. One needs to be identified before this program can effectively proceed. NASA, NSF

or NOAA or some combination of the three are obvious civilian agencies capable of taking this lead responsibility. Table 6 is a cursory timetable for a number of critical events which must take place if a successful observation program is to be mounted in the Spring, 1983.

The following quote from the "Report of the Climate Dynamics Panel to the U.S. Committee for the Global Atmospheric Research Program, Assembly of Mathematical and Physical Sciences, National Research Council, entitled Elements of the Research Strategy for the United States Climate Program" expresses the importance and tractability of this research.

> "4.3.1.2 Cloud Radiation Dynamic Interactions
>
> The importance of horizontally extensive, persistent tropospheric stratiform clouds in modulating the earth's radiation budget is widely accepted. However, improved understanding of cloud-radiation budget/climate interactions requires a knowledge of not only the radiative characteristics of the clouds but also their spatial and temporal extents and the physical and dynamical processes responsible for their formation, persistence, and dissipation. The studies must deal with both low-level stratiform clouds, including marine stratus and strato-cumulus, and upper-level stratiform clouds, particularly cirrus and altostratus. Both modeling and observational studies are required.
>
> The precise design of the observational studies remains to be determined. The observational effort must attempt to define the physical characterisitics, and thermodynamic and dynamic structures of not only the cloud itself but also the large scale environment around it. Observation systems should include aircraft, ships for marine stratiform cloud studies, rawinsondes, lidars, satellites, acoustic sounders, and radiometersondes.
>
> The areal and temporal extent of major stratiform cloud systems must also be determined. These observations can be accomplished primarily from satellite and lidar observations. Some statistical information on the radiative characteristics of the cloud may also be derived from this data set.
>
> A rather complete understanding of the behavior and radiative characteristics of tropospheric stratiform clouds should emerge from these studies. Then, physicaily consistent parameterization techniques may be developed to investigate cloud radiation/climate interactions in both prognostic and diagnostic models.

EVENT TIMETABLE

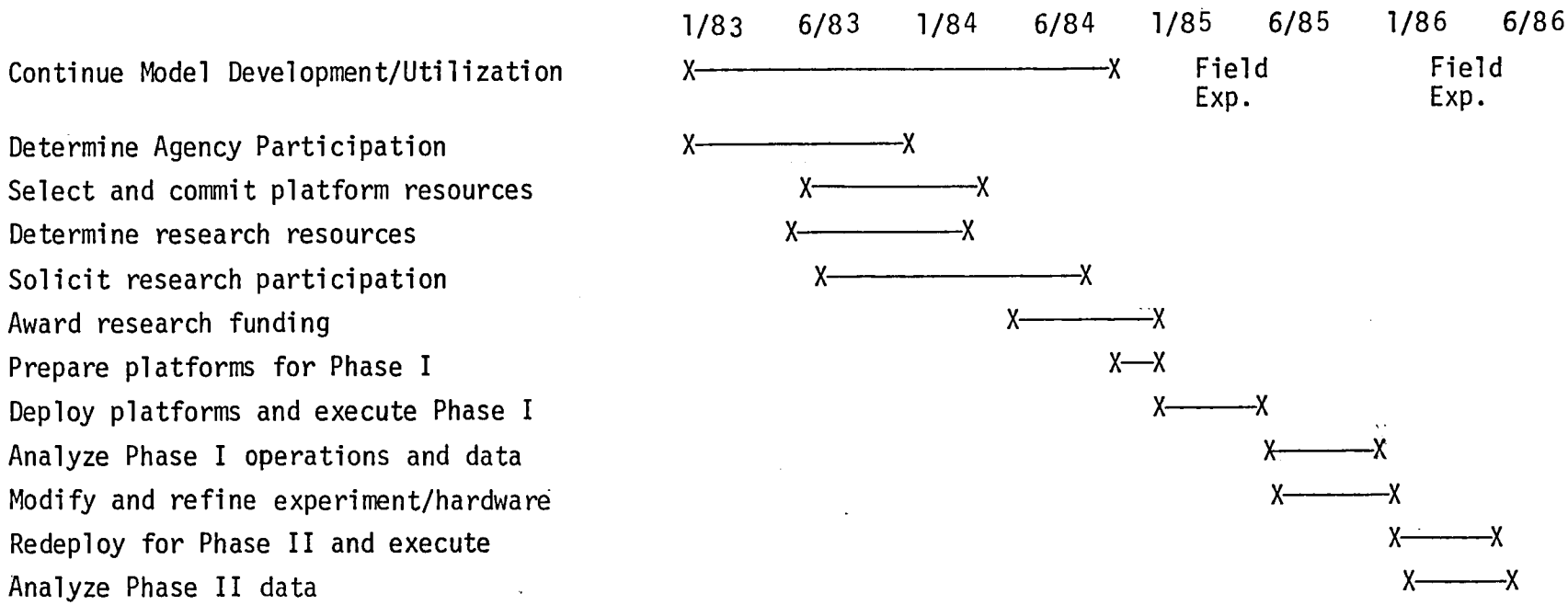

TABLE 6.

This research is feasible using 1977 technology. Furthermore, it can be accomplished largely within or near the continental United States because the cloud phenomena occur frequently over or near the North American continent, the scientific expertise for the various elements resides within the United States, and the aircraft and instrumentation capabilities are large dominated by the United States scientific community. The experimental phase could rely heavily on the National Weather Service rawinsonde network thereby largely eliminating the need for additional, costly rawinsonde equipment. High altitude capability aircraft from NCAR, the National Aeronautics and Space Administration, the National Oceanic and Atmospheric Administration, and the Department of Defense could provide the airborne platform for many of the observations."

7.0 REFERENCES

Allen, J. R., 1971: Measurements of cloud emissivity in the 8-13 μm waveband. J. Appl. Meteor., 10, 260-265.

Arakawa, A., 1966: Computation design for long-term numerical integration of the equations of fluid motion: two-dimensional incompressible flow. Part I. J. of Comp. Phys., 1, 119-143.

Arnason, G., R. S. Greenfield and E. A. Newburg, 1968: A numerical experiment in dry and moist convection including the rain stage. J. Atmos. Sci., 25, 404-415.

Asai, T., and K. Nakamura, 1978: A numerical experiment of airmass transformation over warmer sea, Part I: Development of a convectively mixed layer. J. Meteor. Soc. of Japan, 56, 424-434.

Asselin, R., 1972: Frequency filter for time integrations. Mon. Wea. Rev., 100, 487-490.

Braham, R. R. Jr., and P. Spyers-Duran, 1967: Survival of cirrus crystals in clear air. J. Appl. Meteor., 6, 1053-1061.

Coleman, R. F., and K-N Liou, 1980: Light scattering by hexagonal ice crystals. Vol. of Extended Abstract, International Radiation Symposium, Fort Collins, CO., Aug. 11-16, 511-513.

Conover, J. H., 1960: Cirrus patterns and related air motions near the jet stream as derived by photography. J. of Meteor., 17, 532-546.

Cotton, W. R., and G. J. Tripoli, 1978: Cumulus convection in shear flow, three dimensional numerical experiments. J. Atmos. Sci., 35, 1503-1521.

Cox, S. K., 1969: Radiation models of mid-latitude synoptic features. Mon. Wea. Rev., 97, 637-651.

Cox, S. K., 1971: Cirrus clouds and the climate. J. Atmos. Sci., 28, 1513-1515.

Cox, S. K., 1976: Observations of cloud infrared effective emissivity. J. Atmos. Sci., 33, 287-289.

Davis, P. A., 1971: Observations of cloud infrared effective emissivity. J. Atmos. Sci., 33, 287-289.

Deirmendjian, D., 1960: Atmospheric extinction of infrared radiation. Personal communication -- Document, 371-381.

Deirmendjian, D., and R. J. Clasen, 1962: Light scattering on partially absorbing homogeneous spheres of finite size. U.S.A.F. Project Rand, R-393-PR, 44 pp.

Deirmendjian, D., 1967: Scattering and polarization properties of water clouds and hazes in the visible and infrared. Appl. Opts., 3, 187-196.

Feigel'son, E. M., 1973: Radiant heat transfer in a cloudy atmosphere. Israel Program for Scientific Translations, Jerusalem 1973 (available form NTIS), 191 pages.

Fleming, J. R., and S. K. Cox, 1974: Radiative effects of cirrus clouds. J. Atmos. Sci., 31, 2182-2188.

Fouquart, Y., B. Bonnel, C. Fravalo, R. Rosset, and J. C. Vanhoutte, 1980: Radiative properties of stratocumulus clouds. Vol. of Extended Abstracts, International Radiation Symposium, Fort Collins, CO, Aug. 11-16, 462-464.

Fritz, S., and P. Krishna Rao, 1967: On the infrared transmission through cirrus clouds and the estimation of relative humidity from satellites. J. Appl. Meteor., 6, 1088-1096.

Griffith, K. T., and S. K. Cox, 1977: Infrared radiative properties of tropical cirrus clouds inferred from broadband measurements. Atmos. Sci. Paper No. 269, Colorado State University, Fort Collins, CO., 80523.

Griffith, K. T., S. K. Cox, and R. G. Knollenberg, 1980: Infrared radiative properties of tropical cirrus clouds inferred from aircraft measurements. J. Atmos. Sci., 37, 1077-1087.

Hack, J. J., and W. H. Schubert, 1976: Design of an axisymetric primitive equation tropical cyclone model. Atmos. Sci. Paper #263, Colo. State University, Fort Collins, CO., 70 pp.

Hall, W. D., and H. R. Pruppacher, 1976: The survival of ice particles falling from cirrus clouds in subsaturated air. J. Atmos. Sci., 33, 1996-2006.

Hansen, J. E., 1969: Radiative transfer by doubling very thin layers. Astrophysical Journal, 155, 565-573.

Herman, B. M., 1962: Infrared absorption, scattering and total attenuation cross-sections for water spheres. Quart. J. Roy. Meteor. Soc., 88, 143-150.

Heymsfield, A., 1975a: Cirrus uncinus generating cells and the evolution of cirriform clouds. Part I: the structure and circulations of the cirrus uncinus generating head. J. Atmos., Sci. 32, 799-808.

Heymsfield, A., 1975b: Cirrus uncinus generating cells and the evolution of cirriform clouds. Part II: the structure and circulations of the cirrus uncinus generating head. J. Atmos. Sci., 32, 809-819.

Heymsfield, A., 1975c: Cirrus uncinus generating cells and the evolution of cirriform clouds. Part III: numerical computations of the growth of the ice phase. J. Atmos. Sci., 32, 820-830.

Heymsfield, A., 1977: Precipitation development in stratiform ice clouds: a microphysical and dynamical study. J. Atmos. Sci., 34, 367-381.

Hunt, G. E., 1973: Radiative properties of terrestrial clouds at visible and infrared thermal window wavelengths. Quart. J. Roy. Meteor. Soc., 99, 346-369.

Jacobowitz, H., 1970: Emission, scattering and absorption of radiation in cirrus cloud layers. Ph.D. Thesis, Massachusetts Institute of Technology, 181 pp.

Jayaweera, K.O.L.F., 1971: Calculations of ice crystal growth. J. Atmos. Sci., 38, 738-736.

Jiusto, J. E., 1971: Crystal development and glaciation of a super-cooled cloud. J. Rech. Atmos., 5, 69-86.

Korb, G., and F. Moller, 1962: Theoretical investigation on energy gain by absorption of solar radiation clouds. Final Technical Report.

Kuhn, P. M., 1963a: Radiometersonde observations of infrared flux emissivity of water vapor. J. Appl. Meteor., 2, 368-378.

Kuhn, P. M., 1963b: Measured effective longwave emissivity of clouds. Mon. Wea. Rev., 635-640.

Kuhn, P. M., and V. E. Suomi, 1965: Airborne radiometer measurement of effects of particles on terrestrial flux. J. Appl. Meteor., 4, 246-252.

Kuhn, P. M., and H. K. Weickmann, 1969: High altitude radiometric measurements of cirrus. J. Atmos. Sci., 8, 147-154.

Kuhn, P. M., 1970: Airborne observations of the contrail effects on the thermal radiation budget. Personal communication - Document.

Lilly, D. K., 1962: On the numerical simulation of buoyant convection. Tellus 14, 148-172.

Lilly, D. K., 1965: On the computational stability of numerical solutions of time-dependent non-linear geophysical fluid dynamics problems. Mon. Wea. Rev., 93, 11-26.

Lilly, D. K., 1968: Models of cloud-topped mixed layers under a strong inversion. Quant. J. Roy. Meteor. Soc., 105, 303-306.

Liou, Kuo-Nan, 1975a: Theory of the scattering-phase-matrix determination for ice crystals. J. Opt. Soc. Amer., 65, 159-162.

Liou, Kuo-Nan, 1975b: On the transfer of solar radiation in aerosol atmospheres. J. Appl. Meteor., 32, 2166-2177.

Liou, Kuo-Nan, 1975c: On the absorption, reflection and transmission of solar radiation in cloudy atmospheres. J. Atmos. Sci., 33, 799-805.

Liou, Kuo-Nan, and G. D. Wittman, 1979: Parameterization of the radiative properties of clouds. J. Atmos. Sci., 36, 1261-1273.

Liou, Kuo-Nan, K. A. Gebhart, and S. C. Ou, 1980: Radiative equilibrium temperatures in cirrus cloudy atmospheres. Vol. of Extended Abstracts, International Radiation Symposium, Fort Collins, CO., Aug. 11-16, 453-455.

Lipps, F. B., 1971: Two-dimensional numerical experiments in thermal convection with vertical shear. J. Atmos. Sci., 28, 3-19.

Ludlam, F. H., 1948: The forms of ice-clouds. Quart. J. Roy. Meteor. Soc., 74, 39-56.

Ludlam, F. H., 1956: The forms of ice clouds: II. Quart. J. Roy. Meteor. Soc., 83, 357-365.

Murcray, D. G., J. N. Brooks, F. H. Murcray and W. J. Williams, 1974: 10 to 12 μm spectral emissivity of a cirrus cloud. J. Atmos. Sci., 31, 1940-1942.

Oddie, B. C. V., 1958: Some cirrus cloud observations made by the Westminister Shiant Isles Expedition, 204-208.

Ogura, Y., and N. A. Phillips, 1962: Scale analysis of deep and shallow convection in the atmosphere. J. Atmos. Sci., 19, (2) 173-179.

Oliver, D. A., W. S. Lewellen and G. G. Williamson, 1978: The interaction between turbulent and radiative transport in the development of fog and low-level stratus. J. Atmos. Sci., 35, (2) 301-316.

Paltridge, G. W., 1974: Infrared emissivity, shortwave albedo, and the microphysics of stratiform water clouds. J. Geophys. Res., 79, 4053-4058.

Paltridge, G. W., and C. M. R. Platt, 1980: Aircraft measurements of solar and infrared radiation and the microphysics of cirrus clouds. Quart. J. Roy. Meteor. Soc., 107, 367-380.

Plass, G. N., 1968: Radiance and polarization of multiple scattered light from haze and clouds. Appl. Optics, 7, 1519-1527.

Platt, C. M. R., and D. J. Gambling, 1971: Emissivity of high layer clouds by combined lidar and radiometric techniques. Quart. J. Roy

Meteor. Soc., 97, 322-325.

Platt, C. M. R., 1973: Lidar and radiometric observations of cirrus clouds. J. Atmos. Sci., 30, 1191-1204.

Platt, C. M. R., 1975: Infrared emissivity of cirrus simultaneous satellite lidar and radiometric observations. Quart. J. Roy. Met. Soc., 101, 119-126.

Randall, D. A., 1980: Entrainment into a stratocumulus layer with disturbed radiative cooling. J. Atmos. Sci., 37, 148-159.

Schmetz, J., and E. Raschke, 1980: Radiative properties of boundary layer clouds as measured by an aircraft. Vol. of Extended Abstracts, International Radiation Symposium, Aug. 11-16, Fort Collins, CO., 514-516.

Schubert, W. H., 1976: Experiments with Lilly's cloud-topped mixed layer model. J. Atmos. Sci., 33, 436-446.

Schubert, W. H., J. S. Wakefield, E. J. Steiner and S. K. Cox, 1979: Marine stratocumulus convection, Part I: Governing equations and horizontally homogeneous solutions. J. Atmos. Sci., 36, 1286-1307.

Sommeria, G., 1976: Three dimensional simulation of turbulent processes in the undisturbed trade wind boundary layer. J. Atmos. Sci., 33, 216-241.

Starr, D. O'C., and S. K. Cox, 1979: Characteristics of middle and upper tropospheric clouds as deduced from rawinsonde data. Atmos. Sci. Paper #327, Colo. State University, Fort Collins, CO., 72 pp.

Stephens, G. L., 1980: Radiative transfer on a linear lattice: applications to anisotropic ice crystal clouds. J. Atmos. Sci., 39, (9), 2095-2104.

Swarztrauber, P., and R. Sweet, 1975: Efficient Fortran subprograms for the solution of elliptic equations. NCAR TN/IA-109, July, 138 p.

Wakefield, J., and W. H. Schubert, 1976: Design and execution of the marine stratocumulus experiment. Atmos. Sci. Paper #256, Colo. State University, Fort Collins, CO., 70 pp.

Welch, R. M., J. F. Geleyn, G. Korb and W. Zdunkowski, 1976: Radiative transfer of solar radiation in model clouds. Beitr. Phys. Atmos., 49, 128-146.

Welch, R. M., S. K. Cox, and W. G. Zdunkowski, 1980: Calculations of the variability of ice cloud radiative properties at selected solar wavelengths. Appl. Opts., 19, 3057-3067.

Welch, R. M., S. K. Cox, and J. M. Davis, 1980: Solar Radiation in Clouds. Meteorological Monography, Vol. 39, American Meteorological Society, 93 pp.

Yagi, T., 1969: On the relation between the shape of cirrus cloud and the static stability of the cloud level -- studies of cirrus clouds: Part IV. J. Meteor. Soc. Japan, 47, 59-64.

Yamamoto, G., T. Masayuki, and A. Shoji, 1971: Table of scattering function of infrared radiation for water clouds. NOAA Rech. Report NESS 57, 96 pp.

Yamamoto, G., and A. Shoji, 1975: Light scattering by a spherical particle. Appl. Opts., 14, 29-49.

Zdunkowski, W. G., D. Henderson, and J. V. Hales, 1965: The influence of haze on infrared measurements detected by space vehicles. Tellus, XVII, 147-165.

Zdunkowski, W. G., and F. Strand, 1969: Light scattering constants for a water clouds. Reprint from Pure and Applied Geophysics, 74, 110-133.

Zdunkowski, W. G., and W. K. Crandall, 1971: Radiative transfer of infrared radiation in model clouds. Tellus, XXIII, 517-527.

Zdunkowski, W. G., 1974: Solar radiative transfer in clouds using Eddington's approximation. Tellus, XXVI, 3, 361-368.

NASA PROPOSAL BUDGET			5/6/82			
			YEAR 1	YEAR 2 FIELD PHASE	YEAR 3 FIELD PHASE	YEAR 4 ANALYSIS
SALARIES						
	S. COX	2 MM	10000	10750	11556.25	18000(3 MM)
	C. PASQUA	6 MM	12000	13200	14520	15972
	POST DOC	12 MM		20000	22000	24200
	GRA'S	15MM	18750	19688	20672	21705
	SECRETARIAL	6 MM	6000	6600	7260	7986
	FRINGE RATE		0.18	0.19	0.21	0.22
	FRINGE	BENEFITS	5040	9731	11344	14389
TOTAL	SALARIES	& FRINGES	51790	79969	87352	102253
EQUIPMENT *			6000	6000	6000	0
MATERIALS	& SUPPLIES		2000	10000	5000	1000
DOMESTIC	TRAVEL		1500	8000	12000	1000
PUBLICATION	COSTS		1500	1000	2500	3000
COMPUTER	SERVICES		6000	5000	5000	7500
OTHER DIRECT	COSTS					
	PROGRAMMING	SERVICES	10500	11500	12700	14500
	DATA SERVICES		8000	8800	9700	10600
	DATA ACQ. *	(SAT GROUND STATION)		20000	30000	
	EQUIP RENTAL			4000	6000	
	COMMUNICATION		400	800	1200	400
	XEROX & POSTA		300	500	600	200
	GRA TUITION *		7112	7823	8606	9466
	MAGNETIC TAPE		300	500	750	
TOTAL	OTHER DIRECT COSTS		26612	53923	69556	35166
TOTAL	DIRECT	COSTS	95402	163892	187408	149919
INDIRECT	COSTS	@ .348 * IDC EXEMPT	28637	45264	49695	48878
TOTAL	COSTS		124039	209155	237103	198797

SECTION 5

Calculations of the variability of ice cloud radiative properties at selected solar wavelengths

R. M. Welch, S. K. Cox, and W. G. Zdunkowski

a reprint from **Applied Optics**
volume 19, number 18, September 15, 1980

Calculations of the variability of ice cloud radiative properties at selected solar wavelengths

R. M. Welch, S. K. Cox, and W. G. Zdunkowski

This study shows that there is surprising little difference in values of reflectance, absorptance, and transmittance for many of the intermediate-size particle spectra. Parrticle size distributions with mode radii ranging from ~50 to 300 μm, irrespective of particle shape and nearly independent of the choice of size distribution representation, give relatively similar flux values. The very small particle sizes, however, have significantly larger values of reflectance and transmittance with corresponding smaller values of absorptance than do the larger particle sizes. The very large particle modes produce very small values of reflectance and transmittance along with very large values of absorptance. Such variations are particularly noticeable when plotted as a function of wavelength.

I. Introduction

Energy balance climate models and even general circulation forecasting models recently have sought to include improved estimates of particulate scattering and absorption characteristics. Rasool and Schneider[1] and many others have been assessing the impact of man's activities upon climate change. Large scale field programs such as GATE have been observing the radiative characteristics of natural aerosols. However, clouds are the most important modulators of radiation in the earth's and most other planetary atmospheres. Persistent cirrus cloud layers are known to exist over large regions of the globe,[2] ranging in thickness from thin wisps to 5 km or more.

The radiative characteristics of cirrus clouds are, however, not well understood. Mesaurements of the size, shape, orientation, and number densities of cirrus ice crystals show wide variability. Perhaps the greatest obstacle to a proper assessment of the cirrus cloud radiative properties has been the inability to treat nonspherical particles. Liou[3] calculated the radiative characteristics of long cylinders. However, calculations using cylinders do not agree with the experimental measurements from ice clouds. For instance, they produce cloud bows that are not observed and do not produce halos that are observed. Jacobowitz[4] and Wendling *et al.*[5] studied the radiative characteristics of hexagonal ice crystals. However, there is not yet adequate correspondence between theory and measurement. Wendling *et al.*[5] conclude that improved measurement of crystal size, shape, and orientation must be carried out before it is possible to make realistic comparisons between theory and observation.

Many authors have investigated the radiative characteristics of cirrus clouds.[3,6–14] While Liou[10,12] has modeled ice crystals with ice cylinders, other investigators used spherical Mie theory, in spite of the fact that it is known that nonspherical particles scatter more energy at intermediate and large scattering angles than do their spherical counterparts, although Bryant and Cox[13] do show a decrease in backscatter at 180° for a nonspherical particle shape. Welch *et al.*[14] used the Chýlek[15] surface wave suppression theory in an attempt to model the effects of nonsphericity. While good agreement between measurements of scattered radiation and theory has been reported[16] for aerosols, Welch and Cox showed that this technique may produce nonphysical values of absorption efficiency.[17] Recently the method has been the topic of considerable controversy.[18–20]

Due to the current uncertainties in measured cirrus ice crystal parameters, the present paper calculates the radiative characteristics of cirrus clouds for a wide range of cloud thicknesses and particle size distributions. Nonspherical corrections have been included in the computations, applying the recent semiempirical theory

Stephen Cox is with Colorado State University, Department of Atmospheric Science, Fort Collins, Colorado 80523; the other authors are with Johannes Gutenberg Universitat, Fachbereich Physik, Institut fur Meteorologie, D-6500 Mainz, Federal Republic of Germany.

Received 26 February 1980.
0003-6935/80/183057-11$00.50/0.

developed by Pollack and Cuzzi.[20] We have neglected preferential ice crystal orientation as a variable in these calculations although Griffith *et al.*[21] suggest, and more recently Stevens[22] has quantitatively confirmed, that ice crystal orientation may be a significant factor in determining the radiative properties of ice clouds.

II. Properties of Cirrus Clouds

There is wide variability in the microphysical structure of cirrus ice clouds with shapes including bullets, columns, plates, dendrites, stellars, and needles. Obviously no single crystal shape, column, hexagonal plate, or sphere, can be expected to simulate reasonably the proper scattering characteristics of all ice particles. Crystal orientation is another important consideration. It would be reasonable to expect a random orientation of small ice crystals. However, fluid dynamical considerations dictate that cylinders fall with the long axis horizontal.[23] Griffith *et al.*[21] offer this preferential orientation as a partial explanation for observed IR characteristics of cirrus clouds. Lidar backscattering meaurements[24] also indicate a coherent crystal orientation.

A number of ice crystal size distribution and ice water content measurements have been reported in recent years.[21,25-31] Reported ice water contents[27] vary from $\sim 10^{-3}$ g/m^3 at a temperature of -60°C to 0.5 g/m^3 at 0°C. At temperatures warmer than -15°C, ice crystal concentrations were 2–4 orders of magnitude higher than would be predicted from ice nuclei concentrations; this is in agreement with observations.[36] Concentrations of up to 3.8 cm^{-3} have been measured,[29] but concentrations of 0.1–1.0 cm^{-3} have been reported[37] thousands of feet below cirrus clouds. The mean and maximum crystal lengths have been found to be only slightly dependent upon air temperature but directly dependent upon ice water content. Mean ice crystal lengths often range from 100 to 300 μm with large crystals having lengths >1 mm. It should be noted that typical measurement instrumentation is highly sensitive to particle shape. Most investigators do not report the presence of small particle sizes (<100 μm). However, measurements by Heymsfield[26] and inferences by Griffith *et al.*[21] clearly suggest ice crystal lengths even <20 μm. The data of Heymsfield and Griffith *et al.* were the basis for the bimodal size distribution flux calculations reported by Welch *et al.*[14]

III. Radiative Transfer Calculations

A generalized two-stream flux method, developed by Zdunkowski *et al.*[38] and including the δ-function approximation,[39,40] has been used in the present work. Zdunkowski *et al.*[38] showed that all two-stream methods, including δ-Eddington, may be reduced to a simple form:

$$(dF_1)/d\tau = \alpha_1 F_1 - \alpha_2 F_2 - \alpha_3 S(\tau)/\mu_0, \quad (1)$$

$$(dF_2)/d\tau = \alpha_2 F_1 - \alpha_1 F_2 + \alpha_4 S(\tau)\mu_0, \quad (2)$$

$$(dS)/d\tau = -(1 - \omega_0 f)S(\tau)/\mu_0, \quad (3)$$

where F_1 and F_2 are the upward and downward diffuse fluxes, respectively, and S is the direct beam component. μ_0 is the cosine of zenith angle, τ is optical depth, ω_0 is the single scattering albedo, and the coefficients α_i are given by

$$\alpha_1 = U_1[1 - \omega_0(1 - \beta_0)], \quad (4)$$

$$\alpha_2 = U_2\beta_0\omega_0, \quad (5)$$

$$\alpha_3 = (1 - f)\omega_0\beta(\mu_0), \quad (6)$$

$$\alpha_4 = (1 - f)\omega_0[1 - \beta(\mu_0)]. \quad (7)$$

These coefficients are expressed in terms of the backward scattering coefficient of primary scattered parallel solar radiation,[41]

$$\beta(\mu_0) = \tfrac{1}{2}\int_{-1}^{0} P(\mu_0, -\mu')d\mu', \quad (8)$$

and in terms of the global backscattering coefficient,

$$\beta_0 = \int_{-1}^{1} \beta(\mu)d\mu. \quad (9)$$

The various two-stream methods can be reduced to this form, with each merely representing $\beta(\mu_0)$ and β_0 in a different way. The choice of

$$\beta_0 = 3(1 - g)/8, \quad (10)$$

$$\beta(\mu_0) = 0.5 - [(3\mu_0)/4]\,(g - f)/(1 - f), \quad (11)$$

$$U_1 = U_2 = 2.0, \quad (12)$$

results in the practical improved flux method (PIFM) and provides excellent agreement with results calculated using the adding/doubling method. g is the particle asymmetry factor

$$g = \langle\cos\theta\rangle = \tfrac{1}{2}\int_0^{\pi} \cos\theta P(\cos\theta)\sin\theta d\theta, \quad (13)$$

defined as the cosine of the average scattering angle, where $P(\cos\theta)$ is the azimuthally averaged phase function. f is defined as that portion of the scattered energy in the forward diffraction peak and is usually defined as

$$f = g^2, \quad (14)$$

in two-stream methods.

One advantage of the PIFM method is that it does not produce nonphysical values of flux, as is the case for various other approaches. For instance, the δ-Eddington approximation produces negative upward fluxes under some circumstances for small values of ω_0. Such conditions may be studied using the PIFM method. It has been shown[39] that nonphysical flux values may be caused by negative values of backscattering coefficients. This approach was used by Welch *et al.*[42] to identify further under what conditions various two-stream methods become unsatisfactory.

In the present paper, water vapor transmission is approximated through the use of a sum of exponentials[43] based upon expansion coefficients taken from Liou and Sasamori.[44] Absorption by CO_2, O_3, and trace gases is small in the solar spectrum and neglected in the present study. The water vapor atmospheric profile is taken from the GATE (phase III) measurements.[14] Calculations have been performed for nine spectral

regions, with band centers at 0.55, 0.75, 0.95, 1.15, 1.4, 1.8, 2.8, 3.3, and 6.3 μm, with values of the complex indices of refraction taken from Irvine and Pollack.[45]

IV. Model Atmospheres

The cirrus cloud has been assumed to be 3 km thick with a cloud base height of 9 km in all simulations. Therefore, absorption by water vapor above and within the cloud is small. The average cloud optical thickness was varied from $\tau = 0.6$ to 15.0 in all the following calculations. Cirrus clouds with large optical thicknesses have been reported by Reynolds *et al.*[46]

Due to the wide variability of particle size, number density, and ice water content, it is difficult to generalize the radiative characteristics of cirrus cloud particles. Welch *et al.*[14] attempted to surmount this problem by making calculations for a large number of different size distributions using the modified γ distribution

$$n(L) = aL^{\alpha} \exp\left[-\frac{\alpha}{\gamma}\left(\frac{L}{L_c}\right)^{\gamma}\right], \qquad (15)$$

Table I. Ice Crystal Spectra Characteristics Based upon the Modified γ Distribution Along with the Respective Symbol used in the Figures

	Symbol	Crystal type	α	γ	L_c (μm)
1	□	Column	4	1.0	6.0
2	○	Bullet	4	1.0	6.0
3	△	Sphere	4	1.0	6.0
4	+	Column	2	1.0	20.0
5	×	Bullet	2	1.0	20.0
6	◇	Sphere	2	1.0	20.0
7	⧋	Column	2	0.5	70.0
8	⧖	Bullet	2	0.5	70.0
9	⧗	Sphere	2	0.5	70.0
10	⋎	Column	5	1.0	175.0
11	⋈	Bullet	5	1.0	175.0
12	✳	Column	6	1.0	200.0
13	⧖	Bullet	6	1.0	200.0
14	⧺	Column	4	1.0	330.0
15	✡	Bullet	4	1.0	330.0
16	⧗	Sphere	4	1.0	330.0
17	⧺	Bullet	6	1.0	600.0
18	⋎	Column	6	1.0	600.0
19	⋀	Sphere	6	1.0	600.0

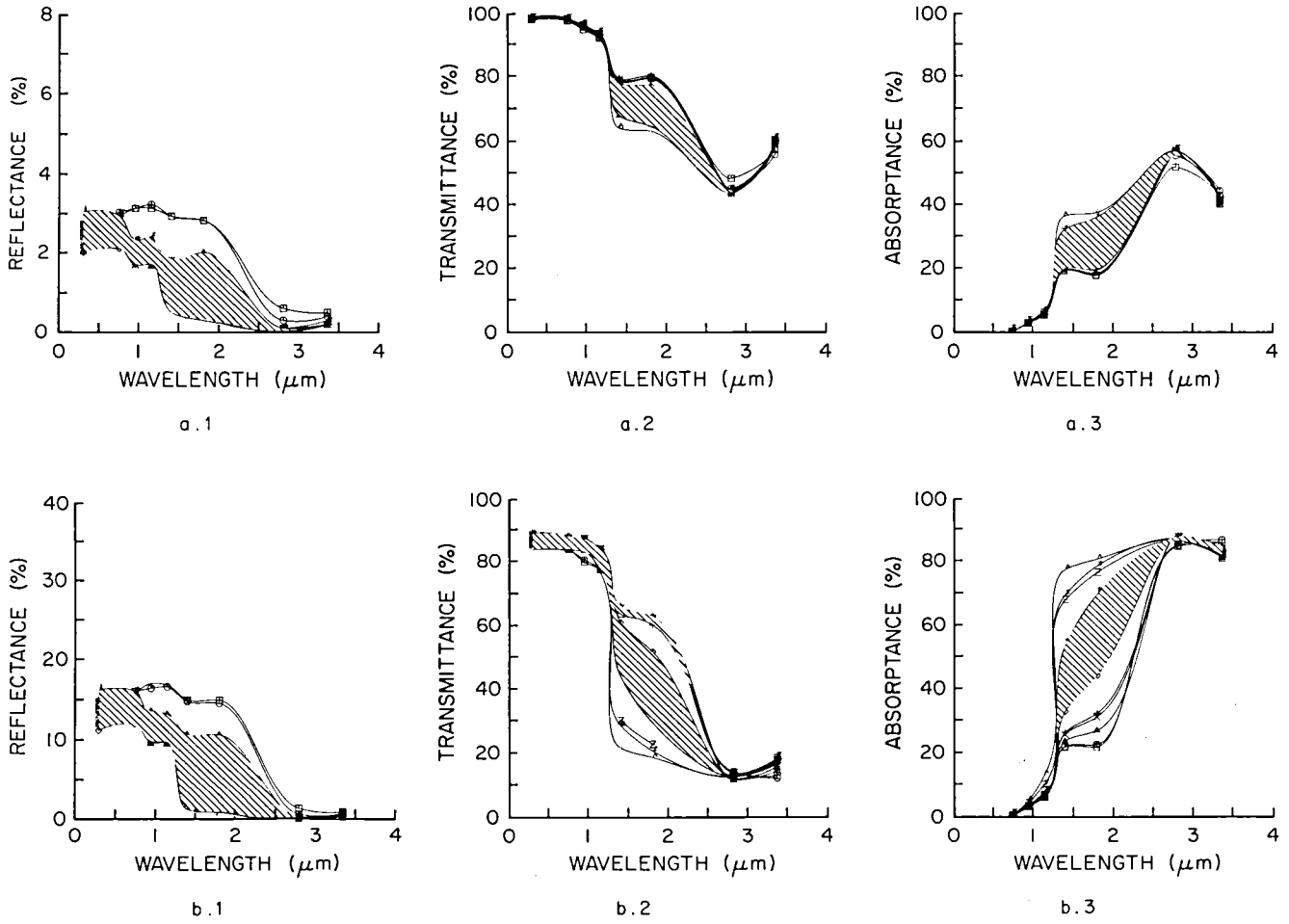

Fig. 1. Ice cloud reflectance, transmittance, and absorptance values for optical thickness $\tau = 0.6$ (a) and $\tau = 3.0$ (b). (Crosshatch areas contain curves not specifically denoted by the symbols visible in the figure; see Table I for symbol definitions.)

where L is the crystal length, and L_c is the distribution mode length. The effective radius is determined from equating equal cross-sectional areas

$$\pi r^2 = LW, \tag{16}$$

where W is the crystal width. Width-to-length ratios are taken from Heymsfield[25] for ice bullets and columns.

For bullets,

$$\begin{aligned} W &= 0.25L^{0.7856}\ (\text{mm}) \quad L \le 0.3\ \text{mm} \\ &= 0.185L^{0.532}\ (\text{mm}) \quad L > 0.3\ \text{mm}; \end{aligned} \tag{17}$$

for columns,

$$\begin{aligned} W &= 0.5L\ (\text{mm}) \quad L \le 0.3\ \text{mm} \\ &= 0.1973L^{0.414}\ (\text{mm}) \quad L \ge 0.2\ \text{mm}. \end{aligned} \tag{18}$$

Spherical Mie theory has been applied using the particle effective radius to obtain scattering and absorption efficiencies and the scattering asymmetry factor g for the different distributions.

Calculations for nineteen different size distributions, with effective mode radius r_c ranging from 6 to 600 μm and with particle shape including bullets, columns, and spheres, are included. Table I lists the relevant microphysical characteristics of the distributions examined in this study. While this list is not exhaustive, it probably brackets most size spectra.

V. Spherical Mie Calculations

Calculated values of cloud reflectance R, transmittance T, and absorptance A are shown as a function of wavelength for optical thicknesses $\tau = 0.6$ [Fig. 1(a)] and $\tau = 3.0$ [Fig. 1(b)]. The calculations were made at wavelengths depicted by the data points; the different symbols represent different distributions and are defined in Table I. The basic shapes of the curves for R, T, and A are preserved as optical thickness is increased. For an optical thickness of $\tau = 0.6$, cloud reflectance varies between 2 and 2.5% up to a wavelength of ~0.8 μm. At larger wavelengths reflectance decreased as a result of increased absorption. At wavelengths $\gtrsim$1.4 μm there is considerable variability in the radiative characteristics for the various size spectra. Crosshatch areas have been used in the figures to denote regions where the number of lines is too dense to resolve easily. The significance of the corsshatch areas is that there is surprisingly little variation in the radiative properties in spite of the wide variability of particle sizes. The values of reflectance and transmittance decrease with increasing particle size, while the values of absorptance increase with increasing particle size. The large variability in values of reflectance suggests a method for remote sensing of particle sizes. The ratio of reflectance at $\lambda = 1.5$–2.0 μm to that at $\lambda = 0.5$ μm ($R_{1.5}/R_{0.5}$) is much larger for the small particle distributions than for the larger size distributions. The fact that the reflectance values in the short wavelength regions ($\lambda < 0.7$ μm) are not as sensitive to the assumed distribution characteristics may provide a means for estimating optical depth. Obviously a far greater wavelength resolution is required to apply such a method to retrieve an estimate of particle size. Nevertheless, these preliminary results indicate that there may be sufficient variability in the cloud radiative characteristics to obtain such information. At larger optical thicknesses there may be far greater opportunity to apply such a method using ground-based transmittance measurements. The ratio $T_{1.5}/T_{0.5}$ provides good resolution for such a procedure. Once again, more detailed wavelength calculations should provide specific wavelengths where such differences are maximized. The method also may lend itself to the discrimination between ice and water phase, as ice and water have different absorption spectra at a given wavelength.

Figure 2 shows values of reflectance, transmittance, and absorptance as a function of optical depth. Figure 2(a) presents broadband results integrated across the entire solar spectrum, while Fig. 2(b) shows results for the wavelength region centered at $\lambda = 1.4$ μm. From Fig. 2(a) we may discern that broadband measurements will not discriminate between the various size distributions very well. In fact, the broadband results for reflectance are not significantly different from those obtained for the 0.55-μm band region (not shown). Cloud absorptance increases rapidly with optical thickness for small values of τ and then levels off at larger values of τ. Values of cloud absorptance generally do not exceed 20%, even for optically thick clouds, except for distributions with very large particle sizes. Of particular importance in the preceeding results in the fact that distributions with L_c varying between 70 and 330 μm do not have significantly different bulk radiative characteristics. These results indicate that knowledge of the exact size distribution may not be necessary to produce reasonable estimates of R, T, and A. The effect of bimodal size distributions upon the radiative properties of clouds have been presented by Welch *et al.*[14] and is not repeated here.

With the preceeding discussion as a basis, the following sections investigate the effect of particle nonsphericity upon these radiative properties.

VI. Theoretical Aspects of Particle Nonsphericity

In recent years there has been considerable progress in the ability to calculate scattering intensities for nonspherical particles. Most of the nonspherical methods are appropriate to specific particle geometries and require massive computer resources. As such they are not appropriate for routine calculations in the free atmosphere where only approximate values of particle size, shape, and orientation may be known. On the basis of results shown in the previous section, only approximate values of particle size and size distribution shape are required to produce reasonable estimates of bulk radiative properties of ice clouds. The question to be addressed in the following section is whether nonsphericity produces significant deviations in the resulting cloud radiative properties.

There have been a great number of scattering measurements for ensembles of particles and analog experiments for particle representations using microwave frequencies.[47–53] Most of these measurements show

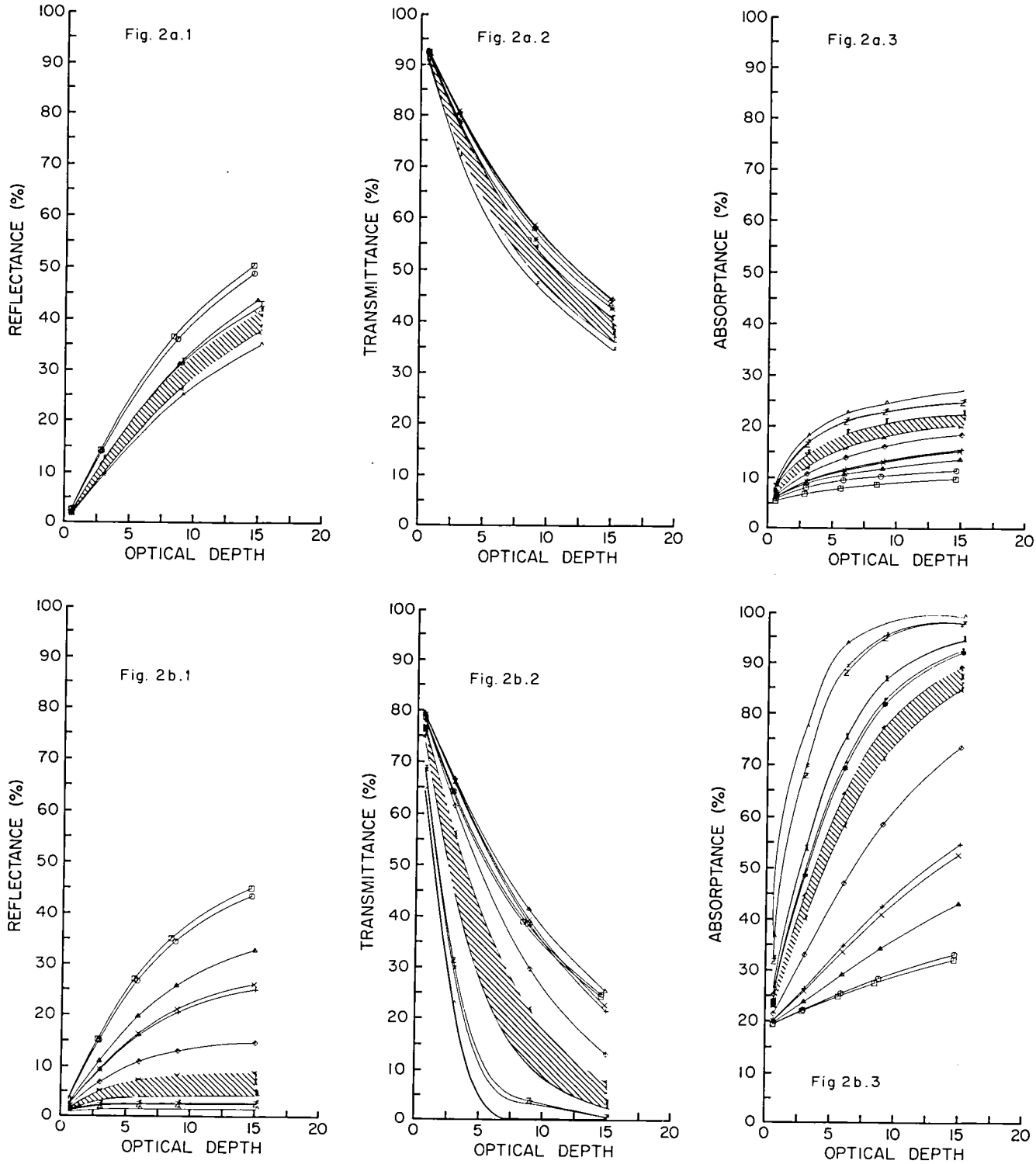

Fig. 2. Ice cloud reflectance, transmittance, and absorptance values as a function of optical depth. (Crosshatch areas contain curves not specifically denoted by the symbols visible in the figure; see Table I for symbol definitions.) (a) Results integrated across the entire solar spectrum; (b) results at 1.4 μm.

that nonspherical particles have a very strong forward diffraction peak, similar to that for spherical particles, but scatter far more energy at intermediate and large scattering angles than do their spherical counterparts.

Chýlek[15] proposed a surface wave suppression theory as a first approximation to nonsphericity. Chýlek *et al.*[16] showed that quite reasonable agreement was obtained for aerosols using this theory when compared to measurements. However, this approach predicts small values of scattered intensity at large and intermediate scattering angles in disagreement with most measurements. Second, the theory predicts that particles with size parameters $\gtrsim 30$ will not show any nonspherical effects. Welch *et al.*[14] applied this approximation for cirrus ice clouds. Unphysical values of absorption efficiency were produced[17] due to the fact that the approximation is nonunitary.[19] Therefore, this approach is limited to scattering intensities only. Application of this method in the present investigation, with these restrictions in mind, produced no significant variation in cloud radiative characteristics, except for the smallest particle distributions.

A recent semiempirical approach has been developed by Pollack and Cuzzi,[20] which reproduces measured nonspherical particle characteristics quite well. This approach indicates that the nonspherical particle asymmetry factor g, defined as the cosine of the average scattering angle, may decrease in value by as much as 20–30% over that of a similar spherical particle. Such behavior is exhibited only for particles with size parameter $X > X_0$, where X_0 is a cutoff value. For $X \leq X_0$, spherical Mie theory, with radii determined from equal volumes rather than equal areas, is appropriate. For the cases studied by Pollack and Cuzzi,[20] X_0 varied from ~10 to 2 with an average value of $X_0 = 4$. In the present investigation for large ice crystals, $X > X_0$, and nonsphericity is invoked. For an ensemble of large irregular particles with $X > X_0$, the theory also predicts that the average scattering efficiency is increased over that of equal volume spheres by a factor equal to the ratio S of their surface areas. For the cases studied by Pollack and Cuzzi, $S \simeq 1.3$ and had only weak dependence upon particle shape. When the value of $2n_iX < 1$, absorption efficiency of nonspherical particles may be assumed equal to that of their spherical counterparts.

VII. Results Based Upon Nonspherical Calculations

The calculations presented in this section are based upon the semiempirical approach developed by Pollack and Cuzzi.[20] However, in the free atmosphere there is no *a priori* information concerning the value of X_0, g, or scattering efficiency scaling factor S. For the following calculations the particle sizes usually are large enough so that $X > X_0$, and the nonspherical approach will be used in all cases.

Welch *et al.*[14] showed that radiative characteristics are extremely sensitive to asymmetry factor g. It was shown that even a 5% change in the asymmetry factor can produce large variations in cloud reflectance, although not in cloud absorptance. In the following results two separate sets of calculations are made; the first analyzes the effect of a variation of g upon cloud properties without any variation of scattering efficiency S, and the second calculation allows both g and S to vary.

Only values of cloud reflectance are shown in Fig. 3. Values of cloud transmittance and absorptance show less variation and are therefore omitted. Figures 3(a) and (b) show cloud reflectance as a function of wavelength at $\tau = 0.6$ for a 10% ($g * 0.9$) and 20% ($g * 0.8$) decrease in asymmetry factor, respectively. Figures 3(c) and (d) show similar variations for $\tau = 3.0$. Comparison of Figs. 1(a) and 3(a) and (b) for $\tau = 0.6$ shows that as the value of the asymmetry factor is decreased, there is a strong increase in scattering and reflectance. The average value of cloud reflectance at $\lambda = 0.55$ μm increases from $\sim R = 2.5\%$ to $\sim R = 4.0\%$ for $g * 0.9$ and to ~6% for $g * 0.8$. In similar fashion comparison of Figs. 1(b), 3(c), and (d) with $\tau = 3.0$ shows that the average value of reflectance at $\lambda = 0.55$ μm increases from ~14% to $\sim R = 22\%$ for $g * 0.9$ and to ~30% for $g * 0.8$. A decrease in g by 20% as indicated by the results of Pollack and Cuzzi leads to increases in the value of reflectance by a factor of 2.0 and 2.5. The ratio $R_{1.5}/R_{0.5}$ still retains the possibility of discriminating between the various size distributions. Likewise, the ratio $T_{1.5}/T_{0.5}$ also retains the possibility for use in remote sensing the size distributions from ground measurements.

Figure 4 shows values of cloud reflectance as a function of optical depth for these same distributions. Figures 4(a) and (b) show cloud reflectance for $g * 0.9$ and $g * 0.8$, respectively. Comparison of Figs. 2(a) and 4(a) and (b) shows that the increase in cloud reflectance with a decrease in the asymmetry factor occurs for all the optical depths studied but with the largest percentage variation occurring at the smaller optical depths. From a measured cloud reflectance of 20%, applying spherical Mie theory and using Fig. 2(a) would lead one to believe that the cloud optical depth was $\sim\tau = 6.0$–7.5. However, a nonspherical particle distribution with $g * 0.8$ produces the same value of reflectance with $\tau = 2.5$–3.0. Therefore, the relationship between reflectance vs optical depth cannot produce realistic estimates in the presence of nonspherical particles.

In the next set of calculations, scattering efficiency has been arbitrarily scaled upward by the factor $S = 1.3$ for all distributions and particle shapes. For the particle shapes studied by Pollack and Cuzzi this factor of $S = 1.3$ occurred frequently. S represents the ratio of the surface area of the nonspherical particle to that of its equivalent volume sphere. The value $S = 1.3$ represents a reasonable estimate for the ratio S; however, more extensive calculations could take into account the actual particle shape variation with length using Eqs. (17 and 18). This complexity was not included in the following results, since bullets and columns are merely two out of a myriad of possible crystal forms. Typically $(2n_iX) < 1$ so that the absorption efficiency calculated for spheres is also appropriate for the nonspherical particles.

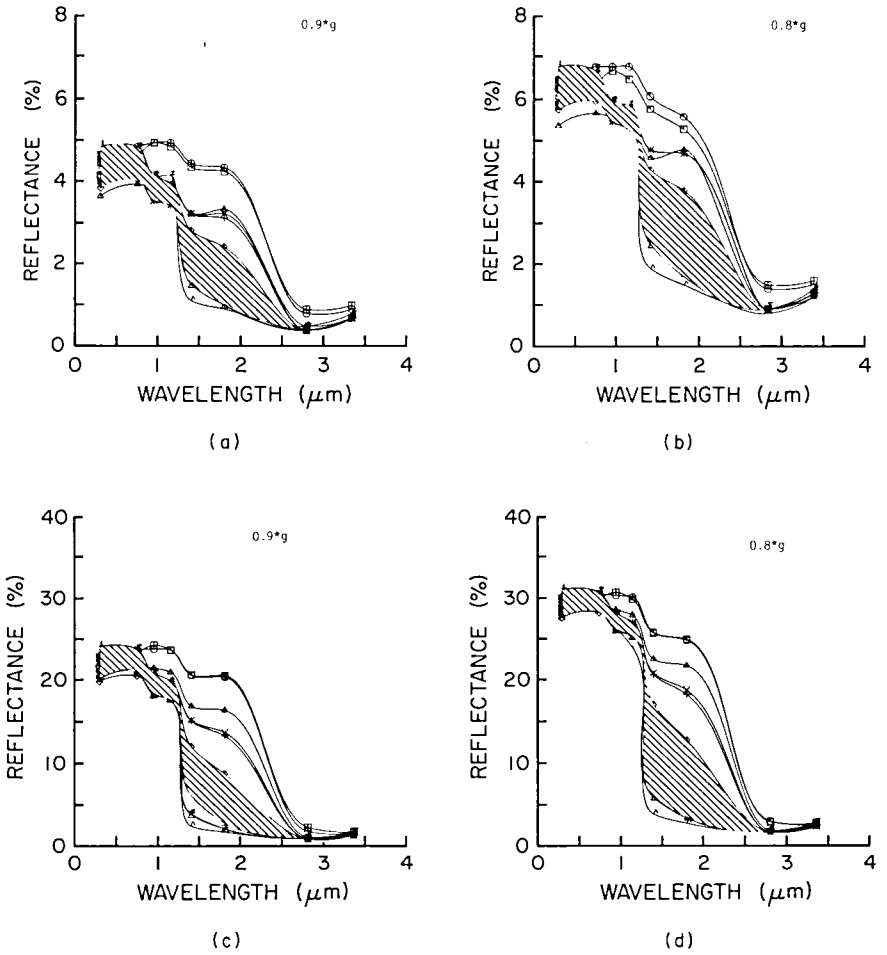

Fig. 3. Ice cloud reflectance for the following conditions: (a) $\tau = 0.6, g' = 0.9g$; (b) $\tau = 0.6, g' = 0.8g$; (c) $\tau = 3.0, g' = 0.9g$; and (d) $\tau = 3.0, g' = 0.8g$. (Crosshatch areas contain curves not specifically denoted by the symbols visible in the figure; see Table I for symbol definitions.)

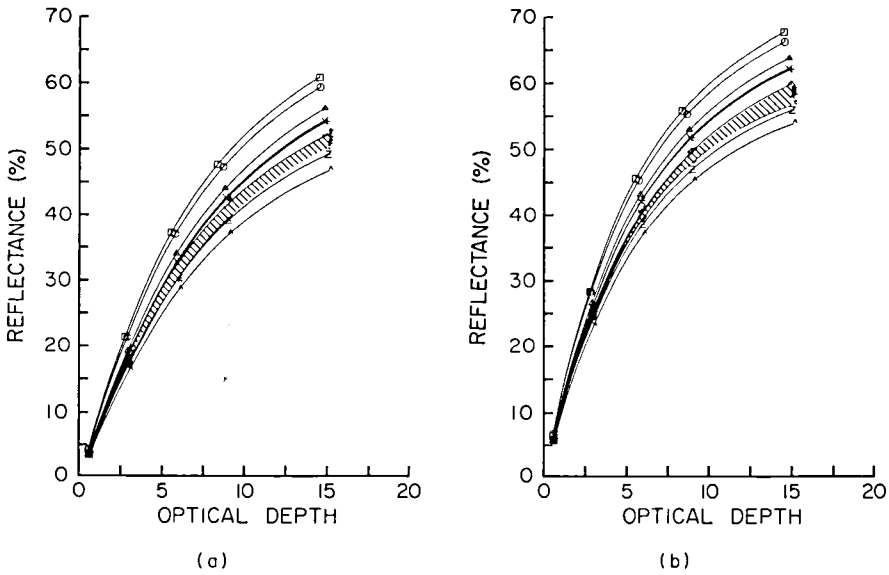

Fig. 4. Ice cloud reflectance values for two different values of the asymmetry factor: (a) $g' = 0.9g$; (b) $g' = 0.8g$. (Crosshatch areas contain curves not specifically denoted by the symbols visible in the figure; see Table I for symbol definitions.)

Figures 5(a), (b), and (c) show values of cloud reflectance R with $S = 1.3$ and for asymmetry factor g scaled by $g * 1.0$, $g * 0.9$, and $g * 0.8$, respectively. The cloud optical depth in this case had also increased by approximately this same scale factor, from 0.6 to ~0.8. Comparison of Figs. 1(a) and 5(a) shows that scaling the scattering efficiency by $S * 1.3$ increases the value of reflectance by approximately this same factor S at most wavelengths. Likewise absorptance is decreased in value (not shown). Comparison of Figs. 3(a) and 5(b) for $g * 0.9$ and Figs. 3(b) and 5(c) for $g * 0.8$ shows that this scaling factor for scattering efficiency merely leads to an almost linear scaling of the resulting reflectance. Similar results occur for an optical depth of $\tau = 3.0$ (now approximately scaled to $\tau = 3.9$).

In this range of optical thicknesses, there is an almost linear relationship between optical depth and cloud reflectance. Therefore, merely using the results in Figs. 2(a) and 4(a) and (b) appropriate for the larger optical depth ($\tau * S$) produces excellent results. Figures 6(a),

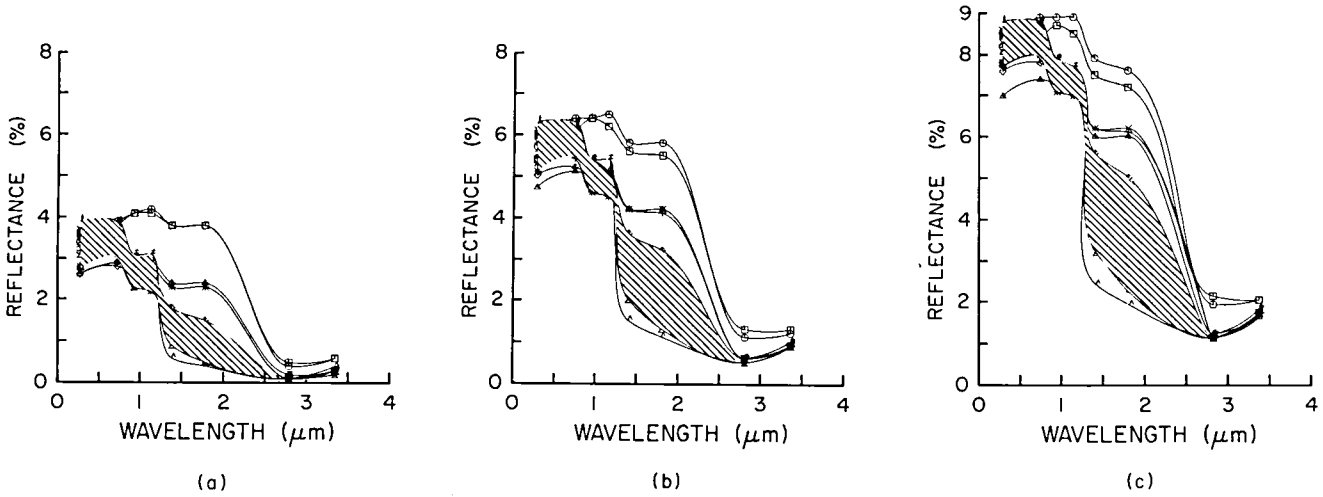

Fig. 5. Ice cloud reflectance with enhanced scattering efficiency for the following conditions: (a) $S = 1.3, g' = g, \tau = 0.6$; (b) $S = 1.3, g' = 0.9g, \tau = 0.6$; (c) $S = 1.3, g' = 0.8g, \tau = 0.6$. (Crosshatch areas contain curves not specifically denoted by the symbols visible in the figure; see Table I for symbol definitions.)

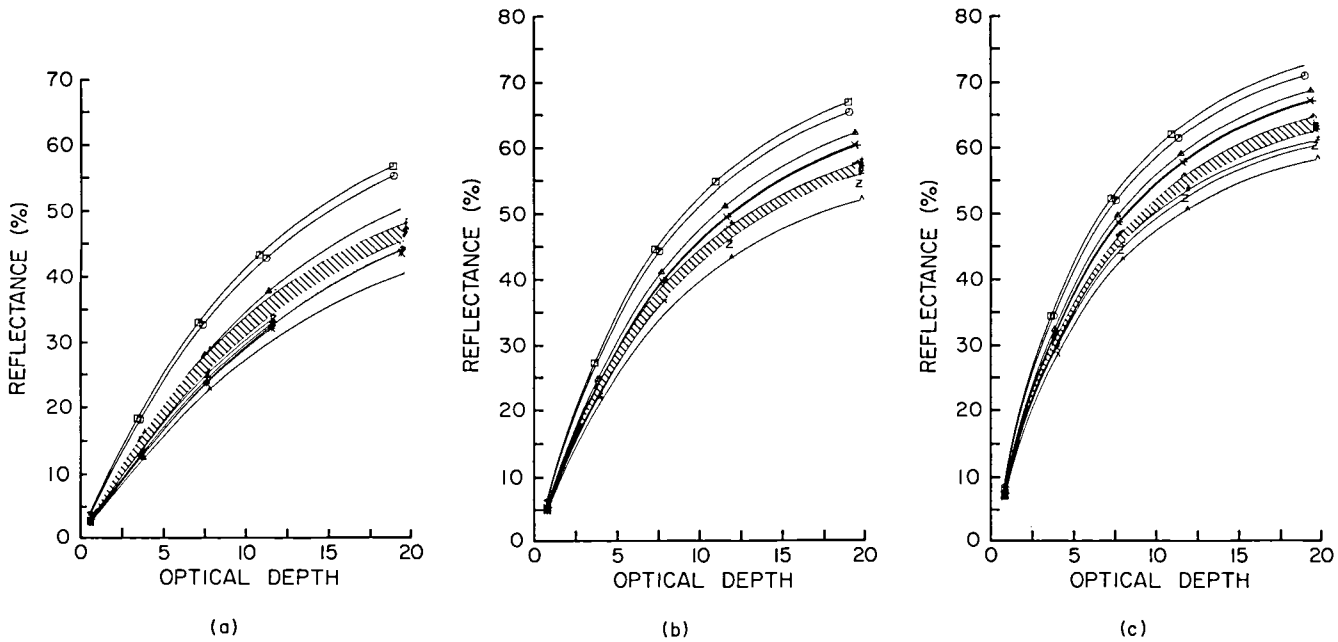

Fig. 6. Broadband ice cloud reflectance for scattering efficiency scaled by a factor of 1.3 for the following conditions: (a) $g' = g$; (b) g' 0.9 g; (c) $g' = 0.8\,g$. (Crosshatch areas contain curves not specifically denoted by the symbols visible in the figure, see Table I for symbol definitions.)

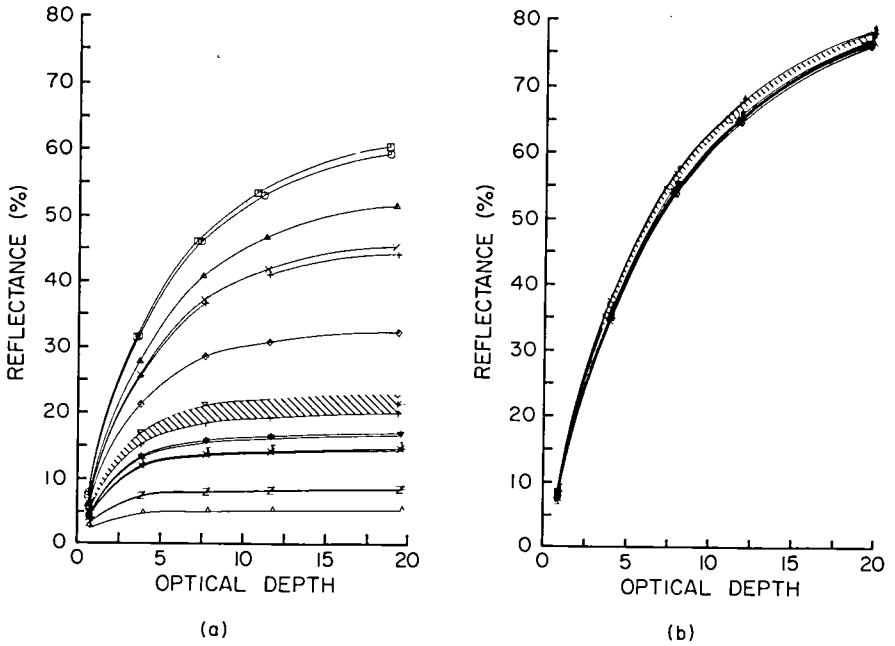

Fig. 7. Ice cloud reflectance with enhanced scattering efficiency enhanced by a factor of 1.3 for a wavelength of (a) 1.4 and (b) 0.55 μm. (Crosshatch areas contain curves not specifically denoted by the symbols visible in the figure; see Table I for symbol definitions.)

(b), and (c) show values of R, T, and A as a function of optical depth with scattering efficiency scaled by S = 1.3 and for $g * 1.0$, $g * 0.9$, and $g * 0.8$, respectively. Comparison of Figs. 2(a) with 6(a), 4(a) with 6(b), and 4(b) with 6(c) shows that the scaled values of R, T, and A all lie along the same curves as for the unscaled values of R, T, and A. Therefore, knowing the basic shape of the curve is all that is necessary. One merely takes those values of R, T, and A appropriate for the scaled optical depth ($\tau * S$).

The results in Fig. 6 were obtained for the broadband (total integrated solar spectrum) results and are also appropriate for $\lesssim$1.0-μm wavelengths. However, there are noticeable differences for the near IR bands, particularly in the 1.0–2.0-μm range. Figure 7(a) shows values of reflectance appropriate for the 1.4-μm band with $S * 1.3$ and $g * 1.0$. The scaled values of reflectance, transmittance, and absorptance no longer lie on the same approximate curves appropriate for unscaled values. Scaled values of reflectance and absorptance are larger, while scaled values of transmittance and absorptance are smaller than their unscaled counterparts. Similar conclusions are valid for an asymmetry factor scaled by $g * 0.9$ and $g * 0.8$. Figure 7(b) shows these same values at a wavelength of 0.55 μm. It can be seen that cloud reflectance is nearly independent of particle size distribution in the visible region, depending rather only upon cloud optical depth.

VIII. Conclusion

The results from this study show that there is surprisingly little difference in values of reflectance, absorptance, and transmittance for many of the intermediate-sized particle spectra. Particle size distributions with mode radii ranging from ~50 to 300 μm, irrespective of particle shape and nearly independent of the choice of size distribution representation, gave relatively similar flux values. The very small particle sizes, however, had significantly larger values of reflectance and transmittance with corresponding smaller values of absorptance than did the larger particle sizes. The very large particle modes produced very small values of reflectance and transmittance along with very large values of absorptance. Such variations are particularly noticeable when plotted as a function of wavelength. For a given value of optical depth, there is a relatively small spread in reflectance at the shorter wavelengths ($\lambda \gtrsim 1$ μm). However, differences between size distributions are greatest in the 1.3–2.0-μm regions. This behavior suggests that it may be possible to obtain an estimate of the average size of the particles present from the ratio of reflectances (or transmittances) at say $\lambda = 1.6$ μm and $\lambda = 0.55$ μm ($R_{1.6}/R_{0.55}$). A large value of this ratio would indicate the presence of small particle sizes, while decreasing values of this ratio would indicate increasing average particle sizes. However, much more detailed calculations are required to demonstrate this ability. It is noted that detailed variations in such ratios may also be useful in determining the presence of ice or water phase. From the comparisons between ice and water clouds made by Welch *et al.*,[14] it would appear that such ratios may be useful in determining the presence of large drops in water clouds.

The present results were primarily aimed at determining the range of variability one might expect in bulk cloud radiative properties as a function of wavelength

and optical depth for various parameterizations of particle size distribution and nonsphericity. Variation of radiative characteristics as a function of particle size was particularly noticeable in the 1–2-μm wavelength range. Nonspherical effects were approximated using the Pollack and Cuzzi[20] semiempirical approach. Asymmetry factor g was scaled by factors of 0.9 and 0.8, while scattering efficiency was scaled by a factor of 1.3 to simulate the increase of scattering by nonspherical particles. It was found that increasing the scattering efficiency by some scale factor S also scaled the optical depth τ by approximately the same factor S. Therefore, from curves of reflectance, transmittance, or absorptance vs optical depth, it is possible to obtain reasonable estimates of these bulk radiative characteristics from the optical depth given by the product of τ and S ($\tau * S$). This procedure is reliable for broadband estimates; it is less reliable for wavelengths between 1.0 μm and 2.5 μm.

The value of cloud reflectance R is particularly sensitive to small variations (10–20%) in the value of asymmetry factor g. A decrease in the value of g, representing a larger value of average scattering angle, leads to increased values of reflectance at all wavelengths. A decrease in g by 20% for clouds of small optical thickness ($\tau \lesssim 5$) leads approximately to a doubling in the value of R. The results of Pollack and Cuzzi indicate that even greater differences may occur, since g is decreased by up to 30% in some cases. At present there is no *a priori* way to determine which scale factors are appropriate to represent the wide variety of particle shapes present in the free atmosphere. The present investigation merely indicates the sensitivity of bulk cloud properties to such variations in parameterization.

The authors express their appreciation to Pauline Martin, Sandy Wunch, and Mark Howes for their role in the preparation of this manuscript. Computer time was provided by the computing facility at the National Center for Atmospheric Research, which is sponsored by the National Science Foundation.

This research was supported by the National Science Foundation under grant ATM 78-12631 and the National Aeronautics and Space Administration under grant NSG 5357.

References

1. S. I. Rasool and S. Schneider, Science **173,** 138 (1971).
2. H. S. Appleman, "Occurrence and Forecasting of Cirrostratus Clouds," World Meteorological Organization, 109-47, Technical Note 40 (1961).
3. K. N. Liou, J. Atmos. Sci. **29,** 524 (1972).
4. H. Jacobowitz, J. Quant. Spectrosc. Radiat. Transfer **11,** 691 (1971).
5. P. Wendling, R. Wendling, and H. K. Weickmann, Appl. Opt. **18,** 2663 (1979).
6. W. G. Zdunkowski and J. D. Pryce, Pure Appl. Geophys. **112,** 739 (1974).
7. J. R. Fleming and S. K. Cox, J. Atmos. Sci. **31,** 2182 (1974).
8. P. M. Kuhn and H. K. Weickmann, J. Appl. Meteorol. **8,** 147 (1969).
9. C. M. R. Platt and D. J. Gambling, Q. J. R. Meteorol. Soc. **84,** 319 (1971).
10. K. N. Liou, J. Atmos. Sci. **31,** 522 (1974).
11. K. T. Griffith and S. K. Cox, "Infrared Radiative Properties of Tropical Cirrus Inferred from Broadband Measurements," Atmos. Sci. Paper 269, Colorado State U., NTIS PB-268531 (1977), 102 pp.
12. D. Roewe and K. N. Liou, J. Appl. Meteorol. **17,** 92 (1978).
13. H. C. Bryant and A. J. Cox, J. Opt. Soc. Am. **56,** 1529 (1966).
14. R. M. Welch, S. K. Cox, and J. M. Davis, "Solar Radiation and Clouds," Meteorological Monographs 39 (1980), 93 pp.
15. P. Chýlek, J. Opt. Soc. Am. **66,** 286 (1976).
16. P. Chýlek, G. W. Grams, and R. G. Pinnick, Science **193,** 480 (1976).
17. R. M. Welch and S. K. Cox, Appl. Opt. **17,** 3159 (1978).
18. C. Acquista, Appl. Opt. **17,** 3851 (1979).
19. C. Acquista and A. Holland, "Energy Conservation: A Test for Scattering Approximations," International Workshop on Light Scattering by Irregularly Shaped Particles, Albany, N.Y., 5–7 June 1979 (1979).
20. J. B. Pollack and J. N. Cuzzi, J. Atmos. Sci. **37,** 868 (1980).
21. K. T. Griffith, S. K. Cox, and R. G. Knollenberg, J. Atmos. Sci. **37,** 1078 (1980).
22. G. L. Stephens, "Radiative Transfer on a Linear Lattice; Application to Anisotropic Ice Crystal Clouds," *J. Atmos. Sci.,* 37, Accepted for publication Sept. (1980).
23. A. Ono, J. Atmos. Sci. **26,** 138 (1969).
24. C. M. R. Platt, J. Appl. Meteorol. **17,** 482 (1978).
25. A. Heymsfield, J. Atmos. Sci. **29,** 1348 (1972).
26. A. Heymsfield, J. Atmos. Sci. **32,** 799 (1975).
27. A. Heymsfield, J. Atmos. Sci. **34,** 367 (1977).
28. A. Heymsfield and R. G. Knollenberg, J. Atmos. Sci. **29,** 1358 (1972).
29. R. T. Ryan, H. Blau, Jr., P. C. Von Thüna, M. L. Cohen, and C. D. Roberts, J. Appl. Meteorol. **11,** 149 (1972).
30. J. D. McTaggart-Cowan, G. Lala, and B. Vonnegut, J. Appl. Meteorol. **9,** 294 (1970).
31. J. Rosinski, C. T. Nagamoto, A. Langer, and F. Parungo, J. Geophys. Res. **75,** 2961 (1970).
32. D. J. Varley, Cirrus Particle Distribution Study, Part 1, AFGL-TR-78-0192 (1978), 71 pp.
33. D. J. Varley and D. M. Brooks, Cirrus Particle Distribution Study, Part 2, AFGL-TR-78-0248 (1978), 106 pp.
34. D. J. Varley, Cirrus Particle Distribution Study, Part 3, AFGL-TR-78-0305 (1978), 66 pp.
35. D. J. Varley and A. A. Barnes, Jr., Cirrus Particle Distribution Study, Part 4, AFGL-TR-79-0134 (1979), 91 pp.
36. P. V. Hobbs, Nature **251,** 694 (1974).
37. R. R. Braham, Jr., and P. Spyers-Duran, J. Appl. Meteorol. **6,** 1053 (1967).
38. W. G. Zdunkowski, R. M. Welch, and G. Korb, "An Investigation of the Structure of Typical Two-Stream Methods for the Calculation of Solar Fluxes and Heating Rates in Clouds," Accepted for publication in Contrib. Atmos. Phys. in press (1980).
39. J. Joseph, W. J. Wiscombe, and J. A. Weinman, J. Atmos. Sci. **33,** 2452 (1976).
40. W. J. Wiscombe, *J. Atmos. Sci.* **34,** 1408 (1977).
41. W. J. Wiscombe and G. W. Grams, J. Atmos. Sci. **33,** 2440 (1976).
42. R. M. Welch, S. K. Cox, W. G. Zdunkowski, and K. Ya. Kondratyev, "Determination of Vertical Profiles of Aerosol Size Spectra from Radiative Flux Measurements, Part II. Theoretical Considerations," submitted for publication to J. Geophys. Res. in press (1980).
43. W. J. Wiscombe and J. W. Evans, J. Comput. Phys. **24,** 416 (1977).
44. K. N. Liou and T. Sasamori, J. Atmos. Sci. **32,** 2166 (1975).
45. W. M. Irvine and J. B. Pollack, Appl. Opt. **13,** 1928 (1968).

46. D. W. Reynolds, T. H. Vonder Haar, and S. K. Cox, J. Appl. Meteorol. **14,** 433 (1975).
47. J. M. Greenberg, R. T. Wang, and L. Bangs, Nature **230,** 110 (1971).
48. J. M. Greenberg, J. Colloid. Interface Sci. **39,** 513 (1972).
49. T. D. Proctor and D. Barker, Aerosol Sci. **5,** 91 (1974).
50. T. D. Proctor and G. W. Harris, Aerosol Sci. **5,** 81 (1974).
51. R. Zerull and R. H. Giese, *Planets, Stars and Nebulae Studied with Photopolorimetry Microwave Analogue Studies,* T. Gehrels, Ed. (U. Arizona, Tucson, 1974), pp. 901–914.
52. A. C. Holland and G. Gagne, Appl. Opt. **9,** 1113 (1970).
53. J. R. Hodkinson, "Light Scattering and Extinction by Irregular Particles Larger Than the Wavelength," in *Electromagnetic Scattering,* M. Kerker, Ed. (Pergamon, London, 1963), 287 pp.

SECTION 6

A CLIMATE INDEX DERIVED FROM SATELLITE MEASURED SPECTRAL INFRARED RADIATION

by Michael D. Abel and Stephen K. Cox

Atmospheric Science
PAPER NO.
335

US ISSN 0067-0340

DEPARTMENT OF ATMOSPHERIC SCIENCE
COLORADO STATE UNIVERSITY
FORT COLLINS, COLORADO

A CLIMATE INDEX DERIVED FROM SATELLITE MEASURED SPECTRAL INFRARED RADIATION

by

Michael D. Abel and Stephen K. Cox

Research Supported by

National Aeronautics and Space Administration
under Grant NSG 5357

Department of Atmospheric Science
Colorado State University
Fort Collins, Colorado

May, 1981

Atmospheric Science Paper Number 335

ABSTRACT

This paper introduces a climate index based on radiative transfer theory and derived from the spectral radiances typically used to retrieve temperature profiles. It is assumed that clouds and climate are closely related and a change in one will result in a change in the other. Because the index developed in this paper is a function of the cloud, temperature, and moisture distributions, it may be used as a climate index. The advantage is that the index is more accurately retrieved from satellite data than cloudiness per se. This index, hereafter referred to as the VIRES index (for Vertical Infrared Radiative Emitting Structure), is based upon the shape and relative magnitude of the broadband weighting function of the infrared radiative transfer equation. The broadband weighting curves are retrieved from simulated satellite infrared sounder data (spectral radiances). This paper describes the retrieval procedure and investigates error sensitivities of this method. It also proposes index measuring options and possible applications of the VIRES index.

Results indicate that the VIRES approach is a very effective use of satellite radiometer measurements. Retrieval advantages include; day and night capability, no need to know cloud radiative properties, retrieval ability when cloud fraction or cloud emittance is less than 1.0, minimal geometric assumptions, retrieved information below sensor resolution, and minimum influence on the index from low tropospheric retrieval errors. These advantages along with the approach of compositing scenes for an average VIRES curve greatly reduce the retrieval

sensitivity to the kind of errors found under assumed normal operating conditions. A detailed error analysis indicated that the most important error sources are instrument system noise, and ill specified temperature and humidity profiles. Accurate VIRES retrievals are illustrated under a number of different error and atmospheric conditions. Furthermore, a statistical technique used to successfully discriminate between VIRES curves derived for different atmospheric conditions is discussed.

Operational VIRES index retrieval strategies and a number of specific applications are proposed. It is suggested that the index be derived from geostationary satellite data and averaged to provide weekly regional values. These index values would be used in a regional climate monitoring mode. They would also be useful for verification of climate model generated infrared radiation to space values.

ACKNOWLEDGMENTS

This dissertation is dedicated to the idea that faith and science are logically complementary and not mutually exclusive as implied by the psalmist who wrote; "Great are the works of the Lord, studied by all those who have pleasure in them". Ps 111:2 RSV. In order to do justice to a set of events, the author believes that it is often necessary to give more than one account of it, in terms of more than one conceptual framework. Thus, scientific convictions can be constructively related to Christian beliefs.

The author wishes to extend his sincere thanks to his advisor Dr. Stephen K. Cox who provided patient guidance and advice, and who arranged for the financial means to support this research. The author also wishes to thank his graudate committee Drs. Paul Mielke, Peter Sinclair and Thomas H. Vonder Haar for their assistance and thoughtful review of this research. The author has also greatly benefitted from discussions with the members of Dr. Cox's research group, especially during project review meetings. Special thanks are due to Ms. Sandy Wunch for typing many drafts of this paper as well as the final manuscript, to Ms. Judy Sorbie for drafting the figures, and to Ms. Pauline Martin for proofreading the final manuscript.

This work has been supported in part by NASA Contract NSG 5357. The author would also like to thank the Air Force Institute of Technology for sponsoring this assignment. Finally, the author happily acknowledges the support, sacrifices, and understanding of his wife Linda and our family during this time of graduate study.

TABLE OF CONTENTS

TABLE OF CONTENTS (Continued)

LIST OF TABLES

LIST OF FIGURES

LIST OF FIGURES (Continued)

LIST OF FIGURES (Continued)

LIST OF SYMBOLS AND ACRONYMS

$B(\nu,T)$	Planck Function
b	Equation coefficient, ln b is the y intercept
c_1, c_2	Plank Function constants
C, D	Empirical constants for retrieval relationship (Equations 6 and 7)
CH_4	Methane
CO_2	Carbon dioxide
CCRC	Clear column radiance correction
COSPAR	Committee on Space Research
d.f.	Degrees of freedom
g	Acceleration due to gravity, 9.8 m s^{-2}
GARP	Global Atmospheric Research Program
GATE	GARP Atlantic Tropical Experiment
GCM	General Circulation Model
H_2O	Water vapor
H_0	Null hypothesis
HIRS	High Resolution Infrared Sounder
IR	Infrared radiation
IRIS	Infrared interferometer spectrometer
ITPR	Infrared temperature profile radiometer
k	Number of like signs, used in the Sign Test
$K(\nu,p)$	Gas mass absorption coefficient, m^2 g^{-1}
$L(\nu,\theta)$	Spectral radiance
L_{cld}	Satellite level spectral radiance from atmosphere above cloud top
L_{cs}	Satellite level spectral radiance due to clear atmosphere

LIST OF SYMBOLS AND ACRONYMS

LWC	Liquid water content, g m^{-3}
m	Equation coefficient, line's slope
N	Fraction of the sky which is cloudy
n	Total number of non zero signs, used in Sign Test
N_2O	Nitrous oxide
NCRP	National Climate Research Program
O_3	Ozone
P	Probability, used in the Sign Test
p	Pressure, mb
p_c	Cloud top pressure level
p_o	Pressure at top of atmosphere
p_s	Surface pressure
p_{wf}	Pressure at weighting function peak level
q	Gas mass mixing ratio
R	Universal gas constant
r^2	Coefficient of determination
RMS	Root mean square
RTE	Radiative transfer equation
SIRS	Satellite IR spectrometer
SW	Shortwave radiation
T	Fisher's combined probability Sign Test statistic
$T_{[p]}$	Ambient temperature profile
TD	Infrared temperature difference between surface and cloud top
VIRES	Vertical Infrared Radiative Emitting Structure
VTPR	Vertical Temperature Profile Radiometer

LIST OF SYMBOLS AND ACRONYMS

W	Gas mixing ratio
χ^2	Chi-Squared distribution
x	Independent variable
y	Dependent variable
z	Vertical distance
α	Effective fractional weighting (clear vs effective cloudy)
$\varepsilon(\nu)$	Spectral infrared emittance
ε_s	Effective infrared broadband surface emittance
θ	Solar zenith angle
λ	Wavelength, μm
ν	Wavenumber, cm^{-1}
σ	Stefan-Boltzman constant
$\tau(\nu)$	Spectral infrared transmittance
$\frac{\partial \tau}{\partial \ell np}$	Infrared radiative transfer equation weighting function

LIST OF SUBSCRIPTS

c	at cloud top level
cld	above cloud
cs	clear sky
o	top of atmosphere
s	surface
ν	wavenumber

I. INTRODUCTION

This paper introduces and describes a climate index called the VIRES index. VIRES (pronounced vī·rēs) is the acronym for Vertical Infrared Radiative Emitting Structure and quite by chance it is also the plural form of the Latin word vis, meaning forces or powers. Thus, the acronym seems especially appropriate since the atmosphere's VIRES is one of the major forcing factors behind the earth's climate. The VIRES index is related to the earth's climate through the earth's radiation budget and therefore, can be considered a climate index. The logic of this may be stated as follows. The climate system is determined by the energy input to the system and the distribution, transformation, and storage of energy in various forms within the system. These processes are mirrored in the components of the earth's radiation budget, one of which is the outgoing emitted thermal radiation (COSPAR Report to ICSU and JOC, 1978b). This cooling to space is described by the VIRES which is primarily a function of cloud distribution.

Atmospheric observation has been and continues to be central to the progress of atmospheric science. Better observations remain one of the needs of the discipline. The recent introduction of meteorological satellite systems has contributed significantly to the growing need of monitoring world-wide weather variables. Satellites not only have world-wide coverage capability with good horizontal and time resolution, they also have a second advantage. Large numbers of observations are made with the same instrument increasing the integrity and comparability of such measurements (Houghton, 1979). The relative if not the absolute accuracy of the satellite measurement is high. More attention

to absolute accuracy has been paid to the sounding type instruments than to any other satellite instrument, (i.e. ITPR, SIRS, IRIS).

The scientific community is still seeking the best ways to use and apply satellite data. Most of the recent successes in using satellite data in a quantitative global way in the atmospheric sciences have come in the areas of solar constant measurement and radiation budget measurements (Heath, 1973; Smith et al. 1977; Vonder Haar and Oort, 1973). Application of satellite data to these problems is fairly straightforward since the principal satellite instrument is a radiometer and the measurement is a spectral or broadband irradiance. Other important areas of research include inference of temperature and humidity profiles, as well as cloud and wind determinations from satellite radiance values. The suitability of satellite observations is reduced since the required information must be inferred from the radiance values measured remotely at the satellite and from the appropriate geometric and radiative transfer principles.

The objective of this study is to describe the Vertical Infrared Radiative Emitting Structure (VIRES) of the atmosphere by using simulated satellite spectral radiation measurements. A process is described that accomplishes this objective using specified cloud radiative properties and mean temperature and gaseous atmospheric profiles. These findings are used to examine the feasibility of using infrared radiative transfer weighting curves (which describe the atmosphere's VIRES by defining how the atmosphere cools to space) as a climate index. This index would be principally dependent on climatological cloudiness, and its variability could be regarded as an indicator of climate variance. The strength of this approach is that it deals

directly with the radiative aspect of the problem thus circumventing the need to infer specific individual clouds directly using the typical parameters of height, base, and amount. The distinction of this technique is that computationally one may be able to simply, accurately, and quickly archive the atmospheric VIRES as a manifestation of global cloudiness in a form that is useful for monitoring climate change, or for validating the statistical characteristics of cooling to space computed by climate models. Many factors account for the strong potential of this approach.

Day to day variations as well as longer period variations in the atmospheres VIRES (which is reflected in satellite measured earth radiances) are primarily caused by clouds. Many techniques using satellite data, some of which are discussed in the next section, have been developed to infer cloudiness in the standard sense. Of course any inference of clouds using such data will by definition be a kind of radiative measure of cloudiness with the drawback that specific radiative cloud properties must be assumed before results are possible. Of course it is desirable to make as few a priori assumptions as possible when analyzing the data for the purpose of obtaining reliable cloud information. By using a radiance measure of cloudiness as proposed in this paper one increases the compatibility between the satellite measurement and the quantity labeled cloudiness. Furthermore, by using a unique form of the technique commonly called the infrared sounder cloud retrieval method for a single field of view, we minimize the assumptions about the spatial scales and geometry, and about the cloud radiative properties while avoiding many time consuming calculations involving iterations through the radiative transfer equation. This new

method is used to find two curve shape parameters which define the atmosphere's VIRES in terms of the infrared weighting curve.

Following the chapter on background information, the specifics of the approach are described. For orientation purposes Figures 1a,b are provided. As described in Figure 1a the procedure starts with satellite spectral data (in this case simulated data) in the 15 μm CO_2 absorption bands and the 10-12 μm window band. These radiances contain information on the VIRES of the atmosphere. Computationally, relative importance is placed on the radiances depending upon where in the vertical most of its energy originates. By assuming known or measured gaseous and temperature profiles one may interpret the scene radiatively by solving for the weighting function peak due to radiatively specified effective clouds and the fractional weighting of a totally overcast effective cloud scene versus a totally clear scene. This scheme results in a spectral weighting curve shape specified by the two variables mentioned in Figure 1a. By design the curve shape is not dependent on the cloud radiative properties specified. For example, if a cloud covering the entire satellite-sensed scene is specified as opaque (black) when its emittance is only 0.5, the routine will compute a proper weighting function peak height (p_{wf}) due to the cloud with 0.5 fractional weighting (α). These two curve shape variables will give the correct weighting function curve, the same curve one gets from an overcast case and cloud emittance of 0.5. Of course, if one insists on interpreting the weighting function peak and fractional weighting as cloud top height and cloud fraction, the accuracy of the cloud fraction value is strongly dependent on how close the assigned cloud emittance is to the true cloud emittance.

Start with satellite spectral radiance values at 12 and 15 μm (in this paper simulated values).	Interpret a single scene radiatively. solve for Wt. Fun. Pk. Level and Fractional Wt. (clear vs. effective clouds), the two curve shape parameters.	Using the cloud shape parameters, compute the IR broadband Wt. curve (how atm. cools to space). Composite many curves for a measure of climatological cloud structure.	Statistically discriminate between curves and calculate a four number climate index, (the VIRES index).
$L_{\nu 1}, L_{\nu 2}, \ldots$	$\rightarrow$ p_{wf}, α	$\rightarrow$ $(\frac{\partial \bar{\tau}}{\partial \ln p}, p)$	$\rightarrow$ 250-450-690-1

Figure 1a. Schematic diagram showing computational steps leading to the proposed atmospheric VIRES climate index.

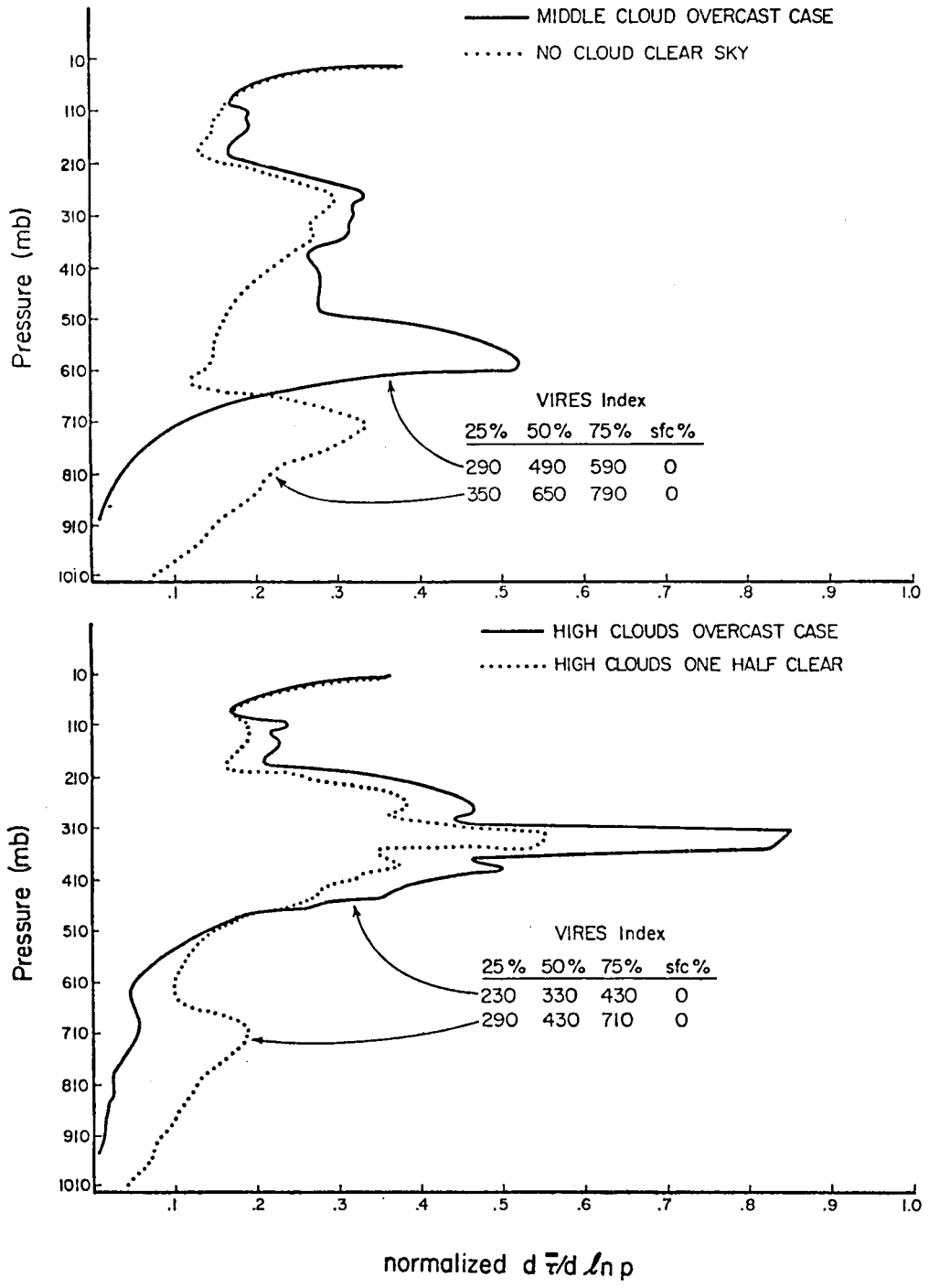

Figure 1b. Schematic diagram showing the relationship between four atmospheric cloud scenarios and the resulting VIRES curves and VIRES indices (reference Chapter VI-B).

Once the two variables determining weighting curve shape are found they may be used in a broadband transfer equation to give a broadband weighting curve (see Figure 1b). This curve combined with the respective temperature profile describes the vertical structure of atmospheric cooling to space. As a test, the value of the earth's emittance to space calculated from the derived weighting curve may be compared to a satellite measured value of the same quantity. As part of this study an error analysis is done to evaluate the influence of several assumptions on the results. In addition, the important question of time and space averaging of the quantities discussed above is also addressed. A technique for discriminating between weighting function curves, and a related climate index is discussed. Finally, the strengths and limitations of using IR broadband weighting curves as a climatic index and representation of cloudiness will be examined.

II. BACKGROUND INFORMATION

There have been many attempts to deduce cloud cover, structure, and radiative properties from satellite data. Table 1 is an outline of most of the approaches, all of which seek to define inferred cloudiness in standard terms. A short summary of the more notable research follows. However, a critique of specific approach shortcomings is not attempted.

Using visible wavelength values Miller and Feddes (1971), have related brightness measurements to cloud amount. Analysis of cloud amount and type from satellite pictures (nephanalysis) has been done using the 'eyeball' method (Clapp, 1964). Another more objective method combines pictures from two geostationary satellites to give a steroscopic view and measure of cloud height (Dalton et al. 1979). Of course these methods are limited to daylight observations and are degraded by variable and cloud look-a-like surface reflectance.

Infra-red window data combined with simplifying assumptions (which greatly reduce the accuracy and applicability) and a 'known' temperature profile when used with appropriate radiation laws will give estimates of cloud height or cloud fraction (Koffler et al. 1973). One also needs to know or estimate cloud radiative characteristics. An example of a technique that uses this type of data is the adjacent field of view method described by Smith et al. (1970). They use the derived cloud information to construct clear column radiance profiles as part of a temperature profile retrieval process. Exact cloud location is still temperature profile dependent. Another totally different approach is described by Rao (1970). He statistically relates

METHODS OF OBSERVING CLOUDS FROM SATELLITES

I. Visible Wavelength Observations
   - A. Reflected Solar Radiances
     1. Threshold
     2. Weighted histogram
   - B. Nephanalysis
   - C. Stereoscopic

II. Infra-red Wavelength Observations
   - A. Window Measurements
     1. Threshold
     2. TD
   - B. CO_2 Gas Band Measurements
     1. Single field of view - RTE iterations
        a. Radiance ratioing
        b. Minimization
     2. Single field of view - empirical RTE*

III. Vis/IR Combined Observations
   - A. Dual channel
   - B. Bi-spectral
   - C. 2-D histogram

*Developed and employed in this paper

Table 1. An outline of satellite cloud retrieval methods.

radiative values to differences between surface and cloud top temperatures (TD) over ocean areas. However, the most straightforward approach is to simply relate cloud top temperature and a known or assumed temperature profile (assuming one measures a single overcast cloud layer). An example of this threshold approach is the work of Cox and Griffith (1978) using GATE data. More recently Campbell et al. (1980) have used geosynchronous satellite IR window observations to produce area cloud top distribution profiles. They wish to assess the impact of the diurnal and spatial changes of these distributions on the earth-atmosphere radiation budget.

Other methods seek to improve accuracy by combining solar brightness and IR window information. However, while improving the accuracy over taking each method separately, one must be content with the limitations of both methods. A good example of this is the bi-spectral technique of Reynolds and Vonder Haar (1977) and expanded upon by Mendola and Cox (1978). They solve simultaneously a set of budget type radiative equations. They also use a method described by Shenk and Curran (1973) to improve retrieval of cirrus clouds. Other methods are often referred to as dual channel. For example, in another paper Reynolds et al. (1978) describe a technique for discriminating different cloud types by visible and IR image subtraction. A similar approach, called the 2-D histogram method, is outlined by Smith (1978). This last technique is designed to handle large quantities of data very quickly. Of course result accuracy is sacrificed for speed. However, for climatological applications the results may be useful.

Because this paper presents a technique using CO_2 gas band measurements, this approach will be discussed in greater detail below.

First it should be mentioned that there are other techniques for determining cloud characteristics from satellite measurements that do not fit neatly into the categories outlined in Table 1. For example, it may be possible in the future to use lidar techniques from space like those described by Platt (1979) for ground based units. Microwave measurements may be used with SW and/or IR measurements in a tri-channel or dual channel approach (Yeh and Liou, 1980). Following this reasoning a 3-D histogram technique has been suggested. A method using IR window and water vapor channels is being pursued by Chen et al. (1980). Finally, a technique that uses spectral infrared measurements from limb scanning is described by Taylor (1974) and by Remsberg et al. (1980).

To conclude this section the single field of view CO_2 gas band measurement technique will now be discussed. It is also referred to as the infrared sounder cloud retrieval method. This approach has many advantages. It requires the fewest a priori assumptions while providing day and night capability. However, it does have problems detecting low clouds. More details on the assumptions involved and limitations will be given later.

The IR RTE in integro-differential form represents the backbone of this method and is given below.

$$L(\nu,\theta) = \varepsilon_s(\nu)\, B(\nu, T_s)\, \tau(\nu, \theta, p_s) + \int_{\ln p_s}^{\ln p_o} B(\nu, T_{[p]}) \frac{\partial \tau(\nu, \theta, p)}{\partial \ln p}\, d \ln p \qquad (1)$$

where L is spectral radiance in W/m^2 sr cm^{-1}, θ is solar zenith angle and ε_s is surface spectral emittance usually taken to be 1 for 10-15 μm wavelengths. The Planck Function B is given below.

$$B(\nu, T) = c_1 \nu^3/[\exp(c_2\nu/T)-1]$$

where ν is wavenumber in cm^{-1}, T is temperature in °K, and c_1 and c_2 are constants. The equation for transmittance τ is given below.

$$\tau(\nu, \theta, p) = \exp[-\frac{q}{g}\int_{p_o}^{p} K(\nu,p) \sec\theta \, dp]$$

where q is the gas mass mixing ratio, g is the acceleration due to gravity, p is pressure with p_o being pressure at the top of the atmosphere and p_s being pressure at the surface, and K is the gas absorption coefficient. Also, $\frac{\partial\tau}{\partial \ln p}$ is commonly referred to as the weighting function. Equation 1 may be rewritten as Eq. (2) for the case of opaque clouds with cloud top height at p_c for cloud fraction N, and 1-N clear sky (cs).

$$L(\nu, \theta) = N\left\{B(\nu, T_c)\,\tau(\nu, \theta, p_c) + \int_{\ln p_c}^{\ln p_o} B(\nu, T_{[p]})\frac{\partial\tau}{\partial \ln p}\, d\ln p\right\}$$

$$+ (1-N)\left\{B(\nu, T_s)\,\tau(\nu, \theta, p_s) + \int_{\ln p_s}^{\ln p_o} B(\nu, T_{[p]})\frac{\partial\tau}{\partial \ln p}\, d\ln p\right\}$$

$$= N L_{\nu cld} + (1-N) L_{\nu cs} \quad . \tag{2}$$

Two basic techniques using these equations to solve for cloud properties have been proposed. One is known as the radiance ratioing method.

It is described in Smith and Woolf (1976), McCleese and Wilson (1976), and Smith and Platt (1978). It is also used by Wielicki and Coakley (1980), who have described its applicability and limitations in detail. An outline of this method follows.

First rewrite Eq. (2) for grey clouds using the relationship $\alpha = \varepsilon_{\nu 1} N$ for a spectral radiance of wavenumber $\nu 1$.

$$L_{\nu 1} = \alpha L_{\nu 1 cld} + (1-\alpha) L_{\nu 1 cs} \tag{3}$$

where α and $L_{\nu 1 cld}$ are the unknowns and $L_{\nu 1 cld}$ depends only on p_c. Rearrange Eq. (3).

$$(L_{\nu 1} - L_{\nu 1 cs}) = \alpha (L_{\nu 1 cld} - L_{\nu 1 cs}). \tag{4}$$

To have one equation with one unknown (p_c), ratio Eq. (4) for two different wavenumber radiances and eliminate α assuming $N \varepsilon_{\nu 1} = N \varepsilon_{\nu 2}$.

$$\frac{(L_{\nu 1} - L_{\nu 1 cs})}{(L_{\nu 2} - L_{\nu 2 cs})} = \frac{(L_{\nu 1 cld} - L_{\nu 1 cs})}{(L_{\nu 2 cld} - L_{\nu 2 cs})} . \tag{5}$$

Iterate through different p_c's until the $L_{\nu 1}$ and $L_{\nu 2}$ that satisfy Eq. (5) are found. Finally take the $L_{\nu 1}$ just found and solve Eq. (4) for α.

A second method is described by Chahine (1974). It is based upon minimization of the RMS difference between the observed radiances and calculated radiances that are a function of cloud top pressure and effective cloud fraction. An iterative scheme is used to choose the cloud pressure and fraction used in the radiative transfer equation calculations. While the first technique is designed to use only two band radiances, the second method may use more than two bands. Requisite lengthy radiative transfer calculations are a disadvantage to operational use of this method.

Both of these techniques and the one developed in this paper assume the profile T(p) is known which implies the clear sky spectral radiance $L_{\nu cs}$ is known. All three methods assume spectral band emittances (ε_ν) are equal, thus the relationship $\alpha_1 = \alpha_2$ is assumed true. All three assume the clear sky spectral band weighting functions are known and are not identical to each other. All three methods assume the satellite radiance measured comes from a scene that contains only the representative grey body cloud top pressure. Measurements in either the 4.3 μm or 15 μm CO_2 band can be used. Sometimes the window channel (11 μm) is also used with the CO_2 bands even though they are widely separated in wavenumber (McCleese and Wilson, 1976). In this case, only as $\varepsilon_\nu \to 1$ does $\varepsilon_{\nu 1} = \varepsilon_{\nu 2}$ (Yamamoto et al. 1970). For this reason poor results can be expected using the window and CO_2 channels together to detect nonblack clouds. Notice that all terminology used in this paper is consistent with recommendations of the IAMAP Radiation Commission except that ν is used for wavenumber instead of κ (Raschke, 1978). The next chapter describes the third technique mentioned above.

III. SHAPE PARAMETER RETRIEVAL THEORY

As stated earlier, the basic approach used in this paper to determine the weighting function curve shape parameters is commonly called the infrared sounder cloud retrieval method for a single field of view. The commonly used procedures are described in detail by Chahine (1975) and by Smith and Platt (1978). Chapter II of this paper contains a brief review of their techniques. Because of the limited number of assumptions needed and the day-night capability, the CO_2 band approach is without question the most accurate for determining high and middle cloud information. Low cloud information in tropical atmospheres is limited primarily due to the high concentration and emittance of water vapor in the lower troposphere which masks the clouds' radiant signature. However, as will be shown this limitation is minimized by retrieving the atmospheres VIRES instead of clouds per se. A brief description of the radiative theory behind this method follows.

Equation 1 gives the IR integral form of the RTE for a plane-parallel clear sky atmosphere with no scatter under the assumption of local thermodynamic equilibrium. A plot of the variation of the transmittance with respect to pressure is called the weighting function. For radiation measured in the CO_2 absorption band or window band in the absence of clouds, the transmittance is a known function (with slight dependence on temperature and water vapor profiles) as is the weighting function.

Equation 2 represents the satellite-received spectral radiance $[L(\nu,\theta)]$ from a scene containing N fraction of radiatively black clouds. For nonblack clouds N takes on a different meaning and is replaced by

α, an effective cloud fraction (see Eq. 3). Because reflectance by black or nonblack clouds is assumed to be small compared to emittance in the IR bands of concern, effective emittance $\varepsilon(\nu)$ and transmittance $\tau(\nu)$ are related by $\varepsilon(\nu) + \tau(\nu) = 1$ for these wavenumber bands. Consequently, we may as stated above replace N with an equivalent fractional cloud cover value equal to the product $\varepsilon(\nu)\ N = \alpha$. Thus, true fractional cloud cover cannot be derived unless the cloud emittance is known.

Neglecting term $L_{\nu cs}$, which is usually calculated from assumed temperature and gas profiles, Eq. (2) has unknowns; p_c and N. If we assume $\varepsilon(\nu_1) = \varepsilon(\nu_2)\ldots$ for the wavebands of interest, then $\alpha = \varepsilon(\nu)\ N$ will be the same value in Eq. (3) written for each of the spectral radiances. We therefore, have a system of at least two equations with two unknowns, p_c and α. So far we have assumed knowledge of gaseous and temperature profiles which allow us to compute the appropriate clear sky spectral radiance $L_{\nu cs}$ and the many $L_\nu(p_c)$ values (using specified cloud radiative characteristics) used to find p_c and α. We also assume that the clouds in the scene all have approximately the same cloud top pressure level p_c. However, we do not need to assume the scene is overcast, nor is it necessary to make assumptions about adjacent scenes.

At this point the method used in this paper diverges from the so-called ratio method and minimization method described in Chapter II. Instead of using Eq. (3) that gives satellite measured radiance L_ν in terms of α, $L_{\nu cs}$, and $L_{\nu cld}$, an empirical equation with L_ν in terms of α, $L_{\nu cs}$ and p_c is derived. This step eliminates the need to solve the IR - RTE for the iteration value of $L_{\nu cld}$. The rationale is outlined

below using simulated satellite radiances. The spectral radiative transfer routine and specific wavenumber bands and cloud radiative characteristics used are described in Chapter IV.

The emphasis is on the relationship between specified effective clouds and the weighting function. With specified effective clouds present the weighting function is drastically changed. For example, Figure 2 shows the effect graphically using wavenumber 747.5 cm^{-1} (5 cm^{-1} band width) and different levels of overcast cloudiness for a typical tropical atmosphere. Cloud emittance is near 1 or is unity since thick clouds are specified using an emittance model (described later) related to specified cloud water content. Figure 3 shows the effect of effective clouds on the weighting function for different amounts of cloudiness for a tropical atmosphere. This is the same effect as changing cloud emittance to less than unity in an overcast case. In other words α is the important shape parameter ($\alpha = N\varepsilon_{\nu}$). Broadband weighting functions show the same general characteristic effects of clouds, except for low altitude effective clouds. Near the ground, water vapor (see Figure 4) acts much like a low effective cloud as far as the atmosphere's VIRES is concerned. This is particularly true in the tropics. Figures 3 and 5 show that small α's result in small changes in the weighting curve shape.

For each wavenumber interval in the CO_2 band there is a different shaped weighting function. Wavenumbers close to the center of the band show clear sky weighting function peaks near the tropopause due to stronger line absorption. Wavenumbers further from center such as 747.5 cm^{-1} show peaks at lower levels in the atmosphere. When there is an effective cloud present, primary or secondary peaks (p_{wf}) occur near

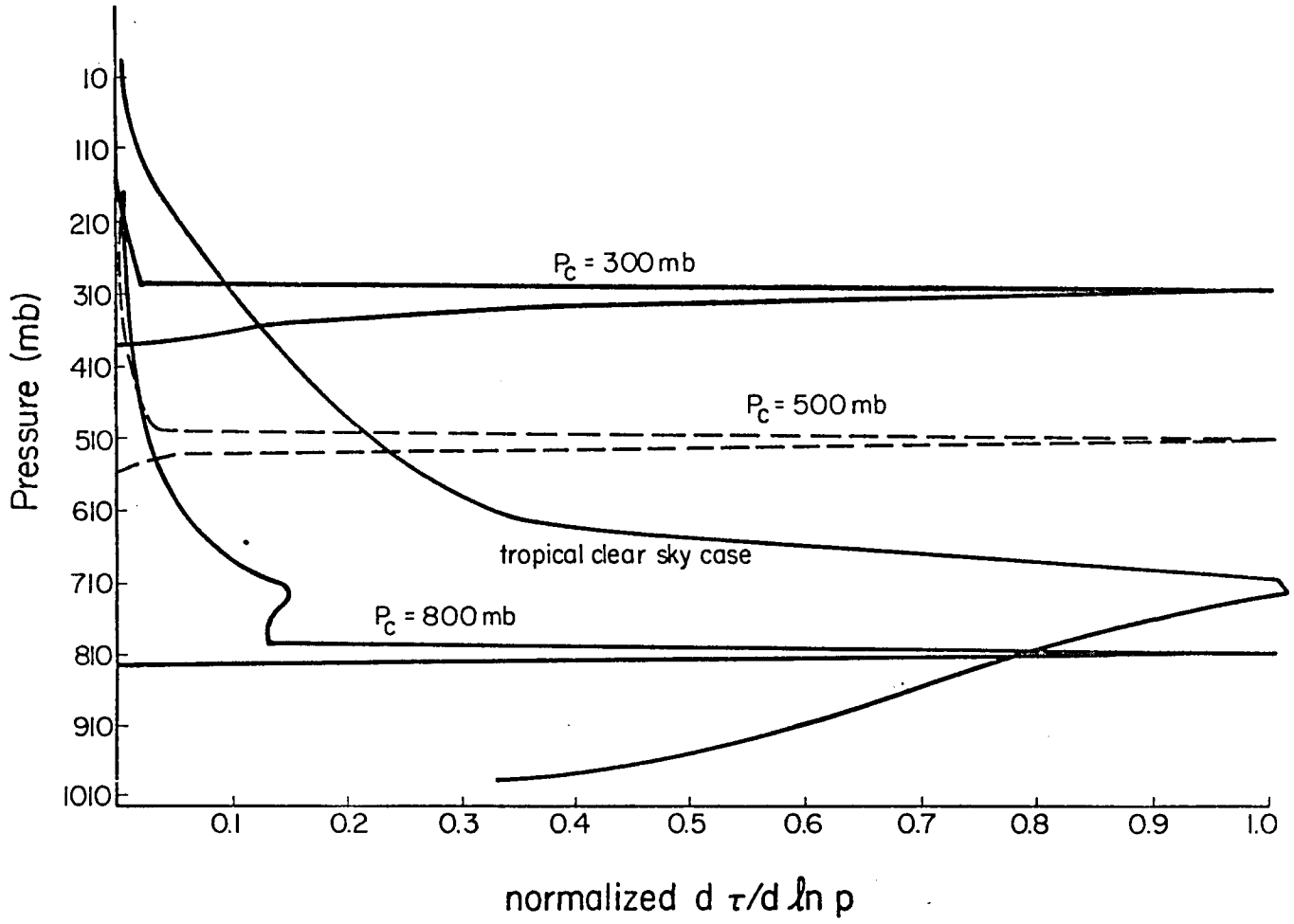

Figure 2. Weighting curves for given p_c and $\alpha = 1$ values, $\nu = 747.5$ cm^{-1}, for a tropical atmosphere.

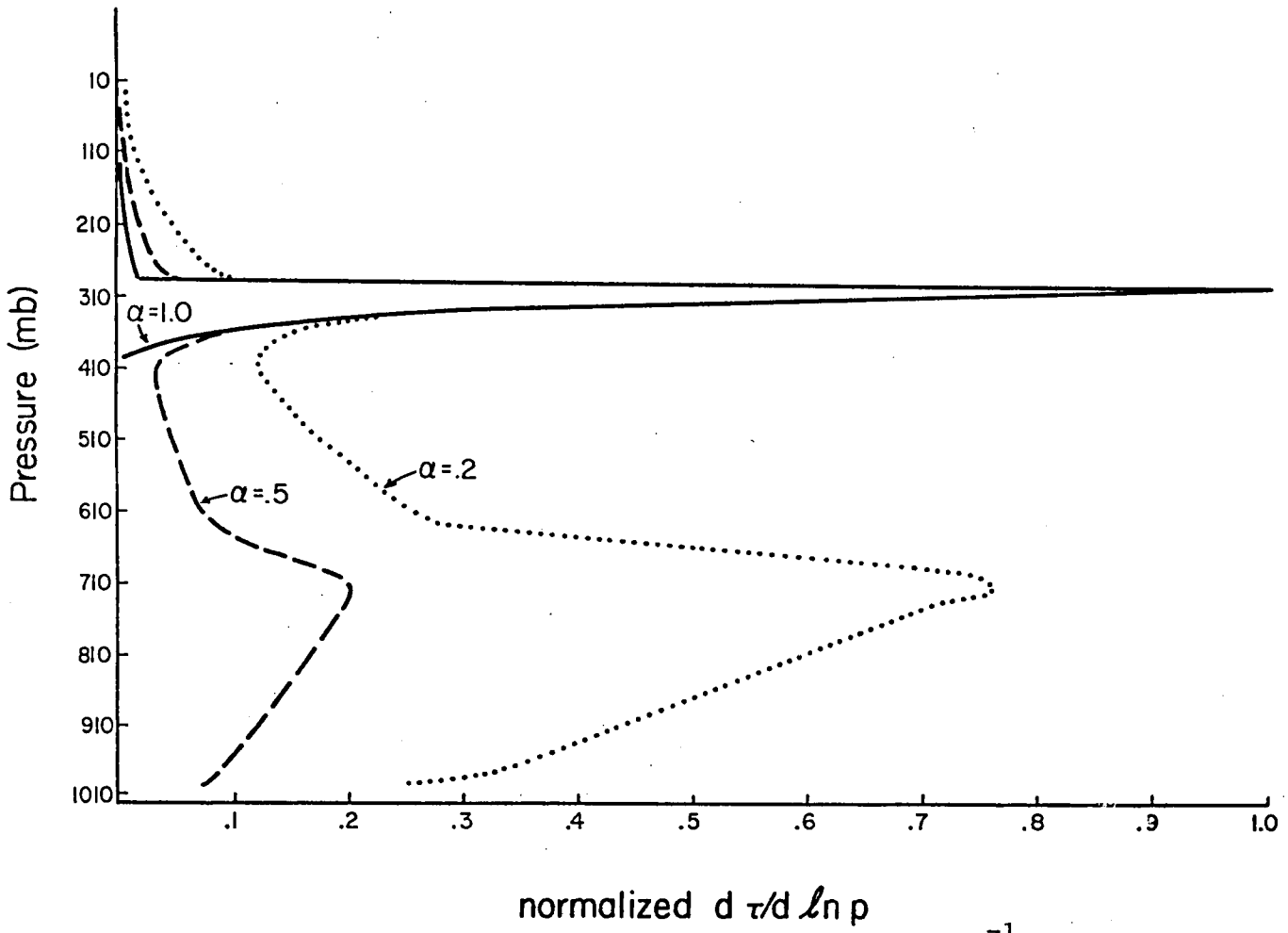

Figure 3. Weighting curves for given p_c = 300 mb and α values, ν = 747.5 cm^{-1}, for a tropical atmosphere.

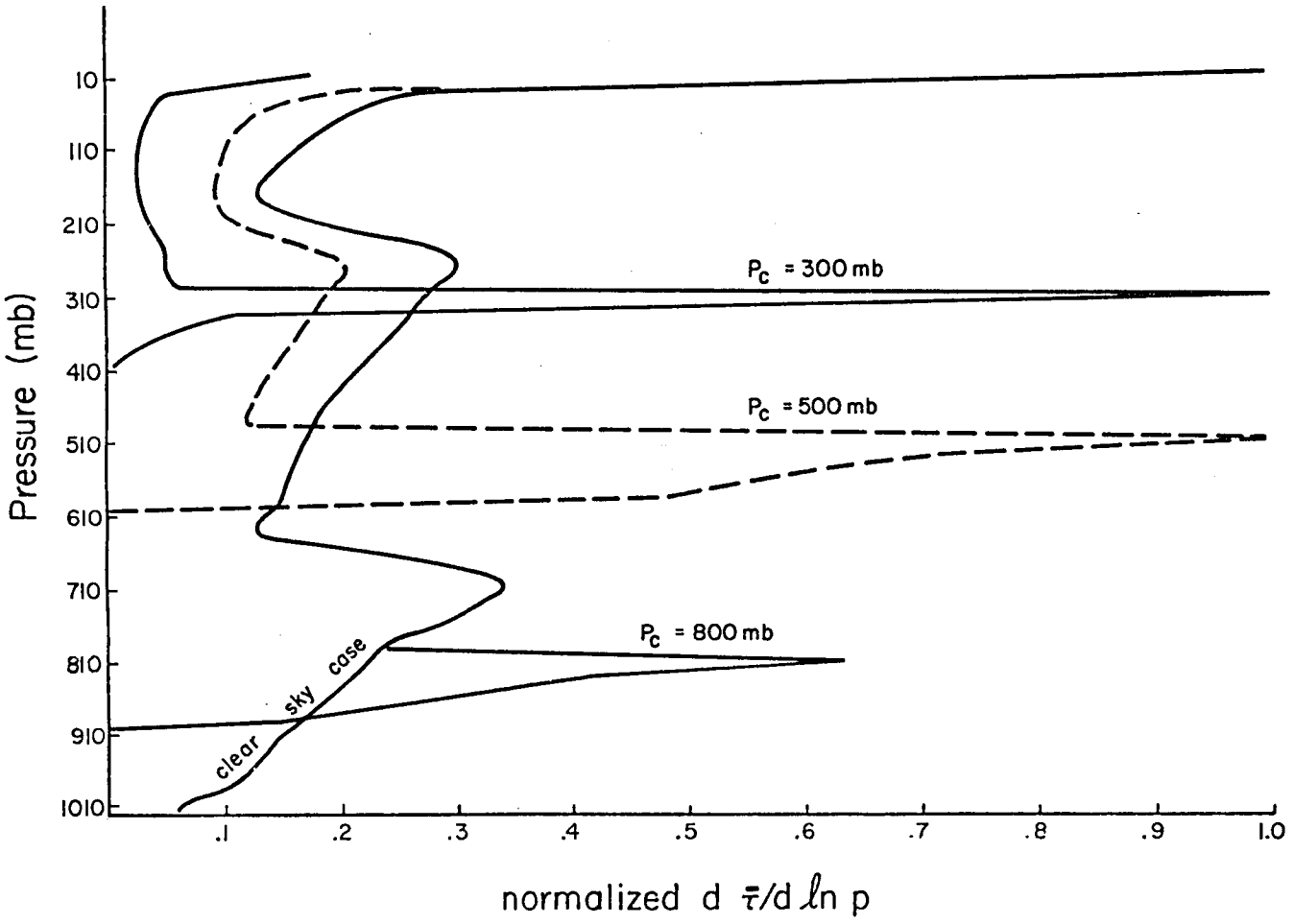

Figure 4. Broadband weighting curves for given p_c and $\alpha = 1$ values for a tropical atmosphere.

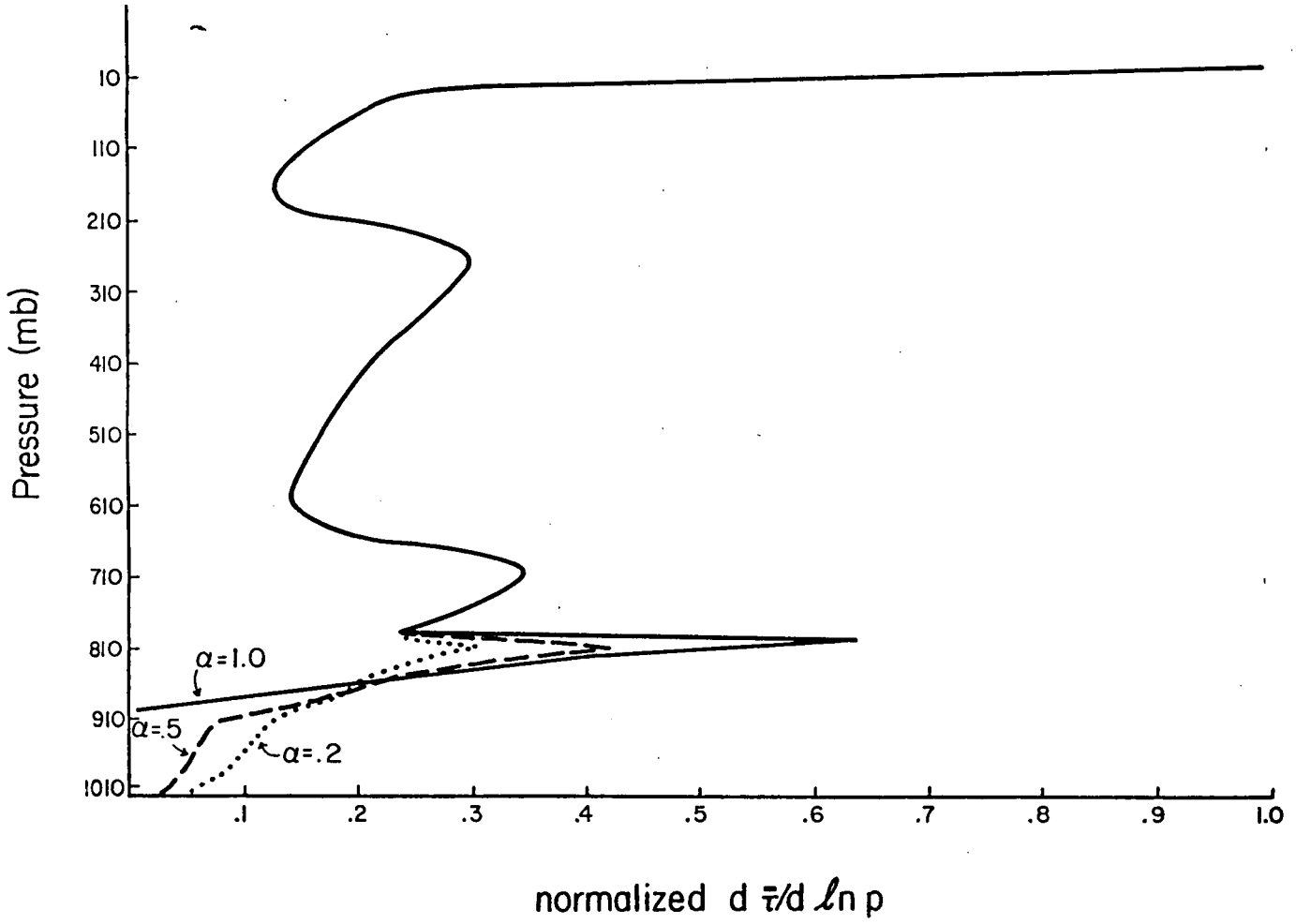

Figure 5. Broadband weighting curves for given p_c = 800 mb and α values for a tropical atmosphere.

the effective cloud top level as seen in Figures 2 and 3. The exact location of the peak is a function of model vertical resolution and in this 20 mb vertical resolution model it is found 10 mb below specified cloud top ($p_c = p_{wf} - 10$).

The most important radiative property in IR bands is cloud emittance as a function of depth into the cloud. Investigation shows that for a model vertical resolution of 20 mb, the level of the weighting function peak due to the cloud is not sensitive to cloud emittance specifications. Even for transluscent clouds the weighting function peak (p_{wf}) is 10 mb below specified effective cloud top (p_c).

To find an empirical relationship between $L_{\nu cs}$, p_{wf}, and α, values of weighting function peak heights (p_{wf}) due to specified effective clouds were plotted against the corresponding values of L (p_c, $\alpha = 1$) for a given temperature humidity profile. Figure 6 shows these plots for a mid-latitude summer profile. Figure 7a,b contains similar plots for a tropical atmosphere. The following relationship was found:

$$\left(\frac{\alpha}{C}\right) \ln \left(\frac{p_{wf}}{D}\right) = (L_\nu - L_{\nu cs}) \qquad (6)$$

The constants C and D depend on spectral wavenumber and atmospheric profile used although for small profile changes (1 to 2°C or 20-30% water vapor) they are nearly constant. The method used to derive and apply Eq. (6) is the topic of Chapter IV.

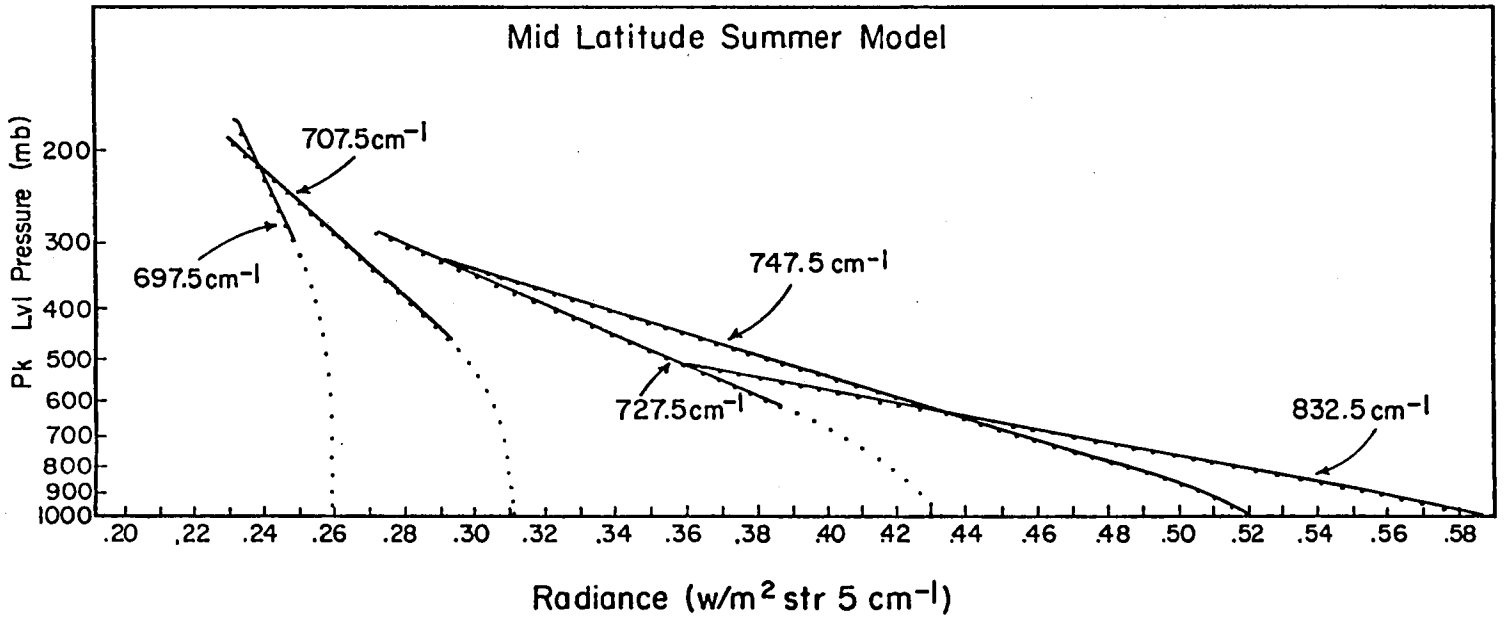

Figure 6. Empirical RTE curves for the mid-latitude summer model for $\alpha = 1$ case.

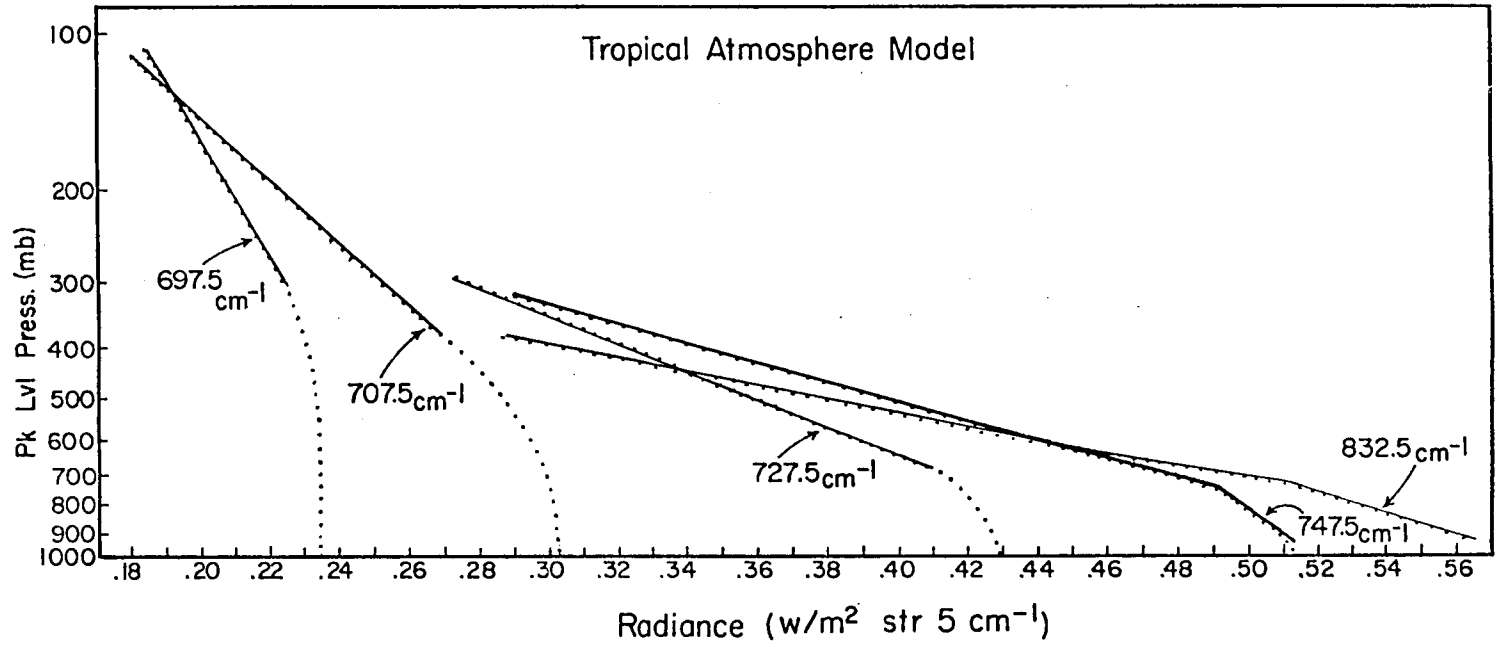

Figure 7a. Empirical RTE curves for the tropical model for $\alpha = 1$ case.

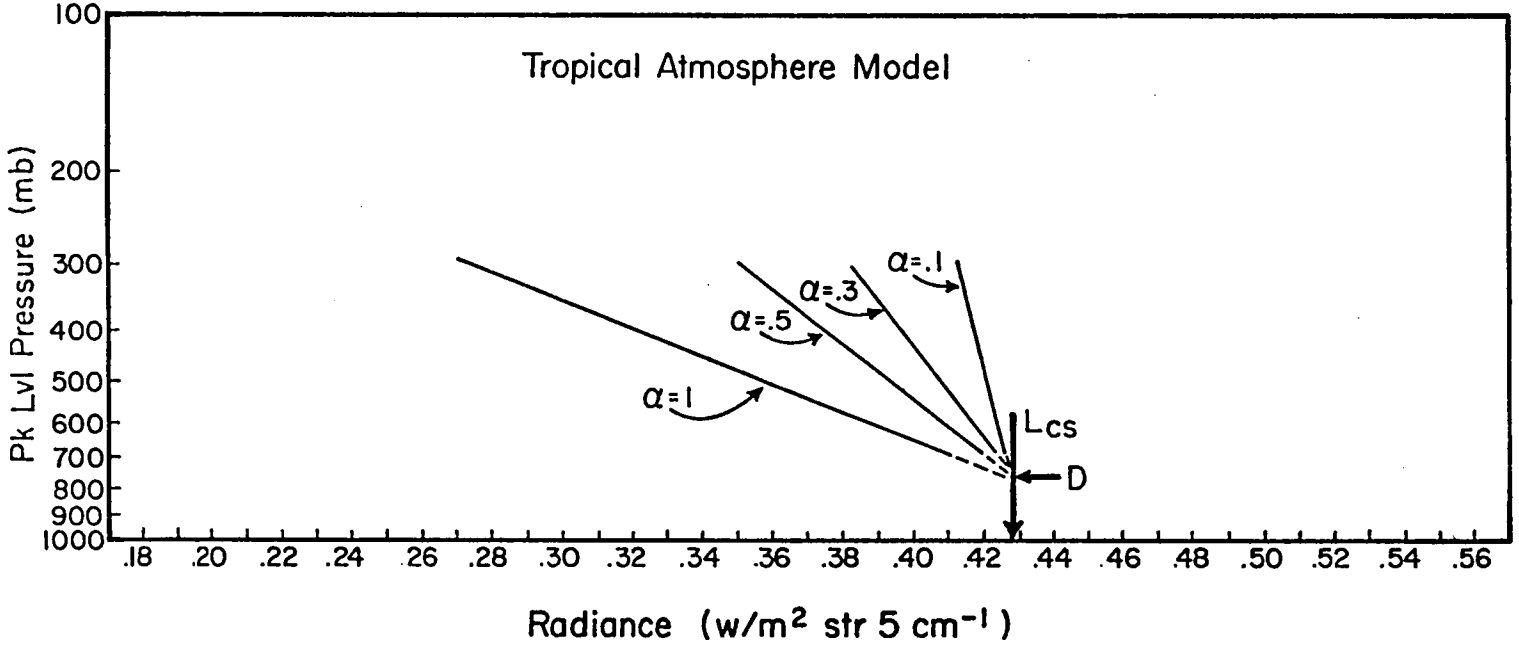

Figure 7b. Empirical RTE curves plotted for ν = 727.5 cm^{-1} and various cases of α, L_{cs} = .428 W/m^2 str 5 cm^{-1}, D = 752 mb.

IV. SHAPE PARAMETER RETRIEVAL PROCEDURE

Radiances received at satellite level are simulated using a spectral radiative transfer equation (RTE) for infrared radiation developed by Cox et al. (1976). Spectral absorption data are taken from Elasser and Culbertson (1960), Smith (1969) and Bignell (1970). For broadband infrared calculations a routine is used that is a broadband approximation to a rigorous line by line spectral radiative transfer equation, and which is described by Cox et al. (1976), and by Griffith and Cox (1977). Both sets of computer code were modified to produce the output requirements of this research. By design both radiative models are computationally fast with the consequence that approximations result in decreased accuracy. For example, N_2O and CH_4 absorption is ignored (Gupta et al. 1978). Nevertheless, the principals of the method described below are not dependent on the absolute accuracy of the radiative calculations.

Spectral bands chosen for use in this research are typical of those used on the satellite-borne radiometers called VTPR - Vertical Temperature Profile Radiometer (NOAA 2-5), HIRS - High Resolution Infrared Sounder (Nimbus 6, TIROS-N) and VAS-VISSR Atmospheric Sounder. Detailed descriptions of the instruments may be found in McMillin et al. (1973), Sissala (1975), and Schwalb (1978). Table 2 gives the central wavenumber of the bands used in this study. These represent typical values and are not necessarily the optimum ones. A 5 cm^{-1} band width is used. Table 2 also gives clear sky atmosphere weighting function properties of these channels.

Central WAVE Number cm^{-1}	Approximate VTPR Channel	Central WAVE Length μm	Clear Standard Atm. Wt. Fun. Pk.	Clear Tropical Atm. Wt. Fun. Pk.	Clear Mid Lat. Atm. Wt. Fun. Pk.
697.5	3	14.337	∿ 210 mb	210 mb	210
707.5	4	14.134	∿ 330 mb	330 mb	330
727.5	5	13.746	∿ 800 mb	710 mb	810
747.5	6	13.378	sfc	730 mb	sfc
832.5	8	12.012	sfc	950 mb	sfc

Table 2. Spectral band values used in the radiative transfer equation to simulate satellite data.

The tropical and mid-latitude atmospheric variables used in this study are given in Tables 3 and 4 respectively. These values were taken from the Handbook of Geophysics and Space Environments (1965) and from U.S. Standard Atmosphere 1976 (1976). As Tables 3 and 4 indicate, the radiative transfer routine is run with a 20 mb tropospheric resolution.

Besides gas and temperature profiles, cloud radiative properties must be specified. As stated earlier and as examined in more detail later, these specified cloud characteristics are not critical to obtaining the proper weighting function curve shape parameters (p_{wf} and α). Figure 8 describes the emittance model used in this research. Table 5 gives the specified cloud parameters. Notice that each of the 45 modeled effective clouds is 100 mb thick (where possible) and that below 300 mb the emittance is unity (black radiating surfaces). The effective cloud tops range from 100 mb to 980 mb at 20 mb intervals.

Since all parameters have been defined, radiance values can now be calculated for each of the six bands given in Table 2. Satellite received radiance values are simulated for each atmosphere and wave band for forty-five overcast cases and one clear sky case. From these 230 spectral radiance values, any simulated set of satellite values for a given atmospheric profile can be generated using Eq. (3). Figures 6 and 7a give plots of L_ν vs. p_{wf} for the overcast case (α values given in Table 5) simulated in this way. The procedure for obtaining the weighting curve shape parameters will be discussed next.

A standard least square linear regression model (Snedecor and Cochran, 1967) is applied to the data in Figures 6 and 7a using a log pressure transformation. The basic model is $y = b \exp(mx)$ and in its

PRESSURE mb	TEMPERATURE °K	W H20 G/KG	W 03 OG/G	W C02 G/KG
1.6	265.0	.010	6.200	.486
20.0	225.6	.020	10.342	.486
40.0	215.3	.010	4.429	.486
60.0	205.6	.010	1.723	.486
80.0	198.7	.010	.623	.486
100.0	195.7	.010	.348	.486
120.0	200.0	.010	.227	.486
140.0	206.0	.010	.200	.486
160.0	211.0	.010	.175	.486
180.0	216.4	.010	.152	.486
200.0	221.0	.010	.138	.486
220.0	225.2	.020	.126	.486
240.0	228.7	.040	.114	.486
260.0	232.3	.070	.104	.486
280.0	235.9	.110	.096	.486
300.0	239.2	.160	.090	.486
320.0	242.5	.220	.085	.486
340.0	245.3	.300	.081	.486
360.0	247.8	.390	.077	.486
380.0	250.2	.480	.074	.486
400.0	252.8	.600	.072	.486
420.0	255.4	.730	.071	.486
440.0	257.9	.870	.069	.486
460.0	260.2	1.030	.068	.486
480.0	262.6	1.200	.067	.486
500.0	264.7	1.400	.066	.486
520.0	266.5	1.630	.065	.486
540.0	268.3	1.870	.064	.486
560.0	270.1	2.110	.063	.486
580.0	271.9	2.300	.062	.486
600.0	273.8	2.490	.061	.486
620.0	275.7	2.680	.060	.486
640.0	277.6	3.290	.059	.486
660.0	279.3	4.680	.059	.486
680.0	281.0	6.070	.058	.486
700.0	282.7	7.460	.058	.486
720.0	284.2	8.560	.058	.486
740.0	285.1	8.810	.057	.486
760.0	286.0	9.050	.057	.486
780.0	286.8	9.290	.057	.486
800.0	287.8	9.540	.056	.486
820.0	288.9	9.990	.056	.486
840.0	290.1	10.520	.055	.486
880.0	291.3	11.570	.054	.486
900.0	293.7	12.090	.053	.486
920.0	294.8	12.800	.052	.486
940.0	295.9	13.550	.051	.486

Table 3. (Page 1)

PRESSURE mb	TEMPERATURE °K	W H20 G/KG	W 03 OG/G	W C02 G/KG
960.0	297.0	14.300	.050	.486
980.0	298.1	15.060	.050	.486
1000.0	299.2	15.810	.049	.486
1013.0	300.0	16.300	.048	.486

Table 3. Tropical atmospheric profile variables.

PRESSURE mb	TEMPERATURE °K	W H2O G/KG	W 03 UG/G	W CO2 G/KG
1.8	270.0	.003	8.600	.486
20.0	229.8	.003	9.775	.486
40.0	222.6	.003	6.597	.486
60.0	219.0	.003	4.260	.486
80.0	217.1	.003	2.782	.486
100.0	216.0	.003	1.813	.486
120.0	216.0	.003	1.258	.486
140.0	216.0	.003	.978	.486
160.0	216.0	.004	.782	.486
180.0	216.2	.006	.675	.486
200.0	220.2	.010	.568	.486
220.0	224.3	.014	.465	.486
240.0	228.4	.019	.365	.486
260.0	231.7	.030	.292	.486
280.0	234.8	.042	.223	.486
300.0	238.1	.064	.189	.486
320.0	241.3	.086	.157	.486
340.0	244.0	.133	.133	.486
360.0	246.5	.188	.112	.486
380.0	249.0	.239	.096	.486
400.0	251.6	.287	.089	.486
420.0	254.2	.336	.082	.486
440.0	256.4	.396	.077	.486
460.0	258.3	.462	.073	.486
480.0	260.3	.527	.069	.486
500.0	262.2	.599	.067	.486
520.0	264.0	.673	.065	.486
540.0	265.7	.748	.063	.486
560.0	267.5	.841	.062	.486
580.0	269.1	.976	.060	.486
600.0	270.7	1.111	.058	.486
620.0	272.4	1.246	.057	.486
640.0	273.9	1.373	.065	.486
660.0	275.3	1.495	.056	.486
680.0	276.8	1.617	.055	.486
700.0	278.3	1.739	.055	.486
720.0	279.7	1.909	.055	.486
740.0	281.0	2.126	.055	.486
760.0	282.3	2.344	.055	.486
780.0	283.6	2.561	.054	.486
800.0	284.9	2.778	.054	.486
820.0	285.9	2.962	.054	.486
860.0	287.9	3.322	.054	.486
880.0	288.9	3.502	.054	.486

Table 4. (Page 1.)

PRESSURE mb	TEMPERATURE °K	W H2O G/KG	W 03 UG/G	W CO2 G/KG
900.0	289.9	3.682	.054	.486
920.0	290.6	3.861	.054	.486
940.0	291.4	4.039	.054	.486
960.0	292.1	4.218	.054	.486
980.0	292.8	4.396	.054	.486
1000.0	293.5	4.575	.054	.486
1013.0	294.0	4.700	.054	.486

Table 4. Mid-latitude summer atmospheric profile variables.

$$\varepsilon_{CLOUD} = 1 - \exp(-K\ LWC\ \Delta z)$$

$$\varepsilon_{CLOUD} = 1 - \tau_{CLOUD} \qquad \Delta z = z_2 - z_1 = \frac{\bar{RT}}{g} \ln \frac{P_1}{P_2}$$

Cloud Top Pressure (mb)	Assumed average cloud ice or liquid water (LWC) content (gm^{-3})	Cloud penetration distance for satellite 11 μm radiance measurements (meters)
100	0.01	1660
200	0.02	830
300	0.05	332
400	0.10	166
500	0.20	83
600	0.33	50
700	0.50	33
800	1.00	20
900	1.00	20
1000	1.00	20

A mass absorption coefficient (K) of 0.045 $m^2 g^{-1}$ was used at all levels thereby allowing cloud emissivity to be determined by variations in cloud water content and cloud thickness. (After Cox and Griffith, 1978).

Figure 8. Description of cloud emittance model used in this paper.

CLOUD TOP	CLOUD BASE	LWC g/cm^3	COMP. τ	COMP. α,N=1	CLOUD TOP	CLOUD BASE	LWC g/cm^3	COMP. τ	COMP. α,N=1
100	200	.010	.15	.85	560	660	.248	.00	1.0
120	220	.011	.15	.85	580	680	.279	.00	1.0
140	240	.013	.13	.87	600	700	.313	.00	1.0
160	260	.016	.10	.90	620	720	.352	.00	1.0
200	300	.021	.08	.92	640	740	.395	.00	1.0
220	320	.025	.06	.94	660	760	.443	.00	1.0
240	340	.029	.04	.96	680	780	.498	.00	1.0
260	360	.034	.03	.97	700	800	.559	.00	1.0
280	380	.040	.02	.98	720	820	.628	.00	1.0
300	400	.047	.01	.99	740	840	.705	.00	1.0
320	420	.055	.01	.99	760	860	.792	.00	1.0
340	440	.064	.00	1.0	780	880	.890	.00	1.0
360	460	.075	.00	1.0	800	900	1.00	.00	1.0
380	480	.087	.00	1.0	820	920	1.00	.00	1.0
400	500	.100	.00	1.0	840	940	1.00	.00	1.0
420	520	.110	.00	1.0	860	960	1.00	.00	1.0
440	540	.124	.00	1.0	880	980	1.00	.00	1.0
460	560	.139	.00	1.0	900	1000	1.00	.00	1.0
480	580	.156	.00	1.0	920	1000	1.00	.00	1.0
500	600	.175	.00	1.0	940	1000	1.00	.00	1.0
520	620	.197	.00	1.0	960	1000	1.00	.00	1.0
540	640	.221	.00	1.0	980	1000	1.00	.00	1.0

Table 5. Specified Cloud Parameters.

linear form it is $\ln y = \ln b + mx$, where m = slope and $\ln b$ is the y intercept value. In this model the known independent variable x is given below:

$$x = L_\nu (p_{wf}, \alpha) = \alpha L_{\nu cld} + (1-\alpha) L_{\nu cs},$$

where L_ν is the satellite measured spectral radiance for a given spot, α is the effective cloud amount, $L_{\nu cld}$ is the radiance from the cloudy area of the spot, and $L_{\nu cs}$ is the radiance from the clear sky portion of the spot. The dependent variable y is equal to p_{wf}. Using the data represented in Figures 6 and 7a one can solve for the equation parameters m and b for $\alpha = 1$ for each wavenumber line.

One could solve for m and b values for a number of α value lines (Figures 6 and 7a represent an $\alpha = 1$ line) using the same procedure. However, an easier and faster approach is to rewrite the linear regression model in terms of α. First note Figure 7b which shows that regardless of the α value line plotted, as L_ν approaches $L_{\nu cs}$, p_{wf} approaches the constant value D. Furthermore, since x is a linear combination using $L_{\nu cs}$ and α, one might expect to be able to write the linear model in terms of $L_{\nu cs}$ and α which in effect gives an equation that represents a family of curves in p_{wf} and α. In other words consider the model

$$y = b \exp (Cx \div \alpha).$$

Analysis showed that for such a model

$$b = D \div \exp (CL_{\nu cs} \div \alpha).$$

This results in the following relationship

$$y = D \exp\left[\frac{C(L_\nu - L_{\nu cs})}{\alpha}\right] = p_{wf}. \qquad (7)$$

In this equation p_{wf} is simply related to both L_ν and α. L_ν is measured and $L_{\nu cs}$ is known. For the $\alpha = 1$ case plotted in Figures 6 and 7a, constant C is simply the lines' slope m, and constant D = exp $(C\ L_{\nu cs} + \ln b)$.

Table 6 gives the respective values of C and D and $L_{\nu cs}$ for each wavenumber band. Computationally these values are used in Eq. (7), which is simply another form of Eq. (6) given in Chapter III. For each wavenumber there is a separate equation with two unknowns p_{wf} and α. One may solve a set of two equations with two unknowns. Two wavenumber equations are chosen. A simple iterative scheme that changes values of α in the two equations is used to solve simultaneously for the values of p_{wf} and α of Eq. (7). Computationally one looks for the best agreement between the two calculated values of p_{wf} as one iterates through the α values.

Each wavenumber family of curves (Eq. 7) represents information from a part of the atmosphere as given in Table 6. As stated in Table 2 and illustrated in Figures 9 and 10 for six spectral bands of interest, clear sky weighting functions peak at certain levels in the atmosphere. Most of the radiance information at a given wavelength comes from the part of the atmosphere above this peak. A relatively small

WAVE NUMBER cm^{-1}	WEIGHTING FUNCTION PEAK LEVEL RANGE (mb)	VARIABLES C*	D**	CCR***
MID LATITUDE SUMMER ATMOSPHERE				
832.5	500 - 690	3.09	1007	.587
832.5	690 - 890	2.87	971	.587
832.5	890 - 995	3.85	998	.587
747.5	320 - 790	4.55	920	.521
747.5	790 - 890	5.95	963	.521
747.5	890 - 995	9.11	996	.521
727.5	295 - 600	6.47	815	.433
707.5	190 - 455	14.0	581	.311
697.5	190 - 295	31.2	396	.259
TROPICAL ATMOSPHERE				
832.5	370 - 630	3.21	942	.578
832.5	630 - 730	2.62	856	.578
832.5	730 - 935	4.47	942	.578
747.5	320 - 730	4.12	795	.513
747.5	730 - 935	10.9	899	.513
727.5	295 - 660	6.00	744	.428
707.5	100 - 400	13.9	600	.302
697.5	100 - 295	26.2	381	.234

* units of $[W/m^2 \text{ str } 5 \text{ cm}^{-1}]^{-1}$

** modified intercept in units of mb, explained in text

*** clear column radiance (W/m^2 str 5 cm^{-1})

Table 6. Cloud retrieval empirical equation variables.

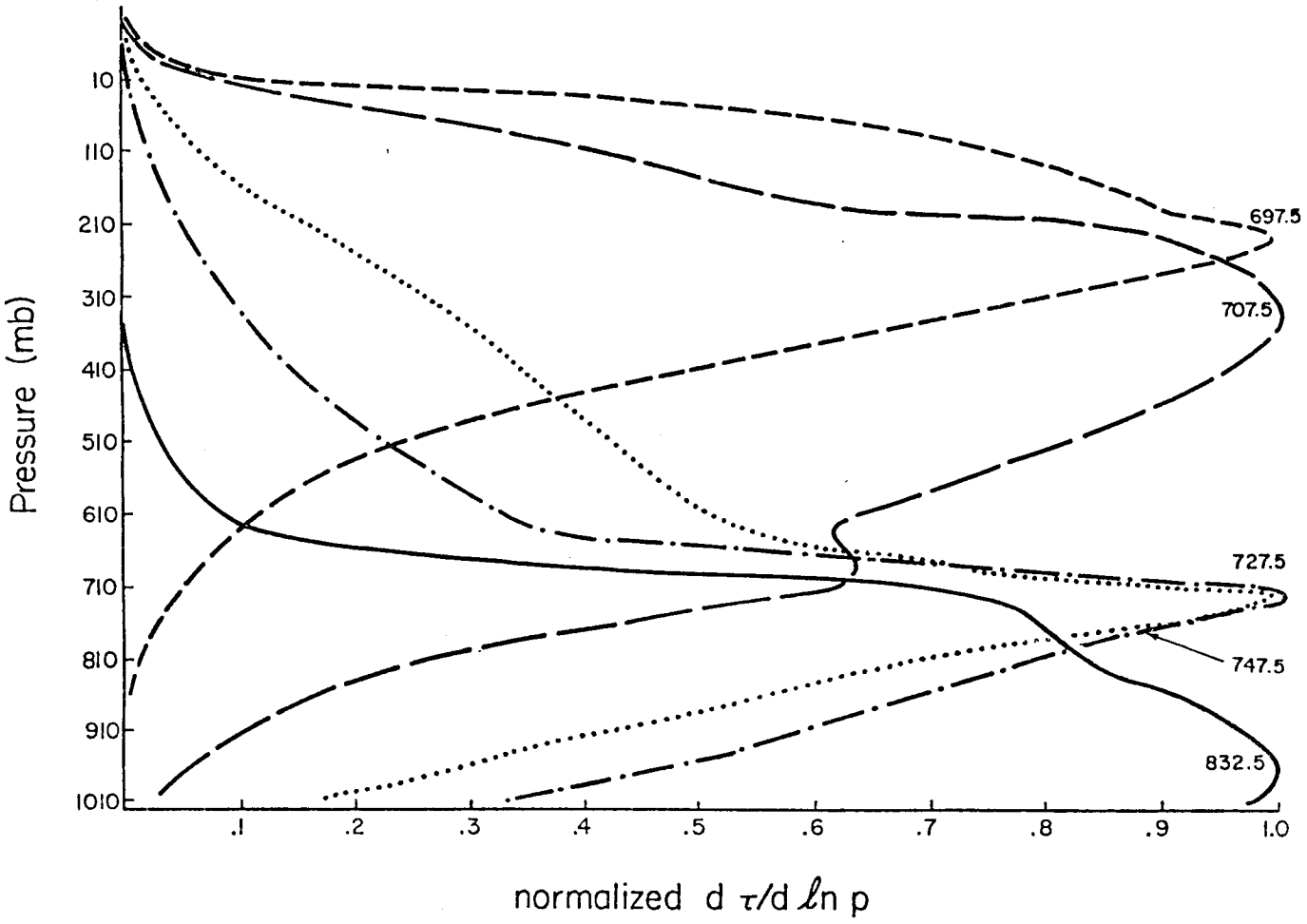

Figure 9. Tropical clear sky spectral weighting curves.

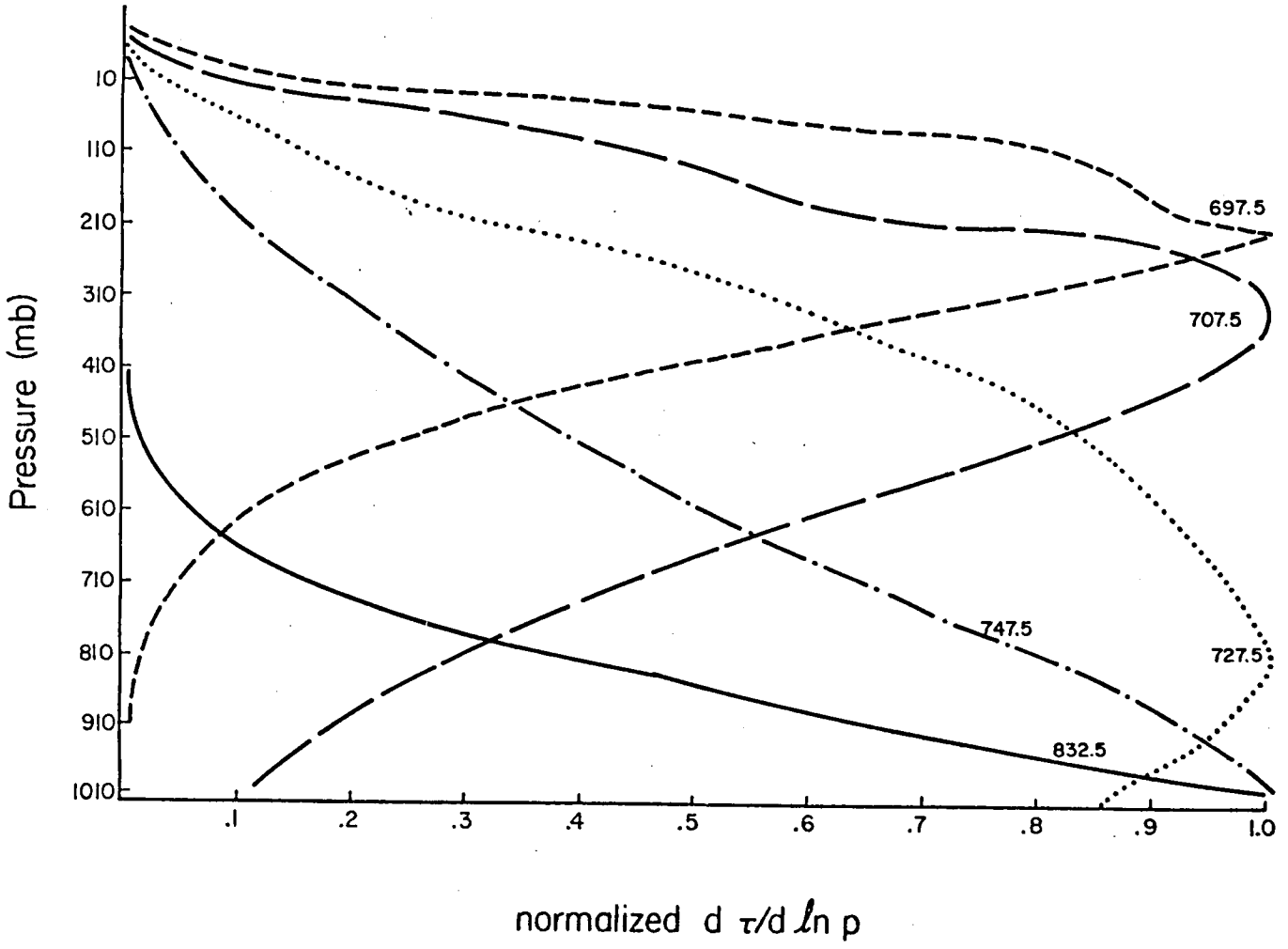

Figure 10. Mid-latitude summer clear sky spectral weighting curves.

portion of the total atmospheric spectral radiance received at satellite level originates below the clear sky weighting function peak level. Thus, any effective radiating surface below this clear sky peak level will not be strongly indicated in the satellite-received radiance value.

This effect can be seen in Figures 6 and 7a. Above the respective wave band natural clear sky weighting function peak, the relationship of ln p_{wf} to L_ν (satellite received spectral radiance) is nearly linear with a flat slope. However, below this point the slope steepens indicating very little change in L_ν for a change in p_{wf} (level of the effective radiating surface since $\alpha = 1$).

This effect is also evident in Figures 11 and 12 which plot wavelength dependent signal to noise ratio as a function of height for the tropical and mid-latitude atmospheres respectively. The signal $L_\nu - L_{\nu cs}$ (see Eq. 7) and the error values are given in Chapter V. In the figures, the solid lines indicate $\alpha = 1$ (overcast case) and the dashed lines are for α less than 1. For α values less than 1, the signal to noise ratio is reduced by a factor of α. For example, if $\alpha = .5$ the signal to noise ratio will be half the value it is for $\alpha = 1$. Note that as $\alpha \to 0$ and as p_{wf} (with constant $\alpha = 1$) $\to$ 1000 mb the signal to noise ratio decreases. In other words less information is available from which to make curve shape retrievals as these boundaries are approached. However, as illustrated in Figures 4 and 5 by the small curve shape change the VIRES of the atmosphere is least sensitive to errors near these boundaries. Figures 11 and 12 seem to indicate that the wavenumber band curves peaking near the surface should give the best results overall. However, the $\varepsilon_{\nu 1} = \varepsilon_{\nu 2}$ assumption limits the use of these widely spaced wavelength curves higher in the atmosphere where

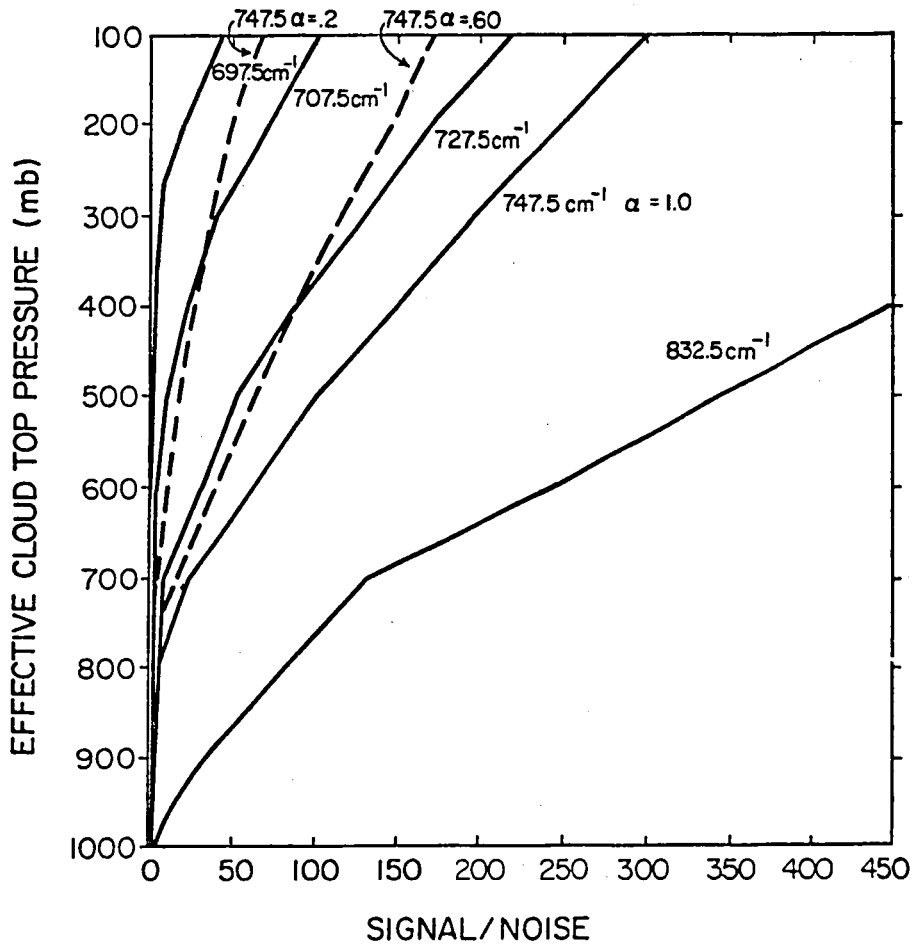

Figure 11. Signal to noise ratio vs. overcast effective cloud top pressure for tropical model. NOTE: Signal = $L_{\nu cs} - L_{\nu}$.

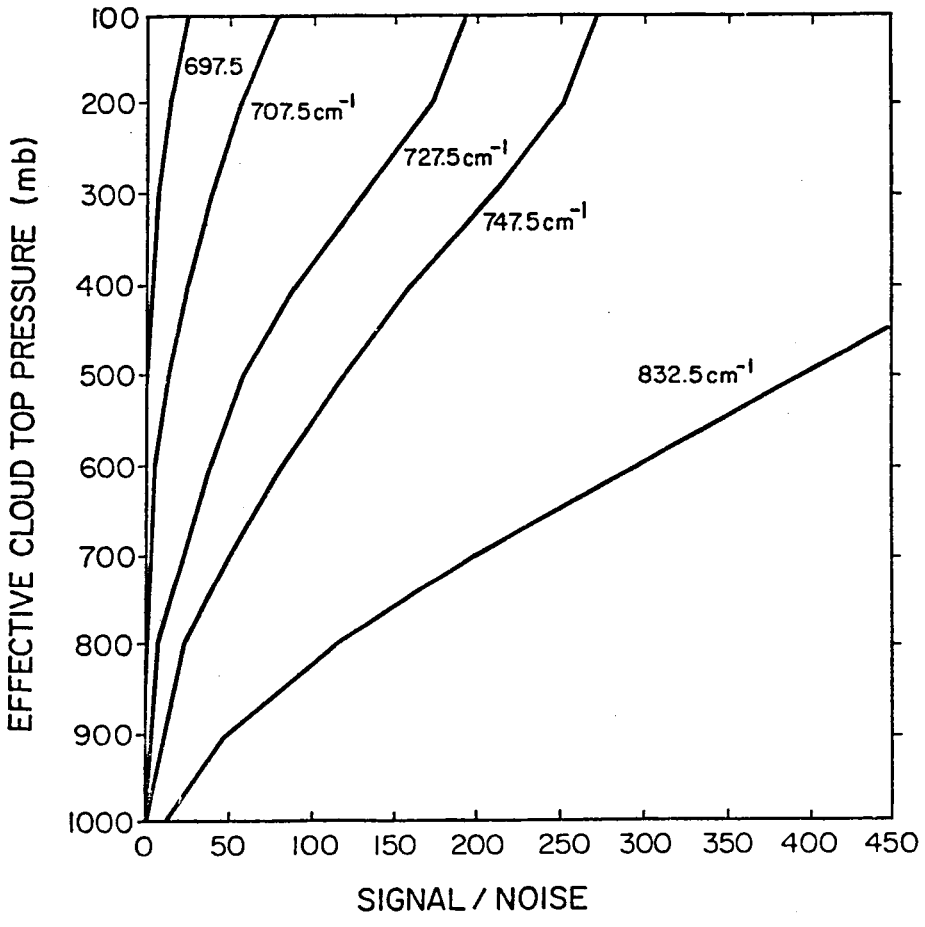

Figure 12. Signal to noise ratio vs. overcast effective cloud top pressure for the mid-latitude summer model.

nonblack clouds are common. Also, the slope and linearity of the curves in Figures 6 and 7a,b for these wavebands limit their use at upper tropospheric levels.

Therefore, since the curve shape parameter radiance signal is related to the clear sky weighting function peak level, only the areas of the atmosphere indicated by solid lines in Figures 6 and 7a,b for the respective wavebands are used in the retrieval calculations. This has the effect of maximizing the useful shape parameter information contained in the satellite radiance values.

Two further points can be made. First, the empirical RTE family of curves approach requires linearity in ln p which restricts the useful part of the curves in Figures 6 and 7a,b as indicated in Table 6. To obtain best results a few of the solid lines plotted in Figures 6 and 7a,b are actually broken down into two or three straight line segments. All lines calculated resulted in the coefficient of determination (r^2) exceeding 0.98. Secondly, for any given level of the atmosphere (100 - 980 mb) there must be at least two different waveband family of curves equations that can be compared to each other in order to determine the proper shape parameters p_{wf} and α. Table 6 indicates that this condition is met and that at times three curves overlap for comparison.

Neglecting input errors for now, it is useful to evaluate the statistical characteristics of the previously described empirical retrieval. Figures 13 and 14 show an evaluation of the bias and RMS error associated with retrieval of the two curve shape parameters p_{wf} and α. RMS error is the standard deviation of retrieval error. Bias error is the mean retrieved value minus the actual simulated value.

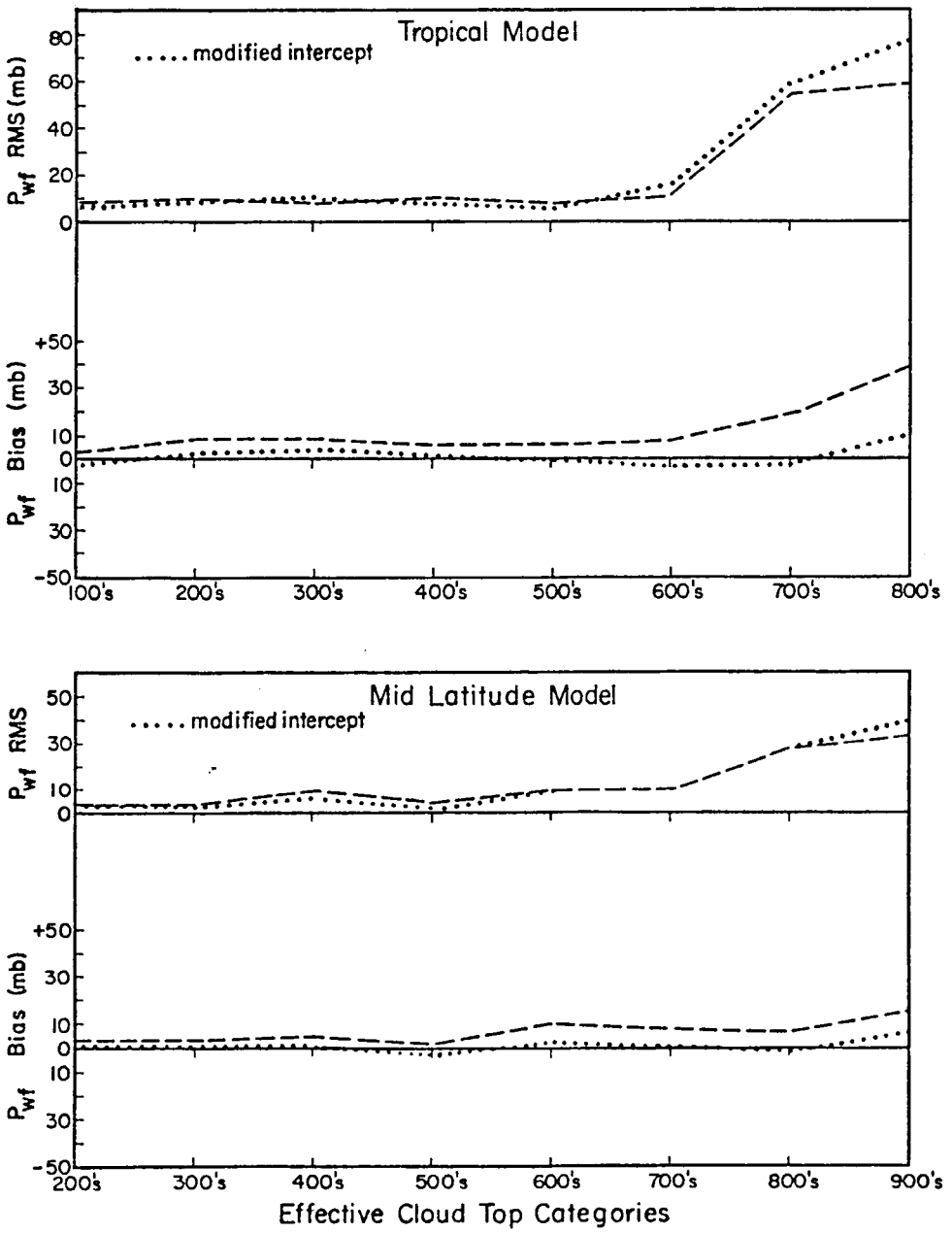

Figure 13. 'No error' empirical model statistical analysis of p_{wf}.

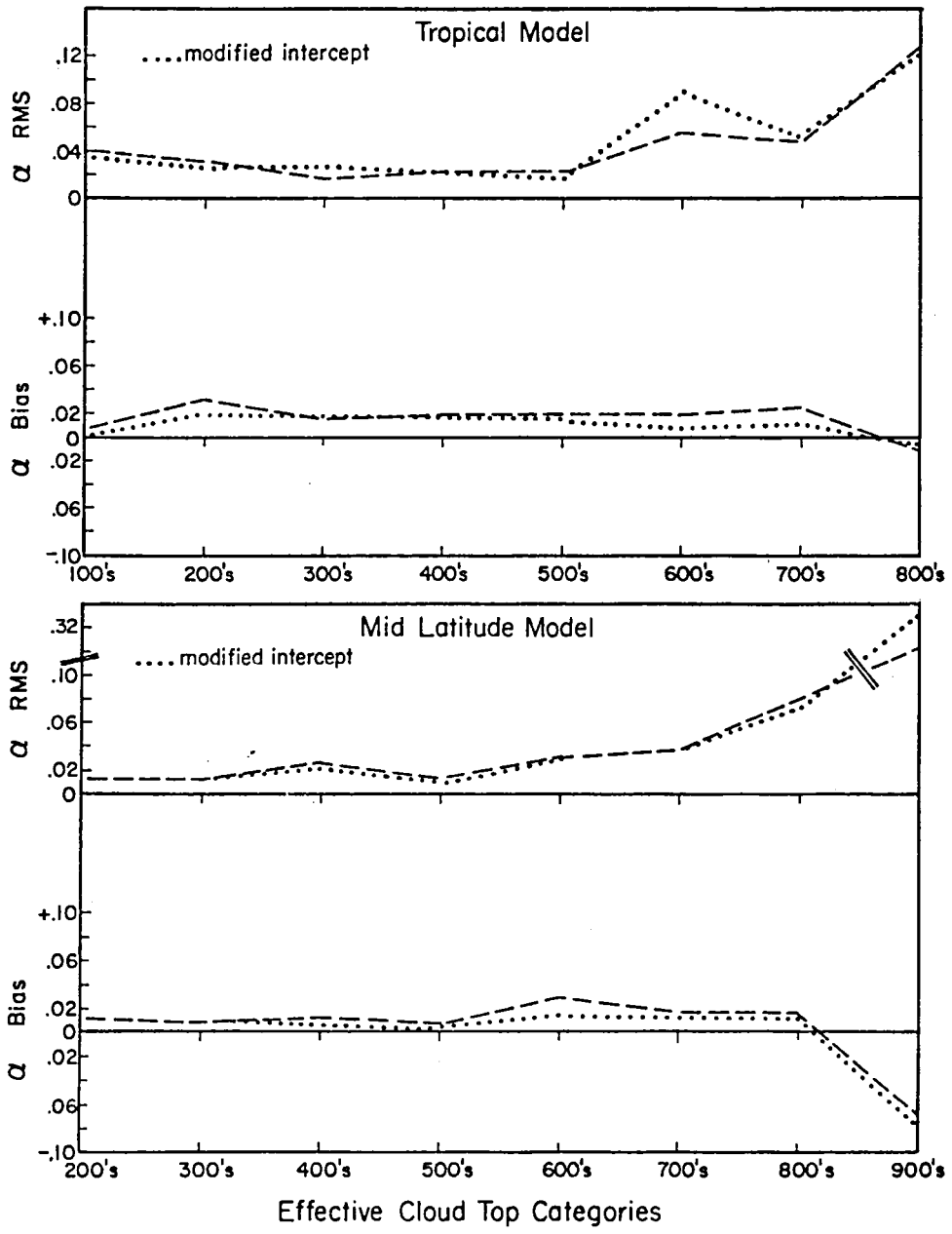

Figure 14. 'No error' empirical model statistical analysis of α.

Each point plotted is an evaluation of 50 values. The 50 values came from the 5 effective cloud top levels in a given 100's category (i.e. 300, 320, 340, 360 and 380 mb) evaluated at 10 clear versus cloudy fractional weightings (i.e. 1.0, 0.9, ..., 0.1). Values were calculated for the tropical atmosphere between 100 and 880 mb and between 200 and 980 mb for the mid-latitude summer atmosphere. Values above the tropopause were not considered because isothermal conditions give no indication of p_{wf} changes in the satellite radiance values (i.e. $\frac{\partial T}{\partial z} \neq 0$). Values at 900 mb and below in the tropical atmosphere were not considered because the high concentration of water vapor at these levels essentially has the same effect on the atmosphere VIRES whether an effective cloud is there or not.

From Figures 13 and 14 it can be seen that the RMS curves are influenced by the signal to noise ratio values discussed previously. As pointed out before, the errors occurring in the retrieval low in the atmosphere have the least effect on the shape of the broadband weighting function curve. However, the error shown by the bias curves is only due to the failure of the empirical RTE to exactly duplicate calculation of the RTE for every combination of p_c and α. The dotted line shows an adjustment made to the empirical method to remove a small consistently high bias. Variable D (an intercept value) of Eq. (7) is slightly reduced to nearly eliminate this bias. Apparently solving for C and D by the method described earlier using $\alpha = 1$ which is at a boundary, results in this $\simeq$ 5 mb bias.

As stated previously and as outlined in Figure 1a the shape parameter p_{wf} and α are used in the broadband computer routine referred to earlier in this chapter. The program is run using the same atmospheric

profile used to compute the C and D values of Eq. (7) and listed in Table 6. One may run the program with many pairs of shape parameters to produce a composite VIRES curve. Chapter VI gives examples of this procedure and explains how the VIRES broadband curves are used to yield the proposed VIRES index. The next chapter evaluates the retrieval errors under realistic system error conditions. Note also that at the end of Chapter V it is shown that one may produce useful composite curves by combining the simulated spectral radiances before curve shape parameter retrieval is performed.

V. SENSITIVITY ANALYSIS

To help assess the feasibility of using the atmospheric VIRES as a climate index in the form of broadband infrared weighting functions, it is useful to know the characteristic errors of inferring these profiles from satellite spectral radiances. First, the uncertainties both random and bias associated with the empirical RTE technique used to retrieve the weighting curve shape parameters p_{wf} and α are examined. Secondly, the sensitivity of the final weighting curve product to reasonable errors is examined. All error sources evaluated are associated with implicit or explicit assumptions.

A. Shape parameter retrieval errors

Error sources examined in this section include system-instrument errors, errors associated with temperature, humidity, and CO_2 profile unknowns, and errors due to specified cloud properties assumptions. The sensitivity of the weighting curve shape parameters to these likely error sources is investigated. The chosen approach and specific error magnitudes are discussed below.

The calculation of the statistics used in this analysis is straightforward. The p_{wf} and α RMS errors are variations of the retrieved values about the retrieval mean p_{wf} and α values. Thus the RMS is a measure of the retrieved values standard deviation about the mean. However, because the RMS is large compared to the mean, the described RMS value is nearly equal to the RMS calculated the standard way. Bias error is the difference between the actual and retrieved mean value.

Important to the calculation of the statistics is the empirical-RTE technique boundary conditions. Naturally the values of α are found between 1.0 and 0. For clear sky conditions α is given the value 0 and p_{wf} = 1000 mb. Clear sky conditions are assigned when $L_\nu \geq L_{\nu cs} - 2\sigma_\nu$, where ν = 747.5 and 832.5 cm^{-1}, and σ_ν is the standard deviation of instrument error at a given wavenumber. Retrieval calculations giving radiating surfaces above the tropopause are taken to indicate the radiating surface location at the tropopause level (100 mb for tropical atmosphere, and 180 mb for mid-latitude atmosphere). Because of the strong influence of water vapor in the tropical model, radiating surfaces calculated to be below 935 mb are taken to indicate clear sky conditions. Specifics of the error analysis are given in the Appendix. A summary of these results including error assumptions follows.

Instrument system noise is assumed to be Gaussian with a mean of zero and a standard deviation of 0.22 mW $m^{-2}sr^{-1}cm$ for the CO_2 channels and 0.11 mW $m^{-2}sr^{-1}cm$ for the window channel. These values represent the state of the art precision of the HIRS instrument on TIROS-N (Schwalb, 1978). It is also assumed that channel errors for a specific spot measurement are correlated. Thus each simulated spectral radiance value was modified in a like manner by an error value distributed as described above and chosen randomly for each set of radiance values. The effect of this approach, compared to random assignment of individual errors to the spectral radiances in a set, is to give $\approx$ 30% smaller overall bias errors and $\approx$ 20% smaller RMS errors to the retrieved curve shape parameters. The bias and RMS errors are smaller because the retrieval routine is better able to find a unique solution when errors are in the same direction and of similar magnitude. Real

characteristic sensor noise of course, lies somewhere between the two descriptions given above. Although example comparisons of the results from the two approaches showed the trend described above, the noise correlation approach was chosen for the overall sensitivity analysis.

Temperature and water vapor profile errors are also assumed to be Gaussian with zero mean. Errors vary randomly from one 20 mb layer to another and temperature errors are assumed not to be correlated with humidity errors. Reasonable temperature and humidity errors are assumed to be $\leq$ 5°C RMS for temperature and an RMS $\leq$ 100% of the correct mixing ratio (Wielicki and Coakley, 1980). Although analysis was done for a number of reasonable values, the results reported on in the Appendix are for a 2°C RMS and an RMS water vapor noise of 50% (Susskind and Rosenfield, 1980; Weinreb and Crosby, 1977).

CO_2 profile maximum errors are assumed to be of magnitude 1%. This represents a value that is $\frac{2}{3}$ of the seasonal change in CO_2 concentration (Bolin and Bischof, 1970; Miller, 1978). CO_2 is assumed to be well mixed in the troposphere and, therefore, the 1% error is applied equally from layer to layer.

For all profile errors a simple correction technique is sometimes useful. Using additional radiative information in the form of a clear column radiance correction (CCRC) decreases error values. Application of CCRC is explained in the Appendix.

Cloud radiative properties must be specified or assumed to be of a certain nature. For emitted radiation the most important property (and only one examined here) is cloud effective emittance. As Platt and Stephens (1980) have recently pointed out, there are scattering and reflection components of effective cloud emittance, especially for ice

clouds. However, for the cloud model used in this research, two properties determine the cloud effective emittance; cloud thickness and cloud liquid water content (LWC). Two errors that are most likely to occur are examined. First a 100 mb thick cloud is specified when in reality a 20 mb thin cloud is present. In other words, cloud emittance is specified too large. Second, a cloud of higher LWC than specified is present. This is the case of cumulonimbus cloud at cirrus level. In this situation cloud emittance is specified too small. This occurs only above 300 mb since below thin level cloud emittance is specified at the maximum value of 1. As stated previously and as shown by this analysis, the retrieval process is essentially independent of cloud radiative properties specified.

Table 7 gives a summary of the error sources and the corresponding bias and RMS order of magnitude error for the two curve shape parameters retrieved. The combination error source includes a random 2°C RMS and 50% RMS water mixing ratio error. It also includes instrument noise as described above. Cloud depth is allowed to randomly vary from 20 to 180 mb and cloud LWC varies randomly from $\pm$ 50% of the specified value. This table shows results that testify to the capability of this retrieval method.

B. Error effects on the weighting curves

The next source of error evaluated is the assumption that the satellite sensor views only one effective cloud layer in non-clear situations. Direct sensitivity of the weighting curve to this error is investigated. The error is examined by means of a sensor resolution argument. We compare two models. In the first model the sensor

Error Sources*	Statistical Values* p_{wf} bias (mb)	p_{wf} RMS (mb)	α bias	α RMS
Empirical RTE	0	5	± .01	.03
Sensor noise	± 15	80	± .04	.15
Temperature + humidity	± 30	160	± .06	.30
Temperature + humidity with CCRC*	± 15	20	± .06	.05
CO_2 profile	± 30	40	± .02	.02
CO_2 profile with CCRC	± 2	10	± .01	.02
Specified emittance	± 2	8	± .01**	.03**
Combination	± 15	160	± .05	.35
Combination with CCRC	± 15	90	± .05	.20

* defined in text

** not plotted in the Figures

Table 7. List of representative errors in shape parameter retrieval due to given error sources.

detects, for example, 200 sets of radiances, representing single layer effective clouds. This model is compared to the second model which senses 100 sets of radiance values for the same area of effective cloud. The second set of radiances are simply averages of the first set of radiances taken by pairs. For both cases curve shape parameters are retrieved assuming single layer effective clouds and composite weighting function curves which represent the same 200 spot (high resolution) area are computed. The two curves are statistically compared to test the one layer error assumption. In the 200 spot specified model the assumption is totally true, while in the 100 pair model the assumption is completely false.

In this analysis the 200 spot area represents a sample from an effective cloud layer distribution. Three different distributions of effective cloud top heights are specified to provide a more complete test. The test in general as well as the distributions are described in detail in the Appendix. The statistical test used is described in Chapter VI.

Table 8 shows the results of the single effective cloud layer assumption analysis. The statistical test values indicate that for the situations of curve compositing the errors associated with the single layer assumption are minimized. For the test cases presented, the retrieved composite weighting function curves are extraordinarily similar to the true (specified) curves. Although the statistical test is designed to indicate curve differences, small T values imply likeness. In other words, if the calculated T values are as large or larger than the critical T value then H_0 (the curves are the same) can be rejected

	DISTRIBUTIONS	SIGN COUNTS FOR SIGN TEST 100 - 380 mb Pos.	100 - 380 mb Neg.	400 - 680 mb Pos.	400 - 680 mb Neg.	700 - 980 mb Pos.	700 - 980 mb Neg.	T Statistic
	FLATS vs FLATR	9	6	9	6	7	8	1.96
(Cut off correction)	FLATS vs FLATR	6	5	1	1	0	0	0
	FLATS vs FLATR*	7	8	9	6	7	8	0.98
(Cut off correction)	FLATS vs FLATR*	7	6	0	2	0	0	1.39
	BIMOS vs BIMOR	7	8	9	6	7	8	0.98
(Cut off correction)	BIMOS vs BIMOR	4	5	1	1	0	0	0
	1PK3S vs 1PK3R	8	7	8	7	4	11	4.17
(Cut off correction)	1PK3S vs 1PK3R	5	7	4	1	0	0	1.45

P values	Critical T values (see text)
.01	16.8
.05	12.6
.10	10.6
.25	7.8
.50	5.4

Table 8. Statistical test of the differences between the curves in Figures 40-42.

at the given P value significance level. Otherwise, H_0 is accepted as true, the differences in the curves being explained by chance happenings.

This last section looks at the sensitivity of the final product broadband weighting curve to the factors that are most important to curve parameter retrieval, temperature and humidity. The two climatological profiles (Tables 3 and 4) are assumed to be correct when using the retrieval method, i.e. when determining C and D values and when calculating the broadband curves from the retrieved curve shape parameters. However, each of these profiles are modified to produce 'actual' cases. Temperature and humidity at each level in the climatological profiles are increased or decreased by a specified percentage to produce these 'actual' cases. From these 'actual' profiles the simulated satellite radiances are calculated. Finally, the broadband weighting curve retrieved assuming a climatological atmosphere (without using CCRC) when an 'actual' profile exists is compared to the weighting curve produced directly from the true atmospheric profile and 'true' specified cloud distribution. The specified cloud profile used is called 1N24 and it represents the actual 24 hour average cloud conditions for the B array north section during Phase III of GATE (see Cox and Griffith, 1978). This cloud distribution as well as those used in Chapter VI and the Appendix are given in Table 9.

Changing the profiles has the following general effects. Increasing the temperature or decreasing the humidity in the profiles gives radiance values higher than those calculated using a climatological profile. Likewise given specified p_{wf} and α values the radiances from a climatological profile will be higher than those

Eff. Cld. Top Pres.	225 Spot Flat 1	215 Spot BIM01	185 Spot 1PK2	190 Spot 1PK4	190 Spot 1PK6	185 Spot 1PK8	240 Spot Flats	230 Spot BIM0S	200 Spot 1PK3S
100	5	2	5	1	1	1	4	2	2
120	5	2	5	1	1	1	4	2	2
140	5	2	5	1	1	1	4	2	2
160	5	2	5	1	1	1	4	2	2
180	5	2	5	1	1	1	4	2	2
200	5	16	20	2	1	1	6	4	5
220	5	16	20	2	1	1	6	4	5
240	5	16	20	2	1	1	5	4	5
260	5	16	20	2	1	1	6	4	5
280	5	16	20	2	1	1	6	4	5
300	5	2	5	5	1	1	6	12	15
320	5	2	5	5	1	1	7	12	15
350	5	2	5	5	1	1	6	12	15
360	5	2	5	5	1	1	7	12	15
380	5	2	5	5	1	1	6	12	15
400	5	1	2	20	2	1	6	4	6
420	5	1	2	20	2	1	5	4	6
440	5	1	2	20	2	1	5	4	6
460	5	1	2	20	2	1	5	4	6
480	5	1	2	20	2	1	5	4	6
500	5	1	1	5	5	1	5	2	4
520	5	1	1	5	5	1	5	2	4
540	5	1	1	5	5	1	5	2	4
560	5	1	1	5	5	1	6	2	4
580	5	1	1	5	5	1	5	2	4
600	5	2	1	2	20	2	4	2	2
620	5	2	1	2	20	2	5	2	2
640	5	2	1	2	20	2	5	2	2
660	5	2	1	2	20	2	4	2	2
680	5	2	1	2	20	2	5	2	2
700	5	16	1	1	5	5	5	4	2
720	5	16	1	1	5	5	6	4	2
740	5	16	1	1	5	5	6	4	2
760	5	16	1	1	5	5	5	4	2
780	5	16	1	1	5	5	6	4	2
800	5	2	1	1	2	20	5	12	2
820	5	2	1	1	2	20	5	12	2
840	5	2	1	1	2	20	5	12	2
860	5	2	1	1	2	20	5	12	2
880	5	2	1	1	2	20	5	12	2
900	5	1	1	1	1	5	7	4	2
920	5	1	1	1	1	5	6	4	2
940	5	1	1	1	1	5	6	4	2
960	5	1	1	1	1	5	6	4	2
980	5	1	1	1	1	5	6	4	2

Table 9. (Page 1)

Eff. Cld. Top Pres. (mb)	215 Spot BIM02	210 Spot BIM03	190 Spot 1PK3	190 Spot 1PK5	190 Spot 1PK7	165 Spot 1PK9	215 Spot 1PK3M	250 Spot 1N24
100	1	1	2	1	1	1	1	1
120	1	1	2	1	1	1	1	1
140	1	1	2	1	1	1	1	1
160	1	1	2	1	1	1	1	1
180	1	1	2	1	1	1	1	1
200	2	2	5	1	1	1	1	4
220	2	2	5	1	1	1	1	4
240	2	2	5	1	1	1	1	4
260	2	2	5	1	1	1	1	4
280	2	2	5	1	1	1	1	4
300	16	16	20	2	1	1	35	4
320	16	16	20	2	1	1	35	4
340	16	16	20	2	1	1	35	5
360	16	16	20	2	1	1	35	5
380	16	16	20	2	1	1	35	5
400	2	2	5	5	1	1	1	5
420	2	2	5	5	1	1	1	5
440	2	2	5	5	1	1	1	6
460	2	2	5	5	1	1	1	5
480	2	2	5	5	1	1	1	5
500	2	16	2	20	2	1	1	5
520	2	16	2	20	2	1	1	4
540	2	16	2	20	2	1	1	4
560	2	16	2	20	2	1	1	4
580	2	16	2	20	2	1	1	4
600	16	2	1	5	5	1	1	4
620	16	2	1	5	5	1	1	4
640	16	2	1	5	5	1	1	5
660	16	2	1	5	5	1	1	5
680	16	2	1	5	5	1	1	5
700	2	1	1	2	20	2	1	5
720	2	1	1	2	20	2	1	5
740	2	1	1	2	20	2	1	5
760	2	1	1	2	20	2	1	4
780	2	1	1	2	20	2	1	4
800	1	1	1	1	5	5	1	4
820	1	1	1	1	5	5	1	4
840	1	1	1	1	5	5	1	4
860	1	1	1	1	5	5	1	5
880	1	1	1	1	5	5	1	5
900	1	1	1	1	2	20	1	5
920	1	1	1	1	2	20	1	5
940	1	1	1	1	2	20	1	5
960	1	1	1	1	2	20	1	4
980	1	1	1	1	2	20	1	4
								64 Clear

Table 9. Model effective cloud distributions (frequency of occurrences).

calculated using cooler or moister profiles. In general then, the p_{wf} values retrieved using radiances from a warmer or drier atmosphere will be a few millibars (20 - 40 mb given the conditions in the next paragraphs) larger (lower in the atmosphere) than the specified value. Just the opposite is true for the cooler or moister case. Typically, retrieved α values remain equal or slightly smaller than the specified α value.

To illustrate the findings, Table 10 gives the results of this analysis for the case of increasing the temperature of the climatological profile by 1% at each level and for the case of increasing the water mixing ratio at each level by 20%. Results for both tropical and mid-latitude cases are given.

It is clear that for these cases the VIRES index (described in the next chapter) is not sensitive to these reasonable assumption errors. The small T statistic values also indicate that the broadband weighting curves are little effected. Looking at the specified and retrieved effective cloud distributions one notices good agreement for the high, middle and combined low and clear categories but poor agreement for the low and clear categories taken separately. This simply supports what has already been said concerning poor retrieval capabilities in the low troposphere. It also shows the advantage of retrieving the VIRES index.

A qualifying statement is in order. A more severe test of this retrieval method would be to not only shift the temperature and humidity profiles but to also change their shape. This was done of course, for the tests in Section A. Also, a rather flat distribution of clouds with some clear sky is a reasonable test, but poorer results would be expected from a sharper (more peaked) distribution. Different shaped

Profile Case	Atmosphere	Mean T 100-1013 mb °K	Precip. H_2O cm	VIRES Index	T Statistic
Actual (+ 20% H_2O)	Tropical	263.2	5.30	270-460-680-0	0
Assume Climatology	Tropical	263.2	4.42	280-480-680-0	
Actual (+ 20% H_2O)	Mid. Lat.	261.7	1.60	280-500-780-.10	2.48
Assume Climatology	Mid. Lat.	261.7	1.34	290-500-780-.15	
Actual (+ 1% Temp)	Tropical	265.8	4.42	280-480-700-0	0
Assume Climatology	Tropical	263.2	4.42	290-490-700-0	
Actual (+ 1% Temp)	Mid. Lat.	264.3	1.34	290-500-800-.11	4.73
Assume Climatology	Mid. Lat.	261.7	1.34	300-520-810-.16	

	SPECIFIED CLOUD DISTRIBUTION IN %				
	High 100-390 mb	Middle 400-690 mb	Low and Clear Combined 700-surface	Low 700-surface	Clear
Actual/Given Trop. and Mid. Lat.	19.2	28.0	52.8	27.2	25.6
Retrieved with + 20% H_2O Trop.	19.2	31.9	48.9	13.5	35.4
Retrieved with + 20% H_2O Mid. Lat.	19.2	28.0	52.8	19.1	33.7
Actual/Given Trop. and Mid. Lat.	19.2	28.0	52.8	27.2	25.6
Retrieved with + 1% T Tropical	16.3	26.0	56.7	10.0	46.7
Retrieved with + 1% T Mid. Lat.	15.2	28.0	56.8	18.0	38.8

Table 10. Example of sensitivity analysis for VIRES index and specified cloud distribution retrievals.

effective cloud distributions and their respective VIRES indexes are examined in the next chapter.

The Appendix has a detailed description of the error investigation as well as a discussion on minimizing the errors. For example, the use of CCRC improves the accuracy of the retrieval over using pre-selected climatological profiles (Crutcher and Mesere, 1970; Jenne et al. 1974; Smith et al. 1972). Nevertheless, the true strength of this climate index approach is that radiation information is used to produce an index directly from radiation theory. Thus, the error prone process of inferring standard physical meteorological variables is avoided.

VI. WEIGHTING CURVES AS A CLIMATE INDEX

A first step in developing a climate index from composite weighting curves is to find an objective way to infer from the curves when there are different types of VIRES (indicators of climatological cloudiness). Section A of this chapter describes a statistical technique and shows that it is a powerful test for objectively determining when two weighting function curves and thus two effective cloud top distributions are different. The remainder of the chapter deals with developing and using a climate index based on the retrieved broadband weighting function curves.

A. Sign Test with Fisher's Method

Utilizing the broadband infrared RTE described earlier, the weighting function curves are computed using a finite differencing scheme which provides one curve value every 20 mb between 100 and 1000 mb. These 45 point values describe the weighting function in the part of the atmosphere influenced by effective clouds. These curves quite obviously represent no standard statistical distribution. Therefore, when comparing two broadband weighting function curves one must use non-parametric statistics.

Because the continuous curve is computed using discrete points, it is easy to compare two curves by pairing their respective point values. A non-parametric statistical test may then be used to test the likeness or difference of the paired values. Although the Wilcoxon Matched Pair Signed Rank Test and the Kolomogorov - Smirnov Test are sometimes useful in such cases, the simple Sign Test gives the best

results in this case. The following is a description of the Sign Test (Beyer, 1971).

In this test, observations from sample x and sample y are paired and the differences are calculated. The null hypothesis (H_0) is that the difference d_i has a distribution with median zero, i.e. the true proportion of positive (negative) signs is equal to $P = \frac{1}{2}$. The probability of positive (negative) signs is given by the binomial probability function f(x) such that

$$f(x) = f(x;\ n,\ P = \tfrac{1}{2}) = \binom{n}{x} \left(\tfrac{1}{2}\right)^n,$$

where x is either the number of positive signs or negative signs, and n is the sum of positive and negative signs. The probability P_i of the samples being the same (true H_0) given x positive (negative) signs is given by the expression

$$P_i\ (x \leq k) = 2\ [\sum_{x=0}^{k} \binom{n}{x}]\ \left(\tfrac{1}{2}\right)^n,$$

where $P_i(x)$ is the Sign Test Probability Function for the two-tailed case. The test is two-tailed because there is no reason to expect more positive signs than negative signs. For example, if k = 3 and n = 15, the probability of x being three or less (either of positive or negative sign) if H_0 is true is given by the following calculation.

$$P_i\ (x \leq 3) = 2\ [\binom{15}{0}\ \binom{15}{1}\ \binom{15}{2}\ \binom{15}{3}]\ \left(\tfrac{1}{2}\right)^{15} = .035156.$$

In other words, 1 - .035156 = .964844 is the probability that H_0 is false. In this case H_0 would be rejected at the 5% level. When they occur, zero differences are excluded because they contribute no information for deciding whether positive or negative differences are more likely.

To evaluate the usefulness of the Sign Test sixteen effective cloud top distributions are specified. Figure 15 and Table 9 describe these distributions in detail. Note that three of these distributions are used for the error analysis in the last chapter and detailed in the Appendix. The specified distributions are intended to represent the type of observed effective cloud top distributions illustrated in Figure 16. The corresponding infrared broadband weighting function curves for these sixteen distributions are given in Figures 17-23 for the tropical atmosphere. These are the curves we wish to discriminate between.

The characteristic shape of the curves in Figures 17-23 result in two problems when using the Sign Test. First, the curves exhibit a characteristic known as crossover. When comparing two curves such as FLATS and BIMOS, or FLATS and 1PK3S in Figure 17, one notices the curves crossover each other many times in the first case and at least once in the second case. Because the curves indicate vertical weighting and total weighting changes little from case to case, the curve that shows large weighting at one vertical position must show small compensating weighting at another point in the vertical. This constraint is the primary cause of curve crossovers. The crossover effect reduces the ability of the Sign Test to discriminate between two obviously different curves. This is clearly seen in Figure 19. 1PK2

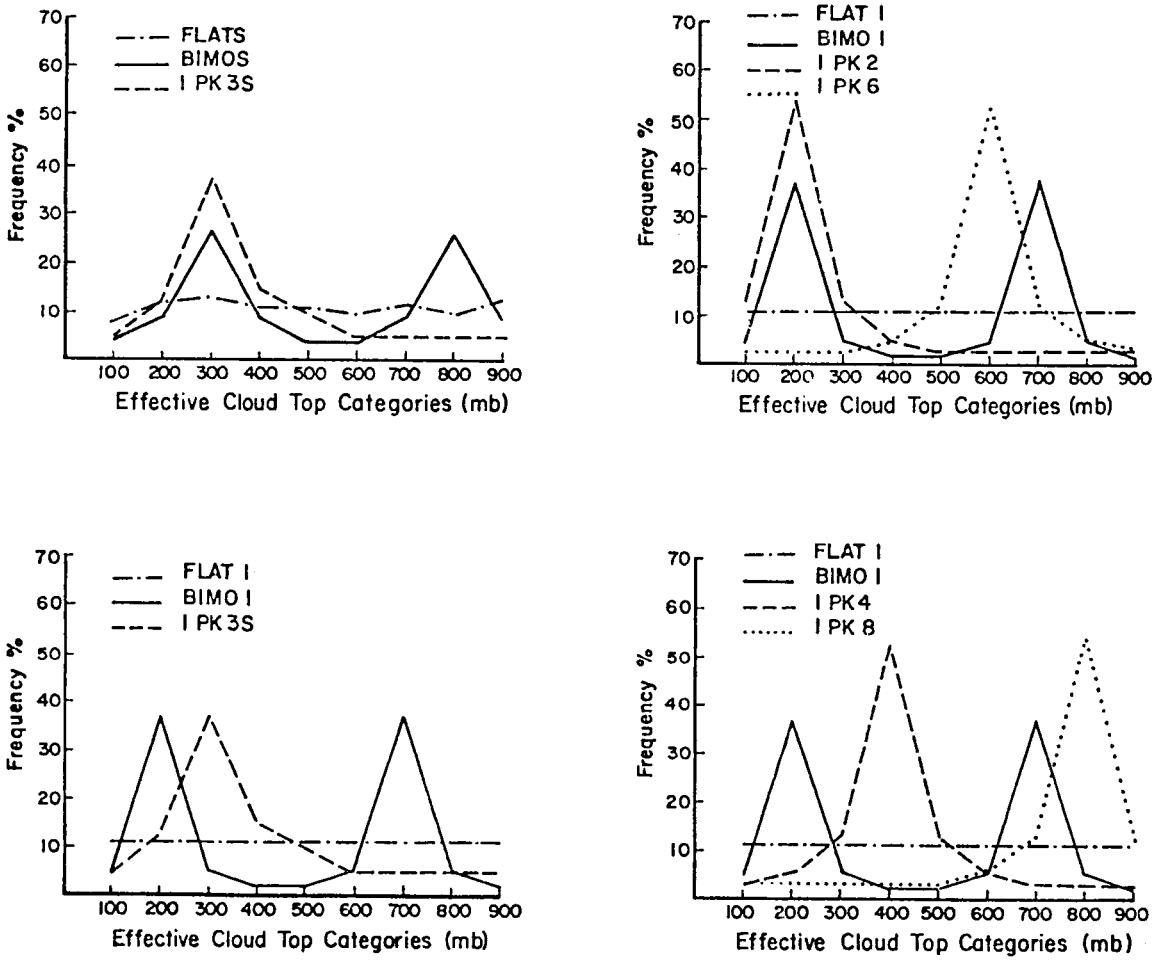

Figure 15. Plots of effective cloud top model distributions.

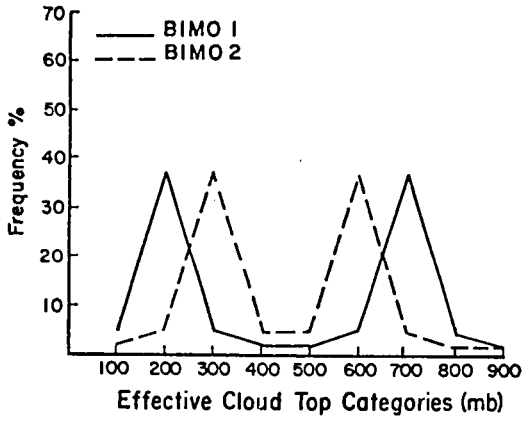

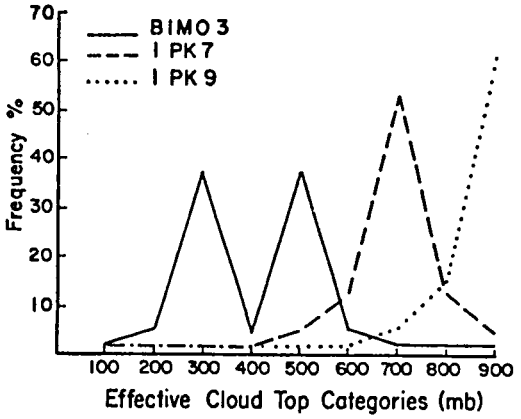

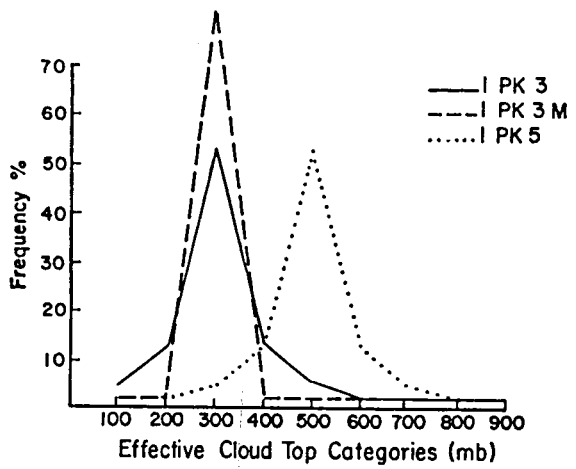

Figure 15 (Continued). Plots of effective cloud top model distributions.

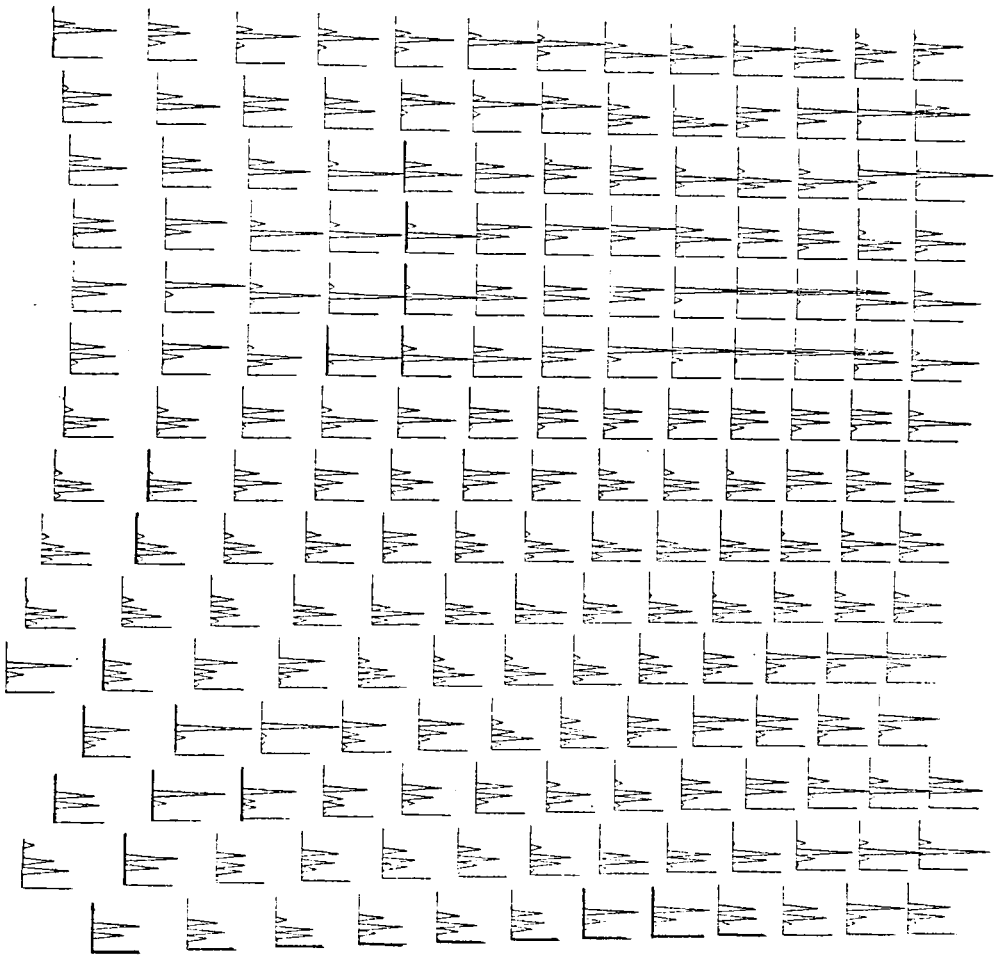

Figure 16. Unpublished figure by G. G. Campbell showing histograms (5°K resolution, 16 cat.) of geosynchronous satellite IR window radiance temperatures that approximate the cloud top distribution. Each histogram represents 200 x 200 km area. The total figure represents data taken on 16 Nov. 1978 at 1500 L for the Pacific Ocean region 10°N - 20°S latitude and 235°E - 265°E longitude.

NOTE: The length of the x-axis represents a 50% frequency and the y-axis has temperature decreasing up the axis.

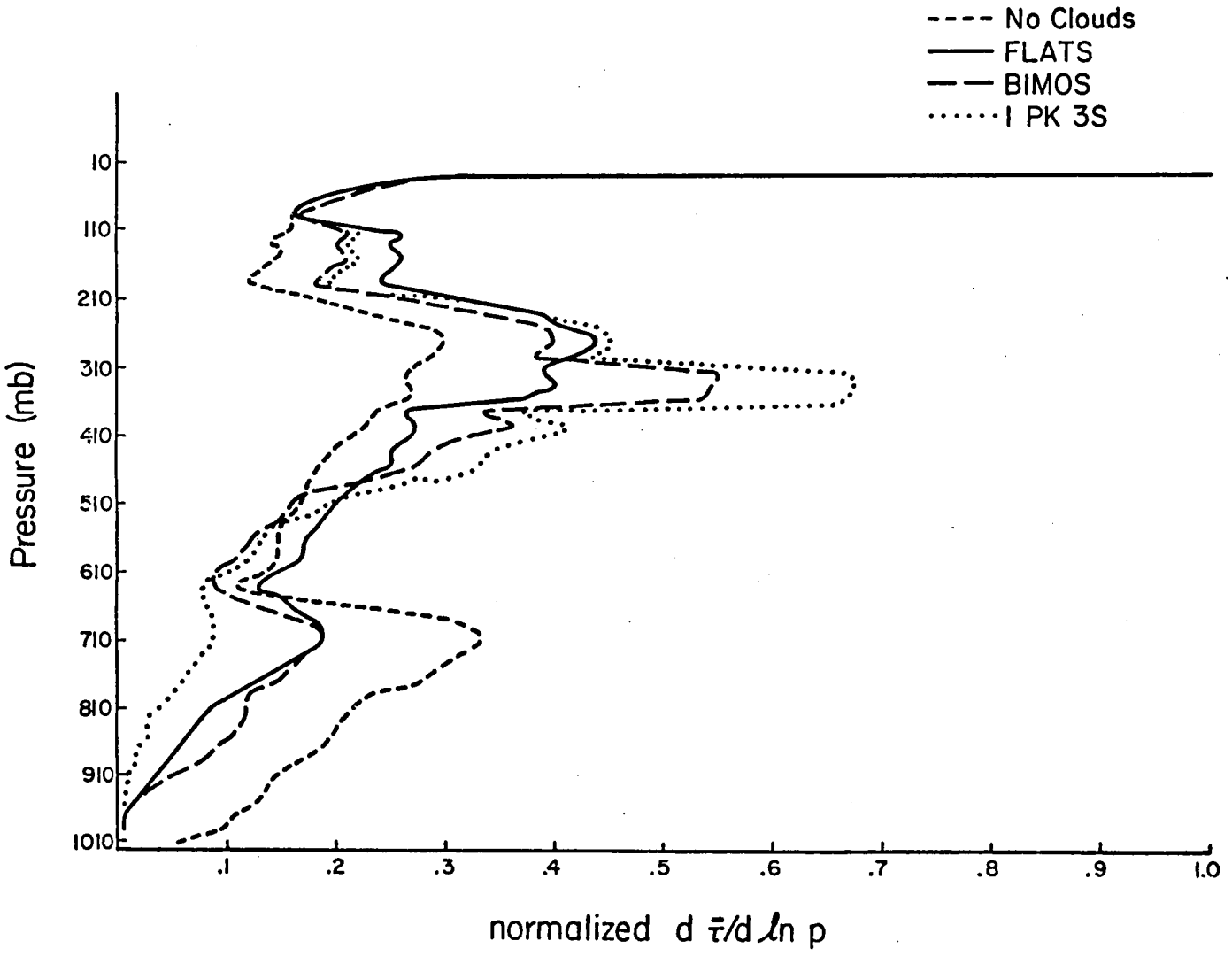

Figure 17. Broadband weighting curves for given specified distributions.

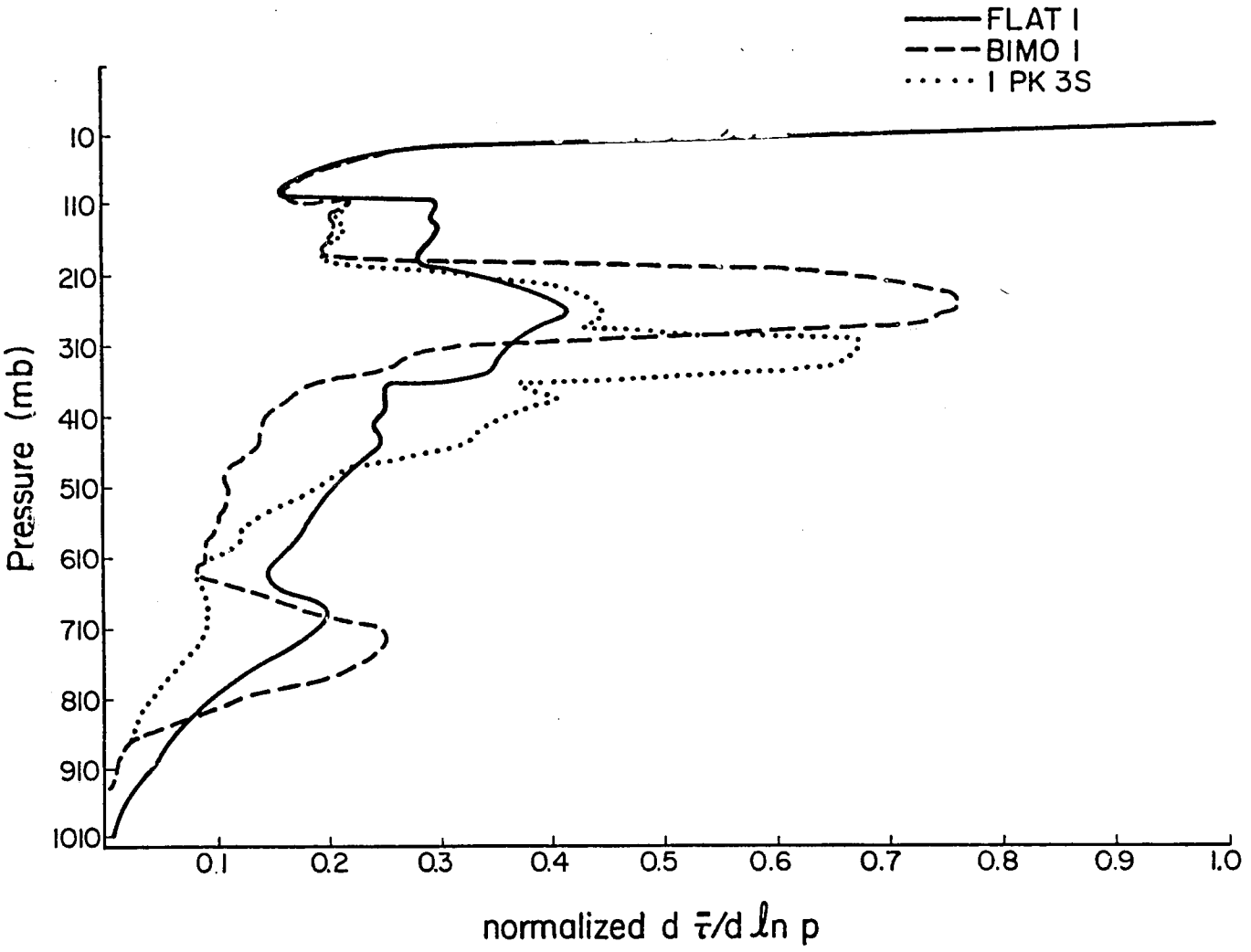

Figure 18. Broadband weighting curves for given specified distributions.

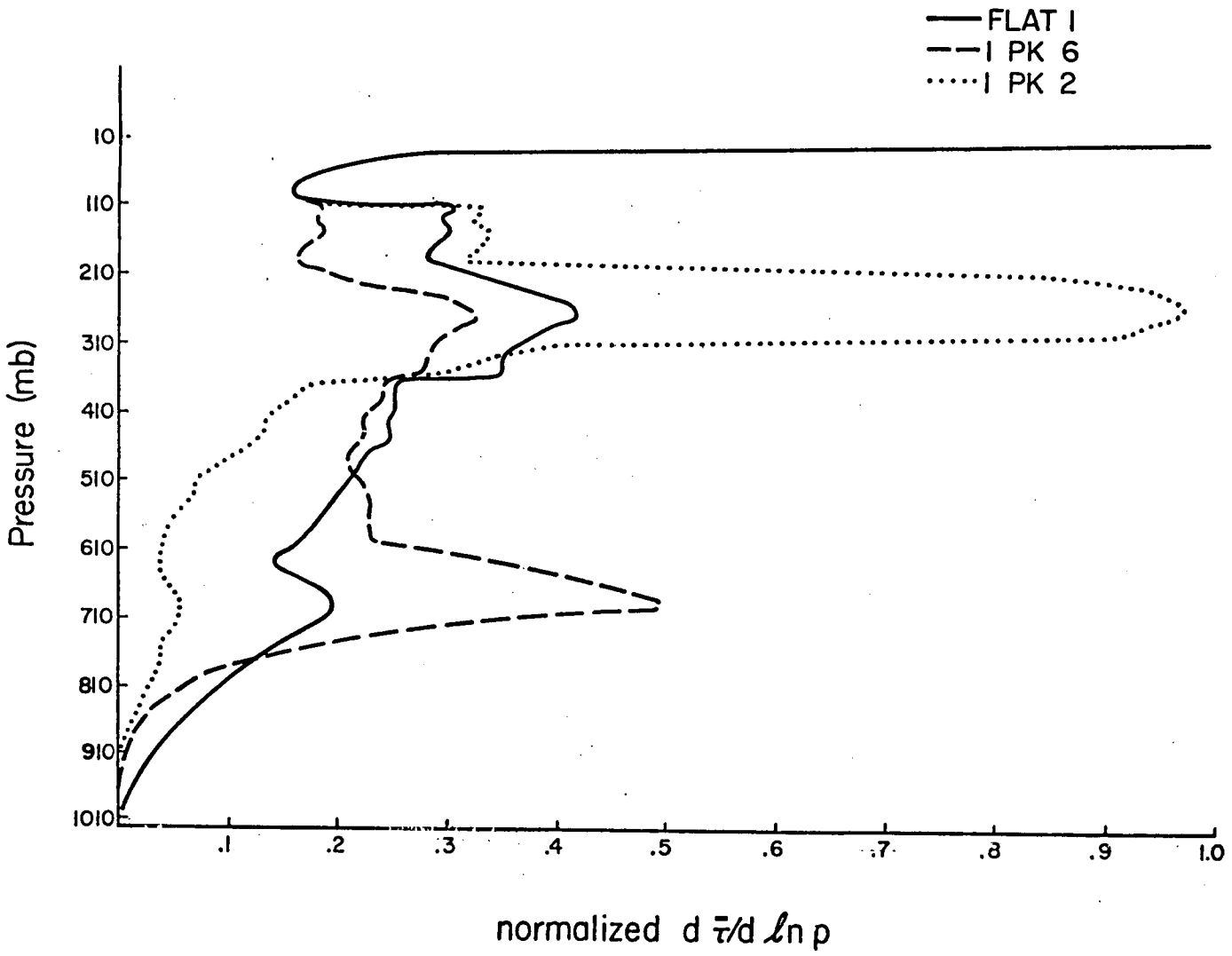

Figure 19. Broadband weighting curves for given specified distributions.

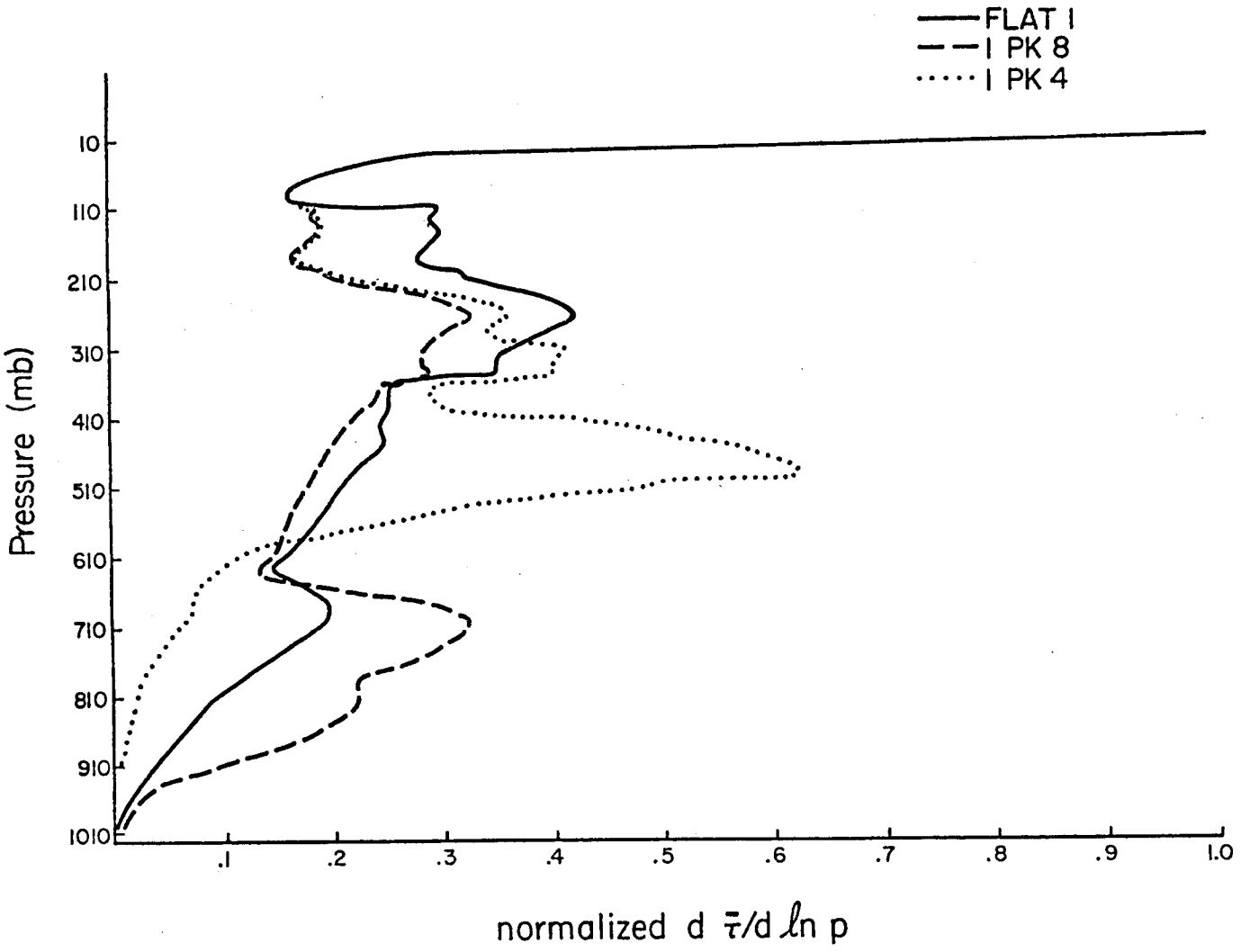

Figure 20. Broadband weighting curves for given specified distributions.

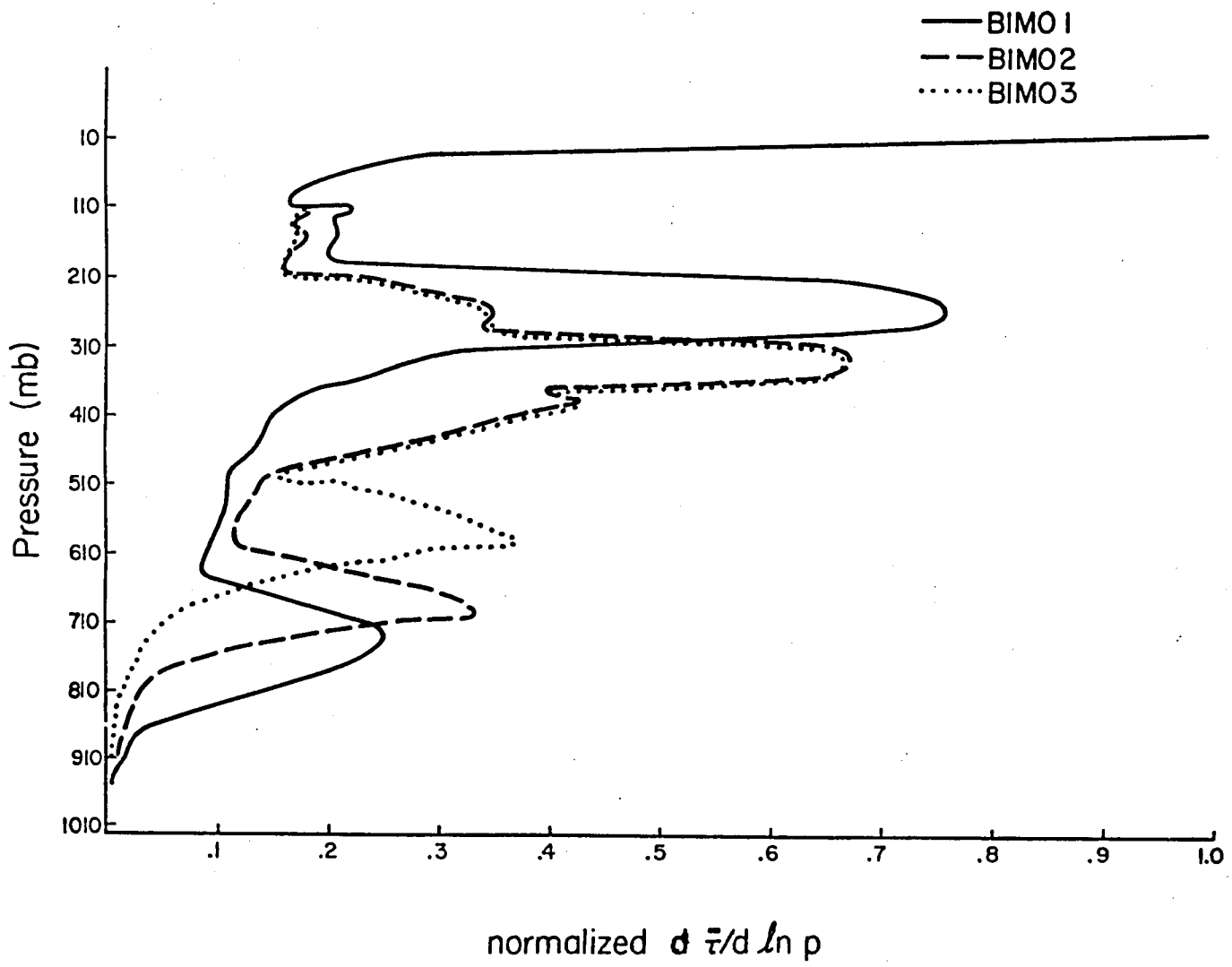

Figure 21. Broadband weighting curves for given specified distributions.

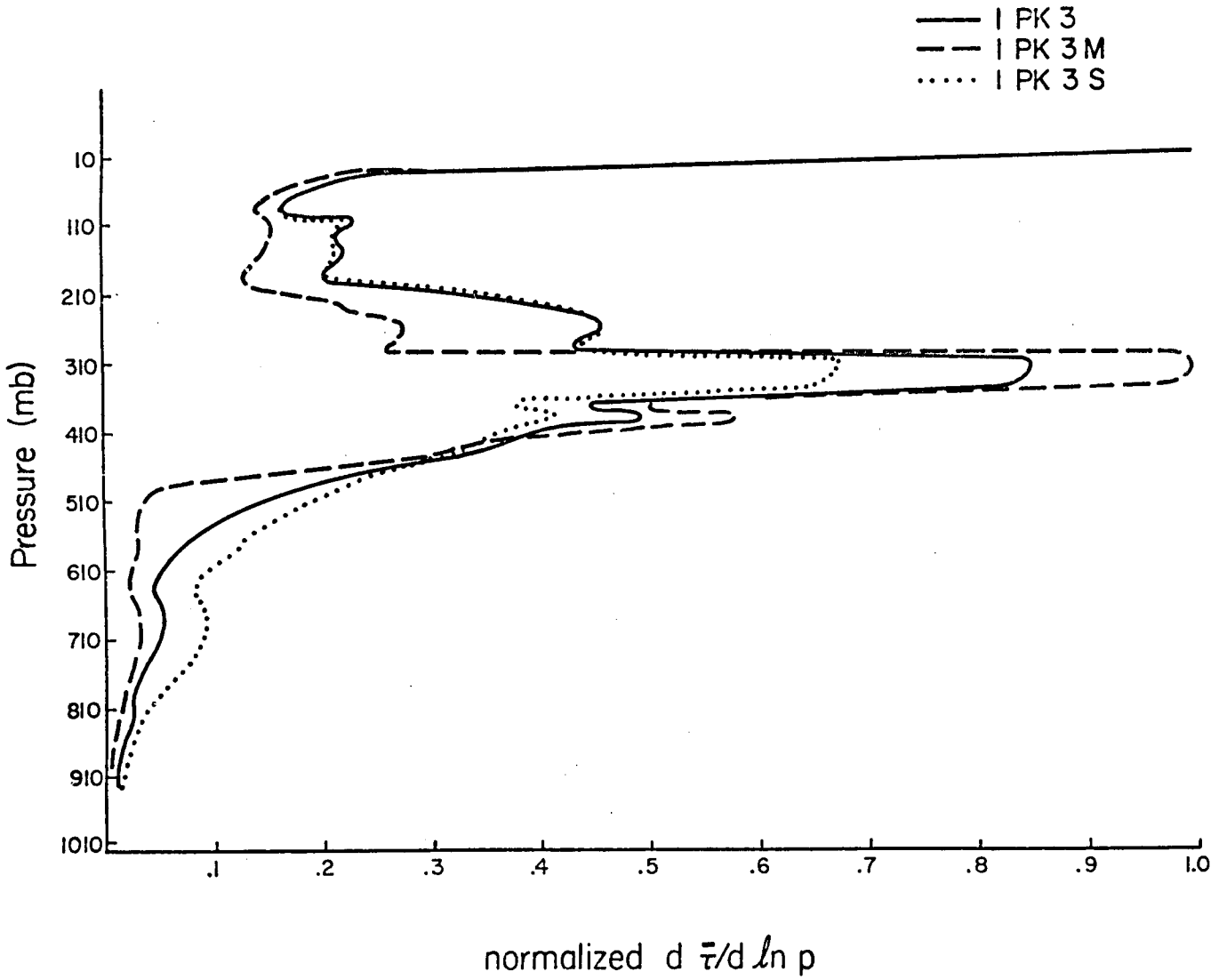

Figure 22. Broadband weighting curves for given specified distributions.

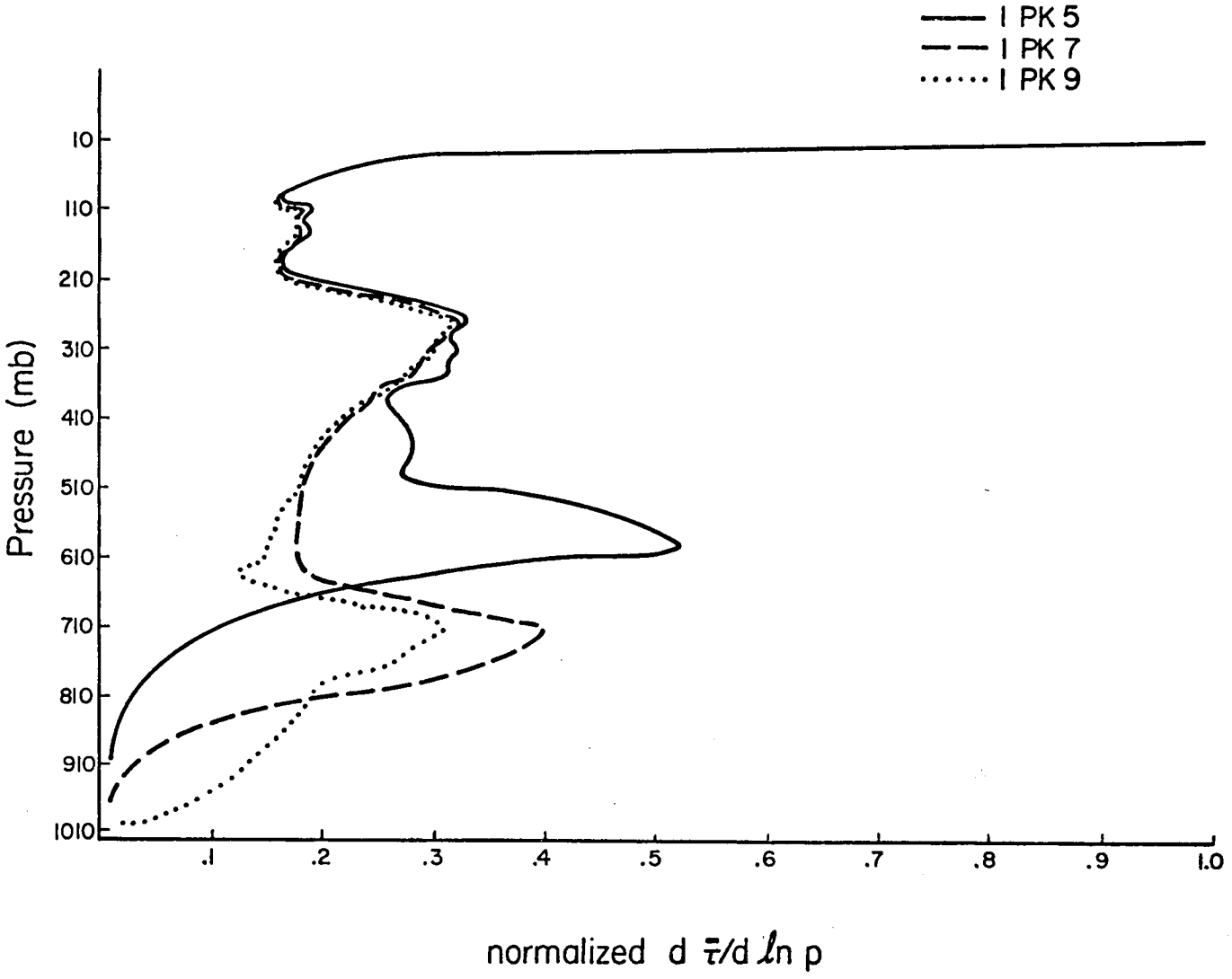

Figure 23. Broadband weighting curves for given specified distributions.

and 1PK6 are compared. For this case n = 45 and x = 19. The Sign Test cannot reject H_0 even at the 25% level. The test shows that there is greater than 1 chance in 4 that these two curves are the same. The crossover effect is to be blamed for this test deficiency.

The crossover effect may be greatly reduced by considering the curves in three equal parts of 15 pairs each instead of taken as a whole (45 pairs). The curves may be divided into three physically distinct parts. This division parallels the well known high, middle and low cloud categories. The part between 980 and 700 mb represents the lower tropospheric area of high water vapor content (approximately 85% of the total). In this area water vapor represents an important source of infrared emission as illustrated by the low level weighting function peak for clear sky in Figure 17. From 380 to 100 mb another naturally occurring clear sky weighting function peak is seen. This is also the area of cirrus cloud formation. Since ice clouds are somewhat different emittors than water clouds it is not unreasonable to examine their respective influence on the weighting curves separately. Finally, the 680 to 400 mb layer is found between the two layers described above. It lacks the consistent large amount of water vapor and the clear sky weighting function peaks. It is also true that the emitting structure within these three divisions are for the most part determined using different pairs of spectral radiative values.

Fisher's Method of Combining Three P Values is used with the Sign Test when comparing corresponding pairs from two curves in three parts (Fisher, 1958). Fisher found that the probability function distribution of - 2 times the sum of the logarithms of m independent P values is Chi-Squared with 2m degrees of freedom. Thus, the three P statistic

values are distributed as Chi-Squared with 6 degrees of freedom. The calculation of the T statistic is done using the values in Table 11 computed from the following equation,

$$T = (-2)\,[\ln P_1 + \ln P_2 + \ln P_3] \approx X^2_{d.f. = 6}.$$

For example, if $\ln P_1 = -4.9$, $\ln P_2 = -6.3$, and $\ln P_3 = -2.1$ (see Table 11), the T statistic is calculated as 26.6. Since for P = .01, $X^2_6 = 16.8$, one would reject H_0 at the 1% level (i.e. less than 1 chance in 100 that the two samples are the same and H_0 is true). The critical T values for a specified P level are given in Table 11.

Table 12 gives the T statistic for the different curve comparisons. By considering a critical value of T = 10.6 (P = 0.10), Table 12 shows that the test indicates curve differences in all cases except one (BIM01 vs. 1PK3S). Notice also that the test says FLAT1 vs. FLATS are different curves when in fact they are nearly identical. These two cases point up the second drawback of this test. Although the test allows for zero differences, the 45 curve point pairs never give an absolute difference value of zero primarily because values are computed beyond reasonable significant figures. Therefore, at times their difference is very small, but as computed for Table 12 there are always 3 sets of 15 sign values calculated with no zeros. Notice that above 100 mb (Figures 17-20) curve points are identical but they are not used in the Sign Test.

To correct this deficiency, when the difference between curve points is smaller than a specified significance level, it is set to

n = 15	
x	lnP
0	-9.7040605
1	-6.99601
2	-4.90827
3	-3.34795
4	-2.13310
5	-1.198131
6	- .49883
7	0

n = 14	
x	lnP
0	-9.010913
1	-6.302863
2	-4.35695
3	-2.8603106
4	-1.717896
5	- .85843
6	- .23521
7	0

n = 13	
x	lnP
0	-8.31777
1	-5.67871
2	-3.79598
3	-2.38287
4	-1.32108
5	- .5429104
6	0

n = 12	
0	-7.62462
1	-5.05967
2	-3.255171
3	-1.92418
4	- .947536
5	- .255649
6	0

n = 11	
0	-6.93147
1	-4.4466
2	-2.72678
3	-1.4847
4	- .59997
5	0

n = 10	
0	-6.2383
1	-3.84043
2	-2.2197
3	-1.06784
4	- .28248
5	0

n = 9	
0	-5.54518
1	-3.2426
2	-1.71654
3	- .67764
4	0

n = 8	
0	-4.8520
1	-2.6548
2	-1.2411
3	- .31943

n = 7	
0	-4.1589
1	-2.0794
2	- .79159
3	0

n = 6	
0	-3.46574
1	-1.5198
2	- .3747
3	0

n = 5	
0	-2.7726
1	- .9808
2	0

n = 4	
0	-2.07944
1	- .4700
2	0

n = 3	
0	-1.3863
1	0

n = 2	
0	- .6931
	0

n = 1	
0	0

Table 11. The logarithm of Sign Test probabilities for given n and x values.

DISTRIBUTIONS	SIGN TEST 100 - 380 mb Pos.	Neg.	400 - 680 mb Pos.	Neg.	700 - 980 mb Pos.	Neg.	T-statistic
FLATS vs. BIMOS	10	5	12	3	4	11	13.4
FLATS vs. BIMO1	10	5	15	0	8	7	21.8
FLATS vs. 1PK3S	6	9	10	5	15	0	22.8
FLAT1 vs. FLATS	6	9	12	3	1	14	21.7 +
FLAT1 vs. BIMOS	10	5	12	3	4	11	13.4
FLAT1 vs. BIMO1	10	5	15	0	8	7	21.8
FLAT1 vs. 1PK2	4	11	15	0	15	0	43.1
FLAT1 vs. 1PK3S	5	10	11	4	15	0	26.1
FLAT1 vs. 1PK4	10	5	6	9	15	0	22.8
FLAT1 vs. 1PK6	15	0	5	10	12	3	28.5
FLAT1 vs. 1PK8	15	0	12	3	14	1	40.1
BIMO1 vs. BIMOS	5	10	13	2	9	6	13.2
BIMO1 vs. 1PK2	2	13	15	0	10	5	31.6
BIMO1 vs. 1PK3S	5	10	4	11	9	6	7.7 +
BIMO1 vs. 1PK4	10	5	3	12	15	0	28.5
BIMO1 vs. 1PK6	11	4	0	15	13	2	33.5
BIMO1 vs. 1PK8	11	4	0	15	0	15	43.1
1PK2 vs. 1PK3S	10	5	0	15	3	12	28.5
1PK2 vs. 1PK4	11	4	0	15	14	1	37.7
1PK2 vs. 1PK6	13	2	0	15	6	9	30.2
1PK2 vs. 1PK8	13	2	0	15	0	15	48.6
1PK3S vs. 1PK4	15	0	3	12	15	0	45.5
1PK3S vs. 1PK6	15	0	5	10	7	8	21.8
1PK3S vs. 1PK8	15	0	6	9	0	15	40.1
1PK4 vs. 1PK6	10	5	8	7	14	1	16.4
1PK4 vs. 1PK8	10	5	9	6	0	15	22.8
1PK6 vs. 1PK8	0	15	15	0	1	14	52.8

+ referred to in the text

Table 12. Sign Test results without zero cutoff correction.

zero. Figure 18 illustrates the small differences between curves BIM01 and 1PK3 below 850 mb. These differences are set to zero. We refer to this procedure as zero cutoff correction. Table 13 which includes more curve comparisons than Table 12 gives the T values with this correction applied. Notice that most of the change occurs in the 700-980 mb group. Also notice that BIM01 and 1PK3S now pass the test for being different while FLATS and FLAT1 as well as 1PK8 and 1PK9 have small T values that indicate likeness. It is also instructive to note that the test does not catch the difference between FLAT1 and BIM0S at the P = 5% level but it does at the P = 10% level. As Figure 15 illustrates, BIM0S represents a flatter bimodal effective cloud top distribution than BIM01 which explains why FLAT1 and BIM01 are judged to be different.

From the P values given in Table 8 it is clear that T values greater than about 10 represent rejection of the null hypothesis. Curves with smaller T values indicate acceptance of H_0: the curves are the same. Referring to Table 13, values of T greater than 10 indicate unlike curves. Of the 48 combinations of curve pairings only 6 cases resulted in T values where H_0 cannot be rejected at the 5% level (two cases are mentioned above). In two of these cases (BIM02 vs. BIM03 and 1PK3 vs. 1PK3M) the effective cloud top distributions are nearly the same, explaining the statistical results. In the other two cases (BIM01 vs. 1PK3 and 1PK8 vs. 1PK7) the large amount of water vapor in the lower troposphere effectively acts as a radiating surface resulting in broadband weighting curve pairs that are quite similar, yet represent different effective cloud top distributions.

Two other points can be made from Table 13. The test is able to distinguish between two slightly different distributions peaking at

DISTRIBUTIONS	SIGN TEST 100 - 380 mb Pos.	Neg.	400 - 680 mb Pos.	Neg.	700 - 980 mb Pos.	Neg.	T-statistic
FLATS vs. BIMOS	9	5	10	2	0	5	13.8
FLATS vs. 1PK3S	5	6	8	4	11	0	15.8
FLATS vs. BIMO1	10	5	13	0	3	6	20.4
FLAT1 vs. FLATS	5	3	0	0	0	0	0.6 +
FLAT1 vs. BIMOS	7	5	11	3	0	5	11.3 +
FLAT1 vs. 1PK3S	5	8	9	4	10	0	16.2
FLAT1 vs. 1PK2	3	11	15	0	11	0	39.0
FLAT1 vs. 1PK3	5	9	11	3	12	0	22.7
FLAT1 vs. 1PK4	10	5	6	9	12	0	18.6
FLAT1 vs. 1PK5	13	0	1	12	12	0	43.2
FLAT1 vs. 1PK6	13	0	2	9	7	3	24.2
FLAT1 vs. 1PK8	13	0	8	2	12	0	36.3
FLAT1 vs. BIMO1	10	5	14	0	3	6	20.4 +
FLAT1 vs. BIMO2	10	5	7	7	10	1	11.3
BIMO1 vs. BIMOS	5	5	9	0	6	5	11.1
BIMO1 vs. BIMO2	10	5	0	10	7	0	23.2
BIMO1 vs. BIMO3	10	5	2	12	8	0	20.8
BIMO2 vs. BIMO3	0	0	3	6	4	0	5.5 +
BIMO1 vs. 1PK2	0	13	11	0	8	0	40.2
BIMO1 vs. 1PK3	5	5	6	6	8	0	9.7 +
BIMO1 vs. 1PK4	10	5	3	10	8	0	16.9
BIMO1 vs. 1PK5	10	4	1	14	8	0	27.1
BIMO1 vs. 1PK6	11	3	0	15	6	2	27.6
BIMO1 vs. 1PK8	11	3	0	15	0	13	41.8
1PK2 vs. 1PK3	10	5	0	9	0	0	13.5
1PK2 vs. 1PK4	10	4	0	14	0	0	21.5
1PK2 vs. 1PK5	12	2	0	15	0	2	29.5
1PK2 vs. 1PK6	12	2	0	15	0	6	35.1
1PK2 vs. 1PK8	12	2	0	15	0	13	44.8

Table 13. (Page 1)

DISTRIBUTIONS	SIGN TEST 100 - 380 mb Pos.	Neg.	400 - 680 mb Pos.	Neg.	700 - 980 mb Pos.	Neg.	T-statistic
1PK3 vs. 1PK4	15	0	0	13	0	0	36.0
1PK3 vs. 1PK5	15	0	3	12	0	3	28.9
1PK3 vs. 1PK6	15	0	4	11	0	7	32.0
1PK3 vs. 1PK8	15	0	4	10	0	13	39.5
1PK4 vs. 1PK5	10	0	6	9	0	3	16.2
1PK4 vs. 1PK6	10	0	8	6	0	7	21.3
1PK4 vs. 1PK8	10	0	9	5	0	13	30.8
1PK5 vs. 1PK6	3	0	11	4	0	7	15.4
1PK5 vs. 1PK8	3	0	13	2	0	13	29.2
1PK6 vs. 1PK7	0	0	11	0	0	10	26.3
1PK6 vs. 1PK8	0	0	11	0	1	12	25.2
1PK8 vs. 1PK7	0	0	0	5	8	5	6.6 +
1PK8 vs. 1PK9	0	0	0	0	4	5	0.0 +
1PK3 vs. 1PK3S	5	0	2	11	0	4	17.3 +
1PK3 vs. 1PK3M	10	5	8	2	0	0	6.8 +
1PK3S vs. 1PK3M	10	5	12	2	6	0	18.0 +
BIM01 vs. 1PK3S	5	5	3	10	8	0	14.5 +
1PK3 vs. 1/2PK3	15	0	4	9	0	15	41.5 +
1PK5 vs. 1/2PK5	3	0	13	2	0	15	32.0 +

+ Referred to in text

Table 13. Sign Test with zero cutoff correction.

the same level. For example, consider the cases 1PK3 vs. 1PK3S and 1PK3S vs. 1PK3M. Table 9 gives the cloud frequency distribution for these two similar cases of a single peak within the 300 mb category. The 1PK3 vs. 1PK3S case represents only a 15% cloud amount difference in the 300 mb category. It is also clear that the test is most sensitive when total 300 mb category cloud amounts are less than 50%. Secondly, the test can distinguish between two cases where the effective cloud top distribution is the same but the proportion of clear versus cloudy varies. For example, 1PK3 represents an overcast case whereas $\frac{1}{2}$ PK3 represents $\frac{1}{2}$ clear sky. The test is also done using 1PK5 and $\frac{1}{2}$ PK5. In summary these results show that the statistical test is capable of distinguishing between VIRES curves representing either cloud distribution shifts in the vertical or in total amount. It is successful in about 90% or more of all cases at the 95% confidence level.

The zero cutoff correction requires further explanation. The small difference value is considered zero when the difference is less than a specified constant. This constant is 5% of the average maximum point value of all points between 100 and 980 mb for all the weighting curves plotted. In reference to Figures 40-43, this is approximately a distance of .02 on the X-axis.

B. Form of the proposed climate index

Because the climate index proposed in this paper is an indicator of climatological cloudiness, it is instructive to review the status and nature of current global cloud climatologies. As mentioned earlier good cloud climatologies are especially needed for climate modeling and

climate monitoring. The VIRES climate index would be in direct competition with standard cloud climatologies to fill certain of these requirements. Therefore, a short review of the standard approach follows. A more detailed synopsis of the currently available cloud climatologies is given in two reports, one by Suomi et al. (1977) and another by Smith (1978).

The most widely used surface based observational data set seems to be that of Telegados and London (1954). Three dimensional distribution of clouds are given for the Northern Hemisphere. However, the spatial resolution of cloudiness is poor and as a consequence even the mean zonal cloudiness values given are of questionable accuracy.

Climatologies of clouds from a combination of ground and satellite sources are given by Sherr et al. (1968) and by Fye (1978). The latter reference describes the U.S. Air Force's three dimensional nephanalysis model. Both sets of climatologies suffer from the lack of spatial and temporal homogeneity in the quality of the compiled data. Nevertheless both climatologies represent global coverage and have three dimensional cloud fields. Furthermore, the Air Force's data base is continually being added to.

The longest uniform time-series of cloud satellite data are in the form of visible wavelength brightness values. From brightness values total cloud amount is inferred. Such climatologies are given by Sadler (1969), Sadler et al. (1976), Miller and Feddes (1971), and Environmental Satellite Imagery (1975-1976). Steiner (1978) summarized the Sadler et al. data, and Avaste et al. (1979) attempted to compare and combine all the brightness derived cloud climatologies given above. Avaste found that the main limitation of this data is its

non-comparability and lack of accuracy. There is also no cloud height information. This last drawback almost eliminates climate and cloud modeling applications.

Inferences of clouds from satellite data using other methods (see Chapter II) have been limited to brief periods and usually less than global coverage. Although most methods strive for three dimensional information, they suffer from a lack of accuracy mainly due to errors in retrieval technique assumptions. As mentioned earlier, all the approaches use standard cloud classification. Some reduce the classification to 3 heights (low, middle and high) and 5 fractional categories, while others use more elaborate classifications in an attempt to be more descriptive. Against this background the proposed VIRES climate index will be discussed.

Figures 17-23 show the final composite form of the infrared broadband weighting functions for 16 different distributions of cloudiness for the typical tropical atmosphere. Because it is too awkward to use the whole curve for purposes of an index, a simpler approach is needed. Of course the two curve shape parameters define the curve for a single case situation, but they will not define the curve for the composite case. Besides being simple, the index should be unique or nearly so for a given cloud distribution.

After much searching an index containing four parameters was found to be suitable. The first parameter of the index represents the level of the atmosphere above which 25% of the energy emitted to space originates. Likewise the next two parameters represent the 50% and 75% levels. The fourth number represents the percentage energy escaping to space from the surface. The approach described above can be

illustrated using the following equation:

$$\frac{\int_{p_i}^{0} \sigma T^4 \frac{\partial \bar{\tau}}{\partial \ln p} \, d \ln p}{\bar{L}_{sat}\uparrow} = i,$$

where $\bar{L}_{sat}\uparrow$ is the broadband infrared radiance measured at satellite level, p_i is one of the first three VIRES index numbers, and i is .25, .50 and .75. Of course other i values may be chosen to define another index.

Table 14 gives the calculated index values for 25 atmospheric VIRES using a tropical and mid-latitude profile atmosphere. The atmospheric levels specified in the index are in mb. For reference purposes Table 15 gives the conversion from mb to meters. The RTE model used produced index values to the nearest 10 mb. Table 14 shows no surface emission from the surface in the tropical case due to water vapor diameter absorption and approximations used in the RTE model. However, ideally a small amount of surface emission would be expected.

Index values given in Table 14 show that weighting curves that are nearly identical give identical indexes (i.e. FLATS and FLATR, BIMOS and BIMOR, 1PK3S and 1PK3R). Specified cloud distributions in the two different atmospheres give the same index at high levels (i.e. 1PK3) but a somewhat different index at lower atmospheric levels (i.e. 1PK8) due primarily to the fact that low level water vapor contributes to the atmospheric VIRES. Notice that low clouds (1PK7, 1PK8, 1PK9) have nearly the same index in the tropical case where low level water vapor

Effective Cloud Top Distribution	TROPCIAL ATMOSPHERE				MID-LAT. SUMMER ATM.			
	25%	50%	75%	Sfc %	25%	50%	75%	Sfc %
FLATS	250	430	650	0	250	450	690	1
FLATR	250	430	650	0	250	450	690	5
FLATR*	250	430	650	0	250	450	690	6
FLAT1	250	430	650	0	250	450	690	1
BIMOS	270	410	670	0	270	430	750	0
BIMOR	270	410	670	0	270	430	750	6
BIMO1	230	370	690	0	230	370	730	1
BIMO2	290	390	630	0	290	390	630	0
BIMO3	270	390	550	0	270	390	550	0
1PK3S	250	350	510	0	250	350	510	0
LPK3R	250	350	510	0	250	350	510	4
1PK2	190	270	390	0	190	270	390	3
1PK3	230	330	430	0	230	330	430	0 +
1PK4	270	430	510	0	270	430	510	0
1PK5	290	490	590	0	310	510	590	0
1PK6	310	550	670	0	310	570	690	0
1PK7	310	570	730	0	330	610	770	0 +
1PK8	310	590	750	0	330	630	850	0 +
1PK9	310	590	750	0	330	650	910	0 +
CLEAR	350	650	790	0	370	790	-	37
½ CLEAR FLAT1	290	530	730	0	310	570	950	21
½ CLEAR BIMO1	270	530	730	0	270	590	930	21
½ CLEAR 1PK3	290	430	710	0	290	450	930	12 +
½ CLEAR 1PK5	310	530	710	0	330	550	890	20
½ CLEAR 1PK7	330	610	750	0	330	670	890	19

+ Referred to in the text

Table 14. Proposed VIRES climate index.

Table 15. Pressure to Height Conversion.

Pressure mb	Mid. Lat. Atm. (m)	Tropical Atm. (m)
110	16280	16330
130	15150	15200
150	14150	14230
170	13330	13430
190	12600	12710
210	11930	12050
230	11340	11450
250	10780	10880
270	10260	10360
290	9760	9860
310	9290	9390
330	8850	8940
350	8430	8510
370	8030	8120
390	7640	7720
410	7270	7351
430	6920	6990
450	6570	6650
470	6240	6320
490	5930	6000
510	5620	5690
530	5320	5390
550	5030	5090
570	4750	4810
590	4480	4540
610	4210	4270
630	3960	4010
650	3710	3750
670	3460	3510
690	3220	3260
710	3000	3030
730	2760	2800
750	2540	2570
770	2320	2350
790	2110	2130
810	1900	1920
830	1690	1720
850	1490	1520
870	1300	1320
890	1110	1120
910	917	933
930	732	745
950	550	561
970	372	379
990	197	201
1007	55	56

emits like a cloud. This is not true for the mid-latitude case where low level water vapor does not contribute much to the atmospheric VIRES. Also notice that similar distributions of clouds but with a different percentage of clear sky have different indexes (i.e. $\frac{1}{2}$ clear 1PK3 vs. 1PK3).

In general the VIRES climate index outlined above may be considered an appropriate and accurate atmospheric descriptor. The parameters in the index indicate the vertical source of emitted earth-atmospheric energy. The index is especially compatible with the original satellite data resulting in minimal anticipated errors. The analysis shows the index has the desired uniqueness characteristic while at the same time remaining straightforwardly simple.

Of course one could consider it a drawback that the index is not compatible with standard measures of cloudiness. However, the index is meant to be closely related to the radiative measurements. Clouds are thought of as simply one constituent (albeit the most important) of the atmospheric VIRES. Furthermore real physical clouds are never considered at all. Only the equivalent radiative effects of specified clouds are taken into account. This approach avoids many difficulties while at the same time providing information that may be used for climate monitoring and for calibration and parameterization of radiative calculations in climate models (the topic of Chapter VII). The next section discusses possible specifications for index use.

C. Climate index specifications

The climate index described in this paper will be used similar to a cloud climatology. It should, therefore, have some of the same

characteristics. Smith (1978) suggests that for purposes of parameterization of cloudiness and radiation in climate models, cloud climatologies should have global coverage with a space resolution of 250 km ($\approx 2\frac{1}{2}°$ Lat. by $2\frac{1}{2}°$ Long.) and a time resolution of 4 hours. Research by Avaste et al. (1979) suggests that for climate monitoring purposes the space resolution be 500 km ($\approx 5°$ Lat. by $5°$ Long.) and time resolution be monthly. A weekly specified time resolution has been suggested by the U.S. Committee for GARP (1975). Before specifying time and space resolution for the proposed climate index let us consider satellite data collection limitations.

Present operational and experimental sun-synchronous weather satellites carry infrared radiometers that have nadir resolutions of at least 30 km. Similar radiometers for geosynchronous satellites will have comparable resolution. Therefore, compiling a VIRES index climatology with useful space resolution seems feasible. However, the global coverage requirement is harder to meet when combined with the time resolution demand.

Satellites such as NIMBUS and TIROS are in sun-synchronous orbits and only make observations over any single earth location twice a day at the same times everyday although the whole globe is covered. Because of diurnal cloudiness variations, twice a day observations give biased results (Harrison et al. 1978, 1980). On the other hand, geosynchronous satellites make observations at all hours but in general can effectively view only between 60°N and 60°S latitude and about 120° of longitude. More complete coverage can be achieved by observing nearly all the low and middle latitudes at each hour by adding a satellite with a mid-inclined orbit which precesses (Harrison et al. 1978).

A good discussion concerning optimizing satellite observations is given by Campbell and Vonder Haar (1978). Nevertheless, it is clear that no one type of satellite offers both the ideal spatial coverage and ideal temporal resolution.

Remembering this limitation, one should consider the importance of cloud classification. Sherr et al. (1968) proposed 29 different cloud climatological regions globally. These regions were based primarily on seasonal distributions of mean monthly cloud cover. Also considered were annual cloud distributions, area precipitation distributions, and different climate classification schemes. Most regions were repeated two or more times throughout the world. Some of Sherr's typical region descriptions are; tropical cloudy, desert marine, mid-latitude clear summer, high latitude clear winter, mediterranean and polar. A similar cloud classification scheme is given by Winston (1969).

By considering cloudiness regions instead of strictly global measurements one might for instance actually have a more sensitive measure for the purpose of climate monitoring. Applications of the climate modeling type might also be stronger on a regional basis. Consequently, global coverage seems to be of secondary importance. Thus, one would expect a climate index derived from geosynchronous satellite data to be the basis of a good climatology except where total global coverage is required. Sun-synchronous satellites could provide additional information if the time bias problem is avoided.

From this discussion one may conclude that the best approach is to take the geostationary satellite information available and average it to a 250 km space resolution and 4 hour time resolution. From these values longer time and larger space scale values can be obtained

with emphasis on weekly regional averages. Of course there should be an attempt to use sun-synchronous satellite data to complete the global picture.

Related to the time resolution problem is the problem of instrument continunity through time. In other words, how do we keep the satellite instrument absolutely calibrated? Without the absolute calibration it becomes necessary to intercompare instruments from different satellites for the purpose of obtaining a homogeneous data set. It is also necessary to detect and correct changes in a specific instrument over time. Of course intercomparisons would be useful as a second check even with absolute calibration. The proposed Space Shuttle may offer the means of intercomparing instruments, although for now such a process is impossible (COSPAR, 1978b). Also, a common ground base laboratory test facility for all satellite instruments would provide a chance to uncover systematic differences.

Calibrating radiation instruments in any absolute sense is very difficult if not impossible (COSPAR, 1978b) especially for SW sensors. Calibration targets such as black bodies are sometimes used successfully for IR instruments. One may also use a transfer technique; observe the same target at the same time with two different instruments whose output can be compared. If one of the instruments has a trusted calibration then the other one may be calibrated. Another approach is to convert radiant energy into heat energy using a known, stable process. The advantage here is that the efficiency of this conversion as a function of temperature can be determined independently and therefore 'known' calibration sources are not needed. Lastly, it can be said that the nature of radiation (e.g. its amplitude, wavelength,

interference and diffraction effects, and polarization) makes calibration of radiometers a complex operation with many uncertainties, especially for SW instruments. Fortunately, the more easily calibrated IR sensitive radiometers are used to derive the VIRES index.

VII. POSSIBLE APPLICATIONS OF A SATELLITE DERIVED CLOUDINESS INDEX

Most of the cloud retrieval methods mentioned in Chapter II have been developed with the idea that deducing global cloud climatology information from satellite data is desirable. Most have tried to conform with classical ground observational definitions of clouds. The present research suggests that a more realistic and progressive point of view is to consider clouds in light of their radiative properties. After all, counting and typing individual clouds on a global climatological basis is probably an impossible task, and the results of such a census may not provide the best information for the application. Therefore, a climatic index that represents cloudiness by means of the infrared broadband weighting function is proposed. How might such an index be used? Perhaps the two most important applications for such a climatological index are in the areas of climate modelling and climate monitoring (Smith, 1978).

A quote from GARP Publication 16 (Stockholm, 1974) relates the importance between climatic processes of clouds and their radiative effects: "... proper treatment of radiative effects of clouds is the single most important factor in the overall parameterization of radiation in a climate model". However, proper treatment of clouds is difficult even for the most advanced climate models. For example, most clouds are sub-grid scale for the typical general circulation model (GCM). Thus, clouds will undoubtedly be parameterized in future models much as they are now. Furthermore, these cloud parameterizations are one of the weakest aspects of the present GCM's. Climate models now lack the ability to meaningfully calculate radiative forcing due to the

failure of cloud-dynamic parameterizations (Webster, 1978). Nevertheless, as newer and better cloud models are developed they must be verified and tuned against actual measurements of global cloudiness (Cox, 1978).

Because climate models necessarily have many assumptions, approximations and parameterizations, verification of their results is quite important. Furthermore, computation of one parameter may be successful because the model contains compensating errors in, for example, the treatment of physical processes. One can have more confidence in the validity of ones model by checking calculated against measured parameters that are both a direct measure of a physical process and available in time and space scale detail. The climatic cloudiness index outlined in this paper is a particularly useful parameter because it is a radiative index that can be compiled for weekly or seasonal worldwide vertical profile values. In other words, the 4-dimensional characteristic of this observable variable would make it a particularly good verification tool for the parameterization of clouds in the GCM radiative calculations.

The values of the proposed index may also be useful in GCM cloud parameterization studies. Instead of dealing directly with clouds in a model, one might go directly from dynamic-thermodynamic considerations to radiative effects (COSPAR, 1978a). Another approach is to relate model derived cloudiness directly to radiative divergence profiles without any model cloud radiative calculations (Cox and Vonder Haar, 1973). Such "direct" parameterization studies will need to use observational data like the cloudiness and radiative information contained in the index.

The second area of potential index application is in climate monitoring. The earth's climate is a function of the earth-atmosphere system reacting to the equator-to-pole gradient of net energy; this net energy budget may be quantified and divided into components by the net radiation budget studies using satellite data (Vonder Haar and Oort, 1973; Campbell and Vonder Haar, 1980a,b). Clouds are the principal modulators of the radiation for they strongly influence the earth's solar albedo and infra-red absorption. To extend and improve the climate monitoring aspect of these radiation budget studies there is a need to determine cloudiness independent of the satellite radiation budget measurements (Vonder Haar, 1979). The index described in this paper would be useful for this purpose.

Because we feel that cloudiness is an important climate variable, and since the VIRES index is strongly a function of cloudiness, it follows that the index itself represents a physical characteristic of the climate system. The temporal and spatial variations of this index can be detected using the statistical method described earlier. This could be done on a global or regional scale in an attempt to detect climatic trends. Regional changes which can be concealed in global averages may provide a more sensitive measure of climatic change. Moreover, climatic anomalies in one area are often correlated with variations in another area. Occassionally there is also a time lag. In such cases climatic forecasts can be made. These teleconnections might be identified and observed easier by processing satellite data into meteorological indexes like the one described in this paper.

The index described in this paper has both information about cloudiness and outgoing longwave radiation. In this respect it would

be especially valuable to the National Climatic Research Program (NCRP). The NCRP Committee proposes satellite observations in the form of a Climatic Index Monitoring Program in addition to conventional meteorological observations (U.S. Committee for GARP, 1975). This VIRES index would represent two indexes in one. Furthermore, it can be computed for the global coverage and weekly frequency required.

There are other possible uses for a radiatively defined cloudiness index. When combined with radiation budget studies a better assessment of atmospheric energetics may be possible (COSPAR WG 6, 1978a). Climatic change may be viewed as an adjustment among compensating feedback processes. Using this index one may be able to identify and quantify coupling between cloudiness and other atmospheric variables. Perhaps by using the index more specific relationships between the cloudiness and the earth-atmosphere energy balance (Hartman and Short, 1980; Herman et al. 1980; Ohring and Clapp, 1980) can be found. Conceivably this index could help determine whether or not a change in cloudiness necessarily results in a change in the climate (Cess, 1976; Ellis, 1978; Coakley, 1979; Van Den Dool, 1980). In this regard the index could shed some much needed light on the role of cloud vertical structure as it applies to the cooling to space portion of the earth-atmosphere radiation budget. The VIRES index would also be useful in understanding more clearly the consequence of tropospheric water vapor emission as it relates to the earth-atmosphere radiative loss.

VIII. CONCLUSIONS

This paper introduces and describes a climate index called the VIRES index. VIRES is the acronym for Vertical Infrared Radiative Emitting Structure and quite by chance it is also the plural form of the Latin word vis, meaning forces or powers. Thus, the acronym seems especially appropriate since the atmosphere's VIRES is one of the major forcing factors behind the earth's climate. The VIRES index is related to the earth's climate through the earth's radiation budget and therefore can be considered a climate index. The logic behind this claim may be stated as follows. The climate system is determined by the energy input to the system and the distribution, transformation and storage of energy in various forms within the system. These processes are mirrored in the components of the earth's radiation budget, one of which is the outgoing emitted thermal radiation (COSPAR Report to ICSU and JOC, 1978b). This cooling to space is described by the VIRES which is primarily a function of the cloud distribution.

This index is an attempt to optimize the use of satellite data for climate purposes by directly utilizing the radiative aspects of the atmosphere while avoiding some of the difficulties of inferring standard meteorological variables from satellite radiances. The VIRES index is based on broadband infrared weighting curves retrieved from operationally measured spectral, earth-emitted radiation in the CO_2 absorption band. These curves describe the vertical structure of infrared radiative emission and are a function of the cloud, temperature and moisture distributions. The most important findings of this research are summarized below.

A. Cloud - VIRES relationship

This paper demonstrates under both tropical and mid-latitude atmospheric conditions the predominate influence of the three dimensional cloud distribution on the atmosphere's Vertical Infrared Radiative Emitting Structure (VIRES). Therefore, the VIRES index can be considered an indicator of cloudiness with the caution that low cloud or high water vapor content can both result in the same VIRES. Also illustrated is the fact that the atmospheric VIRES is responsive to the three dimensional distributions of water vapor and temperature.

B. VIRES retrieval technique

VIRES curves may be inferred directly from satellite measured radiances. A retrieval technique utilizing CO_2 band spectral radiances is described which determines two weighting curve shape parameters (p_{wf} and α). The empirical RTE method was found to be both computationally fast and accurate. The two parameters inferred using the empirical RTE method define a single scene VIRES. The single scene retrievals are composited to give a temporal and spatial average VIRES curve. A sensitivity study and error analysis using simulated satellite data that included the effect of sampling inadequacies quantified the abilities of the empirical RTE retrieval approach.

C. VIRES uniqueness

The VIRES curves calculated for diverse cloud (climate) regimes have been shown to be statistically different in all cases with the following two exceptions. In the moist atmosphere case the high concentrations of low level water vapor radiatively emit to space almost identically like the case with low level cloud. The second exception

occurs for comparisons between two similar cloud shape distributions. The simple non-parametric statistical test compares the points from two VIRES curves every 20 mb. As might be expected, the VIRES index values show (qualitative) uniqueness. Thus, climate change can be effectively monitored using the VIRES index which conveniently and quantitatively expresses the vertical structure of terrestrial emission to space.

D. VIRES index

Although the VIRES curves contain the maximum vertical information, they are cumbersome to work with. Therefore, a useful descriptor of the VIRES curve called the VIRES index was developed. As stated above, the index is able to protray differences in the atmosphere's vertical emitting structure. The first three number parameters in the index represent pressure levels in the atmosphere above which a specified fraction (.25, .50, .75) of the infrared energy lost to space originates. The last parameter represents the fraction of energy lost to space which originated at the earth's surface. The index is especially useful since it represents the VIRES curve information in a shortened, interpretable, and flexible form. The four parameter index prposed in this work may be easily modified to maximize its usefulness for different applications.

E. Suggested applications and sampling strategies

A number of specific applications have been proposed and in general they are related to climate monitoring and climate modeling. For example, to monitor the climate, regional VIRES index averages can be compiled. These values would probably be very sensitive to climate

variations. It is recommended that this basic index, calculated from geostationary satellite radiance measurements, be averaged to a spatial resolution of 250 km (2 1/2° latitude by 2 1/2° longitude) with the smallest time resolution being 4 hours. Of course sun synchronous satellite data may be used to supplement coverage. From these data coarser spatial and temporal averages can be calculated for other specific applications such as regional or global climate modeling. The VIRES index can be used for climate model baselining and verification of radiative calculations. Index values may also be useful to research efforts in the area of cloud parameterizations.

LITERATURE CITED

Avaste, O. G., G. Campbell, E. Smith, S. Cox and T. Vonder Haar, 1979: Determination and analysis of total cloud cover over the oceans 1975-1978. Dept. of Atmospheric Science Report No. 300, Colo. State Univ., Ft. Collins, CO., 73 pp.

Beyer, W. H. ed., 1971: CRC Basic Statistical Tables. The Chemical Rubber Co., Cleveland, Ohio, 310 pp.

Bignell, K. J., 1970: The water vapor infrared continuum. Quart. J. Roy. Meteor. Soc., 96, 390-403.

Bolin, B., and W. Bischof, 1970: Variations of the carbon dioxide content of the atmosphere in the northern hemisphere. Tellus, XXII, 431-442.

Campbell, G. G., and T. H. Vonder Haar, 1978: Optimum satellite orbits for accurate measurement of the earth's radiation budget. Atmos. Sci. Paper No. 289, Colo. State Univ., Ft. Collins, CO., 61 pp.

_____, E. A. Smith and T. H. Vonder Haar, 1980: Cloud amount estimation from geosynchronous satellites: a demonstration of diurnal variation. Proceedings of the 1980 International Radiation Symposium, Ft. Collins, CO., Aug. 11-16, 312-314.

_____, and T. H. Vonder Haar, 1980a: An analysis of two years of Nimbus 6 earth radiation budget observations: July 1975 to June 1977. Atmos. Sci. Paper No. 320, Colo. State Univ., Ft. Collins, CO., 83 pp.

_____, and _____, 1980b: Climatology of radiation budget measurements from satellites. Atmos. Sci. Paper #323, Colo. State Univ., Ft. Collins, CO., 74 pp.

Cess, R. D., 1976: Climate change: an appraisal of atmospheric feedback mechanisms employing zonal climatology. J. Atmos. Sci., 33, 1831-1843.

Chahine, M. T., 1974: Remote sounding of cloudy atmospheres, I. The single cloud layer. J. Atmos. Sci., 31, 233-243.

_____, 1975: An analytical transformation for remote sensing of clear-column atmospheric temperature profiles. J. Atmos. Sci., 32, 1946-1952.

Chen, T. S., L. L. Stowe, V. R. Taylor and P. F. Clapp, 1980: Classification of clouds using THIR data from Nimbus 7 satellite. Proceedings of the 1980 International Radiation Symposium, Ft. Collins, CO., Aug. 11-16, 315-317.

LITERATURE CITED (Continued)

Clapp, P. F., 1964: Global cloud cover for seasons using TIROS nephanalysis. Mon. Wea. Rev., 92, 495-507.

Coakley, J. A. Jr., 1979: A study of climate sensitivity using a simple energy balance model. J. Atmos. Sci., 36, 260-269.

COSPAR Report to ICSU and JOC, 1978a: Status of satellite observing possibilities for study of climate physical processes. NCAR, Boulder, CO., 111 pp.

_____, 1978b: Toward an internationally coordinated earth radiation budget satellite observing system: scientific uses and system considerations. NCAR, Boulder, CO., 76 pp.

Cox, S. K., and T. H. Vonder Haar, 1973: Measurements of solar energy for the study of time dependent meteorological systems. Proceedings of Symposium on Solar Radiation, Smithsonian Institution Radiation Biology Laboratory, Nov. 13-15, 32-35.

_____, M. C. Polifka, K. Griffith, A. Rockwood and D. Starr, 1976: Radiative transfer computational routines for atmospheric science applications. Dept. Atmos. Sci., Colo. State Univ., Ft. Collins, CO., 75 pp.

_____, 1978: Review of parameterizations of radiation and extended cloudiness. JOC Study Conference on Parameterization of Extended Cloudiness and Radiation for Climate Models. Oxford, U.K., 27 Sept. - 4 Oct., 21 pp.

_____, and K. T. Griffith, 1978: Tropospheric radiative divergence during Phase III of the GARP Atlantic Tropical Experiment (GATE). Atmos. Sci. Paper #291, Colo. State Univ., Ft. Collins, CO., 166 pp.

Crutcher, H. L., and J. M. Meserve, 1970: Selected level heights, temperatures and dewpoints for the Northern Hemisphere, NAVAIR 50-1C-52.

Dalton, J. T., M. L. Desjarding, A. F. Hasler and R. A. Minzner, 1979: Digital cloud stereography from geostationary orbit. Proceedings of the 13th International Symposium on Remote Sensing of the Environment (Ann Arbor, Michigan, April 23-27), 1479-1488.

Elasser, W. M., and M. F. Culbertson, 1960: Atmospheric Radiation Tables. Meteorological Monographs, 4, No. 23.

Ellis, J. S., 1978: Cloudiness, the planetary radiation budget, and climate. Ph.D. thesis, Dept. of Atmos. Sci., Colo. State Univ., 129 pp.

LITERATURE CITED (Continued)

Environmental Satellite Imagery, March 1975 - February 1976: NOAA Environmental Data Service, KMRD No. 5.4g, Washington, D.C.

Fisher, R. A., 1958: Statistical Methods for Research Workers. 13th Edition, Hafner Pub. Co. Inc., N.Y., 356 pp.

Fye, F. K., 1978: The AFGWC automated cloud analysis model. AFGWC Tech. Memo. 78-002, HQ AFGWC, Offutt AFB, Nebraska, 97 pp.

Griffith, K. T., and S. K. Cox, 1977: Radiative properties of clouds inferred from broadband measurements. Atmos. Sci. Paper #269, Colo. State Univ., Ft. Collins, CO., 102 pp.

Gupta, S. K., S. N. Tiwari, and J. T. Suttles, 1978: Longwave radiation transfer in the atmosphere. Proceedings of the 3rd Conference on Atmospheric Radiation, Davis, CA., June 28-30, 40-43.

Handbook of Geophysics and Space Environments, 1965: Air Force Cambridge Research Laboratories, Office of Aerospace Research, U.S. Air Force, 649 pp.

Harrison, E. F., G. G. Gibson and P. Minnis, 1978: Sampling analysis for the earth radiation budget satellite system mission based on orbital coverage and cloud variability. 3rd Conf. on Atmospheric Radiation, Davis, CA., 28-30 June.

_____, P. Minnis and G. G. Gibson, 1980: Temporal and spatial variability of cloud cover from GOES data for radiation budget studies. Proceedings of the 1980 International Radiation Symposium, Ft. Collins, CO., Aug. 11-16, 361-363.

Hartman, D. L., and D. A. Short, 1980: On the use of earth radiation budget statistics for studies of clouds and climate. J. Atmos. Sci., 37, 1233-1250.

Heath, D., 1973: Space observations of the variability of solar irradiance in the near and far infrared. J. Geophys. Res., 78, 2779-2792.

Herman, G. F., M. C. Wu, and W. T. Johnson, 1980: The effect of clouds on the earth's solar and infrared radiation budgets. J. Atmos. Sci., 37, 1251-1261.

Houghton, J. T., 1979: The future role of observations from meteorological satellites. Quart. J. Roy. Met. Soc., 105, 1-23.

International Cloud Atlas, Vol. 1, WMO 1956, Geneva, Switzerland.

Jenne, R. L., H. L. Crutcher, H. Van Loon, and J. J. Taljaard, 1974: A selected climatology of the southern hemisphere: computer methods and data availability. NCAR-TN/STR-92, 91 pp., Boulder, CO.

LITERATURE CITED (Continued)

Koffler, R. A., A. G. DeCotiis, and P. Krishna Rao, 1973: A procedure for estimating cloud amount and height from satellite infrared radiation data. Mon. Wea. Rev., 101, 240-243.

McCleese, D. J., and H. M. Wilson, 1976: Cloud top heights from temperature sounding instruments. Quart. J. Roy. Met. Soc., 102, 781-790.

McMillin, L. M., D. Q. Wark, J. M. Siomakajlo, P. G. Abel, A. Werbowetzki, L. A. Lauritson, J. A. Pritchard, D. S. Crosby, H. M. Woolf, R. C. Luebbe, M. P. Weinreb, H. E. Fleming, F. E. Bittner and C. M. Hayden, 1973: Satellite infrared soundings from NOAA spacecraft. NOAA Technical Report NESS 65, National Environmental Satellite Service, Washington, D.C., 112 pp.

Mendola, C., and S. K. Cox, 1978: Cloud analysis from bi-spectral satellite data. Atmos. Sci. Paper #295, Colo. State Univ., Ft. Collins, CO., 75 pp.

Miller, D. B., and R. G. Feddes, 1971: Global atlas of relative cloud cover 1967-1970. U. S. Nat. Envir. Sat. Ser. and USAF ETAC, AD 739434-Rpt. No. 1, 237 pp.

Miller, J., Ed., 1978: Maunalon Observatory, a 20th anniversary report. NOAA Special Report, Air Resources Laboratories, Silver Spring, MD., 158 pp.

Ohring G., and P. Clapp, 1980: The effect of changes in cloud amount on the net radiation at the top of the atmosphere. J. Atmos. Sci., 37, 447-454.

Platt, C. M. R., 1979: Remote sounding of high clouds: I. Calculation of visible and infrared optical properties from lidar and radiometer measurements. J. Appl. Met., 18, 1130-1143.

_____, and G. L. Stephens, 1980: The interpretation of remotely sensed high cloud emittances. J. Atmos. Sci., 37, 2314-2322.

Rao, P. K., 1970: Estimating cloud amount and height from satellite infra-red radiation data. ESSA Technical Report, N.E.S.C. 54, Washington, D. C., 11 pp.

Raschke, E., Ed., 1978: Terminology and units of radiation quantities and measurements. NCAR, Boulder, CO., 17 pp.

LITERATURE CITED (Continued)

Remsberg, E. E., J. M. Russell III, L. L. Gordly, M. Paglia, J. C. Gille, and P. L. Bailey, 1980: Measurement of the radiance signature and distribution of clouds by the LIMB infrared monitor of the stratosphere experiment (LIMS) on Nimbus 7. Proc. of the 1980 International Radiation Symposium, Aug. 11-16, Ft. Collins, CO., 21-22.

Reynolds, D. W., and T. H. Vonder Haar, 1977: A bi-spectral method for cloud parameter determination. Mon. Wea. Rev., 105, 446-457.

_____, M. L. Brown, E. A. Smith and T. H. Vonder Haar, 1978: Cloud type separation by spectral differencing of image pairs. Mon. Wea. Rev., 106, 1214-1218.

Sadler, J. C., 1969: Average cloudiness in the tropics from satellite observations. Internatl. Indian Ocean Expedition Meteorol. Monogr. No. 2, East - West Center Press, Honolulu, 22 pp and 12 plates.

_____, L. Oda and B. J. Kilonsky, 1976: Pacific Ocean cloudiness from satellite observations. Rept. Meteorol. Univ. Hawaii, 137 pp.

Schwalb, A., 1978: The TIROS-N/NOAA A-G Satellite Series. NOAA Tech. Mem., NESS 95, 75 pp.

Shenk, W. E., and R. J. Curran, 1973: A multi-spectral method for estimating cirrus cloud top heights. J. Appl. Meteor., 12, 1213-1216.

Sherr, P. F., A. H. Glaser, J. C. Barnes and H. I. Willand, 1968: World-wide cloud cover distributions for use in computer simulations. NASA CR-61226, Huntsville, Al.

Sissala, J. E., Ed., 1975: The Nimbus 6 user's guide. Goddard Space Flight Center, NASA, Beltsville, MD., 58 pp.

Smith, W. L., 1969: A polynomial representation of carbon dioxide and water vapor transmission. Tech. Report, NESC 47, 20 pp.

_____, H. M. Woolf and W. C. Jacob, 1970: A regression method for obtaining real-time temperature and geopotential height profiles from satellite spectrometer measurements and its application to Nimbus III SIRS observations. Mon. Wea. Rev., 98, 582-603.

_____, H. M. Woolf and H. R. Fleming, 1972: Retrieval of atmospheric temperature profiles from satellite measurements for dynamical forecasting. J. Appl. Meteor., 11, 113-122.

LITERATURE CITED (Continued)

Smith. W. L., and H. M. Woolf, 1976: The use of eigenvectors of statistical convariance matrices for interpreting satellite sounding radiometer observations. J. Atmos. Sci., 33, 1127-1140.

_____, J. Hickey, H. B. Howell, H. Jacobowitz, D. T. Hilleary, and A. J. Drummond, 1977: Nimbus-6 earth radiation budget experiment. Appl. Opt., 16, 306-318.

_____, 1978: Status and plans for cloud climatology programme. JOC Study Conference on Parameterizations of Extended Cloudiness and Radiation for Climate Models (Oxford, 27 Sept. - 4 Oct), 16 pp.

_____, and C. M. R. Platt, 1978: Comparison of satellite-deduced cloud heights with indications from radiosonde and ground-based laser measurements. J. Appl. Meteor., 17, 1796-1802.

Snedecor, G. W., and W. G. Cochran, 1967: Statistical Methods. Sixth Edition, Iowa State Univ. Press, Ames, Iowa, 593 pp.

Steiner, E. J., 1978: A comparison of surface wind parameters, cloud amount, and sea surface temperature in tropical Pacific, 3rd NOAA Climate Conference, Miami, FL., 10-78.

Stockholm, 1974: JOC Study Conference on the Physical Basis of Climate and Climate Modeling, GARP Publications Series No. 16.

Suomi, V. E., F. R. Mosher and D. P. Wylie, 1977: Development of satellite imaging processing techniques from the First GARP Global Experiment. Final Report prepared for NASA, Goddard Space Flight Center under contract NAS 5-23462.

Susskind, J., and J. Rossenfield, 1980: Temperature soundings from TIROS-N. Proceedings of 1980 International Radiation Symposium, Ft. Collins, CO., Aug. 11-16, 90-93.

Taylor, F. W., 1974: Remote temperature sounding in the presence of cloud by zenith scanning. Appl. Opt., 13, 1559-1566.

Telegados, K., and J. London, 1954: A physical model of the northern hemisphere troposphere for winter and summer. New York Univ., Sci. Rept. No. 1, Contract AF 19(122)-165, 55 pp.

U. S. Committee for GARP, 1975: Understanding Climate Change...A program for action. National Academy of Sciences, Washington, D.C.

U.S. Standard Atmosphere 1976, 1976: NOAA, NASA and U.S. Air Force Pub. NOAA-SIT 76-1562, 227 pp.

Van Den Dool, H. M., 1980: On the role of cloud amount in an energy balance model of the earth's climate. J. Atmos. Sci., 37, 939-946.

LITERATURE CITED (Continued)

Vonder Haar, T. H., and A. H. Oort, 1973: New estimate of annual poleward energy transport by Northern Hemisphere Oceans. Phys. Ocean., 3, 169-172.

_____, 1979: Climatic indicators from space. Proceedings of the 13th International Symposium on Remote Sensing of the Environment (Ann Arbor, MI., April 23-27) 327-335.

Webster, P. J., 1978: Sensitivity of climate to variations in cloudiness and the treatment of cloudiness in climate models. JOC Study Conf. on Parameterization of Extended Cloudiness and Radiation for Cliamte Models. Oxford, 27 Sept. - 4 Oct., 417 pp.

Weinreb, M. P., and D. S. Crosby, 1977: A technique for estimating atmospheric moisture profiles from satellite measurements. J. Appl. Met., 16, 1214-1218.

Wielicki, B. A., and J. A. Coakley Jr., 1980: The retrieval of cloud amount and cloud top pressure from infrared sounder data: an error analysis. Proceedings of the 1980 International Radiation Symposium, Ft. Collins, CO., Aug. 11-16, 137-139.

Winston, J. S., 1969: Global distribution of cloudiness and radiation as measured from weather satellites. I: Climate of the free atmosphere, Ed. by D. F. Rex, Amsterdam, Elsevier, 247-280.

Yamamoto, G., M. Tanaka, and S. Asano, 1970: Radiative transfer in water clouds in the infrared region. J. Atmos. Sci., 27, 282-292.

Yeh, H., and K. Liou, 1980: Infrared and microwave sounding of the cloud liquid water content and temperature profile in cloudy atmospheres. Proc. of the 1980 International Radiation Symposium, Ft. Collins, CO., Aug. 11-16, 128-130.

APPENDIX

Retrieval Error Analysis

Chapter V is an introduction and summary of the analysis presented below. For an explanation of the boundary conditions and assumed error values refer to Chapter V. This Appendix contains the following detailed error analysis. Errors due to system-instrument errors are investigated first, followed by errors due to temperature and humidity profile unknowns. The magnitude of errors due to CO_2 profile variations are also examined. Errors due to specified cloud properties are reviewed, followed by a brief analysis of combined error sources. The last source of error examined is the assumption that a single representative radiating surface is in the radiometer field of view. The following sections detail the error findings.

A. Random sensor error effects

Figures 24-31 give the bias and RMS retrieval errors due to random sensor errors for both a mid-latitude and tropical atmosphere. Instrument system noise is assumed Gaussian with a mean of zero and a standard deviation of 0.22 mW $m^{-2}sr^{-1}cm$ for the 15 μm channels, and 0.11 mW $m^{-2}sr^{-1}cm$ for the window channel. These values represent the state of the art precision of the HIRS instrument on TIROS-N (Schwalb, 1978). For calculation purposes the set of spectral values representing a particular atmosphere are modified with random noise errors that are distributed as described above. These modified spectral radiance values are then used in the empirical RTE curve shape parameter retrieval algorithm to solve for the calculated p_{wf} and α values, which are then compared to the known correct values. Statistics are

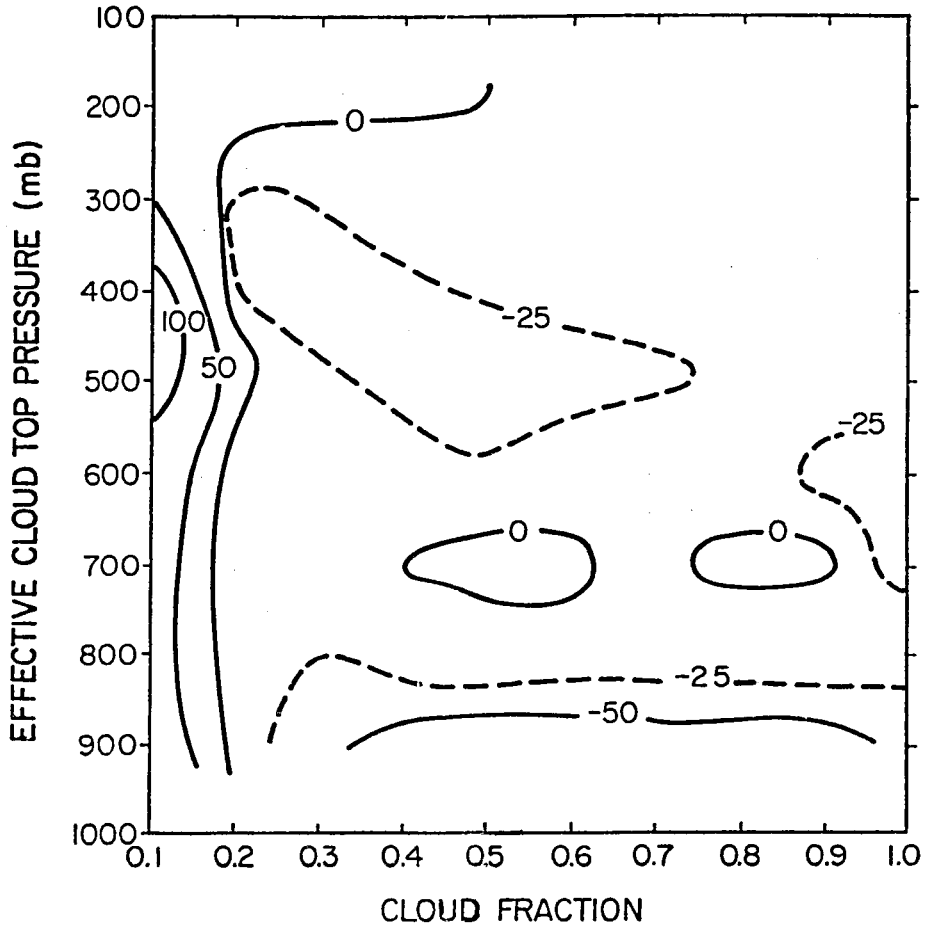

Figure 24. p_{wf} pressure level bias: random sensor errors for mid-latitude summer model.

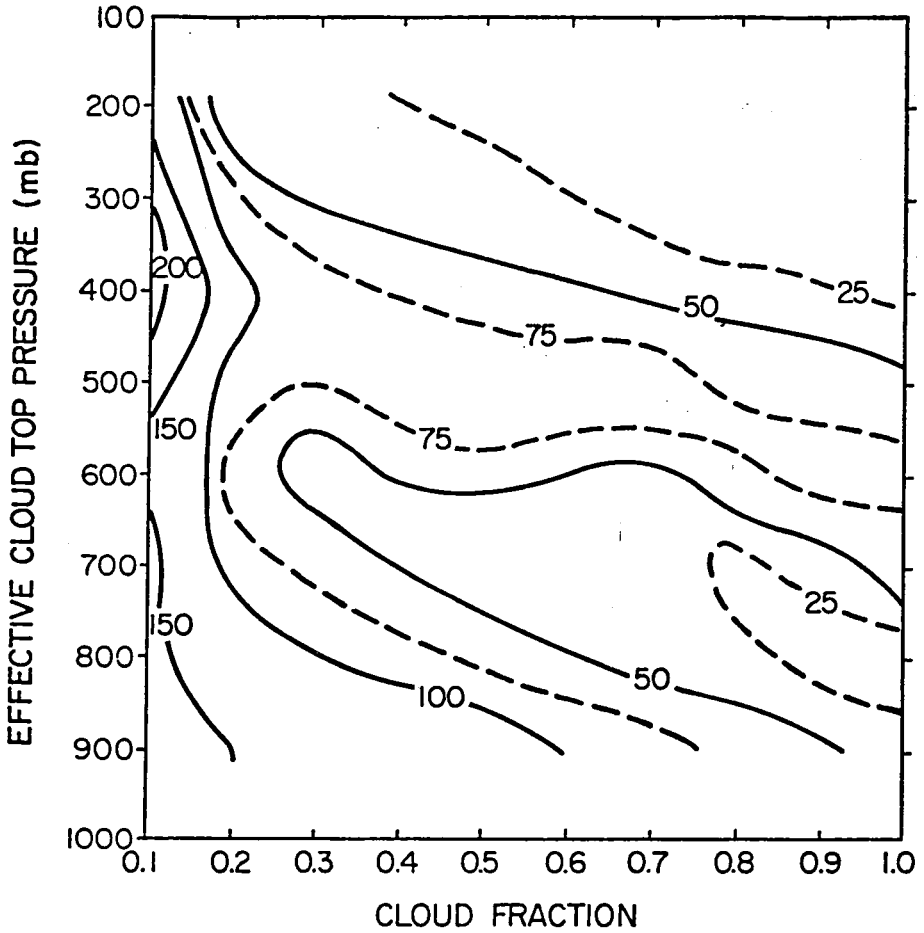

Figure 25. p_{wf} pressure level RMS: Random sensor errors for mid-latitude summer model.

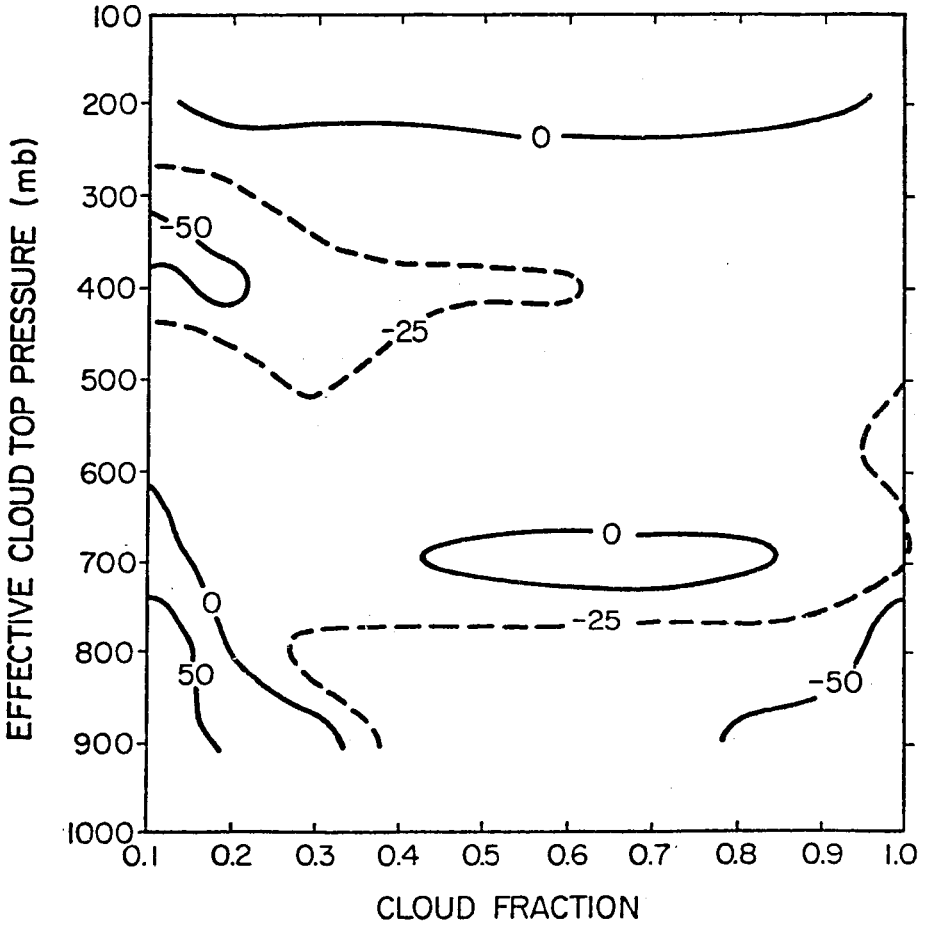

Figure 26. p_{wf} pressure level bias: Random sensor errors for tropical model.

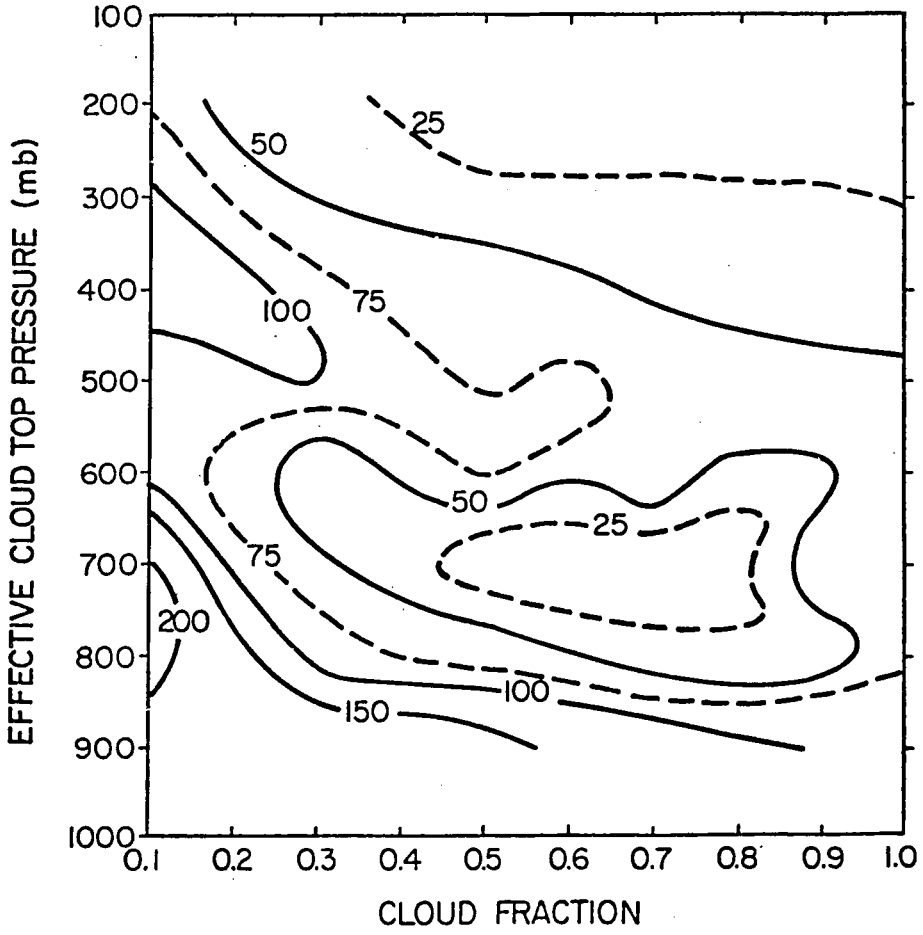

Figure 27. p_{wf} pressure level RMS: Random sensor errors for tropical atmosphere model.

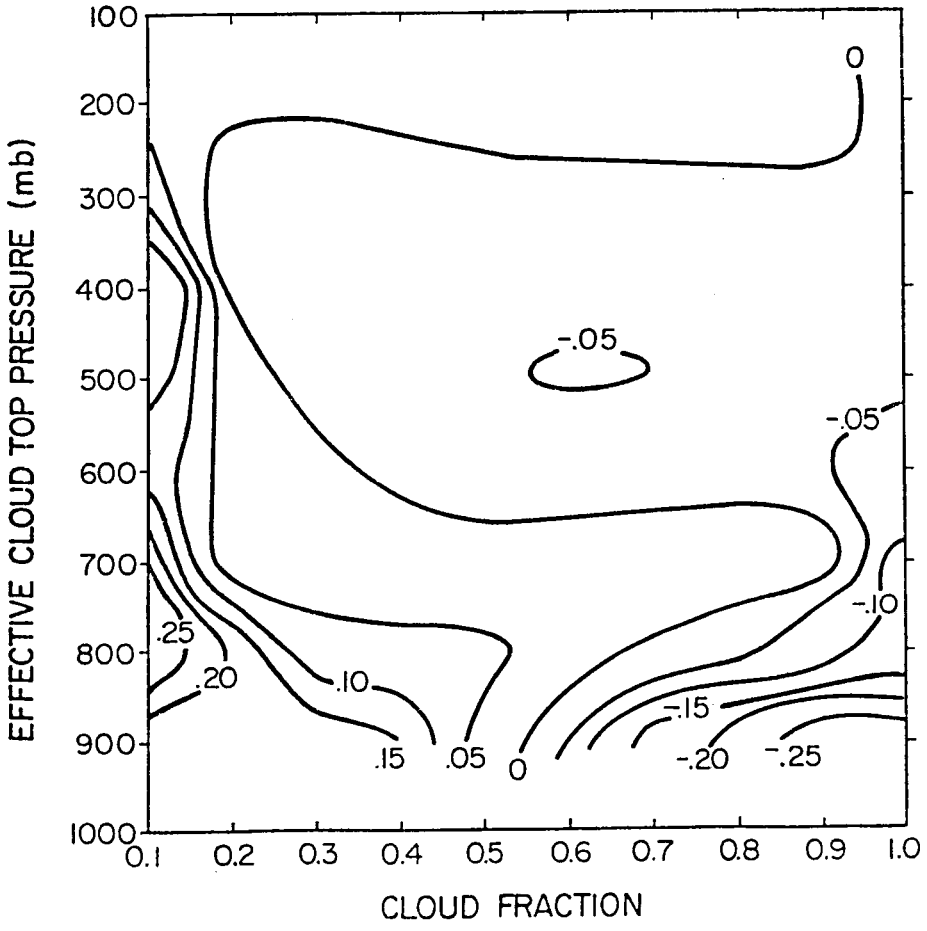

Figure 28. α bias: Random sensor error for mid-latitude summer model.

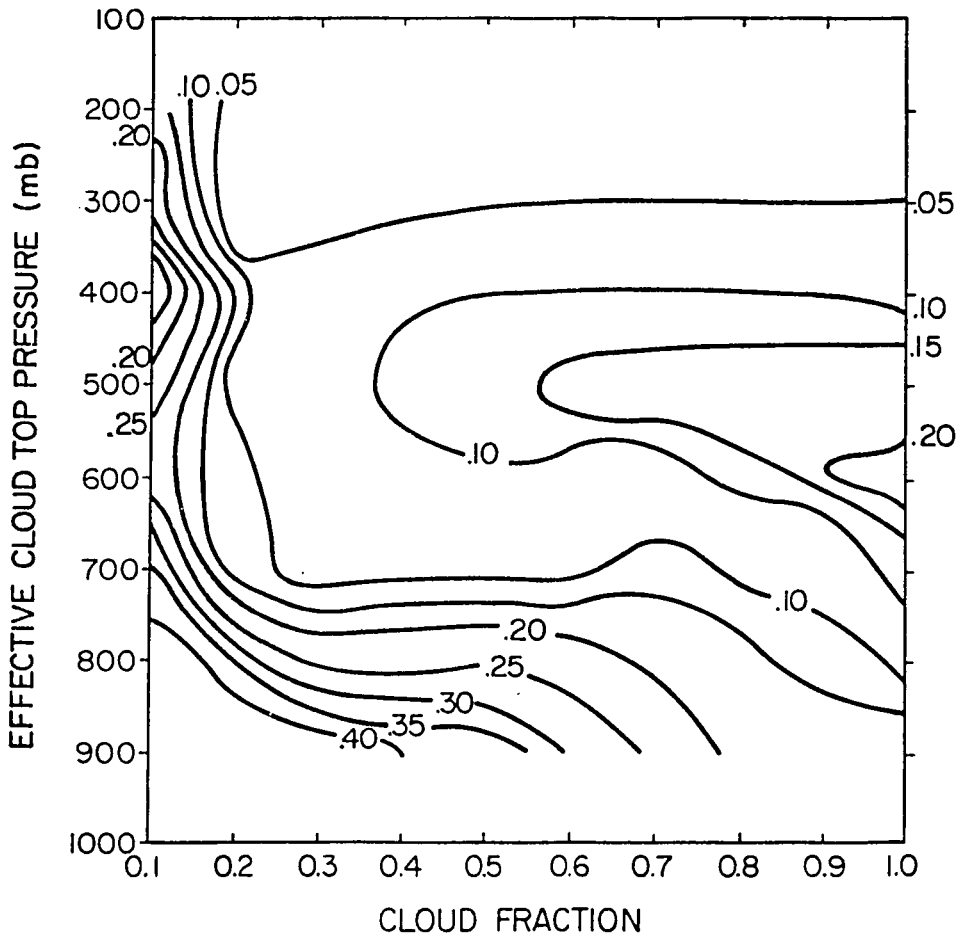

Figure 29. α RMS: Random sensor error for mid-latitude summer model.

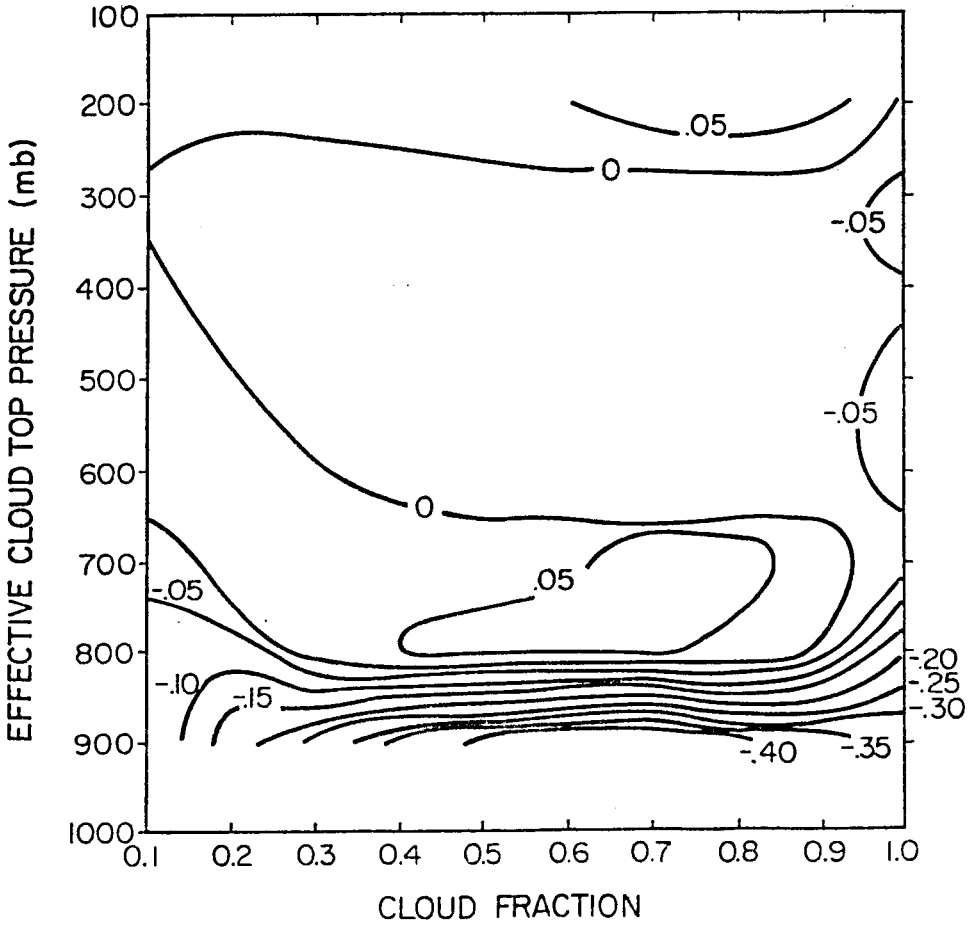

Figure 30. α bias: Random sensor error for tropical model.

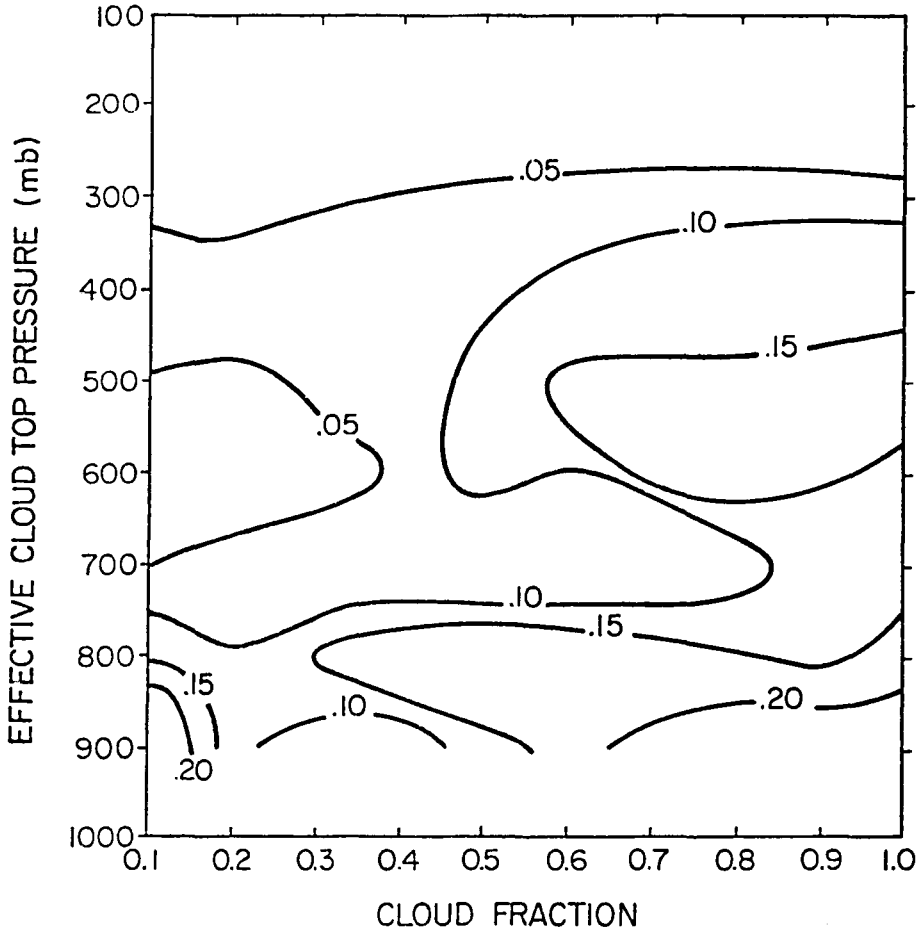

Figure 31. α RMS: Random sensor error for tropical model.

calculated using 60 sets of calculated versus given values for each particular atmospheric condition. As seen in Figures 24-31, one hundred statistics per figure are calculated using combinations of 10 effective cloud top pressures and 10 effective cloud fraction values.

Understanding the bias statistic in Figures 24, 26, 28 and 30 is simplified if one realizes that there is a correlation between the retrieved values of p_{wf} and α. For example, a single spectral radiance may be the result of small p_{wf} and α values or the result of large p_{wf} and α values. For the single spectral radiance there is a spectrum of p_{wf} and α value pairs going from both small to both large that could define a weighting curve for that radiance value. Thus, to satisfy a set of spectral radiances with instrument noise the empirical routine will usually tend to err in the same direction for both p_{wf} and α. For the most part, Figures 24 and 28, and Figures 26 and 30 show this error characteristic.

Furthermore, the bias figures show errors due principally to boundary conditions. The physical constraints of the system force the instrument noise error to show bias errors when $p_{wf} \rightarrow 1000$ mb. In this case radiating surfaces below 1000 mb are not allowed causing the p_{wf} bias error to be negative (bias = calculated - given). At this boundary α bias errors are also generally negative. Figures 24 and 28 show the same effect as $\alpha \rightarrow 0$. By necessity the bias is toward larger α values and as a consequence larger p_{wf} values (positive bias). Figures 26 and 30 show this effect to a lesser degree. Overall this analysis shows the retrieval is highly unbiased due to instrument noise except as $\alpha \rightarrow 0$ and $p_{wf} \rightarrow 1000$ mb. As stated previously, when α is near zero and p_{wf} is near the surface the broadband weighting curve is only

slightly changed from the clear sky case. Thus, these error effects are minimized.

Figures 25, 27, 29 and 31 give the RMS error due to system noise of p_{wf} and α for a mid-latitude and tropical atmosphere. The more gradual increase in RMS errors for p_{wf} and α as $\alpha \to 0$ and $p_{wf} \to 1000$ mb indicates that the RMS error is probably related closely to signal to noise ratio which gradually decreases as $\alpha \to 0$ and $p_{wf} \to 1000$ mb. One also notices that RMS values are slightly larger for the mid-latitude case (Figures 25 and 29). This is probably due to the fact that the tropical atmosphere contains much more water vapor. The presence of water vapor may act as a buffer reducing the impact radiance errors have on the retrieval process. In conclusion, it appears that random noise effects produce p_{wf} and α retrieval errors that are in the mean quite small. Any specific case retrieval errors will be of the magnitude indicated by the RMS figures.

B. Profile error effects

Analysis of profile error effects is extremely difficult due to the computational time involved. Instead of adding random noise 60 times to sets of spectral radiance values (one for mid-latitude and another for tropical atmospheres), the sets of spectral radiance values have to be generated using profiles of temperature, humidity and CO_2 that are modified with errors. To run the spectral RTE for each wavenumber for 60 different error plagued profiles for each of the two basic atmospheres in an attempt to produce figures similar to Figures 24-31 requires a large amount of computer time. Instead of taking this route, a less descriptive but much faster approach is used and

outlined below. It is the same technique described at the end of Chapter IV.

Bias and RMS errors are calculated from 50 values. These values come from calculations made at the 5 effective cloud top levels within a 100's range (i.e. 200, 220, 240, 260 and 280 mb) for 10 fractional effective cloud amounts (i.e. 1.0, 0.9, ..., 0.1). The results given are only for the mid-latitude atmosphere although they are also representative of the tropical atmosphere case.

For example, Figure 32 which represents this approach using instrument noise, may be comprared to Figures 24, 25, 28 and 29. Notice that if the lines in Figure 32 are considered trends representing a single overall statistic, with no importance placed on variations between effective cloud top categories, they compare favorably with the trends indicated in Figures 24, 25, 28 and 29. Thus, the trends indicated in Figures 32-37, especially those trends neglecting the two end groupings are taken as representative of a mean value of bias or RMS. Remember that either end effective cloud category shows effects due to boundary conditions. Despite obvious limitations, these trend values are regarded as sufficiently descriptive for this analysis.

Figure 33 shows the bias and RMS of α and p_{wf} associated with a 2°C RMS and 50% water vapor profile uncertainty specified randomly and independently for each 20 mb layer. The distribution of errors is Gaussian with zero mean. Water mixing ratio errors are given as a percent of the correct mixing ratio at any given level. For this particular analysis instrument noise is set to zero.

For each plot in Figure 33 there are two curves. The dashed line represents the error when the specified climatological temperature and

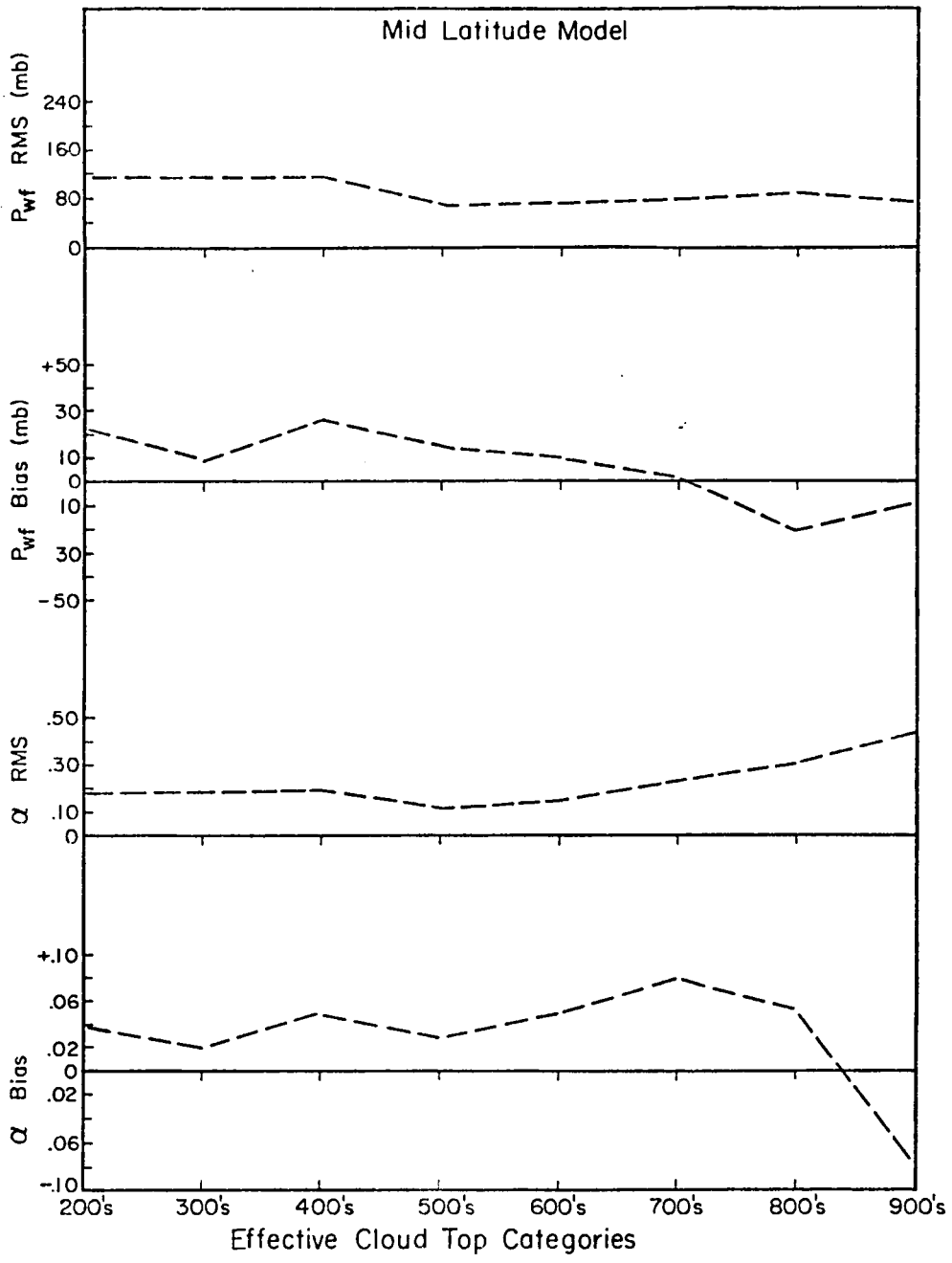

Figure 32. Random sensor error effect on shape parameter retrieval.

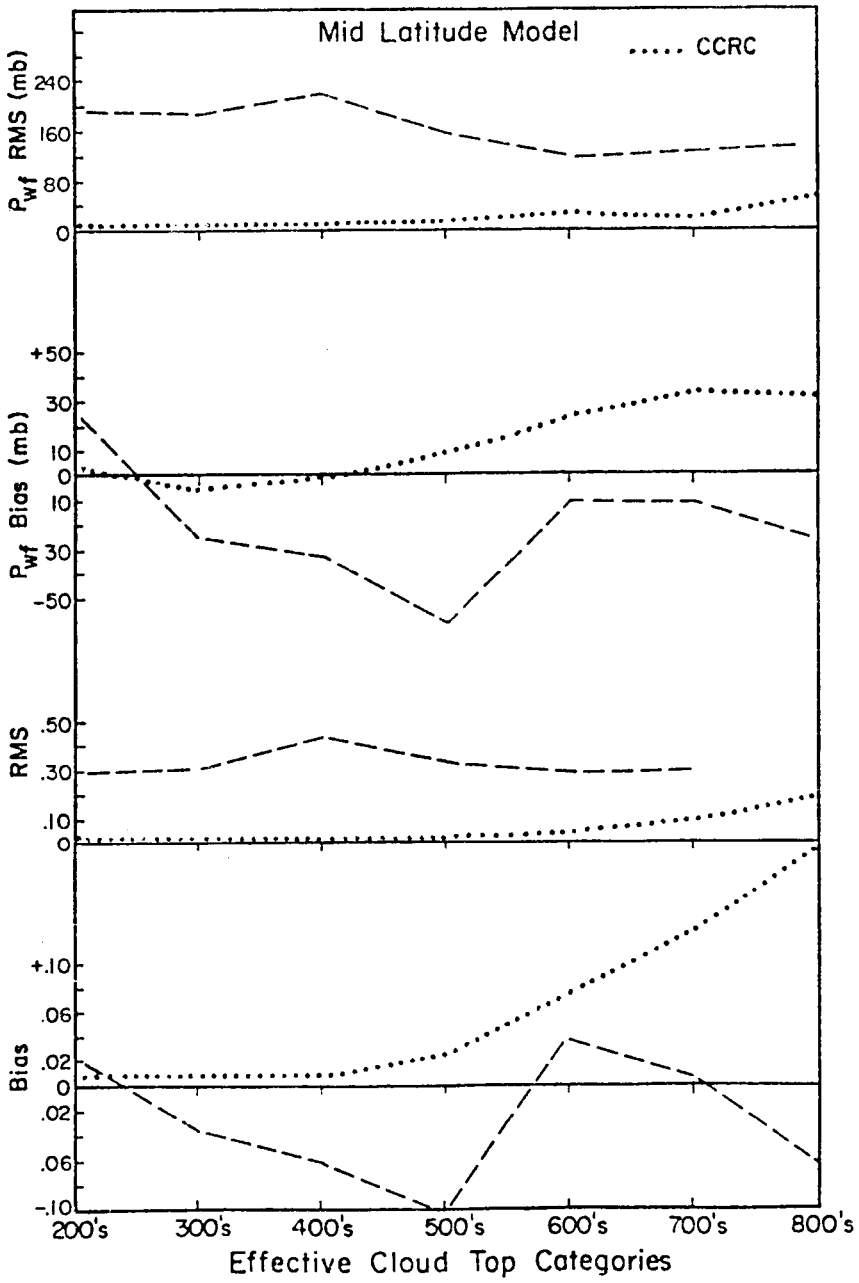

Figure 33. $\pm$ 2° RMS temperature and 50% humidity error effects on shape parameter retrieval.

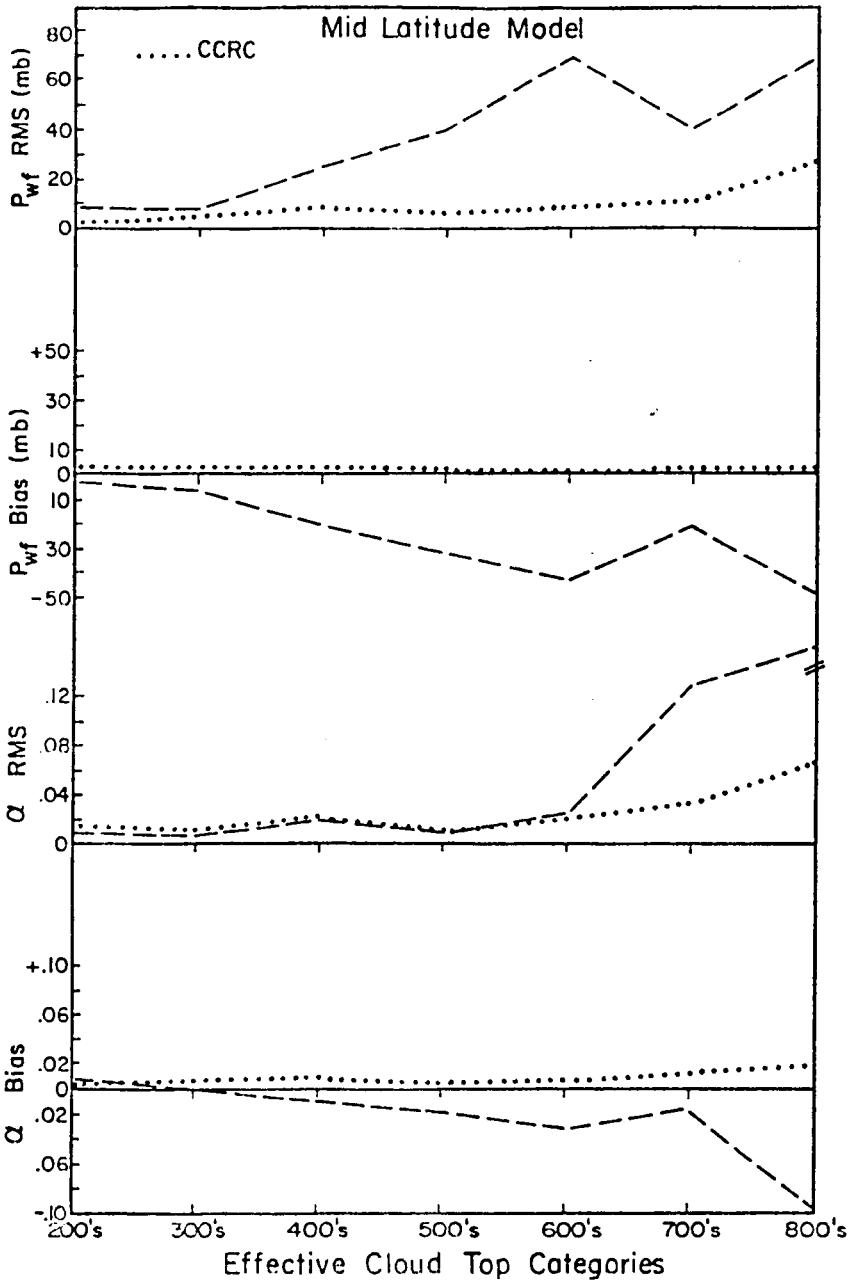

Figure 34. + 1% CO_2 profile error effect on shape parameter retrieval.

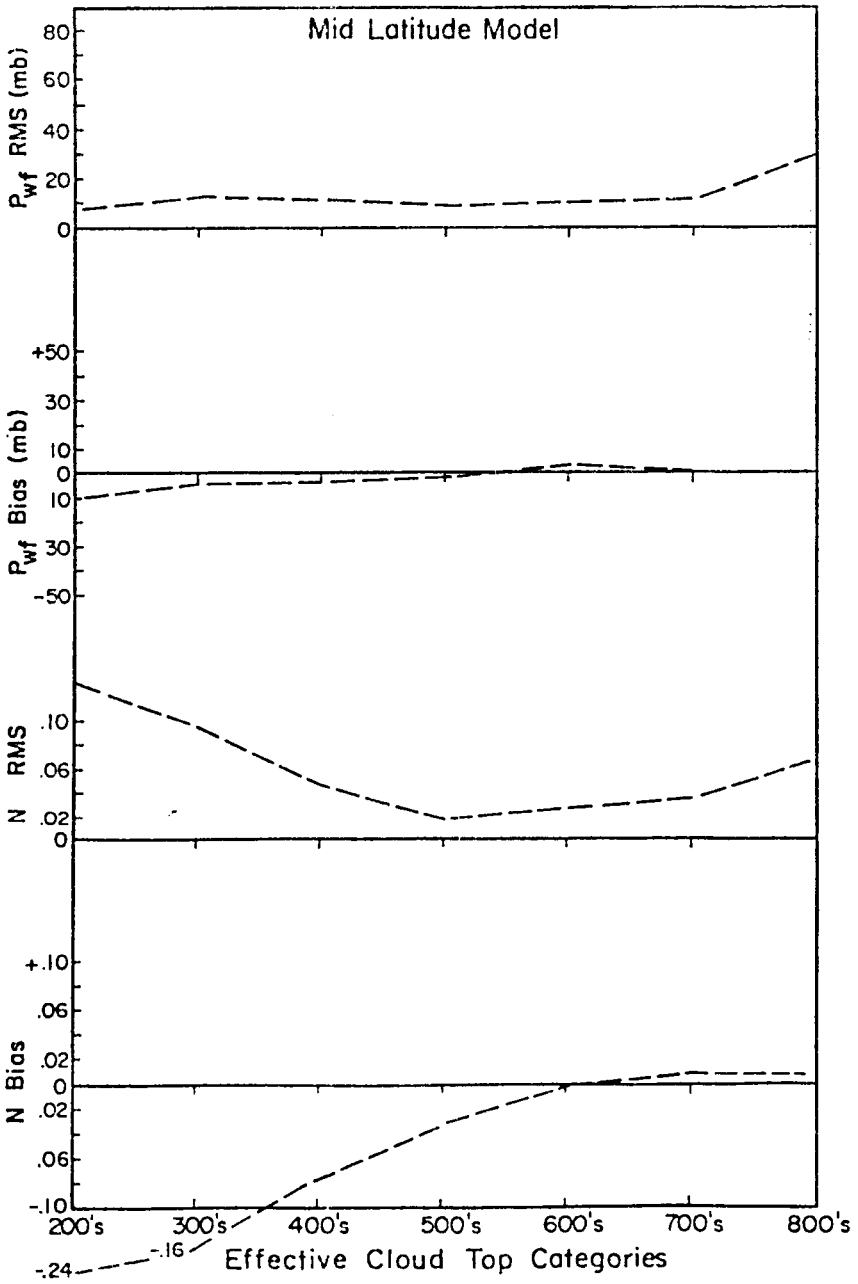

Figure 35. 80 mb cloud thickness error effect on shape parameter retrieval (20 mb vs. 100 mb).

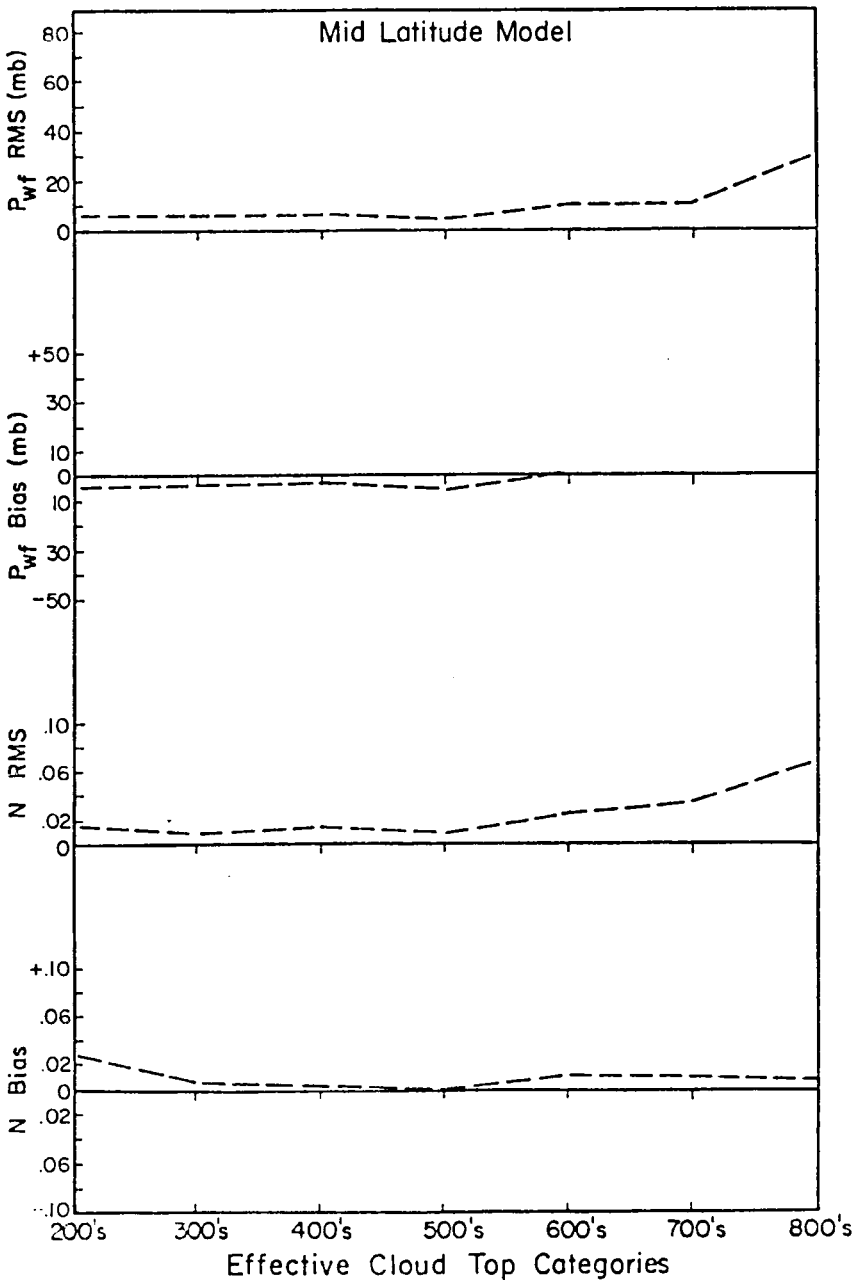

Figure 36. + 50% LWC error effect on shape parameter retrieval.

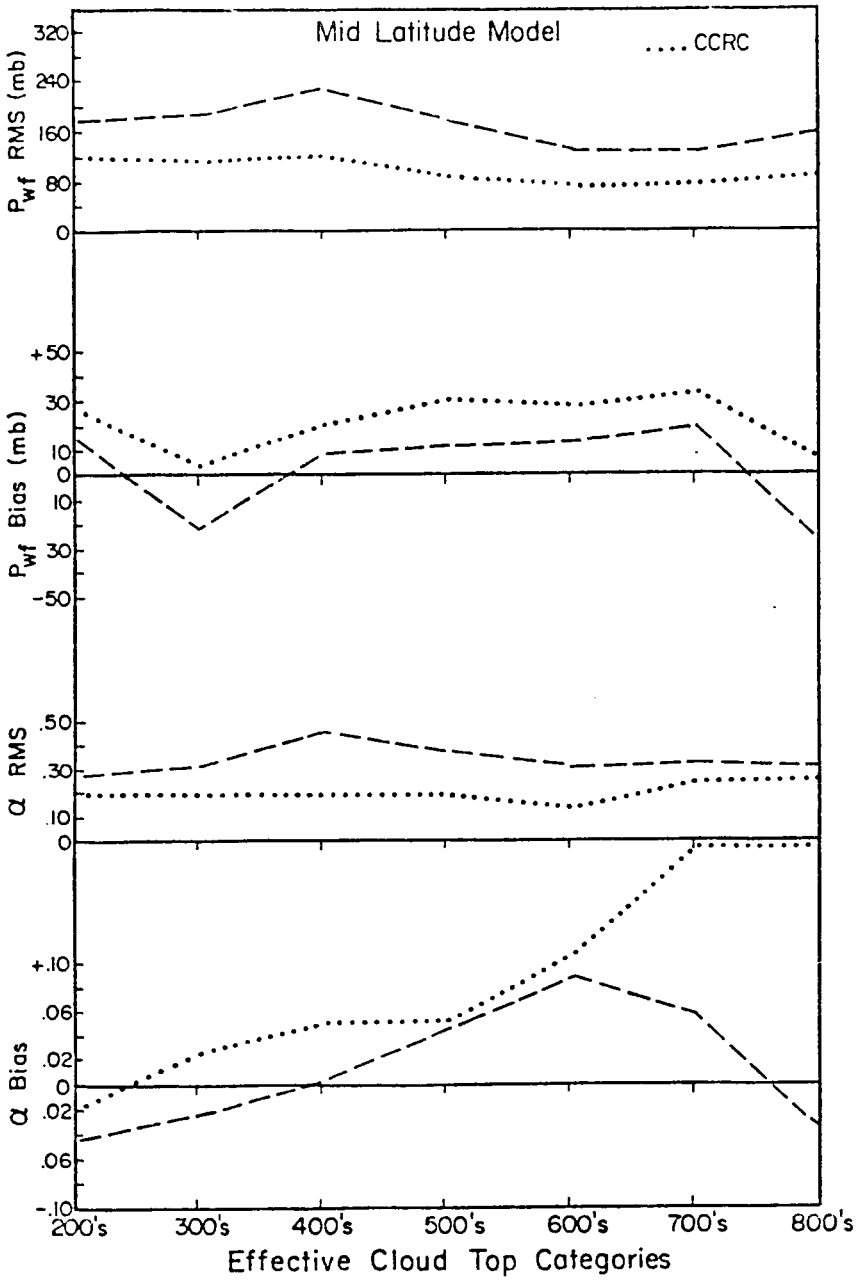

Figure 37. Combined errors effect on shape parameter retrieval.

humidity profile is used. The dotted line represents error analysis when a clear column radiance correction (CCRC) is applied. As can be seen in Figure 33, the application of CCRC, which simply adds one more piece of information ($L_{\nu cs}$), greatly reduces the RMS errors and seems to improve the bias error. The inclusion of the measured $L_{\nu cs}$ information is reasonable since in many cases this information will be available. Even in overcast situations, using the closest $L_{\nu cs}$ measurement should be an improvement over assuming the $L_{\nu cs}$ inferred from the climatological profile is correct.

The CCRC is applied in the following way. Let L_{csc} be the clear sky spectral radiance from a climatological profile. Let L_{csm} be the measured clear sky spectral radiance. Each spectral radiance value used in the retrieval procedure is then multiplied by a factor equal to $(L_{csc} \div L_{csm})_{\nu}$.

Figure 34 gives the RMS bias errors due solely to a + 1% error in the CO_2 profile. The error is not applied randomly but through the whole profile since CO_2 is well mixed in the troposphere. The magnitude represents $\frac{2}{3}$ of the seasonal maximum change in CO_2 observed. Again the CCRC technique eliminates the effect of the error almost entirely. The main effect of the CO_2 error is to change the p_{wf} value from true while α is calculated correctly. When there is more CO_2 than assumed the radiation surface is retrieved higher in the atmosphere that it really is. Notice a change of scale in the RMS plots. Even without the CCRC applied to the CO_2 error the temperature and humidity as well as instrument errors are far more important in terms of RMS error.

C. Effective cloud radiative properties effect

As stated previously, because the empirical RTE retrieval method solves for an α value, theoretically the emittance for the radiating surface being retrieved may be arbitrarily specified. The accuracy of this statement is tested in this section. Errors due to both over and under specifying emittance will be examined by neglecting all other error sources.

Figure 35 shows the effect of assuming effective cloud depths of 100 mb when they are actually 20 mb thick. In other words the emittance is assumed to be much larger than it really is. By comparing Figure 35 to Figures 13 and 14 one can see the RMS and bias errors for p_{wf} are essentially alike. The same is true for α errors which are not plotted. Instead the errors for N are plotted to illustrate that if emittance is assumed too large the N value is simply decreased to give the correct α value ($\alpha = \varepsilon N$). Notice that below 600 mb, 20 mb thick effective clouds behave much like 100 mb thick ones.

Figure 36 gives an analysis of the situation where the emittance is actually greater than specified. This error occurs only at higher levels since emittance below 300 mb is specified at its maximum value. Again N statistics are plotted instead of α statistics. Since emittance is assumed too small at the upper tropospheric levels, the N value calculations are biased positive to give the correct α value. In this case the curves show small variations from those plotted in Figures 13 and 14.

Figure 37 shows the results of combining errors. The errors used are a random 2°C RMS temperature profile error with 50% variation in humidity as explained in Section B. Also included is random

instrument noise as explained in Section A. Furthermore, true cloud depth is allowed to vary randomly from 20 to 180 mb and LWC is allowed to vary randomly from $\pm$ 50% of the specified value.

The consistency of the RMS error from one effective cloud top category to another suggests that the limited sample analyzed gives a typical value of RMS. However, confidence in the bias errors cannot be as high using the consistency argument. It appears that the CCRC procedure reduces the RMS. However, it also seems to add to the bias error. It must be remembered that the error characteristics (level by level independent randomness) used are the severest test of CCRC. For a more trend characteristic error as opposed to random error the CCRC works better as evidenced by the CO_2 values in Figure 34.

In conclusion, this analysis has shown the RMS and bias errors of p_{wf} and α to be of the order of magnitude given in Table 7. These values represent acceptable levels when matched with the approach of using weighting function curves defined by the shape parameters p_{wf} and α as an indication of climatological cloudiness. As pointed out above, a great advantage is gained due to the fact that maximum curve shape parameter errors occur as $p_{wf} \rightarrow 1000$ mb and as $\alpha \rightarrow 0$ and for these values of p_{wf} and α the broadband weighting curve shape remains nearly as it is for the clear sky case.

D. Single p_{wf} level effect

The nature of this error effect, due to errors in the assumption that the satellite sensor is viewing a scene with a single p_{wf} level, requires a different analysis approach. Figure 38 illustrates the effect of two radiating surfaces on the spectral weighting function for

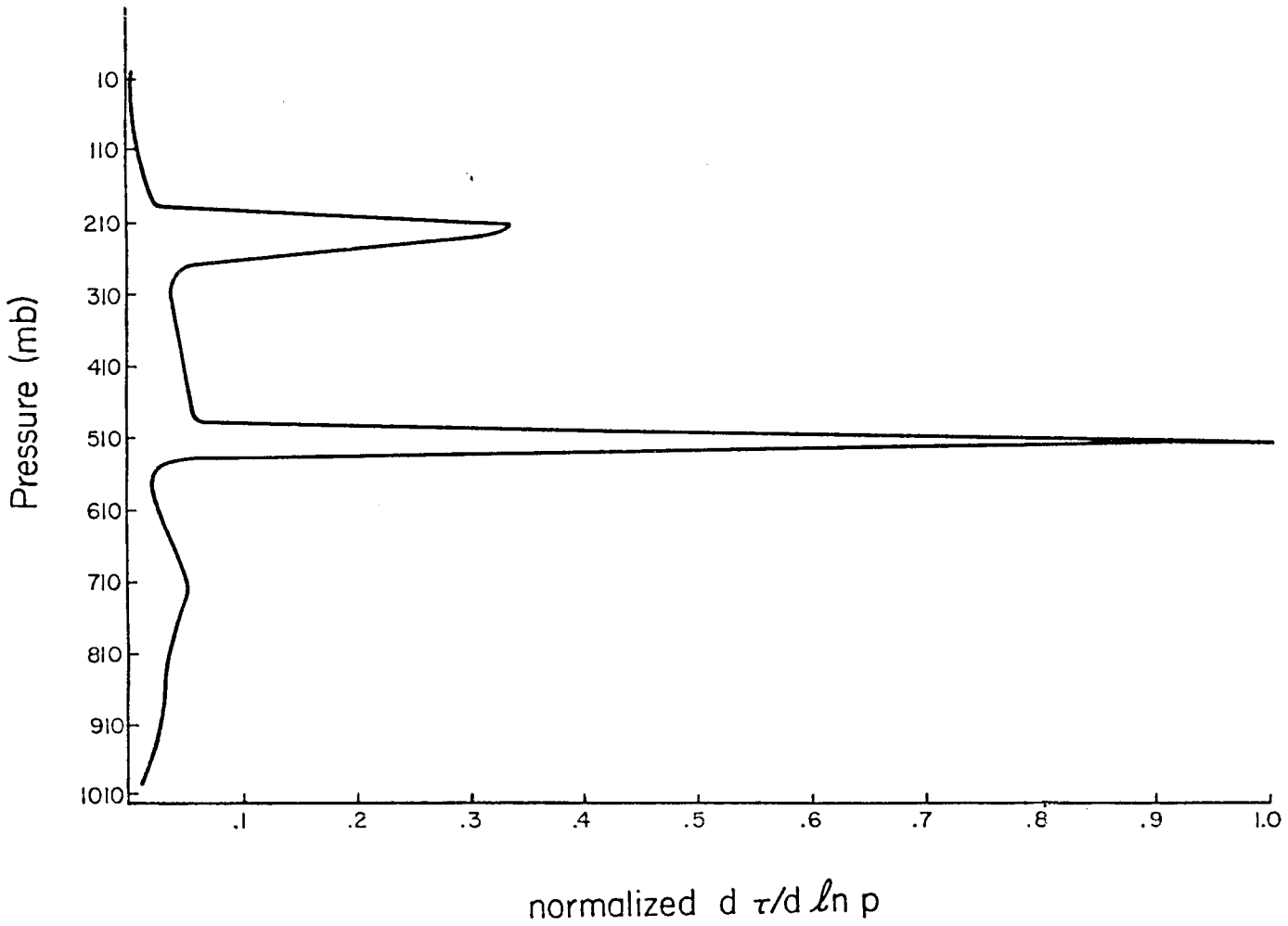

Figure 38. Spectral weighting curve for a case of two separate radiating surfaces in the same scene.

wavenumber 727.5 cm^{-1} using a tropical atmosphere. The values of p_{wf1} and p_{wf2} are 210 and 510 mb respectively. The α values are 0.35 and 0.40 respectively. It is clear that to describe the shape of this weighting function profile takes 4 curve shape parameters. What sort of errors are obtained when the set of spectral radiance values that correspond to these four shape parameters are used in the 2 parameter retrieval program? This problem of two radiating surfaces versus one radiating surface is addressed. To slightly simplify further, α values are restricted to 1.0 for a single specified known scene which when paired translates into a specified known scene that is described by α's of 0.5 and 0.5.

As pointed out in Figure 1 the ultimate objective is to composite broadband weighting curves for purposes of a climate index. Specific scene retrievals are only a secondary consideration. Therefore, the particular source of error described in this section is related to the final composite weighting curve product. To judge error effects, the true versus retrieved composite curves are compared. The composite can be thought of as representing either time or space averages. The experiment most closely resembles a space average.

To do this comparison the following experimental procedure is followed. Assign an effective radiating surface to a simulated spot scene. Do this for many spots ($\sim$ 200 spots) using different p_{wf} values with $\alpha = 1$. There is a set of spectral radiance values for each spot. A composite of curves ($\sim$ 200) described from the spot scenes spectral radiances gives the true weighting curve. Assume the satellite sensor views two scenes at once. In other words, the satellite is assumed to view two effective radiating surfaces instead of one. Thus, each of

the true spot scenes are paired off ($\sim$ 100 pairs). There is a set of spectral radiances for each pair of spot scenes which represent an average of the two separate radiance sets. From this set of spectral radiances, p_{wf} and α values are retrieved and all the resulting weighting curves ($\sim$ 100) are composited to give the retrieved composite weighting function curve. This is done for three separate groups of $\sim$ 200 spot values.

Tables 16 and 17 give the effective cloud top distributions in detail for the three groupings. The flat distribution (FLATS) is modeled after 20 day average GATE B-array cloud data (Cox and Griffith, 1978). The other two distributions (BIMOS and 1PK35) are specified to resemble alternate scenarios. BIMOS represents a specified bimodal distribution, while 1PK35 represents a specified one peak distribution at the 200 mb layer. There are 5 levels within each effective cloud top category (i.e. 400, 420, 440, 460 and 480 mb). The spots are paired off as realistically as possible by category. Within each pair the difference between tops vary according to the values at the bottom of Table 8. For example, if 200 and 300 mb category tops are paired off together their tops may differ between 20 and 180 mb; a 280 mb top may be paired with a 300 mb top or a 200 mb top may be paired with a 380 mb top. Once the top categories are chosen, the exact top differences are determined randomly. The exact specified distribution of top difference values is largely dependent on the total distribution of effective cloud tops. Notice that two 120 pair models of the flat distribution are specified in order to judge result sensitivity to differences in pair separation distributions.

Effective Cld. Top Cat. p_{wf}	240 Spot[1] Freq/%	120 Pair[2] Freq/%	120 * Pair[2] Freq/%	230 Spot[1] Freq/%	115 Pair[2] Freq/%	200 Spot[1] Freq/%	100 Pair[2] Freq/%	20-day GATE B-array %	Effective Cld. Top Cat. p_{wf}
100's	20/8	11/9	10/8	10/4	4/3	10/5	3/3	8	100's
200's	29/12	17/14	18/15	20/9	17/15	25/12.5	19/19	11	200's
300's	32/13	18/15	19/16	60/26	30/26	75/37.5	38/38	11	300's
400's	26/11	12/10	14/12	20/9	13/11	30/15	14/14	13	400's
500's	26/11	11/9	15/13	10/4	9/8	20/10	12/12	13	500's
600's	23/10	15/13	12/10	10/4	3/3	10/5	3/3	13	600's
700's	28/12	14/12	10/8	20/9	8/7	10/5	4/4	11	700's
800's	25/10	23/19	21/18	60/26	29/25	10/5	5/5	10	800's
900's	31/13	0/0	1/1	20/9	2/2	10/5	2/2	10	900's

Table 16. Model effective cloud top distributions by top category.

Paired Cloud Tops Within	120 Pair Model[1] Freq.	%	120 * Pair Model[1] Freq.	%	115 Pair Model[1] Freq.	%	100 Pair Model[1] Freq.	%
0 - 80 mb	0	0	27	22	47	41	33	33
20 - 180 mb	75	62	42	35	19	17	33	33
120 - 280 mb	34	28	20	17	17	15	23	23
220 - 380 mb	8	7	14	12	12	10	6	6
320 - 480 mb	1	1	11	9	6	5	2	2
420 - 580 mb	2	2	5	4	11	10	2	2
520 - 680 mb	0	0	1	1	3	3	1	1

1. specified values 2. retrieved values

Table 16. Model effective cloud top pair separation distribution.

Effective Cloud Top (mb)		240 Spot Freq.[1]	120 Pair Freq.[2]	120 * Pair Freq.[2]		230 Spot Freq.[1]	115 Pair Freq.[2]		200 Spot Freq.[1]	100 Pair Freq.[2]
100		4	0	0		2	1		2	1
120	(FLAT)	4	0	2	(BIMO)	2	0	(1PK3)	2	0
140		4	0	1		2	0		2	0
160		4	5	3		2	2		2	1
180		4	6	4		2	1		2	1
200		6	5	5		4	2		5	4
220		6	2	3		4	4		5	2
240		5	5	6		4	5		5	4
260		6	5	4		4	3		5	6
280		6	0	0		4	3		5	3
300		6	2	2		12	2		15	2
320		7	4	3		12	7		15	10
340		6	3	4		12	9		15	12
360		7	3	5		12	8		15	12
380		6	6	5		12	4		15	3
400		6	1	1		4	2		6	1
420		5	2	3		4	3		6	2
440		5	3	3		4	3		6	4
460		5	3	2		4	3		6	4
480		5	3	5		4	2		6	3
500		5	3	4		2	2		4	2
520		5	4	3		2	3		4	4
540		5	0	3		2	1		4	1
560		6	2	3		2	1		4	2
580		5	2	2		2	2		4	3

Table 17. (Page 1)

Effective Cloud Top (mb)	240 Spot Freq.[1]	120 Pair Freq.[2]	120 * Pair Freq.[2]	230 Spot Freq.[1]	115 Pair Freq.[2]	200 Spot Freq.[1]	100 Pair Freq.[2]
600	4	3	2	2	0	2	1
620	5	3	3	2	1	2	0
640	5	4	3	2	2	2	2
660	4	2	2	2	0	2	0
680	5	3	2	2	0	2	0
700	5	5	3	4	3	2	2
720	6	1	2	4	3	2	0
740	6	0	1	4	0	1	0
760	5	2	1	4	2	2	2
780	6	6	3	4	0	2	0
800	5	6	5	12	3	2	2
820	5	1	2	12	4	2	1
840	5	5	6	12	10	2	1
860	5	7	3	12	8	2	0
880	5	4	5	12	4	2	1
900	7	0	1	4	2	2	2
920	6	0	0	4	0	2	0
940	6	0	0	4	0	2	0
960	6	0	0	4	0	2	0
980	6	0	0	4	0	2	0

1. specified values

2. retrieved values

Table 17. Model effective cloud top distribution.

Because one would not expect each and every set of satellite radiance values to be influenced by a scene with two different radiating surfaces, this test set up may be extreme. On the other hand, occassional scenes with more than two radiating surfaces may be viewed. Overall one may consider this test of the single representative p_{wf} value error to be not quite a worse case situation.

Tables 16 and 17 give the effective cloud top retrieved distributions. Table 18 shows that kind of single p_{wf} and α values the retrieval program calculates from sets of spectral radiances containing the effects of two p_{wf} and α values. In most cases the results seem to provide a fortuitous average type value. Figure 39 gives a more informative summary of this process. Plot A shows the three effective cloud top distributions. Plot B compares the specified top distribution (240 spots) against the retrieved top distribution (120 pairs). Notice that the retrieved top distribution fails to match the specified one in the lower troposphere. This fault is minimized by considering that effective clouds at that level have little influence on the overall broadband weighting function. Notice that both pair models show the same general results. Plots C and D also show favorable comparison between the distribution of specified effective cloud tops and the retrieved ones.

Figures 40-42 show the broadband weighting curve composites for the three effective cloud top distributions. Specified (i.e. 240 spot) curves are compared to retrieved (i.e. 120 pair) curves. In Figure 40 the 120 pair model weighting cuve is not plotted in order to make visual comparison between the two plotted curves easier. All three figures show only minor differences between the specified and retrieved

Effective Cloud Top Pairings	Retrieved Cloud Top	LWC	Retrieved Fraction	Effective Cloud Top Pairings	Retrieved Cloud Top	LWC	Retrieved Fraction
380 - 340	360	.075	1.0	820 - 860	840	1.0	1.0
300 - 340	320	.055	1.0	800 - 840	820	1.0	1.0
360 - 340	340	.064	1.0	200 - 220	220	.025	1.0
380 - 320	340	.064	1.0	240 - 260	240	.029	1.0
380 - 380	360	.075	.96	200 - 220	240	.029	1.0
360 - 360	360	.075	1.0	400 - 480	440	.124	1.0
380 - 380	340	.064	1.0	460 - 440	440	.124	1.0
340 - 320	340	.064	1.0	420 - 480	440	.124	1.0
360 - 300	320	.055	1.0	700 - 780	720	.628	.92
320 - 300	320	.055	1.0	760 - 740	760	.792	1.0
360 - 320	340	.064	1.0	720 - 760	720	.628	.94
320 - 320	320	.055	1.0	940 - 960	900	1.0	.44
300 - 340	320	.055	1.0	980 - 920	900	1.0	.44
360 - 340	340	.064	1.0	900 - 900	880	1.0	.82
300 - 380	340	.064	1.0	100 - 120	100	.010	.90
880 - 860	880	1.0	1.0	540 - 500	520	.197	1.0
880 - 840	860	1.0	1.0	640 - 620	640	.395	1.0
880 - 820	860	1.0	1.0	340 - 240	280	.040	.96
820 - 860	840	1.0	1.0	380 - 280	320	.055	1.0
860 - 860	860	1.0	1.0	300 - 260	280	.040	1.0
880 - 840	860	1.0	1.0	320 - 200	260	.034	1.0
820 - 800	820	1.0	1.0	360 - 260	300	.047	1.0
800 - 880	840	1.0	1.0	360 - 240	280	.040	.92
840 - 860	860	1.0	1.0	380 - 400	380	.087	.98
800 - 860	840	1.0	1.0	380 - 460	360	.075	.92
840 - 840	840	1.0	1.0	340 - 420	360	.075	.94
820 - 840	840	1.0	1.0	820 - 700	720	.628	.84
880 - 800	840	1.0	1.0	800 - 720	760	.792	1.0
800 - 820	820	1.0	1.0	860 - 740	800	1.0	1.0
800 - 880	840	1.0	1.0	800 - 960	840	1.0	.78

Table 18. (Page 1.)

Effective Cloud Top Pairings	Retrieved Effective Cloud Top	LWC	Retrieved Fraction	Effective Cloud Top Pairings	Retrieved Cloud Top	LWC	Retrieved Fraction
880 - 920	880	1.0	.80	400 - 720	500	.175	.88
840 - 980	860	1.0	.66	440 - 780	540	.221	.84
820 - 940	860	1.0	.86	420 - 700	520	.197	.92
860 - 900	880	1.0	.94	480 - 720	580	.279	.94
800 - 980	840	1.0	.70	920 - 640	700	.559	.84
820 - 940	860	1.0	.86	540 - 220	260	.034	.68
300 - 520	380	.087	.90	480 - 160	200	.021	.74
380 - 580	460	.139	1.0	800 - 420	520	.197	.80
340 - 560	420	.110	.96	820 - 400	480	.156	.74
320 - 160	220	.025	.98	300 - 780	340	.064	.58
300 - 180	240	.029	1.0	340 - 760	420	.110	.72
360 - 140	200	.021	.88	520 - 960	560	.248	.62
320 - 100	160	.016	.86	580 - 180	220	.025	.64
340 - 120	180	.018	.88	860 - 360	400	.100	.62
880 - 600	640	.395	.68	800 - 380	460	.139	.74
840 - 660	700	.559	.92	820 - 320	360	.075	.60
880 - 680	700	.559	.78	840 - 340	380	.087	.62
440 - 200	240	.029	.80	880 - 300	320	.055	.54
480 - 280	360	.075	.92	860 - 320	360	.075	.58
460 - 260	340	.064	.94	840 - 360	420	.110	.64
920 - 740	800	1.0	.82	900 - 440	500	.175	.66
960 - 780	820	1.0	.76	700 - 240	260	.034	.56
980 - 760	800	1.0	.64	740 - 280	300	.047	.58
380 - 600	480	.156	1.0	680 - 140	160	.016	.54
360 - 660	460	.139	.90	940 - 380	400	.100	.54
300 - 620	380	.087	.82	820 - 200	220	.025	.56
860 - 560	620	.352	.74	880 - 220	240	.029	.56
840 - 500	580	.279	.78				

Table 18. Satellite Spot to Pair Value Conversion Example.

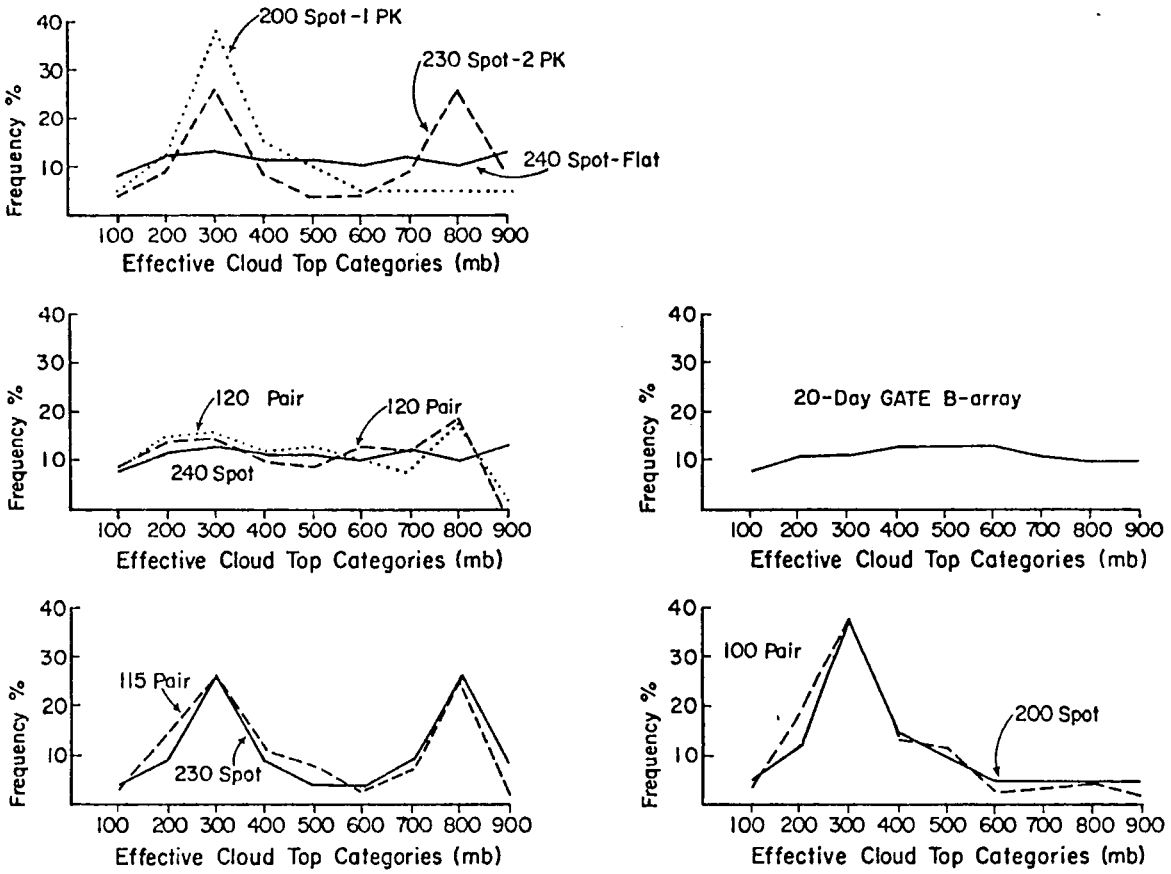

Figure 39. Plots showing comparison between specified effective cloud top distributions and the respective retrieved distributions.

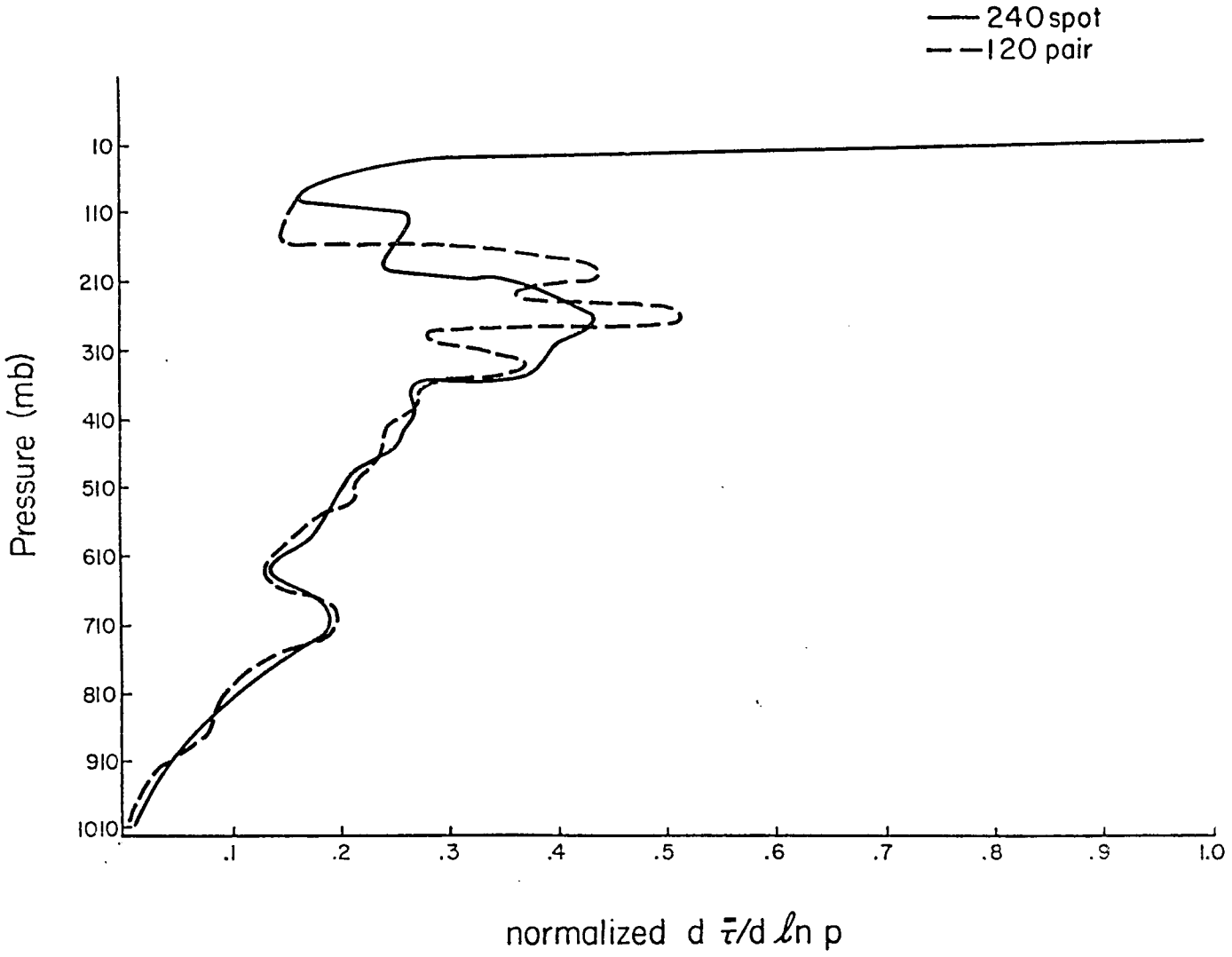

Figure 40. Broadband weighting curves for specified and retrieved flat effective cloud top distribution.

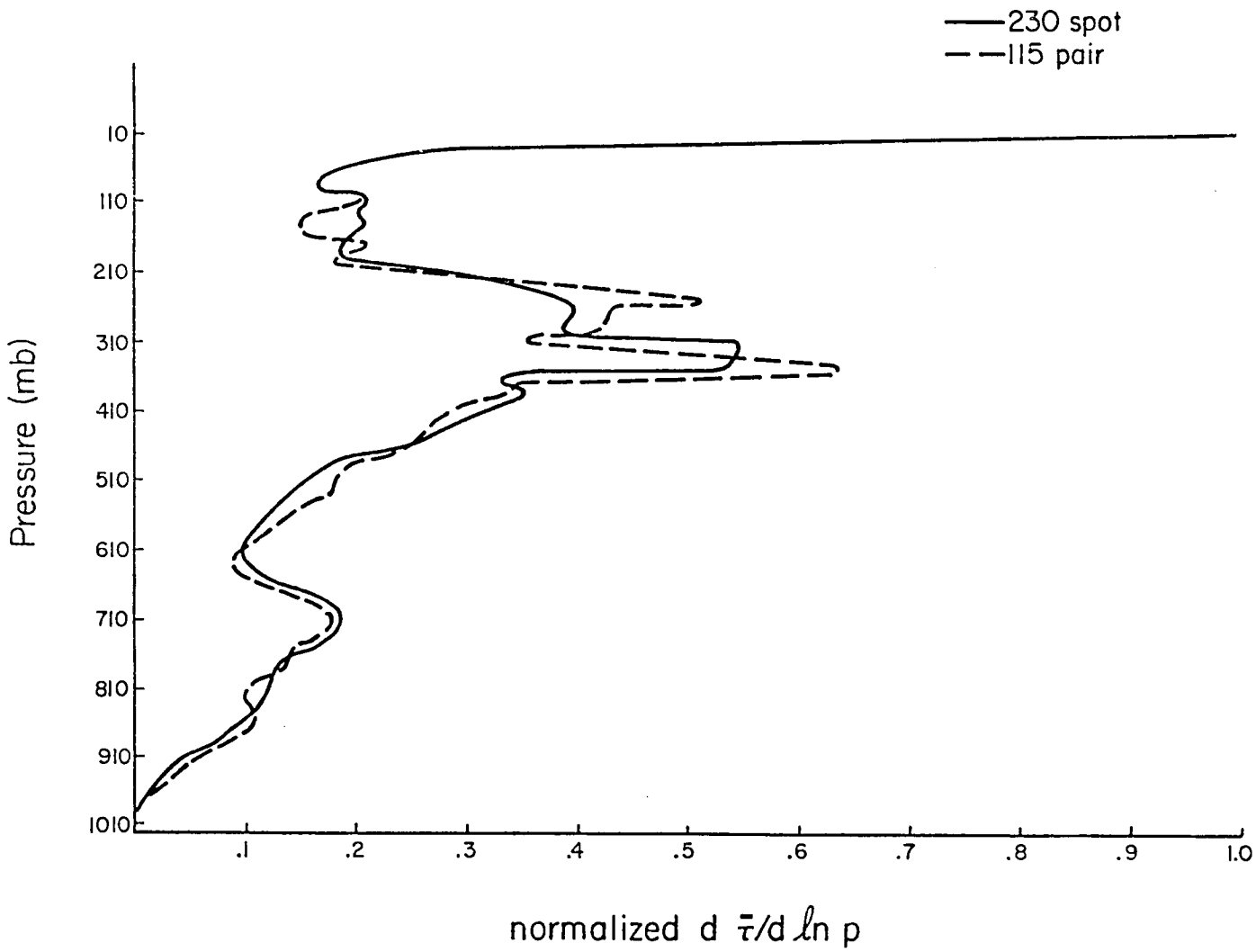

Figure 41. Broadband weighting curves for specified and retrieved two peaked effective cloud top distribution.

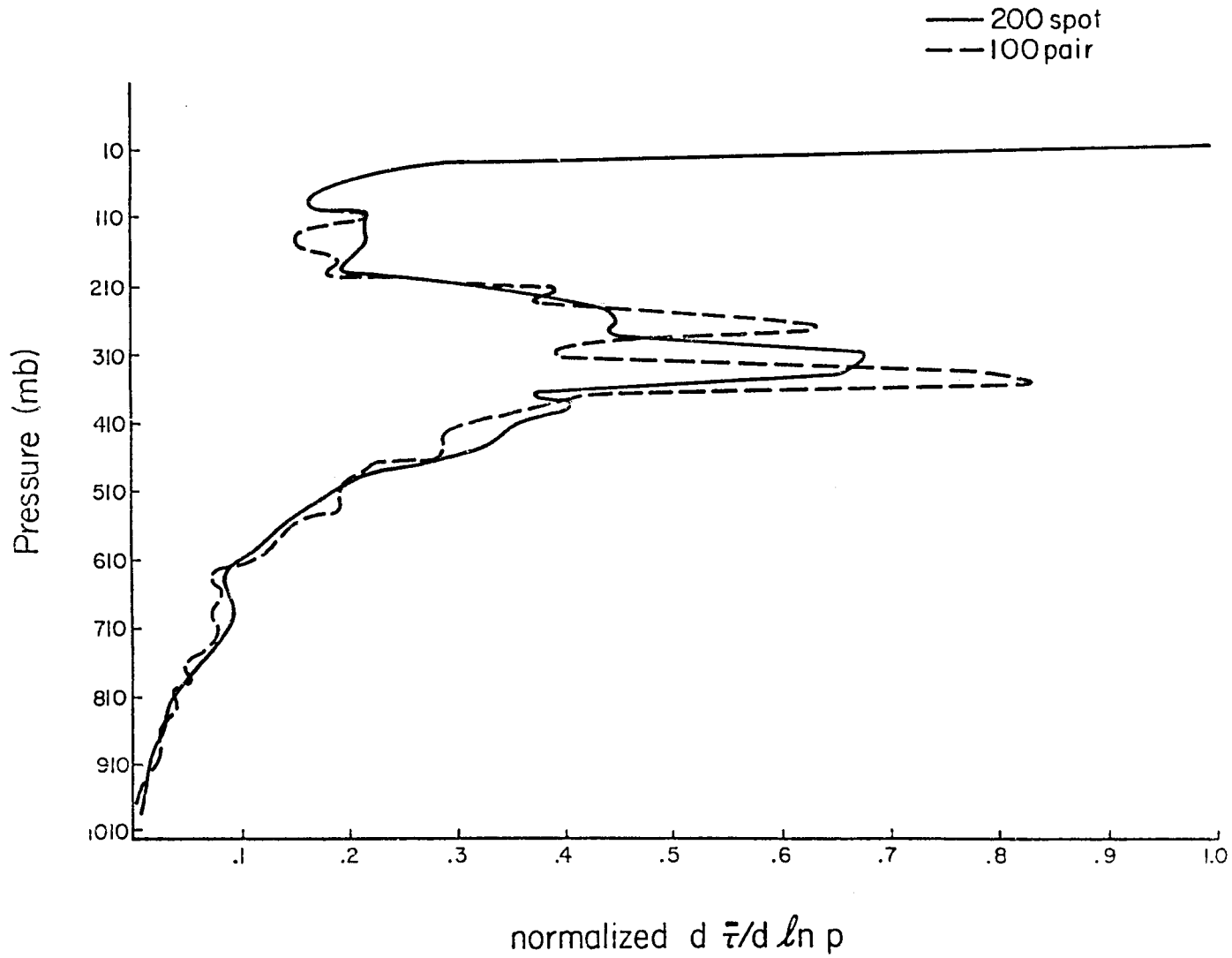

Figure 42. Broadband weighting curves for specified and retrieved one peak effective cloud top distribution.

curves. Notice that errors associated with u-per tropospheric radiating surface retrievals are the greatest. Figure 41 allows direct comparison between high and low atmospheric radiating surfaces and their effect on the weighting curve. Consequently Figure 42, which is the upper tropospheric single peak distribution plot, is taken to represent the severest test case. If retrieval errors are acceptable for this case, then one would expect them to be acceptable for nearly all other effective cloud top distributions.

Table 8 gives the results of a statistical analysis of the differences between the plotted curves in Figures 40-42. The statistical test is fully explained in Chapter VI. The values in Table 8 indicate that for all cases including the so-called worse case there is a high probability that the specified versus retrieved curves are not different.

From this experiment it appears that the assumption of one representative p_{wf} level in the radiometer field of view leads to only small errors when considered for the case of compositing weighting function curves. Of course for the single retrieval case, calculating a single set of p_{wf} and α values can lead to a retrieved weighting curve that is much different from the true one. There may be a question of the representativeness of the effective cloud top distributions specified. Figure 16 gives distribution plots of window radiances which for the most part relate directly to the cloud top distribution. Each plot represents over 900 measurements from a 200 x 200 km section for a specific time from a geostationary satellite. Notice the large number of 1 peak distributions. Although errors in this window radiance data analysis tend to broaden the peaks, they are still quite steep peaks.

It appears from an examination of Figure 16 that the experimental distributions specified above represent nearly a worse case consideration. In other words, steep peaked distributions imply that the assumption of a single radiating surface is for many cases nearly true. The tests above address the problem of the assumption always being false.

E. Minimizing the errors

Throughout this Appendix different techniques have been used to minimize retrieval weighting function errors (sometimes in the form of p_{wf} and α) due to the shortcomings of the basic approach assumptions. These methods include using a clear column radiance correction (CCRC) and stressing the use of composite weighting curves instead of single scene retrievals. The treatment of boundary conditions explained in the Chapter V introduction may also be viewed as a device to limit retrieval errors.

It is also important to view the general approach of using weighting function curves as a major way of minimizing errors. Used as a representation of the atmosphere's vertical infrared radiative emitting structure (VIRES), the composite broadband weighting curves are a measure of climatological cloudiness that is most complimentary to the satellite radiative measurements. As a result, the conditions under which the retrieval of weighting function curve shape parameters is weakest is exactly the condition under which the error effect is least. An advantage important to the approach of averaging over time is the ability to use this retrieval technique day or night with equal reliability.

Finally, to minimize errors further one uses the best information possible. This includes using retrieved clear sky radiance values. A disadvantage of this technique is that to use retrieved temperatures and humidity profiles would mean solving for the C and D values again. Of course sets of C and D values for different scenarios could be pre-calculated. Then the set corresponding closest to the measured profiles could be used. However, for most applications simple season values of C and D for specific areas should be sufficient when used with CCRC.

In summary, this Appendix examined the errors associated with retrieval of the weighting curve shape parameters or with the weighting curve composites. As indicated by Tables 7 and 8 the empirical RTE technique gives results that in the mean represent small errors. Of course only a sample of reasonable simulated error source values are used in the analysis. Nevertheless, the results indicate that the empirical RTE retrieval technique gives usefully accurate results.

BIBLIOGRAPHIC DATA SHEET	1. Report No. CSU - ATS - 335	2.	3. Recipient's Accession No.
4. Title and Subtitle: A climate index derived from satellite measured spectral infrared radiation			5. Report Date
			6.
7. Author(s): Michael D. Abel and Stephen K. Cox			8. Performing Organization Rept. No.
9. Performing Organization Name and Address: Department of Atmospheric Science, Colorado State University, Fort Collins, Colorado 80523			10. Project/Task/Work Unit No. 11. Contract/Grant No. NSG 5357
12. Sponsoring Organization Name and Address: National Aeronautics and Space Administration			13. Type of Report & Period Covered
			14.

15. Supplementary Notes

16. Abstracts

This paper introduces a climate index based on radiative transfer theory and derived from the spectral radiances typically used to retrieve temperature profiles. This index is based upon the shape and relative magnitude of the broadband weighting function. This paper describes the retrieval procedure and investigates error sensitivities of the method.

Results indicate that this index approach is a very effective use of satellite radiance measurements. Retrieval advantages include the following: day and night capability; no a priori cloud radiative property assumptions; retrieval is valid when cloud fraction or cloud emittance is less than unity; minimal geometric assumptions; and minimal influence by undefined low tropospheric emitters.

17. Key Words and Document Analysis. 17a. Descriptors

Climate

Climate monitoring

a) Infrared weighting curves

17b. Identifiers/Open-Ended Terms

17c. COSATI Field/Group

18. Availability Statement	19. Security Class (This Report) UNCLASSIFIED	21. No. of Pages 143
	20. Security Class (This Page) UNCLASSIFIED	22. Price

FORM NTIS-35 (Rev. 3-72)